Carnot 2024 Liège, BE

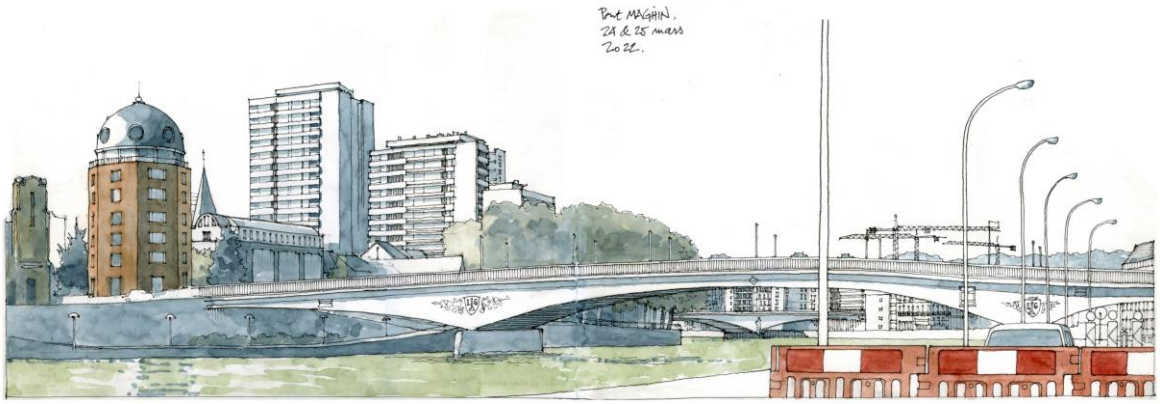
Belgian Symposium of Thermodynamics

16-18 December 2024

University of Liège

Laboratory of Applied Thermodynamics

www.carnot2024.uliege.be



Edited by Alanis Zeoli and Vincent Lemort

2024 Carnot Liège, BE

Proceedings of the 1st Belgian Symposium of Thermodynamics

LIÈGE université

LABORATOIRE DE THERMO DYNAMIQUE UNIVERSITE DE LIEGE

Liège, Belgium, 16-18 December 2024

Although every precaution has been taken to verify the accuracy of the information contained herein, the editors assume no responsibility for any errors or omissions. No liability is assumed for damages that may result from the use of information contained within.

Publication title: Proceedings of the 1st Belgian Symposium of Thermodynamics (Carnot 2024)
Editors: Alanis Zeoli, Vincent Lemort
Series: A&M ULiège Scientific and Technical Publications
Number in series: 1
Electronic publication ISBN: 978-2-9604012-0-2
Liège 2025

Conference information:
Edition name: 1st Symposium of Thermodynamics
Dates: 16-18 December 2024
Location: University of Liège (Belgium)
Organiser: Laboratory of Applied Thermodynamics of the University of Liège

Editors: Alanis Zeoli, Vincent Lemort
Publisher: Aerospace and Mechanical Engineering - ULiège
Year: 2025



License: CC BY-NC-ND 4.0
ISBN: 978-2-9604012-0-2
DOI: 10.5281/zenodo.17964654



Preface

On behalf of the Carnot 2024 Organising Committee, it has been our greatest pleasure to welcome and host you during the 1st Belgian Symposium of Thermodynamics. The Carnot 2024 conference has been organized in Liège and was devoted to the contemporary use of thermodynamics in engineering. In 2024, we celebrated the 200-year anniversary of the publication of Sadi Carnot's Reflections on the Motive Power of Fire and on Machines Fitted to Develop that Power (*"Réflexions sur la puissance motrice du feu et sur les machines propres à développer cette puissance"*). This book laid the foundations of the 2nd Law of Thermodynamics. Although it encountered little success at the time of its publication, its content has been brought to light thanks to Clapeyron and Thomson. Subsequently, Clausius introduced entropy, paving the way to the development of modern classical thermodynamics in a form that is still taught today to physicists and engineers. From the examination of machines emerged macroscopic thermodynamics, and it evolved throughout the 20th century into various subfields exploring, among others, microscopic scales and non-equilibrium processes.

Today, Thermodynamics is a discipline that is used and investigated by many scientists and engineers. Its applications are diverse encompassing power production, heating/air-conditioning/refrigeration, biology, climatology, material sciences, etc. 2024 was therefore an opportune moment to bring together thermodynamicists from both Academia and Industry to discover and bridge different fields of thermodynamics and different applications, but also to share ideas, methods and technological developments… and to show how much thermodynamics is a useful and central discipline, possibly combined with others. In the current context of energy transition, we hope that this meeting will help highlight the role of thermodynamics in the design and operation of energy systems from elementary energy conversion devices to large energy systems.

We are very grateful to all the participants from 12 countries who have decided to continuously support the Carnot 2024 conference by submitting and presenting 68 topics. The conference would not have been possible without all the excellent papers contributed by the authors, as well as without the prestigious invited lectures. During the conference, 35 keynote lectures were given, and 68 posters were presented during dedicated poster sessions. Selected papers will be invited to submit an extended version of their paper to a special issue of Applied Thermal Engineering. Finally, we are pleased to present the Proceedings of the 1st Belgian Symposium of Thermodynamics, containing 52 scientific articles and 16 abstracts.

Prof. Vincent LEMORT

Carnot 2024 Chairman

University of Liège, Belgium

Organising Committee

University of Liège, Laboratory of Applied Thermodynamics, Liège, Belgium

Vincent LEMORT, Chair of the Conference
Samuel GENDEBIEN, Conference coordinator
Alanis ZEOLI, Scientific coordinator
Anne SCHEUER, Administrative secretary

Scientific Committee

Alessia ARTECONI, KU Leuven
Ian BELL, NIST
Julien BLONDEAU, Université Libre de Bruxelles
Yacine BRAHAMI, Tecumseh
Francesco CONTINO, UCLouvain
Cristian CUEVAS, Universidad de Concepción
Quentin DANEL, Sarus
Michel DE PAEPE, Ghent University
Ward DE PAEPE, University of Mons
Pierre DEWALLEF, University of Liège
Rémi DICKES, Copeland
Massimiliano ESPOSITO, University of Luxembourg
Pierre GASPARD, Université Libre de Bruxelles
Samuel GENDEBIEN, University of Liège
Lieve HELSEN, KU Leuven
Koen HILLEWAERT, University of Liège
Steven LECOMPTE, Ghent University
Vincent LEMORT, University of Liège
Nele MOELANS, KU Leuven
Sylvain QUOILIN, University of Liège
Pascal STOUFFS, Université de Pau et des Pays de l'Adour
Ivan VERHAERT, University of Antwerp
Sebastian VERHELST, Ghent University

Sponsors


SAFRAN


COPELAND


Armstrong®
EXPERIENCE MATTERS™


BEBLUE


SFT
Société Française de Thermique


fnrs
LA LIBERTÉ DE CHERCHER


Atic
for HVAC professionals

LIST OF CONTRIBUTIONS

Part 1 – Travelling between Macroscopic and Microscopic Thermodynamics

P. Gaspard
From the thermodynamics of irreversible processes to dissipative structures and active matter 2
ID 1
M. Pedroza-torres, R. Rioboo, V. Lemort
On the role of saturation temperature in thermal management through two-phase mechanically pumped loop . . 10
ID 3
S. Deshpande, M. Vergote, B. Janssens, V. Lemort, A. Adriaens
A Julia-based computational package for predicting temperature-dependent specific heat of rocks using chemical composition 20
ID 5
G. Sonnino
Unveiling novel uncertainty relations: The thermodynamic canonical commutation rules at the mesoscopic scale 23
ID 7
J. Snoeck
State-of-the-art in water-steam cycles 28
ID 17
A. Baghernejad, W. De Paepe
Performance improvement of a single-shaft micro gas turbine: The role of water injection in energy and exergy efficiency 38
ID 20
V. Sileghem, W. Suijs, S. Verhelst
Performance scaling of methanol spark ignition engines using a two-zone semi-predictive zero-dimensional thermodynamic model 47
ID 21
A. Hernández, A. Cendoya, A. Serafino, M. Beaughon, V. Lemort
Enhancing fault detection and diagnosis in organic Rankine cycle systems through proper feature selection in machine learning 57
ID 31
A. Zeoli, A. Pacak, S. Gendebien, V. Lemort
Definition of a novel performance indicator for desiccant wheels 67
ID 33
P. Streit, A. P. Weiß, U. Nägele, U. Bauer, P. Liedl
Theoretical modelling and experimental investigation of a revolving vane expander 73
ID 36
J. Van den Berghe, R. Debroeyer, M. Mendez, Y. Bartosiewicz
A one-dimensional model for supersonic ejectors based on the compound flow theory 77
ID 38
J. Jeßberger, F. Kaufmann, K. Lasch, F. Heberle, D. Brüggemann
Development of a scalable reciprocating compressor model 81
ID 39
J. Spale, V. Vodicka, P. Streit, V. Novotny, L. Volfl, M. Kolovratnik
Experimental investigation of a supersonic axial impulse turbine for a biomass-fired ORC CHP system 85
ID 46
V. Thielens, F. Demeyer, W. De Paepe
Experimental investigation of CH4/H2 blends on the emissions of a micro gas turbine setup with enhanced EGR 90
ID 52
B. Alhabeeb, B. Michel, Y. Brahami, R. Revellin
A new approach for determining primary nozzle throat conditions in two-phase ejector. 95
ID 56
Y. Brahami, M. Metral, David Leray
A dimensionless hermetic reciprocating compressor thermal model 96

ID 57
B. Segers, P. Nimmegeers, P. Billen
Statistical entropy as proxy for the energy requirements for biomass valorisation and its relation to the oxidation state of carbon 97
ID 60
C. Moyaert, A. Kovacs, Y. Marien, D. D'Hooge, P. Nimmegeers, P. Billen
A new method for calculating molecular statistical entropy of polymers in view of circularity. 98
ID 68
N. Leclercq, V. Lemort
A mathematical model for the simulation of two-phase compression in thermal disequilibrium 99
ID 70
F. Azhar Masoodi, R. Goyal
A high-fidelity numerical investigation of over-design load acceptance in a Francis turbine 108
ID 72
J. Gilbert de Cauwer, S. Fakhraddinfakhriazar
Building integrated carbon capture 109
ID 76
L. Leon
Numerical modeling of wet and two-phase compression/expansion in piston machines 110

Part 2 – Heating, Ventilation, Air-Conditioning and Refrigeration

ID 2
G. Vaccaro, P. Santoni, A. Milazzo, A. Rocchetti, L. Talluri
Thermodynamic Analysis and Sustainability: Evaluation of Innovative Mixtures for Heat Pump Cycles 112
ID 9
P. Byrne, A. Labihi, E. Mendes, H. Mesbah, A. Meslem
THERMETRENNES Project: thermal geostructure in the Rennes metro for absorption heat pumps and study of a thermo-active concrete experimental model 121
ID 10
Cristian Cuevas, Aitor Cendoya, Matías Pezo, Daniel Sacasas
Atmospheric water harvesting with active refrigeration systems 130
ID 13
W. Rached, N. Karwa, S. Lintu
A novel heat pump cycle design for very cold weather district heating 140
ID 14
A. Salame, V. Lemort, P. Dufour, M. Nadri, R. Ibsaine
Improving performance of a CO2 Thermally Driven Heat Pump Based on a New Optimal High-Pressure Correlation 150
ID 23
M. Hocevar, E. Mujagic, L. Novak
Analysis of heat pump performance in a tumble dryer based on drying air properties 157
ID 28
S. Alexopoulos, P. Schmitz, Z. Mahdi, D. Högemann, G. Panaras
Simulation of a district heating network with integrated high temperature storage system powered by renewable energy 161
ID 30
Elise Neven, Basile Chaudoir, Vincent Lemort
LaboThApPy: Development of an open-source Python library for thermodynamic system modelling and simulation 165
ID 35
X. Van Heule, M. De Paepe, S. Lecompte
Understanding thermodynamic non-equilibrium expansion 169
ID 37
M. Evens, A. Arteconi
Heat pump monitoring through the adoption of digital twins via neural networks 173
ID 41
M. Ametta, L. Branchini, A. De Pascale, L. Ferrari, G. Francesco Frate, A. Ghilardi, C. Poletto, S.Vasta
REHP-4-TUNE: renewable electric high-temperature heat pumps for thermal users in neutral CO_2 environment 177

ID 44
B. Beguin, T. Van Lierop, G. Léonard
Optimal integration of a high-temperature heat pump in a CO2 capture pilot plant 181
ID 49
M. Goderis, W. Beyne, M. De Paepe
Heat transfer during the dominant-convection melting regime in rectangular enclosures heated from the side . 185
ID 50
J. Van Nieuwenhuyse, S. Lecompte, M. De Paepe
Development of a general heat transfer correlation for horizontal flow of supercritical refrigerants under heating conditions 189
ID 53
M. Everaert, J. Maselyne, S. Lecompte
Experimental evaluation of a thermal load simulation model of a livestock farm 194
ID 54
D. Rojas Plana, S. Quoilin
Flexibility assessment of electric water heaters in virtual power plants for optimal load management 195
ID 55
M. Khairallah, A. Zoughaib, P. Havil, M. Frerejacque
A MILP optimization model for the design of a heat pump system with thermal energy storage for district heating application 202
ID 59
L. Verleyen, A. Dell'Isola, L. Helsen
Comparing air-source with ground-source heat pumps in fully integrated, optimally controlled micro energy communities 206
ID 61
M. Santos, J. Mota, B. Almeida, J. Morgado, J. B. Ribeiro
Thermodynamic and economic analysis of a liquid air energy storage system with thermal integration 207
ID 62
J. Raeymackers, E. Vieren, K. Couvreur, M. De Paepe, S. Lecompte
Analysis of a water-ammonia high-temperature heat pump with a liquid-injected twin-screw compressor 208
ID 66
N. Guilbaud, A. Fabre, P. Stabat
Geocooling for summer comfort in European dwellings 214
ID 67
A. Degelin, I. T'Jollyn, M. De Paepe
Models and methodology for the design and control of thermal energy storage in residential district heating systems 219
ID 69
M. Simon, N. Leclercq, S. Quoilin & V. Lemort
Testing an individual electrical water heater for self-consumption and ancillary services to the grid 223
ID 77
Vincent Natalis, Bernard Leyh
What are students' alternative conceptions of entropy and the second law of thermodynamics? 227

Part 3 – Thermodynamics and the Energy Transition

ID 6
P. Yánez-Rosales, B. del Río-Gamero, J. Schallenberg-Rodriguez
Energy transition in maritime transport: Towards climate neutrality 229
ID 8
N. Arakcheeva El Kori, A. M. Blanco-Marigorta, N. Melián-Martel
Exergy efficiency for desalination processes 230
ID 12
M. Petrollese, M. Esmaeili Shayan
Optimizing hybrid off-Grid energy and water systems with Carnot battery technology and model predictive control 239

ID 16
A. Cendoya, F. Ransy, V. Lemort, P. Dewallef
Numerical modelling of a 50 kWe reversible Carnot Battery coupled with waste heat 244
ID 18
B. Guo, V. Lemort
Potential evaluation of Carnot batteries applied for agricultural energy demands (electricity and cooling) in farms: Based on Carnot cycles 255
ID 19
S. Parsa, S. Verhelst
Accurate Estimation of Ignition Delay in Dual-Fuel Marine Engines Using Methanol or Hydrogen 264
ID 25
H.-J. Wiemer, C. L. Niño Avella, T. Schulenberg
Design study of the Monika ORC-turbine and comparison with experimental results 274
ID 27
S. Alexopoulos, P. Schmitz, Z. Mahdi, D. Högemann, G. Panaras
Simulation model for autonomous energy planning for Othonoi island 284
ID 32
R. Tassanoy, M. De Paepe & S. Lecompte
Integrating Carnot batteries in the electrical grid: a matter of understanding system dynamics? 288
ID 34
A. P. Weiß, P. Streit, J. Spale, V. Novotny, M. Kolovratnik
Experimental pre-verification of a 7 kWel/3,000 rpm radial re-entry turbine for small organic Rankine cycle (ORC) plants 293
ID 40
M. Hauglustaine, A. Laterre, B. Berger, F. Contino
Experimental and numerical investigation of a retrofitted Organic Rankine Cycle towards its integration into a Carnot Battery 297
ID 42
F. Witte, N. Kießling, M. Hofmann
Decarbonizing process steam supply – a framework to assess pathways for industry retrofitting 303
ID 47
M. Lubrano Lavadera, A. Coussement, A. Parente
Steam-assisted MILD-POX: A flexible process for the production of hydrogen 309
ID 48
J. Von Zabienski, F. Kaufmann, C. Schifflechner, H. Spliethoff
First experimental insights on a reversible ORC test rig for geothermal CHP applications 313
ID 51
J. Joseph, D. Rehman, M. Delanaye
High temperature recuperator for micro gas turbine 318
ID 58
M. J. Mendoza Morales, J. Blondeau, W. De Paepe
Optimizing a blue hydrogen fuelled gas turbine combine cycle 319
ID 63
A. Cendoya, B. Chaudoir, T. Janod, V. Lemort, T. Hazar, U. Halaçoğlu, S. Colasson
Carnot battery integration in a geothermal power plant: Study case of Zorlu energy 323
ID 64
J. Mota, M. Santos, J. Baranda Ribeiro
Combined trilateral flash cycle and organic flash cycle for low to medium heat source electricity generation . . 333
ID 65
A. Laterre, V. Lemort, F. Contino
Integrated development of cost-effective Carnot batteries using near-optimum analyses 337
ID 71
F. Ransy, V. Lemort
Comparison of three architectures of thermally integrated Carnot batteries using simulation 338
ID 73
M. Roquet, P. Dewallef
Decarbonisation of existing building stock through low low-temperature district heating network 342

ID 74
T. Stegen, J. Castiaux, N. Diffels, M. Duchesne, B. Cornélusse
Stochastic generator for residential load profiles 343
ID 75
N. Kozlowska, J. Jacquemin, A. Lefebvre, P. Dewallef
Rapid design of energy communities: a heat-driven optimization approach. 344

Carnot 2024 Liège, BE

Part I

Travelling between Macroscopic and Microscopic Thermodynamics

FROM THE THERMODYNAMICS OF IRREVERSIBLE PROCESSES TO DISSIPATIVE STRUCTURES AND ACTIVE MATTER

Pierre Gaspard[1]*

[1] Center for Nonlinear Phenomena and Complex Systems, Université Libre de Bruxelles (U.L.B.),

Code Postal 231, Campus Plaine, B-1050 Brussels, Belgium

* *Corresponding Author:* Gaspard.Pierre@ulb.be

Abstract. A historical perspective is presented on thermodynamics from the pioneering contributions by Carnot and Clausius to recent advances on active matter. Non-equilibrium thermodynamics is developing through the identification of the irreversible processes contributing to entropy production in various types of materials and systems. These processes include friction, viscosity, heat and electric conductions, diffusion, reactions, and more. In 1954, Glansdorff and Prigogine formulated a general evolution criterion, which led to the theory of dissipative structures like chemical clocks, reaction-diffusion patterns, and convection patterns. Non-equilibrium statistical mechanics provides the microscopic foundations for the thermodynamics of irreversible processes.

Keywords. First and second laws of thermodynamics, entropy production, transport properties, chemical reactions.

1 Historical introduction

In 1824, Sadi Carnot published his memoir entitled "Réflexions sur la puissance motrice du feu", a study of heat engines, which led to the formulation of the second law of thermodynamics [1]. The historical context was the development of steam engines (external combustion engines) for industry, mining, and transportation by pioneers like Papin, Savery, Newcomen, Cugnot, Watt, Trevithick, and others; the major issue being the conversion of heat into mechanical work. In his memoir, Sadi Carnot also mentioned that heat is the cause of movements in the atmosphere, oceans, and volcanoes, already opening the scope of thermodynamics to the study of natural phenomena. In his reasonings, he used the laws of ideal gases by Mariotte (1676, $p \propto V^{-1}$) and Gay-Lussac (1802, $p \propto T$) to obtain the following theorem: "In all cases where a quantity of heat is transformed into work, and the body effecting this transformation finally returns to its initial state, another quantity of heat must necessarily pass from a warmer to a colder body, and the magnitude of the latter quantity of heat in relation to the former depends only on the temperatures of the two bodies between which it passes, and not on the nature of the body effecting the transformation", as stated by Clausius in 1854. This result led Clausius to shortly formulate the second law of thermodynamics as: "Heat cannot pass by itself from a cold body to a warmer body" [2,3].

Today, we know many more forms of energy than only heat and work:
• Chemical energy: e.g. in internal combustion engines for boats, trains, cars, aircrafts & rockets; or other processes in chemistry & biochemistry;
• Electric energy: e.g. in electrochemical processes, electric batteries, electric engines, thermoelectricity, plasmas & microelectronics;
• Electromagnetic energy: e.g. in electromagnetic waves, light, lasers & harvested by photovoltaic cells;
• Nuclear energy: e.g. in nuclear fusion (the energy source of stars) & nuclear fission;
• Gravitational energy: e.g. in supernovae & black holes.

Again, the major issue is the conversion of energy from one form into another. Nowadays, this issue also concerns the biosciences (biochemistry, biophysics, and molecular biology), surface science (including heterogeneous catalysis), the nano-sciences, and information science. In all these fields, thermodynamics is needed to understand the mechanisms of energy conversion and their efficiencies, given the limits arising from energy conservation and the non-negativity of entropy production.

In the earliest developments of thermodynamics by Carnot, Clausius, and others during the XIXth

century, the first and second laws of thermodynamics were enunciated in a global formulation, defining energy and entropy for an entire system, possibly in contact with other ones (see Sec. 2). Irreversible processes contributing to entropy production were discovered in different kinds of materials and systems (see Sec. 3). Many irreversible processes such as viscosity, heat conduction, or diffusion are intrinsic local properties of fluids and other continuous media, which led to the local formulation of thermodynamics by Natanson [4], Duhem [5], Jaumann [6,7], Lohr [8,9], and others during the period extending from the 1890s to the 1920s. In the 1930s, the contribution of chemical reactions to entropy production was established by De Donder [10]. Furthermore, Onsager proved his famous reciprocal relations on the basis of microreversibility [11, 12]. Afterwards, a great theoretical synthesis was carried out in the early 1940s with the works of Meixner [13], Eckart [14-16], and Bridgman [17]; and after WWII with those of Prigogine [18,19], de Groot [20], de Groot & Mazur [21], Callen [22], and others on the non-equilibrium thermodynamics of fluids, solutions and electrolytes, which are composed of inert or reactive species (see Sec. 4). Later, the theory was extended to the phases of matter with broken continuous symmetries like crystals, liquid crystals, and superfluids [23]. In the 1950s and 1960s, the thermodynamics of open systems exchanging energy, matter, and entropy with their environment knew significant advances, proving that the entropy produced by irreversible processes in the interior of the system can be evacuated to the exterior, possibly reducing the entropy inside the system [19]. In this way, thermodynamics was shown to be compatible with the formation of patterns and oscillations – called dissipative structures – under far-from-equilibrium conditions [24-26]. These conditions require that the non-equilibrium constraints should exceed some threshold in order for dissipative structures to emerge, which is in relation to the general evolution criterion of Glansdorff & Prigogine [27,28], as briefly explained in Sec. 5. Since then, many spatiotemporal dissipative structures have been discovered and characterized in physics, chemistry, the biosciences, the geosciences, and astronomy.

Recently, research has focused on active matter, which is made of self-propelled particles or other agents locally converting energy into mechanical motion [29-31]. Active matter therefore operates out of equilibrium and its non-equilibrium thermodynamics has become a major topic of interest [32-38], as shortly presented in Sec. 6.

In parallel with these developments, much effort has been devoted to establishing the microscopic foundations of thermodynamics, which is summarized in Sec. 7. Conclusion and perspectives are given in Sec. 8.

2 The laws of thermodynamics

2.1 Global formulation

In the earliest formulations of thermodynamics, the state variables are defined globally for an entire system, which is possibly open exchanging energy and matter with its environment (see Figure 1). Every state variable X can change in time due to exchanges $d_{\mathrm{e}}X$ with the exterior of the system (i.e., its environment) and due to processes taking place in the interior of the system $d_{\mathrm{i}}X$. Therefore, the differential of the state variable can be written as $dX = d_{\mathrm{e}}X + d_{\mathrm{i}}X$ [18,19]. If the state variable obeys a conservation law, the internal contribution is equal to zero, $d_{\mathrm{i}}X = 0$, and $dX = d_{\mathrm{e}}X$.

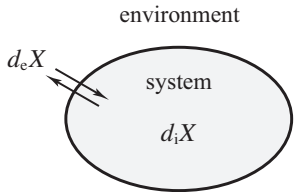


Figure 1: Schematic representation of an open system in contact with its environment. $d_{\mathrm{e}}X$ is the contribution of exchanges and $d_{\mathrm{i}}X$ is the internal contribution to the differential dX of some state variable X.

The first law is the conservation of energy, which can thus be expressed as

$$dE = d_{\mathrm{e}}E + d_{\mathrm{i}}E \quad \text{with} \quad d_{\mathrm{i}}E = 0\,. \tag{1}$$

Similar expressions hold for the conservation of mass and linear momentum. All these conservation laws are justified on the basis of classical or quantum mechanics, which rules the motion of the microscopic particles composing matter.

The second law concerns the entropy, so-called by Clausius in reference to "internal transformation" (εντροπη in Greek) and denoted S [3,39]. In general, the entropy is not conserved, its internal production being always non-negative:

$$dS = d_{\mathrm{e}}S + d_{\mathrm{i}}S \quad \text{with} \quad d_{\mathrm{i}}S \geq 0\,. \tag{2}$$

We have that $d_{\mathrm{i}}S = 0$ for reversible transformations, e.g., at equilibrium; and $d_{\mathrm{i}}S > 0$ for irreversible transformations, i.e., out of equilibrium.

The integration of Eq. (2) over a noncyclic process $S_0 \to S$ gives $\int dS = S - S_0$. On the basis of Carnot's study, Clausius showed that the integral of entropy exchange can be expressed as $\int d_\mathrm{e}S = \int dQ/T$ in terms of the heat dQ exchanged with the environment and the temperature T of the system. Moreover, Clausius introduced the concept of "uncompensated transformation" $N \equiv \int d_\mathrm{i}S$ postulating its non-negativity $N \geq 0$, which is the statement of the second law, and mentioning friction as contributing to $N > 0$. Accordingly, Clausius obtained the formula

$$N = S - S_0 - \int \frac{dQ}{T} \geq 0\,, \tag{3}$$

which is equivalent to $\int d_\mathrm{i}S = \int dS - \int d_\mathrm{e}S \geq 0$, given by integrating Eq. (2) [3,39].

Later, De Donder used the concept of "uncompensated heat", defined as $dQ^\mathrm{n} \equiv T d_\mathrm{i}S \geq 0$ [10].

2.2 Local formulation

In continuous media, the quantities of interest are fields locally defined in every point of the system such as the densities $x(\mathbf{r}, t)$. In this regard, the corresponding global state variable is obtained by integrating the density over the volume of the system according to $X(t) \equiv \int_V x(\mathbf{r}, t)\, d\mathbf{r}$. In general, some density obeys a local balance equation of the following form:

$$\partial_t x + \operatorname{div} \boldsymbol{j}_x = \sigma_x\,, \tag{4}$$

where $\boldsymbol{j}_x$ is the current density or flux and σ_x the production rate density that are associated with the density x. Integrating the balance equation (4) over the volume V of the system and using the divergence theorem, the balance equation of the global formulation is recovered as

$$\frac{dX}{dt} = \frac{d_\mathrm{e}X}{dt} + \frac{d_\mathrm{i}X}{dt} \quad \text{with} \quad \frac{dX}{dt} = \int_V \partial_t x\, d\mathbf{r}\,,$$

$$\frac{d_\mathrm{e}X}{dt} = -\int_{\partial V} \boldsymbol{j}_x \cdot d\boldsymbol{\Sigma} \;\text{ and }\; \frac{d_\mathrm{i}X}{dt} = \int_V \sigma_x\, d\mathbf{r}\,, \tag{5}$$

$d\boldsymbol{\Sigma}$ denoting an element of surface area of the boundary between the system and its environment. In this regard, boundary conditions should be defined, which possibly take into account the non-equilibrium constraints imposed to the system by its environment.

In the local formulation, the first law is the local conservation of energy expressed as

$$\partial_t \varepsilon + \operatorname{div} \boldsymbol{j}_\varepsilon = \sigma_\varepsilon \quad \text{with} \quad \sigma_\varepsilon = 0\,, \tag{6}$$

where ε is the energy density such that the total energy of the system is given by $E = \int_V \varepsilon\, d\mathbf{r}$. Since $\sigma_\varepsilon = 0$, integrating Eq. (6) leads to $d_\mathrm{i}E/dt = 0$ in consistency with the global formulation (1) of the first law. Similar local conservation equations hold for other conserved quantities such as mass and linear momentum.

Next, the second law is expressed by the following local balance equation for entropy:

$$\partial_t s + \operatorname{div} \boldsymbol{j}_s = \sigma_s \quad \text{with} \quad \sigma_s \geq 0\,, \tag{7}$$

where s is the entropy density such that $S = \int_V s\, d\mathbf{r}$ and implying that $d_\mathrm{i}S/dt \geq 0$ in agreement with the global formulation (2) of the second law.

In this way, the first and second laws of thermodynamics can be formulated in continuous media like fluids or solutions.

3 Irreversible processes

3.1 Discoveries of irreversible processes

Since the XIXth century, many irreversible processes contributing to entropy production were discovered either in bulk phases like fluids and solids, or at interfaces between two bulk phases:

- Shear & dilatational viscous pressures (Navier 1822, Lamb 1879):
  $\boldsymbol{\Pi} = -\eta\left(\boldsymbol{\nabla}\mathbf{v} + \boldsymbol{\nabla}\mathbf{v}^\mathrm{T} - \frac{2}{3}\boldsymbol{\nabla}\cdot\mathbf{v}\,\mathbf{1}\right) - \zeta\,\boldsymbol{\nabla}\cdot\mathbf{v}\,\mathbf{1}$;
- Heat conduction: Fourier's law (1822):
  $\boldsymbol{J}_q = -\kappa\boldsymbol{\nabla}T$;
- Diffusion: Fick's law (1855): $\boldsymbol{J}_k = -D_k\boldsymbol{\nabla}n_k$;
- Thermodiffusion (Ludwig 1856, Dufour 1873, Soret 1879);
- Electric conduction: Ohm's law (1827):
  $\boldsymbol{J}_\mathrm{e} = \boldsymbol{\sigma}\cdot\boldsymbol{E}$; $V = RI$.
- Thermoelectricity (Seebeck 1821, Peltier 1834, Thomson 1851);
- Chemical reactions (De Donder 1932);
- Interfacial solid-solid friction (mentioned by Clausius 1865);
- Interfacial fluid-solid sliding friction (Navier 1827, Maxwell 1879);
- Interfacial heat resistance (Kapitza 1941);
- Interfacial diffusion and reactions in heterogeneous catalysis;

where $\boldsymbol{\Pi}$ denotes the dissipative part of the pressure tensor, $\boldsymbol{\nabla}$ the gradient, $\mathbf{v}$ the velocity field, η the shear viscosity, ζ the dilatational or bulk viscosity, $\boldsymbol{J}_q$ the heat flux, κ the heat conductivity, $\boldsymbol{J}_k$ the diffusion flux of species k, D_k its diffusion coefficient, $\boldsymbol{J}_\mathrm{e}$ the electric flux, $\boldsymbol{\sigma}$ the electric conductivity tensor, $\boldsymbol{E}$ the electric field, V the voltage, R the resistance, and I the electric current.

These processes are characterized by phenomenological laws (also called constitutive relations) and the associated parameters that are the transport coefficients and the reaction rate constants.

3.2 The contribution of a reaction to entropy production

Inspired by the works of Gibbs on thermodynamics and using the aforementioned concept of "uncompensated heat", De Donder showed how chemical reactions contribute to entropy production [10,40]. He introduced the concept of affinity for a reaction, defined as minus the change ΔG_r of Gibbs free energy in the reaction:

$$A_r \equiv -\Delta G_r = -\sum_k \mu_k \nu_{kr} \,, \tag{8}$$

where μ_k is the chemical potential of species k and ν_{kr} its stoichiometric coefficient in the reaction r. Afterwards, in 1932, he established that the entropy production rate of a reaction is given by

$$(d_\mathrm{i}S/dt)_r = A_r W_r/T \tag{9}$$

in a well-mixed system, where $W_r = \int_V w_r \, d\mathbf{r}$ is the rate of the reaction in the volume V of the system [10]. The important novelty is that the reactions (as well as the other rate processes) contribute by differences of chemical potentials, which could be uniform across the system, although the transport properties require gradients to drive the system away from equilibrium.

4 The non-equilibrium thermodynamics of reactive fluids

The thermodynamics of continuous media was finally established around WWII on the following assumptions. At the macroscale, we observe the slowest motions ruled by the fundamental conservation laws of energy, momentum, and mass; and also the conservation of particle numbers in the absence of any reaction, or the balance of particle numbers in the presence of slow enough reactions. Furthermore, on long time scales, every element of matter is locally at equilibrium, so that the entropy density s satisfies the following local Gibbs relation:

$$ds = \frac{1}{T} de - \sum_k \frac{\mu_k}{T} dn_k \,, \tag{10}$$

where e is the density of internal energy and n_k the particle density of species k. Subsequently, in reactive fluids, the local balance equation for entropy (7) can be deduced from the local conservation and balance equations for the other quantities, showing that the entropy flux is given by

$$\boldsymbol{j}_s = s\,\mathbf{v} + \frac{1}{T}\boldsymbol{J}_q - \sum_k \frac{\mu_k}{T}\boldsymbol{J}_k \tag{11}$$

in terms of the heat and diffusion fluxes, and the entropy production rate density by

$$\sigma_s = \sum_\alpha A_\alpha J_\alpha \geq 0 \tag{12}$$

in terms of the thermodynamic forces and fluxes associated with each irreversible process (see Table 1) [14-16,18,19,21,22].

Table 1: The thermodynamic forces A_α and fluxes J_α associated with the different irreversible processes of a reactive fluid. T denotes the temperature, $\boldsymbol{\nabla}$ the gradient, $\mathbf{v}$ the velocity, $\boldsymbol{\Pi}$ the tensor of viscous pressure, $\mathbf{1}$ the unit tensor, $\boldsymbol{J}_q$ the heat flux, μ_k the chemical potential of species k, $\boldsymbol{J}_k$ its diffusion flux, ν_{kr} its stoichiometric coefficient in reaction r, and w_r the rate density of the reaction.

irreversible process	**thermodynamic force** A_α	**flux** J_α
shear viscosity	$-\frac{1}{2T}\left(\boldsymbol{\nabla}\mathbf{v} + \boldsymbol{\nabla}\mathbf{v}^\mathrm{T} - \frac{2}{3}\boldsymbol{\nabla}\cdot\mathbf{v}\,\mathbf{1}\right)$	$\boldsymbol{\Pi} - \Pi\mathbf{1}$
bulk viscosity	$-\frac{1}{T}\boldsymbol{\nabla}\cdot\mathbf{v}$	$\Pi = \frac{1}{3}\mathrm{tr}\,\boldsymbol{\Pi}$
heat conduction	$\boldsymbol{\nabla}(1/T)$	$\boldsymbol{J}_q$
diffusion	$\boldsymbol{\nabla}(-\mu_k/T)$	$\boldsymbol{J}_k$
reaction	$-\frac{1}{T}\sum_k \mu_k \nu_{kr}$	w_r

These results should be supplemented by non-equilibrium constitutive relations between the fluxes and the thermodynamic forces:

$$J_\alpha = \underbrace{\sum_\beta L_{\alpha\beta} A_\beta}_{\text{linear response}} + \underbrace{\frac{1}{2}\sum_{\beta\gamma} M_{\alpha\beta\gamma} A_\beta A_\gamma + \cdots}_{\text{nonlinear response}} \tag{12}$$

which must satisfy the Onsager reciprocal relations $L_{\alpha\beta} = L_{\beta\alpha}$ because of microreversibility [11,12] and the Curie symmetry principle holding in the continuous medium of interest [41]. These constitutive relations are linear if the mean free path is smaller than the length scales of variation in the free-energy landscape (which is the case for the viscosities, heat conduction, and diffusion); or nonlinear if the free-energy landscape varies over length scales of the order of molecular sizes (e.g., for chemical reactions). In the latter case, the reaction rate density of a reaction is given by $w_r = w_{+r}\left(1 - \mathrm{e}^{-A_r/k_\mathrm{B}T}\right)$ in terms of the affinity (8)

according to the mass action law holding in dilute solutions.

5 General evolution criterion and dissipative structures

In 1954, Glansdorff and Prigogine obtained the general evolution criterion, which says that, "in a system evolving in a locally stable thermodynamic phase and subjected to stationary constraints, the thermodynamic forces always change with time by decreasing the entropy production rate" [27].

As aforementioned, the entropy production rate is defined by $P \equiv d_{\mathrm{i}}S/dt = \int_V \sigma_s \, d\mathbf{r} \geq 0$, so that $P = \int_V \sum_\alpha A_\alpha J_\alpha \, d\mathbf{r}$. Its time derivative can thus be written as

$$\frac{dP}{dt} = \frac{d_A P}{dt} + \frac{d_J P}{dt} \qquad \text{with}$$

$$\frac{d_A P}{dt} = \int_V \sum_\alpha \partial_t A_\alpha \; J_\alpha \, d\mathbf{r} \quad \text{and}$$

$$\frac{d_J P}{dt} = \int_V \sum_\alpha A_\alpha \, \partial_t J_\alpha \, d\mathbf{r} \,. \tag{14}$$

In systems without convective processes and subjected to the stated conditions, the following inequality is satisfied:

$$\frac{d_A P}{dt} \leq 0 \quad \left(\text{with } \frac{d_A P}{dt} = 0 \text{ in steady states}\right), \tag{15}$$

hence the general evolution criterion. The criterion can be extended to include the convective processes [27,28].

If and only if, linear relations hold between the fluxes and the thermodynamic forces, the general evolution criterion implies the theorem of minimum entropy production, according to which

$$\frac{d_A P}{dt} = \frac{d_J P}{dt} = \frac{1}{2}\frac{dP}{dt} \leq 0 \,. \tag{16}$$

However, such linear relations do not hold in general, leading to the possibility of spatiotemporal pattern formation under far-from-equilibrium conditions. The general evolution criterion can be used to determine the stability or instability of non-equilibrium steady states, showing that instabilities may happen far enough from equilibrium. Beyond the threshold of instability, dissipative structures may thus emerge, in particular, in diffusion-reaction systems [24-26,42].

6 The non-equilibrium thermodynamics of active matter

Significant advances have been recently made in research on the dissipative structures and the thermodynamics of active matter [29-38]. There exist many different sorts of active matter, which may be composed of self-propelled particles or micro-organisms, locally converting energy into locomotion. An example is given by active suspensions of micrometric Janus particles with a catalytic hemisphere, where some reactant is consumed generating propulsion by self-diffusiophoresis [30,33]. In such systems, the internal degrees of freedom of the particles like those describing their orientation may also have slow motions. In this respect, the local conservation equation of the Janus particles should be generalized to their distribution function $f_{\mathrm{C}}(\mathbf{r}, \boldsymbol{\alpha}, t)$ defined in the six-dimensional space of their position $\mathbf{r}$ and orientation $\boldsymbol{\alpha}$:

$$\partial_t f_{\mathrm{C}} + \boldsymbol{\nabla} \cdot (f_{\mathrm{C}} \, \mathbf{v} + \boldsymbol{J}_{\mathrm{Ct}}) + \mathrm{div}_{\mathrm{r}}(f_{\mathrm{C}} \, \boldsymbol{v}_{\mathrm{r}} + \boldsymbol{J}_{\mathrm{Cr}}) = 0 \,, \tag{17}$$

where $\mathrm{div}_{\mathrm{r}}$ denotes the divergence in the orientation subspace [34, 38]. In addition, the local Gibbs relation should be extended into

$$\delta s = \frac{1}{T}\delta e - \sum_k \frac{\mu_k}{T}\delta n_k - \int \frac{\zeta_{\mathrm{C}}}{T}\delta f_{\mathrm{C}} \, do \,, \tag{18}$$

where ζ_{C} is the chemical potential of the Janus particles and do the element of integration in their orientation subspace [19,21,43]. In such systems, the balance equation for entropy (7) can also be deduced and, consistently, the entropy production rate density should include contributions from the Janus particles:

$$\sigma_s = \sum_\alpha A_\alpha J_\alpha + \int \sum_{\gamma=\mathrm{t,r}} \boldsymbol{A}_{\mathrm{C}\gamma} \cdot \boldsymbol{J}_{\mathrm{C}\gamma} \, do \tag{19}$$

with corresponding thermodynamic forces $\boldsymbol{A}_{\mathrm{C}\gamma}$ [34,38].

7 The microscopic foundations of non-equilibrium thermodynamics

Macroscopic theories like hydrodynamics and thermodynamics find their origins in the microscopic motion of atoms composing matter. In particular, the Hamiltonian microdynamics of atoms implies the conservation of energy, which justifies the first law of thermodynamics. However, entropy is a quantity characterizing the statistical disorder associated with a probability distribution defined in the space of microstates of the system, as shown by Boltzmann [44]. Therefore, the second law of thermodynamics should be justified on the basis of statistical mechanics.

The earliest justification is based on the kinetic theory of gases and Boltzmann's kinetic equation for the time evolution of the distribution function $f(\mathbf{r}, \mathbf{p}, t)$ of the positions $\mathbf{r}$ and momenta $\mathbf{p}$ of the particles in a dilute gas [45]:

$$\partial_t f + \frac{\mathbf{p}}{m} \cdot \boldsymbol{\nabla} f = \int \frac{d\mathbf{p}'}{m} d\Omega \, \sigma_{\mathrm{diff}} \, |\mathbf{p} - \mathbf{p}'| (FF' - ff') \,, \tag{20}$$

where m is the mass of the particles, σ_{diff} the differential cross-section of the binary collisions, f & f' the distribution functions of the two particles of momenta $\mathbf{p}$ & $\mathbf{p}'$ incoming a collision, F & F' those of the two outgoing particles, and $d\Omega$ an element of solid angle for the collision direction. If Boltzmann's equation holds, the second law of thermodynamics is satisfied according to the famous H-theorem. Indeed, in dilute gases, the entropy is given by $S = -k_{\mathrm{B}}H = \int_V s\, d\mathbf{r}$, where the entropy density $s(\mathbf{r},t) = k_{\mathrm{B}}\int d\mathbf{p}\, f(\mathbf{r},\mathbf{p},t)\, \ln\frac{\mathrm{e}}{h^3 f(\mathbf{r},\mathbf{p},t)}$ obeys the local balance equation (7) with an entropy production rate density σ_s, which can be proved to be always non-negative, fully justifying the second law in this framework.

As a consequence of the H-theorem, in an isolated system, the relaxation towards equilibrium proceeds in two stages, as shown by Chapman and Enskog in 1917 [46]. Starting from an arbitrary initial distribution function $f(\mathbf{r},\mathbf{p},0)$, first, there is a fast kinetic relaxation towards local equilibrium over a timescale of the order of a few intercollisional times and, afterwards, a slow hydrodynamic relaxation towards global equilibrium, which is asymptotically reached in the long-time limit. In this second stage, the distribution function can be assumed to have a Maxwellian form at the local temperature, particle density, and velocity for every element in the fluid. Therefore, the macroscopic hydrodynamic equations and the values of the transport coefficients can be deduced from the Boltzmann kinetic equation in dilute gases. In this way, the microscopic foundations of non-equilibrium thermodynamics can be established for dilute gases and also for reactive gases [47] and plasmas [48].

These results have been extended to condensed matter with the advent of the methods of non-equilibrium statistical mechanics for many-body systems. In the 1950s and early 1960s, Green [49,50], Kubo [51], Mori [52], McLennan [53], and others obtained formulas for the transport coefficients expressed in terms of microscopic global currents defined for the many-body system. These methods apply to the different phases of condensed matter [54,55]. More recently, the so-called fluctuation theorems have provided further justifications for the non-negativity of the entropy production [56]. In addition, the typical trajectories of non-equilibrium stochastic processes have been shown to be more probable than their time reversal, meaning that directionality – i.e., dynamical order – manifests itself away from equilibrium, as a corollary of the second law of thermodynamics [56].

Nowadays, we understand that microreversibility – i.e., the symmetry of the Hamiltonian microdynamics under time reversal – is always satisfied, but the time-reversal symmetry is broken in the statistical description of non-equilibrium systems. Energy dissipation is explained by the fact that, since the fundamental interactions of nature are local, energy goes from few to many particles after several successive collisions and, thus, from the macroscale down to the microscopic degrees of freedom, generating heat, which is a degraded form of energy. In this regard, the description of macroscopic systems requires coarse graining the microscopic variables, as carried out in non-equilibrium statistical mechanics [56].

8 Conclusion and perspectives

Thermodynamics is the theory of heat and temperature. It is based on the concept of entropy, which evaluates the amount of disorder in the microscopic degrees of freedom that are not under macroscopic control. Thermodynamics distinguishes between reversible and irreversible processes and, thus, allows us to identify the irreversible processes in natural phenomena. Non-equilibrium thermodynamics is known for reactive fluids, active matter, and other phases of matter like crystals, liquid crystals, or superfluids.

Dissipative structures such as oscillations or spatiotemporal patterns can emerge in far-from-equilibrium open systems, which is consistent with the thermodynamics of open systems.

Furthermore, the domains of validity of thermodynamics have been delimited by much effort in classical and quantum statistical mechanics.

Thermodynamics provides the framework to understand the mechanisms of energy conversion and their efficiency in engineering, the physical sciences, and the biosciences [57]. This concerns, in particular, the biological systems, where the metabolism constitutes a chemical reaction network functioning away from equilibrium. Moreover, as envisaged by Brillouin [58] and Landauer [59], thermodynamics plays a fundamental role in the relationship between energy and information, which concerns information science, microelectronics, and also molecular biology in the non-equilibrium processes of replication, transcription, and translation, where connections between thermodynamics and information theory have been established [60].

Acknowledgement

This research was supported by the Université Libre de Bruxelles (ULB).

References

[1] S. Carnot, "Réflexions sur la puissance motrice

du feu et sur les machines propres à développer cette puissance" (Bachelier, Paris, 1824).
[2] R. Clausius, "Ueber eine veränderte Form des zweiten Hauptsatzes der mechanischen Wärmetheorie", Annalen der Physik und Chemie **93**, 481-506 (1854); translated in the fourth memoir of Ref. [3].
[3] R. Clausius, "The Mechanical Theory of Heat" (Van Voorst, London, 1867).
[4] L. Natanson, "Ueber die Gesetze nicht umkehrbarer Vorgänge", Z. physik. Chem. **21**, 193-217 (1896).
[5] P. Duhem, "Traité d'énergétique" (Gauthier-Villars, Paris, 1911, 2 vol.).
[6] G. Jaumann, "Geschlossenes System physikalischer und chemischer Differenzialgesetze", Sitzb. d. Akad. Wiss., Wien, [Math. Naturw. Kl. **120**, abt. 2a, 385-530 (1911)].
[7] G. Jaumann, "Physik der kontinuierlichen Medien", Denksch. d. Akad. Wiss., Wien, [Math. Naturw. Kl. **95**, 461-562 (1918)].
[8] E. Lohr, "Entropieprinzip und geschlossnes Gleichungssystem", Denksch. d. Akad. Wiss., Wien, [Math. Naturw. Kl. **93**, 339-421 (1916)].
[9] E. Lohr, "Das Entropieprinzip der Kontinuitätstheorie", Festsch. d. Deutschen Techn. Hochsch. in Brünn, 176-187 (1924)].
[10] Th. De Donder, "L'affinité", rédaction nouvelle par P. Van Rysselberghe (Gauthier-Villars, Paris, 1936).
[11] L. Onsager, "Reciprocal relations in irreversible processes I", Phys. Rev. **37**, 405-426 (1931).
[12] L. Onsager, "Reciprocal relations in irreversible processes II", Phys. Rev. **38**, 2265-2279 (1931).
[13] J. Meixner, "Thermodynamische und kinetische Behandlung der thermoelektrischen Effekte im Magnetfeld", Ann. Physik **35**, 701-734 (1939); "Einfluß einer Umkehrung des Magnetfeldes auf die galvanomagnetischen und thermomagnetischen Effekte", Ann. Physik **36**, 105-112 (1939); "Zur Thermodynamik der Thermodiffusion", Ann. Physik 39, 333-356 (1941); "Zur Theorie der elektrischen Transporterscheinungen im Magnetfeld", Ann. Physik **40**, 165-180 (1941); "Zur Thermodynamik der irreversiblen Prozesse", Z. physik. Chem. B **53**, 235-263 (1943).
[14] C. Eckart, "The Thermodynamics of Irreversible Processes. I. The Simple Fluid", Phys. Rev. **58**, 267-269 (1940).
[15] C. Eckart, "The Thermodynamics of Irreversible Processes. II. Fluid Mixtures", Phys. Rev. **58**, 269-275 (1940); "Correction", *ibid.* **58**, 924 (1940).
[16] C. Eckart, "The Thermodynamics of Irreversible Processes. III. Relativistic Theory of the Simple Fluid", Phys. Rev. **58**, 919-924 (1940).
[17] P. W. Bridgman, "The Second Law of Thermodynamics and Irreversible Processes", Phys. Rev. **58**, 845 (1940).
[18] I. Prigogine, "Etude thermodynamique des phénomènes irréversibles" (Dunod, Paris & Desoer, Liège, 1947).
[19] I. Prigogine, "Introduction to thermodynamics of irreversible processes", first edition (Charles C. Thomas Publisher, Springfield IL, 1955); second edition (Interscience Publishers, New York, 1961); third edition (Wiley, New York, 1967).
[20] S. R. de Groot, "Thermodynamics of irreversible processes" (North-Holland, Amsterdam, 1951).
[21] S. R. de Groot and P. Mazur, "Non-equilibrium thermodynamics" (North-Holland, Amsterdam, 1962).
[22] H. B. Callen, "Thermodynamics: An Introduction to the Physical Theories of Equilibrium Thermostatics and Irreversible Thermodynamics" (Wiley, New York, 1965).
[23] P. C. Martin, O. Parodi, and P. S. Pershan, "Unified hydrodynamic theory for crystals, liquid crystals, and normal fluids", Phys. Rev. A **6**, 2401-2420 (1972).
[24] I. Prigogine and G. Nicolis, "On Symmetry Breaking Instabilities in Dissipative Systems", J. Chem. Phys. **46**, 3542-3550 (1967).
[25] I. Prigogine and R. Lefever, "Symmetry Breaking Instabilities in Dissipative Systems. II", J. Chem. Phys. **48**, 1695-1700 (1968).
[26] G. Nicolis and I. Prigogine, "Self-Organization in Nonequilibrium Systems" (Wiley, New York, 1977).
[27] P. Glansdorff and I. Prigogine, "Sur les propriétés différentielles de la production d'entropie", Physica **20**, 773-780 (1954).
[28] P. Glansdorff and I. Prigogine, "Thermodynamic Theory of Structure, Stability, and Fluctuations" (Wiley, New York, 1971).
[29] M. C. Marchetti, J. F. Joanny, S. Ramaswamy, T. B. Liverpool, J. Prost, M. Rao, and R. A. Simha, "Hydrodynamics of soft active matter", Rev. Mod. Phys. **85**, 1143-1189 (2013).
[30] R. Kapral, "Perspective: Nanomotors without moving parts that propel themselves in solution", J. Chem. Phys. **138**, 020901 (2013).
[31] C. Bechinger, R. Di Leonardo, H. Löwen, C. Reichhardt, G. Volpe, and G. Volpe, "Active particles in complex and crowded environ-

ments", Rev. Mod. Phys. **88**, 045006 (2016).
[32] F. Jülicher, S. W. Grill, and G. Salbreux, "Hydrodynamic theory of active matter", Rep. Prog. Phys. **81**, 076601 (2018).
[33] P. Gaspard and R. Kapral, "Thermodynamics and statistical mechanics of chemically powered synthetic nanomotors", Adv. Phys. X **4**, 1602480 (2019).
[34] P. Gaspard and R. Kapral, "Active matter, irreversibility, and thermodynamics", Research SPJ **2020**, Article ID 9739231 (2020) (https://doi.org/10.34133/2020/9739231); arXiv:2003.06861.
[35] T. Markovich, E. Fodor, E. Tjhung, and M. E. Cates, "Thermodynamics of active field theories: Energetic cost of coupling to reservoirs", Phys. Rev. X **11**, 021057 (2021).
[36] A. Arango-Restrepo, J. D. Torrenegra-Rico, and J. M. Rubi, "Entropy production in a system of Janus particles", Entropy **27**, 112 (2025).
[37] R. Bebon, J. F. Robinson, and T. Speck, "Thermodynamics of active matter: Tracking dissipation across scales", Phys. Rev. X **15**, 021050 (2025).
[38] P. Gaspard, "The non-equilibrium thermodynamics of active suspensions", New J. Phys. **27**, 094401 (2025).
[39] R. Clausius, "Ueber verschiedene für die Anwendung bequeme Formen der Hauptgleichungen der mechanischen Wärmetheorie", Annalen der Physik und Chemie **125**, 353-400 (1865); translated in the ninth memoir of Ref. [3].
[40] A. Rocci, "Celebrating the birth of De Donder's chemical affinity (1922-2022): from the uncompensated heat to his Ave Maria", Found. Chem. **26**, 37-73 (2024).
[41] P. Curie, "Sur la symétrie dans les phénomènes physiques, symétrie d'un champ électrique et d'un champ magnétique", J. Phys. Théor. Appl. **3**, 393-415 (1894).
[42] A. Goldbeter, "Dissipative structures in biological systems: bistability, oscillations, spatial patterns and waves", Phil. Trans. Roy. Soc. A **376**, 20170376 (2018).
[43] I. Prigogine and P. Mazur, "Sur l'extension de la thermodynamique aux phénomènes irréversibles liés aux degrés de liberté internes", Physica **19**, 241-254 (1953).
[44] L. Boltzmann, "Über die Beziehung zwischen dem zweiten Hauptsatz der mechanischen Wärmetheorie und der Wahrscheinlichkeitsrechnung respektive den Sätzen über das Wärmegleichgewicht", Wiener Berichte **76**, 373-435 (1877).
[45] L. Boltzmann, "Weitere Studien über das Wärmegleichgewicht unter Gasmolekülen", Wiener Berichte **66**, 275-370 (1872).
[46] S. Chapman and T. G. Cowling, "The Mathematical Theory of Non-Uniform Gases" (Cambridge University Press, Cambridge UK, 1939).
[47] I. Prigogine, "Le domaine de validité de la thermodynamique des phénomènes irréversibles", Physica **15**, 272-284 (1949).
[48] R. Balescu, "Equilibrium and Nonequilibrium Statistical Mechanics" (Wiley, New York, 1975).
[49] M. S. Green, "Markoff Random Processes and the Statistical Mechanics of Time-Dependent Phenomena", J. Chem. Phys. **20**, 1281-1295 (1952).
[50] M. S. Green, "Markoff Random Processes and the Statistical Mechanics of Time-Dependent Phenomena. II. Irreversible Processes in Fluids", J. Chem. Phys. **22**, 398-413 (1954).
[51] R. Kubo, "Statistical mechanical theory of irreversible processes. I. General theory and simple applications in magnetic and conduction problems", J. Phys. Soc. Japan **12**, 570-586 (1957).
[52] H. Mori, "Statistical-Mechanical Theory of Transport in Fluids", Phys. Rev. **112**, 1829-1842 (1958).
[53] J. A. McLennan Jr., "The formal statistical theory of transport processes", Adv. Chem. Phys. **5**, 261-317 (1963).
[54] J. Mabillard and P. Gaspard, "Microscopic approach to the macrodynamics of matter with broken symmetries", J. Stat. Mech.: Theory Exp. **2020**, 103203 (2020).
[55] J. Mabillard and P. Gaspard, "Quantum local-equilibrium approach to dissipative hydrodynamics", Phys. Rev. E **107**, 014102 (2023).
[56] P. Gaspard, "The Statistical Mechanics of Irreversible Phenomena" (Cambridge University Press, Cambridge UK, 2022).
[57] T. L. Hill, "Free energy transduction in biology" (Acad. Press, New York, 1977).
[58] L. Brillouin, "Science and Information Theory" (Academic Press, New York, 1956).
[59] R. Landauer, "Irreversibility and Heat Generation in the Computing Process", IBM J. Res. Dev. **5**, 183-191 (1961).
[60] D. Andrieux and P. Gaspard, "Nonequilibrium generation of information in copolymerization processes", Proc. Natl. Acad. Sci. USA **105**, 9512-9521 (2008).

ON THE ROLE OF SATURATION TEMPERATURE IN THERMAL MANAGEMENT THROUGH TWO-PHASE MECHANICALLY PUMPED LOOP

M. Pedroza-Torres[1]*, R. Rioboo[2], V. Lemort[1]

[1] Thermodynamics Laboratory / Université de Liège, Liège, Belgium

[2] Euro Heat Pipes, Nivelles, Belgium

* *Corresponding Author: mptorres@uliege.be*

Abstract. The impact of commercial aviation on the volume of polluting emissions is a problem that has become more relevant over the years, from initiatives at a personal level such as abstaining from the use of aircraft, to approaches at a government level with the dissent via taxes in some countries, there have been various ways of facing a problem whose solution may possibly go through the path of technological development. In today's world, the growing demand for power in the transition to electric aviation systems brings together the need to improve the thermal management systems associated with their correct operation. It is in this context where flow boiling cooling technologies have demonstrated their potential for thermal management. This two-phase solution uses the latent heat of vaporisation as a resource in the extraction of heat, with low requirements in mass flow and near-isothermal operation, resulting in a low temperature difference between hot source and cold sink even for long distances where the addition of pumping stages becomes necessary. In the overall design scheme of a two-phase cooling circuit, adjusting the saturation temperature or mass flow of the coolant are control possibilities in the face of changing conditions of the heat transfer environment. This work presents a set of five criteria to establish a saturation temperature setpoint under steady state conditions. Two application examples are presented, and the results are compared with case studies of two-phase mechanically pumped loop (2ΦMPL) from the aerospace industry.

Keywords. Two-phase, MPL, Flow boiling, Temperature setpoint, Selection criteria.

Nomenclature

A	Area (m^2)
ρ	Density (kg/m^3)
μ	Dynamic viscosity (Pa.s)
R	Gas constant (J/kg.K)
$\dot{Q}$	Heat transfer rate (W)
h_{lv}	Latent heat of vaporisation (J/kg)
M	Mach number (-)
$\dot{m}$	Mass flow rate (kg/s)
P	Pressure (Pa)
T	Temperature (K)
h	Specific enthalpy (J/kg)
γ	Specific heat ratio (-)
v	Velocity
$\dot{V}$	Volumetric flow (m^3/s)

Subscripts

cs	Cross-section
l	Liquid
s	Saturation
snd	Sound
v	Vapour

Acronyms

FoM	Figure of Merit
HTC	Heat Transfer Coefficient
LPD	Low Pressure Drop
LVF	Low Volumetric Flow
RTC	Robust Temperature Control
2ΦMPL	Two-Phase Mechanically Pumped Loop

1 Introduction

Nowadays, there are few problems capable of bringing together so many countries in a common purpose as climate change does. The risks to civilisation and the ecosystem have become tangible over the years, leading to government regulations and initiatives from major technological players that are setting new lines of development [1].

In this regard, the aeronautical industry, committed to the goal of decarbonization [2], has expanded its investment and research horizons towards electrification, a growing market with power dissipation demands proportional to the size and performance of future aircraft [3] [4].

These initiatives bring new challenges in thermal management; the need to acquire, transport, and reject heat within complex structural configurations and high power density per unit area has shifted attention towards two-phase heat transfer solutions, taking advantage of the ability to absorb large amounts of heat by harnessing the latent heat of vaporisation [5] [6].

Passive thermal management alternatives such as heat pipes have demonstrated their capability and reliability over the years in the aerospace environment [7]. However, the mass budget required for use over long distances between heat acquisition and rejection points have shifted focus towards the development of systems with an added pumping stage, such as 2ΦMPLs. These systems allow a new level of control over mass flow, near-isothermal operating conditions, and the theoretical ability to extend their branches to the temperature control of parallel thermal loads. These intriguing capabilities come with numerous questions about the operational requirements of this technology [6].

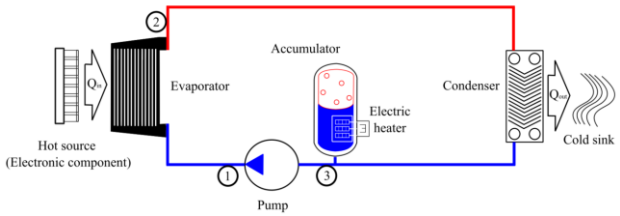
This work presents a set of five criteria to establish a saturation temperature setpoint under steady state conditions. Two application examples are presented, and the results are compared with case studies on thermal control in the aerospace industry: 1) Telecommunication satellite (simulation results with ammonia) [8], and 2) Instruments for measurements in advanced physics (actual set-point selected for operation with carbon dioxide) [9].

2 Fundamentals of a 2ΦMPL

2.1 Basic Mechanics

A simplified representation of a single-loop 2ΦMPL intended for the thermal management of electronic components is shown in Figure 1a, accompanied by its typical behaviour on the pressure-enthalpy diagram (Figure 1b). The description of the operating principle of the loop starts at the accumulator which performs three functions in the configuration shown: 1) supplying liquid to the pump to prevent cavitation, 2) dampening transient excess flow caused by changing conditions in the evaporator, and 3) setting the minimum pressure level within the loop through the controlled activation of an electric heater. Downstream is the pump, which is responsible for maintaining the fluid flow within the system, overcoming pressure losses by increasing the mechanical energy of the flow. The next component is the evaporator, which acquires heat from the hot source while utilising the latent heat of vaporisation to maintain the near-isothermal condition in the working fluid. Finally, the heat is rejected in the condenser, where the working fluid returns to a subcooled condition to complete the cycle again at the accumulator.

a)



b)

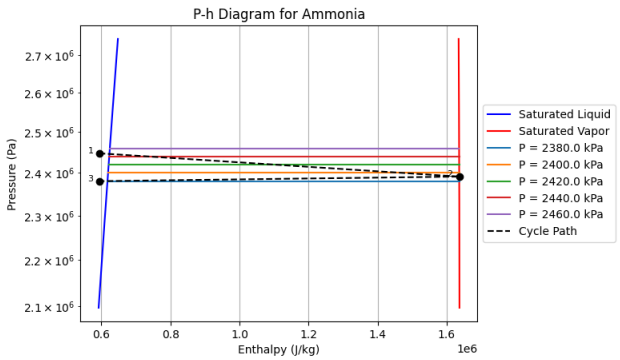


Figure 1: a) 2ϕMPL main components, b) Example of 2ϕMPL P-h diagram.

2.2 Control Strategies

Control strategies for 2ΦMPL systems are still an area under exploration, with thermohydraulic instabilities often occurring at both the component and system levels [10]. Flow restrictors and surface coatings have shown some of the best results in

reducing flow disturbances [11] [12] [13] [14]. However, the disparity in the response times between thermal and hydraulic dynamics makes it a challenging issue, leading to the consideration of heuristic control methodologies (black box approaches) [15]. For clarity in the explanation of the application example in this work, a simple strategy will be considered by setting a nominal temperature value in the working fluid, while response to disturbances will be managed through variations in pump speed.

3 Temperature Setpoint Selection Criteria

3.1 Higher HTC

Improvements in the heat transfer coefficient (HTC) achieved by operating at higher pressure levels have been reported by numerous authors in the phenomenon of flow boiling [16] [17] and can be seen in Figures 2 and 3. The physical argument behind this effect is the reduction in surface tension (due to the increase in saturation temperature), which leads to lower energy requirements for the extension of the liquid film needed for bubble formation. Additionally, operating at higher pressure levels results in smaller bubble sizes, leading to enhanced and more homogeneous nucleation flow. Therefore, according to this criterion operating at the highest possible pressure (saturation temperature) is the best option.

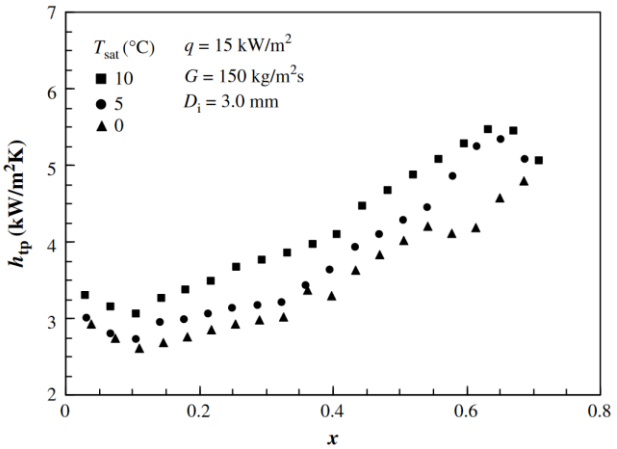


Figure 2: The effect of saturation temperature on heat transfer coefficient for propane **[16]**.

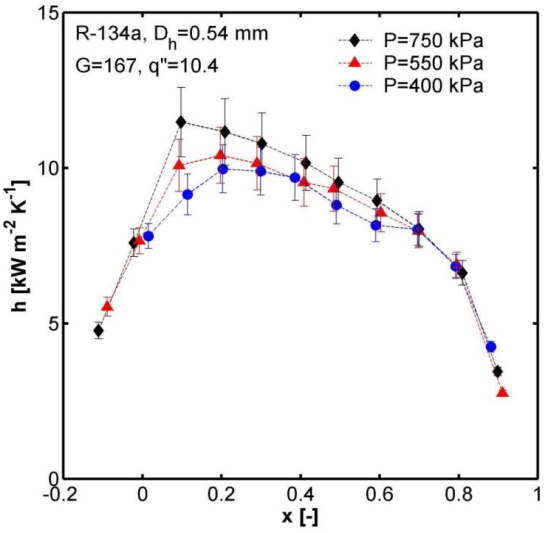


Figure 3: The effect of saturation pressure on the heat transfer coefficient for R-134a **[17]**.

3.2 Higher Latent Heat of Vaporisation

As discussed in the previous paragraph, while the heat transfer coefficient can benefit from setting higher pressure levels (saturation temperature) within the loop, operating in the upper region of the P vs h diagram is associated with lower values of latent heat of vaporisation (Figure 4), which reduces the range of the two-phase region and thus limits the spectrum of isothermal operation. Based on the criterion of high latent heat of vaporisation, it is suggested to operate at the minimum temperature (pressure) settled by the operational requirements of the thermal load.

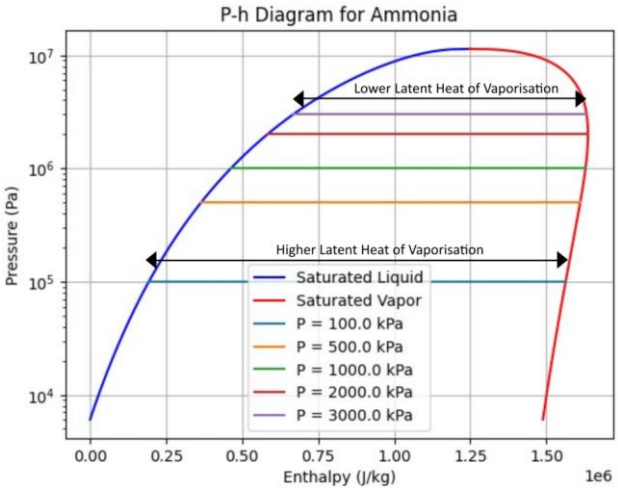


Figure 4: Example of P-h diagram.

3.3 *Robust Temperature Control*

For control purposes, it is beneficial to set a saturation temperature setpoint as close as possible to the critical temperature, where even with relatively large variations in the manipulated variable (pressure regulated from the accumulator), the changes in the controlled variable (saturation temperature) remain minimal [18]. This scenario of control robustness can be assessed by evaluating the gradient between pressure and temperature variations and selecting the temperature with the highest value as shown in Equation (1), based on the analysis of behaviour in the P vs T diagram of the working fluid (Figure 5).

$$T_{RTC\ criterion} = T_s|_{\max\left(\frac{dP}{dT}\right)} \tag{1}$$

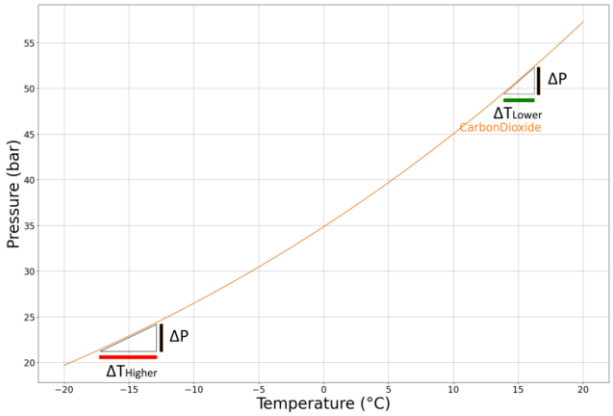


Figure 5: Example of P-T diagram.

3.4 *Lower Pressure Drop*

In a 1ΦMPL (based on sensible heat transfer) the ability to extract heat must be enhanced by increasing mass flow, however the use of latent heat means that for 2Φ-MPL less mass flow is required, and it is possible to reduce the diameter of the pipe, although this will increase the pressure losses. Gerner et al.'s proposal [19] demonstrates how certain formulations allow for distinguishing the contribution of factors in relation to pressure losses for turbulent flow in smooth-walled tubes. A single numerical value (called a Figure of Merit FoM) is proposed to quantify the relationship of multiple thermohydraulic properties. The aim would be to determine the saturation temperature that maximises the value of the Figure of Merit referred to as Low Pressure Drop (LPD FoM) in Equations (2) and (3), by calculating the thermohydraulic properties at that temperature depending on the chosen working fluid.

$$T_{LPD\ criterion} = T_s|_{\max\ (LPD\ FoM)} \tag{2}$$

$$LPD\ FoM = \frac{1}{\frac{\mu_l^{1/4}}{\rho_l (h_{lv})^{7/4}} + \frac{\mu_v^{1/4}}{\rho_v (h_{lv})^{7/4}}} \tag{3}$$

3.5 *Lower Volumetric Flow*

Equation (4) shows the definition of volumetric flow and its inverse relationship with respect to the product of liquid density by latent heat of vaporisation for turbulent flow in smooth-walled tubes [19]:

$$\dot{V} = \frac{\dot{m}}{\rho_l} = \frac{\dot{Q}}{\rho_l h_{lv}} \tag{4}$$

Returning to the concept of the Figure of Merit, it is possible to determine the temperature values that would result in a lower volumetric flow rate (LVF FoM) in Equations (5) and (6), which is directly linked to a reduced pumping requirement.

$$T_{LVF\ criterion} = T_s|_{\max\ (LVF\ FoM)} \tag{5}$$

$$LVF\ FoM = \rho_l h_{lv} \tag{6}$$

3.6 *Sonic Limit Check*

It is suggested that the selected temperature setpoint reduces the influence of compressibility effects, (pressure fluctuations, flow maldistribution, etc.) which would add complexity and difficulties to the thermohydraulic control of the system. Therefore, it is essential to ensure that the vapour velocity in the fluid remains within the subsonic flow category (Mach < 0.8). If not, the operating conditions should be redefined, or a new working fluid should be selected [18].

4 Application Examples

In the following section, the application of the different selection criteria will be demonstrated according to the flowchart shown in Figure 6, based on two case studies with different dissipation requirements for electronic equipment. In each case study, the selection will be made simultaneously for two fluids: Case #1 (R1234yf vs Carbon Dioxide), Case #2 (R1234ze(E) vs Ammonia) the first with potential for aeronautical use (R1234yf / R1234ze(E)), and the second as a reference for comparison, linked to space applications (Carbon Dioxide / Ammonia).

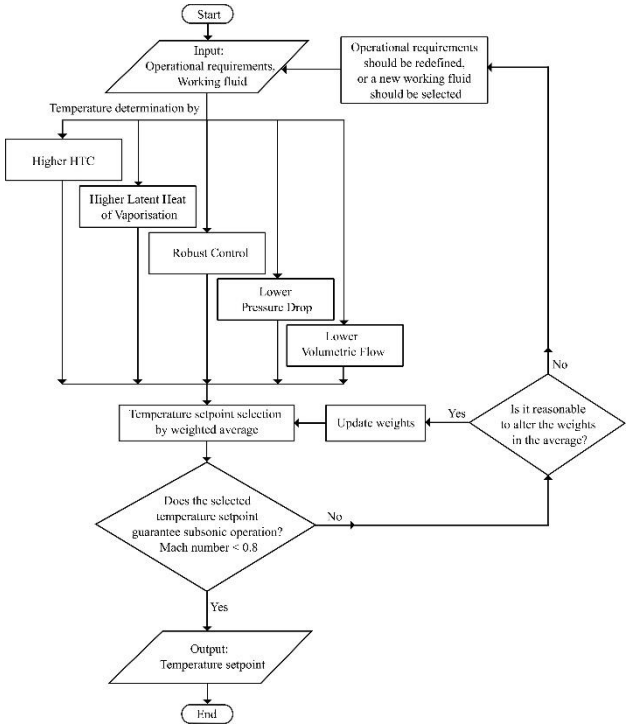


Figure 6: Temperature selection flowchart.

For the sake of simplicity in the explanation, the temperature range for the working fluid was taken as a reduction of the operational temperature requirement at hot source (by adding 5K to the lower limit and subtracting 5K from the upper limit). However, it is worth mentioning that a complete approach requires the estimation of the temperature deltas between fluid and hot source as a consequence of the convective resistance of the fluid, the conductive resistance of the evaporator material and the quality of the evaporator-heat source thermal contact interface.

4.1 Case study #1 (144 W)

In the context of advanced physics research, this first case study establishes some of the basic thermal management requirements for an in-orbit instrument specialised in antimatter detection [9], where the internal distribution of 8 silicon sheets capable of emitting electrical signals based on the impact of the particles under study is described. Around the 8 silicon planes detecting front-end electronics widely distributed at the periphery of the silicon planes (at no less than 192 locations) need to be very stable in temperature while dissipating 144 W of heat. The requirements of the first case study are summarised in Table 1.

Table 1: Operational parameters case study #1.

Power to be dissipated	144 [W]
Operational temperature requirement at hot source	-10 [°C] / 25 [°C]
Temperature range for the working fluid	-5 [°C] / 20 [°C]
Overall mass flow	2 [g/s]
Hydraulic diameter of the two-phase line	2.6 [mm]
Working fluid example (aeronautical application)	R1234yf
Working fluid for comparison (space application [9])	Carbon dioxide

4.1.1 Higher HTC: Figure 7 shows the choice of 20 °C for both R1234yf and Carbon Dioxide, according to the criterion of Higher HTC linked to operation at higher pressure levels.

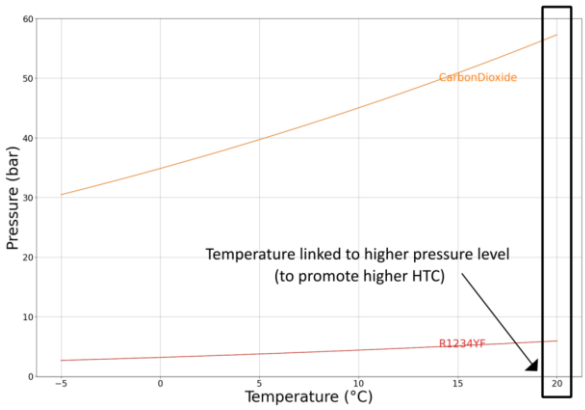


Figure 7: Case #1 (Higher HTC).

4.1.2 Higher Latent Heat of Vaporisation: Figures 8 and 9 shows the choice of -5 °C for both R1234yf and Carbon Dioxide, according to the criterion of Higher Latent Heat of Vaporisation linked to operation at lower pressure levels (lower temperatures).

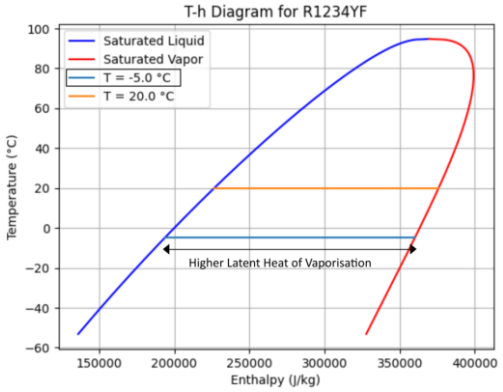


Figure 8: Case #1 (Higher Latent Heat of Vaporisation – R1234yf).

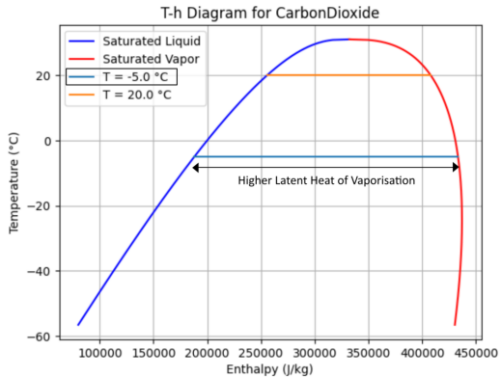


Figure 9: Case #1 (Higher Latent Heat of Vaporisation – Carbon dioxide).

4.1.3 Robust Temperature Control: Figure 10 shows the choice of 20 °C for both R1234yf and carbon dioxide, according to the criterion of Robust Temperature Control linked to operation at the point of largest gradient between pressure manipulation and temperature control.

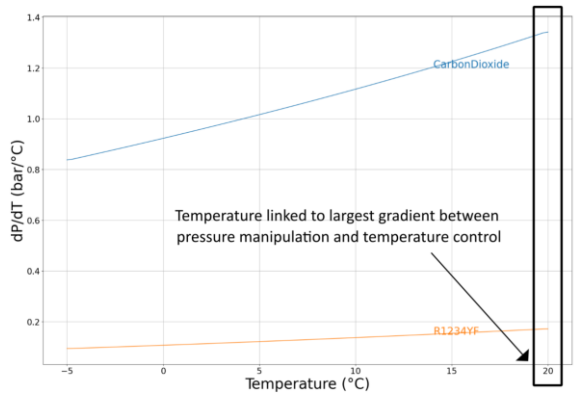


Figure 10: Case #1 (Robust Temperature Control).

4.1.4 Lower Pressure Drop: Figure 11 shows the choice of 20 °C for R1234yf and 2.5 °C for Carbon Dioxide, according to the criterion of Lower Pressure Drop for turbulent flow in smooth-walled tubes.

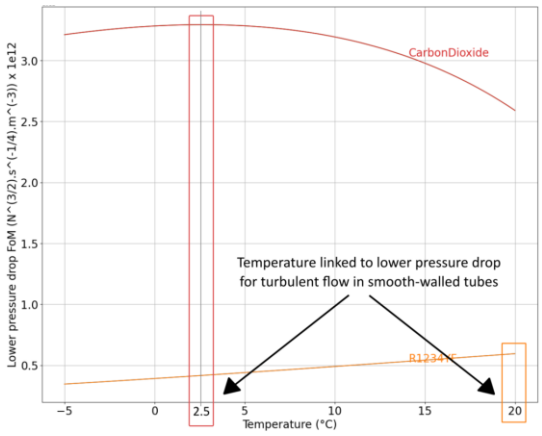


Figure 11: Case #1 (Lower Pressure Drop).

4.1.5 Lower Volumetric Flow: Figure 12 shows the choice of -5 °C for both R1234yf and Carbon Dioxide, according to the criterion of Lower Volumetric Flow with the purpose of reducing pumping power.

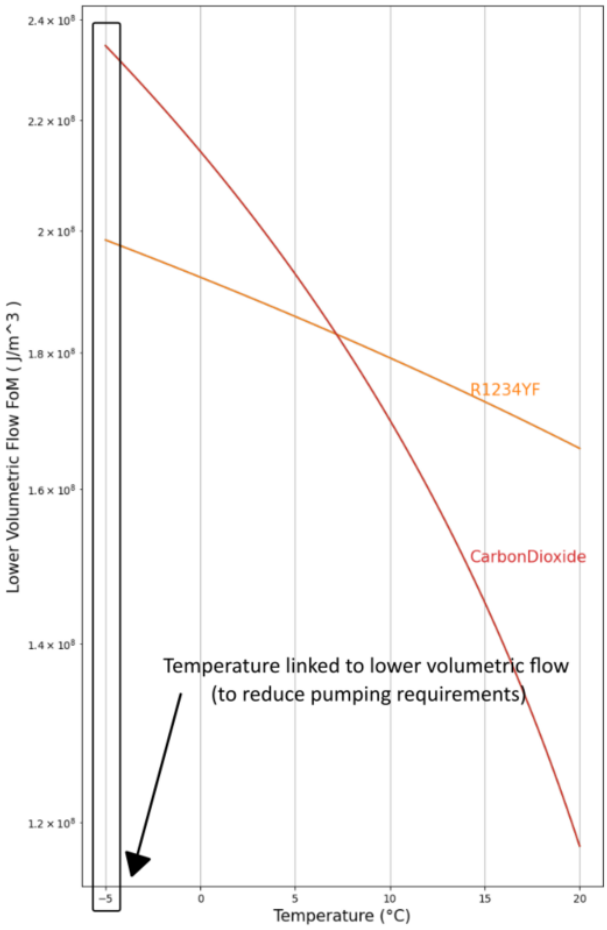


Figure 12: Case #1 (Lower Volumetric Flow).

4.1.6 Weighted average: Once the temperature values for each criterion have been obtained, the weighted average is calculated to determine the saturation temperature setpoint. In this context, two scenarios can be considered: a) known weights, and b) unknown weights.

a) Known weights scenario: Expert knowledge and operational decisions determine the values of the weights used to calculate the setpoint. In this context, various combinations of weights will position the saturation temperature in operating zones that may prioritise heat acquisition, prolong the intervals between interventions in the system, or achieve other objectives. Table 2 compares the temperature setpoints obtained for R1234yf and carbon dioxide for three different combinations of known weights, each serving a different purpose.

Table 2: Case study #1 (Setpoint selection – known weights scenario).

		Selected Temperature [°C]	
Criterion	Weight	R1234yf	Carbon Dioxide
Higher HTC	W1	20	20
Higher Latent Heat of Vaporisation	W2	-5	-5
Robust Temperature Control	W3	20	20
Lower Pressure Drop	W4	20	2.5
Lower Volumetric Flow	W5	-5	-5
Example 1: Equal weights (W1=W2=W3=W4=W5=0.2)			
Weighted average setpoint (Example 1)		**10**	**6.5**
Example 2: Greater heat acquisition (W1=0.7,W2=0.1,W3=0,W4=0.1,W5=0.			
Weighted average setpoint (Example 2)		**15**	**13.25**
Example 3: Less maintenance (W1=0.1,W2=0.1,W3=0.1,W4=0.3,W5=0.4)			
Weighted average setpoint (Example 3)		**7.5**	**`2.25**

b) Unknown weights scenario: In Equation 7 the number of different weight distributions 'N_{WD}' for 'n' indistinguishable objects (number of weight steps) among 'k' different parties (number of criteria) according to the stars and bars formula is equal to:

$$N_{WD} = \frac{(n+k-1)!}{(k-1)!\,n!} \tag{7}$$

Therefore, in the absence of specific weights, the construction of different weight distributions is proposed, after establishing the weight range and the step size for weight increments. As an example, step size for weight increments of 0.1 within the range 0 to 1 establishes $n = 10$ steps to cover the set of possible values $(0 \xrightarrow{Step\ 1} 0.1, \dots, 0.9 \xrightarrow{Step\ 10} 1)$, which assigned in $k = 5$ different positions establish a total of $N_{WD} = 1001$ possible combinations.

From here it is possible to calculate the weighted average associated with the different weight distributions, which gives N_{WD} candidate setpoint temperatures. Taking the set of possible values as a distribution, it is suggested to use the quartiles Q1, Q2 and Q3 as the lower value of the range, setpoint and upper value of the saturation temperature range respectively.

Returning to case study #1, the setpoint for the saturation temperature and its suggested range of variation are presented as a boxplot in Figure 13 for R1234yf and in Figure 14 for carbon dioxide.

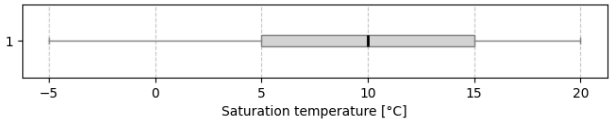


Figure 13: Case #1 (R1234yf setpoint selection – unknown weights scenario).

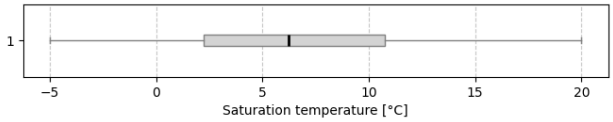


Figure 14: Case #1 (Carbon dioxide setpoint selection – unknown weights scenario).

4.1.7 Sonic Limit Check: At this verification stage it is first recommended to calculate the speed of sound using thermodynamic models and libraries available based on the fluid and temperatures of interest [20]. In the absence of such a resource, the formulation for ideal gases expressed in Equation 8 can be used as a calculation reference:

$$v_{snd} = \sqrt{\gamma \cdot R \cdot T} \tag{8}$$

The second step is to estimate the maximum velocity value developed in the line, for which a complete vaporisation scenario can be taken as a reference (vapor velocity), where the lowest density values for the gas phase will lead to maximum velocity values for an established geometry and mass flow in Equation 9:

$$v_v = \frac{\dot{m}}{\rho_v . A_{cs}} \tag{9}$$

The third and final step is to verify that the speed of the vapor flow remains far from the value of the speed of sound in that medium (to reduce the effects of compressibility) this can be achieved with calculated values less than 0.8 in the Mach number of Equation (10):

$$M = \frac{v_v}{v_{snd}} \tag{10}$$

The sonic limit check for case study #1 is summarized in Table 3 with properties obtained from the CoolProp 6.6.0 library [20].

Table 3: Case study #1 (Sonic Limit Check).

Working fluid	R1234yf			Carbon Dioxide		
Temperature setpoint range [°C]	{5;15}			{2.25;10.75}		
Quartiles	Q1	Median	Q3	Q1	Median	Q3
Temperature [°C]	5	**10**	15	2.25	**6.25**	10.75
Vapor velocity [m/s]	18.16	15.52	13.33	3.59	3.16	2.72
Mach number [-]	0.135	0.115	0.099	0.017	0.015	0.013
Vapour flow regime	Subsonic			Subsonic		

In this sense, the temperature setpoints proposed for the two fluids are far from the sonic limit, and are presented as a baseline for choosing a nominal operating point. For comparison purposes the accumulator setpoint chosen by the reference

2ΦMPL operating with carbon dioxide for thermal management of these dissipation requirements was 0 °C [9], a difference of less than 7 K with the median temperature of the unknown weight method shown above.

4.2 Case study #2 (6000 W)

Within the telecommunications satellite market, new requirements in the power required for signal processing (or in-orbit computing) are linked to increases in size and thermal dissipation requirements, with operating ranges that are increasingly similar to those of aeronautical applications, which has led to joint research programs between aeronautical and aerospace institutions [8]. Regarding this case study, three panels arranged inside a satellite assembly are designed to house 180 active electronic components with a combined dissipation requirement of 6000 W. The requirements of the second case study are summarised in Table 4, its setpoint selection (known weights) in Table 5, setpoint selection (unknown weights) in Figure 15 & 16 and its sonic limit check in Table 6.

Table 4: Operational parameters case study #2.

Power to be dissipated	6000 [W]
Operational temperature requirement at hot source	35 [°C] / 70 [°C]
Temperature range for the working fluid	40 [°C] / 65 [°C]
Overall mass flow	3.15 [g/s]
Hydraulic diameter of the two-phase line	9 [mm]
Working fluid example (aeronautical application)	R1234ze(E)
Working fluid for comparison (space application [8])	Ammonia

Table 5: Case study #2 (Setpoint selection – known weights scenario).

		Selected Temperature [°C]	
Criterion	Weight	R1234ze(E)	Ammonia
Higher HTC	W1	65	65
Higher Latent Heat of Vaporisation	W2	40	40
Robust Temperature Control	W3	65	65
Lower Pressure Drop	W4	65	65
Lower Volumetric Flow	W5	40	40
Example 1: Equal weights (W1=W2=W3=W4=W5=0.2)			
Weighted average setpoint (Example 1)		**55**	**55**
Example 2: Greater heat acquisition (W1=0.7,W2=0.1,W3=0,W4=0.1,W5=0.			
Weighted average setpoint (Example 2)		**60**	**60**
Example 3: Less maintenance (W1=0.1,W2=0.1,W3=0.1,W4=0.3,W5=0.4)			
Weighted average setpoint (Example 3)		**52.5**	**52.5**

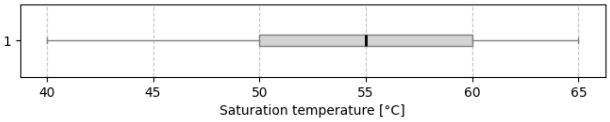


Figure 15: Case #2 (R1234ze(E) setpoint selection – unknown weights scenario).

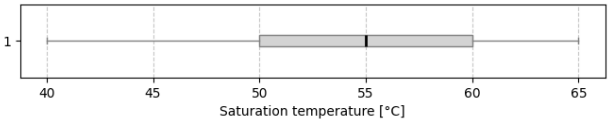


Figure 16: Case #2 (Ammonia setpoint selection – unknown weights scenario).

Table 6: Case study #2 (Sonic Limit Check).

Working fluid	R1234ze(E)			Ammonia		
Temperature setpoint range [°C]	{50;60}			{50;60}		
Quartiles	Q1	Median	Q3	Q1	Median	Q3
Temperature [°C]	50	**55**	60	50	**55**	60
Vapor velocity [m/s]	0.92	0.81	0.71	3.14	2.75	2.42
Mach number [-]	0.007	0.006	0.005	0.008	0.007	0.006
Vapour flow regime	Subsonic			Subsonic		

For comparison purposes the accumulator setpoint chosen by the reference 2ΦMPL prototype operating with ammonia for thermal management of these dissipation requirements was 51.56 °C [8], a difference of less than 4 K with the median temperature of the unknown weight method shown above.

5 Conclusions

- The five criteria presented: 1) Higher HTC, 2) Higher Latent Heat of Vaporisation, 3) Robust Temperature Control, 4) Lower Pressure Drop, 5) Lower Volumetric Flow, provide an analytical alternative for selecting a temperature setpoint that can be adjusted to the operational priorities of the case by modifying their weights in a weighted average formulation.
- In the case of selecting two different fluids for the same thermal management solution the chosen setpoint value may vary (case study #1) or remain the same (case study #2), depending on the behaviour of their thermodynamic diagrams and their performance based on the selected figures of merit.
- While the selection of nominal operating points must encompass the set of challenges in the construction, operation, and control of a 2ΦMPL, the approach presented above is proposed as a reasonable baseline.

Acknowledgement

This work has been made possible thanks to the MPL2030 project, a result of the collaboration between the Walloon government, the Skywin competitiveness cluster, the industrial partnership of Euro Heat Pipes - Calyos, and the academic collaboration between the University of Louvain and the University of Liège.

References

[1] J. Zhang, D. Ballas and X. Liu, “Global climate change mitigation technology diffusion: A network perspective,” Energy Economics, vol. 133, p. 107497, 2024.

[2] C. Jiang, T. D'Alfonso and J. Post, “Aviation decarbonization - Policies and technologies to support decarbonization of the aviation sector,” Transportation Research Part D: Transport and Environment, vol. 127, p. 104055, 2024.

[3] D. Sharar, N. R. Jankowski and B. Morgan, “Review of Two-phase Electronics Cooling for Army Vehicle Applications,” 2010.

[4] S. H. Lee, I. Mudawar and M. M. Hasan, “Thermal analysis of hybrid single-phase, two-phase and heat pump thermal control system (TCS) for future spacecraft,” Applied Thermal Engineering, vol. 100, p. 190–214, May 2016.

[5] Y.-G. Lv, Y.-T. Wang, T. Meng, Q.-W. Wang and W.-X. Chu, “Review on thermal management technologies for electronics in spacecraft environment,” Energy Storage and Saving, vol. 3, p. 153–189, 2024.

[6] J. v. Es and H. J. v. Gerner, “Benefits and Drawbacks of Using Two-Phase Cooling Technologies in Military Platforms,” 2011.

[7] T. Yang, T. Gao, S. Zhao and P. Zhang, "Performance Test of Novel Flat Capillary Pump Loop Heat Pipe under Anti-gravity and Microgravity," Microgravity Science and Technology, vol. 34, June 2022.

[8] J. Hugon, “Development of a Two-Phase Mechanically Pumped Loop (2ΦMPL) for the Thermal Control of Telecommunication Satellites,” 2008.

[9] J. v. Es, A. Pauw, G. van Donk, U. Ragnit, Z. He, B. Verlaat, C. Gargiulo, E. Laudi and P. van Leeuwen, “AMS02 Tracker Thermal Control Cooling System Test Results of the AMS02 Thermal Vacuum Test in the LSS at ESA ESTEC,” 2012.

[10] S. V. Garimella, A. S. Fleischer, J. Y. Murthy, A. Keshavarzi, R. Prasher, C. Patel, S. H. Bhavnani, R. Venkatasubramanian, R. Mahajan, Y. Joshi, B. Sammakia, B. A. Myers, L. Chorosinski, M. Baelmans, P. Sathyamurthy and P. E. Raad, “Thermal Challenges in Next-Generation Electronic Systems,” IEEE Transactions on Components and Packaging Technologies, vol. 31, p. 801–815, 2008.

[11] A. Koşar, C.-J. Kuo and Y. Peles, “Suppression of Boiling Flow Oscillations in Parallel Microchannels by Inlet Restrictors,” Journal of Heat Transfer-transactions of The Asme - J HEAT TRANSFER, vol. 128, March 2006.

[12] G. Hedau, R. Raj and S. K. Saha, “Complete suppression of flow boing instability in microchannel heat sinks using a combination of inlet restrictor and flexible dampener,” International Journal of Heat and Mass Transfer, vol. 182, p. 121937, 2022.

[13] K. C. Leong, J. Y. Ho and K. K. Wong, “A critical review of pool and flow boiling heat transfer of dielectric fluids on enhanced surfaces,” Applied Thermal Engineering, vol. 112, p. 999–1019, 2017.

[14] V. Y. S. Lee, G. Henderson, A. Reip and T. G. Karayiannis, “Flow boiling characteristics in plain and porous coated microchannel heat sinks,” International Journal of Heat and Mass Transfer, vol. 183, p. 122152, 2022.

[15] T. Zhang, J. T. Wen, Y. Peles, J. Catano, R. Zhou and M. K. Jensen, “Two-phase refrigerant flow instability analysis and active control in transient electronics cooling systems,” International Journal of Multiphase Flow, vol. 37, p. 84–97, 2011.

[16] K.-I. Choi, A. S. Pamitran, J.-T. Oh and K. Saito, “Pressure drop and heat transfer during two-phase flow vaporization of propane in horizontal smooth minichannels,” International Journal of Refrigeration, vol. 32, p. 837–845, 2009.

[17] S. S. Bertsch, E. A. Groll and S. V. Garimella, “Effects of heat flux, mass flux, vapor quality, and saturation temperature on flow boiling heat transfer in microchannels,” International Journal of Multiphase Flow, vol. 35, p. 142–154, February 2009.

[18] ADVANCED COOLING TECHNOLOGIES, “Pumped Two-Phase Fluid Selection,” 2024. [Online]. Available: https://www.1-act.com/thermal-solutions/active/pumped-two-phase/.

[19] H. J. v. Gerner, R. C. Van Benthem and J. v. Es, “Fluid selection for space thermal control systems,” in 44th International Conference on Environmental Systems, 2014.

[20] I. H. Bell, J. Wronski, S. Quoilin and V. Lemort, “Pure and Pseudo-pure Fluid

Thermophysical Property Evaluation and the Open-Source Thermophysical Property Library CoolProp," Industrial & Engineering Chemistry Research, vol. 53, p. 2498–2508, 2014.

A JULIA-BASED COMPUTATIONAL PACKAGE FOR PREDICTING TEMPERATURE-DEPENDENT SPECIFIC HEAT OF ROCKS USING CHEMICAL COMPOSITION

Sushrut Deshpande[1]*, Maarten Vergote[1] , Bart Janssens[1] , Vincent Lemort[2] , Arthur Adriaens[1]

[1] Royal Military Academy, Department of Physics, Brussels, Brussels, Belgium

[2] University of Liege, Thermodynamics Laboratory, Liege, Belgium

** Corresponding Author: sushrut.deshpande@mil.be*

Abstract. Accurate prediction of temperature-dependent specific heat in rocks is essential for advanced thermal modelling in geophysical and geothermal applications. This study introduces a comprehensive computational package developed in Julia, designed to calculate the specific heat of various rocks over a temperature range based on their chemical composition. The package leverages the Shomate scheme to match empirical data, ensuring high accuracy in predictions. It includes an extensive database of specific heat values for a wide array of common rock-forming minerals and compounds, while also allowing users to input custom compounds for tailored analyses.

By integrating thermodynamic principles with empirical models, the package effectively computes specific heat variations with temperature, accommodating diverse rock types. The user-friendly interface supports input of chemical composition data—such as SiO_2, Al_2O_3, Fe_2O_3, and other oxides—enabling geologists and engineers to obtain reliable specific heat estimates across different temperatures. This tool is particularly valuable in scenarios where direct measurement of temperature-dependent specific heat is challenging, offering a robust solution for thermal management in geological formations.

Keywords. Rocks, Specific Heat, Temperature variation, Chemical composition

Nomenclature (if relevant)

c_p	Specific heat capacity (J/kg.K)
T	Temperature (K)
A	Coefficients of Polynomial (-)
m	Mass (kg)
Subscripts	
i	Component of mixture

1 Introduction

Estimating the specific heat capacity of solids and fluids is crucial in various fields, including industrial and geological processes as well as thermal energy storage systems. These processes often involve significant temperature variations, making it essential to have accurate approximations of specific heat values, which change with temperature. Additionally, the sizing of the thermal energy storage system is a critical factor that influences its efficiency and effectiveness. This short paper shows methods and techniques to compute specific heat of rocks with variable chemical composition.

2 Theory

2.1 Database

The database provided by [1] contains a list of common rocks types found in the United States. It mainly consists of the study of Westerly Granite, andesite, peridotite , Rockville granite and Basalt. The study includes chemical compositions of these rock samples as well as coefficients of an approximating polynomial for each chemical composition. The work complies the details of the database into a computational package that approximates the specific heat of rocks with an ability to account for variability of chemical composition.

The database categorizes compounds into Oxide based compounds, Sulphur based compounds , Nitrate and Carbonate compounds. The Julia package currently includes Oxide and Sulphur compounds. The database also provides the chemical compositions of several rock samples which can be approximated by techniques mentioned in the following subsection.

2.2 *Mathematical Modelling*

A widely recognized technique for calculating thermodynamic properties is the Shomate equation[2][3]. commonly used to interpolate the enthalpy of a given material. In this context, the same approach is applied to chemical compounds and rock compositions, with coefficients provided in the database [1]. The specific heat, is calculated using the formula:

$$C_p(T) = A_1 + A_2.T + A_3.T^{-2} + \frac{A_4}{T^{-0.5}} + A_5T^2 \quad (1)$$

The Neumann-Klop rule [3] is used to approximate the specific heat of various chemical compositions. This rule states that the specific heat of a composite object can be estimated as the weighted sum of the specific heats of its individual components, with each component weighted by its mass.

$$C_p = \sum_{i=i}^{k} \frac{C_{p,i} m_i}{M}$$

Where "i" is the i^{th} component of the mixture and m is the corresponding mass of the component in the mixture and M is the total mass of the mixture

3 Usage

3.1 *Installation*

The package is open source and can be installed from Github directly :https://github.com/Sush1090/ThermalRocks.jl

It requires the Julia programming language [4] to be installed. A usage guide is available on the Git repository.

3.2 *Example*

Here is an example of approximating the specific heat of Westerly Granite using its individual chemical compositions. The dominant compounds in the rock sample are selected, representing 98.4% of the rock's total mass.

Table 1 : Chemical Composition of Westerly Granite by mass

CaO	SiO_2	Na_2O	K_2O	Al_2O_3
1.98%	69.2%	4.05%	4.46%	15.42%
Fe_2O_3	FeO	MgO		
1.01%	1.49%	0.76%		

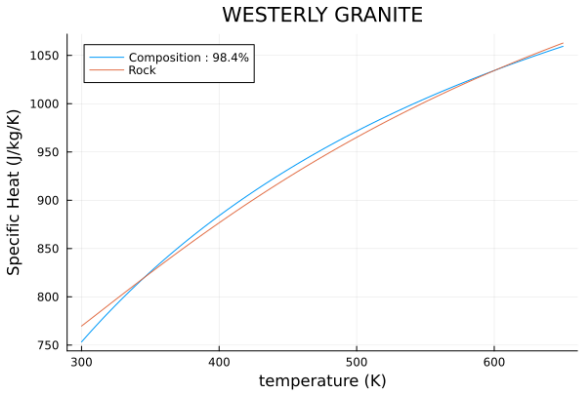


Figure 1: Comparison of composition approximated specific heat with rock sample

The comparison of the approximated specific heat of the rock sample when compared with its individual compositions is shown in Figure 1.It uses about 98% of the total composition by mass of the rock sample. The specific heat computed by the composition closely matches the specific heat of the rock sample.

4 Limitation and possible extensions

The current limitations of the package include a dataset composed solely of sulphur- and oxide based compounds; other compound types are yet to be added. Additionally, the package does not account for phase changes in compositions, which could be significant at extremely high temperatures.

5 Conclusions

In conclusion, *ThermalRocks.jl* offers a practical, open-source tool for estimating the specific heat of various rock types based on their chemical compositions, with particular relevance for high-temperature thermal storage modelling in packed beds. By applying thermodynamic techniques like the Shomate equation and the Neumann-Kopp rule, this package enables precise approximations that account for variations in rock composition, enhancing the accuracy of thermal storage models. With its ease of installation and accessible usage guide, *ThermalRocks.jl* hopes to provide assistance in engineering applications.

Acknowledgement

This work is the part of project: MSP-BCARN-23-05.

References

[1] "Estimating Specific Heat capacity and heat

content of Rocks", Eugene C. Robertson and Bruch S. Hemingway [Online]. Available: https://pubs.usgs.gov/publication/ofr95622.

[2] "Dictionary of Mechanical Engineering (2nd edition)",Marcel Escudier and Tony Atkins, Oxford University Press

[3] Swalin "Thermodynamics of Solids" A Wiley series on the science and technology of materials, 1962

[4] JuliaLang : https://julialang.org/

Unveiling Novel Uncertainty Relations:
The Thermodynamic Canonical Commutation Rules at the Mesoscopic Scale

Giorgio SONNINO*
Université Libre de Bruxelles (ULB), Department Physics, Brussels, Belgium
* *Corresponding Author: giorgio.sonnino@ulb.be*

Abstract. This work investigates thermodynamic processes in small systems within the Onsager region, revealing that quantities such as total entropy production and conjugate thermodynamic variables can be discretized at the mesoscopic scale. By postulating Canonical Commutation Rules (CCRs), thermodynamic measurements are framed as eigenvalue determinations of associated operators. A heuristic nano-gas model, analyzed through classical statistical physics, uncovers the nature of the quantized parameter β, identifying it not as a new fundamental constant but as a minimum value tied to the dimensionless ratio χ, which reflects relative scales between Bohr and molecular levels. This approach provides valuable insights into scattering dynamics, enhancing our understanding of mesoscopic thermodynamics..

Keywords. Mesoscopic Scale, Canonical commutation rules, Thermodynamics of irreversible processes, Onsager's theory, Complex systems.

1 Introduction

Mesoscopic structures have become a vibrant and rapidly evolving research frontier, drawing interest from fields as diverse as physics, chemistry, mineralogy, and the life sciences. The drive toward miniaturization, with devices now reaching nanometer scales, is not only transforming material design but also enhancing our understanding of the fundamental laws governing mesoscopic systems. Building on recent experiments and prior theoretical work, we explore thermodynamic processes in small systems within Onsager's region, starting with a concise overview of Prigogine's key contributions to thermodynamics in this regime. Let us consider a system characterized by n *degrees of advancement* $\xi_1, \cdots, \xi_n$. The deviations of ξ_i from the values $\xi_\mu^{eq.}$, assumed by the degrees of advance when the system is in local equilibrium, are denoted by $\bar{\alpha}_\mu$, that is $\bar{\alpha}_\mu \equiv \xi_\mu - \xi_i^{eq.}$. So, $\bar{\alpha}_\mu$ may represent the fluctuations of the various thermodynamic quantities such as temperature, pressure, etc. According to the principles of thermodynamics, one can introduce for any macroscopic system a state function S, the entropy of the system, which has the following properties. The entropy variation due to the fluctuations reads [1]

$$\Delta S = \Delta_e S + \Delta_I S \quad \text{where} \tag{1}$$
$$\Delta S = \int_{\xi^{eq.}}^{\xi} dS = S(\xi) - S(\xi^{eq.})$$
$$\Delta_e S = \int_{\xi^{eq.}}^{\xi} d_e S \; ; \; \Delta_I S = \int_{\xi^{eq.}}^{\xi} d_I S$$

$\Delta_e S$ denotes the entropy supplied to the system by its surroundings, and $\Delta_I S$ is the entropy produced inside the system, respectively. The second law of thermodynamics states that $d_I S$ must be zero for reversible (or equilibrium) transformations and positive for irreversible system transformations, i.e., $\Delta_I S \geq 0$. The entropy supplied $\Delta_e S$, on the other hand, may be positive, zero, or negative, depending on the interaction of the system with its surroundings. We also have [2]

$$\bar{\sigma} = \frac{\delta}{\delta V}\Big(\frac{d\Delta_I S}{dt}\Big) = \frac{d}{dt}\Big(\frac{\delta \Delta_I S}{\delta V}\Big) = \frac{\partial \Delta_I s}{\partial \bar{\alpha}_\mu}\frac{d\bar{\alpha}_\mu}{dt} = x^\mu j_\mu$$
$$\text{with} \quad j_\mu \equiv \frac{d\bar{\alpha}_\mu}{dt} \tag{2}$$

with j_μ denoting the *thermodynamic fluxes* conjugate to the thermodynamic force x^μ, and δV denotes an infinitesimal spatial volume element occupied by the system. In Eq. (2) we have adopted the Einstein convention of repeated indices. Unless stated otherwise, this convention will also be adopted in the sequel of this manuscript. To work with entropy production strength, which has dimension [Energy]/([Temperature] $\times$ [time]), we adopt the following definition for the thermodynamic forces, the thermodynamic fluxes, and the thermodynamic variables, respectively:

$$X^\mu(\mathbf{r},t) \equiv \sqrt{V}x^\mu;\; J_\mu(\mathbf{r},t) \equiv \sqrt{V}j_\mu;\; \alpha_\mu(\mathbf{r},t) \equiv \sqrt{V}\bar{\alpha}_\mu \tag{3}$$

with $(\mathbf{r}, t)$ denoting the space-time. Eq. (2) links the entropy production strength with the thermodynamic forces and the conjugate fluxes. To obtain the expression for the entropy production strength solely in terms of the thermodynamic forces, it is necessary to relate

the dissipative fluxes to the thermodynamic forces that produce them. These closure relations are called *transport flux-force relations*. For thermodynamic systems in Onsager's region, the most used transport relations are [2]

$$J_\mu = L_{\mu\nu} X^\nu \tag{4}$$

with $L_{\mu\nu} = L_{\nu\nu}$. $L_{\mu\nu}$ is called *Onsager's Matrix* where the entries are the transport coefficients, independent of the thermodynamic forces. Note that to perform calculations, the transport coefficients must be written in a dimensionless form. In terms of the transport coefficients, in Onsager's region, the local entropy production strength can be brought into the form

$$\sigma = L_{\mu\nu} X^\mu X^\nu = V L_{\mu\nu} x^\mu x^\nu = V \bar{\sigma} \tag{5}$$

So, as we wish, σ has dimension:
[Energy]/([Temperature]×[time]) while $\bar{\sigma}$ has dimension [Energy]/([Temperature]×[time]×[Volume]).

• The Space of the Thermodynamic Forces

To continue with the formalism it is necessary to define the space where we can perform calculations. For this, we have to specify two quantities: the *metric tensor* and the *affine connection* [3, 4, 5, 6]. The metric tensor and the affine connection are determined by physics. More specifically, the metric tensor is identified with the symmetric piece of the transport coefficients, and the expression of the affine connection is determined by imposing the validity of the Glansdorff-Prigogine *Universal Criterion of Evolution* [3], [6] (see Fig. 1). For the second law of thermodynamics, the square distance between two infinitely close points in the space of the thermodynamic forces is always a nonnegative quantity. Notice that in the thermodynamic space, the total entropy production σ_T in Onsager's region reads:

$$\sigma_T(t) = \frac{1}{V} \int_V L_{\mu\nu} X^\mu X^\nu \sqrt{L} d^n X \tag{6}$$

with L denoting the determinant of Onsager's matrix and V the volume occupied by the system, respectively.

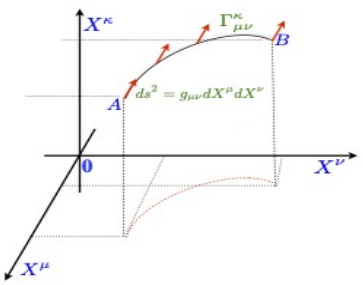


Fig. 1 - The Thermodynamic Space. The thermodynamic forces span the space, the metric tensor is identified with the symmetric piece of the transport coefficients, and the expression of the affine connection is determined by the *Universal Criterion of Evolution.*

2 Quantization of the Entropy Production Strength

• A Heuristic Approach

One of the main objectives of the Brussels School of Thermodynamics, founded by Théphile De Donder and Ilya Prigogine, was to investigate systems on a mesoscopic scale to discover the fundamental laws governing them. We start our analysis with the following (heuristic) observation. A *quasi-localized* disturbance of entropy production can be obtained using a linear superposition of modes with close mode numbers. So, if the system is subject to n independent thermodynamic forces, a *local disturbance* of entropy production strength can be represented as a superposition of plane waves with the generic wave number $\mathbf{K}$ compatible with periodicity conditions:

$$\sigma(\mathbf{X}, t) = \frac{1}{(2\pi)^n} \int_{-\infty}^{+\infty} \left(\sigma_{\mathbf{K}} e^{i(\mathbf{K}\cdot\mathbf{X} - \omega_{\mathbf{K}} t)} + \sigma^\star_{\mathbf{K}} e^{-i(\mathbf{K}\cdot\mathbf{X} - \omega_{\mathbf{K}} t)} \right) d\mathbf{K} \tag{7}$$

Notice that the modes are in the space of thermodynamic forces (and not in the ordinary space). As known, Fourier's theorem requires (see Fig. 2):

$$\Delta t \Delta\omega \geq 1 \quad ; \quad \Delta K_\mu \Delta X^\mu \geq 1 \tag{8}$$
(no summation convention on μ; $\mu = 1, \cdots, n$)

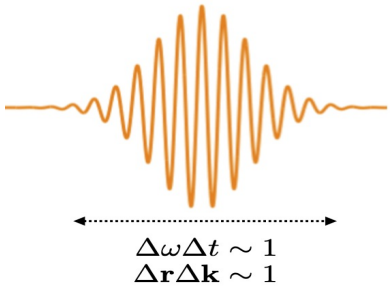


Fig. 2 - Wavpacket. A wavepacket is an infinite set of waves with different wave numbers that interfere constructively in a small region and destructively in the rest of space. Fourier's theorem establishes the general property of the wavepackets: $\Delta t \Delta\omega \geq 1$ or $\Delta \mathbf{r} \Delta \mathbf{k} \geq 1$ Recent experimental results lead to postulate the heuristic idea where, on a mesoscopic scale, in the space of the thermodynamic forces

the entropy production strength is proportional to the frequency and the thermodynamic variable α_μ, conjugate to the thermodynamic forces X^μ, is proportional to the wave-vector K_μ i.e.,

$$\sigma = \not{k}_B\omega \ ; \ \alpha_{\mu,\mathbf{K}} = \not{k}_B\mathbf{K}_\mu \text{ with } \not{k}_B \equiv \beta k_B \qquad (9)$$

with $\not{k}_B$ denoting Boltzmann's constant k_B times a pure number, say β, undetermined at this stage. A combination of Eq. (8) with Eq. (9) yields

$$\begin{aligned} &\Delta t\Delta\sigma \geq \not{k}_B \qquad (10)\\ &\Delta\alpha_\mu\Delta X^\mu \geq \not{k}_B \quad \forall\mu \\ &\text{(no summation convention on } \mu;\ \mu = 1,\cdots,n) \end{aligned}$$

These inequalities establish a fundamental limit on the precision with which certain pairs of physical quantities, such as entropy production rate and time or thermodynamic force and its corresponding thermodynamic variable, can be predicted from initial conditions. In other words, we cannot precisely determine both the entropy production rate of a system and time simultaneously; the more accurately we know the system's entropy production, the less accurately we know the time, and vice versa. Similarly, there is an uncertainty relationship between a thermodynamic force and its corresponding thermodynamic variable. The pairs of variables (t,σ) and (α_μ, X^μ) may be called *canonically conjugate* (in analogy with the quantum mechanics' terminology).

• Discretization of the Total Entropy Production Strength in Onsager's Region

We are now faced with two issues: i) The *heuristic intuitions* expressed in the previous subsection must be supported by a rigorous formalism, and ii) We are dealing with many entities with infinite degrees of freedom as these entities are continually being produced and absorbed. The appropriate mathematical tool to treat these problems is provided by the formalism of the *second quantization* (SQ) largely used in quantum field theory. The second quantization is a mathematical algorithm for dealing with a large assembly of identical entities [7]. This mathematical algorithm is based on introducing canonical commutation rules (CCRs) where the physical quantities are *promoted* to operators. Hence, by the SQ-formalism, we have to promote the single variables σ and t, and X^μ and α_μ to *operators*, which act on some state space of the system, separately, imposing a *bind* between them so that their products behave *as we wish* (see also [8]). At the mesoscopic scale, we have to write:

$$\begin{aligned} &[t,\sigma] = i\frac{\not{k}_B}{2} \qquad (11)\\ &[\alpha_{\mu,\mathbf{K}}, X^\nu_{\mathbf{K}'}] = i\frac{\not{k}_B}{2}\delta_{\mu\nu}\delta_{\mathbf{K}\mathbf{K}'} \qquad \text{with} \quad \not{k}_B = \beta k_B \end{aligned}$$

with $[\cdots]$ denoting the *commutator* between two operators: $[A,B] = AB - BA$ and $\delta_{\mu\nu}$ the Kronecker delta, respectively. In [9] we can find recent experiments where the entropy production in non-equilibrium systems has been measured. To the best of our knowledge, [9] provides the most accurate value of the lowest limit of this constant that appeared up to now in the literature. In [9] we find several examples of experimental traces for the tip position of different mechano-sensory hair bundles as a function of time. The authors estimated the local irreversibility measure obtained from single 30 *sec.* recordings of the oscillations shown in these examples. The sampling rate was $\omega = 2.5kHz$. From these experiments, we can estimate (albeit approximately) the numerical value of β. We find $\beta \sim 1.2\times10^{-8}$ so, $\not{k}_B \sim 1.6\times10^{-31}\ J/K$. In the forthcoming section, we shall provide a (rough) estimation of constant β for a quasi-ideal gas. We shall see that, in this case, β does not appear to be a new fundamental constant but corresponds to the minimum value.
The *total entropy production strength* reads

$$\sigma_T(t) = \frac{1}{V}\int_V \sigma(\mathbf{X},t)\sqrt{L}d^nX = \frac{1}{V}\int_V L_{\mu\nu}X^\mu X^\nu\sqrt{L}d^nX \qquad (12)$$

The local entropy production strength can be split into two contributions

$$\sigma(\mathbf{X},t) = L_{\mu\nu}X^\mu X^\nu = \frac{1}{2}L_{\mu\nu}X^\mu X^\nu + \frac{1}{2}L^{\mu\nu}J_\mu J_\nu \qquad (13)$$

In the space of the thermodynamic forces, the Fourier expansion in a finite box of volume V yields [8]

$$\begin{aligned} \sigma_T(t) &= 2\sum_{\mu=1}^{n}\sum_{\mathbf{K}}\left(\mid X^\mu_{\mathbf{K}}(t)\mid^2 + \mid J_{\mu,\mathbf{K}}(t)\mid^2\right) \qquad (14)\\ &= 2\sum_{\mu=1}^{n}\sum_{\mathbf{K}}\left(\mid X^\mu_{\mathbf{K}}(t)\mid^2 + \omega^2_{\mathbf{K}}\mid \alpha_{\mu,\mathbf{K}}(t)\mid^2\right) \end{aligned}$$

This expression is identical to the Hamiltonian of a harmonic oscillator if we set the value of the *mass* $= 4$ and we identify the following terms: *position*$\rightarrow\ \alpha_{\mu,K}$, *momemtum*$\rightarrow\ 2X^\mu_K$, and *frequency*$\rightarrow\ \omega_K$ (see, for example, [10]). So, we first define two new dimensionless operators $\tilde{X}^\mu_K$ and $\tilde{\alpha}_{\mu,K}$, as follows:

$$\tilde{X}^\mu_{\mathbf{K}} = \sqrt{\frac{2}{\not{k}_B\omega_{\mathbf{K}}}}X^\mu_{\mathbf{K}} \ \ ; \ \ \tilde{\alpha}_{\mu,\mathbf{K}} = \sqrt{\frac{2\omega_{\mathbf{K}}}{\not{k}_B}}\alpha_{\mu,\mathbf{K}} \qquad (15)$$

In terms of these new variables, the expression for $\sigma_T(t)$ reads

$$\sigma_T(t) = \sum_{\mu=1}^{n} \sum_{\mathbf{K}} \not{k}_B \omega_{\mathbf{K}} \left(\mid \tilde{X}^{\mu}_{\mathbf{K}} \mid^2 + \mid \tilde{\alpha}_{\mu,\mathbf{K}} \mid^2 \right) \quad (16)$$

As for the case of the harmonic oscillator, we have to assume the validity of the following *Canonical Commutation Rules* (CCRs):

$$[\tilde{\alpha}_{\mu,\mathbf{K}}, \tilde{X}^{\nu}_{\mathbf{K}'}] = i\delta_{\mu\nu}\delta_{\mathbf{K}\mathbf{K}'} \Rightarrow [\alpha_{\mu,\mathbf{K}}, X^{\nu}_{\mathbf{K}'}] = i\frac{\not{k}_B}{2}\delta_{\mu\nu}\delta_{\mathbf{K}\mathbf{K}'} \quad (17)$$

The two operators of *creation* "$\mathrm{a}^{(\mu)+}_{\mathbf{K}}$änd *destruction* "$\mathrm{a}^{(\mu)}_{\mathbf{K}}$"can be introduced and defined as usual (see, for example, [10]):

$$\mathrm{a}^{(\mu)}_{\mathbf{K}} = \frac{1}{\sqrt{2}} \left(\tilde{\alpha}_{\mu,\mathbf{K}} + i\tilde{X}^{\mu}_{\mathbf{K}} \right); \ \mathrm{a}^{(\mu)+}_{\mathbf{K}} = \frac{1}{\sqrt{2}} \left(\tilde{\alpha}_{\mu,\mathbf{K}} - i\tilde{X}^{\mu}_{\mathbf{K}} \right)$$
$$[\mathrm{a}^{(\mu)}_{\mathbf{K}}, \mathrm{a}^{(\mu')+}_{\mathbf{K}'}] = \delta_{\mu\mu'}\delta_{\mathbf{K}\mathbf{K}'} \quad (18)$$

We finally get the discretization of the total entropy production strength in Onsager's region

$$\boldsymbol{\sigma}_T(t) = \sum_{\mu=1}^{n} \sum_{\mathbf{K}} \not{k}_B \omega_{\mathbf{K}} \left(\mathbf{n}^{(\mu)}_{\mathbf{K}} + \frac{1}{2} \right) \quad (19)$$

where the *number operator* $\mathbf{n}^{(\mu)}_{\mathbf{K}} \equiv \mathrm{a}^{(\mu)+}_{\mathbf{K}} \mathrm{a}^{(\mu)}_{\mathbf{K}}$ has been introduced. To sum up, *in the space of the thermodynamic forces the total entropy production strength behaves as the sum of "*$\mathbf{K}$*"(discretized) independent one-dimensional harmonic oscillators, each oscillating with frequency* $\omega_{\mathbf{K}}$. The constant contribution

$$\sigma_0 = \frac{1}{2} \sum_{\mu=1}^{n} \sum_{\mathbf{K}} \not{k}_B \omega_{\mathbf{K}} \quad (20)$$

is the total entropy production for a macroscopic system generated by very small fluctuations around the thermodynamic equilibrium. To analyze this term we consider the Einstein-Prigogine theory of equilibrium fluctuations. In this theory, the probability P of finding a state in which the values of α_μ lie between α_μ and $d\alpha_\mu$ is [1]

$$P d\alpha_1 \cdots d\alpha_n = P_0 \exp(-\Delta_I S/k_B) d\alpha_1 \cdots d\alpha_n \quad (21)$$

where P_0 ensures normalization to unity. Expression (21) is only valid for small spontaneous fluctuations around the thermodynamic equilibrium and not for systematic deviations from equilibrium. Prigogine showed the validity of the following important result: whatever the thermodynamic system (hydrodynamic, chemical, etc.), due to spontaneous equilibrium fluctuations, the average entropic production is [1]

$$\overline{\Delta_I S} = \int \cdots \int \Delta_I S P d\alpha_1 \cdots d\alpha_n = \frac{n}{2} k_B \quad (22)$$

with n denoting the number of the independent thermodynamic forces. Now we have to calculate the eigenvalues of the $\mathbf{\Delta_I S}$ operator by using the canonical commutation rules. Detailed calculations for getting the expression for the $\mathbf{\Delta_I S}$ operator can be found in [8]. Introducing the operators of creation and destruction $\mathrm{a}^{(\mu)+}_{\mathbf{K}}$ and $\mathrm{a}^{(\mu)}_{\mathbf{K}}$, the number operator $\mathbf{n}^{(\mu)}_{\mathbf{K}}$, and Prigogine's theorem (22), we get the following expression for the entropy production operator:

$$\mathbf{\Delta_I S} = \sum_{\mu=1}^{n} \sum_{\mathbf{K}} \not{k}_B \mathbf{n}^{(\mu)}_{\mathbf{K}} + \frac{n}{2} k_B \quad (23)$$

having discrete positive eigenvalues

$$\Delta_I S = \sum_{\mu=1}^{n} \sum_{\mathbf{K}} \not{k}_B n^{(\mu)}_{\mathbf{K}} + \frac{n}{2} k_B \geq 0 \quad (24)$$

in agreement with the second law of thermodynamics.

3 A Heuristic Model for Determining β for a Quasi-Ideal Gas

We aim to investigate the physical origin of constant β entering the CCRs. We start with the simplest assumption: *by a statistical model for nano-gases we can derive the expression for* β. To this end, we adopt a (very) simple heuristic model for nano-gas with the following assumptions

1) The limit case is reached when the distance b between the molecules of the nano-gas is (approximately) twice the Bohr radius ($b = 2r_B$).
2) The spherical-molecule model is adopted. Beyond the Heisenberg principle, classical statistical physics applies.

Fig. 3 shows the classical spherical model to represent molecules in nano-gases. In our heuristic model, the impact parameter b is twice Bohr's radius and all the molecules of the nano-gas are equal (so, $r'_M = r_M$ with r_M denoting the molecular radius). The volume occupied by a molecule is $V_M = 4/3\pi r^3_M$.

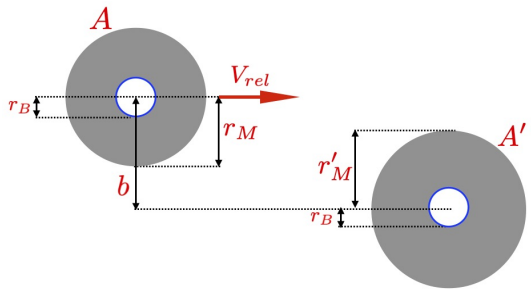


Fig. 3 - Collision between two molecules of a quasi-ideal nano-gas. The impact parameter b is the distance between the two centers of the molecules. In our heuristic model, the molecules are spherical and identical. The model assumes that if $b \leq 2r_B$ the two molecules collide, they *feel* the Heisenberg principle. The limit case is reached when the distance between the two molecules is $b = 2r_B$ and the close packing fraction for spheres is reached (i.e., $n = \pi/(3\sqrt{2})V_M^{-1}$).

At thermal equilibrium, the (classical) uncertainty related to the measurement of the entropy production strength σ reads [11]:

$$\Delta\sigma \sim \frac{\Delta E}{T\tau} \tag{25}$$

with τ denoting the collision time, T the temperature of the system, and ΔE the energy uncertainty of the classical system, respectively. In [11] we can find a rough estimation of β:

$$\beta = \frac{3\pi}{4}\alpha\left(\frac{V_B}{V_M}\right)\left(\frac{m_e}{m_M}\right) = \frac{3\pi}{4}\alpha\chi \tag{26}$$

with m_e denoting the electron mass, c the speed of light, and α the fine-structure constant, respectively. Note that although the mass of the electron appears in Eq. (26) it plays no role since the product αm_e is independent of the mass of the electron. However, it is important from the physical point of view to put this quantity in evidence. Here, V_B/V_M represents the relative size of the Bohr volume (volume of an atom based on the Bohr radius) to the volume occupied by a single molecule and the ratio m_e/m_M compares the mass of an electron to the mass of a molecule composing the material, respectively. Parameter $\chi \equiv (V_B m_e)/(V_M m_M)$ denotes the *Bohr-Molecular Ratio* (BMR). By plugging the values $\alpha \simeq 1/137$, $V_B/V_M \sim 10^{-3}$, and $m_e/m_M \sim m_e/m_p = 0.5 \times 10^{-3}$ into Eq. (26) we get $\beta_{Theor.} \sim 0.9 \times 10^{-8}$ which aligns with the experimental value found in [9]: $\beta_{Exp.} \sim 1.2 \times 10^{-8}$.

4 Conclusions

The *Brussels School of Thermodynamics* sought to uncover fundamental laws governing mesoscopic systems. Building on this vision and inspired by recent experiments, this work establishes Canonical Commutation Rules (CCRs) for the mesoscopic scale. These rules reveal that as we approach the mesoscopic level, the simultaneous measurement of canonically conjugate variables, such as entropy production strength σ and time t, becomes increasingly uncertain, satisfying the relation $Deltat\Delta\sigma \geq \not{k}_B/2$. We demonstrate that key thermodynamic quantities, such as total entropy production, can be discretized at the mesoscopic scale. The ultraviolet divergence problem is resolved by applying the correspondence principle to Einstein-Prigogine fluctuation theory in the macroscopic limit. To address whether β is a universal constant and whether it represents the lowest limit, we developed a heuristic model for a quasi-ideal nano-gas. This model captures mesoscopic effects, such as quantum fluctuations, while adhering to classical statistical physics. Our findings indicate that β is not universal but does represent the minimum quantized value. Notably, the theoretical value of β closely aligns with experimental results reported in [9], validating the robustness of our approach.

References

[1] I. Prigogine 1954 *Thermodynamics of Irreversible processes*, (John Wiley & Sons).

[2] S.R. De Groot and P. Mazur *Non-Equilibrium Thermodynamics*, (Dover Publ., Inc., New York, 1984).

[3] G. Sonnino, Phys. Rev. E, **79**, 051126 (2009).

[4] G. Sonnino *et al.*, Phys. Rev. E **94**, 042103 (2016).

[5] G. Sonnino, American Institute of Physics (AIP) Conference Proceedings, **1853**(1), (2019).

[6] G. Sonnino, Springer Nature, **208**, 71, (2022).

[7] C. M. Becchi, Scholarpedia, **5**(6), 7902 (2010).

[8] G. Sonnino, Physica E: Low-dimensional Systems and Nanostructures, **164**, 116058 (2024).

[9] E. Roldán, *et al.*, New J. Phys., **23**, 083013 (2021).

[10] S. Weinberg, *The Quantum Theory of Fields, Volume 1: Foundations*, Cambridge Univ. Press (1995).

[11] G. Sonnino, Entropy 2024, **26**, 1011 (2024). https://arxiv.org/pdf/2406.13435 (2024).

STATE-OF-THE-ART IN WATER-STEAM CYCLES

Jean Snoeck [1]*

[1] XRGY Consulting, Brussels, Belgium

* *Corresponding Author: jean.snoeck@xrgyconsulting.com*

Abstract. The paper first reminds the development of the steam engine technology before addressing the exergy concept and two major applications.
The first application concerns the bottom steam cycle of an advanced Combined Cycle Gas Turbine (CCGT). Thanks to the progress made in gas turbines and in Heat Recovery Steam Generators (HRSG), the plant efficiencies exceed 60% today. Because other papers are devoted to the gas turbines, this one will focus on the performances of the steam cycle applying the exergy analysis.
The second application is relative to the nuclear power plants where particular attention must be paid to the two-phase character of the flow to mitigate the detrimental effects of the liquid phase from both the thermodynamic and mechanical points of view. That section will describe the improvements in blade design and the different measures to mitigate the negative effects of water droplets and films.

Keywords. Steam cycle, Combined cycle gas turbine, Nuclear power plant, Steam turbine.

Nomenclature

c	Absolute velocity (m/s)
e	Specific exergy (J/kg)
h	Specific enthalpy (J/kg)
$\dot{m}$	Mass flow (kg/s)
s	Specific entropy (kJ/kg.K)
T	Temperature (K)
w	Relative velocity (m/s)
y	Wetness rate (-)

Special characters

α	Parameter of the Baumann's rule (-)
β	Parameter of the Baumann's rule (-)
ε	Heat loss (-)
η	Efficiency (-)

Subscripts

dry	Relative to dry conditions
m	Logarithmic mean value
wet	Relative to wet conditions
I	Relative to the hot side of an exchanger
II	Relative to the cold side of an exchanger

1 Introduction [1]

Steam was used as working fluid well before the publication of Sadi Carnot's book.
In 1690 a French physicist, Denis Papin, built a piston steam engine but the first industrial application was developed by the English engineer Thomas Savery in 1698 for pumping water out of the mines. Unfortunately, the steam pump was inefficient for different reasons. The technology improved in 1712 with a first condensing steam engine of 4 kw built by Thomas Newcomer. The next step was set by James Watt in 1765 who proposed an industrial steam engine with a separate condenser to generate 11 kW mechanical power.
In the same period, an intensive scientific activity promoted the development of thermodynamics under the leadership of Anders Celsius (1742), Sir Benjamin Thomson (1789), Lazare Carnot (1793), his son Sadi Carnot (1824), James Joule (1843), Lord William Thomson (1848) and Rudolf Clausius (1850).
Significant improvements were proposed afterwards to the steam cycle with the superheat (Gustave Hirn, 1855) and the definition of the base steam cycle (William Rankine, 1856).
The first one-stage action steam turbine was built by Gustaf de Laval in 1883 and in the year after Sir Charles Parsons proposed the first multiple stage reaction machine.
The steam reheat was introduced after the second

World War and the first supercritical cycle with double reheat was operated in a 325 MW plant at Eddystone (USA) from 1959 to 1976 with the following thermodynamic features: 360 bar/650 °C, 72 bar/565 °C, and 18 bar/565 °C.
The first combined cycle was proposed by Emmet in 1913 with a top mercury vapor cycle and a bottom steam cycle. A few units were built by General Electric from 1928 but, besides the safety issues relative to mercury, the technology became not competitive because of the continuous improvements of the water steam cycles thanks to higher pressures and temperatures and multiple extractions.
Finally, the today well-known Combined Cycle Gas Turbine (CCGT) was proposed in December 1960 by C. Seippel and R. Bereuter in the Brown-Boveri revue.
Because the present paper will address the possible improvements of the steam cycle, it is worthwhile to remind the concept of exergy introduced for the first time in 1889 by Louis-Georges Gouy as "the useful enthalpy" before being clearly defined by Zoran Rant in 1952.

2 Thermodynamic reminders

Energy must always be associated with a quality index. The same quantity of energy can be transported by different vectors such as electricity, solar radiation, nuclear fission, fossil fuel, gas/vapor flow, water fall… but not all those energy vectors will deliver the same amount of mechanical work. The differences can be quantified using a thermodynamic variable called "exergy" which defines the "maximum useful work possible during a process which brings the system into equilibrium with the surroundings." Moreover, exergy allows analysing the processes in details and identifying the weak contributors in the energy conversion chain. The exergy e is defined from the enthalpy h and the entropy s under the form [1]:

$$e = (h - h_0) - T_0(s - s_0) \quad (1)$$

where the subscript 0 refers to the surrounding conditions.
Exergy never appears, always decreases, and disappears when equilibrium is achieved with the surroundings. It can be applied to all processes involved in power plants such as combustion, compression, expansion, heat exchange, fluid mixing. A detailed survey of applications can be found in [2] but within the context of this paper three particular cases only will be reminded. The exergy E of a heat source is the product of the energy content Q with the Carnot efficiency:

$$E = Q\left(1 - \frac{T_0}{T}\right) \quad (2)$$

When the primary energy source is neither nuclear nor chemical but a heat source, the exergy is the only indicator to assess the quality of a thermodynamic cycle. This applies particularly to the Organic Rankine Cycles where the conventional energy efficiency leads to not representative low values.
The exergy efficiency of a heat exchanger is the ratio of the exergy gain on the cold side to the exergy loss on the hot side. It can be written as:

$$\eta_{transex} = \frac{\Delta \dot{E}_{II}}{-\Delta \dot{E}_I} = \frac{\dot{m}_{II}(e_{2II} - e_{2I})}{\dot{m}_i(e_{1I} - e_{2I})} \quad (3)$$

where the subscripts I and II refer respectively to the hot and cold sides. Equation (3) can be transformed into the form:

$$\eta_{transex} = (1 - \epsilon)\left(\frac{T_{IIm} - T_0}{T_{IIm}}\right)\left(\frac{T_{Im}}{T_{Im} - T_0}\right) \quad (4)$$

which shows that even with no heat losses the exergy efficiency is always lower than 100% because the quality index of the transferred energy degrades.
The exergy expansion efficiency of a steam turbine can be computed from the incoming and outgoing steam fluxes under the form:

$$\eta_{expex} = \frac{\dot{m}_{in}h_{in} - \sum_i \dot{m}_{out,i}h_{out,i}}{\dot{m}_{in}e_{in} - \sum_i \dot{m}_{out,i}e_{out,i}} \quad (5)$$

where the subscript "in" refers to the inlet conditions and the subscript "out,i" to the fluxes leaving the machine towards the feedwater heaters and the condenser.

3 Steam technology in combined cycle

The today CCGTs are the best fossil-fired power plants with efficiencies higher than 60%. Those performances result from combining advanced gas turbines with optimized bottom steam cycles where the design of the Heat Recovery Steam Generator (HRSG) plays a key role. Because the gas turbine technology has already been addressed in other papers, this presentation will focus on the HL-class power plants like the ones currently being built in Belgium at Flémalle end Seraing.
The HL-CCGT are designed to deliver around 890 MW gross power with an efficiency of the order of 64% with a three-pressure level steam cycle defined as follows at the turbine flanges:
HP level: 158 bar, 601 °C, 161.3 kg/s,
IP level: 38.6 bar, 603 °C, 165.9 kg/s,
LP level: 4.9 bar, 301 °C, 184.2 kg/s.
The HL-class combined cycle has been computed applying the Thermoflow32 © database for the Siemens HL-machine and typical boundary conditions and data for the HRSG [4] and for the

condenser.
The water/steam cycle is first analysed from the exergy point of view assuming the heat source being the exit conditions of the gas turbine and the cold sink being the condenser. The results are drawn in Figure 2. The exergy losses are the highest in the HRSG and the lowest in the condenser and at the stack. The value relative to the steam turbine is the gross power. A detailed exergy analysis of a steam turbine will rather be performed in the section devoted to the nuclear units which are more complex because of the reheat and the multiple extractions. The most important component in the thermodynamic cycle is the HRSG which transfers the waste heat to the working fluid of the bottom cycle. Therefore, it is worthwhile to analyse the performance of each heat exchanger to identify the possible ways to improvement.
The HRGSs for this kind of cycle are the biggest ever built for a CCGT. John Cockerill article over Flémalle refers to 27000 tubes and to a casing which is 73 m long, 25 m wide and about 30 m high [4]. The temperature profile computed with the Thermoflow32 © model is drawn in Figure 3 and the corresponding exergy diagram in Figure 4. The heat losses have been assumed to 5%. All heat exchangers achieve exergy efficiency close to or above 85%, but the first preheater (PREH1) which is equipped with a recirculation loop to control the inlet temperature of the heat exchanger and prevent condensation on the gas side. It can be shown that recirculation degrades the exergy efficiency because hot feedwater is mixed with cold condensate.

4 Steam technology in nuclear PWR plants

4.1 Water steam cycle

The thermodynamic conditions at the turbine inlet are heavily impacted by the steam generation process in the nuclear island which leads to dry saturated conditions. All details of the exergy analysis from the fuel rod down to the condenser are reported in [2] for a typical 1000 MW-class unit and the global exergy balance is reported in Figure 5.
The highest exergy losses take place in the reactor (52.09%) because of the exergy degradation in heat generation due to the poor pellet conductivity and the poor heat transfer in the pellet/clad gap. Moreover, because the heat is removed from the core with water pressurized at 150 bar, this leads to poor thermodynamic conditions at the turbine inlet. Saturated steam is generated at pressures ranging typically between 58 and 70 bar. The saturated steam first expands in the high-pressure turbine before being dried out, reheated, and injected into the low-pressure turbine, as shown in the thermodynamic cycle reproduced with the software suite Thermoflow32© (Figure 6) from the heat and mass balance issued by the manufacturer [5].
The steam turbine is modelled with 12 groups of stages of which groups 1 to 4 belong to the HP machine, groups 5 to 8 to the left LP machine and groups 9 to 12 to the right LP machine. The turbine is equipped with two condensers connected in series on the cooling water side. Hence the condenser pressures are respectively equal to 0.053 and 0.074 bar and the two LP turbines are not symmetric because of different extraction pressures. The respective expansion lines are drawn in Figure 7. The discontinuities along the expansion lines are due to the moisture removal which results in enthalpy increases at constant pressure.
The isentropic and exergetic efficiencies have been computed from the heat and mass balance generated by the code. The values relative to the turbines and to the groups of stages are drawn in Figures 8 and 9. It is worthwhile to underline that the exergetic efficiencies are slightly higher than the isentropic efficiencies confirming the quality of the design. Attention is also drawn on the lower values of the penultimate groups 7 and 11 due to high local wetness rates. The situation improves in the exit groups thanks to moisture extraction slots on fixed blade surfaces. This point will be discussed in the next section.

4.2 Steam turbine technology

The expansion efficiencies have considerably improved over the years thanks to advanced design methods and technological developments.
The blade profile has been continuously revised to reduce the losses and the sensitivity to incidence angles. CFD programs allow full three- dimensional blade design to better control the radial and tangential equilibrium of the flow path in a wide range of operating conditions (Figure 10).
Specific developments were also required for nuclear steam turbine because of the two-phase character of the steam. Tiny droplets with nanometric diameters appear during the expansion in metastable conditions when the steam still behaves as a gas while the thermodynamic conditions correspond to the two-phase region of the Mollier diagram. This phenomenon called nucleation takes place in

subcooled vapor and initiates the rapid growth of very numerous droplets through heat and mass exchanges with the surrounding vapor. In supersonic flow conditions, an aerothermal shock can occur leading to extra losses. Different forms of the well-known Baumann's rule:

$$\eta_{wet} = \eta_{dry}\left(\alpha - 0.5\,\beta\left(y_{in} + y_{out}\right)\right) \quad (6)$$

have been proposed to correct the expansion efficiency in dry conditions from the wetness rates at the inlet (y_{in}) and at the outlet (y_{out}) of the group of stages.

The droplets coalesce and settle on the blade surfaces to form water films which leave the trailing edge at velocities (c_{water}) much lower than the steam velocity (c_{steam}) (Figure 11). Hence the velocity triangles of steam and water are quite different downstream of the fixed blades and the droplets hit the suction surface of the moving blades causing local erosion. To mitigate this effect, the blade surface is locally reinforced applying flame or laser hardening.

Preventive measures are also applied to remove as much water as possible from the flow path. The water films on the rotating blades are centrifugated to the casing where they are collected in extraction slots and dumped into the feedwater heaters or the condenser [6]. This process is enhanced with an appropriate design of the trailing edges and sufficiently large gaps between the fixed and the rotating blades. A complementary and very efficient measure consists of slots in hollow fixed blades. (Figure 12). High quality sealings are also of utmost importance to achieve high performances in a steam turbine because excessive leaks can result in several MW loss. This component can be heavily damaged by vibrations originated from an unstable bearing behaviour. But those mechanical issues are beyond the scope of this paper and will not be addressed here. Conclusively, the successful design of a steam turbine depends not only on aerothermodynamic criteria but also on many other ones coming under mechanical resistance, rotor dynamics, instrumentation, and control.

5 Conclusion

Impressive progress has been made in the steam cycle technology since the very first steam engines. This was possible thanks to advanced design methods based on thermodynamics and aerodynamics and to the development of new materials sustaining high temperatures and pressures: in CCGTs, the HP steam temperature achieves today 600 °C and the flue gas exit temperature can be lowered below 70 °C. But in such operating conditions, the sulphur content of the natural gas must be carefully monitored to prevent tube corrosion.

On the other side, many efforts have been made to mitigate the detrimental effects of wet steam in nuclear steam turbines: these ones rely nowadays on different technological solutions to improve the efficiency and prevent blade erosion. This is a unique opportunity to retrofit the existing machines and to increase the generation capacity with no nuclear power uprate.

In new PWR plants, two-stage reheaters are implemented where the first stage is fed with steam extracted from the HP turbine. This reduces the flow supplied by the steam generators and increase the gross power of the machine, hence the plant efficiency.

References

1. Joseph Martin et Pierre Wauters : Installations Thermiques Motrices. Analyse énergétique et exergétique. Deuxième édition. Presses universitaires de Louvain, 2011
2. Jean Snoeck: Exergy. From the Thermodynamic Concept to the Applications. Revision 1. September 22, 2018. Exergy_180922.pdf - Google Drive
3. Siemens document : SGT5-9000HL Heavy-duty gas turbine (50 Hz) (siemens-energy.com) 210923-HL-ClassFactSheet-05-pdf_Original_pdf.
4. John Cockerill: https://www.modernpowersystems.com/analysis/huge-hrsg-for-belgiums-latest-combined-cycle-project-10858319/?cf-view
5. Siemens: Heat Flow Diagram No S312-40889 a, New LP Turbine 100% Thermal Load. Mülheim, 19.12.2006.
6. Siemens: Modernization and Upgrades for Utility Steam Turbines (siemens-energy.com)

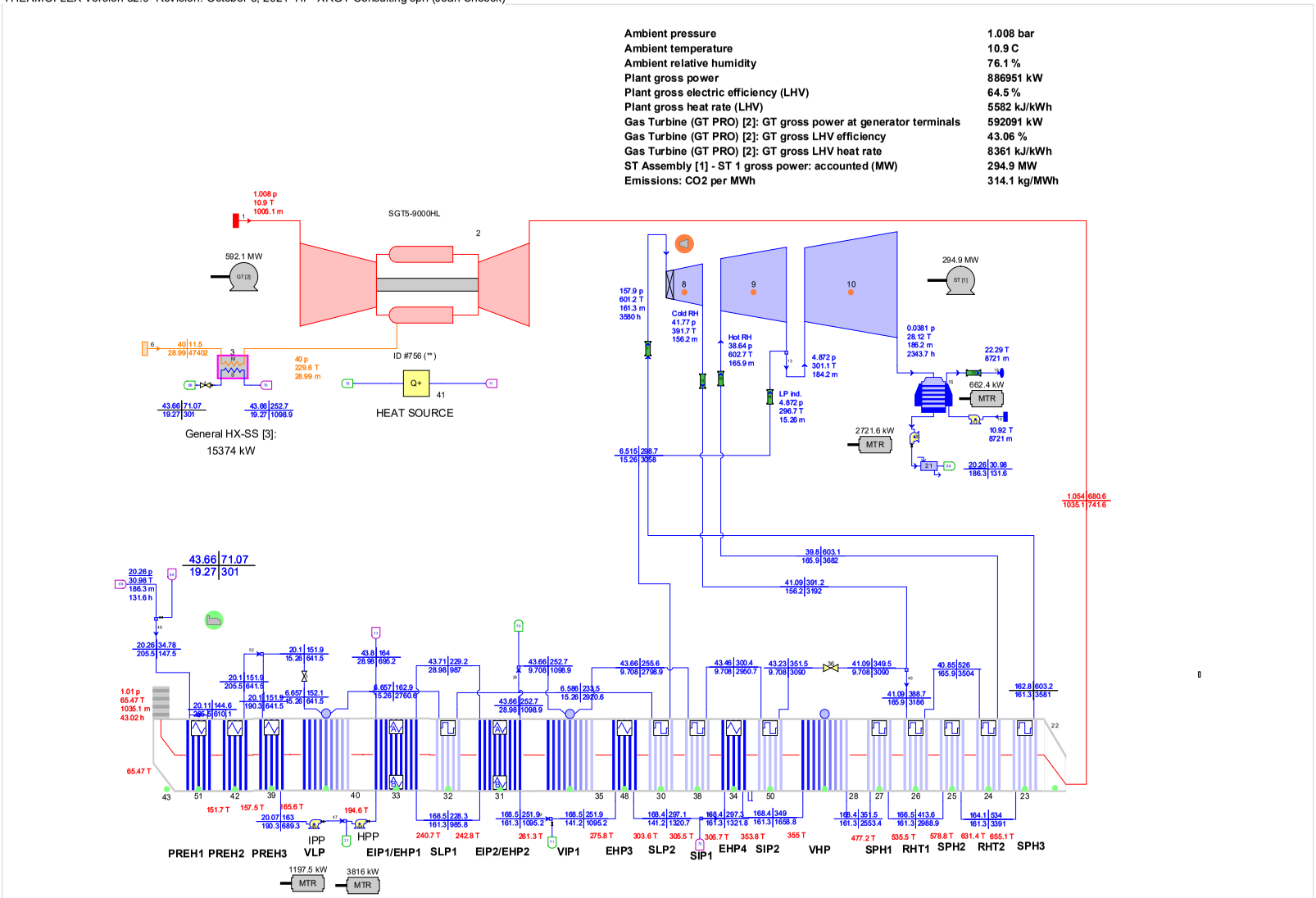


Figure 1: Combined cycle of a HL-class power plant

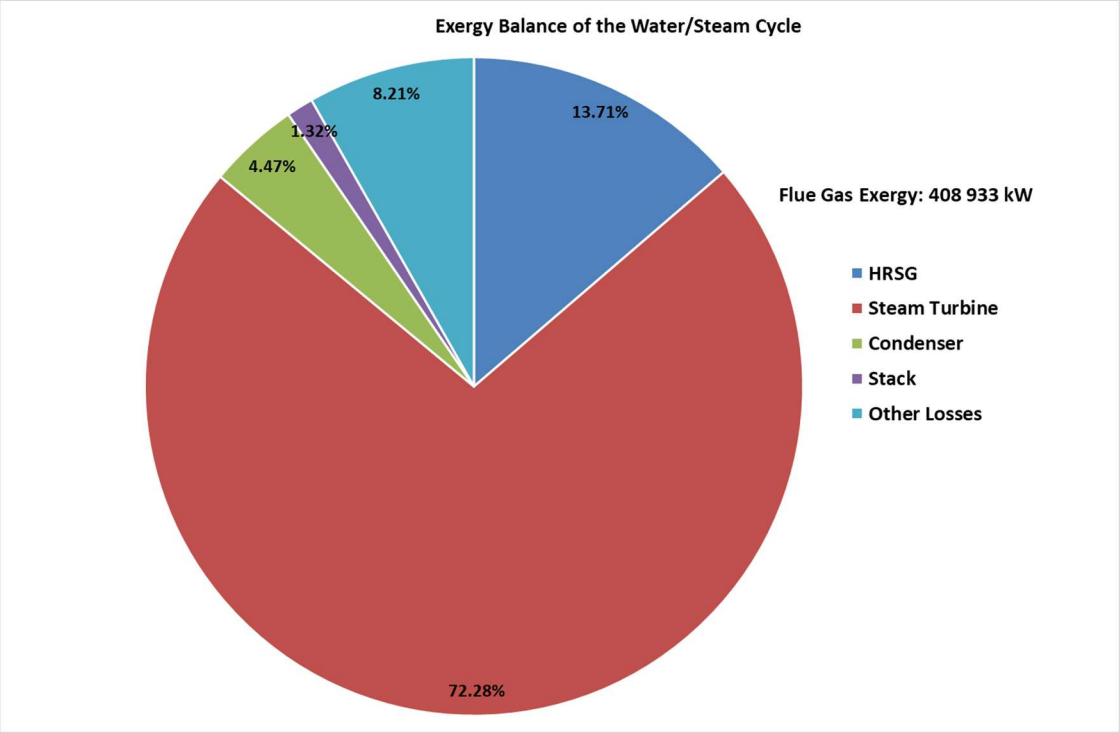


Figure 2: Exergy balance of the water/steam cycle.

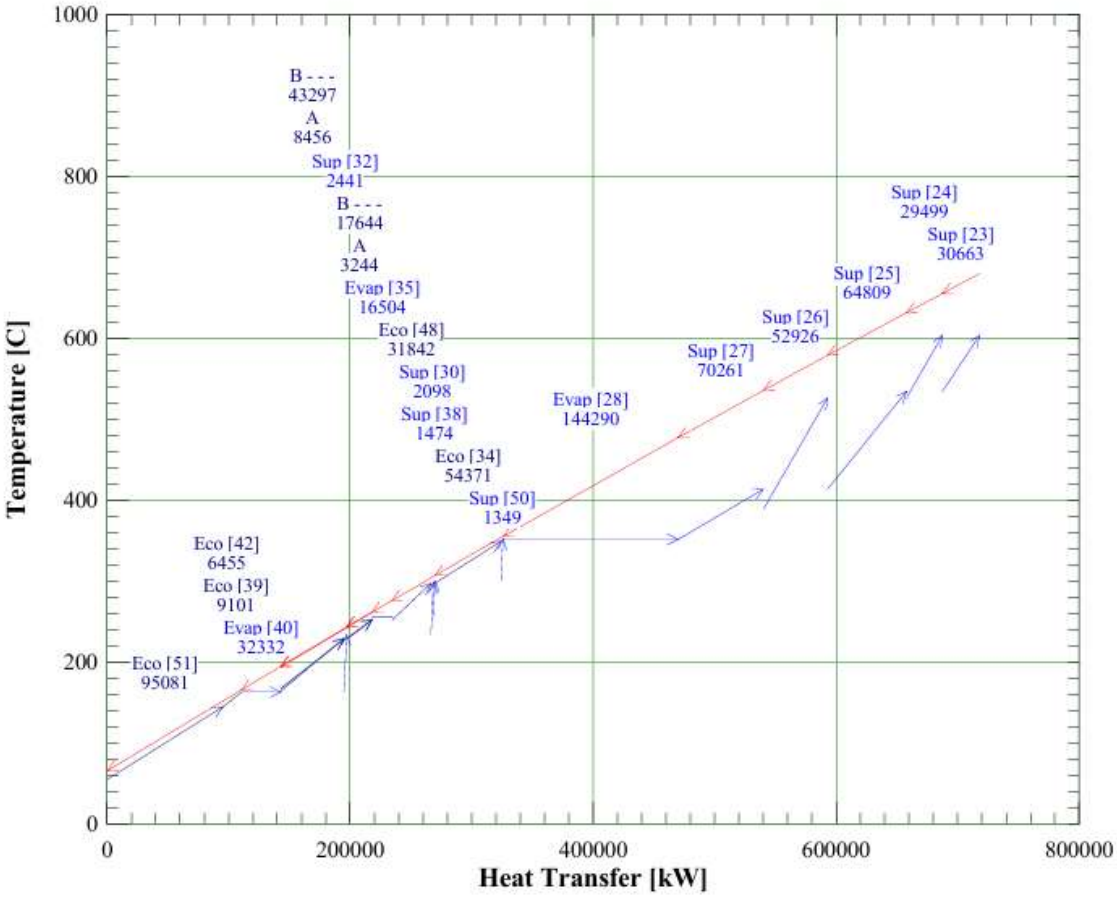


Figure 3: Temperature profile in the HRSG.

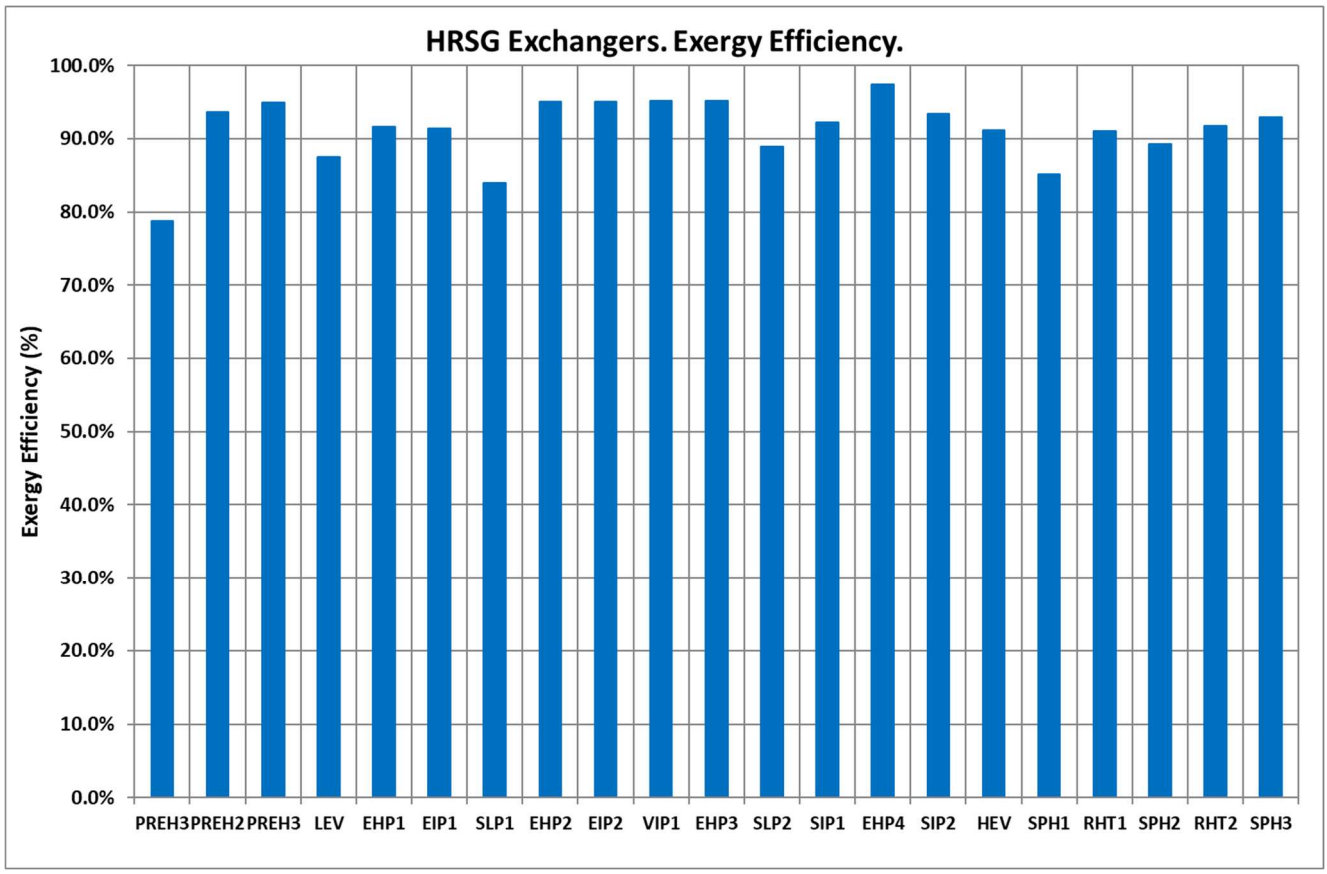


Figure 4: Exergy analysis of the HRSG.

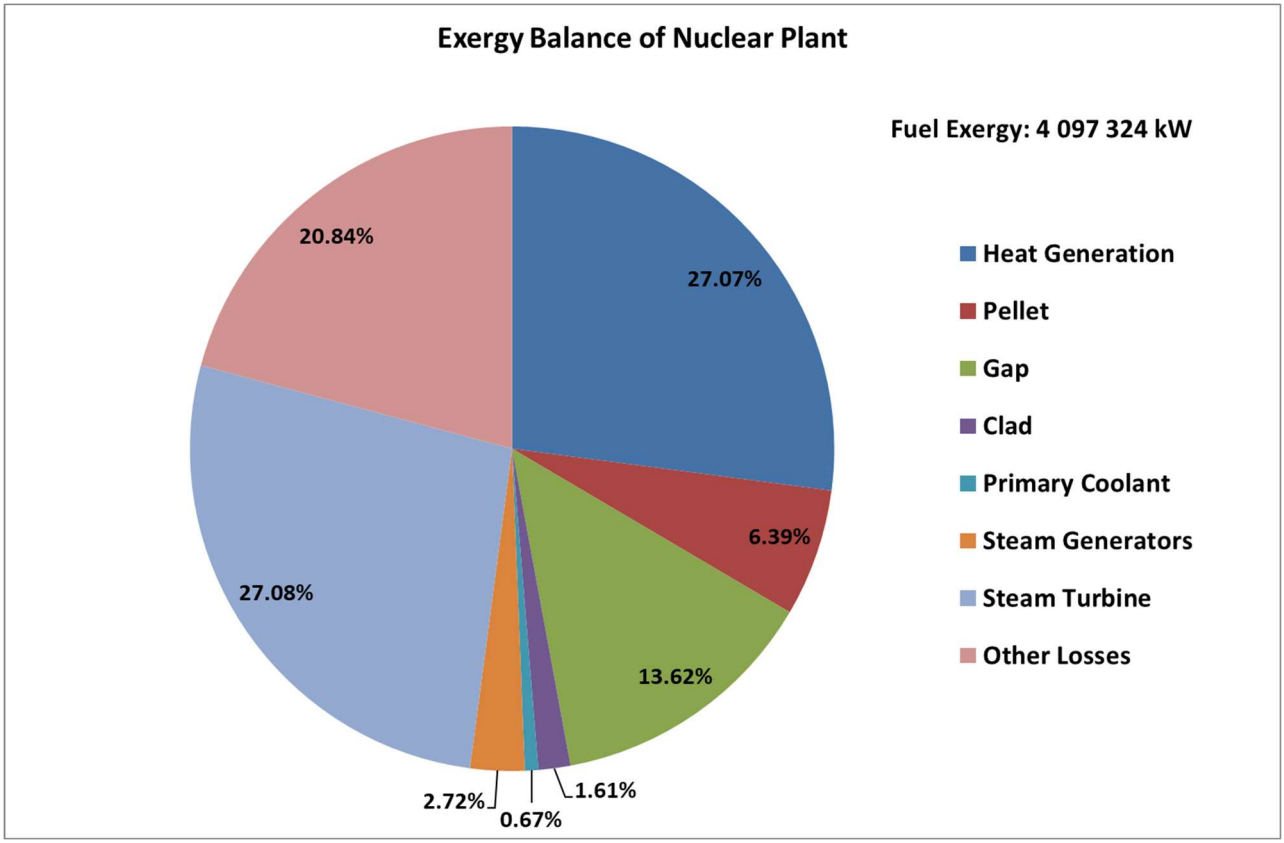


Figure 5: Exergy balance of a 1000 MW-class nuclear plant.

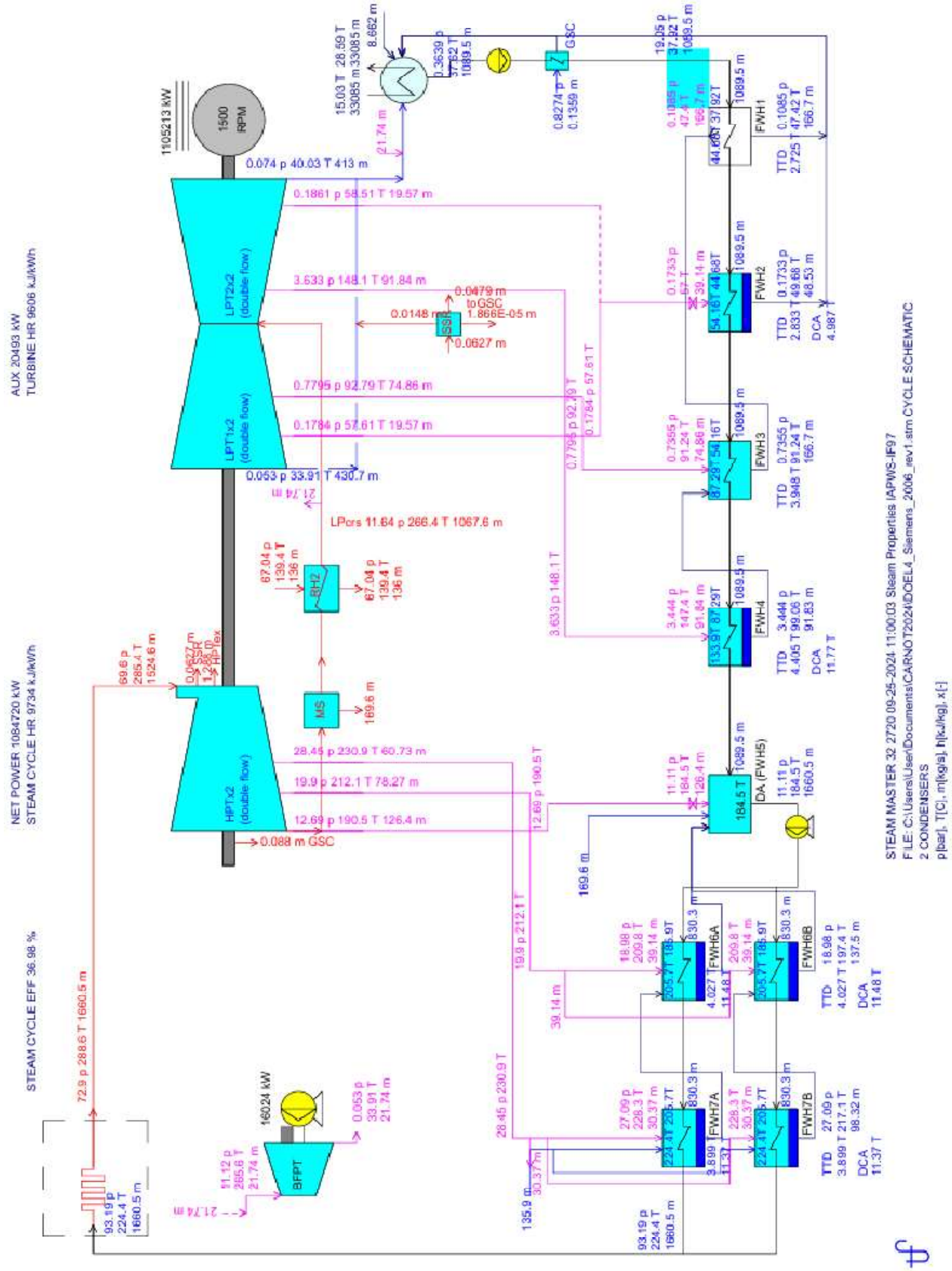


Figure 6: Water/steam cycle of a 1000 MW-class PWR plant.

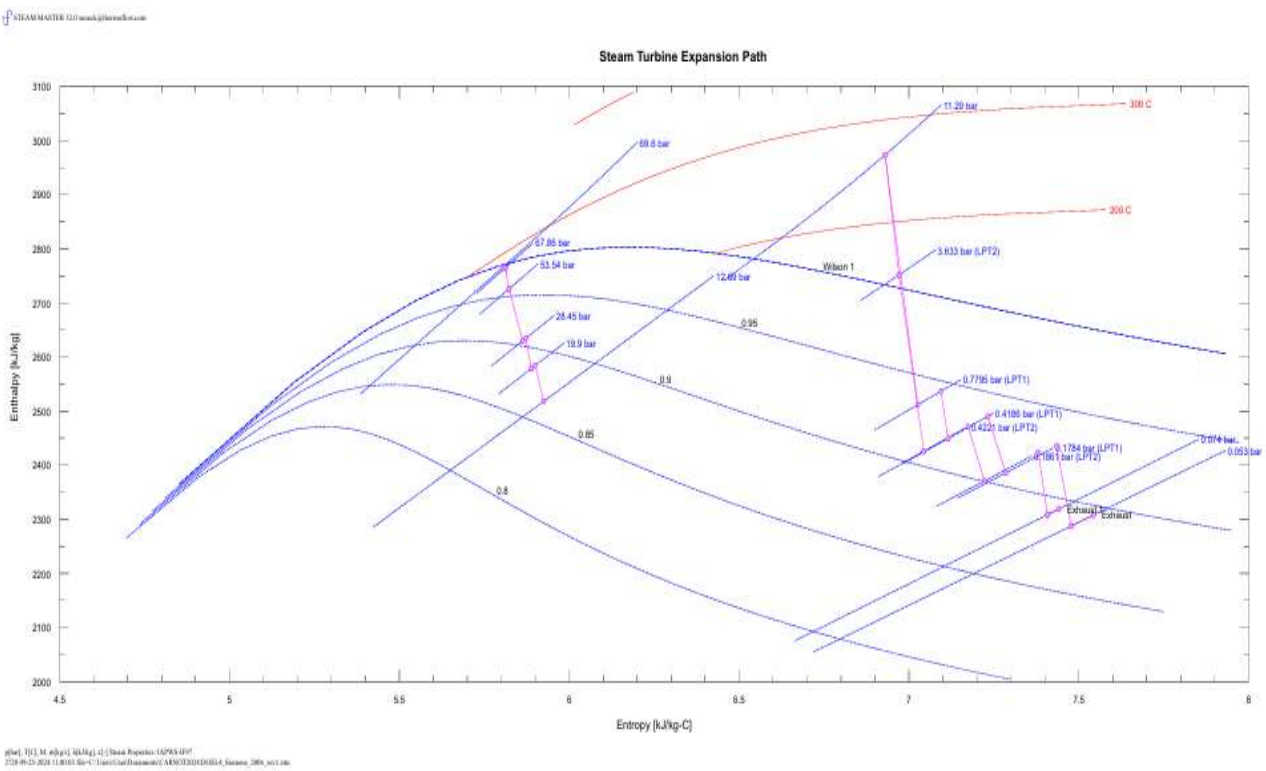


Figure 7: Expansion line of the steam turbine.

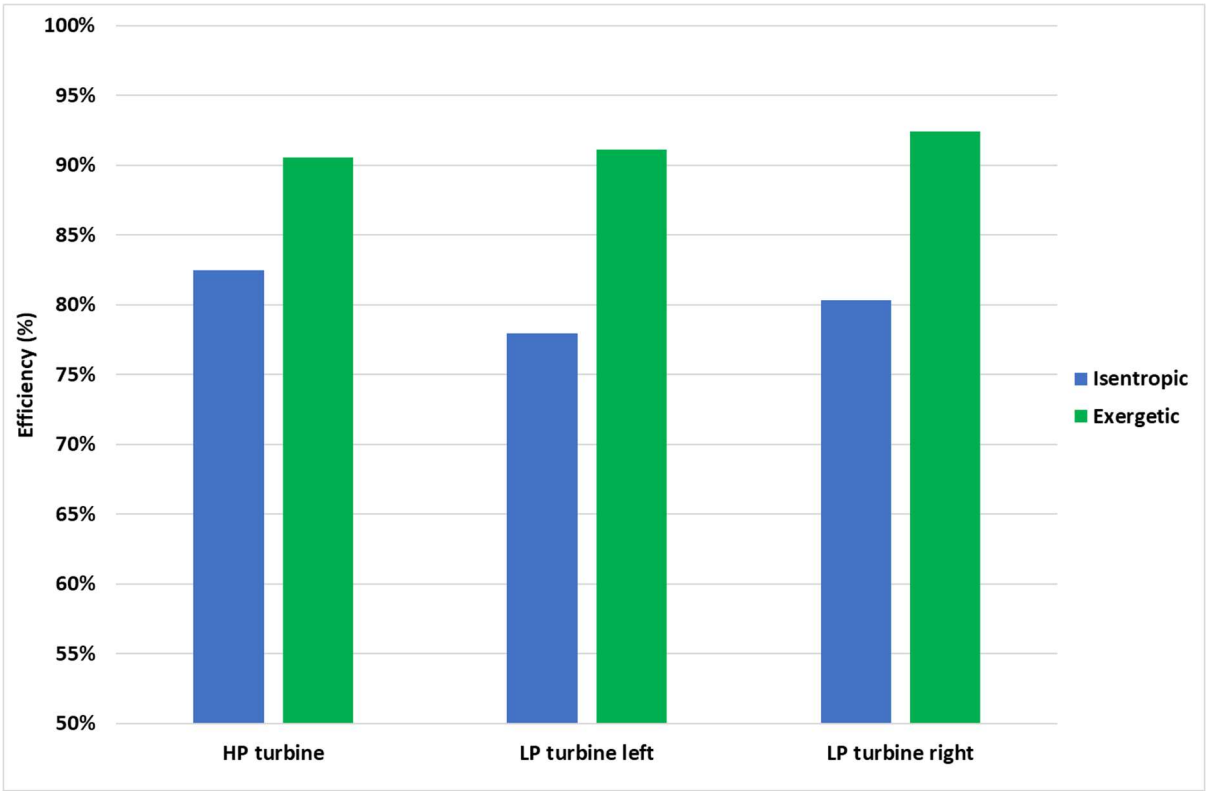


Figure 8: Expansion efficiencies of the HP and LP turbines.

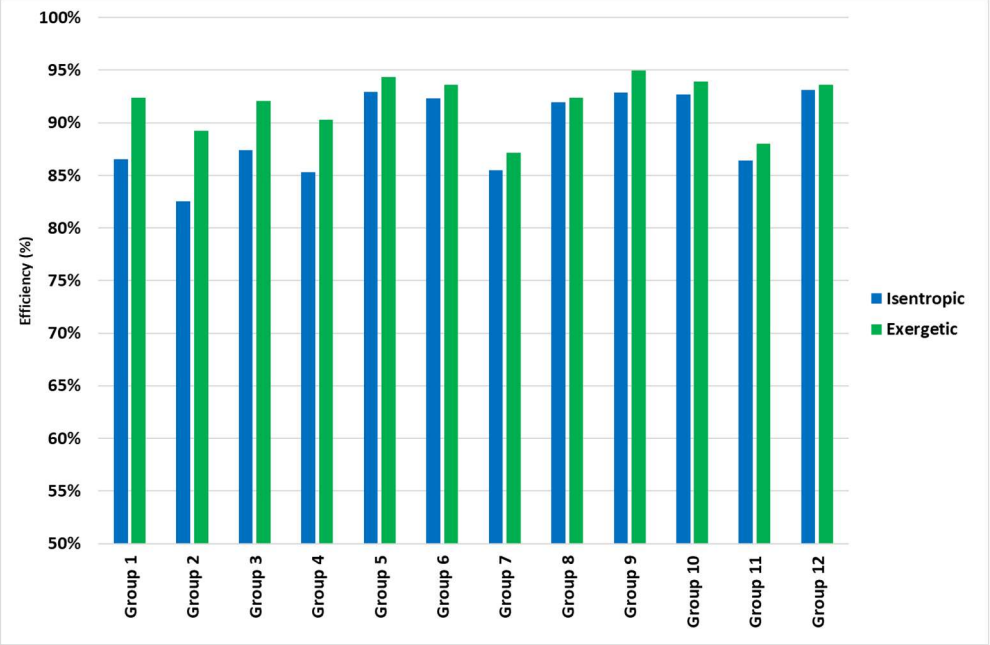


Figure 9: Expansion efficiencies of the stage groups.

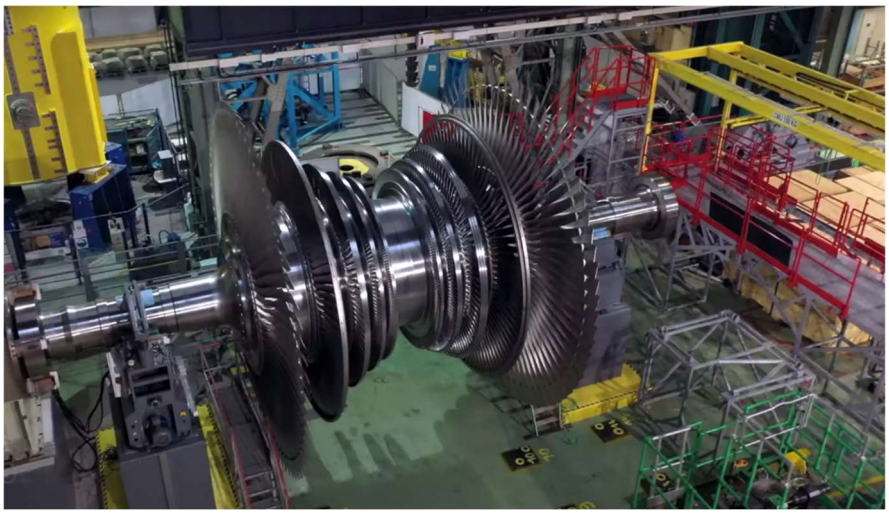


Figure 10: LP turbine rotor [6].

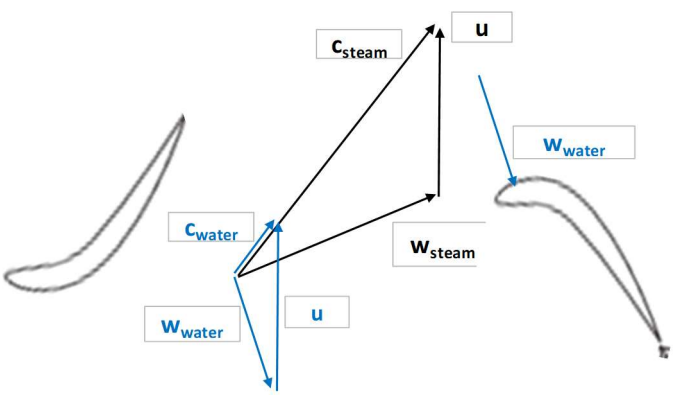


Figure 11: Water and steam velocity triangles.

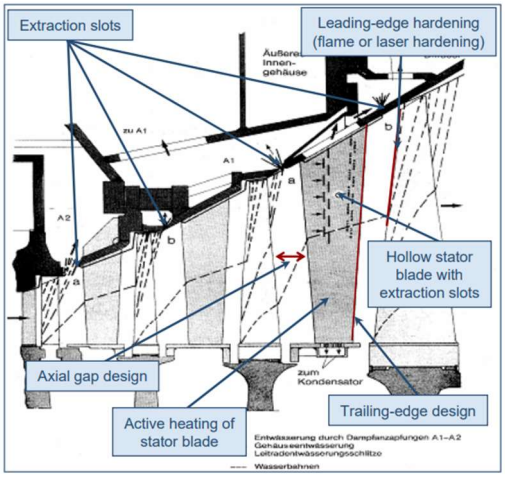


Figure 12: Moisture removal systems [6].

PERFORMANCE IMPROVEMENT OF A SINGLE-SHAFT MICRO GAS TURBINE: THE ROLE OF WATER INJECTION IN ENERGY AND EXERGY EFFICIENCY

Ali Baghernejad[1]*, Ward De Paepe[2]

[1,2] Thermal Engineering and Combustion Unit, University of Mons (UMONS), Place du parc 20, 7000 Mons, Belgium

* *Corresponding Author: ali.baghernejad@umons.ac.be*

Abstract. Micro Gas Turbines (mGTs) have emerged as promising solutions for small-scale, decentralized Combined Heat and Power (CHP) systems due to their compact size and capability to simultaneously provide heat and electricity. However, their relatively low electrical efficiency poses a challenge, particularly for users with variable heat demands. This inefficiency limits their appeal in applications where high electrical output is essential. To address this issue, innovative approaches such as cycle humidification are being explored to enhance the electrical performance of mGTs. More specifically, in this study, we investigated the effect of water injection through a saturation tower on the performance of a mGT cycle with a focus on electrical energy and exergy efficiency. By incorporating the saturation tower, the system utilizes excess heat from exhaust gases more effectively, leading to an increase in both electrical energy and exergy efficiencies. Results indicate that the integration of water injection boosts electrical energy efficiency from 23.76% to 25.91% and enhances exergy efficiency from 22.80% to 24.80%. These findings demonstrate that water injection through a saturation tower significantly improves the performance of the mGT cycle, offering a viable solution for enhancing efficiency in small-scale, decentralized power systems.

Keywords. Micro gas turbine, Humid air turbine, CHP, Electrical efficiency.

1 Introduction

Micro Gas Turbines (mGTs) are a crucial part of the energy sector, offering heating, cooling, and electricity through distributed technology. These compact turbines can operate independently for small-scale power generation or in conjunction with cogeneration systems. They achieve remarkable efficiencies of up to 80% (comprising 30% for electricity and 50% for heat) for a 100 kW_e engine. However, such high efficiencies depend on complete utilization of all exhaust heat for external heating applications. When there is little or no demand for heat, the excess heat generated by the cogeneration unit must be wasted, lowering the overall efficiency, falling back to electrical output only. This can negatively impact the economics of the system and might even result in the unit being shut down.

To tackle this problem, research has focussed on humidification techniques for micro Gas Turbines (mGT) [1]. Introducing hot water or steam produced from flue gases into the cycle adds extra mass, which boosts electrical power production and specific output. Furthermore, humidification allows to recovery waste heat recovered from the flue gases and reintroduce it into the cycle, enhancing so electrical efficiency and allow for operation even during periods of low or no heat demand [2]. Various techniques for humidifying gas turbines have been investigated, each with its own advantages. These techniques include: *Water Injection That Fully Evaporates*: (1) injection into the air intake, commonly known as wet compression, where water is injected before the compressor to reduce compression work and improve efficiency (2) injection into the compressed air after the compressor, as implemented in the HAT cycle, to humidify the air and recover heat. (3) injection into the combustion chamber, primarily aimed at reducing NOx emissions by lowering combustion temperatures."; *Steam Injection*: Steam is injected into the compressed air before the recuperator and into the combustion chamber; *Water Injection in a Saturation Tower (HAT Cycle)*: Water is injected into a saturation tower, where it interacts with the air, becoming humidified before entering the recuperator. The last method, proposed by Rao and Day [3], has shown the highest potential for enhancing electrical efficiency among the humidification techniques [4].

Research on the HAT cycle has encompassed numerous numerical and experimental studies, emphasizing the positive effects and potential of

water injection through a saturation tower in gas turbines, known as the HAT cycle. The study by Araki et al. [5] investigates the Advanced Humid Air Turbine (AHAT) system using both experimental and analytical methods. The research reveals that the AHAT system achieves higher thermal efficiency and power output than conventional gas turbines, primarily due to the beneficial effects of water injection, which enhances specific power output and overall efficiency by increasing mass flow and improving heat recovery. Additionally, the system demonstrated operational stability across various conditions, indicating its robustness and practicality. The AHAT system also offers environmental advantages, including reduced NO_x emissions due to lower combustion temperatures. Lee et al. [6] compared a mGT with hot water and steam injections at the recuperator inlet and the combustor. Their findings indicated that injecting at the recuperator inlet yields higher efficiency than at the combustor for both water and steam injections. Additionally, steam injection generally results in better power generation efficiency compared to water injection. The study of energy and exergy performance of an integrated mGT, compressed air energy storage, and solar dish collector system is presented in [7]. In this study the optimum operating conditions that enhanced the system's electrical efficiency by 4.2% compared to base case conditions before optimization. Montero Carreron et al. [8] demonstrated that while the saturation tower in the mHAT cycle increases enthalpy of the working fluid, it also reduces exergy due to the entropy rise from water evaporation. The primary benefit of water injection in this cycle is the increased heat capacity of the air-vapor mixture, enhancing heat recovery in the recuperator. This improvement leads to lower fuel consumption in the combustion chamber and higher overall efficiency, especially at constant power.

In the experimental view, the performance of a pilot of evaporative gas turbine, focusing on water circuit chemistry and humidification is examined by Ågren et al. [9]. Their study emphasized the critical role of managing water chemistry, including pH and dissolved salts, to prevent scaling and corrosion, which can degrade system efficiency and longevity. Additionally, the researchers evaluated the impact of various humidification methods on the gas turbine's performance, finding that effective humidification enhances power output by increasing the mass flow rate of air. These findings underscore the importance of optimizing both water chemistry and humidification processes to improve the efficiency and reliability of evaporative gas turbine systems. Researchers at Vrije Universiteit Brussel (VUB) transformed a Turbec T100 mGT into an mHAT by adding a spray saturation tower. Experimental results indicated that electrical efficiency increased by up to 4.2% due to water injection at a fixed rotational speed [10]. In another work, Zhang et al. [11] at Shanghai Jiao Tong University explored the dynamic performance of a pressurized packing humidifier in a 100 kW mHAT system. They investigated the influence of the water-air ratio and inlet temperature on the system's performance, demonstrating significant improvements in efficiency with optimized parameters.

Previous works have indicated that introduction of a saturation tower in the mGT cycle is beneficial for electrical efficiency. However, the considered mGTs where larger in scale (semi-industrial, >100 kW_e). The impact on smaller, (semi-)domestic applications has not yet been identified. Hence, the goal of the study presented in this paper is to evaluate the advantages of water injection through the saturation tower from an energy and exergy perspective to fully comprehend the effect that water injection brings in the 10 kW_e single shaft mGT cycle developed by MITIS (micro-10). To perform such analysis, the present paper introduces the Sankey (enthalpy flow) and Grassmann diagrams (exergy flow), to visually represent the enthalpy flow and flow of exergy within the cycle showing the distribution of energy and identifying major losses or gains and, helping to understand the quality of energy transformations and losses within the system, respectively.

2 MGT system and proposed mHAT cycle

The micro-10 mGT developed by MITIS is a compact power generation system designed for distributed energy applications (Fig. 1). The micro-10 mGT follows a classic Brayton cycle with integrated heat recuperation. It includes components such as a radial compressor, a recuperator, a natural gas-fired combustion chamber, and a radial turbine. The turbine drives both the compressor and a generator. The integration of a recuperator allows the system to recover heat from the turbine exhaust, preheating the compressed air before it enters the combustion chamber, which enhances the overall efficiency of the cycle. Turbine Inlet temperature (TIT) and exhaust gas mass flow rate are 800°C and 140 g/s to produce 12 kW_e electricity. The micro-10 mGT is capable of operating in a combined heat and power (CHP) mode. This means that it not only generates electricity but also utilizes the waste heat from the exhaust for heating purposes with thermal power output of 35 kW_{th} which can significantly

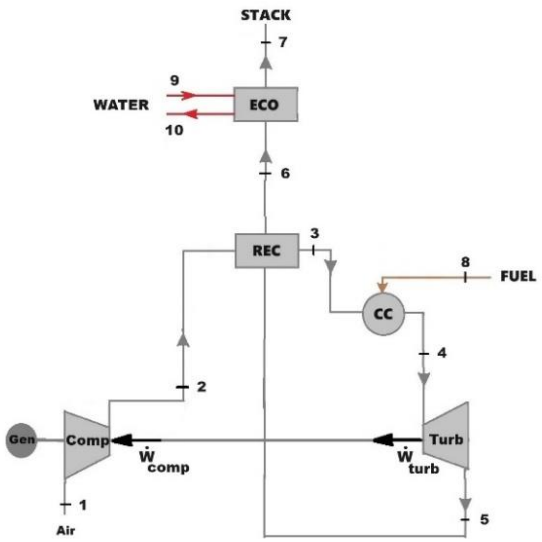


Figure 1. MITIS implementation a single-shaft micro gas turbine (micro-10 mGT)

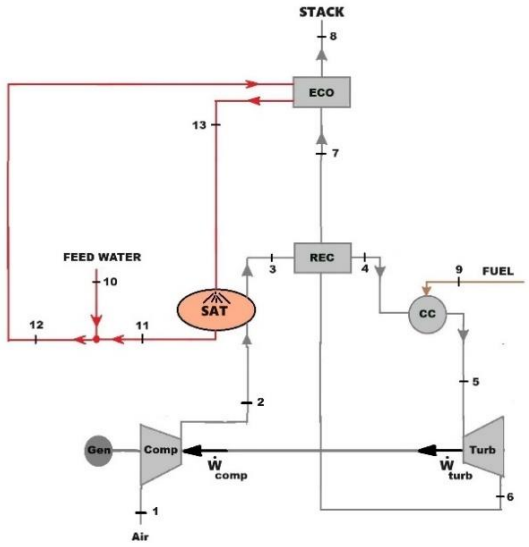


Figure 2. Conversion of a single shaft mGT (micro-10 mGT) in Grey, into an mHAT Cycle via a Saturation Tower (micro-10 mHAT)

increase the total efficiency of the system. Maximum exhaust gas temperature is 270°C (state 6) which can be exploited for various purposes such as hot water production (140 g/s water from 15°C to 70°C), steam generation or other cycle power supply (Organic Rankine Cycle, ad(b)sorption heat pump). The micro-10 mGT is converted into a micro Humid Air Turbine (mHAT) cycle by incorporating a saturation unit after the compressor. This modification enables the system to recover heat from the economizer during periods of low consumer heat demand, using humidification to enhance electrical efficiency. The mHAT system, as illustrated in Fig. 2, retains the traditional components of the mGT, indicated in grey. Heated water from the economizer is sprayed onto the compressed air in the saturation tower. As the air travels through the saturator, its relative humidity increases, which raises both air enthalpy and mass flow, while simultaneously extracting heat from the circulating water at temperatures below boiling. The original economizer is retained in the mHAT cycle, operating with a fixed water flow rate of 140 g/s. However, only 10.3 g/s of this water is required to fully humidify the air in the tower, with the excess water being collected at the bottom of the saturator and redirected back to the economizer.

3 Calculation model and assumptions

The authors utilized their developed and validated models to simulate both mGT and micro heat and power turbine (mHAT) cycles using Aspen Plus, as referenced in [8, 12]. The following section outlines the key assumptions made for the calculations.

In the simulation of the mGT and mHAT cycles, the features of all components, including the Recuperator (REC) and Economizer (ECO) heat exchangers, were kept consistent during the computation of the Heat and Mass Balance (HMB). This approach ensures that the off-design conditions, particularly the different operating conditions of the REC and ECO in the HAT cycle, are accurately captured in the model. The heat exchangers (REC and ECO) are modeled as counter-current gas-gas and gas-liquid exchangers, respectively, with performance computed using correlations for heat transfer and pressure drop. The significant differences in operating conditions (such as variations in mass flow rates and inlet temperatures) between the dry mGT and humidified mHAT cycles are accounted for through Aspen's built-in functionality, ensuring the thermal and hydraulic performance of these components is accurately reflected. To validate the results, we ensured that the HMB aligns with physical expectations by comparing component behaviors under both dry and humidified conditions. For instance, the pinch temperature in the ECO and the effectiveness of the REC were checked to confirm consistency with experimental and literature data [8, 10].

The original micro-10 mGT turbomachinery components are included in the model: The actual map for both the compressor and the turbine are

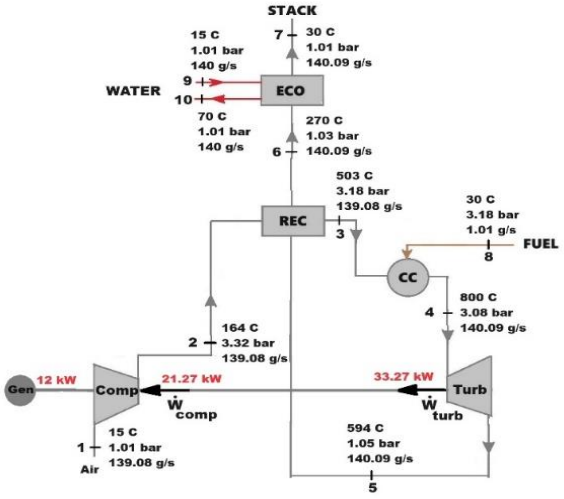


Figure 3. state properties, compressor, turbine and net power for single shaft mGT (micro-10 mGT)

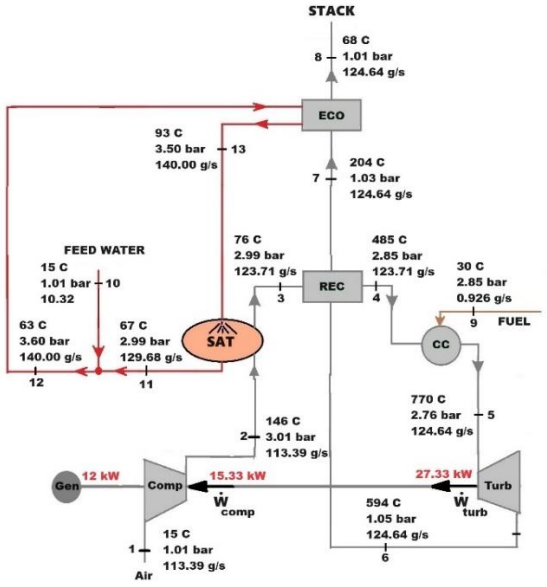


Figure 4. state properties, compressor, turbine and net power for proposed single shaft mHAT (micro-10 mHAT)

introduced in Aspen Plus, regarding both pressure ratio and isentropic efficiency and including the surge limit. The compressors and turbines were operating at an impressive 99% mechanical efficiency. In the mHAT case, the presence of water significantly impacts the properties of the working fluid, specifically the heat capacity ratio (k). Similarly, the isentropic efficiency of the turbine is adjusted for cycles with added humidity using a correction method. This is achieved through eq. (1), where the asterisk (*) denotes the properties of standard dry air, as suggested by Parente et al. [13].

$$\frac{\eta_{is}}{\eta_{is}^{*}} = \frac{k-1}{k^{*}-1}\sqrt{\frac{k^{*}+1}{k+1}\left(\frac{1-(\frac{1}{\pi})^{k^{*}}}{1-(\frac{1}{\pi})^{k}}\right)} \quad (1)$$

The combustion chamber is designed as a classical Gibbs reactor with a 3% pressure loss. Both cycles use methane as fuel, with a lower heating value of 50035 kJ/kg. We assume a combustion efficiency of 100%, meaning complete combustion occurs. Furthermore, we can assume that the pressure loss in the combustors is equal for both the mGT and mHAT cycles due to the insignificant impact of water injection on the combustion process. The recuperator is modelled as a gas-gas heat exchanger operating in a counter-current flow pattern with air side and gas side pressure losses 0.1 bar and 0.04 bar, respectively. Pressure loss for the saturation tower of the mHAT cycle is assumed to be 0.5% based on the experimental results on this such cycles [10].

The simulation models incorporate several control loops to ensure optimal performance:

1. **Turbine Outlet Temperature (TOT)**: This is typically maintained at a constant 594°C by adjusting the fuel flow rate in the reheater.

2. **Net electrical power output**: A constant net electrical power output of 12 kW_e from the generator is achieved by adjusting the rotational shaft speed.

3. **Stack pressure**: A outlet pressure of 1.01 bar is set for stack to maximize energy efficiency of the system by changing air mass flow rate.

4. The final loop determines **the amount of water introduced into the cycle**. This amount of water corresponds to when the economizer has reached its minimum pinch temperature while still adhering to all other conditions outlined.

Fixing the net electrical power at 12 kW allowed for a direct comparison between the mGT and mHAT cycles. By holding the output constant, we could focus on how the proposed modification (water injection) impacts other critical performance metrics, such as electrical efficiency, fuel consumption, and exergy efficiency, without perplexing effects from variations in power output. In real-world applications, micro gas turbines (mGTs) are often operated to meet a specific power demand rather than running at fixed rpm or inlet mass flow rates. This operating mode aligns with typical usage scenarios in small-scale, distributed energy systems, where the primary goal is to satisfy a set electrical demand. The

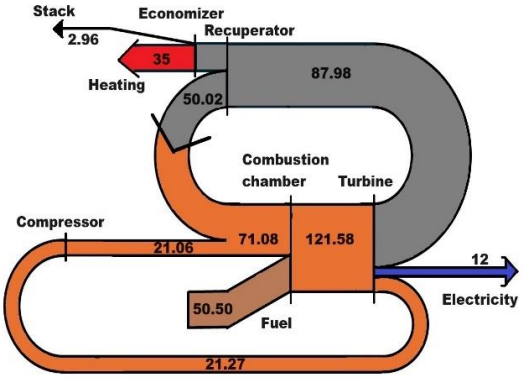


Figure 5. Sankey diagram of mGT cycle working as CHP, with an electrical efficiency of 23.76% and a total efficiency of 93.06%. Energy flows are expressed in kW.

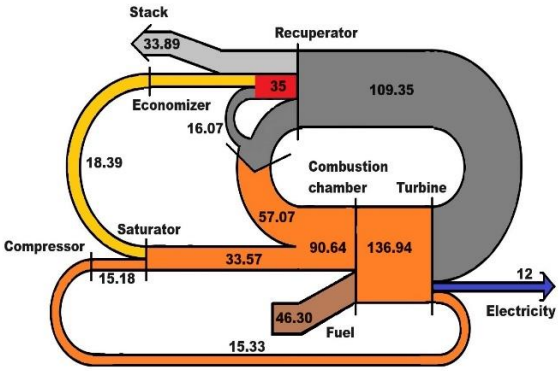


Figure 6. Sankey diagram of mHAT cycle, with an electrical efficiency of 25.91%. Energy flows are expressed in kW.

integration of a saturation tower introduces additional complexity to the system, including changes in the turbine inlet temperature (TIT), mass flow rates, and rotational speed due to water injection. Fixing the power output allowed us to isolate the effects of these interactions and analyze the benefits of the proposed modification in a controlled manner. By maintaining constant power in this study, we aimed to present results that are both practically relevant and easy to interpret for the intended application of the mGT system.

These control mechanisms ensure that the system operates efficiently and within the desired parameters. When water is injected into the cycle after the compressor, an imbalance arises between the compressor and turbine mass flow rates. This imbalance leads to an increase in shaft power output. To maintain a constant electrical power output of 12 kW_e for the mGT and mHAT systems, the control system responds by lowering the rotational shaft speed. This adjustment helps stabilize the power output despite the changes caused by water injection. Additionally, there is a subsequent decrease in the intake air mass flow rate of mHAT cycle compare to dry mGT cycle.

4 Results and discussions

Based on the assumptions mentioned in previous section, the temperature, pressure, and mass flow rate for each stream, along with the net work output from the compressor, turbine, and generator, were computed for both the mGT and mHAT cycles. These results are illustrated in Figs. 3 and 4. The simulations assumed a constant electrical output of 12 kW_e, which was maintained by independently adjusting the shaft's rotational speed, the intake air mass flow, and the flow rate of injected water. In the case of the dry mGT, this setup results in a thermal power output of 35 kW_{th}. However, in the mHAT cycle, no residual thermal power remains available in the economizer. A Sankey diagram is employed to visualize the enthalpy flows between components and to analyze the state properties and results of both cycles. Fig. 5 shows the Sankey flow for the mGT cycle operating as a CHP unit. As indicated before, this system generates 12 kW_e of electrical power and 35 kW_{th} of thermal power from the economizer. The turbines deliver a total power output of 33.27 kW, with 21.27 kW used to drive the compressor via its shaft. As illustrated in the diagram, the recuperator is essential, recovering 50.02 kW from the exhaust gases, which accounts for approximately 41.14% of the 121.58 kW fuel energy input. In the end, only 2.96 kW of energy is lost through the exhaust gases in the stack, after providing thermal energy in the economizer for heating purposes.

The Sankey diagram in Fig. 6 depicts the mHAT cycle for a single-shaft configuration, where the controller ensures a steady electrical power output of 12 kW_e. The diagram highlights the effect of water injection on fuel consumption: the combustion chamber requires just 46.30 kW of fuel, compared to 50.50 kW for the dry mGT. Out of the 35 kW_{th} generated by the economizer in the mGT operating as a CHP unit, 18.39 kW is recovered via water injection in the saturation tower, with an additional 16.07 kW recovered in the recuperator. However, due to the higher water content in the mHAT cycle, the heat capacity of the turbine flow increases. This enables the system to maintain a consistent 12 kW_e power output (limited by the turbo generators) with a

lower required TIT of 770°C in the mHAT cycle, compared to 800°C in the mGT cycle (see Figs. 3 and 4). Although this TIT is achieved at a lower rotational speed in the mHAT cycle than in the mGT cycle, the controller must reduce the fuel flow rate in the combustion chamber accordingly: from 50.50 kW in the CHP mGT unit to 46.30 kW in the mHAT cycle.

In the HAT cycle, the lower (TIT) and mass flow rate lead to a shift in the velocity triangles, reducing the blade loading and adversely affecting turbine efficiency. To account for these changes, the isentropic efficiency of the turbine was corrected in the simulation using a method that adjusts for variations in the heat capacity ratio (k) caused by the addition of water vapor. This correction ensures that the efficiency values reflect the real thermodynamic behavior of the turbine under partial-load and humidified conditions. In the HAT cycle, the lower rpm and reduced mass flow rate also influence the compressor's operating point on its performance map. This deviation from the design point results in a minor drop in isentropic efficiency. The compressor's efficiency was recalculated using actual performance maps integrated into Aspen Plus, which account for off-design operation. While the efficiency drop is not as pronounced as in the turbine, it is a factor that marginally offsets the overall gains from water injection. Despite the adjustments, compressor and turbine efficiencies decreases slightly compared to the dry mGT cycle due to suboptimal blade loading and changes in the flow characteristics. While compressor and turbine efficiency is slightly degraded due to partial-load operation, the system-level efficiencies (electrical and exergy) improve in the HAT cycle. This improvement is primarily due to the enhanced heat recovery in the saturation tower and recuperator, which compensates for the reduced component efficiencies.

The saturation tower in our study does not rely on a natural draft cooling tower mechanism but operates as a counterflow humidifier. In this configuration: Compressed air at 146°C enters the tower and flows counter to the injected hot water at 93°C. The compressed air is cooled to 76°C, achieving 100% relative humidity (saturation), while a fraction of the injected water evaporates. Excess water is collected at the bottom of the tower and returned to the economizer for reheating. A comprehensive HMB is computed for the saturation tower. The key steps include: Energy Balance: The energy required to evaporate 10.32 g/s of water is sourced from the sensible cooling of the compressed air (146°C to 76°C) and the cooling of the injected water from 93°C to its equilibrium temperature at the outlet. This energy exchange ensures that the outlet air achieves saturation without exceeding 100% relative humidity. Mass Balance: The evaporated water mass corresponds to the water vapor content needed to saturate the compressed air. Excess water (un-evaporated) is collected and returned to the economizer at a temperature of approximately 67°C. While the compressed air cools from 146°C to 76°C, it is the evaporation process, rather than direct heat exchange, that drives the cooling of the injected water. The outlet temperature of 67°C is achieved due to the water-air interactions in the tower, which are modeled to ensure thermodynamic consistency. The following assumptions are integral to the model: The relative humidity of the air leaving the saturation tower is 100% (saturation condition). Heat and mass transfer correlations used in the Aspen Plus model are validated against experimental data from similar cycles. The temperature of excess water is consistent with experimental observations reported in the literature for similar systems [8, 10].

The water injected into the saturation tower evaporates, replacing some of the air that would normally pass through the turbine, which reduces the compressor's airflow demand (15.33 kW vs. 21.27 kW). Consequently, the shaft's rotational speed decreases due to humidification, reducing the net power required by the compressor. This ultimately leads to an increase in electrical efficiency from 23.76% in the mGT cycle to 25.91% in the mHAT cycle.

It should be noted that the variable rpm operation requires precise electronic control of the generator's output frequency. In our study, the following approach was assumed: A frequency converter is employed to ensure the generator’s electrical output remains at the desired frequency irrespective of the shaft’s rotational speed. This approach is standard in systems where variable rpm operation is necessary, such as in micro gas turbines with load-following capabilities. The frequency converter adjusts the generator’s electrical output frequency by decoupling it from the mechanical rotational speed, ensuring compatibility with grid or standalone systems. In our simulations, the variable rpm was implemented with the assumption that an efficient electronic control system is in place. The efficiency losses associated with electronic frequency control were considered negligible in the scope of this study. While the current study focuses on thermodynamic performance, integrating a detailed analysis of the electrical subsystem, including control strategies and their efficiencies, would provide a more holistic

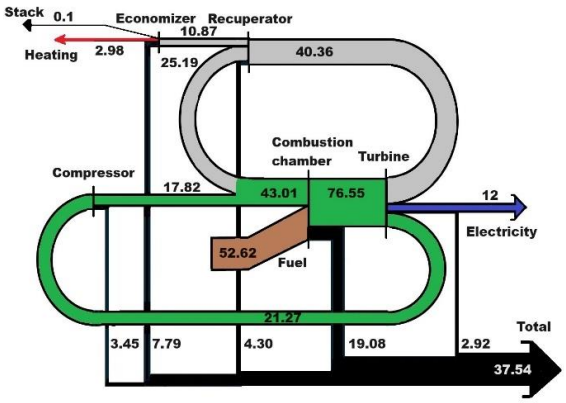


Figure. 7. Grassmann diagram of mGT cycle working as CHP, with an exergy efficiency of 28.46%, of which 22.80% corresponds to electricity and 5.66% to heat production. Exergy f lows are expressed in kW

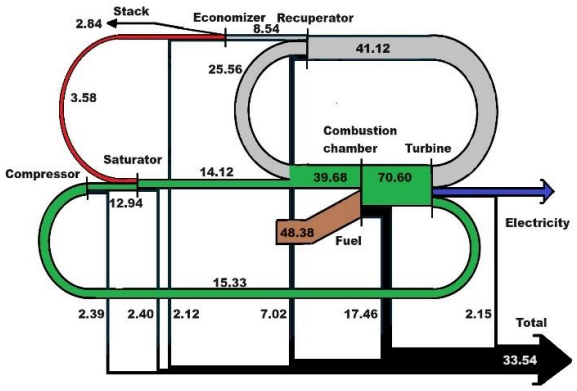


Figure. 8. Grassmann diagram of mHAT cycle, with an exergy efficiency of 24.80%. Exergy flows are expressed in kW.

evaluation. This will be addressed in the future studies.

To more effectively assess the performance of mGT and mHAT cycles, a second law analysis using Grassmann diagrams is highly beneficial. These diagrams, depict exergy flows and the points of exergy destruction instead of just energy flows. This analysis method allows us to pinpoint where exergy losses occur within the cycle, providing critical insights that can guide efforts to optimize and improve system efficiency. Figures 7 and 8 present the Grassmann diagrams for both the mGT and mHAT cycles, illustrating the exergy flows within each system. In the mGT cycle, the second law efficiency is calculated to be 28.46%, with 22.80% of this efficiency attributed to the electrical power output. The thermal power output, which is 35 kW_{th}, has an exergy content of only 2.98 kW, contributing a modest 5.66% to the overall exergy efficiency. On the other hand, the mHAT cycle has a lower exergy efficiency of 24.80%, focused solely on electricity generation.

In the mHAT cycle, while the economizer and water flow rate remain the same, the water loop within the mHAT system controls the water temperature. Given the exhaust gas temperature, the available heat in the economizer, and fixed parameters such as the water flow rate, the injection temperature for the water used to saturate the compressed air in the mHAT cycle is set at 93°C, with a pressure of 3.50 bar. After passing through the saturation tower and mixing with feedwater, the water temperature decreases to 63°C before returning to the economizer. As a result, the exhaust gases exiting towards the stack have a higher temperature of 68°C and a significantly increased exergy content of 2.84 kW.

In terms of exergy destruction, the mGT cycle experiences a value of 37.54 kW, while the mHAT cycle shows a slightly reduced value of 33.54 kW. Although converting the mGT into an mHAT adds complexity, both cycles effectively utilize fuel exergy in the burner. Approximately 71.34% of the fuel exergy is destroyed in the mGT cycle, compared to 69.32% in the mHAT cycle, particularly when external heat demand is low. In the mHAT cycle, the saturation tower introduces a net exergy gain of 3.58 kW from the water provided by the economizer, but it also incurs an exergy loss of 2.40 kW. While the saturation tower enhances energy recovery, as evidenced by the Sankey diagram, and improves exergy recovery in the recuperator, it also lowers the inlet temperature on the cold side of the recuperator from 164°C to 76°C. This larger temperature difference between the hot and cold streams leads to significantly higher exergy destruction in the recuperator with water injection: 7.02 kW in the mHAT cycle compared to 4.3 kW in the mGT cycle. Conversely, the increased temperature difference negatively impacts the exergy performance of the economizer showing more exergy destruction (7.79 kW) compared to the mHAT cycle (2.12 kW).

To summarize, incorporating water injection in the mGT has a significant impact on exergy. It leads to a slightly increased exergy recovery in the recuperator, with 25.56 kW in the mHAT case compared to 25.19 kW in the mGT case, due to the higher heat capacity and lower compressor flow rate. Consequently, the shaft experiences a decrease in

rotational speed, resulting in less power required for the compressor (15.33 kW vs. 21.27 kW). This ultimately reduces the exergy fuel input from 52.62 kW in the mGT case to 48.38 kW in the mHAT case.

Table 1 presents the first and second law efficiencies for both the single-shaft mGT and single-shaft mHAT cycles. The data show that converting the mGT into an mHAT cycle and using exhaust gas heat for preheating the injected water results in a decrease of 36.59% in heating energy efficiency and a 3.90% reduction in heating exergy efficiency. However, this heat recovery approach also leads to modest increases in electrical efficiency, with electrical energy efficiency improving by 2.15% and electrical exergy efficiency increasing by 2%.

Table 1: Comparative results of energy and exergy efficiencies for the mGT and mHAT cycles

Parameter	mGT cycle	mHAT cycle	%variation
Electrical energy efficiency (%)	23.76	25.91	+2.15
Electrical exergy efficiency (%)	22.80	24.80	+2
Heating energy efficiency (%)	69.30	-	-36.59
Heating exergy efficiency (%)	5.66	-	-3.90
CHP energy efficiency (%)	93.06	25.91	-67.15
CHP exergy efficiency (%)	28.46	24.80	-3.66

5 Conclusions

In the study presented in this paper, we examined the conversion of an mGT cycle into an mHAT cycle by integrating water injection for CHP applications, with a detailed analysis of the thermodynamic performance of both cycles. Water injection is utilized to harness excess heat from exhaust gases during periods of low external heat demand. Sankey and Grassmann diagrams are employed to illustrate the enthalpy and exergy flows within the system, highlighting the benefits of water injection in enhancing electrical energy and exergy efficiency.

Advantages from a First-Law Perspective are:

- Increased Recuperator Efficiency: The mHAT cycle allows for greater energy recovery in the recuperator, with 57.07 kW compared to 50.02 kW in the dry mGT cycle, due to the aftercooling effect of the saturator and the higher heat capacity of the flow.
- Lower Turbine Inlet Temperature Requirements: The mHAT cycle reduces the required turbine inlet temperature, leading to an overall increase in heat capacity through the turbine.
- Reduced Fuel Consumption: Fuel flow is decreased from 50.50 kW to 46.30 kW while maintaining a constant electrical output of 12 kW_e.
- Improved Electrical Efficiency: Electrical efficiency is increased from 23.76% in the dry mGT cycle to 25.91% in the mHAT cycle.

The Sankey diagram offers insights into energy flows, but it doesn't account for the varying effectiveness of different energy forms, such as heat and electricity. To compare these forms on a consistent basis, it is essential to analyze their exergy content using the second law of thermodynamics, which is visually represented through Grassmann diagrams. The analysis reveals several key findings:

- Exergy Destruction: Both the mGT and mHAT cycles destroy around 70% of the fuel's exergy input in the combustion chamber, indicating significant exergy loss during combustion.
- Exergy Utilization: The mGT cycle, with its higher stack temperature, more effectively utilizes the available exergy compared to the mHAT cycle. This is because higher stack temperatures typically result in better exergy recovery.
- Overall Exergy Efficiency: The mGT cycle achieves a total exergy efficiency of 28.46%, with 22.80% of this efficiency attributed to electricity production. This higher efficiency is largely due to the superior utilization of exergy made possible by the higher stack temperature. In contrast, the mHAT cycle, despite its modifications, exhibits a lower overall exergy efficiency of 24.80%.

Acknowledgement

This project has Funded by the European Union. Views and opinions expressed are however those of the author(s) only and do not necessarily reflect those of the European Union or CINEA. Neither the

European Union nor the granting authority can be held responsible for them.

References

[1] W. De Paepe et al., “Toward Higher Micro Gas Turbine Efficiency and Flexibility- Humidified Micro Gas Turbines: A Review”, Journal of Engineering for Gas Turbines and Power, no. 140, pp. 081702-1, 2023.

[2] W. De Paepe et al., “Micro Gas Turbine Cycle Humidification for Increased Flexibility: Numerical and Experimental Validation of Different Steam Injection Models”, Journal of Engineering for Gas Turbines and Power, no. 141(2), pp. 021009, 2019.

[3] A. Rao and W. Day, “HAT cycle status report”, In: Eleventh conference on gasification power plants; 1992.

[4] M. Jonsson and J. Yan, “Humidified gas turbines—a review of proposed and implemented cycles”, Energy, no. 30(7), pp. 1013–1078, 2005.

[5] H. Araki et al., ”Experimental and analytical study on the operation characteristics of the AHAT system”, Journal of Engineering for Gas Turbines and Power, no. 134(5), pp. 051701–051701, 2012.

[6] J. Lee et al., “The influence of water and steam injection on the performance of a recuperated cycle microturbine for combined heat and power application”, Applied Energy, no. 87, pp. 1307–1316, 2010.

[7] A. Mohammadi and M. Mehrpooya, “Exergy analysis and optimization of an integrated micro gas turbine, compressed air energy storage and solar dish collector process”, Journal of Cleaner Production, no. 139, pp. 372-383, 2016.

[8] M. M. Carrero et al., “Does humidification improve the micro Gas Turbine cycle? Thermodynamic assessment based on Sankey and Grassmann diagrams”, Applied Energy, no. 204, pp. 1163–1171, 2017.

[9] N. Ågren et al., “First experiments on an evaporative gas turbine pilot power plant: water circuit chemistry and humidification evaluation”, Journal of Engineering for Gas Turbines and Power, no. 124(1), pp. 96–102, 2002.

[10] W. De Paepe et al., “Experimental Characterization of a T100 Micro Gas Turbine Converted to Full Humid Air Operation”, Energy Procedia, no. 61, pp. 2083-2088, 2014.

[11] Q. Zhang et al., “Experimental analysis of the air humidification process for humid air turbine cycle using a two-phase measurement system”, Applied Energy, no. 279, pp. 115892, 2020.

[12] W. De Paepe et al., “Waste heat recovery optimization in micro gas turbine applications using advanced humidified gas turbine cycle concepts”, Applied Energy, no. 207, pp. 218–229, 2017.

[13] J. Parente et al., “Micro humid air cycle: part A – thermodynamic and technical aspects”, In: Proceedings of ASME turbo expo 2003, no. GT2003-38326, pp. 221–229, 2003.

PERFORMANCE SCALING OF METHANOL SPARK IGNITION ENGINES USING A TWO-ZONE SEMI-PREDICTIVE ZERO-DIMENSIONAL THERMODYNAMIC MODEL

ir. Victor Sileghem*, Dr. ir. Ward Suijs, Prof. Dr. ir. Sebastian Verhelst

Ghent University, Department of Electromechanical, Systems and Metal Engineering, Ghent, Belgium

* *Corresponding Author: Victor.Sileghem@UGent.be*

Abstract. Methanol is an appealing low or net zero carbon fuel, and its use in internal combustion engines is regarded as a viable option in Power-to-X-to-Power systems. Although methanol is naturally suited for spark ignition (SI), this is not easily applied to large bores and low speeds, resulting in a lack of experimental data. Still, methanol's high knock resistance allows for potentially larger bore sizes than current high octane fuels. This paper presents a two-zone zero-dimensional combustion model coupled to a knock integral model, which is used to predict the performance of methanol-fuelled port-fuel injected (PFI) SI engines. Special attention is paid to the development of a semi-predictive combustion duration model, which responds to operating conditions, particularly inlet pressure and spark timing. To this end, multiple correlations provided in literature are compared. Experimental data from a heavy-duty Scania D12 PFI SI engine is used to select the best-fitting correlation, and to calibrate the knock model. Predictions of the maximum operating load, and corresponding efficiency, were made for engines with bore sizes ranging from 80 mm to 260 mm. For a constant mean piston speed of 12.32 m/s, engines up to 170 mm are pressure-limited rather than knock-limited. From there on, knock gradually starts to decrease the achievable load. When setting a target of 25 bar indicated mean effective pressure (IMEP), PFI SI operation with methanol would allow to replace diesel engines up to a bore size of 180 mm. When using lean operation, this limit can be extended to 230 mm or 260 mm bore engines for a λ value of 1.4 and 1.6 respectively.

Keywords. Methanol, Spark Ignition, Performance Scaling, Knock, Simulation

1 Introduction

The increased penetration of renewable energy systems such as wind and solar energy brings about the need for renewable energy storage to overcome the mismatch between electricity demand and supply over different time scales [1]. For long-term balancing, internal combustion engines running on alternative fuels are seen as a viable solution within the Power-to-X-to-Power system [2]. Methanol is particularly interesting for its versatile production pathways – as a biofuel, e-fuel or a hybrid form thereof [3] – as well as its unique attribute of being the simplest hydrogen carrier that is liquid at atmospheric conditions. Methanol is naturally suited for spark ignition (SI) operation. However, the SI concept is not easily applied to engines with a large bore and low speed that are used for power generation. Consequentially, there is a lack of both experimental and numerical data on large bore methanol-fuelled SI engines [4]. The main limit to engine efficiency and power density is engine knock. However, methanol's high knock resistance, due to its high autoignition temperature, high laminar burning velocity and charge cooling effect, provides potential for larger bore sizes compared to existing high octane fuels such as natural gas [5]. Before large-scale testing is performed, it is of interest to assess the potential of methanol-fuelled SI engines through performance scaling laws or simulations. Three common scaling law practices, the Willans Line method, similitude and curve-fitted equations, were assessed in an earlier publication [6]. The first two were deemed impractical for the current research problem, while the curve-fitted equations require a large amount of empirical input and cannot be extrapolated to other fuels or engine technologies.

Therefore, the goal of this work is to build an engine simulation model to predict engine efficiencies and power densities over a wide engine size spectrum (80 – 260 mm). The model requires three key components: a combustion model, a knock model and an optimisation procedure to determine the maximum achievable engine load. The combustion model calculates engine pressures, temperatures and performance values such as indicated mean effective pressure (IMEP) and indicated thermal efficiency

(η_i) while the knock model monitors the end gas conditions and detects the occurrence of knock. The optimisation procedure is used to control input parameters such as spark timing (θ_s), and inlet pressure and temperature (P_{in} and T_{in}) to influence the engine load and combustion phasing until the maximum achievable IMEP is reached. The combustion model, the knock model and the optimization procedure are discussed in Sections 3, 5 and 6 respectively.

A zero-dimensional (0-D) modelling approach is chosen over a quasi- or multidimensional approach due to the trade-off between accuracy and computational costs. Literature provides many examples where a 0-D combustion model is coupled to a knock model. Elmqvist et al. [7] integrated a knock integral model into a non-predictive combustion model to predict the optimal spark timing of a knock-limited 86 mm bore engine at different engine speeds and air-to-fuel ratios λ. The knock integral model predicts autoignition of the unburned gas mixture by comparing the actual time in the cylinder (dt) to the autoignition delay time (τ_{ID}) of this gas mixture at every time step [8]:

$$KI = \int \frac{1}{\tau_{ID}} dt \qquad (1)$$

If the KI_{int} reaches unity during the closed engine cycle, knock is said to occur. Similarly, Caton et al. [9] explored a wider range of parameters such as compression ratio, engine speed, inlet pressure, spark timing, heat transfer and exhaust gas recirculation on a gasoline-fuelled 101.6 mm bore engine. Simpler as well as more advanced knock models exist. Lewis et al. [10] also compared the residence time of the mixture in the cylinder to τ_{ID}, but only considered a single time step: the moment of peak cylinder pressure. Even more pragmatic, Dimitrov et al. [11] used the maximum temperature of the unburned gas mixture to set a knock criterion during the preliminary design of a large gas engine.

A key focus of this work is to address the significant impact of operating conditions (speed, spark timing, inlet pressure,…) on the burn duration, which is especially important when considering situations where knock can occur [12]. To this end, three burn duration correlations [13], [14], [15] are introduced in Section 4. Their performance is assessed in Section 7 by comparison to an experimental data set on a heavy-duty methanol-fuelled SI engine. This data set is also used for calibration of the knock model. First, the experimental data set is introduced, after which the model components are systematically discussed. Finally, simulation results are discussed in Section 8.

2 Experimental data

Experimental data on a Scania D12 engine by Mahendar et al. [16] is used as calibration and validation data for the combustion and knock model. The research engine is modified from a 127 mm bore multi-cylinder diesel engine to a methanol-fuelled port-fuel injected (PFI) SI engine. The engine has a compression ratio (CR) of 13:1, a stroke/bore ratio and a connecting rod/stroke ratio of S_0/B_0 = 1.21 and L_0/S_0=1.65 respectively. An independent external compressor and a back-pressure valve simulate the presence of a turbocharger. Detailed information is provided in [16].

The experiment was designed to evaluate part load performance as well as knock-limited operation at increased levels of air dilution. The experiments were performed at a constant engine speed (N_0) of 1200 rpm, resulting in a mean piston speed ($c_{m,0}$) of 6.16 m/s. The entire achievable operating range is covered by performing boost pressure sweeps. For high load operating conditions, a constant inlet temperature of 30 °C was maintained. The current data set is limited to borderline knock conditions, meaning that the spark timing was advanced to either MBT (maximum brake torque) timing or to KLSA (knock limited spark advance) timing. In the case of KLSA timing, the safety margin used to avoid knock is unknown however. Figure 1 shows the operating range in terms of air-to-fuel ratio λ and indicated mean effective pressure IMEP.

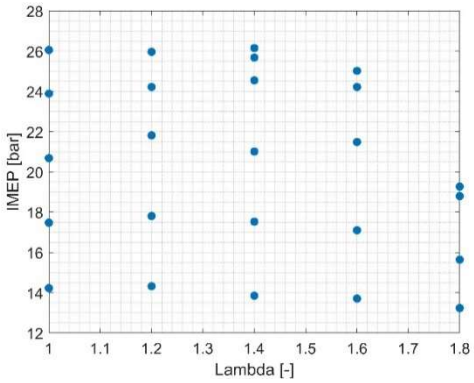


Figure 1: The full load experimental matrix on the methanol-fuelled PFI SI Scania D12 engine [16].

3 Two-zone combustion model

The combustion in an SI engine, governed by flame propagation, is modelled via a two-zone framework which distinguishes between a burned and unburned region. Equations for pressure rise rate, burned and unburned temperature, work, heat loss and enthalpy

loss are derived from an open system energy balance applied to the cylinder contents [17]:

$$\frac{dQ}{d\theta} - P \cdot \frac{dV}{d\theta} = \frac{dU}{d\theta} + \frac{\dot{m}_1 \cdot h_1}{\omega} \quad (2)$$

Where U is the internal energy, Q is the heat loss to the combustion chamber surfaces, P cylinder pressure and V the cylinder volume. The instantaneous blowby flow is represented by $\dot{m}_1$, with h_1 the enthalpy of the blowby gas and ω the angular rotation speed of the engine. This work builds upon an existing homogeneous two-zone finite heat release model with a constant burn duration θ_d [17], which is expanded with an improved heat loss model, a blowby model and a burn duration model.

The heat loss is calculated for both the burned ($\dot{Q}_b$) and unburned ($\dot{Q}_u$) zone. Each zone i has an individual heat transfer coefficient h_i and contact area A_i with the cylinder walls at temperature T_w:

$$\dot{Q}_i = h_i \cdot A_i \cdot (T_i - T_w) \quad (3)$$

A standard wall temperature of 350 K is used [17]. The heat transfer areas are estimated by a $x^{1/2}$-relationship [17]:

$$A_b = A_s \cdot x^{1/2} \quad (4)$$

$$A_u = A_s \cdot (1 - x^{1/2}) \quad (5)$$

Instantaneous heat transfer coefficients are calculated from the temperature and pressure (T_i, P_i), characteristic gas velocity (U_i) and cylinder bore size D through the correlation by Woschni [18].

The blowby term in Equation (2) is modelled using a blowby coefficient C to determine the total mass in the cylinder m [17]:

$$m(\theta) = m_1 \cdot e^{-\frac{C \cdot (\theta - \theta_1)}{\omega}} \quad (6)$$

Where m_1 is the initial mass at the intake valve closure (IVC) timing. A default value of the blowby coefficient is used: $C = 0.8\ s^{-1}$. The enthalpy of the blowby gas is approximated as:

$$h_1 = (1 - x^2) \cdot h_u + x^2 \cdot h_b \quad (7)$$

as more unburned gas is expected to leave the cylinder than burned mass [17].

The most crucial term to evaluate is the mass fraction burned x, which imposes a burn rate to the model and is often described by a cosine law:

$$x(\theta) = \frac{1}{2} \cdot \left[1 - \cos\left(\frac{\pi \cdot (\theta - \theta_s)}{\theta_d}\right)\right] \quad (8)$$

Here θ_s denotes the start of combustion and θ_d the burn duration. The effect of operating conditions (θ_s, N, P_{in}, λ,…) on the burn duration θ_d is implemented using correlations reported in literature.

4 Empirical burn duration correlations

Multiple case-dependent correlations for the burn duration are reported in literature. Those by Lindström et al. [13], Alam et al. [14] and Rousseau et al. [15] were found the most suitable for a first iteration of the model.

Linström et al. [13] define the burn duration between the point where the heat release reaches 2% of its maximum and the 99.9% mass fraction burned point. They propose a correlation relative to a base condition $\theta_{d,0}$:

$$\widehat{\theta_d} = \theta_{d,0} \cdot \frac{F_{SL}}{F_{SL,0}} \cdot \frac{F_{\theta_s}}{F_{\theta_{s,0}}} \cdot \frac{F_N}{F_{N,0}} \quad (9)$$

$$F_{SL} = \frac{1}{S_L(\lambda, T_{spark}, P_{spark}, x_{rg})} \quad (10)$$

$$F_{\theta_s} = 1.60 - 0.053 \cdot \theta_s + 9.1 \cdot 10^{-4} \cdot \theta_s^2 \quad (11)$$

$$F_N = 2.31 - 55.5/\sqrt{N} \quad (12)$$

The burn duration is influenced by the laminar burning velocity S_L at the spark timing, the spark timing θ_s and engine speed N. The correlation by Vancoillie et al. [19] is used to evaluate S_L. As can be seen, an increased laminar burning velocity results in a shorter θ_d. Similarly, an advanced spark timing (expressed in °ca before top dead centre (bTDC)) moves the combustion phase closer to TDC, which shortens θ_d. The second order polynomial induces an increased θ_d when the spark timing is advanced too far before TDC (see Equation (11)). Equation (12) shows that an increased engine speed N results in a longer θ_d. These correlations were developed based on a data set of gasoline-fuelled operating points.

Alam et al. [14] define θ_d between 10% and 90% mass fraction burned. Their correlation does not use a reference condition, and includes effects of the spark timing θ_s, compression ratio r_c, inlet pressure P_{in}, mean piston speed c_m and equivalence ratio ($\phi = \lambda^{-1}$).

$$\widehat{\theta_d} = A - B \cdot r_c - C \cdot P_{in} + D \cdot c_m - E \cdot \phi \quad (13)$$

$$F = G + H \cdot |\theta_s| \quad (14)$$

The coefficients A through H are all positive by design, except for F. These were determined based on data of methane-fuelled SI engines [14]. The intake pressures and mean piston speeds are expressed in bar and m/s respectively. Equation (13) shows a linear increase of θ_d for higher c_m, resulting from the

prolonged duration on a crank angle basis when maintaining a constant burn duration in seconds. Increased values of the remaining parameters (r_c, P_{in}, and ϕ) result in a shortened θ_d. The effect of spark timing is modelled to be minimal at TDC.

Lastly, Rousseau et al. [15] define θ_d between 1% and 95% mass fraction burned, and propose an exponential equation of λ, θ_s and P_{in}:

$$\widehat{\theta_b} = A \cdot P_{in}^{B} \quad (15)$$

$$A = C \cdot \lambda + D \quad (16)$$

$$B = -0.8133 \cdot \lambda + 1.0101 \quad (17)$$

$$C = 196.79 \cdot e^{-0.097 \cdot \theta_s} \quad (18)$$

$$D = 101.83 \cdot \ln(\theta_s) - 291.63 \quad (19)$$

The coefficients for these correlations are based on a natural gas-fuelled SI engine, with a validation range of $0.8 < P_{in} < 1.7$ bar, $1.37 < \lambda < 1.70$ and $8 < \theta_s < 23$ °ca bTDC. Similarly as before, θ_d decreases for a higher P_{in} or a lower λ. Only a minor influence of θ_s is modelled.

The performance of these correlations will be assessed in Section 7, by comparing their outcomes with the burn durations derived from the Scania D12 data set [16]. Therefore, the mass fraction burned profile is derived from the cylinder pressure trace using a method developed by Tunestål [20]. Subsequently, the burn duration is derived through the method proposed by Wiebe [21].

5 Knock model

The knock integral (Equation (1)) is converted to time steps in crank angle degrees according to:

$$KI = \frac{1}{6N} \int \frac{1}{f \cdot \tau_{ID}(\lambda, T_u, P, x_{rg})} d(°ca) \quad (20)$$

The kinetic mechanism from Pichler [22], developed for methanol-fuelled SI engines, is used to calculate τ_{ID}. More detail is provided in [23]. The factor f is added for calibration. Its value is based on a single operating point: Mahendar et al. [16] state that for $\lambda = 1$, the engine only requires spark retard beyond 21 bar IMEP, at inlet conditions of 150 kPa and 303 K. Hence, f is determined to have a KI value of unity at the exhaust valve opening (EVO) timing under these conditions, resulting in $f = 0.167$. This constant is seen to vary significantly between engines due to the complex influence of engine design on knocking behaviour [23], so assuming a constant value for f implies that the calculated scaling laws (Section 8) should be regarded as perfectly scaled versions of the baseline Scania D12 engine in all aspects.

6 Optimization procedure

The combined model is subject to an optimisation procedure that determines the maximum achievable load for differently sized versions of the baseline Scania D12 engine. Each engine starts with a baseline of an initial retarded spark timing of -10 °ca bTDC, an in-cylinder pressure of 101.5 kPa at IVC timing, and an in-cylinder temperature of 30 °C at IVC timing.

The two-zone combustion model calculates the trajectories of pressure and temperature for both zones, together with the indicated mean effective pressure (IMEP) and indicated thermal efficiency (η_i). Simultaneously, the knock model predicts the occurrence of knock. From this point onwards, if knock does not occur, the spark timing is advanced by 1 °ca increments until the 50% mass fraction burned point reaches -10 °ca bTDC, which is seen as the minimum spark advance for maximum torque (MBT timing), or until knock occurs. If the spark timing can be advanced up to MBT timing, the engine has not reached its maximum IMEP yet. In that case, intake pressure at IVC is increased by 5 kPa, representing an increased boost pressure. This load control mechanism is illustrated in Figure 2.

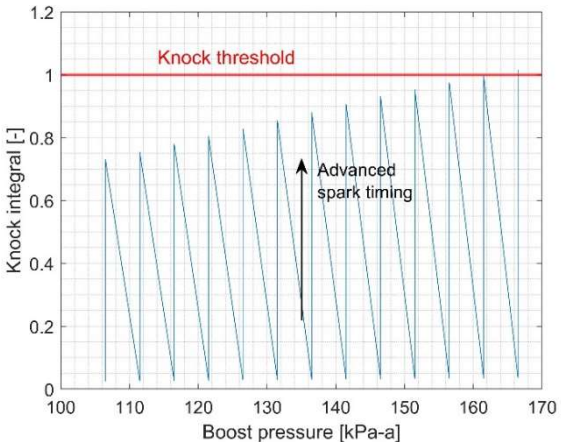


Figure 2: Illustration of the load control mechanism.

Starting from the left-hand, spark timing is advanced until MBT timing is reached. As the resulting knock integral remains below unity, the boost pressure is systematically increased until the knock limit is reached. For this example, this occurs at an inlet pressure of 165.5 kPa and a spark timing of 2 °ca bTDC. The associated IMEP is called the knock-limited IMEP. The in-cylinder temperature at IVC is

assumed constant, regardless of the boost pressure. The model can be further improved by implementing appropriate scavenging and turbocharger models. Additionally, the maximum IMEP is limited by the peak pressure. Therefore, the predicted maximum cylinder pressure is compared to a limit of 150 bar.

In Section 8, this procedure is used to calculate the maximum achievable IMEP, limited by either peak pressure or knock, for differently sized engines. The proportions of the combustion chamber (s/B, L/B and r_c) are held constant to the values specified in Section 2. The rotational engine speed however should not be considered constant, as this is limited by the inertial forces acting on the pistons for heavy-duty engines. Instead, a constant mean piston speed c_m is maintained, as this parameter remains rather constant across different engines. Note that for constant values of $c_{m,0}$ and λ, θ_d expressed in °ca (see Equation (13)) will therefore not by influenced by engine size, but only by spark timing and inlet pressure. This is legitimised as follows: an engine having twice the bore size operates at half the engine speed. For a constant flame speed, the flame front thus has twice the time available to travel double the distance, resulting in a θ_d expressed in °ca.

7 Model development and validation

With all three model components addressed, the experimental data is used to select the best-fitting burn duration correlation. Implementation of this correlation completes the model, after which its correct working will be validated.

7.1 Semi-predictive burn duration model

For the current application, the most important operating parameters are θ_s and P_{in}. Figure 3 shows the experimental burn duration (defined between spark timing and 95% mass fraction burned) as a function of air-to-fuel ratio λ and gauge inlet pressure $P_{in,g}$. The trend seems to be dominated by the air-to-fuel ratio λ. Starting from stoichiometric operation, the burn duration almost doubles when going to a λ value of 1.8. The reduced reaction rate and relatively low burning rates in diluted mixtures produce an almost linearly increasing trend [24]. An increased boost pressure $P_{in,g}$ only has a minor influence. Especially mixtures with a λ value below 1.6 seem unaffected by $P_{in,g}$. For leaner mixtures, θ_d seems to become a little shorter for some points, but other points show the inverse effect. The performance of the correlations by Lindström et al. [13], Alam et al. [14] and Rousseau et al. [15] is assessed by comparison with this experimental data.

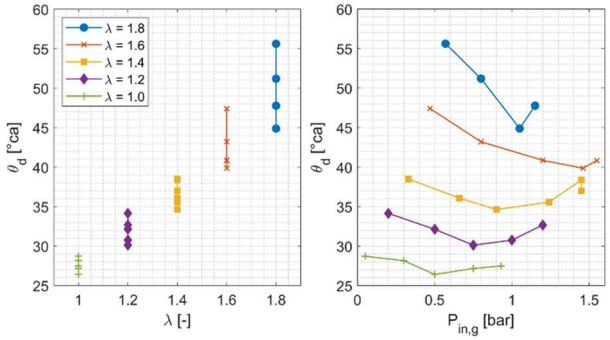


Figure 3: The effect of input variables (λ and $P_{in,g}$) on θ_d for the high load points on the Scania D12.

First, Figure 4 compares the predicted burn durations by Lindström et al. [13] and the measured values, together with perfect fit lines $x = y$ and $x = 2 \cdot y$ for reference. Overall, the correlation overestimates the measured values. The error remains reasonable for lower values of λ, but the measured values are overpredicted by 100% at $\lambda = 1.8$.

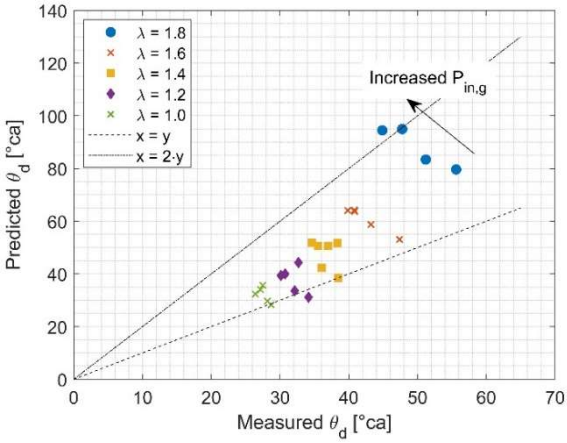


Figure 4: Predicted θ_d versus measured values for different λ values using the correlation of Lindström et al. [13].

The discrepancy can partly be explained by the use of different definitions for θ_d between experiments and correlation, but further analysis shows that the correlation overestimates the impact of a reduced laminar burning velocity S_L at leaner conditions. Figure 5 shows the function $F_{SL}/F_{SL,0}$ that expresses the relative influence of the S_L on θ_d (see Equation (10)). A central point from the experimental matrix is chosen as reference ($\lambda = 1.4, P_{in,g} = 0.33\ bar$, see Figure 1), so $F_{SL}/F_{SL,0}$ equals unity there. This factor is halved for $\lambda = 1$, while it reaches a value of almost 3 for $\lambda = 1.8$. Although the changing S_L will certainly affect θ_d, its impact will not be of this magnitude. The laminar burning velocity predominantly influences the initial combustion

phase, after which the main, fast burning phase is mainly governed by the turbulence intensity [25]. Additionally, for constant values of λ, the predicted burn duration increases with $P_{in,g}$. This is in agreement with the general behaviour of S_L, which tends to decrease linearly with pressure [19]. The experimental burn duration shows the opposite trend however.

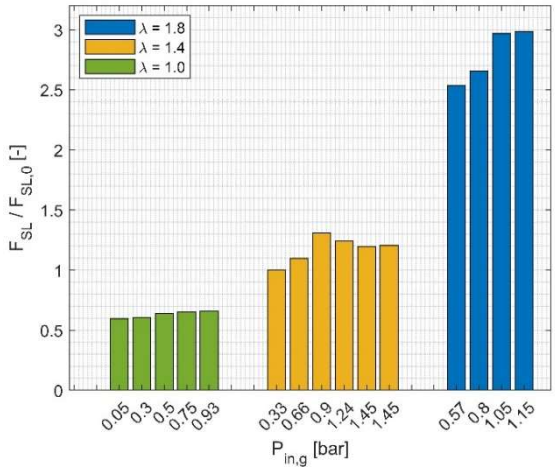


Figure 5: Relative influence of the laminar burning velocity on θ_d for different $P_{in,g}$ at three λ values.

Next, Figure 6 shows the predicted θ_d by the correlation of Alam et al. [14]. Much better results are obtained, showing an acceptable increase in the burn duration for leaner mixtures. Yet, the effect of an increased $P_{in,g}$ is not fully captured. Figure 3 showed that $P_{in,g}$ only has a significant effect at the upper lean limit, while for richer mixtures, θ_d remains more or less unaffected by pressure.

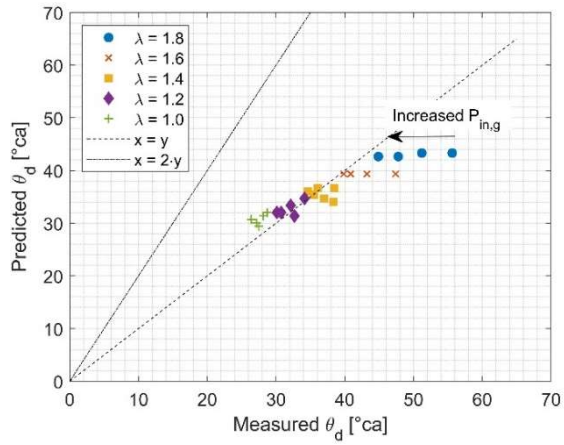


Figure 6: Predicted θ_d versus measured values for different λ values using the correlation of Alam et al. [14].

Lastly, Figure 7 shows the predicted θ_d using the correlation of Rousseau et al. [15], which takes the effects of both $P_{in,g}$, θ_s and λ into account (see Equation (15)). For leaner mixtures with $\lambda \geq 1.4$, the predictions agree well with the experiments. However, results deviate as soon as we leave the validation range of the correlation. Therefore, the coefficients should be returned to a wider set of data.

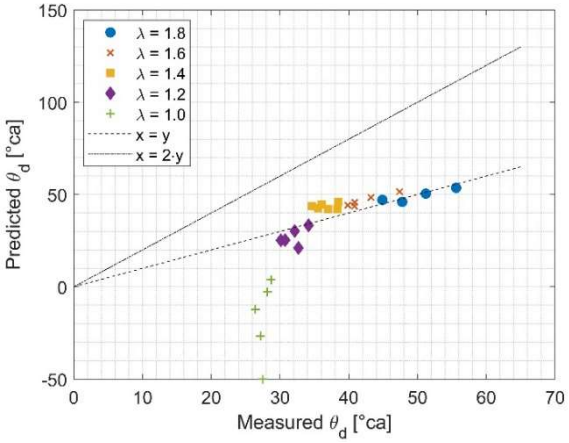


Figure 7: Predicted θ_d versus measured values for different λ values using the correlation of Rousseau et al. [15].

Based on the results presented above, the burn duration correlation by Alam et al. [14] is selected as optimal fit. For optimal model performance however, the coefficients of Equation (13) should ultimately be retuned for the operating range of interest, and, more interestingly, specifically for methanol fuel. The semi-predictive combustion model can be further improved by using the Wiebe law to describe the burn rate [21], instead of the cosine law (Equation (7)). This requires correlations not only for the burn duration, but also for the Wiebe form factor and efficiency factor. Although this is included in the correlations by Lindström et al. [13], Alam et al. [14], no satisfactory fit with the experimental data was obtained.

7.2 Model validation

By implementing the semi-predictive burn duration correlation of Alam et al. [14], the model is complete. Before the model is used to predict performance parameters, its correct working is validated. First, the combustion model is validated against the experimental data by Mahendar et al. [16], who performed load sweeps at different λ values by increasing P_{in}. Figure 8 compares these experimental IMEP values to the model's predictions for the same intake conditions and spark timings. The linear trend is predicted reasonably well, except for the leanest

mixtures ($\lambda = 1.8$), which can be expected as the burn duration model also deviates at these conditions (see Figure 6).

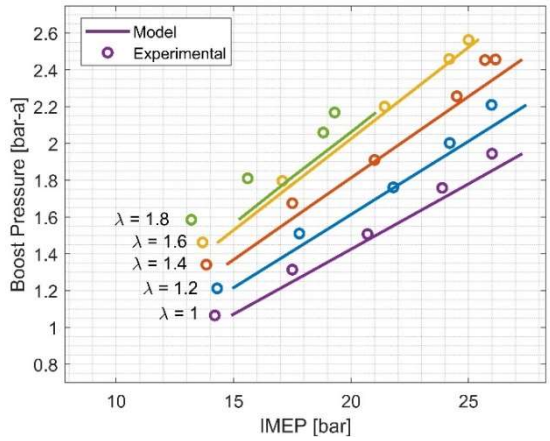


Figure 8: The predicted IMEP versus experimental values as a function of P_{in} at different λ values.

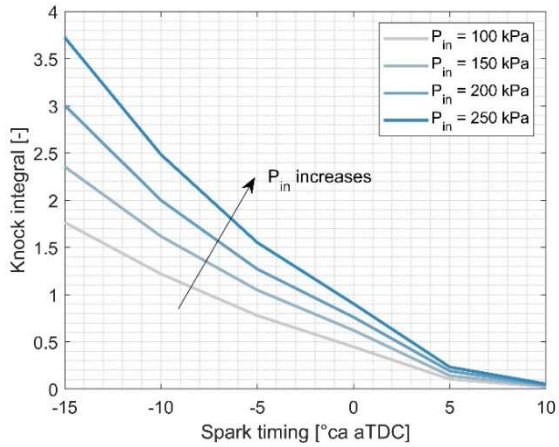


Figure 9: Knock integral values at EVO for different spark timings and P_{in} ($\lambda = 1$).

Next, the working of the coupled combustion and knock model is assessed. Figure 9 shows the value of the knock integral at EVO for advanced spark timings and increased inlet pressures at $\lambda = 1$. Clearly, the knock integral value increases drastically for advanced spark timings, due to the higher unburned temperatures. An increased P_{in} shows a minimal impact at first, but becomes significant once the spark timing is advanced and combustion occurs earlier in the compression stroke. Note that for an inlet pressure of 150 kPa, the knock integral at EVO exceeds unity at a spark timing of 4.5 °ca bTDC. This operating point was used as the calibration point for the knock model, as discussed in Section 5.

This shows that both the predicted power output and knock integral values of the combined model show a satisfactory behaviour. Thus, the model is ready to estimate the performance of scaled versions of the Scania D12 engine.

8 Scaling performance parameters

The complete model is used to calculate the maximum power output, limited by either peak pressures or knock, and corresponding efficiency for differently sized engines through the procedure discussed in Section 6. The engine bore size is increased in increments of 10 mm, starting from 80 mm (automotive size) to 260 mm (marine size). Three mean piston speeds are investigated: the baseline value of 6.16 m/s, as well as its double and triple values of 12.32 m/s and 18.48 m/s respectively.

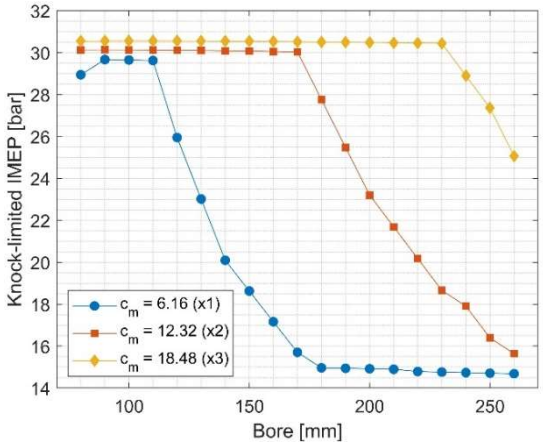


Figure 10: Maximum IMEP as a function of bore size for different mean piston speeds at $\lambda = 1$.

The results are shown in Figure 10. Starting with the lowest c_m, engines up to a bore size of 110 mm are not limited by knock, but by the peak in-cylinder pressure limit. This pressure limit results in a near constant IMEP value of 29.6 bar. Higher loads can be obtained for these engines by investing in a sturdier engine block. From 110 mm onwards, the IMEP becomes knock-limited. Here, the main influencing factor is the reduced rotational engine speed at higher bore sizes, which results in an increased burn duration in seconds (see Section 6). This provides the end-gas with more time to autoignite, resulting in a reduced IMEP. This trend continues up to a bore size of 180 mm, where the IMEP is limited to only 15 bar. For even larger engines, the trend stagnates. Here, boost pressure can no longer be applied without causing knock, even for the latest spark timings. Hence, the model stops and tries to advance the spark timing until the knock integral reaches unity. The downward trend could be continued by implementing negative $P_{in,g}$, which simulates a throttle valve in the intake line.

The knock constraints are significantly reduced by doubling the mean piston speed ($c_m = 12.32\ m/s$). Now, engines are knock-free until a bore size of 170 mm and no throttling is required within the current engine size range. When setting a target of 25 bar IMEP, which is common for heavy-duty diesel operation [16], methanol-fuelled PFI SI engines would be a viable replacement for engines up to a 190 mm bore. For an even higher mean piston speed of 18.54 m/s, engines are limited by peak pressures up to a 230 mm bore. Such mean piston speeds however are at the limit of current conventional SI engines. Current heavy-duty natural gas SI engines have a mean piston speed of about 10.2 m/s [6]. Realistic performance values should therefore be sought between the first and second curve.

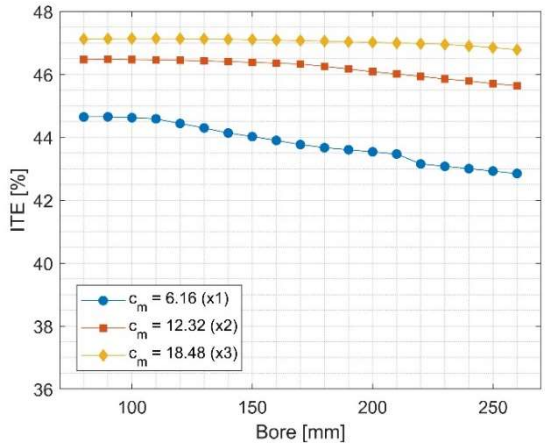


Figure 11: Indicated thermal efficiency as a function of bore size for different mean piston speeds at $\lambda = 1$.

When comparing efficiencies, Figure 11 shows an increased efficiency for higher c_m, due to the reduced heat losses from the shorter residence time of the mixture. However, this advantage could be partially negated with the implementation of a friction model to predict brake thermal efficiencies. Considering individual curves, the curve for $c_m = 6.16 m/s$ can be seen to drop in three stages. After a constant efficiency in the pressure-limited region, the efficiency gradually reduces together with the knock-limited IMEP. Once the intake reaches atmospheric pressure, the IMEP and efficiency do not decrease significantly anymore. The spark timing is retarded to remain below the knock limit however. The other curves show a similar trend, albeit to a lesser extent due to the reduced impact of knock.

Lastly, the impact of diluted air-to-fuel mixtures is investigated at a mean piston speed of 12.32 m/s. The trendlines for the maximum IMEP for λ ranging from 1 to 1.6 are shown below.

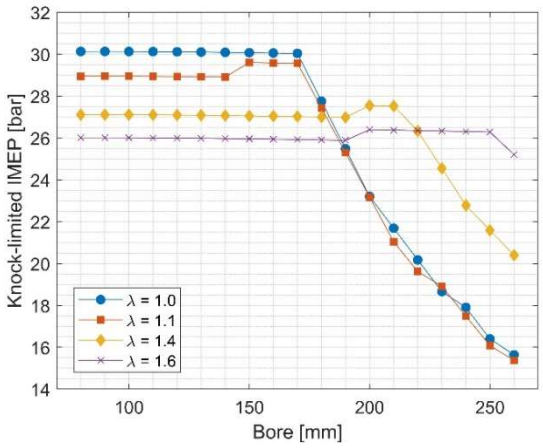


Figure 12: Maximum IMEP as a function of bore size for different λ values at c_m = 12.32 m/s.

Firstly, within the pressure-limited zone, the maximum achievable IMEP is reduced for diluted mixtures due to the increased boost pressure. Starting from a maximum IMEP of 30 bar at $\lambda = 1$, only 26 bar can be achieved at $\lambda = 1.6$. On the other hand, the increased ignition delay times of diluted mixtures extends the knock-free zone to larger engines. Furthermore, since the engine load is reduced for the same boost pressure, the temperature of the unburned gas also decreases, resulting in a longer ignition delay time. For $\lambda = 1.4$, engines remain knock-free until 210 mm, while knock only starts at 250 mm for $\lambda = 1.6$. With a target IMEP of 25 bar, knock-free operation is possible up to 190 mm engines at $\lambda = 1$. This can be extended up to 230 mm and 260 mm for leaner conditions.

9 Conclusions

This paper aimed to predict the maximum achievable load and corresponding efficiency for methanol-fuelled port-fuel injected spark-ignited engines of different sizes. To this end, a combustion model was coupled to a knock model. A homogeneous two-zone combustion model with a constant burn duration was expanded with a blow-by model and a zone- (burned/unburned) and crank angle-specific heat transfer model. Most importantly, a semi-predictive burn duration model was implemented, accounting for the impact of operating conditions (P_{in}, N, λ,…) on the burn duration. To this end, correlations by Lindström et al. [13], Rousseau et al. [15] and Alam et al. [14] were compared to experimental data of a methanol-fuelled heavy-duty Scania D12 engine in PFI SI-operation [16]. The burn duration correlation by Alam et al. provided the best fit. This combustion model was coupled to a knock integral model, which was supplied with autoignition delay times calculated

using the kinetic mechanism by Pichler [22], and was calibrated to a single knock-limited operating point from the Scania D12 data set. The combined model was subject to an optimisation procedure to determine maximum load and corresponding efficiency. Engine bore sweeps were conducted for three mean piston speeds (6.16 m/s, 12.32 m/s and 18.48 m/s) and four relative air-to-fuel ratios (1, 1.1, 1.4 and 1.6). The following trends are observed for a constant mean piston speed and air-to-fuel ratio:

- Smaller engines have a constant maximum engine load, limited by peak pressure. A more robust engine block is needed to fully exploit methanol's knock-resistance.
- For larger engines, the maximum IMEP is systematically reduced due to the increased knocking tendency.
- This trend continues, until knock occurs even at atmospheric inlet pressures. In this case throttling of the intake is required to achieve knock-free operation without spark retard.

For a mean piston speed of 12.32 m/s, the peak-pressure limited IMEP is 29.6 bar. Such engines become knock-limited at a bore size of 170 mm. A 260 mm bore engine would be limited to 15.6 bar IMEP in this case. The knock constraints can be partly lifted by increasing the mean piston speed to 18.54 m/s. These engines are pressure-limited up to 230 mm bore and achieve a maximum IMEP of 25 bar at a 260 mm bore. However, as such engine speeds are the current upper limit of conventional engines, a more realistic solution is to adopt diluted air-fuel mixtures. This reduces the peak-pressure limited IMEP, but extends knock-free operation to larger engines. If a target value of 25 bar IMEP is set, knock-free engines up to 190 mm are possible if running at stoichiometric conditions. If lean operation is allowed, bore sizes op to 230 and 260 mm are possible for λ=1.4, and λ=1.6 respectively. Alternatively, faster or less knock-restricted combustion systems can be used, such as active or passive pre-chamber spark-ignited engines.

Acknowledgement

This research was conducted as part of Ph.D. projects funded by the Energy Transition Fund of the Belgian federal government, under the "Belgian Energy Transition" project (best-energy.be), and by the Ghent University Special Research Fund (BOF23/DOC/091). These financial supports are gratefully acknowledged.

References

[1] Md. S. Alam, F. S. Al-Ismail, A. Salem, and M. A. Abido, 'High-Level Penetration of Renewable Energy Sources Into Grid Utility: Challenges and Solutions', *IEEE Access*, vol. 8, pp. 190277–190299, 2020, doi: 10.1109/ACCESS.2020.3031481.

[2] F. Feijoo, A. Pfeifer, L. Herc, D. Groppi, and N. Duić, 'A long-term capacity investment and operational energy planning model with power-to-X and flexibility technologies', *Renewable and Sustainable Energy Reviews*, vol. 167, p. 112781, Oct. 2022, doi: 10.1016/j.rser.2022.112781.

[3] E. Anetjärvi, E. Vakkilainen, and K. Melin, 'Benefits of hybrid production of e-methanol in connection with biomass gasification', *Energy*, vol. 276, p. 127202, Aug. 2023, doi: 10.1016/j.energy.2023.127202.

[4] Y.-H. Pu, Q. Dejaegere, M. Svensson, and S. Verhelst, 'Renewable Methanol as a Fuel for Heavy-Duty Engines: A Review of Technologies Enabling Single-Fuel Solutions', *Energies*, vol. 17, no. 7, p. 1719, Apr. 2024, doi: 10.3390/en17071719.

[5] S. K. Mahendar, A. Erlandsson, and L. Adlercreutz, 'Challenges for Spark Ignition Engines in Heavy Duty Application: a Review', presented at the WCX World Congress Experience, Apr. 2018, pp. 2018-01–0907. doi: 10.4271/2018-01-0907.

[6] W. Suijs and S. Verhelst, 'Scaling Performance Parameters of Reciprocating Engines for Sustainable Energy System Optimization Modelling', *Energies*, vol. 16, no. 22, p. 7497, Nov. 2023, doi: 10.3390/en16227497.

[7] C. Elmqvist, F. Lindström, H.-E. Ångström, B. Grandin, and G. Kalghatgi, 'Optimizing engine concepts by using a simple model for knock prediction', SAE Technical Paper, 2003.

[8] J. C. Livengood and P. C. Wu, 'Correlation of autoignition phenomena in internal combustion engines and rapid compression machines', *Symposium (International) on Combustion*, vol. 5, no. 1, pp. 347–356, Jan. 1955, doi: 10.1016/S0082-0784(55)80047-1.

[9] J. A. Caton, 'Thermodynamic Considerations Related to Knock: Results From an Engine

Cycle Simulation', *Journal of Engineering for Gas Turbines and Power*, vol. 140, no. 9, p. 092805, Sep. 2018, doi: 10.1115/1.4039750.

[10] A. Lewis, E. Ortiz-Soto, G. Lavoie, and D. N. Assanis, 'Scaling and dimensional methods to incorporate knock and flammability limits in models of high-efficiency gasoline and ethanol engines', *International Journal of Engine Research*, vol. 16, no. 2, pp. 181–196, Feb. 2015, doi: 10.1177/1468087414530387.

[11] D. Dimitrov, G. Kammel, E. Egert, N. Wermuth, and A. Wimmer, 'Development of an 1D multicylinder engine model to predict knocking and emissions of large gas engines', *Trans Motauto World*, vol. 8, no. 3, pp. 92–95, 2023.

[12] J. M. Borg and A. C. Alkidas, 'On the application of Wiebe functions to simulate normal and knocking spark-ignition combustion', *International journal of vehicle design*, vol. 49, no. 1–3, pp. 52–69, 2009.

[13] F. Lindström, H.-E. Angstrom, G. Kalghatgi, and C. E. Möller, 'An Empirical SI Combustion Model Using Laminar Burning Velocity Correlations', presented at the 2005 SAE Brasil Fuels & Lubricants Meeting, May 2005, pp. 2005-01–2106. doi: 10.4271/2005-01-2106.

[14] S. S. Alam, S. W. Rosa, C. Depcik, S. Preetham Burugupally, E. McDaniel, and J. D. Hobeck, 'Modification of the Wiebe function for methane-air and oxy-methane- based spark-ignition engines', *Fuel*, vol. 303, p. 121218, Nov. 2021, doi: 10.1016/j.fuel.2021.121218.

[15] S. Rousseau, B. Lemoult, and M. Tazerout, 'Combustion characterization of natural gas in a lean burn spark-ignition engine', *Proceedings of the Institution of Mechanical Engineers, Part D: Journal of Automobile Engineering*, vol. 213, no. 5, pp. 481–489, May 1999, doi: 10.1243/0954407991527044.

[16] S. K. Mahendar, T. Larsson, and A. C. Erlandsson, 'Alcohol lean burn in heavy duty engines: Achieving 25 bar IMEP with high efficiency in spark ignited operation', *International Journal of Engine Research*, vol. 22, no. 11, pp. 3313–3324, Nov. 2021, doi: 10.1177/1468087420972897.

[17] C. R. Ferguson and A. T. Kirkpatrick, *Internal combustion engines: applied thermosciences*. John Wiley & Sons, 2015.

[18] G. Woschni, 'A universally applicable equation for the instantaneous heat transfer coefficient in the internal combustion engine', SAE Technical paper, 1967.

[19] J. Vancoillie, S. Verhelst, and J. Demuynck, 'Laminar Burning Velocity Correlations for Methanol-Air and Ethanol-Air Mixtures Valid at SI Engine Conditions', presented at the SAE 2011 World Congress & Exhibition, Apr. 2011, pp. 2011-01–0846. doi: 10.4271/2011-01-0846.

[20] P. Tunestål, 'Self-tuning gross heat release computation for internal combustion engines', *Control Engineering Practice*, vol. 17, no. 4, pp. 518–524, Apr. 2009, doi: 10.1016/j.conengprac.2008.09.012.

[21] I. Wiebe, 'The combustion speed in internal combustion piston engines', *Collected works of piston engine research, Laboratory of Engines, Academy of Sciences, USSR, Moscow.(Translated to English by M. Kiisa, KTH 1993)(a)(b)*, 1956.

[22] C. Pichler and E. J. K. Nilsson, 'Reduced Kinetic Mechanism for Methanol Combustion in Spark-Ignition Engines', *Energy Fuels*, vol. 32, no. 12, pp. 12805–12813, Dec. 2018, doi: 10.1021/acs.energyfuels.8b02136.

[23] W. Suijs, J. Dierickx, Y.-H. Pu, Y. Wang, and S. Verhelst, 'Calibrating the Livengood–Wu integral knock model for differently sized methanol engines', *Fuel Communications*, vol. 19, p. 100121, Jun. 2024, doi: 10.1016/j.jfueco.2024.100121.

[24] A. Gorczakowski and J. Jarosiński, 'Lean-burn combustion systems in spark ignitron engines: advantages and limitations', *Journal of KONES*, vol. 15, pp. 97–102, 2008.

[25] S. Verhelst and C. G. W. Sheppard, 'Multi-zone thermodynamic modelling of spark-ignition engine combustion – An overview', *Energy Conversion and Management*, vol. 50, no. 5, pp. 1326–1335, May 2009, doi: 10.1016/j.enconman.2009.01.002.

ENHANCING FAULT DETECTION AND DIAGNOSIS IN ORGANIC RANKINE CYCLE SYSTEMS THROUGH PROPER FEATURE SELECTION IN MACHINE LEARNING

Andrés Hernández[1]*, Aitor Cendoya[1], Aldo Serafino[2], Michel Beaughon[2], Vincent Lemort[1]

[1] Université de Liège, Thermodynamics Laboratory, Liège, Belgium

[2] Enertime, R&D division, Courbevoie, France

* *Corresponding Author: jahernandez@uliege.be*

Abstract. In the current energy scenario, enhancing energy efficiency is crucial for sustainable development. Organic Rankine Cycle (ORC) systems play a significant role by recovering waste heat and converting it into useful energy. However, the efficiency and robustness of ORC systems are often compromised by various types of faults, leading to increased maintenance costs. This study focuses on fault detection and diagnosis (FDD) to improve system reliability and reduce maintenance expenses in ORC systems. The proposed methodology utilizes machine learning, specifically support vector machines (SVM), to detect and classify faults such as evaporator fouling and operational deficiencies in the expander and pump. A critical aspect of this approach is the careful choice of features for classification, which can either significantly enhance SVM's effectiveness or lead to misclassification of certain faults. Simulation results explore various feature sets to illustrate their impact on the FDD methodology's efficacy. These scenarios are evaluated in terms of prediction accuracy, demonstrating that proper feature selection improves the long-term efficiency and reliability of ORC systems.

Keywords. Fault detection and diagnosis, Organic Rankine cycle, Support vector machine.

Nomenclature (if relevant)

P	Pressure (Pa)
T	Temperature (°C)
h	Specific enthalpy (J/kg)
$\dot{Q}$	Heat transfer rate (J/s)
$\dot{m}$	Mass flow rate (kg/s)

Special characters

η	Efficiency (-)
η_s	Isentropic efficiency

Subscripts

su	supply
ex	exhaust
hf	Hot fluid
cf	Cold fluid
ev	Evaporator
cd	Condenser
exp	Expander

1 Introduction

The increasing global demand for energy efficiency and sustainability has intensified interest in technologies such as Organic Rankine Cycles (ORCs) for waste-heat recovery and renewable energy generation [1]. The fluctuating nature of the waste heat source make the ORC system to operate frequently at off-design conditions [2], therefore during long-term operation it becomes particularly difficult to identify from the sensor data available, if there exists a fault in a component or sensor, or if it is due to the specific operating conditions. Thus, given these vulnerabilities developing fault detection and diagnosis (FDD) techniques to maintain optimal performance and reliability for these complex energy systems is currently of high interest [3]. Note that effective FDD in ORCs not only reduces downtime and operational costs but also contributes to extending the lifecycle of these systems, enhancing their overall economic viability.

FDD in energy systems has evolved significantly, with various approaches. Model-based approaches, for instance, leverage the physical dynamics of an industrial heat exchanger to predict normal behaviour and detect deviations that may indicate faults [4]. In the context of ORC systems for geothermal

applications, dynamic modelling has proven useful for detecting performance anomalies, helping to support control system design and robust fault diagnosis using residual analysis [5].

Data-driven methods, including machine learning, have been increasingly applied to FDD tasks across complex systems, where they offer adaptability to system variations and the potential for high accuracy. Most scientific contributions of FDD are in the field of refrigeration systems and for heating, ventilation and air conditioning HVAC, as for example [6], where predictive frameworks are explored to automatically assess the system's state of degradation from unlabelled data. Whilst in [7] it is highlighted for the case of Air Conditioning how soft faults decrease the system performance (i.e., increases energy consumption) and are more difficult to detect, thus requiring more sensors.

Hybrid approaches that combine model-base-driven techniques are particularly promising for complex applications, as they can accommodate both the complex dynamics and diverse fault types present in these systems. Methods such as digital twin frameworks and advanced filtering algorithms, including extended Kalman filters and one-class Support Vector Machine (SVM), have been explored for real-time FDD applications in energy systems, including air handling and chiller units [8,9]. Where these frameworks not only enhance fault detection but support decision-making by providing actionable insights into system health and performance.

At the best author knowledge literature on FDD for ORC systems is scarce. For instance, [10] demonstrated the application of machine learning in fault detection for ORC systems dedicated to waste-heat recovery, illustrating the power of supervised learning models to detect four different faults using six sensor data.

This study aims to identify the strengths and limitations of Support Vector Machine for FDD and propose a methodology to optimally define the number and type of features (i.e., sensors or variables) used to train the machine learning algorithm. The findings will contribute to a deeper understanding of fault management strategies in ORC systems, promoting the development of more resilient and efficient energy recovery solutions.

2 Methodology

In this section the description of the organic Rankine cycle architecture is presented, as well as a general analysis of the faults considered in this study and the simulation approach.

2.1 ORC process architecture

The ORC power unit considered corresponds to a 50kWe expander, using refrigerant R1234yf as working fluid and with architecture as depicted in Figure 1.

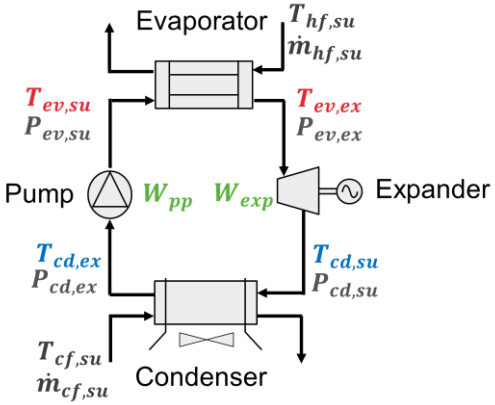


Figure 1: Process architecture.

The refrigerant in liquid state is pumped up, increasing its pressure at the moment of reaching the evaporator inlet, then heat is exchanged between the refrigerant and the secondary fluid which is in this case water at an average temperature $T_{hf,su} = 90$°C and mass flow rate $\dot{m}_{hf,su} = 12.5$ kg/s. The refrigerant boils and is heated up until a superheating state at the expander inlet. The vapour passes through the expander, making it rotate thus producing electrical power when connected to a generator, leading to a drop in temperature and pressure in the refrigerant at condenser input. The condenser ensures that the refrigerant will be back in a liquid state thus closing the loop. Water is used as secondary fluid in the condenser, at an average temperature $T_{cf,su} =$ 10°C and mass flow rate $\dot{m}_{cf,su} = 22.5$ kg/s.

The simulator is built considering refrigerant R1234yf as a working fluid, while its properties are computed using CoolProp [11] in Python. Braze Plate Heat exchanger for both, condenser and evaporator are selected due to their high efficiency for liquid applications. The methodology followed for these heat exchangers corresponds to a discretization according to the different refrigerant zones [12]. The condenser and evaporator are discretized in three zones (zi); superheating (sh), two-phase (tp) and subcooled (sc) zone. Those models are based on physical principles, and the solving process is carried out based on iteration of the saturation pressure at vapour quality. The problem is considered solved

when the difference between the real area and the area computed is lower than a tolerance value of 1 x 10 -6 [12].

The energy balance of the condenser is presented in Equation 1 for the refrigerant side. Additionally, the heat transfer equation presented in Equation 2 is considered to represent any change in the heat exchanger performance by a change in the operational conditions or geometry. For this equation a counter arrangement is considered between the refrigerant and the water loops.

$$\dot{Q}_{cd} = \sum_{i}^{sh,tp,sc} \dot{m}_r \cdot \left(h_{r,su,zi,cd} - h_{r,ex,zi,cd}\right) \quad (1)$$

$$\dot{Q}_{cd} = \sum_{zi}^{sh,tp,cd} \varepsilon_{zi,cd} \cdot \dot{C}_{min,zi,cd} \cdot \left(T_{r,su,zi,cd} - T_{w,su,zi,cd}\right) \quad (2)$$

The effectiveness of the heat transfer process can be computed by Equation 3 and 4, for the single phase and the two-phase zone, respectively.

$$\varepsilon_{zi,cd} = \frac{1 - e^{\left(-NTU_{zi,cd}\cdot\left(1-C_{r,zi,cd}\right)\right)}}{1 - C_{r,zi,cd} \cdot e^{\left(-NTU_{zi,cd}\cdot\left(1-C_{r,zi,cd}\right)\right)}} \quad (3)$$

$$\varepsilon_{tp,cd} = 1 - e^{\left(-NTU_{tp,cd}\right)} \quad (4)$$

The overall heat transfer coefficient in each zone (UA_(zi,cd)) considers the possibility of fouling in the heat exchanger which basically represent the thermal resistance of the fouling thickness in the heat transfer. The UA_(zi,cd)is computed as the sum of the thermal resistance of the water and refrigerant, beside is necessary to consider the thermal resistance of the plates (R_(zi,cd)). To relates the overall heat transfer within the effectiveness of the process Equation 5 is employed, which allows to compute the area, which will the comparison value for the iteration problem.

$$NTU_{zi,cd} = U_{zi,cd} \cdot A_{zi,cd} / \dot{C}_{min,zi,cd} \quad (5)$$

The BPHXs are validated against SWEP manufacturer data for the design condition. The model considered in the validation corresponds to:

• Model B633MH, within 278, 250 and 160 plates.

• Model B439H, within 220, 140 and 120 plates.

The developed model presents an error below 5% for the heat power capacity, 4 K for the exhaust refrigerant temperature and below 10% for the pressure drops.

A centrifugal pump is employed in this configuration due to its high efficiency, where the isentropic efficiency is extracted from the manufacturer curves for the operational range. The pump Movitec V F010/11 from KSB is chosen.

The expander is modelled by thermodynamic equations, assuming that the expansion is an isentropic process. For that an isentropic efficiency of 0.7 [21] is considered, and a volumetric efficiency of 0.95. The Equation 6 is employed to compute the expander power.

$$\dot{W}_{exp} = \dot{M}_r \cdot \varepsilon_{exp} \cdot \left(h_{r,e,ex,exp} - h_{r,su,exp}\right) \quad (6)$$

The nominal conditions of the ORC system are presented in Table 1, where the secondary fluid temperatures and mass flow rates can be analysed. Moreover, the parameters for the expander and pump are also presented, with their respective operational speed.

Table 1: Nominal simulation conditions.

Simulation condition	value
Heat source temperature ($T_{hf,su}$)	90 °C
Heat source mass flow rate ($\dot{m}_{hf,su}$)	12.5 kg/s
Heat sink temperature ($T_{cf,su}$)	10 °C
Heat sink mass flow rate ($\dot{m}_{cf,su}$)	22.5 kg/s
Expander isentropic efficiency	0.7
Pump isentropic efficiency	0.7
Expander speed (N_{exp})	3000 rpm
Pump speed (N_{pp})	2400 rpm

2.2 Faults description

In the present study 4 conditions are considered: the healthy state, heat exchanger fault, expander fault and pump fault. First an attempt for physical interpretation is provided and then the form how the simulator emulates the fault is described.

2.2.1 Heat exchanger fault: some of the most common faults in heat exchangers include fouling, leaking and blocking. Over extended operating periods, fouling faults arise due to crystallization, sedimentation, coking, corrosion, and similar processes. This results in a layer of fouling that gradually builds up on the surface of the heat exchanger. Because the heat conductivity of this

fouling layer is very low, it directly reduces the heat exchanger's efficiency, leading to significant economic losses [15]. For instance, when the evaporator operates at low efficiency, the input temperature to the expander drops, reducing the ORC's work capacity. In this study fouling is emulated by proportionally decreasing the number of plates as fouling occurs. Other types of faults are not considered at the moment.

2.2.2 Expander fault: The expander generates mechanical work by expanding high-temperature, high-pressure organic fluid, directly influencing the system's power output. Expanders are classified as either speed or volume type, with faults typically categorized into thermal performance and mechanical functional faults. Thermal performance faults often show as irregular discharge volume, abnormal pressure differences, and elevated exhaust temperatures, usually due to issues with parts like the air valve, piston ring, or cooling channels. Mechanical functional faults, on the other hand, manifest as unusual vibration, noise, or overheating, stemming from loosened components, wear-induced gaps, or structural cracks. These faults significantly decrease expander efficiency and, if left unaddressed, may lead to severe system failures. Due to the critical impact of mechanical faults, this paper focuses on diagnosing a specific type of mechanical fault, which is emulated as a decrease in the expander isentropic efficiency.

2.2.3 Pump fault: The pump functions to transport and pressurize the working fluid, with types generally classified as positive displacement, dynamic, or electromagnetic, based on how pressure is applied. Pumps are prone to various faults, including reduced speed, blockage, and leakage. When such issues arise, the pump cannot achieve the required pressure, resulting in a reduced mass flow rate of the working fluid. In this work a centrifugal pump is considered with fault emulated by a drop in the isentropic efficiency.

Finally, 4 sets of training data are collected from the ORC thermodynamic model, including a no-fault data set and three data sets with different typical faults, to detect whether a fault occurs in the system as summarized in Table 2.

Table 2: Summary of simulation fault conditions.

Data set	Simulation condition	Class label
No fault	Healthy state	0
Fault 1	Heat exchanger fouling	1
Fault 2	Mechanical fault in expander	2
Fault 3	Mechanical fault in pump	3

2.3 Data generation

In order to stablish during the simulation study conditions similar as the ones encountered on a real application, closed loop control for superheating and subcooling are employed with setpoint in $\Delta T_{sh,ref} = 7$ K and $\Delta T_{sc,ref} = 2$ K.

Additionally, for each simulation condition from Table 2, a random Gaussian distribution is employed for $T_{hf,su}$ and $T_{cf,su}$, with standard deviation 6 and 2, respectively.

3 FDD through Support Vector Machine

In this section the mathematical description of the machine learning classification algorithm implemented as FDD solution is presented, as well as the features selection and the tuning methodology.

3.1 Support Vector Machine (SVM)

The support vector machine, developed in [16], is a highly powerful and flexible model rooted in statistical learning theory. It is effective for both linear and nonlinear classification, regression, and outlier detection, especially with small sample sizes and high-dimensional data [17].

Support vector machines are supervised learning algorithms used for classification that work by finding an optimal hyperplane that maximizes the margin between two classes. In mathematical terms, for a set of training points (x_i, y_i) where $x_i \in \mathbb{R}^n$ and $y_i \in \{-1,1\}$, the objective of SVM is to maximize the margin $\frac{2}{\|w\|}$ between the classes.

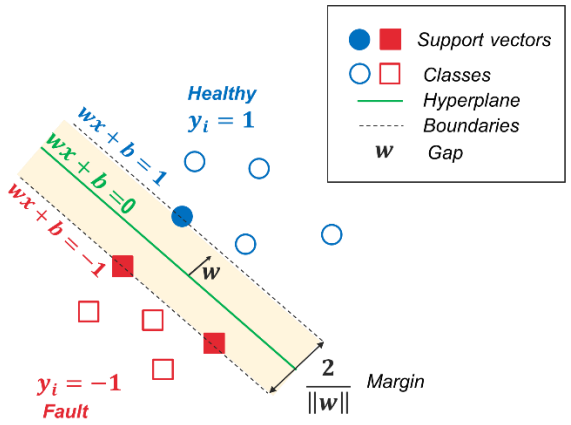


Figure 2: Principle of Support Vector Machine.

This is achieved by solving the optimization problem:

$$\textbf{min} \quad \frac{1}{2}\|w\|^2 + C\sum_{i=1}^{N}\xi_i \tag{7}$$

$$subject\ to: \quad y_i(w \cdot x_i + b) \geq 1 - \xi_i \tag{8}$$
$$for\ i = 1,2,\dots,N \ \text{ and } \ \xi_i \geq 0$$

Where w is the weight vector, and b is the bias term. Note that in order to prevent overfitting and achieving a proper trade-off between achieving a low error on the training data and minimizing the model complexity the regularization parameter C is used, with ξ_i the slack variables representing the degree of misclassification of each data point.

A small value of C allows the optimizer to increase the margin, even if it means misclassifying more points. It makes the decision surface smoother (high bias, low variance). A large value of C tries to classify all training examples correctly by giving the model the freedom to select more complex decision boundaries (low bias, high variance).

Additionally, when the data is not linearly separable, SVM introduces a kernel function $\mathbf{K}(x_i, y_i)$ to transform the data into a higher-dimensional space, enabling linear separation. In this study the Radial Basis Function (RBF) kernel is used as transformation function:

$$\mathbf{K}(x_i, y_i) = \exp(-\gamma\|x_i - x_j\|^2) \tag{9}$$

The parameter γ determines the spread of the kernel, a larger value makes the kernel narrower, meaning each training point has a more localized influence. This can lead to a model that fits the training data closely (risking overfitting). Whilst a smaller value makes the kernel function broader, causing each point to have a more significant influence on the decision boundary, which can help the model generalize better.

In conclusion the optimization problem from Equation 7, Equation 8 and Equation 9, together generate a solution called in machine learning a soft-margin SVM algorithm. Where C controls the regularization and margin, allowing for a trade-off between margin size and classification error, while γ adjusts the influence range of each data point in nonlinear SVMs with kernels.

3.2 Optimal trade-off tuning

A first step before tuning the algorithm consists in normalising the data set between {-1,1}. This can be achieved by applying the following relation

$$\mathbf{X} = \frac{x_i - \mu}{\sigma} \tag{10}$$

with μ the media and σ the standard deviation of each data set. Subsequently, in order to find the optimal C and γ parameters defined in previous section, one can perform an exhaustive search over a specified parameter grid, e.g., C: [0.01, …, 1000] and γ: [0.001, 0.01, 0.1, 100], by evaluating each combination of C and Gamma values using cross-validation.

3.3 Feature selection

In the context of support vector machines and machine learning in general, a feature is an individual measurable property or characteristic of the data being analysed. Features are the input variables used by the SVM model to distinguish between different classes in classification tasks. In the case of FDD for ORC systems using SVM, it is necessary to select between the different sensors available the ones more relevant to correctly detect the different faults.

Due to the limited amount of literature on FDD for ORC systems, there is no clear reference on which sensors or sensor combinations should be used for different fault types. However, considering similar systems, one can use industrial refrigeration systems as a reference. For example, in [6], nine features are selected, namely evaporating temperature, condensing temperature, temperature differences at various cycle components, and superheat. An additional interesting study applied for chillers is encountered in [18], where thirteen different features are employed among them the instantaneous input power, temperature and pressures at different components inputs and outputs, subcooling level, chiller efficiency, and superheat.

In SVM for classification, there is a key trade-off between the number of features (dimensions of the data) and the number of classes (distinct categories being classified). This trade-off affects both the computational complexity of the model and its generalization to new data. In a simple approach one can employ all sensor data available to train a SVM classifier, or use knowledge from the system to interpret from the physics of the system the more suitable features, additionally, one can use algorithms such as the Relief method to optimally select the most important features [19] and [20].

The Relief algorithm is a feature selection method that identifies important features by evaluating their ability to distinguish between classes. For each randomly chosen instance in the dataset, Relief finds

the nearest neighbour from the same class (near-hit) and from a different class (near-miss). It then adjusts the weight of each feature based on how similar its value is in the target instance compared to the near-hit and near-miss instances. If a feature's values are similar within the same class and different across classes, it receives a higher weight, indicating its importance for classification. After multiple iterations, features with the highest weights are selected as the most relevant.

SVM is inherently a binary classifier, therefore, to extend Support Vector Machines (SVM) for multi-class classification (e.g., with 4 classes for the defined healthy and faults to be studied), one can use the One-vs-One (OvO) approach, in which a separate SVM classifier it is trained for every possible pair of classes. For a problem with k classes, this results in $k(k-1)2^{-1}$ classifiers. In the case of 4 classes, it would create 6 binary classifiers (one for each pair of classes). During classification, each classifier makes a vote, and the class that receives the majority of votes across all classifiers is chosen as the predicted class. This method although can be computationally intensive it is effective, especially with smaller numbers of classes as in the present study.

4 Results and analysis

Datasets are generated using the simulation model based on the descriptions in Table 2, with additional severity levels for each fault set at 10%, 30%, and 50%. The algorithms are trained using known data and subsequently tested on unknown data across different scenarios, each representing faults with varying degrees of severity.

The testing procedure is as follows: the algorithm is trained based on the healthy scenario and for each fault type at 10% of severity level. Afterwards, the classification algorithm is tested for the other severity cases i.e., 30% and 50%.

4.1 Scenario 1: All sensor data

In the first scenario, all available sensor data is used as features to evaluate the algorithm's performance. This scenario assumes that the user believes having more information available can enhance the machine learning (ML) predictions. The sensor values to be used as features are listed in Table 3. Note that in this case, raw measured data (RMD) is used to create the features. However, in other cases, calculated data (CD) or secondary variables, which are derived from algorithms or combinations of primary variables, may be used.

Table 3: Variables used as features in scenario 1.

Feature	Type	Feature	Type
$T_{hf,su}$	RMD	$P_{ev,ex}$	RMD
$\dot{m}_{cf,su}$	RMD	$T_{cd,su}$	RMD
$\dot{m}_{hf,su}$	RMD	$P_{cd,su}$	RMD
$T_{ev,su}$	RMD	$T_{cd,ex}$	RMD
$P_{ev,su}$	RMD	$P_{cd,ex}$	RMD
$T_{ev,ex}$	RMD	-	-

The next step is to perform a grid search to tune the C and γ parameters, where the result of each combination is a mean score that reflects how well the SVM model performs on unseen data, as determined by cross-validation. This procedure is then applied to the training datasets (healthy and fault datasets with 10% severity). The results are presented as reference for the nonlinear region encountered, as depicted in Figure 3, leading to $C = 10$ and $\gamma = 0.1$.

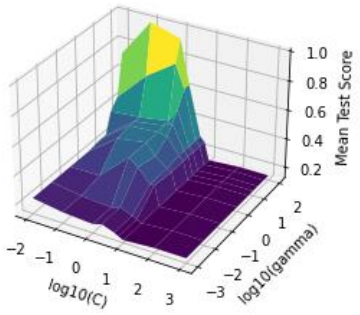


Figure 3: Optimal SVM tuning by cross-validation.

The prediction capabilities of the tuned SVM classifier are then tested on unseen datasets, specifically for severity cases of 30% and 50%. As an example of its performance, the prediction results of the SVM for fault detection and diagnosis (FDD) using features from scenario 1 are presented in Figure 4. In this case, the algorithm fails to predict 8 out of 56 data samples. Notably, it mainly struggles to distinguish between the healthy (class 0) and evaporating fouling (class 1), as outlined in the classification presented in Table 2, whilst for faults in the expander and the pump are correctly detected.

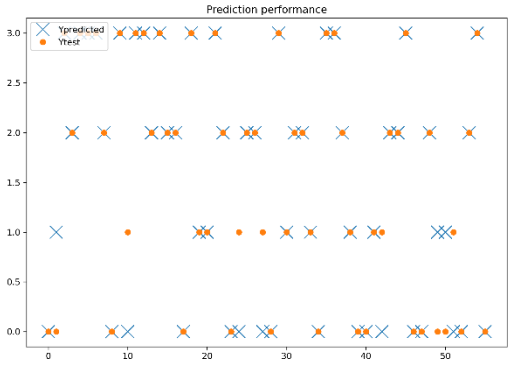


Figure 4: Scenario 1: Prediction performance of FDD with 30% fault severity (error: 8/56).

4.2 Scenario 2: All sensor data + combinations

In the second scenario, all sensor data is used during the training phase, along with additional variables derived from combinations of sensor data. In scenario 1, the main errors occurred because the classifier struggled to distinguish between healthy data points and evaporator fouling. To address this issue, additional information related to system performance should be included. Examples of such variables include the rate of heat transfer $\dot{Q}$, cycle efficiency η, and the power consumed W by the pump or produced by the expander. These additional variables could provide valuable insights, potentially enabling the SVM algorithm to achieve greater accuracy. Table 4 lists the variables used as features, indicating whether each is a raw measured data (RMD) variable or a calculated data (CD) variable. The heat transfer and cycle efficiency are defined as follows:

$$\dot{Q}_{ev} = \dot{m}_{wf}(h_{ev,su} - h_{ev,ex}) \tag{11}$$

$$\eta_{ORC} = \frac{(W_{exp} - W_{pp})}{\dot{Q}_{ev}} * 100 \tag{12}$$

Table 4: Variables used as features in scenario 2.

Feature	Type	Feature	Type
$T_{hf,su}$	RMD	$T_{cd,ex}$	RMD
$\dot{m}_{cf,su}$	RMD	$P_{cd,ex}$	RMD
$\dot{m}_{hf,su}$	RMD	W_{exp}	RMD
$T_{ev,su}$	RMD	W_{pp}	RMD
$P_{ev,su}$	RMD	η_{ORC}	CD
$T_{ev,ex}$	RMD	$\dot{Q}_{cd}$	CD
$P_{ev,ex}$	RMD	$\dot{Q}_{ev}$	CD
$T_{cd,su}$	RMD	$\dot{m}_{wf}$	RMD
$P_{cd,su}$	RMD	-	-

After defining the features, a grid search is performed to tune the C and γ parameters, resulting in $C = 1$ and $\gamma = 0.1$. The training procedure is then applied to 70% of the samples from the healthy and fault datasets with 10% severity, while the remaining 30% is reserved for testing.

The prediction performance for the dataset with 30% severity is shown in Figure 5. It is observed that the FDD algorithm successfully distinguishes between the different faults without any errors. Particularly, it accurately differentiates between healthy data and the evaporator fouling condition without issues. The algorithm is able to classify both datasets i.e., 30% and 50% severity with no error.

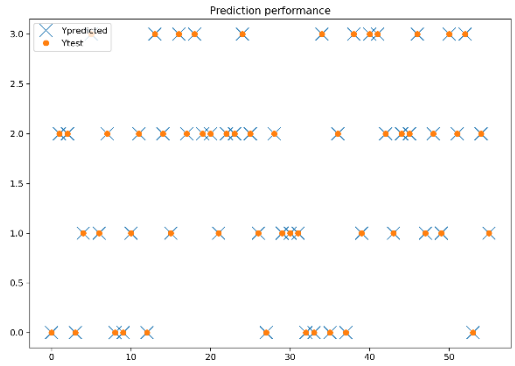


Figure 5: Scenario 2: Prediction performance of FDD with 30% fault severity.

4.3 Scenario 3: Optimizing features

Following the improved results from scenario 1 achieved in scenario 2 by including additional information, an investigation is conducted to determine whether all features used are truly necessary. The Relief algorithm, as described in Section 3.3, is applied to the healthy and 10% severity datasets during training to identify whether fewer features can be used without compromising accuracy in fault detection and diagnosis. Scenario 3 initially considers the same features as in scenario 2, where the weights assigned by the Relief algorithm to each feature represent its relevance or importance in contributing to the classification task. These weights are particularly useful for determining whether a feature can be eliminated, as they specifically indicate how well a feature helps distinguish between classes while considering similarities between samples. The results of this analysis are illustrated in Figure 6.

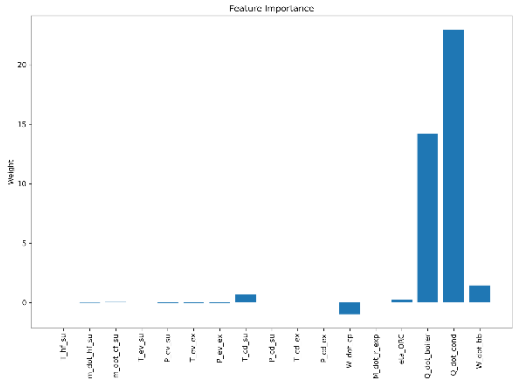


Figure 6: Scenario 2: Prediction performance of FDD with 30% fault severity.

The results shown in Figure 6 suggest that not all features are relevant for accurately classifying fault conditions. Various methods for reducing the number of features can be considered, such as applying a threshold value, selecting a specific percentage, or defining a minimum number of features. In this study, the features with the highest numerical weight values were selected, as shown in Table 5.

Table 5: Variables used as features in scenario 3.

Feature	Type
W_{pp}	RMD
$\dot{Q}_{cd}$	CD
$\dot{Q}_{ev}$	CD

After considering the three selected features, the grid search is performed to tune the C and γ parameters, resulting in C=0.1 and γ=1. The training procedure is then applied to 70% of the samples from the healthy and fault datasets with 10% severity, while once more the remaining 30% is reserved for testing. The trained FDD SVM algorithm is assessed in terms of prediction performance on the 30% and 50% severity fault datasets. The FDD successfully classifies the faults with no errors, achieving the same performance as in scenario 2. However, in scenario 2, 17 features were required, but in this case, only 3 features were necessary. The prediction capabilities for the case of the scenario 3 are depicted in Figure 7.

A final summary of the results obtained for the different proposed scenarios is presented in Table 6, which lists the total accuracy as well as the scores based on fault severity.

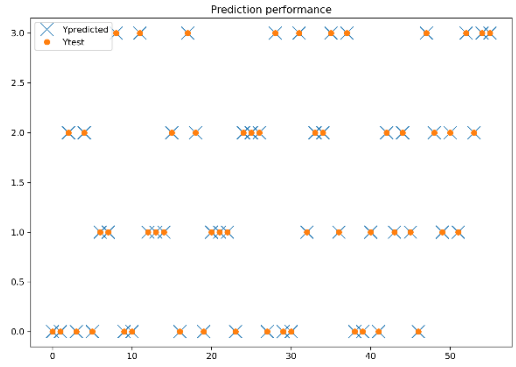


Figure 7: Scenario 3: Prediction performance of FDD with 30% fault severity.

Table 6: Accuracy score of the diagnosis using the proposed SVM-FDD for different fault severities.

Scenario	Number features	Severity	Total Accuracy	Score
1	11	10%	43.75%	7/16
	11	30%	85.71%	48/56
	11	50%	85.71%	48/56
2	17	10%	100%	16/16
	17	30%	100%	56/56
	17	50%	100%	56/56
3	3	10%	100%	16/16
	3	30%	100%	56/56
	3	50%	100%	56/56

5 Conclusions

This paper presents a fault detection and diagnosis (FDD) algorithm for organic Rankine cycle (ORC) power systems, which utilizes a support vector machine (SVM) to classify various operational conditions. Four conditions are considered in this study: the healthy state, evaporator fouling fault, and mechanical faults in the expander or pump. Additionally, the severity of faults is explored at three levels: 10%, 30%, and 50%.

The SVM algorithm is trained using the healthy state and 10% severity fault data, and tested on datasets with 30% and 50% fault severity. The results demonstrate strong predictive performance, with the model effectively generalizing to unseen data.

Regarding model tuning, a grid search approach is employed to identify the optimal tuning parameters for the SVM. Furthermore, the study emphasizes the importance of proper feature selection across three scenarios, ranging from raw sensor data to more

complex variables derived from the measurements. These additional features provide valuable insights to improve the algorithm's performance.

Using the Relief algorithm for feature selection, the number of features is reduced from 17 to just 3, while maintaining excellent predictive performance with no errors.

A limitation of the present study is the reliance on labelled data during the training process. Consequently, future work will focus on the development of self-learning algorithms capable of working with datasets where only a small portion of the data is labelled, and the rest remains unlabelled. This is particularly important for fault detection and diagnosis (FDD), as it can be challenging to obtain sufficient data representing various fault conditions, or to simulate such conditions effectively. For example, emulating the presence of non-condensable gases in Organic Rankine Cycles (ORCs) can be difficult. Self-learning algorithms can address this by using the labelled data to train an initial model, then iteratively improving the model by predicting labels for the unlabelled data and incorporating those predictions into the training process

Acknowledgement

This project has received funding from the European Union's Horizon Europe research and innovation programme under grant agreement No 101069740.



The information presented on this document reflects only the authors' view. The Agency is not responsible for any use that may be made of the information it contains.

References

[1] C. Wieland, C. Schifflechner, K. Braimakis, F. Kaufmann, F. Dawo, S. Karellas, G. Besagni, C. Markides, "*Innovations for organic Rankine cycle power systems: Current trends and future perspectives"*, Applied Thermal Engineering, Volume 225, p. 120201, ISSN 1359-4311, 2023.

[2] Dickes, R., *Charge-sensitive methods for the off-design performance characterization of organic Rankine cycle (ORC) power systems*, PhD Thesis, University of Liege, 2019.

[3] Wang, J., Zuo, Q., Liao, G., Luo, F., Zhao, P., Wu, W., He, Z., & Dai, Y. *"Machine Learning–Based Fault Detection and Diagnosis of Organic Rankine Cycle System for Waste-Heat Recovery".* Journal of Energy Engineering, 2021.

[4] D. Dragan, "Fault Detection of an Industrial Heat-Exchanger: A Model-Based Approach", Journal of Mechanical Engineering, Vol. 57 (6), p. 477-484, 2011

[5] S. Choi, S. Krumdieck, "*Dynamic modeling of organic Rankine cycle (ORC) system for fault diagnosis and control system design*", Proceedings 38th New Zealand Geothermal Workshop, 23 - 25, Auckland, New Zealand, November 2016.

[6] R. van de Sand, "A Predictive Maintenance Model for Heterogeneous Industrial Refrigeration Systems", PhD thesis, Tor Vergata University of Rome, Italy, 2021

[7] A. Elmouatamid, B. Fricke, J. Sun, P. Pong, "*Air Conditioning Systems Fault Detection and Diagnosis-Based Sensing and Data-Driven Approaches*", Energies, Vol. 16, p. 4721, 2023.

[8] H. Hosamo, P. Ragnar, K. Svidt, D. Han, H. Nielsen, "*A Digital Twin predictive maintenance framework of air handling units based on automatic fault detection and diagnostics*", Energy and Buildings, Vol. 261, p. 111988, ISSN 0378-7788, 2022

[9] K. Yan, Z. Ji, W. Shen, "*Online fault detection methods for chillers combining extended Kalman filter and recursive one-class SVM*", Neurocomputing, Vol. 228, p. 205-212, ISSN 0925-2312, 2017

[10] J. Wang, Q. Zuo, G. Liao, F. Luo, P. Zhao, W. Wu, Z. He, Y. Dai, *"Machine Learning-Based Fault Detection and Diagnosis of Organic Rankine Cycle System for Waste-Heat Recovery"*, Journal of Energy Engineering, Vol. 147(4), p. 04021016, 2021

[11] I. H. Bell, J. Wronski, S. Quoilin, and V. Lemort, '*Pure and Pseudo-pure Fluid Thermophysical Property Evaluation and the Open-Source Thermophysical Property Library CoolProp'*, Ind. Eng. Chem. Res., vol. 53, no. 6, pp. 2498–2508, Feb. 2014

[12] C. Cuevas, J. Lebrun, V. Lemort, and P. Ngendakumana, '*Development and validation of a condenser three zones model'*, Applied Thermal Engineering, vol. 29, no. 17–18, pp. 3542–3551, Dec. 2009.

[13] B. Eck and B. Eck, *Fans: design and operation of centrifugal, axial-flow and cross-flow fans*, 1. engl. ed. Oxford: Pergamon Pr, 1973

[14] V. Lemort, S. Declaye, and S. Quoilin, '*Experimental characterization of a hermetic*

scroll expander for use in a micro-scale Rankine cycle', Proceedings of the Institution of Mechanical Engineers, Part A: Journal of Power and Energy, vol. 226, no. 1, pp. 126–136, Feb. 2012

[15] Markowski, M., M. Trafczynski, and K. Urbaniec. "Identification of the influence of fouling on the heat recovery in a network of shell and tube heat exchangers." Appl. Energy 102 (Feb): 755–764, 2013.

[16] V. Vapnik, "The nature of statistical learning theory". Berlin: Springer, 2000.

[17] L. Qiao, and Q. Chen. "Forecasting models for hydropower unit stability using LS-SVM." Math. Probl. Eng. 2015 (1): 1–9, 2015

[18] K. Yan, J. Zhiwei, S. Wen, *"Online fault detection methods for chillers combining extended kalman filter and recursive one-class SVM"*, Neurocomputing, Volume 228, p. 205-212, ISSN 0925-2312, 2017

[19] M. Robnik-S˘ikonja, I. Kononenko, *"Theoretical and empirical analysis of ReliefF and RReliefF"*, Mach. Learn. 53 (1–2) (2003) 23–69.

[20] Y. Sun, J.Li, *"Iterative Relief for feature weighting"*, in: Proceedings of the 23rd International Conference on Machine Learning, ACM, 913–920, 2006.

[21] M. Pezo, C. Cuevas, E. Wagemann, A. Cendoya, "Net Zero Energy Building technologies - Reversible Heat Pump/Organic Rankine Cycle coupled with Solar Collectors and combined Heat Pump/Photovoltaics - Case study of a Chilean mid-rise residential building", Applied Thermal Engineering, 252, 123683, 2024

DEFINITION OF A NOVEL PERFORMANCE INDICATOR FOR DESICCANT WHEELS

Alanis Zeoli[1]*, Anna Pacak[2], Samuel Gendebien[1], Vincent Lemort[1]

[1] Laboratory of Applied Thermodynamics, Department of Aerospace and Mechanics, University of Liège, Belgium

[2] Department of Cryogenics and Aviation Engineering, Faculty of Mechanical and Power Engineering, Wrocław University of Science and Technology, Poland

* *Corresponding Author: alanis.zeoli@uliege.be*

Abstract. Desiccant wheels (DW) are key components in the desiccant evaporative cooling systems used for air-conditioning in buildings. They dehumidify the air stream by adsorbing the water vapour contained in the air through sorption effect. The equations behind the physics of the DW can be complex to integrate into a system simulation tool. This paper offers a simplified approach to evaluate the performance of a DW by enhancing the similarities between the thermodynamic processes of evaporative cooling and desiccant dehumidification. The new performance indicator is defined similarly to the wet bulb effectiveness of direct evaporative coolers. It is then applied to a DW in operation in a real system installation.

Keywords. Desiccant wheel, Dehumidification, Evaporative cooling, Performance indicator.

Nomenclature

c_p	Specific heat capacity (J/kg.K)
h	Specific enthalpy (J/kg)
$h_{fg,0}$	Water vaporisation enthalpy at 0°C (J/kg)
$\dot{m}$	Mass flow rate (kg/s)
P	Pressure (Pa)
q	Specific heat flux (J/kg)
$\dot{Q}$	Heat flux (W)
T	Temperature (°C)
Special characters	
ε	Effectiveness (-)
ω	Specific humidity (kg/kg)
Subscripts	
a	Humid air
in	Incoming
out	Outdoor air
reg	Regeneration air
v	Water vapour
w	Water
wb	Wet bulb

1 Introduction

Cooling accounts for nearly 20% of the total electricity demand of buildings worldwide and this share is expected to increase with global warming [1]. Alternative air-conditioning methods have become a significant area of interest to tackle the drawbacks of vapour-compression systems. Amongst them, desiccant evaporative cooling systems (DECS) couple desiccant dehumidification and evaporative cooling, offering a promising solution by primarily utilising low-grade energy sources such as solar energy, waste heat from industrial processes and district heating networks.

Desiccant wheels (DW) are key components of DECS as they dehumidify the incoming air stream through water adsorption. The inner matrix of the DW is covered with a desiccant material that adsorbs water through sorption effect. The water is then released on the secondary side during the regeneration process. The equations underlying the desiccant dehumidification process can rapidly become complex and semi-empirical models have been developed to describe the DW operation [2], [3].

This paper offers a simplified approach to evaluate the performance of a DW by enhancing the similarities between the evaporative cooling and desiccant dehumidification processes. Those processes are described based on the fundamental laws of thermodynamics and studied to establish the definitions for performance indicators. The newly defined performance indicator is then applied to an operating DW in a real system installation.

2 (De)humidification processes description

This section thoroughly describes the processes of evaporative cooling and desiccant dehumidification.

2.1 *Evaporative cooling process*

Evaporative cooling occurs through direct contact between an air stream and a water film. Heat is transferred from the air stream to the water film, hence evaporating water. The water vapour is then homogeneously mixed in the air stream. Figure 1 shows a schematic representation of the evaporative cooling process and the associated evolution of the air stream conditions in a psychrometric diagram.

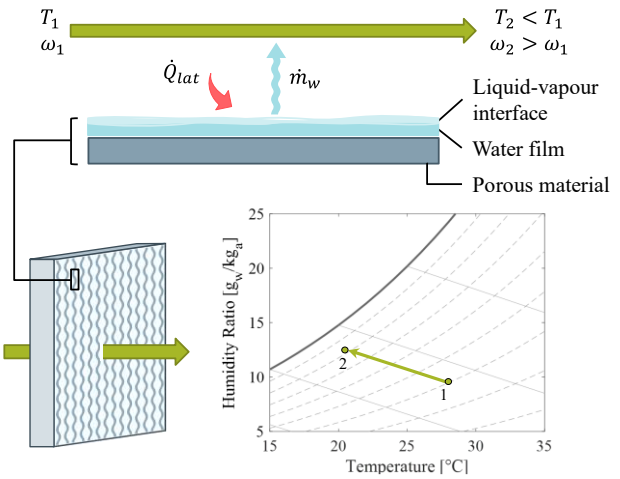


Figure 1: Schematic representation of the evaporative cooling process.

2.2 *Desiccant dehumidification process*

The desiccant dehumidification process occurs through an intermediate media, a desiccant material such as silica gel. As the air stream enters into contact with the desiccant material, moisture is adsorbed from the air and stored in liquid form at the surface of the desiccant. During the sorption process, latent and sorption heat is released to the primary airflow, which leaves the DW heated and dehumidified. Some additional heat transfer occurs due to sensible energy storage in the inner matrix of the DW during the regeneration process. Figure 2 shows a schematic representation of the desiccant dehumidification process and the associated evolution of the air stream conditions in a psychrometric diagram.

3 Methodology

In this section, the two previously described processes are analysed from a thermodynamic point of view to enhance the similarities between both processes and lay the foundations for defining a new performance indicator for the desiccant wheels.

3.1 *Thermodynamic process analysis*

Defining a control volume in which the considered process takes place is necessary to perform a thermodynamic analysis of the processes.

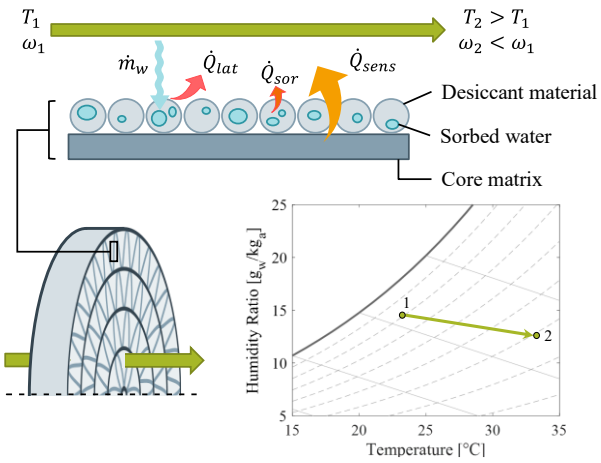


Figure 2: Schematic representation of the desiccant dehumidification process.

Figure 3 gives a general representation of the studied thermodynamic process which can be adapted to represent either the evaporative cooling process or the desiccant dehumidification process. The control volume consists of a box containing air and water. Heat and mass transfers occur through the system boundaries. In its most general form, energy conservation inside the system can be written as

$$\dot{m}_a \cdot h_{a,1} + \dot{m}_w \cdot h_w + \dot{Q}_{in} = \dot{m}_a \cdot h_{a,2} \qquad (1)$$

and can be considered at steady-state under the following assumptions:

- The water flow rate should compensate exactly the amount of water added in (resp. removed from) the air, which can be written as

$$\dot{m}_w = \dot{m}_a \, (\omega_2 - \omega_1) \qquad (2)$$

- The water that enters (resp. leaves) the reservoir does not carry sensible energy inside (resp. outside) the system. It should be at the average temperature of the water inside the reservoir.
- There is only latent heat transfer between air and water.

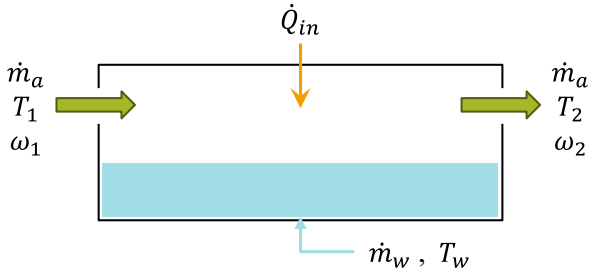


Figure 3: Schematic representation of the studied thermodynamic process.

Eq. (1) can be developed using equations (2)-(5), as shown in Eq. (6).

$$h_a = c_{p,a} \cdot T_a + \omega \left(c_{p,v} \cdot T_a + h_{fg,0}\right) \quad (3)$$

$$h_w = c_{p,w} \cdot T_w \quad (4)$$

$$h_{fg,2} = h_{fg,0} + \left(c_{p,v} - c_{p,w}\right) T_{a,2} \quad (5)$$

$$\left(c_{p,a} + \omega_1 \cdot c_{p,v}\right)\left(T_{a,2} - T_{a,1}\right) = \left(\omega_2 - \omega_1\right)\left[-h_{fg,2} + c_{p,w}\left(T_w - T_{a,2}\right)\right] + q_{in} \quad (6)$$

Eq. (6) can also be expressed as

$$q_{sens} = -q_{lat} + q_{sens,w} + q_{in} \quad (7)$$

- q_{sens} is the sensible energy gained by the air during the process. It is positive if the air is heated.
- q_{lat} is the latent heat of vaporisation of the water. It is positive if water evaporates in the air.
- $q_{sens,w}$ is the sensible energy brought by the water entering the system.
- q_{in} is the "parasitic" heat transfer occurring through the system boundaries.

3.2 *Application to the evaporative cooling process*

The thermodynamic analysis can be applied to the evaporative cooling process, considering some additional assumptions:

- There is no heat transfer across the system boundaries. The evaporative cooling process can be considered adiabatic.
- If the water enters the control volume at a temperature close to the outlet temperature of the air, the term of the sensible energy of the water can be neglected compared to the term related to the latent heat of vaporisation.

When applied to the evaporative cooling process, Eq. (7) gives:

$$q_{sens} = -q_{lat}\ , \quad (8)$$

indicating that the airflow loses sensible energy that is converted into latent heat for the vaporisation of water. As illustrated in the psychrometric diagram in Figure 4, the evaporative cooling process is isenthalpic and the air saturation limits the maximum humidification rate. The evaporative cooling process performance can be measured by comparing the actual to ideal latent heat fluxes, corresponding to the ratio of actual to ideal sensible heat fluxes. The lowest temperature reached by the air through the evaporative cooling process is the wet bulb temperature, which leads to the definition of the *wet bulb effectiveness*, an indicator widely used in the literature [4].

$$\varepsilon_{wb} = \frac{q_{lat}}{q_{lat,max}} = \frac{q_{sens}}{q_{sens,max}} = \frac{T_1 - T_2}{T_1 - T_{2b}} \quad (9)$$

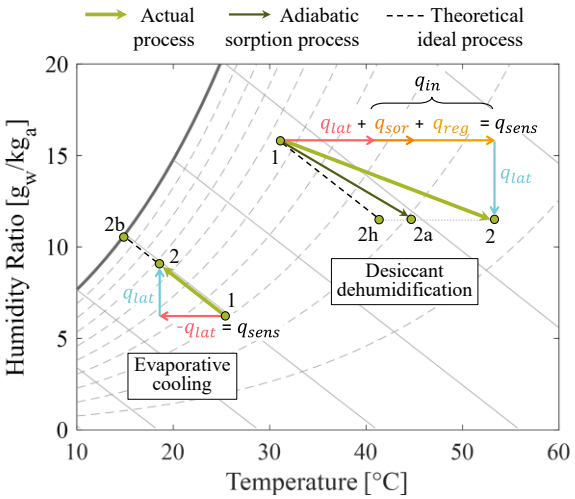


Figure 4: Representation of the actual and ideal evolutions for the evaporative cooling and desiccant dehumidification processes and decomposition into simplified heat fluxes.

3.3 *Application to the desiccant dehumidification process and definition of a new KPI*

The same methodology can be applied to the desiccant dehumidification process by considering two additional heat fluxes:

- The sorption process is an exothermic reaction. Moisture is removed from the air and bonds with the sorbent, releasing heat, called *heat of sorption* (q_{sor}), into the air stream [5].
- For the desiccant wheel to work continuously, the desiccant material should be regenerated, *i.e.* the moisture adsorbed from the airflow should be removed from the desiccant through heating. As the desiccant wheel rotates, the newly regenerated desiccant material reaches the primary side. The inner matrix of the DW is still at a temperature close to the regeneration temperature and heat is subsequently transferred to the primary air. The heat transfer due to the regeneration process (q_{reg}) is proportional to the temperature difference between the process and regeneration sides.

The thermodynamic analysis can be applied to the desiccant dehumidification process under the following assumptions:

- The aforementioned heat transfers are accounted for in the q_{in} term of Eq. (6).
- If the water leaves the control volume at a temperature close to the outlet temperature of the air, the term of the sensible energy of the water can be neglected compared to the term related to the latent heat of vaporisation

Finally, Eq. (7) gives:

$$q_{sens} = -q_{lat} + q_{sor} + q_{reg} = -q_{lat} + q_{in} \qquad (10)$$

In this case, the water condensation into the desiccant material releases heat absorbed by the airstream in the form of sensible heat. As illustrated in Figure 4, the additional heat transfer q_{in} causes a deviation of the actual process from the ideal theoretical process. The heat of sorption causes a deviation from the *isenthalpic* dehumidification, while the heat transfer due to the regeneration process causes a deviation from the *adiabatic* dehumidification. In other words, q_{reg} reflects the irreversibility linked to the regeneration process, while q_{sor} characterises the desiccant material's ability to bond with water.

Similarly to the wet bulb effectiveness, we can define two new indicators for the DW to quantify the closeness to the ideal process under a similar dehumidification rate. The *isenthalpic effectiveness* expresses the closeness of the actual process to an isenthalpic dehumidification:

$$\varepsilon_h = \frac{q_{sens,s}}{q_{sens}} = \frac{-q_{lat}}{-q_{lat} + q_{in}} = \frac{T_{2h} - T_1}{T_2 - T_1} \qquad (11)$$

The *adiabatic effectiveness* expresses the closeness of the actual process to adiabatic dehumidification:

$$\varepsilon_a = \frac{q_{sens,a}}{q_{sens}} = \frac{-q_{lat} + q_{sor}}{-q_{lat} + q_{in}} = \frac{T_{2a} - T_1}{T_2 - T_1} \qquad (12)$$

The adiabatic and isenthalpic effectiveness are both defined for a constant dehumidification rate because we are interested in characterising the temperature deviation from the ideal evolution when the dehumidification rate is fixed.

4 Results and discussion

4.1 Application of KPI to a real test case

The dehumidification rate and effectiveness of a DW depend on the air conditions at the inlets. Lower temperatures on the primary side drive the sorption process, resulting in larger dehumidification rates [6]. Conversely, the regeneration process is driven by higher temperatures on the secondary side, resulting in an enhanced sensible heat transfer from the core matrix of the DW and the primary air stream.

The effect of the DW inlet air conditions on the dehumidification rate and DW effectiveness has been studied on a real desiccant wheel, rotating at a constant speed, in a desiccant evaporative cooling system test case in Denmark [7], [8]. It has been decided to compute the isenthalpic effectiveness rather than the adiabatic effectiveness because the latter requires information about the heat of sorption, which computation is not straightforward [9].

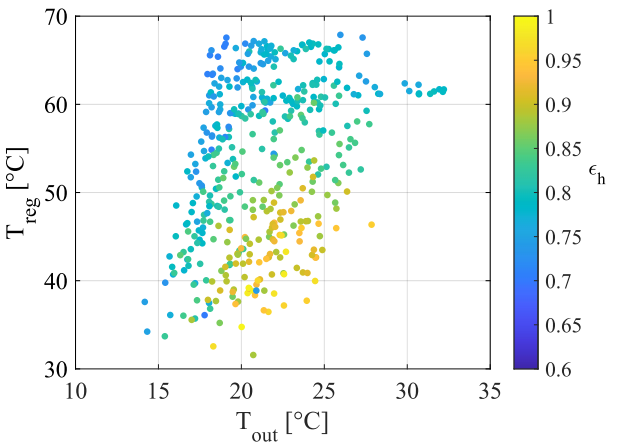


Figure 5: Evolution of the isenthalpic effectiveness depending on the outdoor and regeneration temperatures.

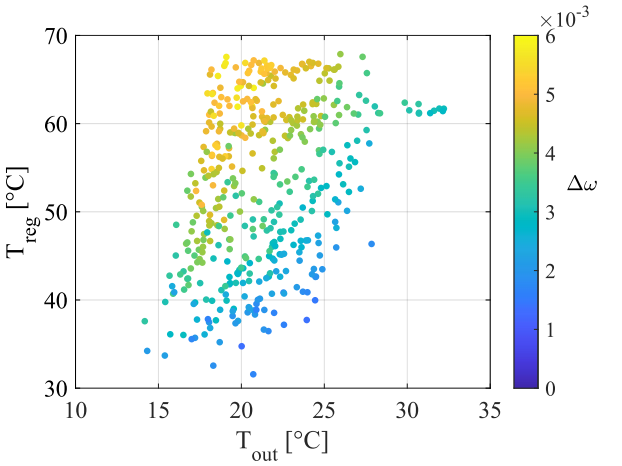


Figure 6: Evolution of the dehumidification rate depending on the outdoor and regeneration temperatures.

Figures 5 and 6 show the evolution of the dehumidification rate and the computed values of the isenthalpic effectiveness for the tested outdoor and regeneration temperatures. The isenthalpic effectiveness mostly varies between 0.75 and 0.95, the highest values being reached for higher outdoor temperatures and lower regeneration temperatures. Since the extra sensible heat transfer is proportional to the difference between the regeneration and outdoor temperatures, those conditions result in the dehumidification process closest to the ideal one.

4.2 Empirical correlations

It has been established that the dehumidification rate and the isenthalpic effectiveness at a fixed rotation speed depend only on the outdoor and regeneration temperatures. Empirical correlations can be developed to ease the modelling of constant rotation

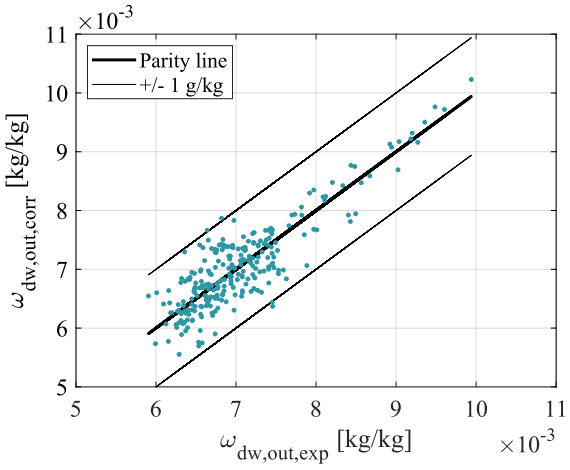


Figure 7: Measured and calculated specific humidity at the desiccant wheel outlet.

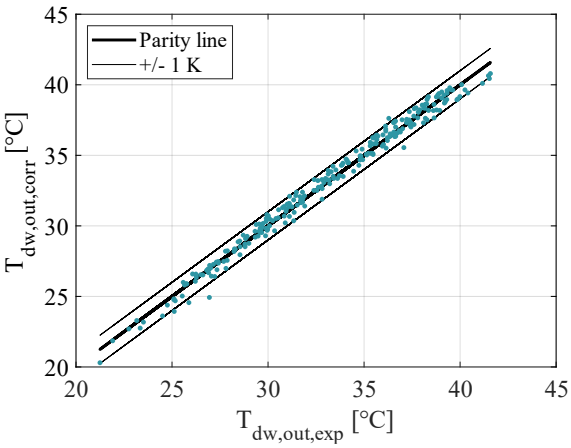


Figure 8: Measured and calculated temperature at desiccant wheel outlet.

speed desiccant wheels in practical applications. The correlation expressions take the following form:

$$X = A \cdot (T_{out})^m \cdot (T_{reg})^n \qquad (13)$$

where X represents the parameters $\Delta\omega$ and ε_h; and A, m and n are constant coefficients which depend on the operating and geometrical parameters of the DW. The computed coefficients for the studied DW are detailed in Table 1.

Table 1: Values of coefficients adopted in the $\boldsymbol{\Delta\omega}$ and $\boldsymbol{\varepsilon_h}$ correlations.

X	A	m	n
$\Delta\omega$	$2.385 \cdot 10^{-4}$	-0.9966	1.4569
ε_h	1.6664	0.2630	-0.3825

The comparison between measured and calculated temperature and specific humidity at the DW outlet is shown in Figures 7 and 8. 40% of the dataset is used to fit the model parameters and the other 60% is used for model validation. With these simplified correlations, the outlet air conditions can be computed with an accuracy of ±1 K for the temperature and ±1 g/kg for the humidity.

4.3 Limitations

The performance of a desiccant wheel strongly depends on its chemical and physical properties. In this work, the analysed desiccant wheel is made of aluminium foils covered with silica gel and channels with sinusoidal cross-sectional area. The correlations developed in Eq. (13) should be calibrated based on experimental data. It should be noted that one set of coefficients is valid only for one desiccant wheel geometry and for a constant rotation speed.

In this case, the air conditions at the DW outlet depend only on the inlet temperatures. Temperature ranges for the inlet conditions should be established to define the validity range of the correlations. Figure 9 represents the set of inlet air conditions that have been observed for the considered DW on the process and regeneration sides. On the regeneration side, the inlet specific humidity was rather constant since the regeneration air source was the indoor environment. For applications with inlet air conditions subject to wider variation ranges, the proposed empirical correlation could be modified to account for the inlet specific humidity on the regeneration side.

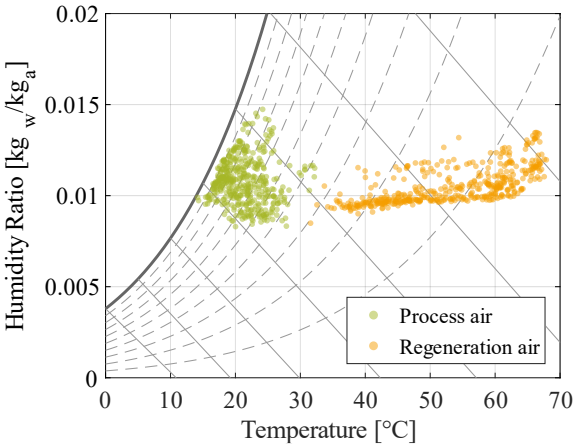


Figure 9: Operation range of the air conditions at the inlets of the DW on process and regeneration sides.

5 Conclusions

In this paper, a novel performance indicator for desiccant wheels has been developed from the thermodynamic analysis of the evaporative cooling and desiccant dehumidification processes. It is shown that the desiccant dehumidification process can be viewed as a combination of isenthalpic

dehumidification and sensible heating, leading to the definition of the isenthalpic effectiveness.

The application of the definition of the isenthalpic effectiveness to an actual operating DW shows that the isenthalpic effectiveness is a suitable indicator to characterise the performance of the DW. Empirical correlations are proposed for the computation of the dehumidification rate and the isenthalpic effectiveness depending on the outdoor and regeneration temperatures. With the proposed correlations, the outlet air conditions are predicted with an accuracy of ±1 K for the temperature and ±1 g/kg for the specific humidity.

Acknowledgement

This study is a part of the International Energy Agency (IEA) EBC Annex 85 "Indirect Evaporative Cooling" project activities. The work was co-financed by the program of Polish National Centre for Research and Development "Lider XII [contract No. LIDER/29/0151/L-12/20/NCBR/2021].

References

[1] *The Future of Cooling - Opportunities for energy efficient air conditioning*, International Energy Agency, 2018.

[2] G. Panaras, E. Mathioulakis, V. Belessiotis, and N. Kyriakis, "Experimental Validation of a Simplified Approach for a Desiccant Wheel Model", in *Energy and Buildings*, vol. 42, pp. 1719-1725, Oct. 2010, doi: https://doi.org/10.1016/j.enbuild.2010.05.006.

[3] S. De Antonellis, M. Intini, and C. M. Joppolo, "Desiccant Wheels Effectiveness Parameters: Correlations Based on Experimental Data", in *Energy and Buildings*, vol. 103, pp. 296-306, Sep. 2015, doi: https://doi.org/10.1016/j.enbuild.2015.06.041.

[4] Z. Duan *et al.*, "Indirect evaporative cooling: Past, present and future potentials", in *Renewable and Sustainable Energy Reviews*, vol. 16, no. 9, pp. 6823–6850, Dec. 2012, doi: 10.1016/j.rser.2012.07.007.

[5] A. Gabelman, "Adsorption Basics: Part 1", Back to Basics, *American Institute of Chemical Engineers*, 2017.

[6] A. Pacak, A. Jurga, B. Kaźmierczak and D. Pandelidis, "Experimental Verification of the Effect of Air Pre-Cooling in Dew Point Evaporative Cooler on the Performance of a Solid Desiccant Dehumidifier", in *Int. Com. in Heat and Mass Transfer*, vol. 142, pp. 106651, Mar. 2023: doi: https://doi.org/10.1016/j.icheatmasstransfer.2023.106651.

[7] H. Johra, "Instant District Cooling System: Project Study Case Presentation", Dept. of the Built Environment, Aalborg University, Denmark, DCE Technical Report 290, 2021, doi: https://doi.org/10.54337/aau468741799.

[8] H. Johra, 2024, "Operation data of a desiccant evaporative cooling system implemented in an office building in Denmark during spring and summer 2022", distributed by Zenodo.

[9] A. Nuhnen and C. Janiak, "A practical guide to calculate the isosteric heat/enthalpy of adsorption *via* adsorption isotherms in metal–organic frameworks, MOFs," *Dalton Trans.*, vol. 49, no. 30, pp. 10295–10307, 2020, doi: 10.1039/D0DT01784A.

THEREOTICAL MODELLING AND EXPERIMENTAL INVESTIGATION OF A REVOLVING VANE EXPANDER

Philipp Streit[1*], Andreas P. Weiß[1], Ulf Nägele[2], Ulrich Bauer[3], Philipp Liedl[4]

[1] Centre of Excellence for Cogeneration Technologies, East Bavarian Technical University of Applied Sciences Amberg-Weiden, Kaiser-Wilhelm-Ring 23, 92224 Amberg, Germany

[2]Nägele Mechanik GmbH, Gottlieb-Daimler-Straße 72, 71711 Murr

[3]Ulrich Bauer, Griesstraße 19, 72793 Pfullingen

[4]Steinbeis-Beratungszentrum Technologische Transformation, Baumreute 31, 73730 Esslingen am Neckar

** Corresponding Author: ph.streit@oth-aw.de*

Abstract. Theoretical and experimental studies on a Revolving Vane Expander (ReVE) are discussed in this paper. The concept and the working mechanism of this type of volumetric expander are examined and the benefits and drawbacks compared to other volumetric expander types are discussed. A brief insight into the modelling results of a simple Excel 1D-model is given. Furthermore, data of the expander measured with pressurized air are published and compared to the modelled data. Through the examination of the model and the comparison to the measurements, improvement potentials for the expander and the model are recognized.

Keywords. Volumetric Expander, Revolving Vane Expander, 1D-model, Organic Rankine Cycle

1 Introduction

Organic Rankine Cycles (ORC) are a proven technology for low-temperature waste heat recovery in the industry. [1] For applications below 10 kW_{el} volumetric expanders are most used due to their cost-effectiveness, as they are often adapted from mass-produced refrigeration compressors. One of the main disadvantages of volumetric expanders are the high frictional losses, which contribute significantly to the losses in this small power range. These frictional losses are largely caused by the high relative velocities of the rotating and non-rotating parts in contact of the expander. Furthermore, significant wear is the result. The Revolving Vane Expander (ReVE) reduces these frictional losses by reducing the relative velocities of the casing (outer cylinder) and the rotor in relation to each other. This advantage could make the ReVE a promising expander for the future in this power range. Figure 1 shows a cut through the expander. The three main parts of the expander are the vane (1), the rotor (2) and the casing, the so-called cylinder (3). The rotor is positioned eccentric to the cylinder of the expander. The vane connects the rotor and the cylinder via two bearing points but can retract and extend. The working fluid enters the expander axially via the hollow shaft and through a bore in the rotor to the working chamber (green arrows). The working fluid leaves the expander via the bore in the ejection chamber (red arrow). The expander rotates in the clockwise direction (black arrow). The working fluid enters the working chamber (green volume) under high pressure.

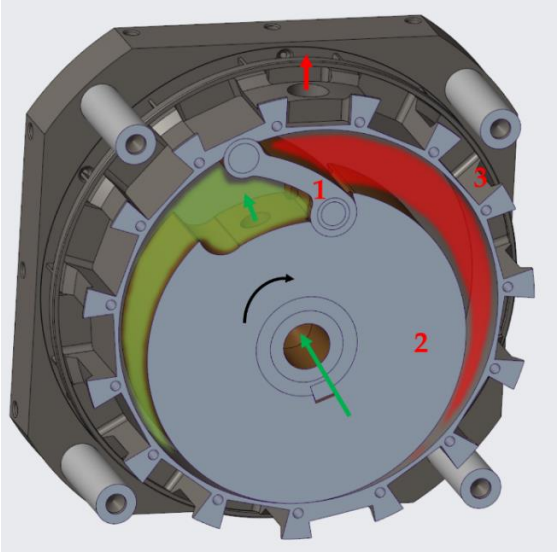


Figure 1: Cut through the Revolving Vane Expander in CAD

The high pressure causes a force on the vane which turns the entire geometry and the volume can expand in the clockwise direction due to the eccentric

position of the rotor to the cylinder. At the same time, the working fluid of the previous expansion is pushed out through the outlet bore via the decreasing volume of the ejection chamber (red volume). As soon, as a full rotation has been completed, the fluid that was in the previous expansion chamber, is now in the ejection chamber and new fluid enters the working chamber over the inlet bore and the hollow shaft – the process repeats. Due to the firm connection of the rotor and the cylinder, the relative motion between these two parts is small, and therefore, friction and wear as well. Main disadvantage of the expander is the induced high forces on the bearings through the inertia of the corotating outer cylinder. Due to the eccentric position of the rotor to the cylinder, the cylinder has to accelerate and decelerate at each revolution, while the rotor remains at constant circumferential velocity. Furthermore, this type of expander requires a high level of manufacturing effort due to the many moving parts and a high level of manufacturing accuracy. Table 1 shows the basic data of the considered expander:

Table 1. Basic geometric data of the expander

Parameter	Value	Unit
Outer diameter	188	mm
Inner diameter	158	mm
Eccentricity	15	mm
Expander Length	50	mm
Swept volume	441	ccm
Inlet cross section	78.54	mm^2
Outlet cross section	314.16	mm^2

2 Modelling of the expander

This section only provides a brief insight into the results of the model. For more information on the modelling of the Revolving Vane Expander, the reader is referred to the work of Subiantoro et al., Naseri et al. and Ooi et al. [2–4] which have had a significant research contribution for this type of expander.

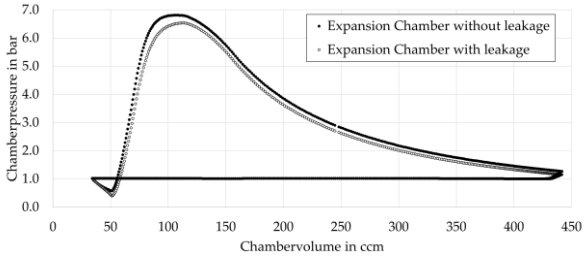


Figure 2. Modelled chamber pressure over chamber volume of the expander with and without leakage

Figure 2 shows the modelled pressure evolution in the working chamber and the ejection chamber of the expander over the chamber volume. The source pressure was set at 7.5 bar and the outlet pressure at 1 bar. The leakages in the chamber were modelled using measured values for leakage mass flow rates at different rotor positions and different chamber pressures. To implement these measurements, the expander was fixed in different positions and charged with different pressures. These measurements were used to generate a leakage mass flow rate matrix, which the model can use to determine the corresponding leakage mass flow rate for different positions and pressures. The curve in Figure 2 clearly shows that the course with leakage mass flow rate results in a lower working chamber pressure than the course without leakage. As can also be seen in the Figure, the chamber draws a vacuum, as the previously mentioned inlet opening cross-section can also be shifted to different positions in the model. Here in the modelled example, it is at 30°. By modelling the pressure in the chamber, it has already been established that a later inlet than 0° in the circumferential direction only has a negative effect on the expansion efficiency of the expander. This becomes clear, as due to the vacuum at the beginning of the expansion, no work output of the expansion chamber can be created. Even the opposite is the case. Due to the vacuum in the expansion chamber and the prevailing ambient – or even higher - pressure in the ejection chamber, a force acts against the direction of rotation on the vane.

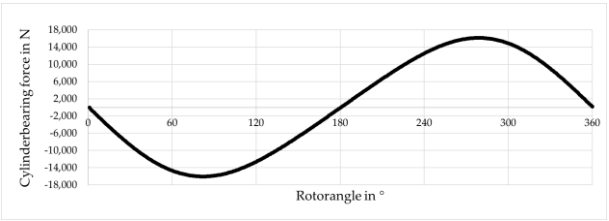


Figure 3. Cylinder bearing forces over rotor angle at 3000 rpm

Figure 3 shows the bearing load over the rotor angle. The diagram shows the load curve for 3,000 rpm. Here, the cylinder mass and geometry of the measured expander out of the CAD were used to calculate the inertia. The Figures show that the bearing load increases up to 16 kN - positive and negative. The course also shows that the maxima are at approx. 90° and 270°, the minimum at 180°. This seems logical, as the maximum eccentricity is at 180° and the maximum acceleration and deceleration of the cylinder take place before and after the maximum eccentricity. The maximum accelerations – positive and negative - and the inertia of the cylinder induce

corresponding torques, which then cause forces on the cylinder bearing. With these amplitudes, it is highly questionable whether the expander could have been operated at this rotational speed at all.

3 Results and discussion

In this section, the results of the modelling are compared with the results of the measurement of the Revolving Vane Expander. The inlet position for the measurement was set at 30° and the length of the inlet opening was set at 40°. This position and width also correlate with the modelled curves just shown. The measurements were carried out with compressed air at the pressurized air facility *PDLT* at the OTH Amberg-Weiden [5].

Figure 4 shows the comparison of the mass flow rate of the measured expander with the values from the model over the rotational speed. At first glance, the courses are similar, with the curve of the modelling at 400 rpm being slightly lower than the curve from the measurement, but then rising more sharply. These deviations can best be explained by the transient effects of the inflow. The speed-dependent sliding of the inlet cross-section in the valve with the inlet opening bore in the rotor very probably results in transient effects that are not represented in the modelling. The transient effect of the constriction of the flow will be more pronounced at high rotational speeds than considered in the model. In the model, the inlet mass flow rate is determined for each degree step based on the prevailing opening cross-section, source and chamber pressure. What also comes apparent by the numbers in the Figure, which is the same for all the following Figures, is the considered rpm range. The range lasts from 400 rpm to 1,000 rpm, as for lower rpms than 400, the expander went into an area of strong strokes. Therefore, determination of mass flow rate, torque and rpm was very difficult. Rotational speeds above 1,000 rpm were not considered, as the expander began to beat strongly at these higher rpms and the test stand was not designed for these strong impacts.

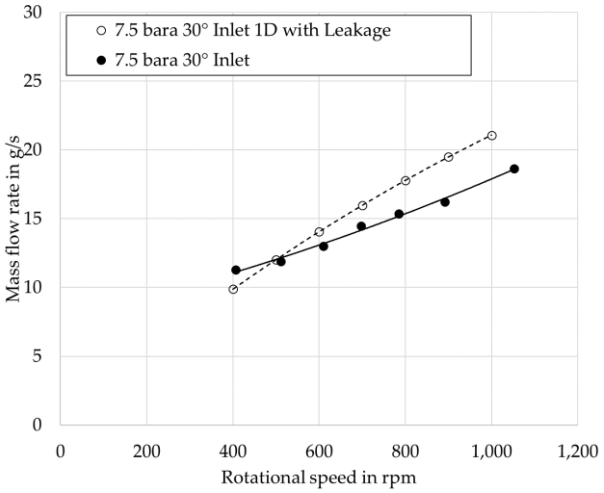


Figure 4. Modelled (open circles) and measured (full circles) mass flow rate over rotational speed

The torque distribution over the rotational speed of the expander in the model and measurement in Figure 5 shows a comparable course. Due to the higher mass flow rate after 300 rpm in the model, the pressure in the chamber of the expander is also higher and thereby the torque. Both curves show a similar slope, where the modelling shows about 2 Nm (400 rpm) to around 4 Nm (1,000 rpm) higher torque than measured. This slighter drop in torque in the modelling also correlates with the steeper increase in mass flow rate towards higher rotational speeds. For rpms lower than 300 rpm, where the modelled mass flow rate is lower than measured, the torque should also be lower. This is not the case, which implies, that the model still leaks some negative influences on the energy conversion.

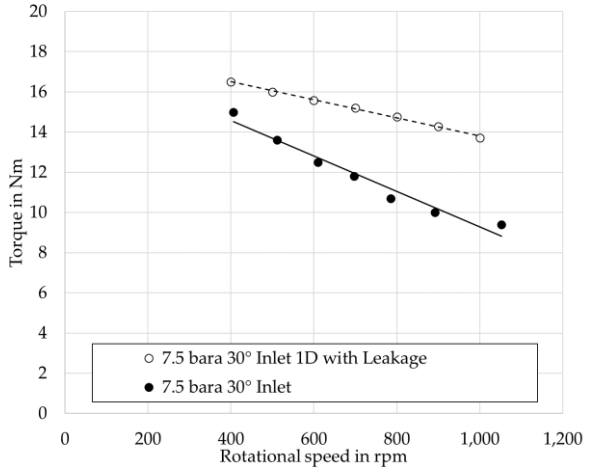


Figure 5. Modelled (open circles) and measured (full circles) torque over rotational speed

For a complete comparison, Figure 6 shows the modelled and measured isentropic expansion efficiency of the expander. The efficiency course of

the two curves can be derived from the two previous Figures of the mass flow rate and the torque. What is immediately apparent is that the two curves are very similar. The curves are relatively flat over the entire rotational speed range. It is also clear that the model is consistently approx. 5 - 7 %-P above the measured expansion efficiency. Nevertheless, measured expansion efficiency is with about 45% at least competitive compared to available volumetric expander in this low power range (< 10 kW_{el}) [6].

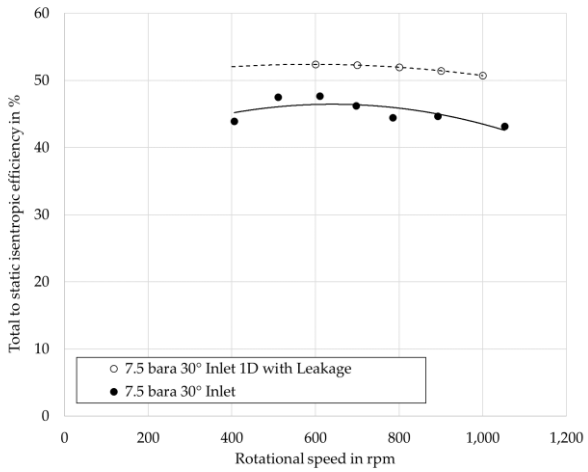


Figure 6. Modelled (open circles) and measured (full circles) isentropic expansion efficiency (ts) over rotational speed

4. Summary and conclusions

After this presentation of the Revolving Vane Expander and the comparison of the measurement results with the modelled results in this short paper, the following conclusions can be drawn. The first major drawbacks could already be identified through the simplified observation in the 1D Excel model. These are primarily the high torque amplitudes and the resulting forces on the bearings due to the inertia of the corotating outer cylinder. Furthermore, it was made clear that a later inlet position of the inlet valve after 0° only has a negative influence on the expansion efficiency of the expander. When looking at the modelling results compared to the measured results, it becomes clear that although the simple model with the empirical leakage modelling already provides a good guideline for the performance numbers, the model still needs to be further improved. A further, optimized Revolving Vane Expander is now to be designed and measured during the project. This expander should eliminate the negative points identified by the model and the measurement. Above all, the high inertia of the cylinder and the acceleration and deceleration. Thus, generate a higher power output and expansion efficiency. The 1-D model is to be further optimized on the basis of the results of the next expander. In the future it should be possible to extract the optimum design specifications from the model for certain applications and boundary conditions. Thereby it should be possible to provide corresponding highly efficient and reliable Revolving Vane Expanders for Organic Rankine Cycles.

Acknowledgement

Supported by:

Federal Ministry for Economic Affairs and Climate Action

on the basis of a decision by the German Bundestag

4 References

[1] Tartière T, Astolfi M. A World Overview of the Organic Rankine Cycle Market. Energy Procedia 2017;129:2–9. https://doi.org/10.1016/j.egypro.2017.09.159.

[2] Alison Subiantoro, Ooi KT. Introduction of the Revolving Vane Expander.

[3] Naseri A, Norris S, Subiantoro A. Theoretical modelling and experimental investigation of the modified revolving vane expander (M-RVE). Energy Conversion and Management 2022;252:114997. https://doi.org/10.1016/j.enconman.2021.114997.

[4] Teh YL, Ooi KT. Theoretical study of a novel refrigeration compressor – Part I: Design of the revolving vane (RV) compressor and its frictional losses. International Journal of Refrigeration 2009;32(5):1092–102. https://doi.org/10.1016/j.ijrefrig.2008.09.006.

[5] Jan Misak, Harald Wirth, Andreas P. Weiß. 20 Jahre angewandte Forschung am Prüfstand für Druckluftantriebe und-technik (PDLT) an der OTH Amberg-Weiden. OTH Forschungsbericht 2021:174–9; Available from: https://www.oth-aw.de/files/oth-aw/Aktuelles/Veroeffentlichungen/Forschungsbericht/OTH_Forschungsbericht_2021.pdf. [October 02, 2024].

[6] Imran M, Usman M, Park B-S, Lee D-H. Volumetric expanders for low grade heat and waste heat recovery applications. Renewable and Sustainable Energy Reviews 2016;57:1090–109. https://doi.org/10.1016/j.rser.2015.12.139.

A ONE-DIMENSIONAL MODEL FOR SUPERSONIC EJECTORS BASED ON THE COMPOUND FLOW THEORY

Jan Van den Berghe[1,2]*, Romain Debroeyer[2], Miguel Alfonso Mendez[1], Yann Bartosiewicz[2]

[1] von Karman Institute for Fluid Dynamics, Environmental and Applied Fluid Dynamics, Sint-Genesius-Rode, Belgium

[2] Université Catholique de Louvain, Institute of Mechanics, Materials, and Civil Engineering, Louvain-la-Neuve, Belgium

* *Corresponding Author: jan.vandenberghe@vki.ac.be*

Abstract. We present a 1D ejector model based on compound flow theory and the momentum balance between two one-dimensional streams. The model reproduces the dividing streamline between the streams and the axial distribution of cross-stream averaged quantities, including momentum exchanges between the streams and the walls using friction closure laws. A formulation based on the Prandtl-Meyer relation and oblique shocks is proposed to describe the pressure equalisation between the streams, from the outlet of the primary nozzle until the pressures equalise. From that point, the compound equations including momentum exchange are integrated. The model predictions were validated against experimental data and axisymmetric RANS simulations in on- and off-design operation. The agreement confirms that the model can serve as a valuable tool for the analysis and design of ejectors, as well as its integration into complex thermodynamic cycles.

Keywords. Supersonic ejectors, Compressible flow, Choking.

1 Introduction

Ejectors are passive flow devices that entrain a flow from a low-pressure source by expanding a flow at high pressure through a nozzle into a mixing pipe (see Figure 1), where both streams mix and reach an intermediate pressure at the outlet of the diffuser. Their performance is typically evaluated with axisymmetric Reynolds-Averaged Navier Stokes (RANS) simulations [1] or predicted by 0D models [2], which rely on conservation laws between key sections and calibrated efficiency coefficients.

A compromise between these options consists of one-dimensional models, which are relatively scarce. These predict the axial distribution of relevant quantities in the primary and the secondary stream, using quasi-1D conservation equations in two coupled 1D domains. The cross-sections of these channels depend on the dividing line between the streams, which has an infinite number of admissible distributions. An additional constraint is therefore required to close the model. Most authors assume a uniform static pressure across the streams at a given axial position [3-6]. This restricts the solution to a unique dividing *streamline* (implying no mass exchange between the streams) and is the base of the compound flow theory [7]. This theory also provides a mechanism for mass flow blockage where the compound sonic condition consists of a combination of the streams, as opposed to the separate streams becoming sonic (referred to as 'Fabri choking'). Compound choking has been shown to be the more general mechanism [7, 8]. However, the primary jet is usually under- or over-expanded in ejectors, leading to a shock train in the mixing pipe with non-uniform static pressure [1]. A notable contribution in these conditions is the work of del Valle et al. [9], who retrieved the dividing streamline with potential flow and Prandtl-Meyer expansion theory but used Fabri choking for mass flow limitation.

To the authors' knowledge, none of the existing models based on the compound flow theory admit different static pressures at the inlet of the mixing pipe. This work proposes a mechanism to equalise the static pressures of both streams over a finite distance. The compound flow theory is applied from that point on.

2 Model definition

2.1 General definition

The structure of the model is shown schematically in Figure 1. It consists of two parallel 1D domains which represent the two streams continuously from

$$\begin{aligned} d_x(\rho_i A_i u_i) &= 0\,, \\ d_x\left(\rho_i A_i u_i^2\right) &= -A_i d_x p_i + F_i\,, \\ d_x\left(\rho_i A_i u_i h_{t,i}\right) &= 0\,, \end{aligned} \qquad (1)$$

the separate inlets to the common outlet in the diffuser. The governing equations are the steady quasi-1D Euler equations with force terms F:

where d_x denotes the axial derivative, ρ is the density, A is the cross-section's area, u is the velocity, p is the static pressure, h_t is the total enthalpy and the index $i \in [p, s]$ indicates the primary or the secondary stream. The variables thus

represent local cross-stream averages as function of the axial coordinate x. The fluid is assumed to follow the ideal gas law.

A friction force $F_{w,i} = 0.5\, f_w \rho_i u_i^2 l_w$ is applied at the wall of the separate inlets and of the secondary stream in the mixed domain, where the friction coefficient f_w is computed with Van Driest's [10] formula and l_w denotes the perimeter of the wall. The primary stream is assumed to be choked in the primary nozzle, so it can be computed independently from the rest of the ejector. The flow variables and the cross-sections in the mixing pipe are computed with the compound flow equations, including momentum exchange through a friction force at their interface, which acts equally on both streams but in the opposite direction:

$$F_{ps} = 0.25\, C\, f_{ps}(\rho_p + \rho_s)(u_p - u_s)^2 l_{ps}\,, \qquad (4)$$

where friction coefficient f_{ps} is computed with Papamoschou's [11] formula and l_{ps} denotes the perimeter of the primary stream. The constant C is added as a calibration parameter. The forces in the mixing pipe are defined as follows:

$$F_p = -F_{ps} \quad \text{and} \quad F_s = F_{ps} - F_{w,s} \qquad (5)$$

We refer to [7] for the numerical solution of these equations and more details. Note that the primary jet is generally under- or over-expanded [1], so the assumption of equal static pressure is invalid near the outlet of the primary nozzle. Furthermore, the finite thickness of the nozzle lip requires some attention in the cross-section definitions.

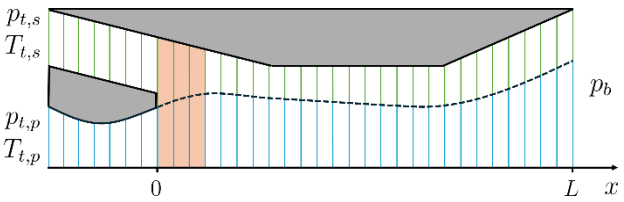


Figure 1: The ejector model consists of two coupled 1D domains, with pressure equalisation in the shaded area (see 2.2) and compound equations downstream.

2.2 Precautions near the primary nozzle outlet

The finite thickness of the primary nozzle lip causes a mismatch of the secondary cross-section at the inlet of the mixing pipe, as shown in Figure 2. The primary cross-sections at the left and right side of the interface match, so the flow states are identical: $y_{p,L} = y_{p,R}$ (where y denotes a suitable state vector, e.g. the density ρ, static pressure p and velocity u). The state of the secondary stream on the right side is found using conservation of mass, momentum and energy (implying $T_{t,s,L} = T_{t,s,R}$). The right state is computed iteratively: from a guessed velocity $u_{s,R}$, the static temperature follows from the definition of the total temperature, and the density follows from the mass flow rate. The static pressure $p_{s,R}$ is computed with the ideal gas law, which allows to compute the residual of the momentum equation:

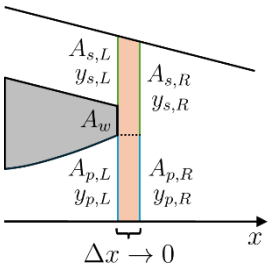


Figure 2: The finite thickness of the nozzle lip causes a mismatch in the secondary cross-section.

$$\dot{m}_s u_{s,L} + p_{s,L} A_{s,L} + p_{s,R} A_w = \dot{m}_s u_{s,R} + p_{s,R} A_{s,R}\,. \qquad (6)$$

The resulting static pressure $p_{s,R}$ is generally different from $p_{p,R}$, violating the assumption of the compound equations [7]. The proposed pressure equalisation mechanism is shown in figure 3 and is inspired by the 2D shock train which is formed in reality. If the primary pressure is lower than the secondary pressure (over-expansion), an oblique shock is formed to compress the flow to the same static pressure, which deviates the flow inwards. The shock angle α follows from the static pressures and the primary Mach number (which is greater than unity since the primary nozzle is choked) [12]:

$$\frac{p_s}{p_p} = \frac{1}{\gamma + 1}\left(2\gamma M_p^2 \sin^2\alpha - \gamma + 1\right). \qquad (7)$$

The deviation angle θ follows from the shock angle:

$$\tan\theta = -\frac{2\cot\alpha\left(M_p^2 \sin^2\alpha - 1\right)}{M_p^2(\gamma + \cos 2\alpha) + 2}, \qquad (8)$$

where the minus sign is introduced to deviate the flow towards the centreline. If the primary pressure is greater than the secondary pressure, the primary stream expands outwards. This process is assumed to be isentropic, so the total pressure $p_{t,p}$ is conserved from the initial state to the expanded state, which has the static pressure p_s and the Mach number $\widetilde{M}_p$:

$$p_{t,p} = p_s\left(1 + 0.5(\gamma - 1)\widetilde{M}_p^2\right)^{\gamma/(\gamma-1)}. \qquad (9)$$

The deviation angle follows from the difference in the Prandtl-Meyer angle ν related to the Mach numbers M_p and $\widetilde{M}_p$:

$$\theta = \nu(\widetilde{M}_p) - \nu(M_p)\,, \tag{10}$$

where $\nu(M)$ is given by [12]:

$$\nu(M) = \sqrt{\frac{\gamma+1}{\gamma-1}}\tan^{-1}\left(\sqrt{\frac{\gamma-1}{\gamma+1}(M^2-1)}\right) - \tan^{-1}\left(\sqrt{M^2-1}\right)\,. \tag{11}$$

The gradient of the cross-sections is directly related to the deviation angle θ and the radius of the primary cross-section r_p:

$$d_x A_p = d_x A - d_x A_s = 2\pi r_p \tan\theta\,. \tag{12}$$

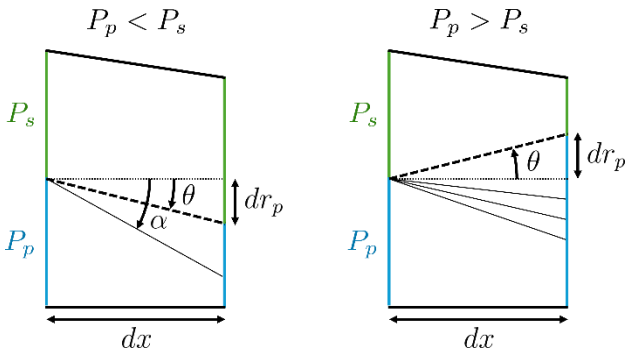


Figure 3: The dividing streamline (dashed line) is computed locally by the pressure equalisation mechanism with an oblique shock or an isentropic expansion (Mach lines in full lines).

Equations (7)-(12) form a closed system of equations with (1), (2), (4) and (5) that can be integrated in space until the static pressures equalise.

3 Results

Figure 4 compares the static pressure predicted by the model with the wall pressure from axisymmetric RANS simulations and experiments in an on-design operating point [13]. The origin of the x-axis corresponds to the inlet of the constant-area section, which extends to $x/L = 1$. The parameter C (equation 4) was calibrated to match the experimental critical back pressure and equals 1.8. Hence, the original correlation tends to underpredict the friction between the streams, which could be due to the large scatter in the underlying data [11].

The pressure equalisation mechanism acts in a relatively short distance from the exit of the primary nozzle as highlighted in the bottom of figure 4. The primary jet is overexpanded, so it is compressed through equations (7), (8) and (12). Downstream the location at which pressures have equalised, the compound equations are integrated (see [7]), reaching a compound-sonic flow at the inlet of the constant area section ($x = 0$) with a pressure ratio $p/p_{ts} \approx 0.6$. This sonic state is reached further downstream in the RANS simulation. Both the model and the RANS simulation underestimate the static pressure in the mixing pipe and overestimate the secondary mass flow rate (see table 1). The reason for this mismatch remains an open question. The predicted pressure accurately matches the reference at the wall up $x = 0$. The reference pressures oscillate downstream due to the shock train, which consists of several cells in the CFD and the experiments and is two-dimensional. The pressure equalisation mechanism only approximates the first cell. The shock in the diffuser is not captured due to the lack of a compound shock model.

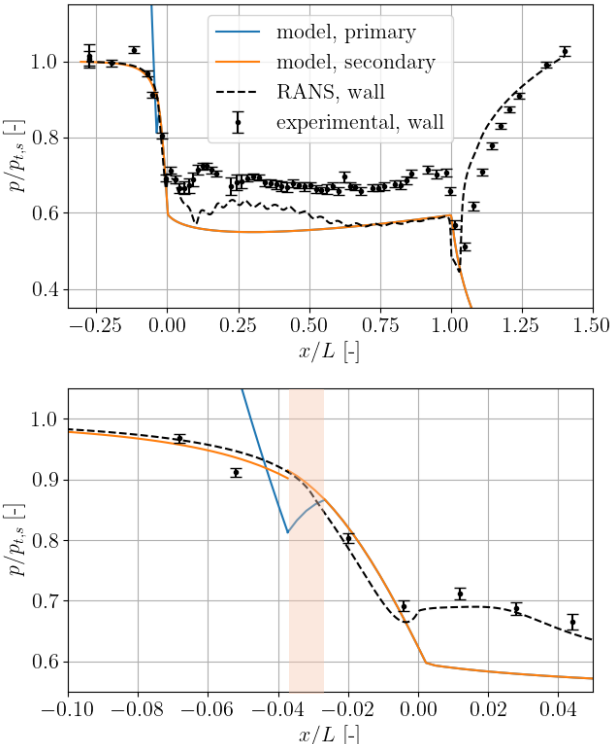


Figure 4: The static pressure in both streams as predicted by the model and at the wall from RANS simulations and experiments in on-design operation.

Figure 5 displays an off-design operating point, where the parameter $C = 2.5$ has been calibrated to match the secondary mass flow rate. The predictions agree well with the reference data, except near the inlet of the constant area section where the pressure recovery is overpredicted by the model. This might be an indirect consequence of the assumption of the uniform pressure profile: it restricts the dividing streamline to a unique solution, which can result in

sharp, non-physical deviations. This is especially the case at the inlet of the constant-area section. The corner at the wall directly affects the primary stream in the model through the assumption of uniform pressure, whereas its effect is less immediate due to the presence of the shock train. Notably, the RANS simulation overpredicts the secondary mass flow rate despite its accurate prediction of the static pressure.

Table 1: Secondary mass flow rates (cf. figure 4).

$\dot{m}_s$ (kg/s)	**Experimental**	**RANS**	**Model**
On-design	0.193 ± 0.002	0.198	0.202
Off-design	0.148 ± 0.002	0.164	0.148

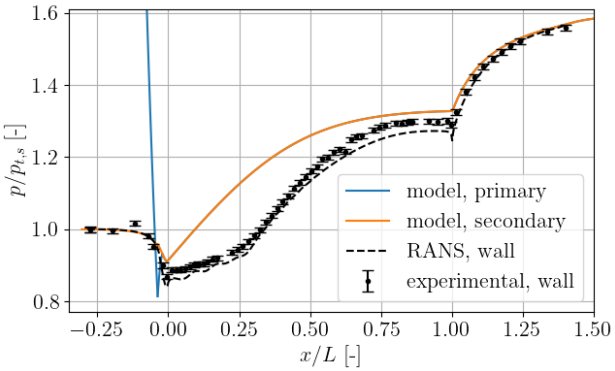


Figure 5: The static pressure in off-design operation.

4 Conclusion

We have presented a 1D ejector model based on compound choking combined with a novel pressure equalisation mechanism. It predicts the correct axial distribution of flow variables such as the static pressure and can quantify the secondary mass flow rate in off-design conditions if the friction between the streams is modelled correctly. The overestimated flow rate in on-design conditions and the overestimated static pressure in off-design conditions are likely caused by the 2D effects of the shock train at the exit of the primary nozzle. Further investigation is ongoing to clarify and to mitigate the observed discrepancy between the model and the data, as well as an extension with energy exchange between the streams. Nevertheless, we believe that the model fosters the understanding of various physical effects, which can be studied independently.

References

[1] Y. Bartosiewicz et al., “Numerical and experimental investigations on supersonic ejectors”, International Journal of Heat and Fluid Flow 26 (1), pp. 56-70, 2005.

[2] A. Metsue et al., “An improved thermodynamic model for supersonic real-gas ejectors using the compound-choking theory”, Energy p. 121856, 2021.

[3] L. Clark, “Application of compound flow analysis to supersonic ejector-mixer performance prediction”, in 33rd Aerospace Sciences Meeting and Exhibit, p. 645, 1995.

[4] D. Papamoschou, “Analysis of partially mixed supersonic ejector”, Journal of propulsion and power 12 (4), pp. 736-741, 1996.

[5] G. Grazzini, F. Mazzelli, A. Milazzo, “Constructal design of the mixing zone inside a supersonic ejector”, International Journal of Heat and Technology 34 (S1), pp. S109-S118, 2016.

[6] K. Banasiak, A. Hafner, “1D computational model of a two-phase R744 ejector for expansion work recovery”, International Journal of Thermal Sciences 50 (11), pp. 2235-2247, 2011.

[7] J. Van den Berghe, M.A. Mendez, Y. Bartosiewicz, “An extension of the compound flow theory with friction between the streams and at the wall”, Journal of Fluid Mechanics, 2024.

[8] O. Lamberts, P. Chatelain, N. Bourgeois, Y. Bartosiewicz, “The compound-choking theory as an explanation of the entrainment limitation in supersonic ejectors”, Energy 158, pp. 524-536, 2018.

[9] J. G. del Valle et al., “A one dimensional model for the determination of an ejector entrainment ratio”, International Journal of Refrigeration 35 (4), pp. 772-784, 2012.

[10] E. R. Van Driest, “Turbulent boundary layer in compressible fluids”, Journal of the Aeronautical Sciences 18 (3), pp. 145-160, 1951.

[11] D. Papamoschou, “Model for entropy production and pressure variation in confined turbulent mixing”, AIAA journal 31 (9), pp. 1643-1650, 1993.

[12] A. H. Shapiro, “The dynamics and thermodynamics of compressible fluid flow”, New York: Ronald Press 1953.

[13] L. Brosteaux, Q. Doucet, “Experimental characterization of an axisymmetric supersonic air ejector”, master thesis, UCLouvain, 2021.

DEVELOPMENT OF A SCALABLE RECIPROCATING COMPRESSOR MODEL

Jaromir Jeßberger[1]*, Kristina Lasch[1], Florian Kaufmann[2], Florian Heberle[1], Dieter Brüggemann[1]

[1]Chair of Engineering Thermodynamics and Transport Processes (LTTT), Center of Energy Technology (ZET), University of Bayreuth, Prof.-Rüdiger-Bormann-Strasse 1, DE-95447 Bayreuth, Germany

[2] Chair of Energy Systems, Technical University of Munich, Boltzmannstr. 15, 85748 Garching, Germany

** Corresponding Author: jaromir.jessberger@uni-bayreuth.de*

Abstract. The transition from a fossil fuel-dominated heating market to a renewable system represents a significant challenge for the present era. The integration of high-temperature heat pumps (HTHP) is a crucial aspect of this transition and cannot be overlooked. In the absence of a substantial corpus of experimental data, it is imperative that models demonstrating resilience and robust performance be employed in the design and planning of heat pump projects. The compressor represents the most significant and intricate component within the heat pump cycle, with a multitude of available technologies currently on the market. This submission focuses on reciprocating piston compressors, which are widely used in heat pump processes due to their flexibility and extensive range of available sizes. The literature demonstrates a variety of approaches to simulating the performance of the compressor, including physical models, empirical models, and semi-empirical models. The objective of this study is to develop a semi-empirical model based on experimental data obtained from a test rig and to convert it into a scalable polynomial model in accordance with the approach proposed by Kaufmann et al. [1]. Following the validation of the model with the test rig, a comprehensive validation with manufacturer data will be conducted. This will result in the creation of a low-order model that combines the advantages of low computational cost, high accuracy, physically correct predictions over a wide operational range and scalability to different machine capacities. Additionally, the variation of working fluids will be analysed and validated using datasets provided by manufacturers.

Keywords: Reciprocating compressor, Simulation, Semi-empirical model, Upscaling, polynomial model

Nomenclature

HTHP	High-temperature heat pump
k	Fitting coefficients
N	Compressor speed (rpm)
P	Power consumption (kW)
p	Pressure (bar)
SH	Superheating
T	Temperature (°C)
V	Volume (m³)
$\dot{V}$	Volume flow rate (m³/s)

Special characters

η	Efficiency (%)
Π	Pressure ratio (-)

Subscripts

comp	Compressor
dis	Discharge side
exp	Experimental
norm	Normalized
sim	Simulated
suc	Suction side

1 Introduction

The use of simulation models serves several purposes, including the validation of measurement data, the creation of digital twins, and the prediction of operating behaviours outside the measurement range. Therefore, it is of the utmost importance that models are as accurate as possible for the optimisation of thermal systems such as heat pumps and refrigeration systems. However, the accuracy of a model is not the sole determinant of its efficacy; the computational effort required is also a significant factor. In the context of modelling physical and technical systems, a distinction is drawn between three classes of models, each characterised by a distinct level of accuracy and complexity. Empirical models are entirely based on experimental data and utilise bespoke polynomial functions devoid of intrinsic physical meaning for the purpose of mapping the measurement data. They are relatively straightforward to develop and require minimal computing power; however, they are typically unsuitable for making predictions outside the

measurement range. Semi-empirical models combine physical equations, such as thermodynamic relationships, with empirical parameter equations. This allows for a more accurate representation of the physical behaviour, thereby enabling extrapolation beyond the measurement range. Deterministic or geometric models represent the complete machine geometry and fluid dynamics of a technical system on the basis of physical and thermodynamic equations. While these models have the highest predictive accuracy, they are also complex to develop and require large computing resources [2]. Consequently, this paper focuses on semi-empirical and empirical models for the modelling of reciprocating piston compressors.

In addition to the aforementioned purposes for compressor models, another crucial objective is the development of validated compressor models that can be employed for compressors of varying scales. In this study a semi-empirical model, published by Li [3,4] is fitted to experimental data of a reciprocating piston compressor in a high-temperature heat pump test rig, with a maximum electrical energy consumption of 12 kW. In the next step, a polynomial model is developed to simulate the operation behaviour of the compressor, as function of the pressure ratio, the normalized volume flow rate and the superheating of the suction gas.

2 Methodology

The compressor model published by Li [3,4] is a simplified semi-empirical model for scroll and reciprocating piston compressors, with the mass flow rate, power consumption and discharge temperature as output values. The 11 empirical parameters are fitted to 8 experimental operation points over the operation range of the high-temperature heat pump test rig published by Jeßberger et al. [5,6]. Initially, the Matlab [7] solver fmincon is employed to optimize each of the three output parameters individually. Subsequently, a simultaneous optimisation is conducted using a combined residual function (see equation (1)).

$$\begin{aligned} RES &= \frac{1}{3}\sqrt{\frac{1}{N}\sum_{i=1}^{N}\left(\frac{\dot{V}_{suc,model,i}-\dot{V}_{suc,exp,i}}{\dot{V}_{suc,exp,i}}\right)^2} \\ &+\frac{1}{3}\sqrt{\frac{1}{N}\sum_{i=1}^{N}\left(\frac{P_{comp,model,i}-P_{comp,exp,i}}{P_{comp,exp,i}}\right)^2} \\ &+\frac{1}{3}\sqrt{\frac{1}{N}\sum_{i=1}^{N}\left(\frac{T_{dis,model,i}-T_{dis,exp,i}}{T_{dis,exp,i}}\right)^2} \end{aligned} \quad \textbf{(1)}$$

Furthermore, a validation dataset comprising 33 experimental operation points is used to assess the model's predictive accuracy. Afterwards, a synthetic dataset is generated using the validated model for a constant suction gas pressure of 2 bar, pressure ratios between 1.5 and 10 and compressor speeds between 758 rpm and 2100 rpm.

Based on this dataset a 1st degree polynomial for the volumetric efficiency η_{vol} and a 3rd degree polynomial for the isentropic efficiency η_{isen} are developed, as function of the pressure ratio Π, the superheating of the suction gas SH_{suc} and the normalized volume flow rate $\dot{V}_{suc,norm}$. The normalized volume flow rate leads to:

$$\dot{V}_{\mathrm{suc,norm}} = \frac{\dot{V}_{\mathrm{suc}}}{V_{\mathrm{stroke}} \cdot N_{\mathrm{comp,ref}}} \quad \textbf{(2)}$$

With the stroke volume of the compressor V_{stroke}, the volume flow rate at the compressor suction side $\dot{V}_{suc}$ and the compressor speed in the design operation point $N_{comp,ref}$. The normalized volume flow rate is introduced, regarding Kaufmann et al. [1], to make the compressor model valid for different scales. The equations for the volumetric and isentropic efficiency are thus derived as follows:

$$\eta_{vol} = k_1 + k_2 x + k_3 y + 0.1\, z \quad \textbf{(3)}$$

and

$$\begin{aligned} \eta_{isen} = k_1 + k_2 x + k_3 y + k_4 x^2 + k_5 xy \\ + k_6 y^2 + k_7 x^3 + k_8 x^2 y \\ + k_9 y^3 + k_{10} xy^2 + 0.1\, z \end{aligned} \quad \textbf{(4)}$$

Where x is the normalized volume flow rate $\dot{V}_{suc,norm}$, y the pressure ratio Π and z the superheating of the suction gas SH_{suc}. The coefficients of both polynomial functions are determined using a linear least squares fitting procedure based on the synthetically generated data set.

In the following chapters the preliminary results are presented and an outlook regarding the next steps is given.

3 Results

For the fitting of the semi-empirical model to the experimental data 8 datapoints were selected. An increase in the number of operation points neither improved or degraded the model's performance so the remaining 33 data points were used as a validation

dataset. Over 95 % of the simulation results of the mass flow rate are within the 5 % tolerance range, while for the compressor output, 100 % of the values are even within this deviation limit. The Root Mean Square Errors (RMSE) of the isentropic efficiency leads to 1.6 % and for volumetric efficiency to 1.3 %. This underlines the high model quality. Using this validated semi-empirical model, the synthetic dataset is created, presented in Figure 1 for the isentropic efficiency and in Figure 2 for the volumetric efficiency.

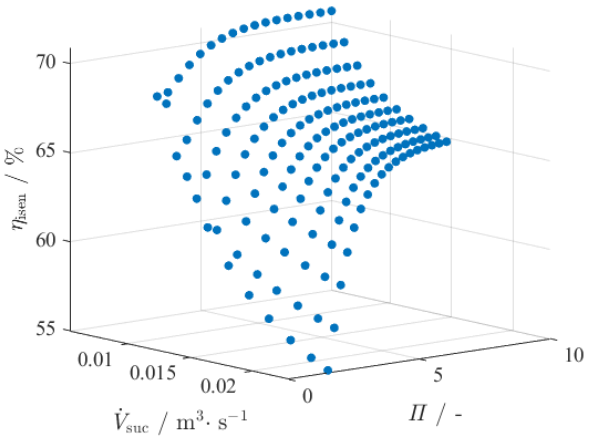


Figure 1: Synthetic dataset for isentropic efficiency as function of volume flow rate and pressure ratio.

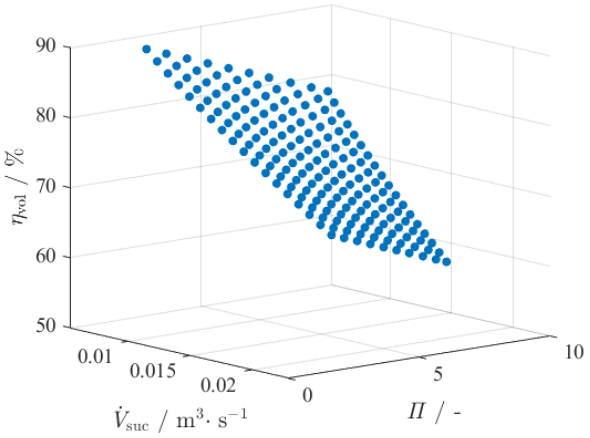


Figure 2: Synthetic dataset for volumetric efficiency as function of volume flow rate and pressure ratio.

Following, the synthetic dataset is used for the fitting of the coefficients of the polynomial model, compare equation (3) and (4). The resulting coefficients are presented in Table 1.

Taking the calculated coefficients into account, the isentropic and volumetric efficiency can be calculated as function of normalized volume flow rate, pressure ratio and superheating of the suction gas.

Table 1: Coefficients of the polynomial model.

coefficient	η_{vol}	η_{isen}
k_1	95.42	87.17
k_2	0.01	-88.37
k_3	-3.86	1.81
k_4		75.84
k_5		5.55
k_6		-0.49
k_7		-24.40
k_8		-1.71
k_9		-0.19
k_{10}		0.03

The results are presented in Figure 3, where the 3D-plots represent the complete scope of validity of the model for both efficiencies. The blue datapoints represent the synthetic dataset and can be reproduced with a RMSE of 0.21 % for the volumetric efficiency, using a first-degree polynomial. For the isentropic efficiency, the RMSE increases to 0.83 %, as its calculation based on the semi-empirical model is more susceptible to inaccuracies due to the more complex dependence on the pressure ratio and volume flow. Furthermore, an increase in the polynomial order does not lead to any significant improvement in the model quality. The green markers represent the validation dataset of the 33 experimental datapoints. Their deviations are shown in the parity plots below. With regard to volumetric efficiency, it can be observed that over 95 % of the values lie within the 5 % deviation limit. Similarly, for isentropic efficiency, 85 % of the values are also within the aforementioned limit. The RMSE is 1.36 % and 2 %, respectively. These results indicate a high level of goodness of fit, which is notable given the simplicity of the final polynomial compressor model and the scatter of the experimental data.

In the following section a conclusion is given and the next steps regarding the finalizing of the model are pointed out.

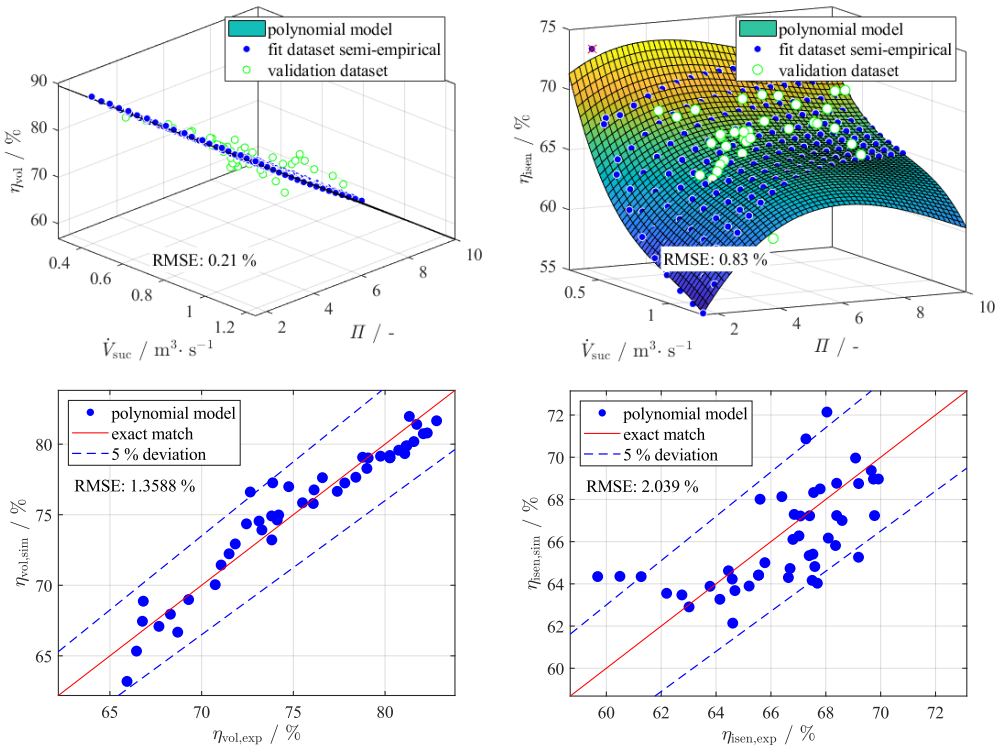


Figure 3: Deviations of the polynomial model to the synthetic dataset and to the experimental dataset.

4 Conclusions

The presented study shows the status of the work in progress, developing a scalable compressor model for reciprocating piston compressors. Therefore, the model presented by Li [4] was adapted to experimental data of a HTHP piston compressor, published by Jeßberger et al. [5,6]. The semi-empirical model demonstrates excellent performance following fitting to 8 experimental operational points, which were validated with an additional 33 operational points. A polynomial model was developed based on the semi-empirical model by fitting it to a dataset created by the semi-empirical model. The polynomial model demonstrates satisfactory performance across the entire compressor operational range with respect to both isentropic and volumetric efficiency. The next stage of the study will entail the validation of the polynomial model using performance datasets of compressors of varying sizes and manufactured by different companies, as sourced from the published literature, as well as the variation of the working fluid.

Acknowledgement

The authors gratefully acknowledge the Bavarian State Ministry of Science and Arts within the framework of the "Geothermal Alliance Bavaria" project for funding.

5 References

[1] Kaufmann F, Irrgang L, Schifflechner C, Spliethoff H. Fast and accurate modelling of twin-screw compressors: A generalised low-order approach. Applied Thermal Engineering 2024;257:124238. https://doi.org/10.1016/j.applthermaleng.2024.124238.

[2] Santos GZ, Ronzoni AF, Hermes CJ. Performance characterization of small variable-capacity reciprocating compressors using a minimal dataset. International Journal of Refrigeration 2019;107:191–201. https://doi.org/10.1016/j.ijrefrig.2019.07.014.

[3] Li W. Simplified steady-state modeling for hermetic compressors with focus on extrapolation. International Journal of Refrigeration 2012;35(6):1722–33. https://doi.org/10.1016/j.ijrefrig.2012.03.008.

[4] Li W. Simplified steady-state modeling for variable speed compressor. Applied Thermal Engineering 2013;50(1):318–26. https://doi.org/10.1016/j.applthermaleng.2012.08.041.

[5] Jeßberger J, Heberle F, Brüggemann D. Maximising the potential of deep geothermal energy: Thermal output increase by large-scale heat pumps. Applied Thermal Engineering 2024;257:124240. https://doi.org/10.1016/j.applthermaleng.2024.124240.

[6] Jeßberger J, Arpagaus C, Heberle F, Brendel L, Bertsch S, Brüggemann D. Experimental investigations of upscaling effects of high-temperature heat pumps with R1233zd(E). International Journal of Refrigeration 2024;164:243–56. https://doi.org/10.1016/j.ijrefrig.2024.04.023.

[7] The MathWorks Inc. MATLAB: 2023. Natick, Massachusetts, United States: The MathWorks Inc.

Experimental Investigation of a Supersonic Axial Impulse Turbine for a Biomass-Fired ORC CHP System

Jan Spale[1,2,*], Vaclav Vodicka[1], Philipp Streit[2,3], Vaclav Novotny[1,2], Lukas Volfl[1,2], Michal Kolovratnik[2]

[1] Czech Technical University in Prague, University Center for Energy Efficient Buildings, Energy Systems in Buildings, Bustehrad 27343, Czechia

[2] Czech Technical University in Prague, Faculty of Mechanical Engineering, Department of Energy Engineering, Prague 160 00, Czechia

[3] East Bavarian Technical University of Applied Sciences Amberg-Weiden, Centre of Excellence for Cogeneration Technologies, Amberg 92224, Germany

* *Corresponding Author: jan.spale@cvut.cz*

Abstract.

A supersonic axial impulse turbine has been developed to operate with hexamethyldisiloxane (MM) as the working fluid in a biomass-fired Organic Rankine Cycle (ORC) combined heat and power (CHP) prototype unit. The turbine is designed for a nominal electrical output of 8 kWel at a rotational speed of 18,000 rpm, with a design-point isentropic efficiency of 69 %. The design process utilized an in-house developed 1D meanline design code using genetic algorithm optimization to tune key design parameters. A hermetically sealed magnetic high-speed coupling is used to transmit power to an off-the-shelf CNC spindle, which acts as a high-speed generator. The generated power is delivered to the grid through a variable frequency drive. This paper, presented as work-in-progress, describes the turbine design, including both aerodynamic and mechanical assembly aspects. Finally, the paper presents preliminary experimental results from the field test in the biomass CHP ORC unit. Lessons learned during the initial testing phases are also highlighted, providing feedback for future improvements and optimization of small-scale ORC systems utilizing siloxane working fluids.

Keywords. Turboexpander, Organic Rankine cycle, Supersonic, Combined heat and power, Biomass, Experimental

1 Introduction and motivation

Small-scale distributed ORC systems, especially in biomass-fired setups, offer an effective way to generate both heat and electricity in a sustainable local manner. [1] However, scaling ORC technology towards a commercial product introduces unique challenges, particularly in designing efficient and cost-effective expanders, which are crucial for the system's performance and cost-effectiveness. [2]

Turbine design for small-scale ORC systems (<50 kWel) must account for the specific properties of organic fluids, such as non-ideal compressible flow behavior and high molecular complexity. [3] Traditional volumetric expanders dominate this segment due to their cost-effectiveness, off-the-shelf availability, and low sensitivity to varying thermal loads. Turbines offer an alternative with a potential for higher peak efficiencies and lower maintenance needs despite their higher initial costs and narrower operational range. [4]

This work explores the development and optimization of a supersonic axial impulse turbine using MM as the working fluid within a biomass-fired ORC CHP system. [2] The ORC unit schematics is shown below in Figure 1. The turbine design, tailored for a nominal 8 kWel output, leverages an in-house Python 1D meanline design tool optimized by a genetic algorithm to refine key design parameters. This manuscript combines aerodynamic design, mechanical considerations, and preliminary experimental results, with the goal of providing insights into performance improvements and the practical application of turbine technology in small-scale ORC systems.

2 Design methodology

The design of the supersonic axial impulse ORC turbine for the system with MM as the working fluid uses a Python 1D meanline tool. This approach uses velocity loss correlations for supersonic flow and REFPROP [5] for fluid properties and the meanline design methodology was previously reported in [3]. The lumped velocity loss correlations from turbine drives of rocket turbopumps were used. [6] These correlations were previously experimentally verified to provide reasonable results also for small-scale highly loaded ORC axial impulse turbomachinery. [4] The design was further optimized using a genetic algorithm (GA). Table 1 summarizes the cycle boundary conditions imposed to the turbine design.

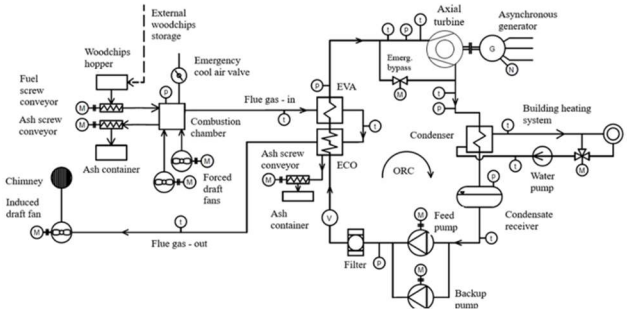


Figure 1: Piping and instrumentation diagram of the biomass-fired CHP ORC unit at CTU

The optimization routine leverages GA to refine key design parameters such as midspan diameter, blade angles, and rotational speed, aiming to maximize isentropic efficiency within the bounds of manufacturability according to Eq.(1,2). Constraints are imposed to limit flow angles and ensure feasible blade dimensions (see list below), with the goal of achieving a compact yet effective turbine layout for the target application.

- Midspan diameter (D_{mid}): 80–200 mm
- Rotational speed (n): 10,000–25,000 rpm
- Nozzle out. flow angle (α_2): 10–18°
- Blade height ratio ($\frac{h}{D_{mid}}$): 0.03–0.1
- Rotor in. flow angle (β_2): 15–30°

A tournament-selection GA (population size 80, 50 generations) was used, combining blend crossover (probability 0.5) and polynomial mutation (probability 0.2) to explore these parameter ranges systematically. For each individual, the in-house Python 1D meanline code evaluates isentropic efficiency as a global objective function under the nominal cycle boundary conditions (Table 1). The design code provides geometric and manufacturing feasibility checks.

$$f(\vec{x}) = \eta_{is}(\vec{x}); \text{ where} \quad (1)$$

$$\vec{x} = [D_{mid}, n, \alpha_s, \frac{h}{D_{mid}}, \beta_r] \quad (2)$$

Table 1: ORC boundary conditions for the turbine design

Parameter	Value	Units
Turbine inlet pressure p_{evap}	550	kPa
Turbine inlet temperature T_{in}	180	°C
Turbine inlet superheat T_{SH}	10	K
Turbine outlet pressure p_{cond}	55	kPa
Working fluid	MM	-
MM mass flow rate $\dot{m}_{wf}$	0.25	kg.s^{-1}

The aerodynamic design incorporates Method of Characteristics (MOC) for the divergent part of the supersonic nozzle design [7] using the Python *open-moc* script and a vortex-flow method [8] for the rotor profiles. Stator nozzles and rotor vanes are manufactured as prismatic blades, stator blades are de Laval nozzles and rotor blades constant channel width buckets and the rotor is shrouded to minimize tip leakage flow. Low pressure vapor exits the turbine through the diffusor to partially recover the kinetic energy at the turbine outlet. The impulse stage geometry is shown in Figure 2 in the blade-to-blade plane and the key design parameters in Table 2.

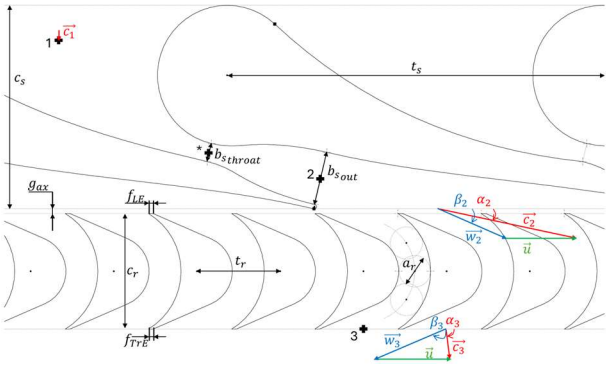


Figure 2: Cascade profile geometry in the blade-to-blade plane

Table 2: Key turbine design parameters

Parameter	Value	Units
Midspan diameter D_{mid}	135	mm
Rotational speed n	18 000	rpm
Nozzle out. Mach Ma_2	1.89	-
Nozzle out. flow angle α_2	13	°

Rotor in. flow angle β_2	23.5	°
Blade height h	5.5	mm
Number of blades Z_s, Z_r	10, 47	-
Rotor in. rel. Mach Ma_{rel2}	1.07	-
Isentropic efficiency $\eta_{is_{t-s}}$	68.1	%
Mechanical power output P_{mech}	8	kW

CFD full stage simulations using ANSYS CFX were used to validate the turbine's aerodynamic design, focusing on shockwave formation and its interactions with boundary layers, evaluating the overall performance of the turbine stage. A 3D model incorporating real-gas properties captured the non-ideal behavior of MM during vapor expansion. The CFD results informed minor adjustments to the blade profiles and clearances, helping to improve efficiency and understand the turbine flow behavior in both design and off-design conditions.

The mechanical design of the turbine assembly accounts for the high rotational speeds and includes a hermetically sealed magnetic coupling to transmit power to a high-speed generator. A water-cooled CNC spindle asynchronous motor is used as an AC high-speed generator, thus an electrical cabinet including active front end rectifier unit and a variable frequency drive is necessary for the turbine rotational speed governing and to deliver grid frequency to the local distribution network. Standard off-the-shelf shielded ball bearings greased for life with a high temperature lubricant are used. The whole turbine assembly is shown in Figure 3.

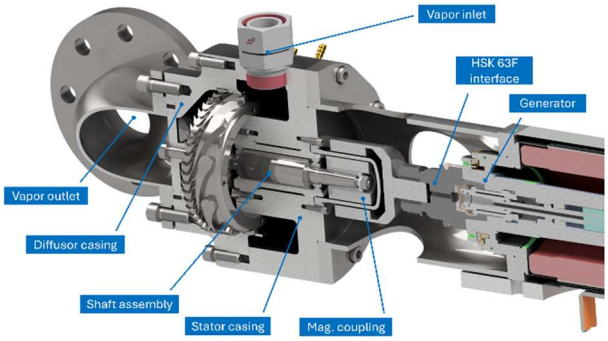


Figure 3: Cross-section view of the supersonic axial impulse turbine assembly

3 Experimental investigation

The ORC prototype unit (Figure 1) delivers heat and electricity to the CTU UCEEB research center and is used for testing various expanders. Control logic employs constant superheat PID control by varying the gear pump speed; without turbine inlet valves, the turbine inlet pressure varies with thermal input.

Due to inherently unsteady woodchips combustion, the turbine inlet pressure can fluctuate by ±10–20 kPa over a 30-minute steady-state run. The condensing pressure is fixed by the building's return water temperature (operated in CHP mode) and a 3-way valve, forcing the turbine to accommodate variable loads.

The ORC test rig uses an industrial PLC for logging and control, gathering data from the following primary sensors. Pressure transducers are ceramic capacitive elements, 0–1 MPa for high pressure, 0–400 kPa for condenser side with accuracy ±0.5 % of full scale. Temperature sensors are Pt100 resistance thermometers with accuracy ±(0.3 °C + 0.005 | T |). These are placed in thermo wells at the turbine inlet/outlet and the condenser inlet/outlet, with an overall expanded uncertainty of ±1.7 °C in the relevant 50–200 °C range with a confidence interval of 95 %. The turbine flowmeter measures volumetric flow rate of liquid MM. The range is 0–56.7 l.min^{-1} and its accuracy ±1 % of full scale. Measured liquid density is temperature and pressure-compensated via REFPROP, resulting in about 1.3 l.min^{-1} uncertainty in calculating the working fluid mass flow, the most significant source of error in the evaluation chain. Electrical power output is evaluated from the variable frequency drive (VFD) and with experimentally obtained generator efficiency curves. The combined accuracy is ±2 % of measured shaft power in the 5–10 kW range. An external handheld vibration sensor is used periodically to check shaft displacement and detect bearing anomalies. Vibration thresholds were set to ensure operation remains below ISO 10816-1 "Satisfactory" criteria. [9] These sensors enable real-time monitoring of the cycle conditions and evaluate isentropic efficiency calculations with a total uncertainty within ±2–4 percentage points, based on its absolute values.

Isentropic efficiency is calculated by comparing mechanical power output to the ideal isentropic enthalpy drop, using temperature and pressure measurements at the turbine inlet and outlet, and electrical power from the VFD with measured electric chain efficiency (Eq. (3)). An industrial PLC logs flow rates, pressures, temperatures, and electrical power for continuous monitoring and efficiency evaluation. Turbine performance was evaluated over 30-minute steady states at various pressure ratios and rotational speeds. Pressure probes measure static pressure distribution along the expansion, and a vibration meter monitors vibration intensity to prevent bearing damage.

$$\eta_{is} = \frac{P_{mech}(P_{el}, \eta_{el})}{\dot{m}_{wf}(\dot{V}_{wf}, p_{liq}, T_{liq}) \cdot \Delta h_{is}(p_{in}, p_{out}, T_{in})} \quad (3)$$

4 Preliminary results

To vary the pressure ratio (PR), the thermal input to the cycle was adjusted by changing the fuel conveyor speed (higher heat input results in pressure increase). At each pressure ratio, turbine efficiency was measured across different rotational speeds, controlled by the VFD unit via Modbus communication from the PLC. Figure 4 presents in a) the isentropic total-to-static efficiency of the turbine evaluated according to Eq.(3) and in b) turbine mechanical power output at each steady state (rpm, pressure ratio).

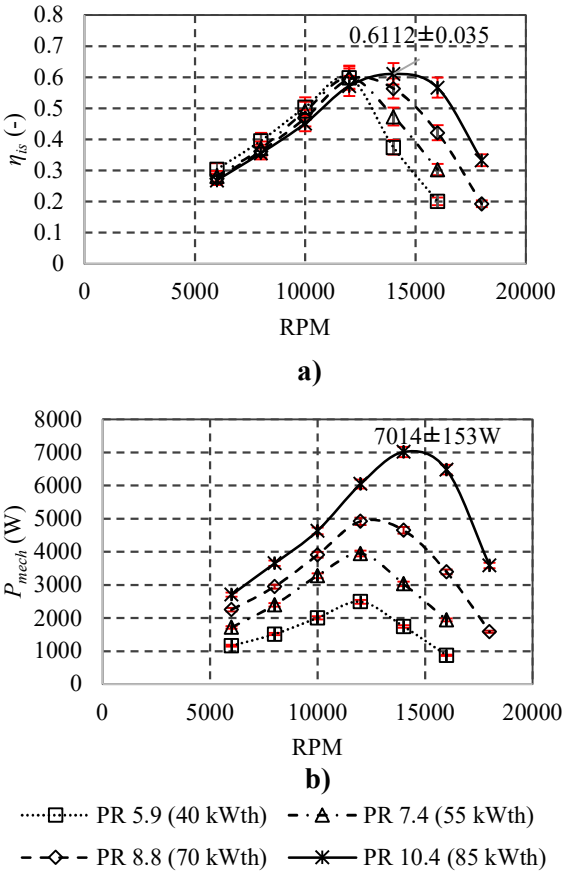


Figure 4: Experimental results of the ORC turbine test campaign, a) isentropic efficiency, b) mechanical power output

The static pressure distribution in the turbine at various points is shown in Figure 5. The nozzle works according to the design, the rotor shows a low pressure increase, probably as a result of a normal shock in the channels or the dynamic jet impinging the pressure probes tangentially at the rotor outlet, thus partially measuring the dynamic component of pressure.

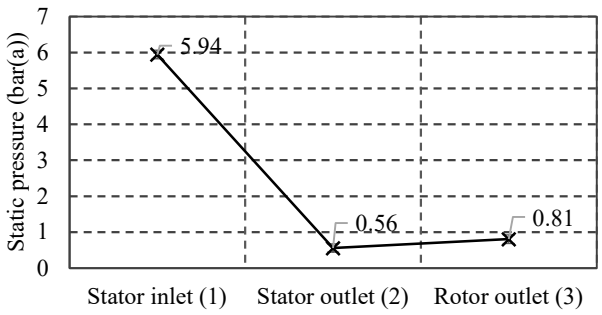


Figure 5: Static pressure along the turbine expansion at nominal pressure ratio

5 Conclusions and Future Work

This paper briefly introduces a work-in-progress in the experimental development of a small-scale supersonic axial impulse turbine for a prototype biomass-fired ORC CHP unit. The initial experimental campaigns yield the following conclusions:

- The cost-effective mechanical assembly proved reliable, showing low vibration intensity and no visible damage after 100 operational hours.
- Maximum power output (7 kW measured vs. 8 kW predicted) and isentropic efficiency (61.12 % compared to 68.1 %) was lower than modeled and occurred at a lower rotational speed (15,000 rpm vs. 18,000 rpm design), possibly due to shockwave formation at the stator trailing edge and deviations in the stator outlet flow angle.
- Measured efficiency curves are asymmetrical, with a steep decrease in power output beyond the maximum, indicating rotor choking at higher pressure ratios.
- Pressure probe measurements indicate correct operation of the supersonic nozzle at the design point but suboptimal rotor performance, suggesting normal shock choking the channels.

The future work will investigate long-term reliability under fluctuating biomass-fired ORC conditions following the building heat demand, as well as exploring advanced control strategies (VFD speed governing according to pressure ratio) to improve adaptability in small-scale CHP applications.

Acknowledgement

This material is based upon work supported by the Grant Agency of the Czech Technical University in Prague, grant No. SGS24/087/OHK2/2T/12. This work is also co-financed from the state budget by the Technology agency of the Czech Republic under the Theta Program with project no. TS01030218.

References

[1] J. Mascuch, V. Novotny, V. Vodicka, J. Spale, and Z. Zeleny, "Experimental development of a kilowatt-scale biomass fired micro – CHP unit based on ORC with rotary vane expander," *Renew. Energy*, 2018, doi: 10.1016/j.renene.2018.08.113.

[2] J. Spale, V. Vodicka, Z. Zeleny, J. Pavlicko, J. Mascuch, and V. Novotny, "Scaling up a woodchip-fired containerized CHP ORC unit toward commercialization," *Renew. Energy*, vol. 199, pp. 1226–1236, Nov. 2022, doi: 10.1016/j.renene.2022.08.144.

[3] A. P. Weiß *et al.*, "Customized ORC micro turbo-expanders - From 1D design to modular construction kit and prospects of additive manufacturing," *Energy*, p. 118407, Jul. 2020, doi: 10.1016/j.energy.2020.118407.

[4] A. P. Weiß, T. Popp, J. Müller, J. Hauer, D. Brüggemann, and M. Preißinger, "Experimental characterization and comparison of an axial and a cantilever micro-turbine for small-scale Organic Rankine Cycle," *Appl. Therm. Eng.*, vol. 140, no. January, pp. 235–244, 2018, doi: 10.1016/j.applthermaleng.2018.05.033.

[5] M. L. Huber, E. W. Lemmon, I. H. Bell, and M. O. McLinden, "The NIST REFPROP Database for Highly Accurate Properties of Industrially Important Fluids," *Ind. Eng. Chem. Res.*, vol. 61, no. 42, pp. 15449–15472, Oct. 2022, doi: 10.1021/acs.iecr.2c01427.

[6] T. W. Reynolds, "Aerodynamic Design Model II Turbine M-1 Fuel Turbopump Assembly," 1966.

[7] N. Anand, S. Vitale, M. Pini, G. J. Otero, and R. Pecnik, "Design Methodology for Supersonic Radial Vanes Operating in Nonideal Flow Conditions," *J. Eng. Gas Turbines Power*, vol. 141, no. 2, pp. 1–9, 2019, doi: 10.1115/1.4040182.

[8] L. J. Goldman and M. R. Vanco, "Computer program for design of two-dimensional sharp-edged-throat supersonic nozzle with boundary layer correction," E-6261, Aug. 1971. Accessed: Mar. 13, 2024. [Online]. Available: https://ntrs.nasa.gov/citations/19710023317

[9] "ISO 10816-1:1995(en), Mechanical vibration — Evaluation of machine vibration by measurements on non-rotating parts — Part 1: General guidelines." Accessed: Nov. 08, 2024. [Online]. Available: https://www.iso.org/obp/ui/#iso:std:iso:10816:-1:ed-1:v1:en

EXPERIMENTAL INVESTIGATION OF CH_4/H_2 BLENDS ON THE EMISSIONS OF A MICRO GAS TURBINE SETUP WITH ENHANCED EXHAUST GAS RECIRCULATION

Vincent THIELENS[1,2]*, Frederiek DEMEYER[2], Ward DE PAEPE[1]

[1] University of Mons, Thermal Engineering and Combustion Unit, Mons, Belgium

[2] Engie R&I Laborelec, Mechanics and Thermal Processes, Linkebeek, Belgium

* *Corresponding Author:* vincent.thielens@umons.ac.be

Abstract. In the context of the energy transition towards a zero-carbon society, amine-based carbon capture has been identified as a transient solution to enable the continued use of fossil fuels while mitigating CO_2 emissions. To reduce the penalty associated with carbon capture, exhaust gas recirculation (EGR) is employed to increase the concentration of CO_2 in the exhaust gases and to reduce the overall mass flow of these gases. However, operating close to stoichiometric combustion conditions increases CO emissions, which limits the EGR rate and thus the penalty reduction. To overcome this challenge, hydrogen cofiring has been proposed as a promising method to stabilize combustion under near-stoichiometric conditions. However, the impact of hydrogen cofiring as an EGR facilitator has never been tested, and its effects on performance and emissions still require thorough investigations. To fill this gap, experiments are conducted using a 3 kW_e micro gas turbine (MTT EnerTwin®), fuelled with pure methane and a blend containing 20% hydrogen. In this study, the effects on emissions are investigated, specifically for NO_x, CO, CO_2, and O_2. The modified setup, designed to allow for higher EGR rates, provides insights on how hydrogen cofiring can stabilize combustion and improve carbon capture efficiency. While the highly diluted conditions encountered in the mGT combustor do not enhance the thermal NO_x formation when hydrogen is added, H_2 cofiring significantly depletes CO emissions (up to a factor 10). Furthermore, the stabilizing effect of hydrogen on the combustion allows higher EGR rate and exhaust gases more concentrated in CO_2 (additional 1.3% compared to pure methane). These findings could be crucial when extrapolating the behaviour of micro gas turbines to industrial-scale systems and evaluating the potential of hydrogen to reduce the overall system penalty of carbon capture technologies.

Keywords. Micro gas turbine, hydrogen, exhaust gas recirculation, NO_x reduction, CO emission.

Nomenclature

EGR	Exhaust Gas Recirculation
HHV	Higher Heating Value
mGT	micro Gas Turbine
LHV	Lower Heating Value

Subscripts

e	electrical
th	thermal

1 Introduction

Exhaust Gas Recirculation (EGR) has already been identified by ElKady et al. [1] and Lieuwen et al. [2] as a technological pathway allowing to decrease NO_x emissions in gas turbines. More recently, the potential of EGR in post-combustion carbon capture has proven to increase the CO_2 concentration while decreasing the flow rate of exhaust gases to treat, due to the fraction enclosed in the recirculation loop. This decreases the energy required at the stripper for the desorption process as well as the size of the installation. Furthermore, De Paepe et al. [3] and Gülen et al. [4] have shown that EGR both depletes O_2 and NO_x levels beneficial to the thermal stability of amines according to Fostas and al. [5].

Nevertheless, experiments realized in the Thermal Engineering and Combustion Unit of UMONS have shown that CO emissions are growing exponentially once dry O_2 concentration goes below 16% at the combustor inlet. Whereas this limit has already been announced by El-Kady et al. [1], it significantly reduces the potential of EGR by letting higher recirculation ranges inaccessible due to constraints on the emissions. H_2 can here help by reducing the

amount of C-atoms in the fuel and stabilizing the combustion.

In terms of H_2 addition in mGTs, Jamshidiha et al. [6] have highlighted the increase of NO_x due to the higher temperature encountered in the combustion chamber. Nevertheless, Schefer et al. [7] have shown that H_2 enrichment leads to more OH radicals promoting the oxidation of CO to CO_2. This tendency has also been put forward by du Toit et al. [8].

To experimentally assess the potential of hydrogen on the factors limiting EGR, namely CO emissions and flame-out, blends of CH_4 containing 0% and 20% of H_2 respectively have fuelled a 3 kW_e micro gas turbine. During these experiments, the dry concentrations of O_2, CO_2, CO, NO and NO_2 are monitored while different EGR rates are applied.

The setup presented in this paper thus addresses the lack of experimental validation on the use of hydrogen as a mean of decreasing CO emissions while extensive levels of EGR are applied on micro gas turbines. Even if the experiments are run on a modified mGT, the results observed give some insight into the use of distinguished CH_4/H_2 blends at industrial scale.

2 Methodology

To understand the impact of hydrogen injection on the emissions, when EGR is applied, a micro gas turbine has been modified and a testing campaign established to compare CO_2 and O_2 concentrations with the theoretical laws. The level of CO and NO_x in the exhaust gases are also measured and compared for the cases with and without hydrogen enrichment.

2.1 Experimental setup

The micro gas turbine EnerTwin® from MTT is used for combined heat and power purposes. The mGT can produce up to 3.2 kW_e of electrical power and has a thermal power of 7-15.6 kW_{th}. Due to the presence of a cogeneration setup, the total efficiency can exceed 94%, while the net grid output efficiency remains between 10% and 16%. In terms of fuel compatibility, the mGT allows fuels containing up to 23% of H_2.

As depicted in Figure 1, the fresh air enters the mGT (1) before being compressed (4). The high-pressure air is then preheated (5) by means of an internal recuperator and flows into the combustion chamber where fuel is burned (16, 17, 18). After the combustion (6), the hot exhaust gases are expanded over the turbine (7) and the remaining energy is transmitted to the compressed air (8) and to the water in the economizer (9). The exhaust gases then flow out to the chimney (13). To work under constant conditions, the incoming air is preheated with an added electrical resistance (3). To apply various levels of EGR, two valves have been added to the setup. The first one allows the flow to be recirculated to the compressor inlet (10, 11), while the second one increases the backpressure (12, 13) forcing recirculation.

The micro gas turbine has been equipped with several sensors for the monitoring of the pressure, temperature, and composition of the flow at separate locations. The gas analyser, a Testo® 350, measures the dry concentration of O_2, CO_2, CO, NO and NO_2.

O_2 is measured with an absolute accuracy of 0.2 vol.%, while the gas analyser allows an accuracy of (0.3 vol.% + 1% of the read value) for CO_2. The inlet gas line is connected to the mixing station where different fuels can be chosen. For the preheating of the components (e.g., internal recuperator, combustion chamber), natural gas is used.

2.2 Test campaign

The test campaign starts with a preheating phase of 2 hours. The set-point of the turbine is fixed at 70% of its nominal load (3.2 kW_e) and the PID controller regulates the tension across the electrical resistor for ensuring a stable inlet temperature of 25 °C. After the preheating period, the valve switches from natural gas to the bottles of pure methane or the blend methane (80%) with hydrogen (20%). The molar fraction of hydrogen in the blend is provided with a relative accuracy of 5%.

When the mGT stops during operation, due to any issue differing from flameout, natural gas is used for a shorter preheating phase (20 minutes) before resuming the ongoing test.

2.3 Analytical predictions

While methane has a LHV and a HHV respectively equal to 50 and 55.5 MJ/kg, hydrogen admits values much higher of 120 and 141.7 MJ/kg. As shown in Figure 2, the increase in the higher and lower heating values between pure methane and the 20%-H_2 blend will necessarily lead to a decrease in the fuel mass consumption of roughly 4% combined with an increased volume flow of 16%.

The equilibrium equation has been used to compute the dry fraction of CO_2 and O_2 for the two cases (namely pure methane with Equation 1 and 20% H_2 with Equation 2), where S is the number of moles of air per mole of fuel. The combustion of pure methane theoretically allows to reach 11.7% of CO_2 on a dry

basis in the exhaust gases at stoichiometry. Working with a blend containing 20% of hydrogen decreases this maximal value by 0.6% abs. (maximum of 11.1%). Looking at the concentration in oxygen, the deviation reaches a maximum of 0.029% for a given recirculation rate when the CH_4/H_2 blend is burned. On a capture perspective, the addition of hydrogen leads to exhaust conditions less concentrated in carbon dioxide as well as in oxygen, and therefore appears disadvantageous.

$$CH_4 + S(0.21\,O_2 + 0.79N_2) \rightarrow CO_2 + 2H_2O + (0.79S)\,N_2 + (0.21S - 2)O_2 \quad (1)$$

$$C_{0.8}H_{3.6} + S(0.21\,O_2 + 0.79N_2) \rightarrow 0.8CO_2 + 1.8H_2O + (0.79S)\,N_2 + (0.21S - 1.7)O_2 \quad (2)$$

3 Results and discussion

For the two fuels chosen, respectively pure methane and the blend 20% H_2 – 80% CH_4, the evolution of the fractions in O_2 and CO_2 is tracked for different EGR ratios. Afterwards, the evolution of pollutant emissions, namely NO_x and CO, are described.

3.1 O_2 emissions

The dry O_2 fraction is measured in the exhaust gases and compared with the equilibrium calculation derived from Equations 1 and 2. The comparison between the combustion of pure methane (reference scenario - upper part of Figure 3) and its difference with the combustion of the blend (lower part of Figure 3) shows similar values. The addition of hydrogen allows only a higher absolute deviation of 0.029% abs. and thus more oxygen in the exhaust gases.

3.2 CO_2 emissions

The monitoring of the dry CO_2 fraction in the exhaust gases indicates that a higher concentration can be obtained with the blend (7.8%) than with pure methane (6.5%), where a lower EGR rate can be applied due to flameout. The presence of H_2 indeed stabilizes the combustion and allows higher EGR rate, leading to exhaust gases more concentrated in CO_2. The combustion of methane follows the theoretical law (upper line in Figure 4) while the experiments with the blend show small deviations from the expected trend (gap between the dots and the line in the lower part of the Figure 4). This difference is explained by the errors coming from the accuracy of the blend composition (2% rel.) as well as the accuracy of the gas analyser (0.3 vol.% + 1% of the read value).

3.3 NO_x emissions

The NO_x emissions are measured in the exhaust gases in ppm on a dry basis. Up to 60% EGR, NO_x emissions are increasing as the recirculation loop fictively increases the residence time in the combustion chamber. However, higher EGR rates lead to a significant NO_x reduction due to the oxygen depletion. As it can be observed in Figure 5, the fuel change does not impact the NO_x concentration in the exhaust. Indeed, the high dilution rate, as illustrated with the air-fuel ratio around 9, when no EGR is applied, decreases the flame temperature in the combustion chamber. The presence of hydrogen is not sufficient to increase the fraction of thermal NO_x in the exhaust gases due to the limited H_2 fraction.

3.4 CO emissions

The CO emissions are monitored in the exhaust and presented in Figure 6 as functions of the CO_2 concentration. As this pollutant emission is the main limiting factor, this representation justifies itself to understand the penalty associated to the concentration in CO_2. The CO concentration evolves exponentially with the CO_2 concentration as the oxygen entering the combustion chamber is decreasing. Under the hypothesis of working at the legal limit on CO emissions, it can be observed that H_2 injection, due to its strong capability to reduce the CO emissions, makes it possible to move towards a higher CO_2 concentration. A gain between 1 and 2.5% in absolute CO_2 dry concentration can be obtained with a blend containing 20% H_2 while maintaining the CO concentration constant. This trend is expected by the reduction of carbon atoms in the fuel, by the enhanced reactivity of hydrogen (higher temperature helping the completeness of the combustion), by the promotion of additional radicals OH, accelerating the reaction in Equation 3 as well as by the higher oxygen concentration in the exhaust gases also leading to the complete oxidation of CO.

$$CO + OH \rightarrow CO_2 + H \quad (3)$$

4 Conclusions

In amine based post-combustion capture, the use of exhaust gas recirculation is presented as a way of increasing the CO_2 concentration for penalty reduction. However, the main limiting factor identified is the formation of carbon monoxide while getting closer to stoichiometric conditions. While CO

production has already been experimentally observed, hydrogen co-firing has never been addressed and evaluated as a way of decreasing the pollutant formation. Within the modified 3kWe-mGT, EGR has been applied and two fuels have been used: pure methane as a reference fuel and a blend containing 20% of H_2. The test outcome shows that the injection of hydrogen allows higher CO_2 concentrations by pushing forward the flameout limit, drastically lowering CO emissions and a no-change in the NO_x emissions (potentially due to the limited H_2 blend concentration). H_2 should be thus further investigated as a way of enhancing higher EGR rates while decreasing the emission of carbon monoxide.

Acknowledgement

Vincent THIELENS is a Research Fellow of the Fonds de la Recherche Scientifique – FNRS. This work was supported by the Fonds de la Recherche Scientifique – FNRS under Grant No J.0033.23 ACCURATE.

References

[1] A. M. ElKady, A. Evulet, A. Brand, T. P. Ursin, and A. Lynghjem, 'Application of Exhaust Gas Recirculation in a DLN F-Class Combustion System for Postcombustion Carbon Capture', *J. Eng. Gas Turbines Power*, vol. 131, p. 034505, Feb. 2009.

[2] T. C. Lieuwen and V. Yang, *Gas turbine emissions*, vol. 38. Cambridge university press, 2013.

[3] W. De Paepe, M. Montero Carrero, S. Giorgetti, A. Parente, S. Bram, and F. Contino, 'Exhaust gas recirculation on humidified flexible micro gas turbines for carbon capture applications', in *Turbo Expo: Power for Land, Sea, and Air*, American Society of Mechanical Engineers, 2016, p. V003T06A011.

[4] S. C. Gülen and C. Hall, 'Gas Turbine Combined Cycle Optimized for Post-Combustion Carbon Capture', in Turbo Expo: Power for Land, Sea, and Air, vol. Volume 3: Coal, Biomass and Alternative Fuels; Cycle Innovations; Electric Power; Industrial and Cogeneration Applications; Organic Rankine Cycle Power Systems. Jun. 2017, p. V003T08A008.

[5] B. Fostås, A. Gangstad, B. Nenseter, S. Pedersen, M. Sjøvoll, and A. L. Sørensen, 'Effects of NOx in the flue gas degradation of MEA', *Energy Procedia*, vol. 4, pp. 1566–1573, 2011.

[6] M. Jamshidiha, M. Kamal, M. Cafiero, A. Coussement, and A. Parente, 'Experimental and numerical characterization of hydrogen combustion in a reverse-flow micro gas turbine combustor', *Int. J. Hydrog. Energy*, vol. 55, pp. 1299–1311, 2024.

[7] R. Schefer, 'Hydrogen enrichment for improved lean flame stability', *Int. J. Hydrog. Energy*, vol. 28, no. 10, pp. 1131–1141, 2003.

[8] M. Du Toit, N. Engelbrecht, S. P. Oelofse, and D. Bessarabov, 'Performance evaluation and emissions reduction of a micro gas turbine via the co-combustion of H2/CH4/CO2 fuel blends', *Sustain. Energy Technol. Assess.*, vol. 39, p. 100718, 2020.

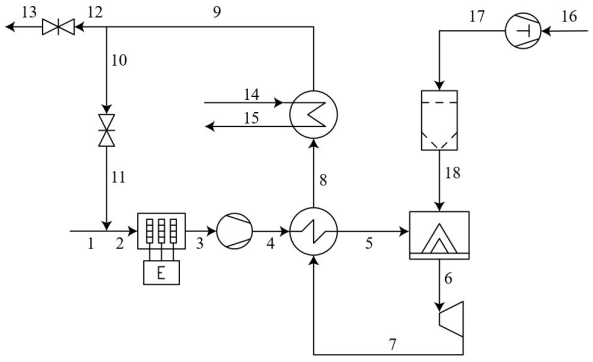


Figure 1: The 3 kW_e-mGT EnerTwin® from MTT has been modified with an external EGR loop and an electrical heater.

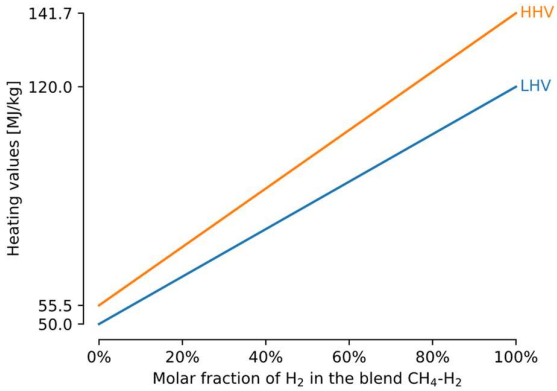


Figure 2: With a blend containing 20% of H_2, the lower and higher heating values are respectively of 64 and 72.7 MJ/kg.

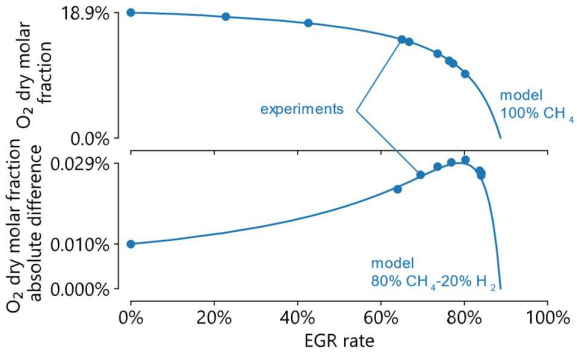


Figure 3: Analytical chemistry predicts that O_2 exhaust concentration reaches a maximum of 18.9% with pure methane (upper figure), while this concentration is slightly higher with the blend (lower figure). (line: theoretical law – dot: experimental points)

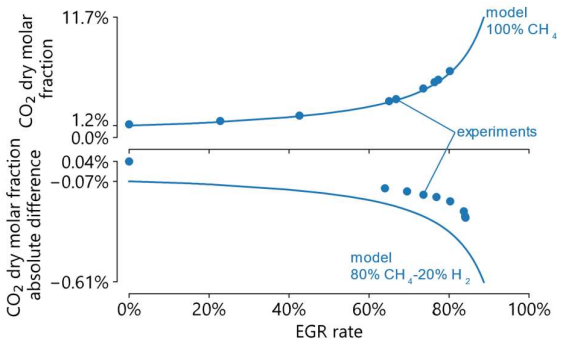


Figure 4: Analytical chemistry predicts that CO_2 concentration increases from 1.2% to 11.7% in the exhaust when the fuel is pure methane (upper figure), while this concentration is slightly lower with the blend (lower figure). (line: theoretical law – dot: experimental points)

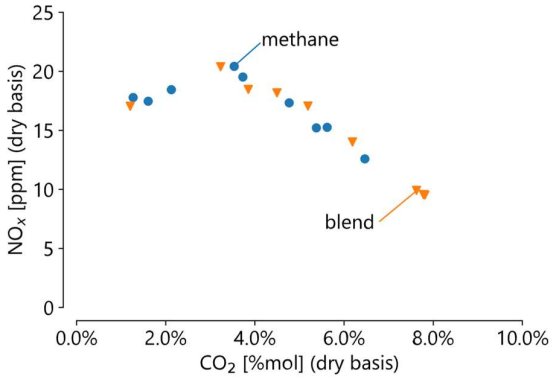


Figure 5: The fuel change does not significantly impact the NO_x production.

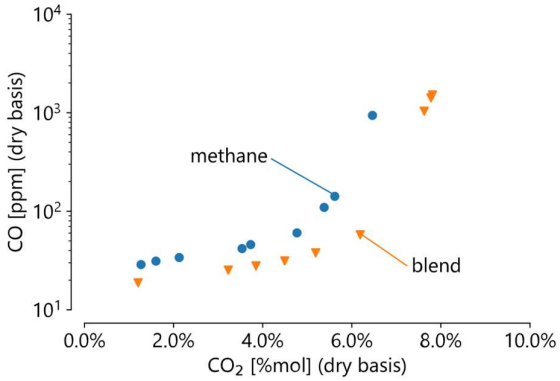


Figure 6: The use of hydrogen in the fuel allows to reduce the CO emissions.

A NEW APPROACH FOR DETERMINING PRIMARY NOZZLE THROAT CONDITIONS IN TWO-PHASE EJECTOR

Baqer Al-Habeeb[1]*, Benoît Michel[1], Yacine Brahami[2], Rémi Revellin[1]

[1] INSA Lyon, CNRS, CETHIL, UMR5008, 69621 Villeurbanne, France [2] Tecumseh Europe Sales & Logistics S.A.S, 38290 La Verpillière, France * *Corresponding Author:* baqer.al-habeeb@insa-lyon.fr

Abstract. Two-phase ejectors are used in refrigeration systems as well as in various industrial applications. Designing such an ejector requires calculating the sonic velocity at the primary nozzle throat. Given the numerous sonic velocity correlations available in the literature, which often yield different results, this study proposes a novel approach that relies solely on conservation equations (mass and energy) to determine the thermodynamic conditions at the throat for design purposes. The results showed that the proposed approach consistently produced a convergent-divergent nozzle under all computed operating conditions including primary and secondary pressures, using R1234yf as a working fluid. In contrast, the considered sonic velocity correlations frequently resulted in a converging nozzle across a wide range of the operating conditions. Additionally, the proposed method demonstrated good agreement in predicting the primary nozzle throat diameter with experimental data from the literature using R134a as a working fluid with a deviation of -8% while the tested correlations exhibited larger deviations of -12 to +186%.

Keywords. Ejector, Two-phase flow, Sonic velocity, Chocked flow.

A DIMENSIONLESS HERMETIC RECIPROCATING COMPRESSOR THERMAL MODEL

Yacine Brahami[1], Maxime Metral[1], David Leray[1]

[1] Tecumseh Europe Sales & Logistics S.A.S, 38290 La Verpillière, France * *Corresponding Author: yacine.brahami@tecumseh.com*

Abstract. Hermetic compressors are home for multiple physical phenomena, which interact in a complex manner. Developing models is a delicate compromise between simplicity, generality, precision and computational costs, but also accessibility of experimental data. We propose a semi-empirical thermal model for hermetic reciprocating compressors. The objective is to predict the mass flow rate, absorbed power and discharge temperature, together with various internal compressor temperatures and motor operating point. Doing so, the model should take as fitting parameters only external compressor measurements, which is the industry standard. The specificity of this model is the use of dimensionless equations, which, in the context of rapidly changing refrigerants, could largely extend the validity to the cost of a few additional fitting parameters. In this preliminary work, the model is validated against single refrigerants.

Keywords. Reciprocating compressors, Semi-empirical models, Dimensionless numbers.

STATISTICAL ENTROPY AS PROXY FOR THE ENERGY REQUIREMENTS FOR BIOMASS VALORISATION AND ITS RELATION TO THE OXIDATION STATE OF CARBON

Britt Segers[1], Philippe Nimmegeers[2], Pieter Billen[1]

[1] iPRACS, University of Antwerp, Belgium

[2] EnvEcon, University of Antwerp, Belgium

* *Corresponding Author:* britt.segers@uantwerpen.be

Abstract. Biomass is currently a heavily researched resource as an alternative to the fossil-based economy. However, the transition from fossil resources to biomass is not straightforward due to the high diversity in biomass composition and the wide range of potential end products that can be produced. In selecting the optimal pathways linking resources to end products, the amount of energy required to do so must be taken into account. Determining the energy requirements for each of these pathways requires a considerable amount of time, data, and expertise. This study proposes a statistical entropy-based method as a proxy for energy demand. As entropy is a state variable, only information on the start and end points need to be considered, regardless of the path taken. Statistical entropy has the potential to quantify the compositional complexity and geospatial distribution of the biomass resource and its potential end products. Therefore, the potential of statistical entropy as a proxy for the energy demand is investigated for case studies in which poplar (lignocellulosic biomass) is valorised through different processes (reductive catalytic fractionation, gasification, and pyrolysis) targeting different end products (lignin oil, syngas, and pyrolysis oil). The determined difference in complexity found is a proxy for the energy requirements as the path of least thermodynamic resistance is sought. In addition to energy, entropy differences can be related to the difference in oxidation state of the resource and the end product.

Keywords. Statistical Entropy Analysis, Decision support, Energy demand, Biomass valorisation, Oxidation State.

A NEW METHOD FOR CALCULATING MOLECULAR STATISTICAL ENTROPY OF POLYMERS IN VIEW OF CIRCULARITY

Cristina Moyaert[1], Attila Kovacs[1], Yoshi Marien[1], Dagmar D'hooge [2], Philippe Nimmegeers[1], Pieter Billen[1]

[1] University of Antwerp, Belgium

[2] University of Ghent, Belgium

* *Corresponding Author: Cristina.Moyaert@uantwerpen.be*

Abstract. This paper presents a novel application of Statistical Entropy Analysis (SEA), based on Shannon's theorem, to quantify the complexity of polymers at the molecular level. In a case study of free radical-induced grafting (FRIG) of polybutadiene with styrene, we explore how SEA—an emerging concept in scientific fields related to the Circular Economy—can be extended to assess polymeric systems. By analysing entropy on five distinct molecular levels—including mixing complexity (involving additives), molecular weight distribution, and structural complexities (subconformation level) such as crosslinking, H-grafting, T-grafting, and chain building—our methodology offers a detailed assessment of polymer complexity. While the primary goal is to quantify the complexity of polymer systems, we also aim to explore the potential relationship between entropy and energy, specifically in terms of the energy required for polymer recycling. Primary data for this study was acquired through coupled-matrix Monte Carlo simulations. These simulations provided detailed characteristics on distributions for all polymer chains in the system, including the number of monomer units per chain, crosslinking and grafting data, and specific monomer distributions within T-grafts and H-grafts. At the mixing level, amounts and types of additives were estimated based on literature and expert input from the same research team. Preliminary results indicate an increase in entropy at all levels as the reaction progresses, with a distinct S-shaped curve observed at the subconformation level. This curve shows a surge in entropy during 20-30% conversion, corresponding to the peak of reaction kinetics and a rapid increase in polymer complexity. After this phase, entropy continues to increase, though at a slower rate, until the system reaches a steady state. By advancing SEA at the molecular level, this study contributes a new theoretical framework for understanding polymer behaviour, with potential implications for material recovery and energy optimization in polymer chemistry.

Keywords. Circular Economy, Polymer Science, Statistical Entropy, Sustainability Assessment.

A MATHEMATICAL MODEL FOR THE SIMULATION OF TWO-PHASE COMPRESSION IN THERMAL NON-EQUILIBRIUM

Nicolas Leclercq[1]*, Vincent Lemort[1]

[1] University of Liège, Thermodynamics Laboratory, Liège, Belgium

* *Corresponding Author:* n.leclercq@uliege.be

Abstract. When a pure refrigerant in a two-phase state undergoes a reduction of volume, the volume of the vapour phase is going to follow closely the total reduction of volume, while the liquid phase volume variation is negligible in comparison to this total reduction. This variation of vapour volume induces a rise in temperature, creating a thermal disequilibrium between the two phases, whereas the mechanical equilibrium is maintained. Heat transfer, condensation and evaporation are thereby going to occur between the two phases, leading to variations in pressure that are difficult to predict. In this paper, a mathematical model for simulating a two-phase compression (or expansion) assuming a thermal non-equilibrium is proposed. This model is intended to be used as a core model for the simulation of displacement compressors using deterministic modelling. The model is applied to a piston-cylinder setup simulating a simple variation of volume over time, as well as a resting phase allowing to reach a final state in both thermal and mechanical equilibrium. External heat transfers and leakages are considered in the equations but will be set at zero in the simulation. The simulated fluid is the refrigerant R1233zd(E). The results of this application are discussed in terms of work consumption and isentropic efficiency, showing that irreversibilities are unavoidable when working in thermal non-equilibrium.

Keywords. Two-phase compression, Thermal non-equilibrium, Mathematical model, Deterministic model.

Nomenclature

Q	Vapour quality (mass fraction) (-)
V	Volume (m³)
T	Temperature (K)
p	Pressure (Pa)
v	Specific volume (m³/kg)
u	Specific internal energy (J/kg)
h	Specific enthalpy (J/kg)
m	Mass (kg)
$\dot{Q}$	Heat transfer rate (W)
ṁ	Mass transfer rate (kg/s)
A	Area (m²)
U	Internal energy (J) / heat transfer coefficient (W/(m²K))

Special characters

θ	Angle (rad)
ω	Rotational speed (rad/s)
ε_{is}	Isentropic efficiency (-)
ρ	Density (kg/m³)
Φ̇	Energy transfer rate (W)
α	Vapour volume fraction or void fraction (-)

Subscripts and superscripts

g	Vapour phase
l	Liquid phase
ϕ	Any phase
cv	Control volume
σ	At saturation
$cond$	Condensation

1 Introduction

The deterministic modelling of compression and expansion processes is widely used to help understanding the behaviour of displacement machines. Such modelling technique is able to predict variation of temperature and pressure induced by the reduction/expansion of volume. Along with the prediction of internal leakages, heat transfer and mechanical losses, the performance of displacement machines can be accurately predicted with a limited number of empirical parameters.

Two-phase compression modelling can be used for several purposes:

- In oil-flooded compression/expansion considering the heat exchange between the liquid phase (mainly oil) and the vapour phase (refrigerant), in screw and scroll compressors [1], [2]
- In compression-resorption heat pumps using wet compression to improve the coefficient of performance, using twin-screw compressors [3], [4]
- In the modelling of liquid slugging, useful to predict the behaviour of compressors under the presence of liquid during cold start-up [5], [6], [7]

- In the compression/expansion of pure-refrigerant or oil-refrigerant mixture with low superheat, used, for instance, in the trilateral flash cycle using Lysholm turbine, single-screw expanders or in the regen-by-two cycle, using scroll compressors and expanders [1], [8], [9].

Amongst the cited authors, several assume a thermal equilibrium between the two phases for simplicity reasons ([2], [4], [5], [6], [8]). In [6], the two phases are modelled separately, but the evaporation rate is analytically determined to always reach the thermal equilibrium. As a pure fluid (R290) is being used, no concentration equation is applied. The thermodynamic variables used are the density and the temperature, but no information is provided regarding the equation of state. The authors of [2], [4] model a two-phase compression using mixtures (oil-refrigerant or ammonia-water), inducing the use of a concentration equation. Moreover, in both papers, the use of pressure, temperature and concentration as independent thermodynamic variables allows the calculation of the remaining properties. Finally, in [5], [8], an homogeneous phase is modelled using a pure fluid. The authors of [5] provide an analytical formula for the calculation of the variation rate of vapour quality with the shaft angle ($\mathrm{d}Q/\mathrm{d}\theta$). Thereby, it seems that the vapour quality and the temperature are used as thermodynamic variables to determine the state of the fluid. In [8], the two-phase density and a uniform temperature are used to determine the state of the fluid in a two-phase scroll compressor deterministic model.

On the other hand, several authors ([1], [3]) propose a thermal non-equilibrium modelling. A deterministic model applied to an oil refrigerant-mixture expansion using a single-screw expander is developed in [1]. This model uses a concentration equation for the oil content and uses the density and the temperature as independent thermodynamic variables for both liquid and vapour phases. Although it does not show how the condensation/evaporation effect of the refrigerant can be figured out, it constitutes a base for the mathematical developments shown in this article. In [3], the author developed a two-phase compression model for a twin-screw compressor used in compression-resorption heat pumps, using the pressure, temperature and sorbent concentration as independent thermodynamic variables with the Ziegler-Trepp equation of state (EoS).

In this paper, a model similar to the expansion model of [1] is developed. The equations are solved to calculate the specific volume and temperature variation rates of both phases with the shaft angle of the displacement machine. The model takes into account the non-equilibrium between the two phases, considering the mass and heat exchanges between them. The interactions between the two phases are thoroughly described, in the case of the compression as well as an expansion. The equations are applied to a simple piston-cylinder setup filled with a saturated liquid-vapour R1233zd(E) mixture. The volume contained in the piston-cylinder setup is decreased at a fixed rate, until reaching a constant value where the system can rest until the thermal equilibrium is re-established. The evolution of pressure inside the cylinder is tracked, as well as the temperatures and masses of the liquid and vapour phases. The external heat transfer and leakages are taken into account in the equations; however, they will be neglected in the piston-cylinder application. The model developed in the paper constitute a base for a scroll compressor deterministic model, intended to be validated by the authors using experimental data from [10].

2 Mathematical model

The mathematical model is split into 3 parts: the interface interactions, the mass conservations equations and the energy conservation equations. The objective is to obtain the variation of pressure, under a variation of volume in which the two-phase fluid is initially at rest, in thermal and mechanical equilibrium. For the sake of simplicity, since the model is intended for use as a compressor deterministic model, the derivatives will be expressed in terms of shaft angle variation (θ), and the speed of the compressor is given by the variable ω (in rad/s). As already stated, the two independent thermodynamic variables used to define the properties of both phases are the temperature and the density. Those variables are used along with the Helmhotz equation of state to determine other thermophysical properties such as the pressure, enthalpy and entropy. The variation of volume of the liquid phase with regards to the pressure being negligible, the pressure of the control volume is going to be set based on the vapour phase properties. To decrease the computational time of the model, the abstract state module of CoolProp has been used to compute the thermophysical properties.

A representation of the studied control volume can be found in Figure 1. The control volume is subject to a volume variation rate $\mathrm{d}V_{CV}/\mathrm{d}\theta$ distributed into volume variations of the vapour and liquid phases, $\mathrm{d}V_g/\mathrm{d}\theta$ and $\mathrm{d}V_l/\mathrm{d}\theta$, respectively. The computations of the temperature and specific volume of both

phases along the variation of volume with the shaft angle are computed using the backward Euler method, where the specific volume is converted into the density for the equation of state afterward:

$$T_\phi^k(\theta) = T_\phi^{k-1}(\theta) + \frac{\mathrm{d}T_\phi}{\mathrm{d}\theta}\mathrm{d}\theta \quad (1)$$

$$v_\phi^k(\theta) = v_\phi^{k-1}(\theta) + \frac{\mathrm{d}v_\phi}{\mathrm{d}\theta}\mathrm{d}\theta \quad (2)$$

Where ϕ stands for the liquid or vapour phase and $\mathrm{d}\theta$ is the shaft angle step used. The mass and energy conservation equations will thereby help in determining $\mathrm{dT_\phi/d\theta}$ and $\mathrm{dv_\phi/d\theta}$, for both phases.

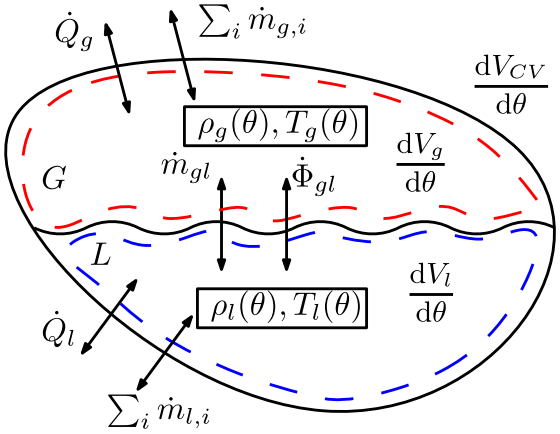


Figure 1: Definition of the control volume and the interactions with its environment.

2.1 Interface interactions

A pure fluid in a two-phase state, respecting thermal and mechanical equilibrium, can be seen as an heterogeneous mixture of a saturated vapour and saturated liquid, in given proportion, quantified by a mass fraction called the vapour quality, defined as:

$$\mathrm{Q} = m_g/(m_l + m_g) \quad (3)$$

Where g stands for the vapour phase and l for the liquid phase.

When such a fluid in two-phase state undergoes a decrease of volume, with neither external and internal heat transfer nor mass transfer, the density of the vapour phase is going to increase as well as its temperature, inducing a rise in pressure. Regarding the liquid phase, its change in temperature and in volume is negligible under the effect of the pressure only, creating a thermal non-equilibrium between the two phases, while the mechanical equilibrium is maintained all along the compression. The liquid phase therefore becomes a subcooled liquid phase, due to the rise of pressure at constant temperature. Depending on the shape of the vapour saturation curve, increasing the pressure of the saturated vapour phase may or may not create condensation. Most refrigerants used being dry fluids, the rise of pressure of the saturated vapour phase is going to create a new liquid phase, at the vapour phase temperature, as illustrated in Figure 3. If the mass and heat transfer are considered between the two phases, the new liquid phase is going to mix with the original liquid phase, thereby increasing its temperature. The difference in temperature between the vapour and liquid phase is also resulting in condensation/evaporation between the two phases, thereby inducing a mass transfer. These two effects have a role in the change of volume and mass of both liquid and vapour phases, having a significant impact on the resulting pressure. The difficulties encountered in the modelling of those effects have been described in [9], where the two-phase expansion of pure refrigerant R134a in a Lysholm turbine is investigated. Several authors have modelled the interaction between the two phases in thermal non-equilibrium under some assumptions. In both [7], [11], the energy transfer rate from the liquid phase to the vapour phase (either by heat transfer or mass transfer) $\dot{\Phi}_{lg}$ and from the vapour phase to the liquid phase $\dot{\Phi}_{gl}$ are defined as:

$$\dot{\Phi}_{gl} = \dot{Q}_{gl} + \dot{m}_{gl}h_g \quad (4)$$

$$\dot{\Phi}_{lg} = \dot{Q}_{lg} + \dot{m}_{lg}h_l \quad (5)$$

Where $\dot{\mathrm{Q}}_{lg}$, $\dot{Q}_{gl}$ are the heat transfer rates and $\dot{m}_{gl}$, $\dot{\mathrm{m}}_{lg}$, the mass transfer rates. The interface between the vapour phase (G) and the liquid phase (L) can thereby be defined and the interactions are represented in Figure 2. This interface can be seen as an infinitely thin boundary between the two extended control volumes represented by the vapour and liquid phases. Therefore, the gradient of temperature that can appear between the two phase is not embedded inside the interface but in the extended control volumes boundaries, allowing to respect the temperature continuity though the control volumes boundaries and the interface.

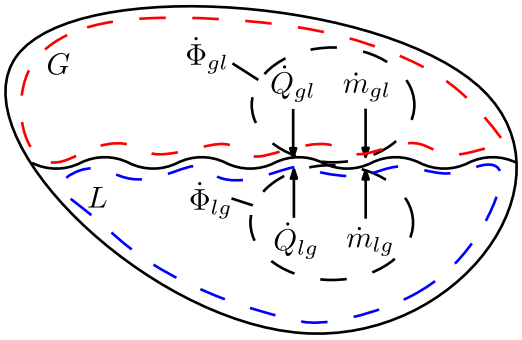


Figure 2: Interface interactions.

From the mass and energy conservation at the interface, the following equalities can be deduced:

$$\dot{m}_{gl} + \dot{m}_{lg} = 0 \tag{6}$$

$$\dot{\Phi}_{gl} + \dot{\Phi}_{lg} = 0 \tag{7}$$

The heat transfer rates toward the interface can be defined considering an interface at the saturation temperature from the pressure p, they can be written as[1]:

$$\dot{Q}_{gl} = AU_l \left(T_g - T^{\sigma}(p)\right) \tag{8}$$

$$\dot{Q}_{lg} = AU_g \left(T_l - T^{\sigma}(p)\right) \tag{9}$$

Where AU_l, AU_g are the heat transfer coefficients from the interface to the liquid phase and vapour phase, respectively. Isolating the mass flow rate from the vapour phase to the liquid phase $\dot{m}_{gl}$ from equations (4), (5), (6) and (7) gives:

$$\dot{m}_{gl} = \frac{-\left(\dot{Q}_{gl} + \dot{Q}_{lg}\right)}{\left(h_g - h_l\right)} = \frac{-\left(\dot{Q}_{gl} + \dot{Q}_{lg}\right)}{\Delta h^{SH} + \Delta h^{\sigma} + \Delta h^{SC}} \tag{10}$$

Where Δh^{SH} is the sensible heat of superheating (from the saturated vapour state reference), Δh^{SC} is the sensible heat of subcooling and Δh^{σ} is the latent heat. The problem identified with this definition is the fact that it does not take into account the partial evaporation (also called flash)/partial condensation coming from the compression of the saturated vapour phase/expansion of the saturated liquid phase as illustrated in the Figure 3. As previously explained, the compression of the saturated vapour present in the two-phase mixture results in the creation of a liquid phase at the temperature of the vapour phase, which is going to mix with the liquid phase and thereby change its temperature, resulting in a change of volume of the liquid phase. Depending on the initial vapour quality of the compression, this effect can be negligible, especially for low vapour qualities where the amount of liquid coming from the saturated vapour compression would be too small to affect significantly the liquid phase temperature. The same effect is observed during the expansion of a saturated liquid phase, which creates a vapour phase at the liquid phase temperature (see blue transformation in Figure 3). This partial evaporation is also called flashing.

Eventually, the mass transfer from the vapour phase to the liquid phase m^{σ}_{gl} and the mass transfer from the liquid phase to the vapour phase m^{σ}_{lg} can simply be defined as follows:

$$m^{\sigma}_{gl} = m_g \cdot \max\left(0, \frac{v^{\sigma}_g(p) - v_g}{v^{\sigma}_g(p) - v^{\sigma}_l(p)}\right) \tag{11}$$

$$m^{\sigma}_{lg} = m_l \cdot \max\left(0, \frac{v_l - v^{\sigma}_l(p)}{v^{\sigma}_g(p) - v^{\sigma}_l(p)}\right) \tag{12}$$

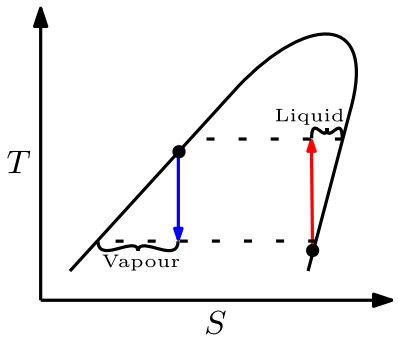


Figure 3: Saturated vapour compression in red, saturated liquid expansion in blue.

Where v is the specific volume and σ stands for the saturation properties. Finally, the corresponding energy transfer from one phase to the other can be defined as follows, where the enthalpy of vaporisation is considered inherently of the compression/expansion of the saturated phase.

[1] The notations AU_l and AU_g, to the authors perspective, could be switched in both equations. However, the adopted notation appears in this form in the literature.

$$\Phi_{gl}^{\sigma} = m_{gl}^{\sigma} \cdot h_{l}^{\sigma}(p) \quad (13)$$

$$\Phi_{lg}^{\sigma} = m_{lg}^{\sigma} \cdot h_{g}^{\sigma}(p) \quad (14)$$

2.2 Mass conservation equations

The total mass transfer rate condensed from the vapour phase to the liquid phase is defined as:

$$\frac{dm_{cond}}{d\theta} = \frac{1}{\omega}\dot{m}_{gl} + \frac{1}{d\theta}\left(m_{gl}^{\sigma} - m_{lg}^{\sigma}\right) \quad (15)$$

The mass conservation equations can simply be written considering the mass flow rates entering/leaving both phases and the interaction between them (condensation rate) that is represented by Equation (15):

$$\frac{dm_{g}}{d\theta} = \frac{1}{\omega}\left(\sum_{i}\dot{m}_{g,i} - \frac{dm_{cond}}{d\theta}\right) \quad (16)$$

$$\frac{dm_{l}}{d\theta} = \frac{1}{\omega}\left(\sum_{i}\dot{m}_{l,i} + \frac{dm_{cond}}{d\theta}\right) \quad (17)$$

The specific volume variation rates can then be defined with the following definition:

$$\frac{dv_{\phi}}{d\theta} = \frac{1}{m_{\phi}}\frac{dV_{\phi}}{d\theta} - \frac{V_{\phi}}{m_{\phi}^{2}}\frac{dm_{\phi}}{d\theta} \quad (18)$$

Where the volume variation rates of both phases can be linked together with the control volume variation rate:

$$\frac{dV_{g}}{d\theta} = \frac{dV_{CV}}{d\theta} - \frac{dV_{l}}{d\theta} \quad (19)$$

Finally, the derivative of the liquid volume $dV_l/d\theta$ can be conveniently expanded to explicit the dependency from the liquid phase temperature T_l, while neglecting the effect of pressure:

$$\frac{dV_{l}}{d\theta} = v_{l}\frac{dm_{l}}{d\theta} + m_{l}\frac{dv_{l}}{d\theta} \quad (20)$$

$$= v_{l}\frac{dm_{l}}{d\theta} + m_{l}\left(\frac{\partial v_{l}}{\partial T}\right)_{p}\frac{dT_{l}}{d\theta}$$

The whole system of equations is therefore dependant on the variation rate of the liquid phase temperature, that is going to be computed from the energy conservation equations.

2.3 Energy conservation equations

The conservation of energy is applied in the same way for both phases, with derivatives expressed relative to time first:

$$\frac{dU_{\phi}}{dt} = \sum_{i}\dot{m}_{\phi,i}\,h_{\phi,i} + \dot{W}_{\phi} + \dot{Q}_{\phi} \pm \dot{\Phi}_{cond} \quad (21)$$

Where U_ϕ is the internal energy of the phase represented by ϕ. The boundary work rate exchanged with the corresponding phase can be rewritten as:

$$\dot{W}_{\phi} = -p\frac{dV_{\phi}}{dt} \quad (22)$$

Regarding the condensation energy transferred rate, it comes from interface interactions and can be defined as:

$$\dot{\Phi}_{cond} = \dot{\Phi}_{gl} + \frac{\omega}{d\theta}\left[m_{gl}^{\sigma} \cdot h_{l}^{\sigma}(T_l) - m_{lg}^{\sigma} \cdot h_{g}^{\sigma}(T_g)\right] \quad (23)$$

This term is taken with a negative sign for the vapour phase and with a positive sign for the liquid phase, in the energy conservation equation. Equation (21) can be rewritten with derivatives relative to the shaft angle θ:

$$\frac{dU_{\phi}}{d\theta} = \frac{1}{\omega}\sum_{i}\dot{m}_{\phi,i}\,h_{\phi,i} - p\frac{dV_{\phi}}{d\theta} + \frac{1}{\omega}\dot{Q}_{\phi} \pm \frac{1}{\omega}\dot{\Phi}_{cond} \quad (24)$$

The left-hand term of Equation (24) can be reformulated using the mass and the specific internal energy of the corresponding phase:

$$\frac{dU_{\phi}}{d\theta} = \frac{d\left(m_{\phi}u_{\phi}\right)}{d\theta} = u_{\phi}\frac{dm_{\phi}}{d\theta} + m_{\phi}\frac{du_{\phi}}{d\theta} \quad (25)$$

Moreover, knowing that, derived from the Maxwell equations:

$$\left(\frac{\partial u_{\phi}}{\partial v}\right)_{T} = \left[T_{\phi}\left(\frac{\partial p}{\partial T}\right)_{v} - p\right] \quad (26)$$

The derivative $du_\phi/d\theta$ of Equation (25) can be expressed as follows:

$$\frac{du_{\phi}}{d\theta} = \left[\left(\frac{\partial u_{\phi}}{\partial T}\right)_{v}\frac{dT_{\phi}}{d\theta} + \left[T_{\phi}\left(\frac{\partial p}{\partial T}\right)_{v} - p\right]\frac{dv_{\phi}}{d\theta}\right] \quad (27)$$

By substituting the expression of $dv_\phi/d\theta$ from Equation (18), $dU_\phi/d\theta$ can be developed as follows:

$$\frac{\mathrm{d}U_\phi}{\mathrm{d}\theta} = u_\phi \frac{\mathrm{d}m_\phi}{\mathrm{d}\theta} + m_\phi \left(\frac{\partial u_\phi}{\partial \mathrm{T}}\right)_v \frac{\mathrm{d}T_\phi}{\mathrm{d}\theta} \quad (28)$$

$$+T_\phi \left(\frac{\partial p}{\partial T}\right)_v \frac{\mathrm{d}V_\phi}{\mathrm{d}\theta} - T_\phi \left(\frac{\partial p}{\partial T}\right)_v v_\phi \frac{\mathrm{d}m_\phi}{\mathrm{d}\theta}$$

$$-p\frac{\mathrm{d}V_\phi}{\mathrm{d}\theta} + pv_\phi \frac{\mathrm{d}m_\phi}{\mathrm{d}\theta}$$

Given the fact that $u_\phi + \mathrm{p}v_\phi = h_\phi$ and simplifying the term $-\mathrm{p}\mathrm{d}V_\phi/\mathrm{d}\theta$ is both Equation (24) and (28), the term in $\mathrm{d}T_\phi/\mathrm{d}\theta$ can be isolated, giving:

$$m_\phi \left(\frac{\partial u_\phi}{\partial T}\right)_v \frac{\mathrm{d}T_\phi}{\mathrm{d}\theta} = \frac{1}{\omega}\sum_i \dot{m}_{\phi,i}\, h_{\phi,i} + \frac{1}{\omega}\dot{Q}_\phi \quad (29)$$

$$\pm\frac{1}{\omega}\dot{\Phi}_{cond} - h_\phi \frac{\mathrm{d}m_\phi}{\mathrm{d}\theta}$$

$$-T_\phi \left(\frac{\partial \mathrm{p}}{\partial \mathrm{T}}\right)_v \left(\frac{\mathrm{d}V_\phi}{\mathrm{d}\theta} - v_\phi \frac{\mathrm{d}m_\phi}{\mathrm{d}\theta}\right)$$

For the liquid phase, the derivative of the volume can be substituted from Equation (20), isolating the term in $\mathrm{d}T_\mathrm{l}/\mathrm{d}\theta$ therefore gives:

$$m_l \frac{\mathrm{d}T_l}{\mathrm{d}\theta}\left[\left(\frac{\partial u_l}{\partial \mathrm{T}}\right)_v + T_l \left(\frac{\partial \mathrm{p}}{\partial T}\right)_v \left(\frac{\partial v_l}{\partial \mathrm{T}}\right)_\mathrm{p}\right] = \quad (30)$$

$$\frac{1}{\omega}\sum_i \dot{m}_{l,i}\, h_{\mathrm{l},i} + \frac{1}{\omega}\dot{Q}_l + \frac{1}{\omega}\dot{\Phi}_{cond} - h_l \frac{\mathrm{d}m_l}{\mathrm{d}\theta}$$

The derivative of the liquid phase temperature $\mathrm{d}T_l/\mathrm{d}\theta$ can therefore be calculated only based on the interface interactions, the external heat transfer and mass flow rates, and does not depend on the total volume reduction. The last term of Equation (30) takes into account the fact that if some liquid is added/removed at the same enthalpy as the liquid phase, its temperature is not going to change.

The vapour phase volume variation rate $\mathrm{d}V_g/\mathrm{d}\theta$ can now be computed from Equation (19). Isolating the term in $\mathrm{d}T_g/\mathrm{d}\theta$ gives, for the vapour phase:

$$\mathrm{m_g}\frac{\mathrm{dT_g}}{\mathrm{d}\theta}\left(\frac{\partial \mathrm{u_g}}{\partial \mathrm{T}}\right)_\mathrm{v} = \frac{1}{\omega}\sum_i \dot{m}_{\mathrm{g},i}\, h_{\mathrm{g},i} + \frac{1}{\omega}\dot{Q}_\mathrm{g} \quad (31)$$

$$-\frac{1}{\omega}\dot{\Phi}_{cond} - h_g \frac{\mathrm{d}m_g}{\mathrm{d}\theta}$$

$$-T_\mathrm{g}\left(\frac{\partial \mathrm{p}}{\partial \mathrm{T}}\right)_v \left(\frac{\mathrm{d}V_\mathrm{g}}{\mathrm{d}\theta} - v_\mathrm{g}\frac{\mathrm{d}m_\mathrm{g}}{\mathrm{d}\theta}\right)$$

Thus, the variation of the vapour phase temperature depends on the mass and heat transfers as well as the variation of its volume. Once again, the fourth left-hand term takes into account the mass exchange with the same enthalpy as the vapour phase, which would not change the temperature. The last term takes into account the variation of internal energy due to the change in specific volume, at a constant pressure.

Equations (30) and (31) requires the calculation of several derivatives, for instance, the derivative $\left(\partial \mathrm{u}_\phi/\,\partial \mathrm{T}\right)_\mathrm{v}$ can not always be replaced by the specific heat at constant volume, as sometimes, two-phase conditions can occur in one of the phase, leading to more internal energy balancing the phase change. These derivatives are therefore going to be directly calculated when those two-phase conditions are met, using a backward difference method for the vapour phase and a forward difference method for the liquid phase, to ensure the no-crossing of the saturation curves:

$$\left(\frac{\partial \mathrm{u_g}}{\partial \mathrm{T}}\right)_\mathrm{v} = \frac{\mathrm{u}(\mathrm{v_g}, \mathrm{T_g}) - \mathrm{u}(\mathrm{v_g}, \mathrm{T_g} - \mathrm{dT})}{\mathrm{dT}} \quad (32)$$

$$\left(\frac{\partial \mathrm{u}_l}{\partial \mathrm{T}}\right)_\mathrm{v} = \frac{\mathrm{u}(\mathrm{v}_l, \mathrm{T}_l + \mathrm{dT}) - \mathrm{u}(\mathrm{v}_l, \mathrm{T}_l)}{\mathrm{dT}} \quad (33)$$

Regarding the term $(\partial v_l/\,\partial \mathrm{T})_\mathrm{p}$, it must be computed as a function of the pressure and the temperature, i.e., subcooled conditions close to saturation must be ensured. To avoid property calculation error, a temperature shift $\Delta T = 1$ [K] is introduced, which does not significantly change the results of the derivative. The derivative is thereby calculated as:

$$\left(\frac{\partial v_l}{\partial \mathrm{T}}\right)_\mathrm{p} = \frac{\mathrm{v}(p, \mathrm{T_l} - \Delta T + \mathrm{dT}) - \mathrm{v}(\mathrm{p}, \mathrm{T_l} - \Delta T - \mathrm{dT})}{2\mathrm{dT}} \quad (34)$$

Finally, the derivative $(\partial \mathrm{p}/\,\partial \mathrm{T})_v$ is calculated similarly for a subcooled and superheated state, where a shift is introduced to ensure being in the single-phase region:

$$\left(\frac{\partial p}{\partial \mathrm{T}}\right)_\mathrm{v} = \frac{\mathrm{p}(\rho_\phi, \mathrm{T}_\phi + \Delta T + \mathrm{dT}) - \mathrm{p}(\rho_\phi, \mathrm{T}_\phi + \Delta T - \mathrm{dT})}{2\mathrm{dT}} \quad (35)$$

The remaining derivative to be calculated is $(\partial \mathrm{p}/\,\partial \mathrm{T})_v$ in the two-phase region, which can be done using the Clapeyron equation:

$$\left(\frac{\partial \mathrm{p}}{\partial \mathrm{T}}\right)_\mathrm{v} = \frac{h_g^\sigma(p) - h_l^\sigma(p)}{T_\phi\left(v_g^\sigma(p) - v_l^\sigma(p)\right)} \quad (36)$$

2.4 Summary

Eventually, the system of equation can be solved step by step to obtain the four derivates required to obtain the updated state after an angle step. As a reminder, those four derivatives are $dv_g/d\theta$, $dv_l/d\theta$, $dT_g/d\theta$ and $dT_l/d\theta$. First, the derivatives from Equations (32), (33), (34), (35) and (36) should be calculated using the previous state of temperature and density. The interface interactions should then be defined, using the heat transfer coefficients from the interface

Table 1: Initial state before the compression.

V_i[cm³]	Q_i[-]	α_i[-]	P_i[Pa]	T_i[K]
80	0.4	0.9889	$1.5 \cdot 10^5$	302.2

to the liquid phase U_l and to the vapour phase U_g in order to obtain the condensation mass flow rate $dm_{cond}/d\theta$ and condensation energy transfer rate Φ_{cond}, from Equations (15) and (23). Then, the mass derivatives of both phases can be calculated using the mass conservation Equations (16) and (17). Afterwards, using the mass flow rate and heat transfer rate of the liquid phase (as the pressure effect is neglected), $dT_l/d\theta$ can be calculated, using Equation (30). The latter term allows to define the variation of volume of the vapour phase $dV_g/d\theta$ via Equations (20) and (19) and, therefore, the derivatives $dv_g/d\theta$, $dv_l/d\theta$ using Equation (18). Finally, Equation (31) can be used to obtain $dT_g/d\theta$ and the backward Euler method of Equations (1) and (2) can be used to obtain the next temperature and specific volume of both phases.

3 Results and discussion

In this section, the two-phase compression model is going to be applied to a simple piston-cylinder setup represented in Figure 4.

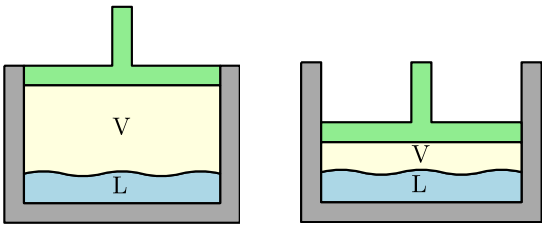


Figure 4: Piston-cylinder setup to simulate a two-phase compression, initial state on left and final state on right.

The two-phase compression with given initial conditions is going to be thoroughly analysed using pressure-enthalpy and temperature-entropy diagram. Then, the energy consumption of the compression is going to be calculated and an isentropic efficiency defined. In this application, pure refrigerant R1233zd(E) in a two-phase state is going to be compressed, and the state evolution of the two phases analysed along the compression. The volume defined by the piston-cylinder setup is going to be decreased linearly with a rate similar to what can be observed in a scroll compressor running at a speed of 2000 RPM, with a volume ratio of 5 reached after approximately 0.01 second. Then the system is going to be left at rest until the thermal equilibrium is reached again. The initial state can be found in Table 1, where Q_i stands for the initial vapour quality in mass fraction while α_i is the volume fraction or so-called void fraction.

In this simulation, heat transfer coefficients from the phases to the interface U_Φ have been randomly fixed at 70000 W/(m²K) and the area A is simply taken as being the cylinder cross-section area.

The variation of the temperatures of both phases as well as the pressure ratio over time can be found in Figure 5. Point 1 corresponds to the initial state, point 2 to the state right after volume reduction and point $2''$ after the resting period, after which the thermal equilibrium is reached again.

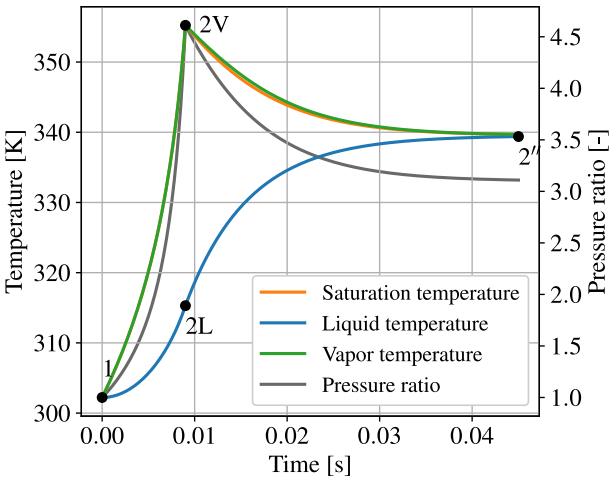


Figure 5: Evolution of the temperatures of both phases and evolution of the pressure ratio with time.

The pressure ratio reaches its maximum just after the reduction of volume and the same holds for the vapour phase temperature. Regarding the liquid phase temperature, due to the high heat transfer coefficients used, it follows closely the vapour phase temperature, allowing to re-establish the equilibrium after a resting period of less than 0.05 second. During

the resting period, the pressure decreases due to condensation decreasing the vapour phase density, generating an expansion with an increasing volume but a decreasing mass, inducing a reduction in the vapour phase density.

The pressure-enthalpy and temperature-entropy diagrams of the transformation can be found in Figure 6 and Figure 7.

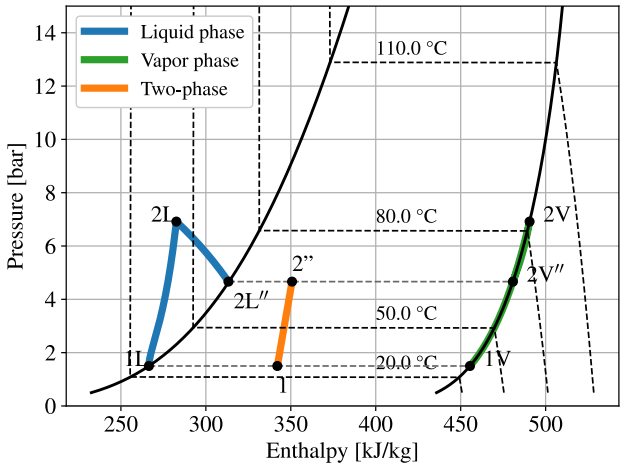


Figure 6: Pressure-enthalpy diagram of the two-phase compression.

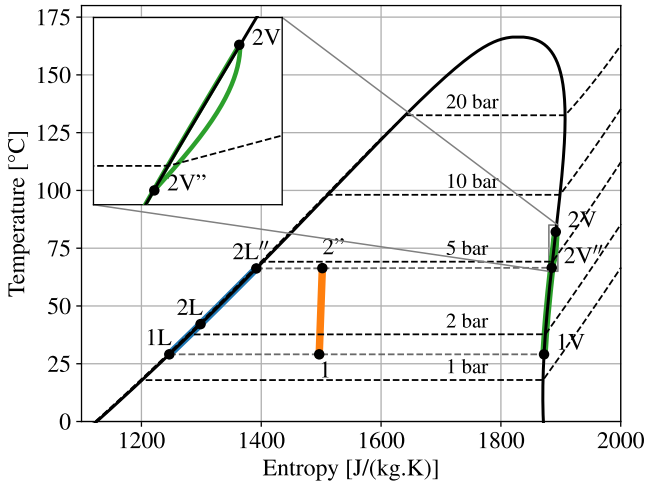


Figure 7: Temperature-entropy diagram of the two-phase compression.

The observation of those two diagrams allows a deep understanding of what is occurring along the compression in both phases. The first observation that can be made is the fact that the vapour phase follows the vapour saturation line during the compression, while the liquid phase becomes subcooled due to the rise of pressure. During the resting period, the saturated vapour becomes superheated due to the expansion (decrease in density) generated by the condensation between the two phases. Therefore, a pseudo-state, where a superheated phase is mixed with a subcooled phase is met during the resting phase, until the equilibrium is re-established, allowing to reach back two saturated phases at the same temperature.

The energy consumption of the compression can be calculated in two different ways, calculating both terms of the energy conservation equation applied to the studied case (no heat exchange considered):

$$\Delta U = W_{cp} \tag{37}$$

Calculating the results from both side of the equation allows checking the consistency of the model. The right-hand side of the equation gives:

$$\Delta U = \frac{m_g}{m_{cv}} u_g(\rho_g, T_g) + \frac{m_l}{m_{cv}} u_l(\rho_l, T_l) - m_{cv} u(Q_i, T_i) = 18.66 \text{ [J]} \tag{38}$$

While the left-hand side can be calculated as:

$$W_{cp} = -\int_{V_i}^{V_f} p dV = 18.82 \text{ [J]} \tag{39}$$

The difference between the two values can be explained by the numerical errors introduced by the Euler backward method.

Finally, the isentropic efficiency of the process can be calculated, using the definition hereunder. The definition is only valid when the thermal equilibrium is reached (same temperature for both phases), which is respected in this case.

$$\varepsilon_{is} = \frac{m_{cv} \Delta u_{is}}{\Delta U} = 86.45 \text{ [\%]} \tag{40}$$

Which means that, even without external heat transfer, nor leakage, nor friction introduced, a two-phase compression creates irreversibilities due to the heat transfer between the two phases. If the heat transfer coefficients U_ϕ were higher, the difference between the phases temperatures would be lower, resulting in a higher isentropic efficiency. A complete analysis of the evolution of this isentropic efficiency under various conditions will be part future works from the authors.

4 Conclusions

In this work, a two-phase compression (and expansion) mathematical model with thermal non-equilibrium has been introduced. The model takes as inputs heat transfer, mass transfer and the control volume evolution with a fictitious shaft angle and gives as outputs the thermodynamic properties evolutions of the two phases. The interface interaction along the control volume reduction allows to determine the evolution rate of the specific volumes as well as the temperatures of both phases a by applying mass and energy balance equations.

Moreover, the simulation of a simple piston-cylinder setup is analysed, showing how, under specific initial conditions and heat transfer coefficients at the interface, the temperature of both phases evolve as well as the pressure, even when the system is left at rest. Finally, an isentropic efficiency is introduced, showing that irreversibilities are unavoidable when compressing two-phase fluid.

Acknowledgement

The project source of the results presented in this paper has received funding from the European Union's Horizon 2020 research and innovation programme under grant agreement N° 851541.

References

[1] D. Ziviani, 'Theoretical and Experimental Characterization of Single-Screw Expanders for ORC Applications', Universiteit Gent, Gent, 2017.

[2] I. H. Bell, V. Lemort, E. A. Groll, J. E. Braun, G. B. King, and W. T. Horton, 'Liquid-flooded compression and expansion in scroll machines - Part I: Model development', *International Journal of Refrigeration*, vol. 35, no. 7, pp. 1878–1889, Nov. 2012, doi: 10.1016/j.ijrefrig.2012.07.010.

[3] D. Zaytsev, 'Development of Wet Compressor for Application in Compression-Resorption Heat Pumps', University of Delft, Delft, 2003.

[4] V. Gudjonsdottir, C. A. Infante Ferreira, and A. Goethals, 'Wet compression model for entropy production minimization', *Appl Therm Eng*, vol. 149, pp. 439–447, Feb. 2019, doi: 10.1016/j.applthermaleng.2018.12.065.

[5] Z. Liu and W. Soedel, 'A mathematical model for simulating liquid and vapor two-phase compression processes and investigating slugging problems in compressors', *HVAC and R Research*, vol. 1, no. 2, pp. 99–109, 1995, doi: 10.1080/10789669.1995.10391312.

[6] J. Lin, N. Guo, L. Hong, J. Wu, J. Jiang, and T. Zhao, 'Simulation of single and two-phase refrigerant compression in rotary compressors', *Appl Therm Eng*, vol. 211, Jul. 2022, doi: 10.1016/j.applthermaleng.2022.118465.

[7] N. Guo, J. Lin, and J. Wu, 'Simulation on two-phase refrigerant compression in the cylinder of rotary compressors using CFD method', *Sci Rep*, vol. 14, no. 1, Dec. 2024, doi: 10.1038/s41598-024-56856-y.

[8] N. Leclercq and V. Lemort, 'Modeling and Simulation of a Two-phase Scroll Compressor', in *International Compressor Engineering Conference*, International Compressor Engineering Conference 2022, 2022. [Online]. Available: https://docs.lib.purdue.edu/icec

[9] H. Öhman and P. Lundqvist, 'Experimental investigation of a Lysholm Turbine operating with superheated, saturated and 2-phase inlet conditions', in *Applied Thermal Engineering*, 2013, pp. 1211–1218. doi: 10.1016/j.applthermaleng.2012.08.035.

[10] N. Leclercq, B. G. Bederna, and V. Lemort, 'Experimental Testing of a Scroll Compressor with Two-Phase Refrigerant Flows', in *13th International Conference on Compressors and Their Systems*, Springer, 2024, pp. 239–250. doi: 10.1007/978-3-031-42663-6_19.

[11] R. Revellin, S. Lips, P. Neveu, and J. Bonjour, 'A comprehensive non-equilibrium thermodynamic analysis applied to a vapor-liquid two-phase flow of a pure fluid', *International Journal of Multiphase Flow*, vol. 42, pp. 184–193, Jun. 2012, doi: 10.1016/j.ijmultiphaseflow.2012.02.008.

A HIGH FIDELITY NUMERICAL INVESTIGATION OF OVER-DESIGN LOAD ACCEPTANCE IN A FRANCIS TURBINE

Faiz Azhar Masoodi[1*], Rahul Goyal[1]

[1] Department of Energy Science and Engineering, IIT Delhi, New Delhi-110016, India

** Corresponding Author: faiz.azhar.masoodi@iitd.ac.in*

Abstract. An impediment in realizing the operational flexibility of hydraulic turbines is the development of hydrodynamic instabilities under off-design operation. In particular, the vortex breakdown phenomenon encountered in the draft tube leads to a complete disruption of velocity field and development of pressure fluctuations, thereby compromising efficiency and health of the machine. This work encapsulates a high-fidelity simulation of a load acceptance procedure involving development of vortex breakdown during transition from the best efficiency point (BEP) to high load (HL) in a model Francis turbine. A simultaneous rotation of guide vanes and runner during the load change is achieved using the dynamic meshing capability of OpenFOAM v2012 software. The mesh near the guide vane region is optimally morphed to ensure acceptable quality as the guide vanes rotate to effect the load change. A hybrid model capable of resolving large scales of unsteady flow is used to achieve turbulence closure. The simulation is performed using 320 cores of a high performance computer. Dilation of the vortex core is seen with a central stagnation of axial flow within it. Intermittent axial flow reversals are seen within the stagnation region. The centrally stagnant flow is enveloped by a fast axial outflow which decelerates toward the wall. Steep radial gradients of axial velocity are seen at the interface of stagnation region and surrounding outflow, indicating strong shearing. The vortex core is visualized using the iso-surface of $\lambda 2$. Short time Fourier transforms are used to analyze the pressure fluctuations.

Keywords. Building stock, Low temperature district heating network, Building simulation.

BUILDING INTEGRATED CARBON CAPTURE

Jacques Gilbert de Cauwer[1]*, Salar Fakhraddinfakhriazar[1]
Grégoire Léonard[1], Vincent Lemort[1]
[1] University of Liège, Chemical Engineering, Liège, Belgium
* *Corresponding Author: jgilbert@uliege.be*

Poster Abstract. The great question regarding the renewable energy transition revolves around how to accelerate and successfully implement the shift from traditional, fossil-fuel-based energy sources to renewable and sustainable alternatives. This transition is crucial for addressing climate change, reducing environmental impact, and ensuring a more sustainable future. Energy has been crucial for human welfare, yet the reliance on finite fossil resources raises concerns. The disproportionate energy consumption, coupled with plants' inadequate capacity to recycle emitted CO_2, contributes to its rising atmospheric concentrations and climate changes. Consequently, a global challenge emerges, where affluent populations must reduce/change their energy consumption while impoverished regions strive for increased access. In this context, developing new technologies that could mimic nature's photosynthesis process to convert CO_2 into hydrocarbon is pertinent. At our latitude, since the availability of the sun's energy is modulated by seasons, it is desirable to develop new processes akin to nature that could transform this energy in summer and store it for wintertime. CO_2 can be captured at a point of emission, like in flue gases, or it can be captured directly in air (Direct Air Capture: DAC). The DAC option is challenging, as the CO_2 concentration is rather small. Therefore, buildings equipped with large ventilation systems can be an option to integrate a DAC technology. There are two research objectives for this project. The first one is to design an "air contactor" functionalized to capture carbon dioxide. This part is focused on the synthesis of materials that can develop a very high surface area and have a minimum impact on the ventilation air stream. The second part is to study the integration of the DAC system within the technical systems of the building. Since the DAC system will require energy to function, it is the objective of this project to study its different interactions/synergies between the HVAC system and the PV electricity production. In this context, Dymola/Modelica™ will be used to simulate dynamically the interactions between the different systems. The carbon capture potential on a typical commercial building is rather small when compared with point source capture on industrial emissions. However, the number of buildings where a DAC system could be installed can be counted in millions in the EU only. Another interesting point to consider is the fact that a local DAC system can probably fit well with the distributed PV energy production found in most buildings. Finally, reducing the carbon footprint of buildings is one of our policy objectives, as the buildings sector accounts for around a third of our carbon emissions.

Keywords. Carbon dioxide, DAC, Building, Dynamic simulation

References

[1] Philippe Couty, "First solar hydrogen storage in a private building in western Switzerland: building energy analysis and schematic design", CISBAT 2019, Journal of Physics: Conference Series.
[2] Fahad Ben Salamah, "Building-Integrated Carbon Capture: A Study on the Design and Potential of Carbon Emission Offsets from Buildings", PhD Thesis, Arizona State University.

NUMERICAL MODELING OF WET AND TWO-PHASE COMPRESSION/EXPANSION IN PISTON MACHINES

Lucas Leon[1]

[1] ENSAM – SARUS, France

* *Corresponding Author: lucas.leon@ensam.eu*

Abstract. This research aims to optimize piston expansion and compression machines developed by the French company SARUS. These machines are designed to improve the energy efficiency of industrial processes, such as the recovery of waste heat from gas networks, gas liquefaction, the recovery of industrial waste heat via heat pumps, and the enhancement of refrigeration cycles. The novel architecture of the developed machines, the presence of fluids in a two-phase state, and pulsating phenomena require a local-scale study of flows, leading to the development of a CFD (Computational Fluid Dynamics) model. Numerical modeling reduces the need for experimental campaigns, though it should not entirely replace them. Indeed, experimental measurements are essential to validate the results of CFD models, and the company will provide them, such as pressure measurements in the pipes and cylinder, and flow rates in the pipes at the machine outlets. This study will contribute to optimizing the machines under development.

The CFD models will lead to a better understanding of the thermodynamic behavior of the machine and the flow within the cylinder, before proceeding to the development of a reduced-order model (0D, 1D) integrated into the MODELICA language.

The complexity of two-phase flows arises from the need to consider interactions and exchanges between phases, which can involve mass, momentum, and energy, making their simulation even more complex. A primary challenge of this work is to establish a model that accurately accounts for all the physical phenomena at play. The movement of mechanical components also requires the use of dynamic meshing. Additionally, some of the company's projects require consideration of pulsating phenomena within the systems, caused by significant pressure variations in the pipes near the expansion machines, which reduce their efficiency. The combination of all these elements characterizes the originality of this research topic.

Keywords. Fluid Mechanics, CFD, Multiphase flows, Expanders.

Part II

Heating, Ventilation, Air-Conditioning and Refrigeration

THERMODYNAMIC ANALYSIS AND SUSTAINABILITY: EVALUATION OF INNOVATIVE MIXTURES FOR HEAT PUMP CYCLES

G. Vaccaro[1], P. Santoni[1], A. Milazzo[1], A. Rocchetti[1], L. Talluri[1]*

[1] Università degli Studi di Firenze, Department of Industrial Engineering, Florence, Italy

* *Corresponding Author: lorenzo.talluri@unifi.it*

Abstract. The impact of heat pumps on climate change is closely tied to the choice of working fluid. Refrigerant fluids, currently state-of-the-art for this technology, predominantly consist of synthetic hydrofluorocarbons (HFCs) with a high global warming potential, making them environmentally unsustainable if released into the atmosphere.

HFCs, engineered for maximum performance in heat pumps, pose environmental concerns due to their high global warming potential. Transitioning to more sustainable fluids is expected to result in a lower COP. However, the need for an alternative working fluid also provides an opportunity to explore new technological configurations and perspectives.

One significant challenge in heat pumps is the heat exchange irreversibility occurring in evaporators and condensers, which leads to impactful losses. Typically, heat pumps operate between fluids that do not undergo a phase change, thus having a finite heat capacity.

This paper proposes a thermodynamic analysis of a simple heat pump cycle to assess mixtures of CO_2 and various organic substances as potential working fluids. The cycle incorporates an internal heat exchanger and is designed to warm a finite heat capacity flow on the hot side, covering transcritical conditions. The optimization of composition and fundamental parameters, including COP, heating capacity, and gas cooler pressure, is performed for each mixture, with comparisons made to the base CO_2 cycle. Two case studies are considered in order to have insights on the optimal working conditions for CO_2 mixtures.

Keywords. Heat pump, CO_2, Mixtures, Sustainability, Thermodynamic.

Nomenclature (if relevant)

COP	Coefficient of Performance
DH	District Heating
DME	Dimethyl Ether
GSHP	Ground source Heat Pump
HFC	Hydrofluorocarbons
HFO	Hydro-fluoro olefins
HTHP	High Temperature Heat Pump
IHX	Internal Heat Exchanger
ODP	Ozone Depletion Potential
P	Pressure (bar
T	Temperature (°C) – (K)

Special characters

η	Efficiency (-)

Subscripts

cr	critical
gc	gas cooler

1 Introduction

The transition toward a sustainable energy future, pursued by many countries, demands the decarbonisation of energy-intensive sectors like heating and cooling, which represents about 50% of energy consumption in Europe [1]. Heat pumps, especially with the expanding production of renewable energy, serve as a significant resource for this energy transition. In recent years, there has been growing interest in researching and developing heat

pumps that utilize fluids with low Ozone Depletion Potential (ODP) and Global Warming Potential (GWP) to mitigate environmental impact. CO_2, readily available, non-flammable, and possessing minimal GWP, holds appeal in these applications. However, CO_2's low critical temperature (31°C) presents a challenge for cycle efficiency, necessitating transcritical operation, especially in warmer environments. In a transcritical cycle, CO_2 displays a variable temperature within the gas-cooler, facilitating better temperature profile matching. Yet, operating under transcritical conditions entails high pressures at the gas-cooler, demanding careful configuration and material selection, thereby increasing system costs. To address these challenges, solutions like internal heat exchangers (IHX), parallel compressors, ejectors, or dedicated mechanical sub cooling systems have been proposed.

A potential solution to enable sub-critical operation and enhance COP involves using CO_2-based mixtures: by adding refrigerants, hydrocarbons or other natural fluids to carbon dioxide in small concentrations to yield non-flammable mixtures with low GWP. The growing number of scientific publications on "CO_2 mixtures heat pumps and refrigeration cycles" underscores rising interest in CO_2-based mixtures. Table 1 resume the latest publications on this topic.

Table 1: Recent works on CO_2 mixtures heat pumps and refrigeration cycles.

Reference	Mixture	Notes
Bouteiller P., et al., 2017 [2]	CO_2/ R1234yf CO_2/Propane	The aim is to use CO_2 mixtures containing propane and R1234yf in a heat pump to elevate the mixture's critical temperature.
Tobaly et al., 2018 [3]	CO_2/Propane	Research into CO_2 mixtures for refrigeration or air conditioning in hot climates reveals consistent reductions in operating pressure. Additionally, under certain conditions, there is a potential increase in COP by up to 20%.
Sun et al., 2019 [4]	CO_2/R32	Experimental studies have examined CO_2 and R32 mixtures in a water-to-water heat pump. Results indicate that at a CO_2 mass fraction of 0.6, the heating COP is boosted by 23.3%.
Yu et al., 2019 [5]	CO_2/R41	Various mixtures of CO_2 and R41 were tested on an experimental heating/cooling system designed for automotive air conditioning.
Wang et al., 2021 [6]	CO_2/R32	A mixture of CO_2 and R32 could potentially avoid the challenges encountered in efforts to enhance the efficiency of CO_2 systems.
Li et al., 2022 [7]	CO_2/R32 CO_2/R41 CO_2/R1234yf CO_2/R152a	A thermodynamic analysis, considering an external temperature ranging from -20°C to 10°C. Highest COP reached with the CO_2/R32 mixture.
Liu et al., 2022 [8]	Combination of R744, R41, R170, RE170, R600a, R1234yf, R1234ze, R290	Evaluation of the performance of air heat pumps for heating domestic hot water, using fifteen binary zeotropic mixtures. The maximum COP achieved is 4.17, attained by the CO_2/DME mixture at a ratio of 30/70%.
Luo et al., 2022 [9]	CO_2/R600a	Experimental study of an air-to-water heat pump with CO_2/R600a as the working fluid. An external air temperature ranging from -30°C to 0°C was considered, with the water being heated from 50°C to 75°C.
Ganesan et al., 2023a [10]	CO_2/butane CO_2/pentane	Analysis of a cascade heat pump system for producing hot water at temperatures higher than 100°C (HTHP). The system configuration comprises two cascading cycles: Low Stage (LS) and High Stage (HS). CO_2/butane mixtures were considered in the LS cycle and CO_2/pentane mixtures in the HS cycle, with varying concentrations of CO_2 (2, 4, 6, 8%).

Ganesan et al., 2023b [11]	CO_2/butane CO_2/pentane	Analysis focuses on a cascade heat pump employing two CO_2-based mixtures: CO_2/butane in the LS cycle and CO_2/pentane in the HS cycle, with varying CO_2 concentrations of 5, 10, 15, and 20%.
Mazer et al., 2023 [12]	CO_2+ R32/R290/R1234yf/R410a	Three different heat pump configurations designed for residential space heating and hot water production. The highest COP attained reaches 6.
Vaccaro et al., 2023 [13]	CO_2/R1234yf CO_2/R1233zd(E) CO_2/R1234ze(E) CO_2/n-pentane CO_2/propane CO_2/iso-butane CO_2/DME	The study explores the impact of adding a second element in CO_2 transcritical cycles, examining various configurations from the base refrigeration cycle to the double evaporator ejector cycle. Results indicate that all investigated mixtures exhibit improved COP compared to pure CO_2.
Sicco et al., 2024 [14]	CO_2/R152a	Experimental work on a mixture of CO_2 and R152a, showing that a maximum COP improvement of 11.6% with a mixture featuring a 5% of R152a.
Vaccaro et al., 2024 [15]	CO_2/propane CO_2/iso-butane CO_2/propylene CO_2/DME	Adding CO_2 with 8% of DME gives a COP increase of 25%, but the mixture is non-flammable. Therefore, this mixture would represent a safe option, combining the advantages of CO_2 (low GWP, high VHC) with good energy efficiency

As evidenced by the literature review, there seems to be a lack of insights into selecting optimal CO_2 mixtures for high-temperature heat pumps. This gap arises from various factors that need consideration, such as flammability, sustainability, economic feasibility, and thermodynamic performance. Therefore, the aim of this paper is to shed light on the selection process of the suitable secondary fluid in the mixtures, with a focus on two case studies.

2 METHODOLOGY

2.1 Fluid selection

In this study, 8 working fluids were considered as the secondary component of CO_2-based mixtures for heat pump cycles: R152a, R1233zd(E), R1234ze(E), n-pentane, propane, propylene, isobutane, and dimethyl ether. R152a, R1233zd(E), and R1234ze(E) were chosen as representatives of well-known hydrofluorocarbons and hydro-fluoro olefins with low Global Warming Potential (GWP). N-pentane, propane, propylene, and isobutane were selected as reference hydrocarbons, while dimethyl ether served as a reference for the alcohol category. All chosen fluids exhibit favourable environmental characteristics (zero Ozone Depletion Potential, low GWP, low toxicity) and significantly lower critical pressures compared to CO_2, as summarized in Table 2. HFCs and HFOs have low flammability levels, whereas hydrocarbons and dimethyl ether are highly flammable. However, when the percentage of secondary fluids in the mixture is small, the resulting mixtures often fall into the category of non-flammable or mildly flammable [15].

Table 2: Main characteristics of assessed fluids [16], [17].

Fluid	**T_{cr} [C]**	**P_{cr} [bar]**	**GWP**	**NBP [K]**	**ASHRAE safety classification**
R152a	113.26	40.8	124	249.1	A2L
R1233zd(E)	165.6	35.7	1	291.4	A1
R1234ze(E)	109.4	36.3	7	254.2	A2L
N-pentane	196.5	33.6	5	309.2	A3
Propane	96.7	42.5	3.3	231.0	A3
Propylene	91.06	45.55	2	225.4	A3
Isobutane	134.7	36.4	3	261.4	A3
Dimethyl ether	127.2	53.67	1	248.4	A3

CO_2	30.98	73.77	1	194.7[1]	A1

2.2 System configuration

Two configurations of the Heat Pump cycle (the base cycle consisting of a compressor, gas cooler, valve, and evaporator, and the cycle incorporating an IHX, Figure 1) were simulated to evaluate the benefits and drawbacks of CO_2-based mixture solutions in enhancing CO_2 heat pump systems.

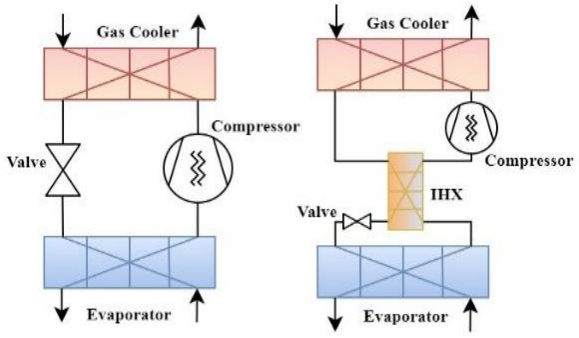


Figure 1: a) Base Configuration Cycle, b) Cycle with IHX.

A fixed compressor isentropic efficiency of $\eta = 0.7$ was assumed across all configurations. Other fixed parameters are detailed in Table 3 and vary according to the two case studies. The first case study, derived from Piemonte, 2019 [18], involves a Ground Source Heat Pump linked to a District Heating Network. Conversely, the second case study, outlined in Pellegrini et al., 2023 [19], features a High-temperature Heat Pump that raises the recuperated heat from a paper industry process and delivers it at a temperature of 120°C.

Table 3: Main variable assumption for all assessed cycles.

Parameter	GSHP for DHN	HTHP for Paper Industry
Hot fluid outlet temperature	90	120
Hot fluid inlet temperature	65	80
Internal Heat exchanger efficiency	0.8	0.8
Pinch point temperature at gas cooler	2	2
Pinch point temperature at evaporator	2	2
Cold fluid outlet temperature	7.6	25
Cold fluid inlet temperature	15	39

The working cycles are solved numerically by employing locally evaluated real fluid properties. All simulations were conducted using Python Software integrated with the NIST Refprop fluid library release 10 [16]. This method is deemed the most reliable for assessing the thermodynamic properties of CO_2-based mixtures [20]. The primary assumptions include heat pump cycles operating under steady-state conditions, negligible kinetic and potential energies, and negligible pressure losses in cycle components and piping.

3 RESULTS

In both case studies, fluid performance comparisons were conducted against the base configuration of the cycle. However, only for the most effective fluid combination the cycle with the IHX was investigated.

3.1 Ground Source Heat Pump for District Heating Network

Table 4 presents a comparison among different additional secondary fluids and demonstrates the dual advantageous impact of incorporating a small amount of a secondary fluid into a CO_2-based transcritical heat pump: (i) a boost in the Coefficient of Performance (COP) and (ii) a reduction in gas cooler pressure. Each fluid mixture attains a maximum COP value for a specific gas cooler pressure due to the balancing effects of heating capacity and compression work increase as the gas cooler pressure rises. Furthermore, each mixture exhibits its peak COP when the evaporator exit is in a saturated condition. In contrast, CO_2, which does not hold any glide at the evaporator, achieves its optimal COP with a superheat of about 7°C. This distinction is emphasized in the table 4, specifically in the final two lines. Compared to pure CO_2, all mixtures enhance COP and lower gas cooler pressure compared to the saturated CO_2 condition, yet the highest efficiency is observed for CO_2/propylene blends followed closely by CO_2/R152a and CO_2/DME combinations. This

[1] In the case of CO_2, must be intended as Normal Sublimation Point instead of Normal Boiling Point.

rise in COP is attributed to improved heat exchange alignment at both the evaporator and gas cooler in contrast to the CO_2 cycle. Additionally, the best mixtures exhibit a gas cooler pressure reduction of 15 to 25% compared to the pure CO_2 scenario. Furthermore, all mixtures boast low Global Warming Potential (GWP), and those containing a small proportion of the secondary fluid are either non-flammable or mildly flammable. The optimal mixture in this context appears to be CO_2 and DME, offering exceptional performance, a GWP of 1, and non-flammability when the DME percentage is below 12% [15]. It's worth noting that the CO_2 cycle, with superheating at the evaporator exit, aligns closely with the performance of the mixtures in terms of both COP and the reduction of gas cooler pressure.

Table 4: Obtained results for each assessed fluid, optimal composition, GSHP for DH case.

Fluid	%	Tcr [C]	Pcr [bar]	Pgc [bar]	GWP	COP
CO_2/R152a	91/9	40.66	78.5	169	12	1.99
CO_2/R1233zd(E)	95/5	33.34	72.6	176	1	1.95
CO_2/R1234ze(E)	90/10	39.49	78.6	171	1.6	1.97
CO_2/n-pentane	98/2	35.16	77.0	180	1.1	1.94
CO_2/propane	80/20	37.30	67.7	164	1.4	1.90
CO_2/propylene	78/22	48.52	77.9	142	1.2	2.01
CO_2/Isobutane	92/8	37.99	75.1	169	1.2	1.94
CO_2/Dimethyl ether	95/5	40.84	80.2	167	1	1.99
CO_2	100	30.98	73.8	197	1	1.87
CO_2 with SH	100	30.98	73.8	182	1	1.93

3.1.1 CO_2-DME

An examination of the CO_2-DME mixture has been conducted, comparing the base cycle configuration with that of the IHX. In Figure 2, the P-h diagram of the cycle is depicted, emphasizing that the optimal condition for maximizing the COP with the mixture is to have at the exit of the IHX saturated vapour.

In contrast, Figure 3 illustrates the comparison between the IHX and the base cycle concerning COP, compression ratio, and pressures at the gas cooler. Since the primary focus of the study was to enhance the CO_2 heat pump transcritical cycle with a small amount of secondary fluid, the analysis was conducted up to a composition of 70/30.

As observed from the figure, the IHX significantly enhances the coefficient of performance (with an average increase of approximately 15% at each composition), while also reducing the pressure at the gas cooler and the compression ratio. Notably, for the base cycle, there is a peak in the maximum COP at a 5% composition of DME, whereas for the IHX cycle, this peak is absent. This phenomenon can be explained by the fact that, for a given mixture composition, shifting point 0 to the left (i.e., decreasing the vapour quality at the evaporator exit) reduces the glide. Consequently, achieving the desired glide value may be re-established by increasing the quantity of added fluid to the mixture, thereby improving the COP. Additionally, it is worth noting the increasing downward slope of the isotherms on the right side of the saturation zone, which renders the glide very sensitive to the position of point 0.

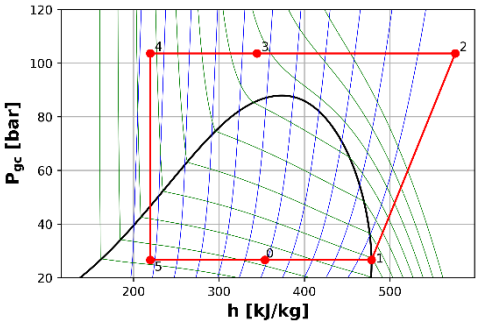


Figure 2: P-h diagram of IHX Cycle.

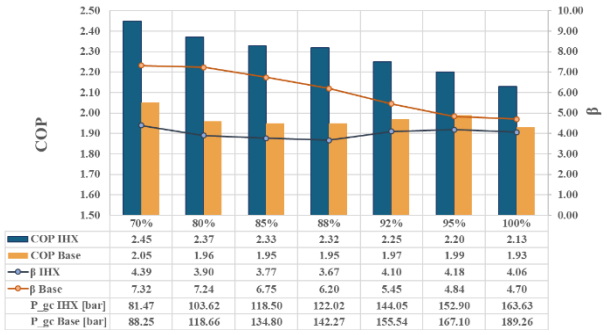


Figure 3: Comparison of performance of Base and IHX cycle at various percentage of CO_2 – GSHP for DH Case Study.

3.2 *Paper Industry*

Similarly to the GSHP for DH case study, Table 5 offers a comparison of various additional secondary fluids for the HTHP for the paper industry case study. Notably, the most significant distinction lies in the higher temperature disparity at both the evaporator and the gas cooler, leading to distinct optimal composition percentages for certain mixtures. Specifically, only fluids with a high critical temperature, such as R1233zd(E), n-pentane, and isobutene, demonstrate optimized composition when added to CO_2. Conversely, all other fluids exhibit a monotonically increasing trend of COP with the rise of the secondary fluid percentage, owing to the working conditions at the evaporator, which closely approximate the pseudo-critical point, resulting in close saturation curves. Fluids that do not significantly increase the critical temperature (and the glide) operate within a range close to the required evaporator glide of 14°C, thus not providing and optimizing composition. Therefore a composition of 80/20 has been selected in order to show the increase of performance and the reduction of gas cooler pressure for these mixtures.

Once again, compared to pure CO_2, almost all blends enhance COP and reduce gas cooler pressure, with the CO_2/DME blend showing the highest efficiency, followed by CO_2/R152a and CO_2/R1234ze(E) combinations. The top-performing mixtures demonstrate an even greater pressure reduction at the gas cooler (ranging between 35 to 50% compared to the pure CO_2 scenario and the prior case study). All blends exhibit low Global Warming Potential (GWP), and those with a small portion of the secondary fluid are either non-flammable or mildly flammable.

Once again, the optimal blend in this context appears to be CO_2 and DME, offering outstanding performance with a 38% increase in COP while still remaining in the mildly flammable zone.

Table 5: Obtained results for each assessed fluid, optimal composition, Paper Industry case.

Fluid	**%**	**Tcr [C]**	**Pcr [bar]**	**Pgc [bar]**	**GWP**	**COP**
CO_2/R152a	80/20	51.52	81.4	186	25.6	2.0
CO_2/R1233zd(E)	87/13	37.48	70.6	198	1	1.92
CO_2/R1234ze(E)	80/20	47.71	81.4	204	2.2	1.94
CO_2/n-pentane	95/5	41.30	81.2	214	1.2	1.87
CO_2/propane	80/20	37.30	67.7	222	1.4	1.75
CO_2/propylene	80/20	44.90	77.9	201	1.2	1.92
CO_2/Isobutane	83/17	47.40	76.5	191	1.3	1.89
CO_2/Dimethyl ether	80/20	64.18	87.9	150	1	2.10
CO_2	100	30.98	73.77	301	1	1.53
CO_2 with SH	100	30.98	73.77	246	1	1.83

3.2.1 CO_2-DME

Figure 4 shows the comparison between the IHX and the base cycle concerning COP, compression ratio, and pressures at the gas cooler for the paper industry case study. Again, the IHX significantly enhances the coefficient of performance (with an average increase of approximately 16% at each composition), while also reducing the pressure at the gas cooler and the compression ratio. Notably, both the base cycle and the IHX cycle do not present a peak in the COP varying the composition. As previously discussed this is due to reduced glide at the evaporator as it is close to the pseudo critical point (therefore the liquid and vapour saturation curves are close to each other).

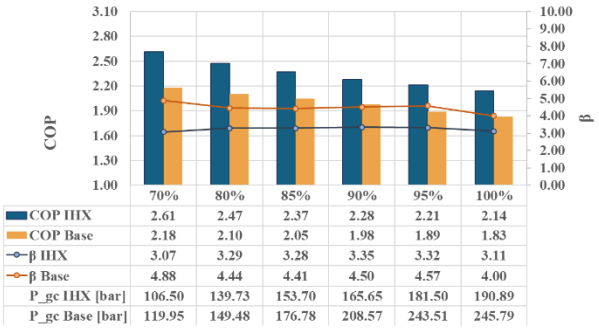


Figure 4: Comparison of performance of Base and IHX cycle at various percentage of CO_2 – Paper Industry Case Study

3.3 *Comparison of a two case studies – CO_2/DME*

Figure 5 and 6 depict the temperature profiles as a function of the heat exchanged at the evaporator and the gas cooler for pure CO_2 with a saturated condition at the evaporator exit, optimized superheat condition, and a CO_2-DME mixture.

In Figure 5, the results for the GSHP for DH illustrate that the temperature profiles of CO_2 with superheating are more closely aligned with those of the mixture, especially at the gas cooler. The CO_2/DME 95/5 mixture exhibits superior performance due to the better alignment of the profile at the evaporator.

Similarly, Figure 6 examines the paper industry case study. It's noteworthy how the effect of the mixture is particularly significant at the evaporator, where there's optimal matching of the temperature profile. Conversely, for the transcritical gas cooler, the alignment between the cooling CO_2 and the heating water is already quite satisfactory. The primary distinction from the GSHP case study lies in the increased fraction of DME necessary to align with the evaporator glide, which, in this instance, amounts to 20%.

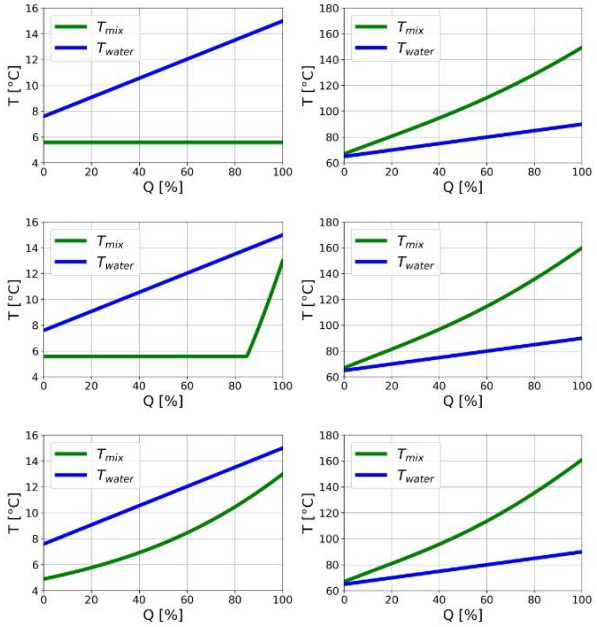


Figure 5: Temperature-Heat diagram at a), c), e) evaporator and b), d), f) gas cooler, for pure CO_2 without superheating at evaporator exit (a, b), with superheating (c, d) and with a 95/5 mixture of DME for the GSHP case study

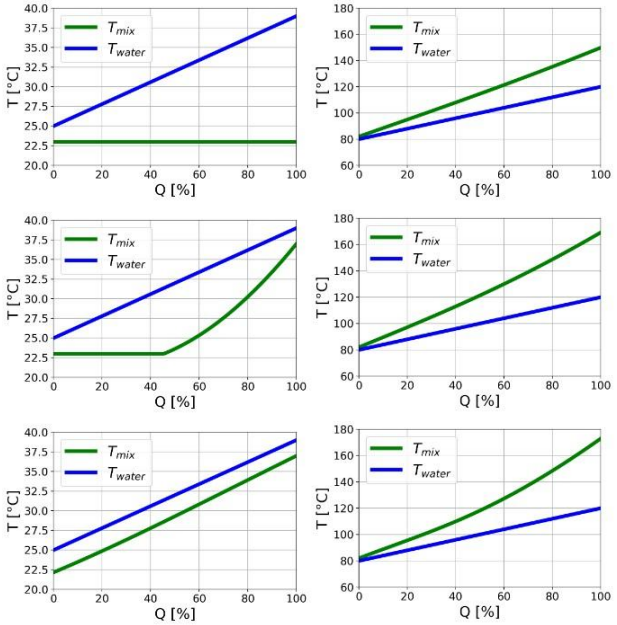


Figure 6: Temperature-Heat diagram at a), c), e) evaporator and b), d), f) gas cooler, for pure CO_2 without superheating at evaporator exit (a, b), with superheating (c, d) and with a 80/20 mixture of DME for the HTHP for paper industry case study

4 Conclusions

The thermodynamic analysis developed in this work was utilized for evaluating the efficiency of several CO_2 based mixtures under different operating conditions. The key results from the study may be summarised as follows:

- The utilization of a secondary fluid in CO_2 transcritical heat pump allows both an increase of the COP and a reduction of the gas cooler pressure.
- Another relevant result that was obtained was the higher advantage that the CO_2 mixtures provide at the evaporator compared to the gas cooler, as the temperature profiles are closer in the case of finite heat capacity case studies in transcritical configurations.
- The choice of the secondary fluid is strongly affected by several factor: flammability, toxicity, environmental concerns. CO_2-DME seems to be a good solution as low percentage of DME allow for a high COP gain, still keeping the mixture non-flammable.
- When evaporator temperatures closely approach the pseudo-critical point, the evaporation glide diminishes significantly, inhibiting the attainment of a local optimum for the composition. Consequently, there is an increase in COP as the

proportion of the secondary component rises in the mixture.

Acknowledgement

Supported by PNRR - Missione 4 “Istruzione e Ricerca” - Componente C2 Investimento 1.1 “Fondo per il Programma Nazionale di Ricerca e Progetti di Rilevante Interesse Nazionale (PRIN)”, “Next generation inverse cycles using CO_2 based mixtures as refrigerant (CO_2MIX)”, project code: P2022C494T, MUR D.D. financing decree n. 1385 of 01/09/2023 (CUP B53D23026960001) funded by the European Commission under the NextGeneration EU programme"

References

[1] IRENA, Power to heat and cooling: Status, 2023. Available at: https://www.irena.org/Innovation-landscape-for-smart-electrification/Power-to-heat-and-cooling/Status (last accessed 08/03/2024)

[2] Bouteiller, P., Terrier, M. F., & Tobaly, P. (2017, February). Experimental study of heat pump thermodynamic cycles using CO_2 based mixtures-Methodology and first results. In AIP Conference Proceedings (Vol. 1814, No. 1). AIP Publishing.

[3] Tobaly, P., Terrier, M. F., & Bouteiller, P. (2018, June). CO_2+ propane mixture as working fluid for refrigeration in hot climates. Experimental results of energy efficiency tests. In 13th IIR Gustav Lorentzen conference on natural refrigerants: natural refrigerant solutions for warm climate (pp. 18-20).

[4] Sun Z., Cui Q., Wang Q., Ning J., Guo J., Dai B., Liu Y., Xu Y., Experimental study on CO_2/R32 blends in a water-to-water heat pump system, Applied Thermal Engineering, 162, 2019.

[5] Yu B., Yang J., Wang D., Shia, J., Guo Z., Chen J., 2019, Experimental energetic analysis of CO_2/R41 blends in automobile air-conditioning and heat pump systems, Applied Energy, 239, 1142–1153

[6] Wang Y., He Y., Song Y., Yin X., Cao F., Wang X., 2021, Energy and Exergy Analysis of the Air Source Transcritical CO_2 Heat Pump Water Heater Using CO_2-Based Mixture as Working Fluid, Energies, 14, 4470.

[7] Li C., Liu Z., Sun B., Wang Y., Gao S., Zhang T., Wang B., Thermodynamic analysis of CO_2 blends for vehicle heat pump at cold ambient temperature, Frontiers in Energy Research, Sec. Process and Energy System Engineering, 2022.

[8] Liu J., Zhou L., Lin Z:, Zhang X., Performance evaluation of low GWP large glide temperature zeotropic mixtures applied in air source heat pump for DHW production, Energy Conversion and Management, 274, 2022.

[9] Luo J., Yang K., Zhao Z., Chen G., Wang Q., Experimental investigations on the performance of a single-stage compound air-source heat pump using CO_2/R600a in cold regions, Applied Thermal Engineering, 205, 2022.

[10] Ganesan P., Eikevik TM., Hamid K., Wang R., Yan H., Thermodynamic analysis of cascade high-temperature heat pump using new natural zeotropic refrigerant mixtures: R744/R600 and R744/R601, International Journal of Refrigeration, 154, 2023.

[11] Ganesan P., Eikevik, New zeotropic CO_2-based refrigerant mixtures for cascade high-temperature heat pump to reach heat sink temperature up to 180 °C, Energy Conversion and Management: X, 20, 2023.

[12] Mazer MFP., da Rosa OC., da Silva AK., Thermodynamic modeling of a residential heat pump for combined space and water heating using binary CO_2-based mixtures, International Journal of Refrigeration, 155, 2023.

[13] Vaccaro, G., Milazzo, A., Talluri, L. (2023). Thermodynamic assessment of transcritical refrigeration systems utilizing CO_2-based mixtures. International Journal of Refrigeration, 147, 61-70.

[14] Sicco, E., Martínez-Ángeles, M., Toffoletti, G., Nebot-Andrés, L., Sánchez, D., Cabello, R., Llopis, R. (2024). Experimental evaluation of CO_2/R-152a mixtures in a refrigeration plant with and

without IHX. International Journal of Refrigeration.
[15] Vaccaro, G., Milazzo, A., Talluri, L. (2024). A proposal for a non-flammable, fluorine-free, CO_2-based mixture as a low TEWI refrigerant. International Journal of Refrigeration, 158, 157-163.
[16] REFPROP, NIST, available at: https://www.nist.gov/srd/refprop (last accessed 08/03/2024)
[17] ASHRAE, Standard and guideline, available at: https://www.ashrae.org/technical-resources/standards-and-guidelines (last accessed 08/03/2024)
[18] Piemonte C., Examples of realisation of geothermal district heating systems, available at: https://www.unionegeotermica.it/pdfiles/8-PIEMONTE.pdf (last accessed 08/03/2024)
[19] Pellegrini M., Guzzini A., Saccani C., Feasibility study for the application of a high-temperature heat pump in the pulp and paper industry: an Italian case study, proceedings of 14th IEA Heat Pump Conference, 15-18 May 2023, Chicago.
[20] Bertini M., Fiaschi D., Manfrida G., Niknam PH., Talluri L., Evaluation of the property methods for pure and mixture of CO_2 for power cycles analysis, Energy Conversion and Management, Vol. 245, 2021.

THERMETRENNES PROJECT: THERMAL GEOSTRUCTURE IN THE METRO OF RENNES FOR ABSORPTION HEAT PUMPS AND STUDY OF A THERMO-ACTIVE CONCRETE EXPERIMENTAL MODEL

Paul Byrne[1]*, Abdelouhab Labihi[2], Eduardo Mendes[1], Habib Mesbah[1], Amina Meslem[1]

[1] Laboratoire Génie Civil Génie Mécanique, Université de Rennes, France

[2] Pôle Cristal, Dinan, France

* *Corresponding Author: paul.byrne@univ-rennes.fr*

Abstract. During the construction of Line b of the metro of Rennes, France, 30 km of HDPE tubes were installed in diaphragm walls and in concrete slabs of four stations. Powered by these geothermal probes, absorption heat pumps provide part of the heating and domestic hot water production demands for residential buildings. Additional heat is provided by natural gas boilers. The glycol water coming from the heat pump evaporators and circulating inside the geothermal loops is heated mainly by the ground but also by the heat released by human activity. The THERMETRENNES project aims to study the thermomechanical behaviour of the metro station in its environment through experimental measurement campaigns and numerical simulations. The University of Rennes contributes by designing, building, instrumenting and studying an experimental model representative of an active wall element. The experimental model developed at the LGCGM and the results of the thermomechanical behaviour obtained during thermal cycling, alternating between the temperature regimes in winter and summer, usually observed in these geostructures, is firstly detailed. Secondly, the performance of the heating and domestic hot water production system observed in situ during the first months of operation is analysed.

Keywords. Absorption heat pump, Geostructure, Thermo-active wall, Metro, Thermomechanical behaviour.

1 Introduction

Geostructures are infrastructures that recover geothermal energy. Over the last twenty years, the idea has emerged that, when constructing a building or an infrastructure (tunnel, parking lot, metro line, etc.), installing closed water loops would enable to mutualize investment costs in civil engineering and energy production. The first steps of development were focused on foundation piles, which have a simple geometry and are widely used. The sizing tools used for vertical geothermal probes are not suitable for sizing what have come to be called geothermal piles, as these are much shorter and larger in diameter than vertical geothermal probes. Since the early 2000s, a large amount of work has developed new models for the energetic and thermomechanical design of piles, and validated them through numerical and experimental studies [1-5]. There are numerous operational applications of this technology, especially in Austria, Germany, the UK and Switzerland [6-11]. The technology was initially applied to piles. Numerous studies and design methods have been proposed to evaluate both their energy potential [12-14] and their geotechnical behavior [15-17]. Di Donna et al. reported the number of existing energy geostructures by country. Belgium, Italy and France also count some applications [18]. Underground thermo-active structures interact thermally with a larger volume of soil than energy piles.

The metro of Rennes is the first in France and one of the first in Europe to have part of its network equipped with geothermal heat exchangers (figure 1) to produce renewable and affordable heat for collective dwellings and tertiary buildings. The objectives of the THERMETRENNES project are to maximize the lessons learned from this initiative by the metropolis of Rennes and to seize the opportunity to develop the sector, reassuring investors and

building managers about the technical and economic performance of such installations by providing reliable sizing tools for engineering offices.



Figure 1: Geothermal loops before concrete pouring.

Achieving these objectives involves fundamental research work to better understand the multi-physical (heat transfers, thermomechanical behaviour...) and multi-scale (both spatial and temporal) coupling phenomena that occur in the geostructure, the surrounding subsoil and within the station. This research is based on three aspects:

1. Instrumentation of one of the four thermo-activated stations to obtain information on the thermal and mechanical parameters of the structure, the subsoil and the interior of the station, as well as on the underground flows, the temperature profiles in the ground and in the structure, and the energy performance of all heat exchangers.

2. Experiments carried out on a laboratory model in LGCGM, University of Rennes, to more accurately measure the temperature evolutions near the heat exchanger and to assess the thermomechanical behaviour of the concrete.

3. Finally, modelling is carried out, based on the data measured on site and in the laboratory, to better narrow down the inputs and validate the model outputs. Using Comsol Multiphysics, his modelling explores the long-term performance of the structure, better understanding the influence of the different thermal, mechanical, geometric, geological and hydrogeological parameters that affect thermal transfers in the thermo-active geostructure.

Heat pump-assisted geothermal energy, also known as shallow geothermal energy or very low geothermal energy, uses the ground near the surface as a source of heat or cold to power a heat pump that controls the temperature level of the energy delivered to the customer. Heat exchangers installed underground can be either open loops (aquifer collection) or closed loops. In closed loops, the piping material is generally high-density polyethylene (HDPE).

Despite the growing interest in these technologies, currently there is no standardized tool or procedure for the energetic and thermomechanical sizing of thermo-active geostructures, due to the lack of real operational feedback. The thermo-active geostructures currently in operation can be considered as pilots, or even demonstrators. The main objective of the THERMETRENNES project, co-funded by ADEME, is to get the maximum feedback from the operation of one of the four thermo-active stations on line b of the metro of Rennes.

The task of the LGCGM team in this project is to build and test a representative experimental model of the geostructures that represents the cast-in-place walls of the stations on line b of the Rennes metro. The evolution of temperatures and deformations inside the concrete was measured during thermal cycling imitating the summer and winter modes that can be experienced in geothermal loops. The results of this study provides the project partners with data for use in global simulations of metro stations. The work presented in this article first presents the experimentation using the representative model built in the laboratory and the performance analysis of an absorption heat pump recovering energy from the geostructure to heat 54 apartments representing 3422 m^2 of floor area distributed in two buildings (figure 2). The second part of this article reports and completes the analysis of the performance of the absorption heat pump connected to the geothermal system of one metro station. The measurements were collected and primarily analysed by the design office Egis, also in charge of the construction of the metro.



Figure 2: Two buildings heated by an absorption heat pump connected to the geostructure.

2 Experimental model

2.1 Model configuration

An elementary model of a concrete wall was built in the same configuration as a metro station in Rennes (figure 3).

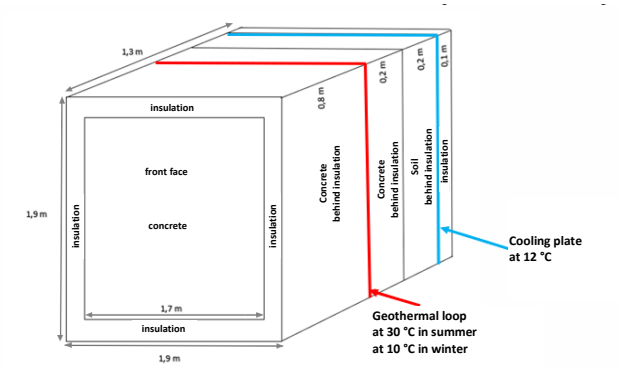


Figure 3: Scheme of the experimental model.

The structure of the model consists of a reinforced concrete wall of 170 cm width, 170 cm height and 100 cm thickness (figures 4 and 5).



Figure 4: Bottom insulation, frames, HDPE water loop and wall forms.



Figure 5: Concrete block.

The width and depth correspond to the dimensions of a real geothermal loop inside the walls of a metro station. As in the real geostructure, the "geothermal" water loop was placed at a distance of 80 cm from the front face (figure 3). A layer of soil of 20 cm thickness was poured behind the concrete wall. A cooling metallic plate was installed behind the soil layer to maintain the surface at the stable temperature of 12 °C as the one of the ground at a depth of 30 m in Rennes (figure 6). Thermostatic baths were used to control the water temperatures in the modelled geothermal loop and in the cooling plate water loop (figure 7). Five faces of this wall are insulated with panels of 10 cm thickness (figure 8). Only the front face is exposed to heat exchange with the environment. The gaps between the insulating panels were filled up with expanding foam in order to limit peripheral heat loss and to approach a mono-dimensional configuration in terms of heat fluxes distribution. A photograph of the finished model is shown in figure 9.



Figure 6: Cooling plate.



Figure 7: Thermostatic bath of the geothermal loop.



Figure 8: Top side insulation.



Figure 9: Finished experimental set-up.

The instrumentation consisted of vibrating strings in order to measure deformations and temperatures inside the concrete, K-type thermocouples for inlet and outlet water temperatures and a data acquisition system. The uncertainties of the experimental measurement system are given in table 1. The uncertainty propagation calculation results for heat fluxes are within an error margin lower than 10 %.

Table 1: Uncertainties of sensors and calculated heat flux

Value	Device or method	Uncertainty
Temperature	K-type thermocouple	± 0.1 °C
Deformation	Socotec Vibrating chord	± 1 µm/m
Temperature	Socotec Vibrating chord	± 0,1 °C
Thermal conductivity	CTmètre Conductivity meter	± 3 %
Heat flux	Calculation	5.3 to 9.7 %

2.2 Experimental results

The experimental tests consist of thermal cycles alternating between a winter mode in which the water loop average temperature is set at 10 °C and a summer mode in which the it is set at 30 °C. The first cycling protocol is presented in figure 10. This cycling experiment was repeated and showed the same results.

An analysis was conducted based on the temporal evolution of the temperature at the central vibrating chord of concrete block named Cpt8. The concept of time constant and exponential evolution was utilized to better analyse the choice of periodicity between summer/winter cycle changes. Figure 11 illustrates the situation observed.

1st THERMAL CYCLING SCHEDULE - 10/04/2024 to 24/04/2024							
WEEK	Monday	Tuesday	Wednesday	Thursday	Friday	Saturday	Sunday
1st Week	X 08/04/2024	X 08/04/2024	W Starting date Start at 11:00 am 10/04/2024	W 11/04/2024	S Changing Setup at 11:00 am 12/04/2024	S 13/04/2024	S 14/04/2024
2nd Week	W Changing Setup at 11:00 am 15/04/2024	W 16/04/2024	S Changing Setup at 11:00 am 17/04/2024	S 18/04/2024	W Changing date at 11:00 am 19/04/2024	W 20/04/2024	W 21/04/2024
3rd Week	S Changing Setup at 11:00 am 22/04/2024	S 23/04/2024	S Ending date Finish at 11:00 am 24/04/2024	X 25/04/2024	X 26/04/2024	X 27/04/2024	X 28/04/2024
Legend: X → NO CYCLING W → CYCLING IN WINTER SETUP S → CYCLING IN SUMMER SETUP							

Figure 10: Cycling schedule.

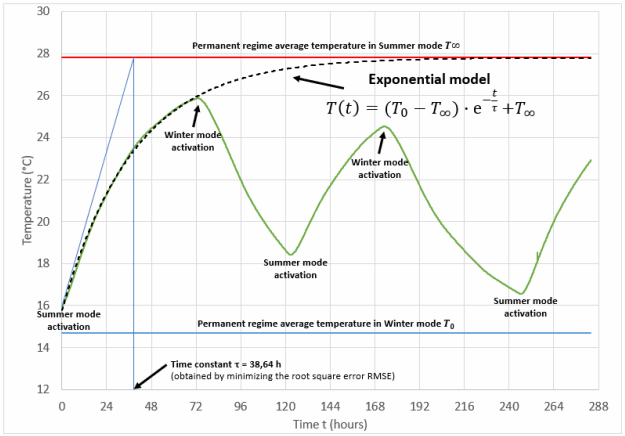


Figure 11: Temperature evolution at the centre of the block.

The time constant was obtained by minimizing the root mean square error between experimental and modelled evolutions. It is equal to 38.64 h. The minimum and maximum temperatures T_0 and T_∞ are equal to 14.8 °C and 27.9 °C respectively. The average temperature of the water measured flowing behind the cooling plate is equal to 11.9 °C. The average temperature of the geothermal loop is 9.7 °C during the winter mode and 29.6 °C during the summer mode. The thermal conductivities of the

concrete and the soil are 2.04 $W.m^{-1}.K^{-1}$ and 0.25 $W.m^{-1}.K^{-1}$ respectively. The temperature differences and heat fluxes are detailed in table 2. The total heat flux obtained experimentally is 36.8 $W.m^{-2}$ in winter mode and 30.9 $W.m^{-2}$ in summer mode. The results of thermal response tests run by Egis design office gave results between 20.0 and 24.6 $W.m^{-2}$. These results are in the same order of magnitude. However, the discrepancy can be attributed to the configuration of some parts of the real circuit where heat transfers are less efficient. The experimental model results can also be influenced by the good peripheral insulation that is not present in the real case.

Table 2: Heat fluxes inside the concrete block.

Mode	Designation	ΔT [K]	Heat flux [$W.m^{-2}$]
Winter	From cooling plate To geothermal loop	2.12	2.4 ± 0.2
Winter	From concrete centre (Cpt8) To geothermal loop	5.07	34.5 ± 1.8
Winter	Total	-	36.8 ± 1.9
Summer	From geothermal loop To cooling plate	1.65	11.2 ± 1.1
Summer	From geothermal loop To concrete centre (Cpt8)	17.65	19.7 ± 1.1
Summer	Total	-	30.9 ± 1.6

The temperature variation inside the concrete block caused deformations due to thermal expansion and contraction. Figure 12 shows the evolutions recorded by vibrating chords situated at the centre of the block (Cpt8), nearer to the front (Cpt7) and closer to the geothermal loop (Cpt4). The variations of deformations are lower at the centre and higher near the geothermal loop. Vibrating chord Cpt7 (near the front face) is sensitive to the daily variations of ambient air. The maximum deformation is lower than 30 ± 1 µm/m which is far below the values that would create dramatic mechanical deformations such as cracking inside the geostructure. Indeed, for C25/30 reinforced concrete, Young's modulus is 33,000 MPa and tensile strength is estimated at 2.6 MPa, resulting in a risk of cracks appearing at a strain of 800 µm/m.

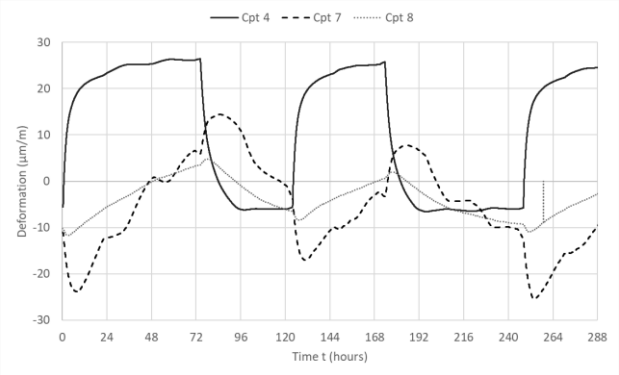


Figure 12: Deformations measured by three vibrating chords.

3 Performance analysis of the geothermal absorption heat pump

3.1 Description of the heating system and monitoring equipment

The scheme of the heating system is presented in figure 13. It can operate only in a heating mode. The heat pump (HP) is connected to the geothermal system via a heat exchanger and two circulating pumps on the heat-source side and to a 1000 L tank on the heat-sink side. The gas boiler is connected to a second water tank of 800 L. The uncertainties of sensors of the monitoring system are given in table 3.

Table 3: Uncertainties of sensors of the monitoring system

Value	Device or method	Uncertainty
Temperature	PT100	± 0.1 °C
Flow rate	Ultrasonic	± 1 % in m^3/h
Thermal energy	Itron CF Echo II Calculation	± 3 % in kWh
Gas counter	Itron Quantometre Calculation	± 1.5 % in kWh

3.2 Results of monitoring campaign

The absorption heat pump is a Robur water-to-water heat pump GAHP GS HT of 41.6 kW nominal heating capacity and 1.65 nominal Gas Utilization Efficiency (GUE or thermal COP) in an evaporator inlet temperature / Delivery temperature regime of 10 °C / 50 °C (W10W50). As a remainder, the global COP of an absorption heat pump includes electrical energy consumed by the pump in addition to thermal energy consumption. The nominal heat input by natural gas is 25.2 kW. It was used for space heating

and domestic hot water production. The thermal consumptions and productions were monitored during the 2022/2023 campaign (figure 14).

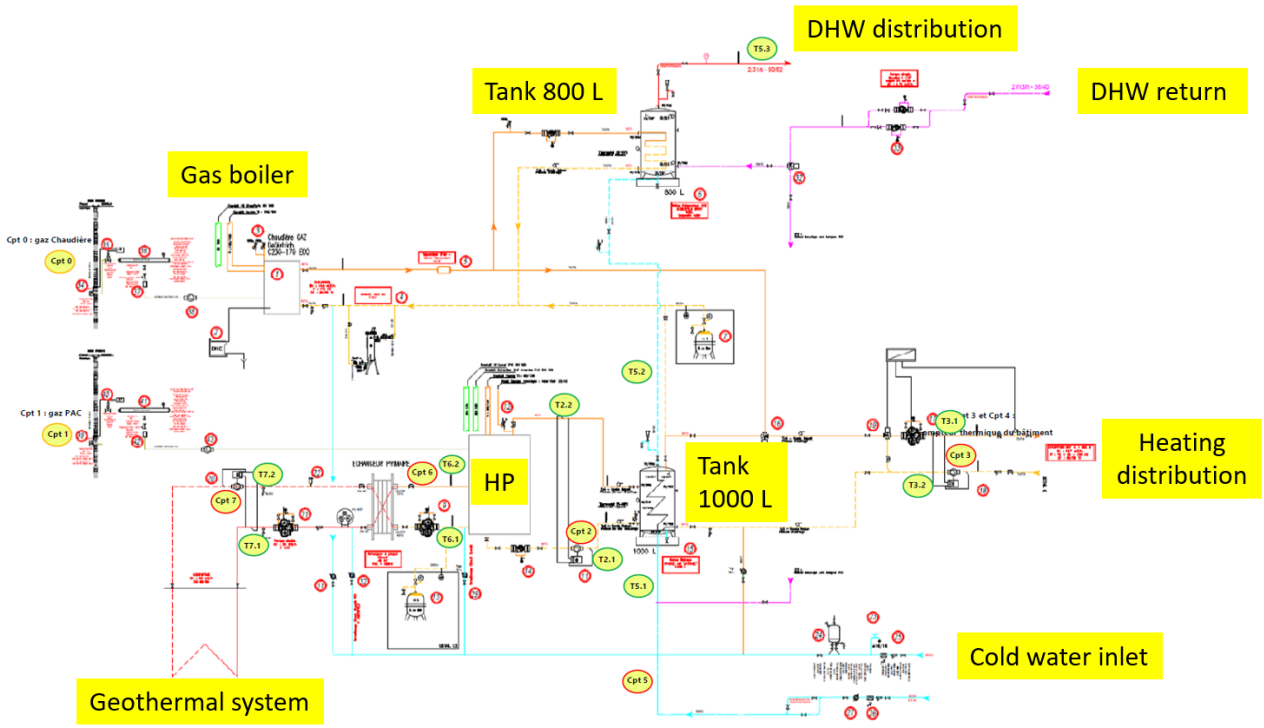


Figure 13: Heating system.

A De Dietrich C230 EVO condensing gas boiler was installed to be used as a complementary heating device. During the colder days of the winter and for DHW production during the summer, the gas boiler consumed more heat than the absorption heat pump (figure 15). The heat production by the gas boiler was unfortunately not monitored because of a defective counter. This monitoring campaign also suggests that the control management could be improved to operate the absorption heat pump more often rather than the gas boiler. Figure 16 shows the small variations of the GUE of the heat pump. A small decrease in December can be attributed to a fault of the heat pump that can be noticed on figure 17 by a sudden decrease of delivery temperature. During summer, the absorption heat pump only satisfied a low part of the domestic hot water (DHW) demand. The lower heat demand led to shorter operating cycles, more heat losses and thus lower average performance. The annual GUE is measured at 1.575, which is slightly under the value announced by the manufacturer (1.65 for W10W50) because the heat sink temperature is higher. Indeed, the average HP outlet temperature during the heating period between 18 October and 8 May is equal to 56.1 °C (Figure 17). The standard deviation is ± 3.6 K. This is higher than the nominal delivery temperature equal to 50 °C. This discrepancy can explain the fact that the experimental GUE is slightly lower than the nominal one. The DHW distribution temperature oscillates quite importantly between 55 and 80 °C during the heating period (Figure 18). The temperature lift up to 80 °C is supplied by the condensing gas boiler. Around the 23rd of May, a maintenance operation enabled to reduce the maximum temperature to 69 °C and the variation to a smaller interval of 10 K.

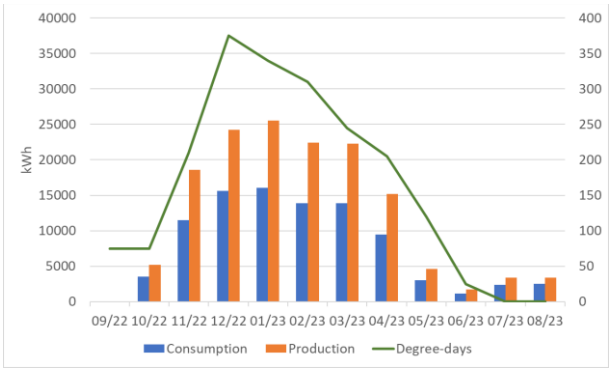


Figure 14: Energy consumption and production of the absorption heat pump during the 2022/2023 season.

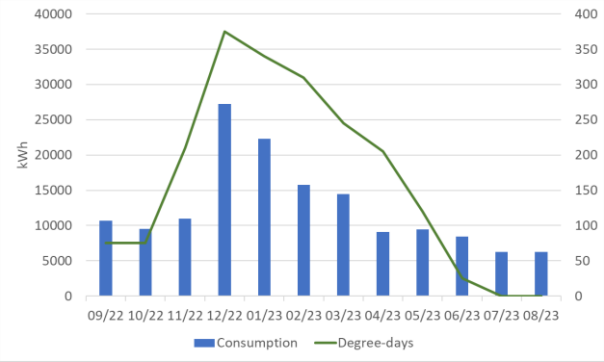


Figure 15: Energy consumption of the gas boiler during the 2022/2023 season.

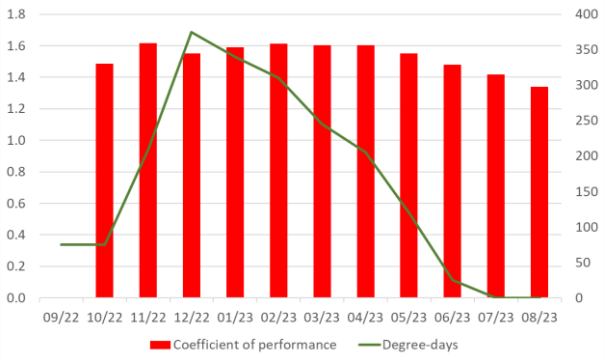


Figure 16: GUE of the absorption heat pump during the 2022/2023 season.

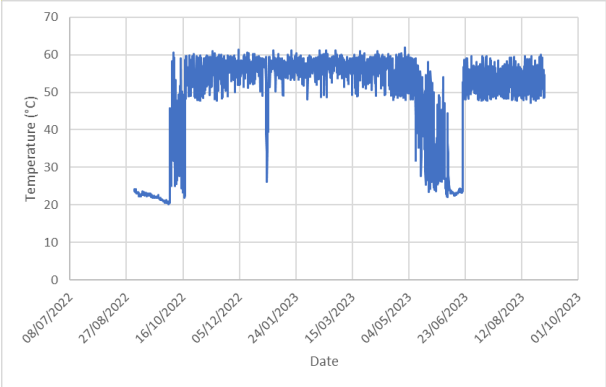


Figure 17: HP outlet temperature of the absorption heat pump during the 2022/2023 season.

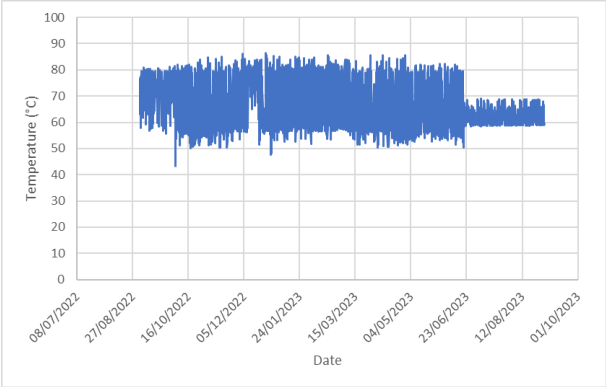


Figure 18: DHW temperature during the 2022/2023 season.

3.3 Comparison with other monitoring campaigns

Table 4 reports the results of GUE of absorption heat pumps in Rennes, Belgium and three other locations in France.

The same absorption heat pump was tested by Davila et al. [19]. in other operating conditions. Two sites were monitored in Belgium. Outdoor air was the heat source. The piping systems were not exactly the same between the two sites. For one of them, the absorption heat pump was assisted by solar energy for DHW production. The indicator COP_{TH} calculated by Davila et al. is equal to the GUE. The closest conditions to the ones monitored in Rennes are an outdoor air of 12 °C and delivery temperatures of 45 °C and 55 °C. The COP_{TH} values are respectively of 1.38 and 1.22, so 1.3 if interpolated for a delivery temperature of 50 °C. It seems more favourable to operate on water at 10 °C than air at 12 °C as a heat source. A more detailed monitoring system could measure the refrigerant temperatures and confirm this conclusion. As in Rennes, a performance drop of around 10 % was observed by Davila et al. during summer. This decrease was attributed to low frequency of use, which increased the relative impact of thermal losses during start and stop phases.

Other monitoring campaigns on absorption heat pumps of same brand and equivalent heating capacity were analysed by ADEME (French agency for ecological transition) [20-22]. In Rumilly, the average seasonal GUE of three absorption heat pumps was estimated at 1.4. In Toulouse, the GUE was 1.42 for a lower delivery temperature of 40 °C and air at 7 °C as a heat source. In Luynes, the heat pump operated also with air at 7°C as a heat source and at high temperature (A7W60). The average GUE during winter of 1.16 was consequently lower, and even 9 % under the expected value announced by the manufacturer in those conditions. The monitoring campaigns presented by ADEME reveal a series of advantages and drawbacks of operating absorption heat pumps. They also provide some paths of improvement.

The main advantages are the following:

- Less noise and vibrations than vapour compression heat pumps,
- Better performance than gas boilers,
- Stable performance using ground source,
- Possibility of doing free geocooling during summer with the geothermal loop.

The main drawbacks are the following:

- Lower performance than vapour compression heat pumps (VCHP),
- More technical maintenance because of specific chemical products, partial vacuum and risk of crystallization,
- Higher OPEX than VCHP,
- Higher CAPEX than VCHP.

The main improvement paths are the following:

- Heating auxiliaries must be controlled according to heat pump operation,
- The control management of the absorption heat pump within the whole heating system must be adjusted depending on the season and thermal demands,
- A water logic based on outdoor temperature reduces the delivery temperature and increase the COP when the outdoor temperature is milder than the base temperature.

Table 4: GUE of absorption heat pumps measured during monitoring campaigns

Location	Temperature regime*	GUE or COP_{TH}
Rennes	W10W56	1.575
Belgium	A12W55	1.3
Rumilly	W10W52	1.4
Toulouse	A7W40	1.42
Luynes	A7W60	1.16

*W=water; A=air

4 Conclusions

The recovery of geothermal energy through thermo-activated walls in underground metro stations lacks precise information regarding the safety and effectiveness of the technology. Also destinated to decision-makers and project managers, THERMETRENNES project intends to develop and validate simpler design methods and good practices for the operation and future development of such facilities. In addition, combining the results of the experimental and simulation models with the data monitored in the metro station provides a complete study.

An elementary model of a concrete wall, as typically found in four metro stations of Line b in Rennes, was constructed and validated. The model was equipped with vibrating chords to measure temperatures and deformations plus type K thermocouples. The ground temperature was successfully controlled at 12 °C, matching the conditions 30 meters underground in Rennes, as well as the water inlet temperature in the concrete, set at either 10 °C or 30 °C, simulating winter and summer modes.

For a detailed study of temperature and deformation behaviours, thermal cycles were performed. They revealed that the heat fluxes of around 30-35 $W.m^{-2}$ were representative of the real case by comparison with the results of thermal response tests between 20 and 25 $W.m^{-2}$. The assessment of heat loss and gains should be continued in further studies. The time constant of the exponential evolution was evaluated at around 40 h. During thermal cycles, the deformations observed were far too low to damage the geostructure.

A monitoring campaign was finally performed on the operation of an absorption heat pump connected to the geostructure of a metro station in Rennes. The GUE or thermal COP was calculated and compared to results from other case studies in Belgium and France. The performance measured in each study is close to the expected one. In general, the GUE is much higher than the efficiency of the condensing gas boiler. However, it remains lower than the COP of a vapour compression heat pump. Absorption heat pumps produce less noise and vibrations than vapour compression heat pumps. To reduce the CAPEX difference, the building should be connected to the natural gas network.

The most important takeaways from this study are the following:

(1) No critical thermo-mechanical behaviour will occur in geostructures due to thermal cycling between winter and summer operations.
(2) Operation of absorption heat pumps is stable with geothermal sources.
(3) Maintenance and control are crucial for all heating systems but specifically for absorption heat pumps to maintain good performance levels.

This study provides significant insights about the thermo-mechanical behaviour of the geostructures found in the metro station of Rennes and of the connected absorption heat pumps. Looking ahead, thermo-activated concrete walls seem to have a strong potential and should be studied in every new project of metro and even every new other infrastructure.

Acknowledgement

The authors would like to acknowledge ADEME, the French Agency for Ecological Transition for the funding of THERMETRENNES project, Rennes Métropole and the design office Egis for the authorization to exploit the data of the commissioning campaign.

References

[1] F. Loveridge et al., "energy geostructures: a review of analysis approaches, in situ testing and model scale experiments", geomech. Energy environ., vol. 22, 2020.

[2] L. Laloui, M. Nuth, and L. Vulliet, "Experimental and numerical investigations of the behaviour of a heat exchanger pile," int. J. Numer. Anal. Methods geomech., vol. 30, no. 8, pp. 763–781, 2006.

[3] Y. Hamada et al., "Field performance of an energy pile system for space heating", Energy build., vol. 39, no. 5, pp. 517–524, 2007.

[4] A. Di donna, A. F. Rotta loria, and L. Laloui, "Numerical study of the response of a group of energy piles under different combinations of thermo-mechanical loads", Comput. Geotech., vol. 72, pp. 126–142, 2016.

[5] F. Loveridge and W. Powrie, "G-functions for multiple interacting pile heat exchangers", energy, vol. 64, pp. 747–757, 2014.

[6] D. Adam, "Tunnels and foundations as energy sources - practical applications in austria," 5th int. Symp. Deep found. Bored auger piles (bap v), pp. 337–342, 2009.

[7] P. J. Bourne-webb, "Observed behaviour of energy geostructures", in energy geostructures: innovation in underground engineering, L. Laloui and A. Di donna, eds. Iste ltd and john wiley & sons inc., 2013.

[8] H. Brandl, "Energy foundations and other thermo-active ground structures", géotechnique, vol. 56, no. 2, pp. 81–122, 2006.

[9] D. Pahud, "A case study: the dock midfield of zurich airport", in energy geostructures: innovation in underground engineering, L. Laloui and A. Di donna, eds. Iste ltd and john wiley & sons inc, 2013, pp. 281–295.

[10] P. Riederer et al., "Conception de fondations geothermiques," p. 170, 2007.

[11] M. Anstett et al., Utilisation de la chaleur du sol par des ouvrages de fondation et de soutènement en béton. Guide pour la conception, la realization et la maintenance. Switzerland: société suisse des ingénieurs et des architects, 2005.

[12] D. Pahud, "pilesim: simulation tool for heating / cooling systems," 2007.

[13] M. Alberdi-pagola et al., "A case study of the sizing and optimisation of an energy pile foundation (rosborg, denmark)", Renew. Energy, vol. 147, pp. 2724–2735, 2018.

[14] F. Loveridge and W. Powrie, "Temperature response functions (g-functions) for single pile heat exchangers", Energy, vol. 57, pp. 554–564, 2013.

[15] T. Mimouni and L. Laloui, "behaviour of a group of energy piles," can. Geotech. J., vol. 52, no. 12, pp. 1913–1929, 2015.

[16] A. F. Rotta loria and L. Laloui, "The interaction factor method for energy pile groups," comput. Geotech., vol. 80, pp. 121–137, 2016.

[17] A. Di Donna and L. Laloui, "Numerical analysis of the geotechnical behaviour of energy piles", Int. J. Numer. Anal. Methods geomech., vol. 39, pp. 861–888, 2014.

[18] A. Di Donna, M. Barla, and T. Amis, "Energy geostructures : a collection of data from real applications", Proceedings - IACMAG 2017, 15th International Conference of the International Association for Computer Methods and Advances in Geomechanics, pp. 1063-1071, 2017.

[19] C. Davila, J. Vega and V. Lemort. "Experimental investigation, modeling and in-situ monitoring of a gas-driven absorption heat pump in Belgium". Cleaner Energy Systems, vol. 6, 100087, 2023.

[20] ADEME. Synthèse des résultats d'une campagne de suivi d'un site équipé de trois pompes à chaleur à absorption gaz naturel. Site de Rumilly (74). 2013. Accessed online on 26 February at https://media.xpair.com/pdf/chauffage/Instrumentation-PAC-Gaz-Rumilly.pdf

[21] ADEME. Synthèse des résultats d'une campagne de suivi d'un site équipé de deux pompes à chaleur à absorption gaz naturel. Site de Toulouse (31). 2012. Accessed online on 26 February at https://media.xpair.com/pdf/chauffage/Instrumentation-PAC-Gaz-Dinetard.pdf

[22] ADEME. Synthèse des résultats d'une campagne de suivi d'un site équipé d'une pompe à chaleur haute température à absorption gaz naturel. Site de Luynes (13). 2012. Accessed online on 26 February at https://media.xpair.com/pdf/chauffage/Instrumentation-PAC-Gaz-Luynes.pdf

ATMOSPHERIC WATER HARVESTING WITH ACTIVE REFRIGERATION SYSTEMS

Cristian Cuevas[1]*, Aitor Cendoya[2], Matías Pezo[1], Daniel Sacasas[1]

[1] Universidad de Concepción, Departamento de Ingeniería Mecánica, Concepción, Región Bío Bío, Chile

** Corresponding Author: crcuevas@udec.cl*

Abstract. According to the Food and Agriculture Organization, by 2025, 1800 million people are expected to live under "absolute" water scarcity, (less than 500 m^3 per year per capita), and two-thirds of the world population could be under "stress" conditions. One of the sources of water that could mitigate this problem, is the water in the atmospheric air, which presents a potential $12.9 \cdot 10^{12}$ m^3 of water. This study, proposes to use an active refrigeration system to collect this water. The proposed system is composed by a variable speed scroll compressor, a condenser, an evaporator and a variable speed axial fan. It is designed to produce 150 L/day at an ambient condition of 20ºC and 60% of relative humidity. The system is firstly analysed through a parametric analysis, in order to evaluate the effect of the air temperature settled at the evaporator exhaust. It was concluded that to maximize the harvested water, it is advisable to work with a variable air temperature at the evaporator exhaust, because it depends on the ambient relative humidity. This temperature is modulated with the air mass flow rate circulating though the circuit. Other result presented here corresponds to the monthly water harvested in two Chilean cities. Here the most important conclusion is that the amount of water collected depends on the weather conditions and varies through the different seasons, obtaining a higher water collection during summer and a lower water collection during winter, due to the lower temperatures. Concerning the Specific Energy Consumption, it varies between 0.37 kWh/L and 1.05 kWh/L.

Keywords. Water scarcity, Vapour compression refrigeration system, Atmospheric water harvesting system, Modelling.

Nomenclature

A	Area (m^2)
AWG	Atmospheric Water Generator
a	Constant (-)
b	Constant (-)
$\dot{C}$	Heat capacity rate (W/K)
d	Diameter (m)
h	Specific enthalpy (J/kg)
$\dot{M}$	Mass flow rate (kg/s)
N	Speed (1/s)
NTU	Number of Transfer Units (-)
P	Pressure (Pa)
$\dot{Q}$	Heat flow (W)
RH	Relative humidity (-)
r	Ratio (-)
SEC	Specific Energy Consumption (kWh/L)
t	Temperature (°C)
U	Peripheral velocity (m/s)
UA	Overall heat transfer coefficient (W/K)
V	Volume (m^3)
$\dot{V}$	Volumetric flow rate (m^3/s)
VCR	Vapour Compression Refrigeration
v	Specific volume (m^3/kg)
$\dot{W}$	Power (W)

Special characters

Δ	Difference
ε	Effectiveness (-)
ϕ	Flow factor (-)
λ	Power factor (-)
τ	Time (s)
ω	Humidity ratio (kg/kg)
ψ	Pressure factor (-)

Subscripts

a	Humid air
ad	Adapted

amb	Ambient
c	Contact
cd	Condenser
cp	Compressor
dyn	Dynamic
ev	Evaporator
ex	Exhaust
fa	Fictitious air
HW	Harvested Water
in	Internal
$leak$	Leakage
min	Minimum
noz	Nozzle
r	Refrigerant
ref	Reference
s	Swept or Isentropic
sc	Subcooled
sh	Superheated
su	Supply
thr	Throat
tp	Two-phase
v	Volume
wb	Wet bulb
wl	Liquid water

1 Introduction

Nowadays, most of the freshwater for human consumption comes from rivers, lakes, and groundwater reservoirs [1]. However, these sources have been affected by indiscriminate human use, contamination, and climate change, affecting its availability and sanitation [2]. In this scenario, Chile is one of the most affected countries by the water scarcity crisis [3], in fact, by the end of 2021, 8.25 million people suffered freshwater rationing [4]. Sea water desalination comes up as the most promising alternative water source, nevertheless, brine production in the areas where these plants are installed is a threat to the biodiversity of the surroundings [5]. Isolated areas without piped distribution networks or water trucks will not be able to take advantage of this method [6].

According to this issue, atmospheric water seems as a good alternative, by accounting around $12.9 \cdot 10^{12}$ m^3 [7]. This has led the scientific community to seek new methods for harvesting water from the atmosphere. The existent atmospheric water harvesting methods can be classified into 4 groups: passive methods, active refrigeration methods, sorption methods, and hybrid technologies [8]. Among these, active refrigeration systems are the most used by manufacturers [9]–[15], because they allow greater water harvesting rates than passive methods, which only can operate during limited period of time during a day [16]. Nevertheless, this type of system needs electric power input to operate [17]. On the other hand, the sorption methods employ adsorption materials to collect water from the atmosphere [8], [18], which is then regenerated with thermal energy, such as solar energy, waste heat or heat generated by combustion. A more innovative and complex system corresponds to the hybrid/integrated system, combining two or more methods to increase the performance of one of them, such as desiccant wheels [19], [20], membranes [21], or a combination of both [22].

Since it is a well-developed technology, with several experimental investigations and a generalised use by Atmospheric Water Generator (AWG) manufacturers, this article will be focused on active refrigeration systems [9]–[15]. This technique uses either Vapour Compression Refrigeration (VCR) systems or Thermoelectric cooling systems [23] as a cold source to condense water by cooling the air below its dew point temperature [24]. These system have been studied by Zolfagharkani et al. [25] through numerical methods in some region of Iran, reaching a production rate near 24 L/day, with a Specific Energy Consumption (SEC) of 0.26 kWh/L. These systems do not present a good performance in dry climates [8], [22], [23], [26]. At these conditions, the efficiency decreases considerably due to the higher sensible heat that the evaporator must to remove, reducing the heat capacity of the system to remove the latent heat, which is directly proportional to the collected water [27].

In the same way, for some of these climatic conditions, the system is not able to operate since frosting occurs at the evaporator surface for temperatures lower than 4°C [23], [27]. This problem was highlighted by Raveesh et al. [28], who carried out several simulations in 30 Indian cities. In winter their system was limited by weather conditions, obtaining few operating hours, with low water harvesting rates. VCR systems present good performances in humid climates. The optimal environment condition for VCR systems is 35°C and 95% of relative humidity [26], which allows to harvest water without any problem of frosting.

In spite VCR systems are widely used in AWGs, there still exist a large gap of improvement in these systems, which can be addressed with a correct selection of the system components or integrating other technologies. Furthermore, operating limitations such as dew point temperatures below 4°C and the worst performance in dry climatic conditions continue to be a challenge. In this paper a VCR system is numerically modelled, by using a variable speed compressor and a variable speed axial fan. This combination generates more flexibility in the system operation, increasing the amount of collected water. The scope of this article is to address and to contribute on the understanding of the AWGs based on VCR systems through the evaluation of the performance of one of these systems working with two types of modulation: variable refrigerant mass flow rate and variable air mass flow rate.

2 Methods

2.1 Simulation conditions

Parametric analysis. A first analysis will be developed to identify the variables that can be controlled for the optimum performance of the system, such as, fan speed and compressor speed.

Annual simulation. A second analysis will be developed by considering two Chilean cities, in order to determine the monthly water harvested by the system considered in this study. The system is simulated throughout a typical meteorological year.

2.2 System design

The system is designed considering a basic VCR system, with an evaporator, a compressor, a condenser, and an expansion valve. These components and the connections are represented in Figure 1. The evaporator is used to remove the sensible and latent load from the air, which leads to condensation of the atmospheric water on its surface. The air exhausting the evaporator is conducted to the condenser where is heated and finally discharged to the ambient through an axial fan.

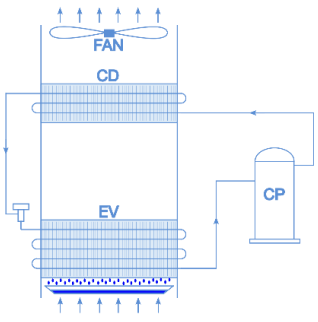


Figure 1: Schematic of the system.

The system is designed to collect around 150 L/day at an average air temperature of 20°C, relative humidity of 60% and atmospheric pressure of 1 atm. This condition was selected as a good compromise for the system size and because it is the average meteorological condition of the Chilean northern cities during the months that the system can operate more efficiently (higher water collection). For the design, the system is forced to operate at an air temperature of 6°C at the evaporator exhaust.

The system is sized with the mathematical model presented hereafter.

2.3 Mathematical modelling

The system model is decomposed into four modular models: variable speed scroll compressor, tube-and-fin air cooled condenser, tube-and-fin air-heated evaporator and variable speed axial fan, which are modelled by using a semi-empirical approach. The refrigerant considered in this study is R410A.

Compressor model. The scroll compressor is modelled in a similar way as proposed by Winandy et al. [29], but taking into account the internal leakages and the discharge check valve pressure drop. It is assumed that the compressor imposes the refrigerant mass flow rate circulating through the system and the refrigerant temperature at the compressor exhaust. Furthermore, the compressor model also allows to determine the compressor input power.

The refrigerant mass flow rate trapped by the compressor is determined with equations 1 and 2. It is divided into the refrigerant mass flow rate coming from the evaporator $\dot{M}_{r,su1,cp}$ and the compressor internal leakage $\dot{M}_{r,leak,cp}$. Finally, the refrigerant mass flow rate trapped by the compressor depends on the compressor swept volume and the compressor speed.

$$\dot{M}_{r,in,cp} = \dot{M}_{r,su1,cp} + \dot{M}_{r,leak,cp} \quad (1)$$

$$\dot{M}_{r,in,cp} = \frac{V_{s,cp} \cdot N_{cp}}{v_{r,su2,cp}} \quad (2)$$

The compressor input power is divided into the internal compression power and the compressor electromechanical losses, as indicated in equation 3. The internal compression takes into account an isentropic compression from *su*2 to *ad* and an isochoric compression from *ad* to *ex*3, as indicated in equation 4. The electromechanical losses are here assumed to follow the law indicated in equation 5.

$$\dot{W}_{cp} = \dot{W}_{in,cp} + \dot{W}_{loss,cp} \quad (3)$$

$$\dot{W}_{in,cp} = \dot{M}_{r,in,cp} \cdot \left[\left(h_{r,ad,cp} - h_{r,su2,cp}\right) + v_{r,ad,cp} \cdot \left(P_{r,ex3,cp} - P_{r,ad,cp}\right)\right] \quad (4)$$

$$\dot{W}_{loss,cp} = \dot{W}_{loss0,cp} + \dot{W}_{loss2,cp} \cdot \left(\frac{N_{cp}}{N_{ref,cp}}\right)^2 \quad (5)$$

The parameters of the compressor model are identified from the catalogue data of the Copeland compressor XPV0182 by considering 120 points. The model is able to predict the refrigerant mass flow rate, the refrigerant exhaust temperature and the compressor input power with Root Mean Square Errors of 4.0%, 4.7ºC and 6.8%, respectively. Then, the model is modified, by introducing the ambient loss, and it is verified with 1448 catalogue data, by predicting the refrigerant mass flow rate and the compressor input power with a Root Mean Square Errors of 3.2% and 6.1%, respectively. Table 1 presents the parameters identified for the model, with some description for the parameters not included in the equations presented previously.

Table 1: Parameters of the compressor model.

Parameter	Value	Description
$A_{thr,noz,cp}$	6.715×10^{-8} m^2	Leakage area
$d_{r,ex,cp}$	0.00285 m	Equivalent diameter of the exhaust valve
$r_{v,in,cp}$	1.987	Built-in volume ratio
$UA_{ex,ref,cp}$	0.0001 kW/K	Supply overall heat transfer coefficient
$UA_{su,ref,cp}$	3 kW/K	Exhaust overall heat transfer coefficient
$V_{s,cp}$	18.98 cm^3	Swept volume
$\dot{W}_{loss0,cp}$	0.1416 kW	Compressor electromechanical loss parameter
$\dot{W}_{loss2,cp}$	0.0306 kW	Compressor electromechanical loss parameter
$M_{r,ref,cp}$	0.098 kg/s	Reference mass flow rate
$N_{ref,cp}$	50 Hz	Reference compressor speed
$UA_{cp,amb}$	0.0053 kW/K	Ambient overall heat transfer coefficient

Condenser model. The condenser was modelled by using a three zones approach: superheated, two-phase, and subcooled, as proposed by Cuevas et al. [30]. Each zone is evaluated through two energy balances and one fluid-to-fluid heat transfer equation determined with the ε-NTU method, as indicated in equations 6 to 8 for the superheated zone.

$$\dot{Q}_{r,sh,cd} = \dot{M}_{r,cd} \cdot \left(h_{r,su,sh,cd} - h_{r,ex,sh,cd}\right) \quad (6)$$

$$\dot{Q}_{a,sh,cd} = \dot{M}_{a,cd} \cdot \left(h_{a,ex,sh,cd} - h_{a,su,sh,cd}\right) \quad (7)$$

$$\dot{Q}_{sh,cd} = \varepsilon_{sh,cd} \cdot \dot{C}_{min,sh,cd} \cdot \left(t_{r,su,sh,cd} - t_{a,su,sh,cd}\right) \quad (8)$$

The heat exchanger effectivenesses of the superheated and subcooled zones are determined by considering a counterflow configuration, but for the two-phase zone the effectiveness is determined with the equation proposed for phase change. The two-phase and subcooled zones are analysed in a similar way as presented for the superheated zone.

Evaporator model. The evaporator is modelled following the approach shown previously for the condenser. In this case it is divided into 2 zones: two-phase and superheated. The main difference in this heat exchanger is on the air side, because it is designed to condense the water from the atmospheric air. Here the assumption proposed by Braun [31] and the modelling approach proposed by Ding et al. [32] are used. Therefore, the heat flow of the cooling coil is defined as the maximum between the heat flow determined by assuming that the cooling coil works in a completely dry regime on the air side and the heat flow determined by assuming a completely wet regime.

The heat transfer in dry regime is determined as described for the condenser, but for the wet regime a fictitious moist air is defined, which is characterized through a fictitious heat capacity. In wet regime, the heat flow on the air side is determined as indicated in equations 9 and 10.

$$\dot{Q}_{a,wet,coil} = \dot{M}_{a,coil} \cdot \left(h_{a,su,wet,coil} - h_{a,ex,wet,coil}\right) - \dot{M}_{a,coil} \cdot \left(\omega_{a,su,wet,coil} - \omega_{a,ex,wet,coil}\right) \cdot h_{wl} \quad (9)$$

$$\dot{Q}_{a,wet,coil} = \dot{C}_{fa,wet,coil} \cdot \left(t_{wb,su,wet,coil} - t_{wb,ex,wet,coil}\right) \quad (10)$$

The fluid-to-fluid heat transfer is also determined with the ε-NTU method and with the same assumptions mentioned previously to determine the heat exchanger effectiveness.

In wet regime, the exhaust conditions of the air are determined as indicated in ASHRAE HVAC Systems and Equipment [33], by considering a constant surface temperature and by assuming that the air in contact with the heat exchanger surface is saturated. Thus, the air exhaust conditions are determined with equations 11 to 14.

$$h_{a,su,wet,coil} - h_{a,ex,wet,coil} = \varepsilon_{c,wet,coil} \cdot \left(h_{a,su,wet,coil} - h_{c,wet,coil}\right) \quad (11)$$

$$\omega_{a,su,wet,coil} - \omega_{a,ex,wet,coil} = \varepsilon_{c,wet,coil} \cdot \left(\omega_{a,su,wet,coil} - \omega_{c,wet,coil}\right) \quad (12)$$

$$\varepsilon_{c,wet,coil} = 1 - exp\left(-NTU_{c,wet,coil}\right) \quad (13)$$

$$NTU_{c,wet,coil} = \frac{1}{R_{a,coil} \cdot \dot{C}_{a,dry,coil}} \quad (14)$$

Table 2 summarizes the references used to determine the heat transfer coefficients on the air and on the refrigerant sides.

Table 2: References used to determine the heat transfer coefficients.

Refrigerant side	
Reference	Description
Incropera et al. [34]	Correlation used to determine the heat transfer coefficient in single phase and in laminar flow.
Gnielinski [35]	Correlation used to determine the heat transfer coefficient in single phase and in turbulent flow.
Thome et al. [36]	Correlation used to determine the condenser two-phase heat transfer coefficient.
Shah [37]	Correlation used to determine the evaporator two-phase heat transfer coefficient.
Air side	
Kays and London [38]	Correlation fitted from the curves presented in this reference.

Table 3 summarizes the methodology used to determine the pressures losses on the air and on the refrigerant sides.

Table 3: References used to determine the pressure losses.

Refrigerant side	
Reference	Description
Incropera et al. [34]	Correlation used to determine the friction factor in laminar and turbulent flow.
Friedel [39]	Correlation used to determine the friction factor in two phase flow for the evaporator and for the condenser.
Collier and Thome [40]	From this reference are obtained the equations used to determine the pressure variation due to the fluid acceleration.
Air side	
Kays and London [38]	The pressure drop includes the effect of the contraction, acceleration, friction and expansion, as suggested in the methodology of this reference. The correlation for the friction factor is fitted from the curves presented in this reference.

Fan model. The fan is modelled through 3 dimensionless factors: flow factor, pressure factor and power factor, which are defined in equations 15 to 17.

$$\phi_{fan} = \frac{\dot{V}_{a,fan}}{A_{fan} \cdot U_{fan}} \quad (15)$$

$$\psi_{fan} = \frac{\Delta P_{total,fan}}{P_{dyn,periph,fan}} \quad (16)$$

$$\lambda_{fan} = \frac{\phi_{fan} \cdot \psi_{fan}}{\varepsilon_{s,fan}} \quad (17)$$

Then, for the fan modelling one of these factors is defined as an independent variable, which is the pressure factor in this case, and the other two factors are determined through polynomials laws identified from the fan catalogue data.

$$\lambda_{fan} = a_0 + a_1 \cdot \psi_{fan} + a_2 \cdot \psi_{fan}^2 \quad (18)$$

$$\phi_{fan} = b_0 + b_1 \cdot \psi_{fan} + b_2 \cdot \psi_{fan}^2 \quad (19)$$

The constants of the polynomial laws are identified with the catalogue data of the axial fan W3G-400 of the manufacturer ebmpapst. The power factor allows

to determine the fan isentropic effectiveness, then the actual fan power is determined as:

$$\dot{W}_{fan} = \frac{\dot{W}_{s,fan}}{\varepsilon_{s,fan}} \quad (20)$$

Where the isentropic fan power is determined with the air volumetric flow rate and the total pressure drop on the air side:

$$\dot{W}_{s,fan} = \dot{V}_{a,fan} \cdot \left(\Delta P_{a,cd} + \Delta P_{a,ev}\right) \quad (21)$$

Integrated system model. Every model is interconnected with the other models to define the overall system model. Figure 2 presents the interconnections between each model, by showing the inputs and outputs of the overall model. For the system model, the black variables represent the model inputs, the red variables must be verified to avoid any working condition outside the equipment domain and the other variables are used for analysis or for the connection between the different equipment.

Heat exchanger sizing. The condenser and the evaporator are sized to collect 150 litres per day at 20ºC and 60% of relative humidity. Both are also sized to introduce a total pressure drop on the air side lower than 150 Pa at the maximum air flow rate. Another considered parameter was the compressor pressure ratio, which was considered higher than 2 for any working condition.

With these constraints, among others, the obtained condenser and evaporator sizes are the one presented in Table 4.

Table 4: Heat exchanger dimensions.

Variable	Condenser	Evaporator
Tube external diameter	9.53 mm (3/8")	9.53 mm (3/8")
Tube thickness	0.81 mm	0.81 mm
Longitudinal pitch	21 mm	21 mm
Transverse pitch	25 mm	25 mm
Number of rows	3	5
Number of circuits	2	3
Number of tubes per circuit and per row	10	6
Fin thickness	0.3 mm	0.3 mm
Fin pitch	2 mm	2.5 mm
Heat exchanger height	0.500 m	0.450 m
Heat exchanger depth	0.063 m	0.105 m
Heat exchanger width	0.714 m	0.643 m
Total number of tubes	60	90

For the annual simulations, two monthly indicators are determined with the results of the modelling: the monthly harvested water and the monthly Specific Energy Consumption, as defined in equations 20 and 21.

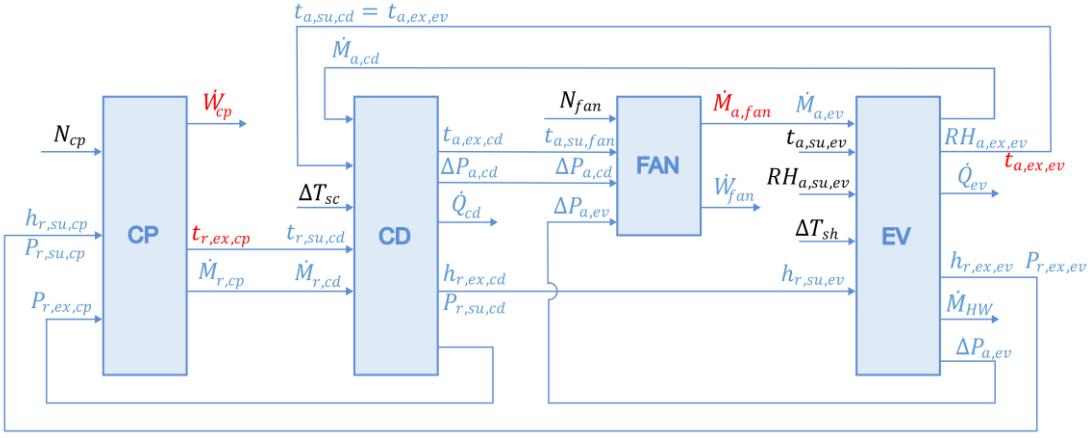


Figure 2: Principle of the system modelling.

$$V_{HW} = \int_0^{\tau_{final}} \dot{V}_{HW} \cdot d\tau \quad (20)$$

$$SEC = \int_0^{\tau_{final}} \frac{\left(\dot{W}_{cp} + \dot{W}_{fan}\right)}{\dot{V}_{HW}} \cdot d\tau \quad (21)$$

Simulation constraints. The constraints in the operation of the system are: compressor speed between 15 Hz and 120 Hz, maximum compressor input power of 3.6 kW and air mass flow rate between 0.14 kg/s and 0.7 kg/s. When the working conditions are outside of these limits, the system is forced to work within these safe conditions by modifying the compressor speed or axial fan speed in order to modulate the refrigerant mass flow rate or the air mass flow rate.

3 Results and discussion

3.1 Parametric analysis

As the harvested water depends on the air mass flow rate circulating through the evaporator and humidity ratio at the evaporator exhaust, which in turn depends on the air conditions at the evaporator exhaust, a parametric analysis is developed to determine the effect of the air temperature at the evaporator exhaust, which is here modified by controlling the axial fan speed. Figures 3, 4 and 5 present the results obtained for different air temperatures at the evaporator exhaust at different ambient temperatures (20ºC, 25ºC and 30ºC) and relative humidities (from 20% to 100%). This study does not consider relative humidities lower than 20% due to the poor performance of the system and due to frosting formation.

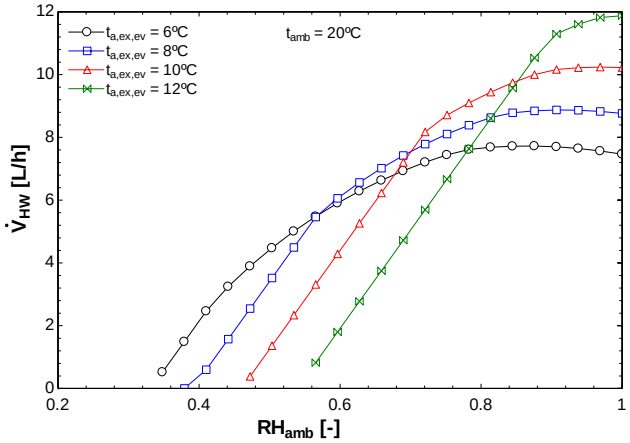


Figure 3: Harvested water for an ambient temperature of 20ºC and different relative humidities.

It is observed that to maximize the harvested water is recommendable to use variable air temperature at the evaporator exhaust (variable air mass flow rate). This trend is more important at high ambient temperatures than at low temperatures.

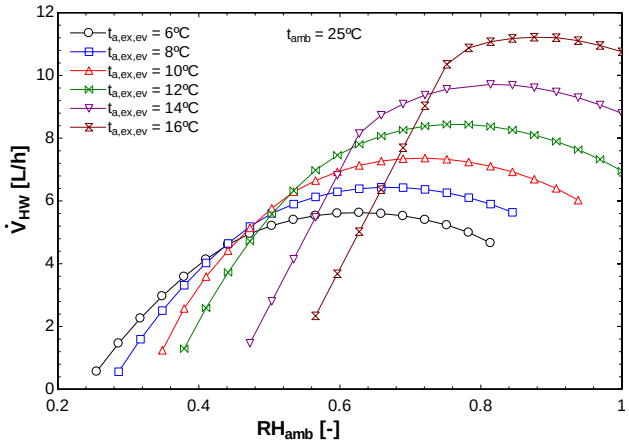


Figure 4: Harvested water for an ambient temperature of 25ºC and different relative humidities.

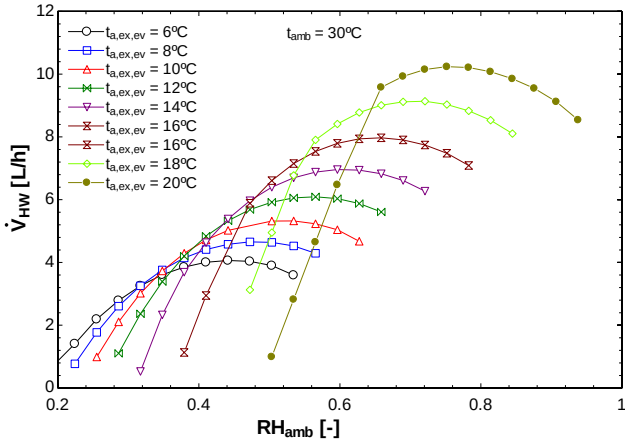


Figure 5: Harvested water for an ambient temperature of 30ºC and different relative humidities.

For example, for ambient temperatures of 20ºC, the improvement in the water harvested is only observable at high relative humidities, from 80% upwards. On the other hand, for an ambient temperature of 30ºC, the improvement in the water harvested begins from a relative humidity of 45%.

It is also observed that, for a given ambient temperature, the maximum harvested water depends on the air temperature at the evaporator exhaust and the relative humidity.

3.2 Annual harvested water

Another study developed consists in an annual simulation of the system, but considering a constant air temperature at the evaporator exhaust. In this case a temperature of 6ºC was considered. Two Chilean cities with problems of water scarcity are selected: Copiapó and Petorca. In order to simplify the

simulation of the system, the weather conditions are classified by using the BIN method, using the wet bulb temperature as reference.

Figure 6 presents the monthly harvested water for a Typical Meteorological Year (TMY). As expected, the system collects more water during summer and in some months of autumn and spring. During July the water harvested decreases down to 36 litres per day in the case of Petorca city.

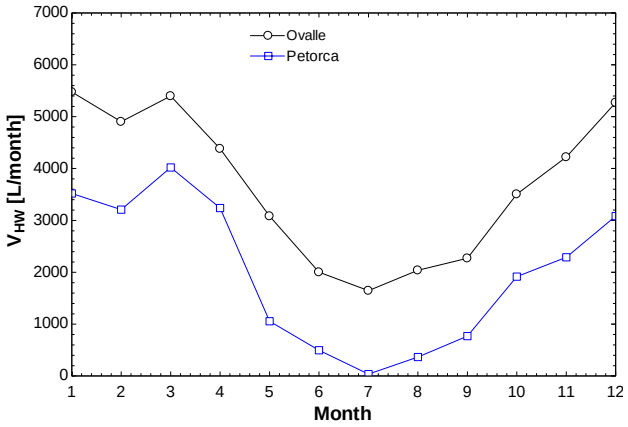


Figure 6: Monthly collected water.

Another important indicator is the Specific Energy Consumption, which is presented in Figure 7. A lower SEC indicates a more performant system in terms of energy consumption per litres of harvested water. In this case, Petorca presents the better SECs values during summer. In both cities, this indicator varies between 0.37 kWh/L and 1.05 kWh/L.

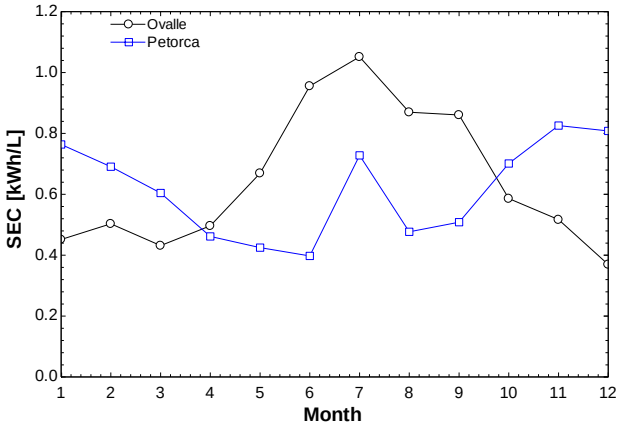


Figure 7: Monthly Specific Energy Consumption.

The values obtained for the SEC are within the values presented in the literature and could be improved by implementing a control with a variable air temperature at the evaporator exhaust in order to maximize the harvested water.

Concerning the operating hours, in Copiapó the system operates 8514 hours (97%) and in Petorca 6121 hours (70%). The main reason of the non-operating hours is the low temperature of the ambient air, since at dew point temperatures lower than 6ºC frosting appears on the evaporator surface.

4 Conclusions

This paper presents the results of the simulation of an atmospheric water harvesting system based on a vapour compression refrigeration system. The system is studied through a parametric analysis and considering the climate conditions of two Chilean cities. The system analysed was designed to produce 150 L/day under ambient conditions of 20ºC and 60% of relative humidity. From the parametric analysis, the following conclusions are obtained:

- The amount of the harvested water depends not only on the weather conditions but also on the operating conditions of the refrigeration system and its control.
- One of the variables affecting the amount of collected water is the air temperature settled at the evaporator exhaust (depending on the air mass flow rate), which must be adjusted in function of the weather conditions to maximize the harvested water.
- In general, the higher the ambient temperatures, the higher the required air temperature at the evaporator exhaust to maximize the collected water.

From the simulations of two Chilean cities the following conclusions are obtained:

- The results of the simulations of the cities present a marked seasonal dependence, with a higher water production in summer and in some months of autumn and spring. In winter the water production decreases due to the lower temperatures, which produces some problems of frosting on the evaporator surface.
- Concerning the water production, the maximum water collected was 5477 litres for January in the city of Copiapó and the lower 36 litres during July in the city of Petorca.
- In terms of the energetic indicator, the SEC obtained for both simulations vary between 0.37 kWh/L and 1.05 kWh/L. These values are similar to the ones obtained by other authors and could be improved by implementing a control with a variable air temperature at the evaporator exhaust.

Acknowledgement

This work was funded by the ANID FONDEF ID22I10051.

References

[1] United Nations, Summary Progress Update 2021: SDG 6 — water and sanitation for all, 2021. [Online]. Available: https://www.unwater.org/publications/summary-progress-update-2021-sdg-6-water-and-sanitation-all

[2] World Meteorological Organization, WMO Statement on the State of the Global Climate in 2019, 2020. Accessed: Aug. 09, 2023. [Online]. Available: https://library.wmo.int/doc_num.php?explnum_id=11108

[3] Water Resource Institute, Aqueduct Water Risk Atlas. https://www.wri.org/applications/aqueduct/water-risk-atlas/#/?advanced=false&basemap=hydro&indicator=w_awr_def_tot_cat&lat=50.84757295365389&lng=-22.148437500000004&mapMode=view&month=1&opacity=0.5&ponderation=DEF&predefined=false&projection=absolute&scenario=optimistic&scope=baseline&threshold&timeScale=annual&year=baseline&zoom=2 (accessed Aug. 09, 2023)

[4] R. Alvarado, Chile lidera la crisis hídrica en América Latina, 2022. https://uchile.cl/noticias/184816/dia-mundial-del-agua-chile-lidera-la-crisis-hidrica-en-america-latina (accessed Aug. 09, 2023).

[5] A. Alvez, D. Aitken, D. Rivera, M. Vergara, N. McIntyre, and F. Concha, At the crossroads: can desalination be a suitable public policy solution to address water scarcity in Chile's mining zones?, J Environ Manage, vol. 258, p. 110039, Mar. 2020, doi: 10.1016/j.jenvman.2019.110039

[6] Y. Zhou and R. S. J. Tol, Evaluating the costs of desalination and water transport, Water Resour Res, vol. 41, no. 3, pp. 1–10, Mar. 2005, doi: 10.1029/2004WR003749

[7] I. Al Keyyam, M. Al-Nimr, S. Khashan, and A. Keewan, A new solar atmospheric water harvesting integrated system using CPV/T – Stirling engine – Absorption cooling cycle and vapor compression refrigeration cycle, Int J Energy Res, vol. 45, no. 11, pp. 16400–16417, Sep. 2021, doi: 10.1002/ER.6888

[8] G. Raveesh, R. Goyal, and S. K. Tyagi, Advances in atmospheric water generation technologies, Energy Convers Manag, vol. 239, p. 114226, Jul. 2021, doi: 10.1016/j.enconman.2021.114226

[9] Aeronero, Thunder, Atmospheric Water Generator Aeronero. https://aeronero.life/product/thunder (accessed Jul. 11, 2023).

[10] Watergen, M1 | Water from Air Generator | Watergen. https://www.watergen.com/commercial/gen-m1/ (accessed Oct. 19, 2022)

[11] RainofLife, RoL 50 AWG specifications. Jul. 2023. [Online]. Available: https://rainoflife.com/en/rol50/

[12] Veragon, Air To Water Products. https://veragon.com/products/ (accessed Jul. 11, 2023).

[13] Hendrx, HR-90HK. https://www.hendrxwater.com/product/17.html (accessed Jul. 11, 2023)

[14] Atlantis Solar, Atlantis Solar. https://www.atlantissolar.com/atlantis_h2o_elite.html (accessed Jul. 11, 2023)

[15] T. Products, Tsunami Products - Atmospheric Water Generators. 2023. [Online]. Available: https://www.tsunamiproducts.com/products

[16] H. Jarimi, R. Powell, and S. Riffat, Review of sustainable methods for atmospheric water harvesting, International Journal of Low-Carbon Technologies, vol. 15, no. 2. Oxford University Press, pp. 253–276, May 01, 2020. doi: 10.1093/ijlct/ctz072

[17] H. Nikkhah et al., A comprehensive review on atmospheric water harvesting technologies: From thermodynamic concepts to mechanism and process development, Journal of Water Process Engineering, vol. 53, p. 103728, Jul. 2023, doi: 10.1016/j.jwpe.2023.103728

[18] D. Ybyraiymkul et al., Innovative solid desiccant dehumidification using distributed microwaves, Sci Rep, vol. 13, no. 1, Dec. 2023, doi: 10.1038/s41598-023-34542-9

[19] A. Heidari, R. Roshandel, and V. Vakiloroaya, An innovative solar assisted desiccant-based evaporative cooling system for co-production of water and cooling in hot and humid climates, Energy Convers Manag, vol. 185, pp. 396–409, Apr. 2019, doi: 10.1016/j.enconman.2019.02.015

[20] R. Tu and Y. Hwang, Performance analyses of a new system for water harvesting from moist air that combines multi-stage desiccant wheels and vapor compression cycles, Energy Convers

Manag, vol. 198, p. 111811, Oct. 2019, doi: 10.1016/j.enconman.2019.111811
[21] W. Wang, S. Xie, Q. Pan, Y. Dai, R. Wang, and T. Ge, Air-cooled adsorption-based device for harvesting water from island air, Renewable and Sustainable Energy Reviews, vol. 141, p. 110802, May 2021, doi: 10.1016/J.RSER.2021.110802
[22] A. Cendoya, C. Cuevas, and E. Wagemann, Numerical Evaluation of a Hybrid Atmospheric Water Harvesting System for Human Consumption, Journal of Water Process Engineering, Volume 56, December 2023, 104464. doi: 10.1016/j.jwpe.2023.104464
[23] H. Nikkhah et al., A comprehensive review on atmospheric water harvesting technologies: From thermodynamic concepts to mechanism and process development, Journal of Water Process Engineering, vol. 53. Elsevier Ltd, Jul. 01, 2023. doi: 10.1016/j.jwpe.2023.103728
[24] L. Cattani, P. Cattani, and A. Magrini, Air to Water Generator Integrated System Real Application: A Study Case in a Worker Village in United Arab Emirates, Applied Sciences (Switzerland), vol. 13, no. 5, Mar. 2023, doi: 10.3390/app13053094
[25] S. Zolfagharkhani, M. Zamen, and M. M. Shahmardan, Thermodynamic analysis and evaluation of a gas compression refrigeration cycle for fresh water production from atmospheric air, Energy Convers Manag, vol. 170, pp. 97–107, Aug. 2018, doi: 10.1016/J.ENCONMAN.2018.05.016
[26] J. Patel, K. Patel, A. Mudgal, H. Panchal, and K. K. Sadasivuni, Experimental investigations of atmospheric water extraction device under different climatic conditions, Sustainable Energy Technologies and Assessments, vol. 38, p. 100677, Apr. 2020, doi: 10.1016/J.SETA.2020.100677
[27] B. Gido, E. Friedler, and D. M. Broday, Assessment of atmospheric moisture harvesting by direct cooling, Atmos Res, vol. 182, pp. 156–162, Dec. 2016, doi: 10.1016/J.ATMOSRES.2016.07.029
[28] G. Raveesh, R. Goyal, and S. K. Tyagi, Parametric analysis of atmospheric water generation system and its viability in Indian cities, Thermal Science and Engineering Progress, vol. 39, Mar. 2023, doi: 10.1016/j.tsep.2023.101682
[29] E. Winandy, C. Saavedra, and J. Lebrun, Experimental analysis and simplified modelling of a hermetic scroll refrigeration compressor, Appl Therm Eng, vol. 22, no. 2, pp. 107–120, Feb. 2002.
[30] C. Cuevas, J. Lebrun, V. Lemort, and P. Ngendakumana, Development and validation of a condenser three zones model, Appl Therm Eng, vol. 29, no. 17, pp. 3542–3551, 2009, doi: https://doi.org/10.1016/j.applthermaleng.2009.06.007
[31] J. Braun, S. Klein, and J. Mitchell, Effectiveness models for cooling towers and cooling coils, ASHRAE Transactions (American Society of Heating, Refrigerating and Air-Conditioning Engineers), vol. 95, no. 2, Jan. 1989
[32] X. Ding, J. Eppe, J. Lebrun, and M. Wasacz, Cooling Coil Models to be used in Transient and/or Wet Regimes. Theoretical Analysis and Experimental Evaluation, in Proceedings of the third international conference on System Simulation in Buildings, Liege, 1990.
[33] ASHRAE Handbook: HVAC Systems and Equipment. Atlanta, American Society of Heating, Refrigerating and Air-Conditioning Engineers, 2016.
[34] F. Incropera, T. Bergman, A. Lavine, and D. Dewitt, Fundamentals of Heat and Mass Transfer, 7th ed. Hoboken: John Wiley & Sons, 2011
[35] V. Gnielinski, Ein neues Berechnungsverfahren für die Wärmeübertragung im Übergangsbereich zwischen laminarer und turbulenter Rohrströmung, Forsch Ingenieurwes, vol. 61, no. 9, pp. 240–248, Sep. 1995, doi: 10.1007/BF02607964
[36] J. R. Thome, J. El Hajal, and A. Cavallini, Condensation in horizontal tubes, part 2: new heat transfer model based on flow regimes, Int J Heat Mass Transf, vol. 46, no. 18, pp. 3365–3387, Aug. 2003, doi: 10.1016/S0017-9310(03)00140-6
[37] M. M. Shah, Chart correlation for saturated boiling heat transfer: equations and further study, ASHRAE Trans, vol. 88, no. 1, pp. 185–196, 1982.
[38] W. M. Kays and A. L. London, Compact Heat Exchangers. New York: McGraw-Hill, 1955.
[39] L. Friedel, Improved friction pressure drop correlations for horizontal and vertical two-phase pipe flow, in European Two-phase Group Meeting, Ispra, Italy, 1979, pp. 485–492.
[40] J. G. Collier, J.R. Thome. Convective boiling and condensation, 3rd Edition, Oxford University Press, New York (1994).

A NOVEL HEAT PUMP CYCLE DESIGN FOR VERY COLD WEATHER DISTRICT HEATING

Wissam Rached[1]*, Nitin Karwa[2], Simon Lintu[3]

[1] Honeywell, Energy & Sustainability Solutions, Dublin, Ireland

[2] Honeywell Buffalo Research Laboratory, 20 Peabody Street, Buffalo, USA

[3] Fortum Power and Heat Oy, Espoo, Finland

* *Corresponding Author:* wissam.rached@honeywell.com

Abstract. District heating (DH) provides around 12% of the residential and commercial heat in the EU, with about 70% of it being generated from fossil fuels. It is crucial to prioritize the replacement of fossil fuel-fired boilers in district heating as part of the decarbonization process. There is a consensus within the energy sector that integrating emission-neutral electricity with heat pumps can significantly contribute to decarbonizing Europe. Existing district heating networks have several thousand kilometers of pipes installed, and the supply water temperature can be as high as 115 °C in Nordic countries and Eastern Europe (Poland). The analysis of thermodynamic cycles for heat pumps indicates the potential for developing heat pumps capable of replacing boilers for very high-temperature heat, offering economic and ecological benefits. A partial cascade system with deep subcooling has been identified as the best configuration due to its high efficiency, low cost, and component availability.

Keywords. District heating, very cold weather, heat pump, high temperature, best configuration, fluids.

1 Introduction

Decarbonization policy in Europe encourages replacing gas boilers with heat pumps [1]. According to Connolly et al. [2], existing urban district heating capacity for heating and domestic hot water totals more than 250 TWh/year. Connolly et al. [2] concluded that a considerable reduction in fossil fuel consumption and carbon dioxide emission can be achieved if the district heating networks are widely used in European cities. David et al. [3] show that heat pumps are already part of district heating sources in several European countries. For example, significant installed capacities have existed in Sweden since the 1980's with most of the installed capacities delivering hot water at temperatures up to 90 °C. They mention the temperature lifts and COPs of existing capacities. The maximum temperature lift is 80 °C with COP close to 3.

Arpagaus et al. [4] reviewed the current state-of-the-art high-temperature heat pumps (HTHPs) with heat sink temperatures in the range of 90 to 160 °C. More than 20 HTHPs from 13 manufacturers have been identified on the market that can provide heat sink temperatures of at least 90 °C. Bergamini et al. [5] compared the thermodynamic performance of various High-Temperature Heat Pumps (HTHP) based on a vapor compression cycle using water, ammonia, propane, and isobutane with natural gas boilers to assess their technical feasibility and competitiveness as future replacements. First-law and second-law thermodynamic analyses were performed for single-stage, two-stage, and cascade architectures. They concluded that HTHP can competitively replace gas boilers in delivering heat of up to 180 °C with temperature lifts of up to 160 °C, and two-stage cycles were able to achieve the highest efficiencies. Robinson et al. [6] discussed the design and optimization of turbo compressors using computational fluid dynamic and finite element mechanical analysis techniques. They show that compressor polytropic efficiency values higher than 80% can be achieved by optimizing the design for the refrigerant and the operating conditions. Jaatinen-ärri et al. [7] combined the analyses of a 500 kW two-stage heat pump cycle and centrifugal compressor designs. The study qualitatively assesses the impact of refrigerant (hydrocarbons and hydrofluoroolefins) and operating conditions (temperature lift and evaporation temperature) on the compressor dimensions and rotational speed, and its isentropic efficiency. The study concluded that high-temperature heat pump equipment could be feasible for heat pump temperature lifts of around 100 °C. The study shows that the R1233zd(E) compressor operates at a lower rotational speed and Mach number with a smaller impeller diameter than the pentane compressor. This simplifies the R1233zd(E) compressor design and reduces its overall size.

R1233zd(E) and isopentane compressors can achieve isentropic efficiencies between 78 to 83%. The isentropic efficiency depends on the temperature lift.

While high-temperature heat pump cycles have been studied by previous researchers, district heating systems demand high flexibility of operation in areas that have very cold winters. Figure 1 shows the bin temperature data for Helsinki showing that 4% of the occurred hours are at temperatures lower than -10°C. During such periods, there is increased heat demand and thermal losses in the piping network, the supply temperature must be raised to up to 115 °C. A higher supply temperature doesn't have a significant impact on the heat generation efficiency of both gas and electrical boilers.

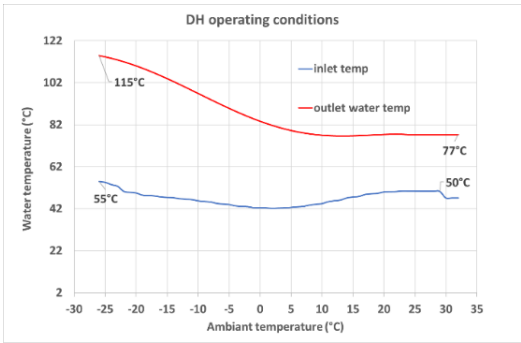


Figure 1: Temperature occurrence by hours and required water temperature rise as a function of the ambient temperature

Reducing the circulating water flow rate in a district heating pipes network allows the use of smaller pipe diameters and delivers the required heating capacity to more end users.

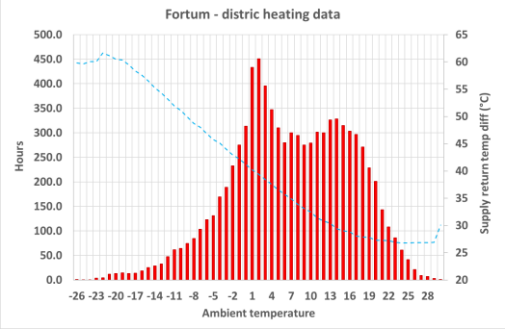


Figure 2: Delivered water and average return water temperatures from the district heating network

However, the need for an increase in heat generation coupled with an increase in supply temperature complicates the design of heat pump systems. The most basic setup would involve a heat pump to consistently generate hot water up to 90 °C and, as needed, operate a booster gas or electric boiler to further heat the water to the desired temperature. There are a few practical challenges with this architecture. Firstly, using both heat pumps and boilers increases the capital investment and maintenance cost. Secondly, the higher heating demand and hot water temperature needs during low ambient induces in some cases a peak demand on electricity networks when the electricity is most expensive. Similarly, gas or electricity prices are also high during extreme winter.

It is technically challenging to economically achieve a water temperature rise of up to 80 °C and a hot water supply temperature of up to 115 °C with a standard single-stage heat pump compared to the combination of a heat pump and an electrical boiler. The same heat pump must be capable of delivering hot water at 77 °C (Fig. 1) in summers with a temperature lift of less than 30 °C (Fig. 2). Mateu-Royo et al. [8] analyzed several advanced high-temperature heat pump configurations with several low GWP refrigerants for industrial waste heat recovery. Configurations like single-stage cycle with economizer, single-stage with ejector, and two-stage cycle with either an economizer or a flash tank perform less when applied to the discussed district heating network (Figure 2). The heat pump cycle needs to adjust for variations in the demanded water temperature and be able to deliver heat at variable temperature lifts. Configurations with an economizer, a flash tank, or an ejector are less beneficial when there is a possibility to achieve high subcooling by exchanging heat with the district heating water return flow.

This paper analyses the impact of cycle architecture, especially the ones with deep subcooling, and the choice of refrigerant on the investment and operational costs of high-temperature district heating heat pumps designed for year-round operation with cold to very cold winters and mild summers, such as Nordic countries and central Europe.

2 Refrigerants selection

Table 1 lists the refrigerants selected for this assessment. These refrigerants are employed within district heating infrastructures.

Table 1: Properties of selected fluids.

Refrigerant	Normal boiling point (°C)	Critical temperature (°C)	Critical pressure (MPa)	ASHRAE Classification
Ammonia	-33.3	132.2	11.3	B2L
R1234ze(E)	-18.9	109.3	3.6	A2L
Isobutane	-11.7	134.6	3.6	A3
Butane	-0.5	151.9	3.8	A3
R1233zd(E)	18.3	165.6	3.6	A1

3 **Heat pump advanced cycle configurations**

For district heating heat pump systems operating in extremely cold climates, cycle configuration needs to be adjusted according to the district heating demands. For this reason, the following cycle configurations are selected to investigate their potential for this application (Figures 3 to 7).

Configurations (A): The reference design (A) is a single-stage cycle heat pump with very high (deep) subcooling and an electrical boiler. During moderate winters and summers, the heat pump can meet the heating demand. However, in cold ambient periods, the heat pump cannot deliver hot water at the required supply temperature.

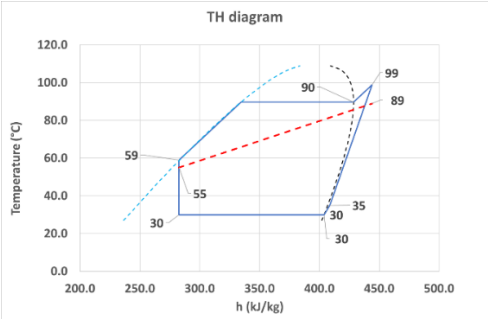


Figure 3: A - Single-stage cycle with deep subcooling

The electrical boiler is used to heat the water to the supply temperature of up to 115 °C. Table 2 summarizes the maximum supply temperatures for each working fluid.

Table 2: Properties of selected fluids and maximum water supply for single-stage cycle

Fluid	R1234ze	NH3	Isobutane	Butane	R1233zd(E)
Critical T (°C)	109	132	134	151.9	165.6
Maximum water supply temperature (°C)	89	92	115	115	115

Configurations (B): Single-stage transcritical cycle. This configuration allows the refrigerant pressure at the compressor outlet to exceed its critical pressure and provide high water temperature when required. Deep subcooling is also used at subcritical conditions to increase COP. For this configuration, the same single-stage unit can cover the complete range of supply temperature, and the electrical boiler can be eliminated. The selected fluids should have a critical temperature lower than 115 °C to achieve supercritical conditions. If the fluid critical temperature is higher than 115 °C, the system will operate at subcritical conditions.

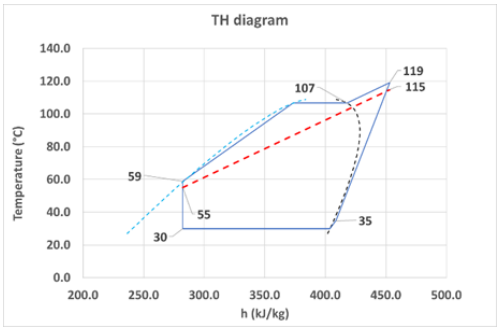


Figure 4: B - Supercritical cycle at high temperature with deep subcooling

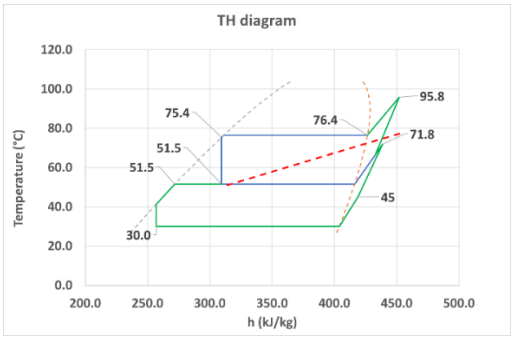


Figure 5: C - Two-stage cycle

Configurations (C): Two-stage cycle with a flash tank: This configuration allows cycles with higher pressure ratios and is an improvement over the single-stage cycle. After the first expansion, a flash tank allows vapor phase recovery and injection between the two compressors. The remaining subcooled liquid in the flash tank is expanded to the evaporator. This configuration can deliver hot water at high temperatures depending on the selected refrigerant. The electrical boiler is used, if needed, to increase water temperature up to 115 °C during very cold ambient temperatures.

Configurations (D): Cascade cycle with deep subcooling: The purpose of this cycle is to cover the production of water at very high temperatures by using two different fluids. The first stage will achieve a maximum temperature increase up to 90 °C and the second stage will deliver on-demand hot water up to 115 °C for DH.

Water is used for both stages to subcool the refrigerant at the condenser's outlets. Suction superheat in the high-stage cycle is achieved by using either an internal heat exchanger within the high-stage cycle or by exchanging heat with the hot discharge vapor of the low-stage cycle.

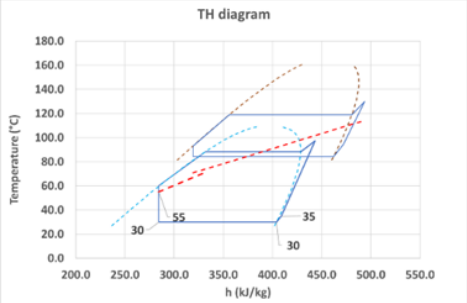


Figure 1: D - Cascade cycle with deep subcooling

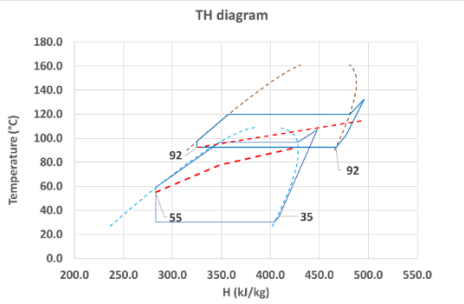


Figure 2: E - Partial cascade cycle with deep subcooling

Configurations (E): Partial cascade cycle with deep subcooling: This configuration uses two cascaded loops, but the high-stage system only partially recovers heat from the low-stage loop. The cascade condenser only partially condenses the refrigerant of the low-stage cycle, and the condensation is completed by heating the DH water. After condensation, the refrigerant is further subcooled by preheating the DH water return flow. The DH water flow is further heated by the high-stage loop. Deep subcooling can be achieved in the high-stage cycle. Like configuration D, an additional suction line heat exchanger is provided in the high-stage cycle.

4 **Modelling details**

The simulation results of the advanced cycle configurations (Figures 3 to 7) are based on thermodynamic calculations with COP optimization. The evaporator operating conditions are fixed for all the cycles. The condensing temperature is calculated as a function of the water inlet/outlet temperature, cycle limitations, fixed temperature pinch through heat exchangers, and COP optimization.

The heat exchanger approach (HEA) is the minimum temperature difference between the refrigerant flow and water flow through the heat exchanger. The HEA is assumed equal to 4 °C for all heat exchangers and all configurations.

At the heat source level, evaporator superheat is equal to 5 °C, and condenser subcooling is equal to 1 °C for all configurations. Configuration D and E use heat exchangers between first-stage discharge and second-stage suction to superheat the second-stage fluid and prevent wet compression and compressor damage.

In a single-stage cycle with deep subcooling, configuration A (Figure 3), initially, the saturated vapor condensing temperature value is assumed to be higher than the water outlet temperature. For each condensing saturated vapor temperature, iterations on compressor capacity are done to match the fixed pinch point temperature difference between the condensing saturated vapor temperature and water temperature. Multiple iterations of the condensing temperature deliver the target water exit temperature to the DH network.

In the supercritical cycle at high temperature and deep subcooling, configuration B (Figure 4), the minimum condenser pinch temperature is fixed as input. Iteration was done on condenser/cooler pressure to get the right pinch value between the two temperature profiles.

In a two-stage cycle with a flash tank, configuration C (Figure 5), the mid pressure is calculated as a function of the evaporating and condensing pressures. The condensing temperature is used for pinch minimization between the refrigerant and water flows. The pinch loop calculations are repeated up to calculation convergence.

In the cascade cycle with deep subcooling, configuration D (Figure 6), The low-stage condensation temperature is used for COP optimization. For each low-stage condensation temperature, iteration on the cooling capacity needed for the high-stage converges when the outlet water temperature matches the fixed outlet water demand. For each low-stage condensing temperature and high-stage cooling capacity, iterations are done on the low-stage compressor displacement to match the heating capacity to the high-stage demand.

In partial cascade cycle with deep subcooling, configuration E (Figure 7), The low-stage condensation temperature is used for COP optimization. For each condensation temperature, iteration on the heating capacity needed for the second stage converges when the outlet water temperature matches the fixed outlet water demand. The lowest-level iterations are on the first stage compressor capacity used for temperature pinch matching through the condenser.

5 Compressor types and performances

Compressors have a major impact on heat pump performances. Not only nominal or design heat pump operating conditions should be considered but also the whole annual operating conditions function of the outside ambient temperature. In this study, the pressure ratio and compressor rotating speed are reviewed for different compressor types to understand their impact on the compressor and heat pump's annual efficiency.

According to each cycle configuration, the pressure ratio across the compressors will vary between very low to very high-pressure ratios as the ambient temperature varies. Heating demand is also a function of the outside temperature, e.g., during summer temperatures, heat demand is lowest, and compressors need to either frequently start and stop or run at reduced speed. The water temperature rise is a function of the ambient temperature in the district heating systems. Figure 1 shows that the required water temperature rise increases from a low of 25 °C in the summer to as high as 60 °C on the coldest winter days. Consequently, good compressor efficiency over a large range of pressure ratios and heating power demands is highly desired.

While there is an interest in using centrifugal compressors for heat pump applications, they may not be suitable when very high-pressure lift, such as in supercritical configurations. Also, published performance data of centrifugal compressors are scarce, this paper will focus on piston and screw compressors only.

5.1 Compressor models

For compressor modelling, the focus is on real compressor power consumption versus isentropic compression. The compressor efficiency is defined as the ratio of isentropic enthalpy difference between discharge and suction over the real compressor electricity consumption. The real compressor electricity consumption is assumed to be equal to the product of the real enthalpy difference between discharge and suction and the mass flow rate.

To calculate compressor efficiency, the manufacturer's polynomial compressor equations are used inside an iterative routine function of the compressor efficiency. Calculated efficiency is plotted as a function of the pressure ratio for different compressor speeds.

Figures 8 and 9 show respectively piston and screw compressor performance curves using R-1234ze(E) refrigerant with an operating envelope suitable for heat pumps up to 90°C.

5.2 Compressor Speed and Pressure Ratio

For the specific piston compressor (Fig. 8), reducing compressor speed helps to increase the efficiency. The efficiency at all pressure ratios is higher at a speed of 25Hz (green dots) than at 55Hz (red dots).

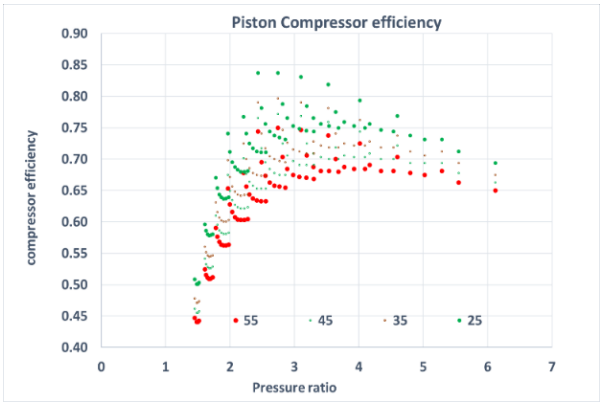


Figure 3: R1234ze(E) Piston compressor efficiency plotted function of pressure ratio and compressor rotating frequency

For the specific screw compressor (Fig. 9), reducing compressor speed decreases the compressor efficiency. The highest efficiency is achieved at a pressure ratio of around 2.5 for displacement between 350-175 m3/h. Speed reduction from 700 m3/h to 175 m3/h reduces the maximum efficiency value by 40%.

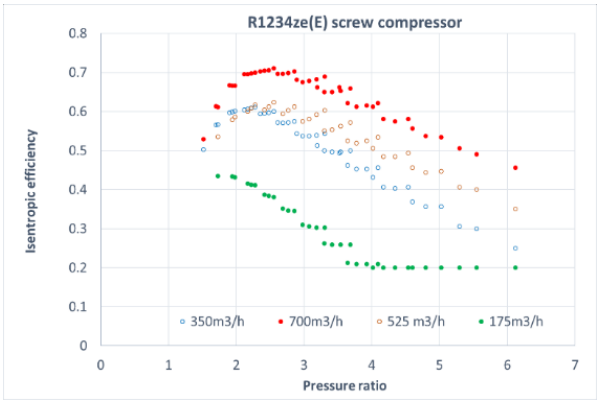


Figure 4: R1234ze(E) Screw compressor efficiency plotted function of pressure ratio and compressor displacement

The compressor efficiency is also impacted by the pressure ratio between the discharge and the suction pressure (Fig 8 and 9).

5.3 Compressor efficiency equation

For the cycle configurations used in this study, we selected a piston compressor efficiency trend curve function of pressure ratio. This curve will be used with all the configurations and all the refrigerants. This scenario is used because there is no available compressor (in manufacturer compressor selection software) suitable for the selected cycle configurations and refrigerants. Also, the impact of speed variation is excluded when executing configuration comparison for the same reason.

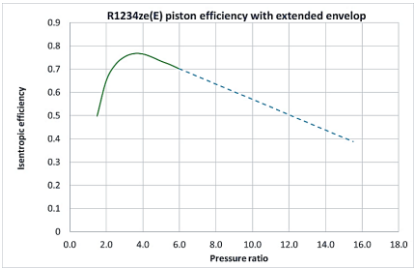


Figure 5: Piston efficiency at a fixed speed

Compressor volumetric efficiency is assumed to be equal to the ratio of mass flow rate over the product of compressor displacement and the suction density. Compressor displacement and mass flow rate are calculated using compressor manufacturer data. Suction density is calculated as a function of the operating conditions. Calculated volumetric efficiency values are fitted with a linear equation function of the pressure ratio.

6 Results and discussions

The task of this paper is to compare different cycle configurations using various working fluids. The annual performances and maximum compressor displacements are considered as main indicators. Each model uses the DH profile shown in Fig. 1 and 2 as input data. The annual performance is calculated as the ratio of the heat delivered over the electricity consumption (SCOP).

For heat source, this paper considers only the case of heat recovery from a data center or any other heat source between 30 to 40 °C, such as condensers of chillers and industrial waste heat.

The HP should deliver 550 kW at -26 °C outside ambient temperature and the DH water flow is assumed constant through the year.

6.1 SCOP Configuration Performance Evaluation

First, to determine the best configuration for our DH case study, we perform the analysis using the same refrigerants. The SCOP (Fig. 11) is the ratio of heat delivered to the DH over the total electricity consumption including the electrical heater, when needed.

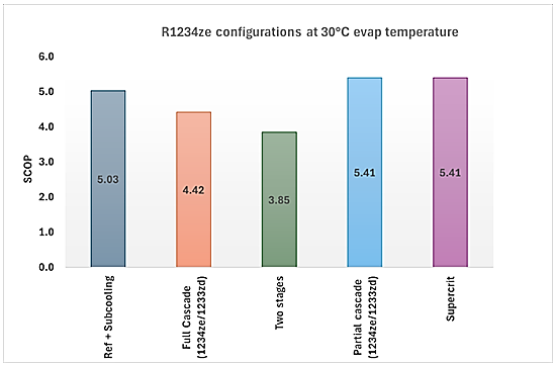


Figure 6: SCOP of DH configuration using R1234ze(E) or R1234ze(E) and R1233zd(E) as working fluids

The Reference configuration with deep subcooling is penalized at very low ambient because the electrical heater is needed to deliver hot water at 115°C

The two-stage configuration has the lowest SCOP because the mid-stage vapor-liquid separator doesn't allow deep subcooling using DH water return flow. Consequently, the SCOP is penalized.

Full cascade configuration is less suitable for a high ambient season when the pressure ratio becomes very low. Under these conditions, a one-stage system can perform better.

Partial cascade and Supercritical configuration: Both configurations achieve the best SCOPs, can take advantage of the deep subcooling, and meet the heating load without an electrical heater.

6.2 Electrical power peak demand

Electrical power peak demand is an important parameter to be considered when selecting a heating system configuration. From SCOP analyses, partial cascade or supercritical configurations can reduce annual electricity consumption by only 7% (Fig. 12). The analysis of power demand reveals that although the reference configuration has a high SCOP, it has a significantly high electricity demand during very cold weather conditions, which occurs for a few hundred hours annually. This leads to a very high power demand, peaking at up to 200%. Therefore, using advanced high-efficiency configurations can help reduce peak electricity demand during times of

high electricity prices. Additionally, the reduced peak load has a positive impact on the electrical grid infrastructure and installation cost.

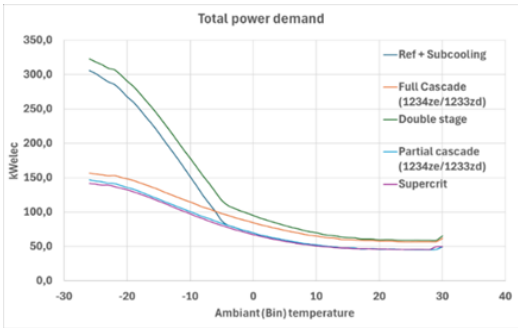


Figure 7: Electrical power demand

6.3 Components and technologies

Predesign thermodynamic cycle analysis gives the potential advantages and disadvantages for each configuration. Advanced configurations need additional components like compressors, heat exchangers, valves, and special control systems. This can have an important impact on the final heat pump cost. Some configurations are infeasible either because of technical constraints or the unavailability of components. For example, the supercritical configuration operates at very high condensing pressures and pressure ratios, which cannot be supported by current compressors and heat exchangers.

6.4 Configuration performance evaluation with different fluids

Different fluids are used for configuration evaluation according to the selected heat source scenario. Only annual performances and compressor displacements are compared (Figure 13).

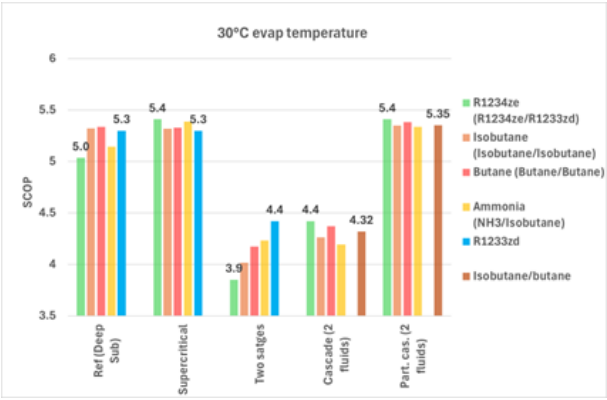


Figure 8: Impact of working fluids and selected configurations on the annual total electricity consumption

For the specific DH case study analysed in this paper, the SCOP values show the same trend for all the working fluids. Two-stage and cascade configurations are the least suitable options for this application. SCOPs of reference configuration with deep subcooling are either lower or equal to supercritical configuration SCOPs. These SCOPs are impacted by the fluid's critical temperature and pressure ratio. The supercritical and partial cascade configurations show equivalent results.

In the context of supercritical configurations, the choice of working fluid has minimal influence on the calculated SCOP. However, in situations requiring elevated water temperatures, the utilization of ammonia leads to a notable increase in both discharge pressure and temperature. Specifically, in a supercritical cycle, Ammonia necessitates a compressor discharge pressure of 63 bar and a temperature of 209°C. Also, Ammonia is corrosive to the usual construction material used with other refrigerant components. These conditions render selecting compressors and components notably demanding and more costly.

The size or displacement of the compressor is an important factor in determining the total heat pump cost. Compressor costs are higher for refrigerants with lower volumetric capacity. Refrigerants with lower volumetric capacity also require larger components, which increases heat pump costs. Figure 14 illustrates the comparison of compressor displacement for various fluids and configurations.

6.5 Impact of the selected fluids on the investment and operational cost:

Mateu-Royo et al. [08] correlated HP component costs to the required compressor displacement and heating capacity. 20% additional cost is mentioned for cascade configuration versus single-stage configuration. As the cost estimations are approximated, we consider that the heat pump's total cost is proportional to the required compressor displacement when using equivalent technologies.

The cost of risk mitigation due to increased flammability or toxicity of the fluid should be considered when calculating the total installed cost of the heat pump. These cost details considerations are beyond the scope of this paper.

We have considered that the refrigerant circuit cost is directly proportional to the compressor displacement (figure 14). For this reason, the R1234ze partial cascade configuration is 15% more expensive than the supercritical configuration. The isobutane and butane systems are 46% and 95% more expensive

than the supercritical R1234ze(E) configuration, respectively.

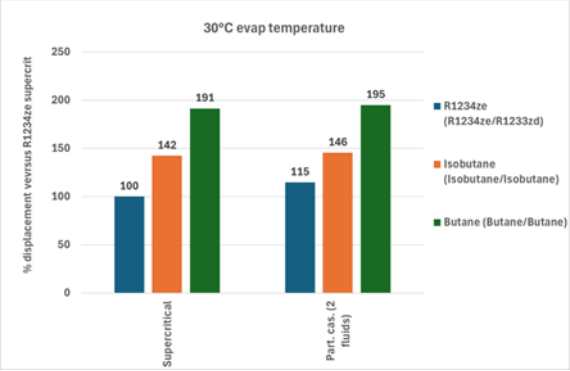


Figure 14: Compressor displacement difference for various fluids when using supercritical and partial cascade configurations

Figure 15 compares the additional electricity costs for partial cascade systems with various working fluids to partial cascade systems with the R1234ze and R1233zd pair. For a constant electricity price of 0.5€/kWh, the partial cascade configuration with the R1234ze/R1233zd pair offers about a 1.1% reduction in electricity consumption compared to isobutane.

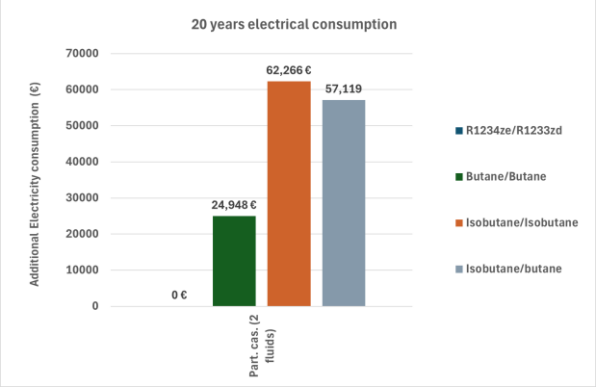


Figure 9: Additional electrical consumption versus R1234ze/R1233zd partial cascade configuration over 20 years

6.6 HP CAPEX and operational cost for partial cascade system:

To estimate heat pump cost versus a single-stage standard heat pump configuration we assume that standard heat pump cost is divided into three parts:

The refrigerant circuit cost includes compressors and heat exchangers, the water loop cost includes water pipes, valves, and hydraulic connections and installed costs include footprint impact and risk mitigation costs.

Table 3: Total CAPEX % cost function of the refrigerant circuit, water circuit, and installation

% cost per kW	Refrigerant circuit	Water circuit	Installation	ATEX & safety requirements
Reference system using R1234ze	30	30	40	6
System with hydrocarbon	Calculated based on displacement and configuration	30	40	15

Heat pump total cost of a standard basic single-stage heat pump using A1 refrigerant is assumed to be 1000 €/kW installed heating capacity.

For cascade configurations, we consider a 20% increase in the refrigerant circuit cost versus single-stage reference configuration.

According to customers feedback, total heat pump cost increases by 15 to 50% when A3 fluids is used versus A1 or A2L fluids. In this paper, we have considered 15% as the minimum cost increase when using A3 refrigerants. This cost increase includes ATEX and additional safety requirements not only for the heat pump itself but also for the whole surrounding. Footprint and building construction requirement costs are not considered as these are equipment and site-specific. Consequently, we have considered a 150€/kW cost increase when using A3 refrigerants versus other options.

Table 4: Volumetric capacity and cascade configuration impact on refrigerant circuit cost

	R1234ze/ R1233zd	Isobutane/ Isobutane	Isobutane/ Butane	Butane/ Butane
Volumetric capacity impact	+15%	+46%	+49%	+95%
Cascade impact	+20%	+20%	+20%	+20%

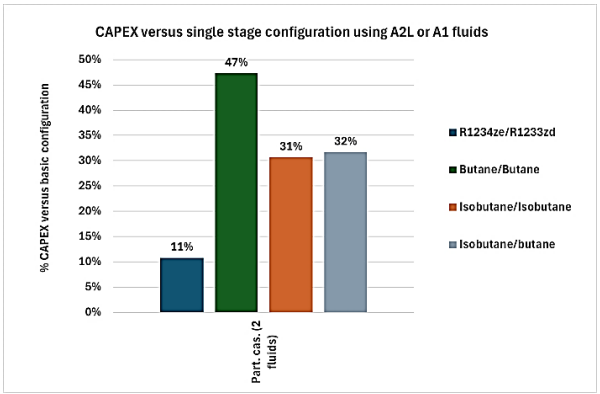


Figure 10: Total cost increase versus reference single-stage heat pump using A1 or A2L refrigerant

Figure 16 shows the CAPEX increase for partial cascade systems with different fluids. This capex increase covers the components, configuration, and safety costs. Figure 17 shows the total CAPEX and OPEX costs over 20 years.

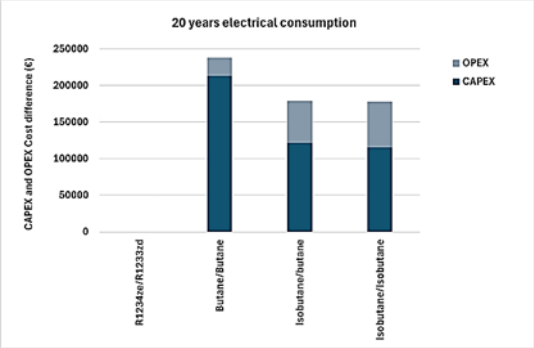


Figure 11: Cost increase over 20 years life span when using A3 versus A2L refrigerant for a 550 kW DH heat pump using heat recovery

7 HP cost assumption for DH in Finland

To cover heating needs for the DH network in the Helsinki climate zone, Fortum investigated project costs based on HP and electrical boiler implementation (Figure 18). The quality of the equipment, electrical system, and plant automation were required to be of high energy industry standard.



Figure 18 : Fortum plants, building for HP and boiler.

Table 6: Project CAPEX

	Capacity kW	Cost k€	Water flow (l/s)	Maximum Temperature °C	Cost k€/kW
Heat pump plant	6000	3800	26.6	95	0.63
Electrical boiler plant	2400	800		115	0.33
Electrical grid		1400			

Table 6 shows the costs of the heat pump plant, electrical boiler plant, and electrical distribution module include the modular building and all auxiliary equipment, excluding foundation works.

7.1 Partial cascade HP option

Partial cascade system can be an option for this project. For this reason, total HP consumption and maximum electricity power are investigated to analyse the cost impact on CAPEX and OPEX and estimate payback scenarios.

7.2 Peak electricity load reduction

Figure 19 shows calculation results according to Fortum operating conditions for the heat pump + boiler and for partial cascade heat pump options. The use of a partial cascade system allows the reduction of installed electrical power by 2000 kW and the elimination of electrical boiler plants.

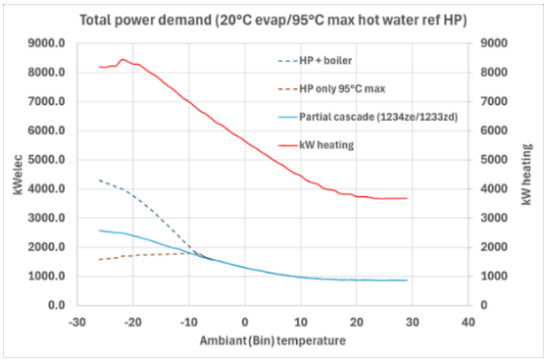


Figure 19: Electrical power consumption and heating power for selected configurations.

7.3 CAPEX cost saving

According to the estimated peak load reduction (2000 kWelec), table 6 shows the impact on electrical grid investment cost reduction.

Table 5: Electrical grid cost saving

Electrical grid without boiler				
	Cost/Kw k€/kW	Capacity kW	Cost k€	Cost saving
Reference system		4600	1400	
Partial Cascade HP	0.304	2600	791	609

The total calculated cost savings is about 1409 K€ for boiler cost + electrical grid cost. Additional cost savings as the plant automation cost reduction (-100k€) and power transfer fees (-37K€/year) will also decrease the cost of the full HP option versus the hybrid HP & boiler option.

7.4 HP cost increase

The use of a cascade system has an impact on heat pump cost versus reference options. According to prior art, a 20% cost increase can be expected as a quick estimation versus a single-stage system. We need to conduct further investigations in collaboration with HP manufacturers to improve cost estimation for available technologies.

8 Conclusions

The study shows that a heat pump alone can supply very high-temperature hot water to meet all district heating needs, even in very low ambient temperatures. By using heat recovered from data centers, a SCOP of around 5 can be achieved using various advanced configurations and fluid combinations. The partial cascade configuration is the most promising design, delivering the highest SCOP with available piston compressors. The use of partial cascade helps to reduce the pressure ratio of the compressors compared to the supercritical configuration and allows for the use of oil-free centrifugal compressors, which offer higher system efficiency at full and part loads. This has a positive impact on the heat pump SCOP and increases the efficiency gap with other options. Besides the availability of components to build up the heat pump, the combination of R1234ze(E) and R1233zd(E) shows an equipment size reduction advantage thanks to the higher volumetric capacity of R1234ze versus hydrocarbon at low evaporating temperatures. The A2L and A1 classification of R1234ze and R1233zd, respectively, also have a beneficial impact on component selection and implementation cost. Consequently, the thermodynamic properties and safety classification give a major cost advantage for HFO over hydrocarbon fluids for this district heating application.

9 References

[01] Funder-Kristensen T et al. Large Heat Pumps for Decarbonized District Heating. 13th IEA Heat Pump Conference Jeju, Korea, April 26-29, 2021.

[02] Connolly et al. Heat Roadmap Europe 1 First Pre-Study for the EU27. Aalborg Universitet, Downloaded from vbn.aau.dk on: April 30, 2024

[03] David A et al. Heat Roadmap Europe: Large-Scale Electric Heat Pumps in District Heating Systems. Energies. 2017; 10(4):578. https://doi.org/10.3390/en10040578

[04] Arpagaus C et al. High-Temperature Heat Pumps: Market Overview, state of the art, research status, refrigerants, and application potentials. Energy. 2018. 152:985-1010 https://doi.org/10.1016/j.energy.2018.03.166

[05] Bergamini et al. Thermodynamic Competitiveness of High-Temperature Vapor Compression Heat Pumps for Boiler Substitution. Energy. 2019. 182:110-121 https://doi.org/10.1016/j.energy.2019.05.187

[06] Robinson C et al. An Integrated Approach to the Aero-Mechanical Optimisation of Turbo Compressors. Current trends in design and computation of turbomachinery. 33. 2011. 3:031026

[07] Jaatinen-Värri A et al. Centrifugal Compressor Design for High-Temperature Heat Pumps. Applied Thermal Engineering. 2024. 239:122087 https://doi.org/10.1016/j.applthermaleng.2023.122087

[08] Mateu-Royo C et al. Advanced High-Temperature Heat Pump Configurations Using Low GWP Refrigerants for Industrial Waste Heat Recovery. Energy Conversion and Management. 2021. 229: 113752 https://doi.org/10.1016/j.enconman.2020.113752

[09] Ameur K et al. Modeling and Numerical Approach for the Design and Operation of Two-Phase Ejectors. Applied Thermal Engineering. 2016. 109: 818 https://doi.org/10.1016/j.applthermaleng.2014.11.022

Disclaimer: Although all statements and information contained herein are believed to be accurate and reliable, they are presented without guarantee or warranty of any kind, expressed or implied. Information provided herein does not relieve the user from the responsibility of carrying out its own tests and experiments, and the user assumes all risks and liability for use of the information and results obtained. Statements or suggestions concerning the use of materials and processes are made without representation or warranty that any such use is free of patent infringement and are not recommendations to infringe on any patents. The user should not assume that all toxicity data and safety measures are indicated herein or that other measures may not be required.

Improving performance of A CO2 Thermally Driven Heat Pump Based on a New Optimal High-Pressure Correlation

Ali Salame[1,2,3], Vincent Lemort[2], Pascal Dufour[3], Madiha Nadri[3]

[1]Boostheat Companyz
Lyon, France,

(+33) 0 6 70 84 61, ali.salame@boostheat.com

[2]University of Liège, Energy Systems Research Unit,
Liège, Belgium,
vincent.lemort@uliege.be

[3] Univ Lyon, Université Claude Bernard Lyon 1, CNRS, LAGEPP UMR 5007,
43 boulevard du 11 novembre 1918, F-69100, VILLEURBANNE, France,

pascal.dufour@univ-lyon1.fr

Abstract. Optimizing the performance of CO2 heat pumps often requires an optimal high pressure setpoint, which traditionally depends on the gas cooler outlet temperature and sometimes the evaporation temperature, as proposed in [8]. Despite the variety of correlations available in the literature, no single generalized correlation can be universally applied to all applications. Consequently, it is advisable to determine the optimal correlation specific to each application to achieve the most accurate and relevant results. Boostheat has developed a new thermally driven heat pump with a three-stage thermal compressor to exploit CO2 in its supercritical state. This study, based on a validated model, investigates the impact of various parameters such as the return water temperature, fume and evaporation temperature on the overall coefficient of performance (COP). Using the most significant parameters, we propose a new optimal high-pressure correlation and compare it with the existing ones.

Keywords. CO2, Thermally driven, Heat pumps, Thermal compressor.

Nomenclature

$\dot{m}$	Mass flow rate (G/s)
$\dot{Q}$	Heat capacity (W)
h	Specific enthalpy (J/kg)
Tr	Temperature ratio
p	Pressure (Bar)
Pr	Pressure ratio
T	Temperature (°C)

Special characters

ω_b	Burner fan speed (Rpm)

Subscripts

COP	Coefficient of performance
LHV	Lower heating value
GWP	Global warming potential
TDHP	Thermally driven heat pump
TC	Thermal compressor
CO2	Carbon dioxide
c	Gas cooler
e	Evaporator
t	Total
w	Return water
$comb$	Combustion
rec	Recovery

1 Introduction

Until 1930, CO2 was considered as a widespread refrigerant. Due to the discovery of superior performance artificial refrigerants (CFC and HFC), CO2 was replaced. Forty-four years later, and due to the accumulation of harmful effects done on the ozone layer by these artificial refrigerants, natural refrigerants and specifically CO2 has gained attention again [9], mainly due to its global warming potential (GWP) and ozone depletion layer (ODP) of 1 and 0, respectively. Other advantages include nontoxicity, nonflammability and availability.

In the past decades, CO2 have shown its potential in heat pump applications, as demonstrated in [10, 11, and 17]. Another distinguishable characteristics of CO2 are lower critical temperature of 31.1 °C and high critical pressure of 73.8 bar, which justify why CO2 heat pump cycles are usually designed to operate in the transcritical state, a higher temperature glide. In fact, the effect of the high pressure on the COP seems to be nonmonotonic in the transcritical region, as the high pressure becomes independent from the rejected heat temperature. Among the first attempts to find the optimal high pressure are introducing a graphical method [5] and by comparing different simulated operating conditions [13].

Other research work [2, 6, 8, and 16] obtained high pressure control correlations as a function of gas cooler outlet temperature, and sometimes including also evaporation temperature, as done by the latter two. Their results were based on either simulated models or experimental data on specific range of parameters, proving that gas cooler outlet temperature has greater effect on the COP than evaporation temperature. An optimal high-pressure correlation as function of gas cooler outlet temperature was developed based on experimental data [14], surpassing the performance of correlations in [2 and 6]. No generalized high-pressure correlation for CO2 heat pump, so we believe that each application will have to develop its own correlation, either based on experimental data, or a validated simulated model.

Most of the developed heat pumps today are electrically driven, so little attention was paid to Thermally driven ones, which have its major strength when being powered by waste heat or solar power. Two major types of TDHP applications are absorption and adsorption machines. In this work, we target one specific TDHP application that uses thermally driven compressors previously analyzed [4], which will be called thermal compressor heat pump (TCHP) in this paper. The performance of this heat pump cycle at different operating conditions can be found in [3]. The previous high-pressure correlation used was dependent solely on the return water temperature to the gas cooler and was obtained from trial and error on a real machine. We aim to carry a parametric analysis on a previously validated dynamic model for the gas cooler, where only steady state is simulated. A mass flow rate empirical correlation is derived as function of total pressure ratio, temperature ratio between hot part and cold part of the thermal compressor (TC) as well as the motor speed. By varying the high-pressure value, the COP is simulated at different return water, burner fan seed and evaporation temperature. The optimal COP and high-pressure values are then plotted in a heat pump map for different ranges of these temperatures. After finding the optimal high-pressure correlation again, we compare it with the existing one and Liao's correlation [8]. The Thermophysical properties of CO2 were calculated using CoolProp [1].

2 Thermodynamic model

2.1 Process Overview.

As illustrated in figure 1, the cycle of a TCHP consists of three TCs, three buffers, one gas cooler, one evaporator, internal heat exchanger, flash tanks, two expansion valves and a recovery heat exchanger. At evaporation pressure, CO2 enters the first stage compressor and leaves at a higher pressure. It is then cooled inside buffer 1 with a water flow, and then mixes with the vapor leaving the flash tank in a one-way valve before entering the second TC. The CO2 then leaves at higher intermediary pressure and cooled again inside the second buffer before entering the third TC. At the CO2's highest pressure level and high temperature, CO2 rejects heat into the water entering the gas cooler. It is then cooled again inside an internal heat exchanger by the CO2 leaving the evaporator. After leaving the internal heat exchanger, the CO2 refrigerant is expanded in a high-pressure valve, then enters a flash tank, where the CO2 in its gaseous state is reinjected between the first and second TCs through a one-way valve, and the remaining liquid leaves and expands in a low-pressure valve before finally entering the evaporator. For the water side (heating circuit): smaller part of the water flow goes to the buffers and the TCS, where it is subdivided again between the first two buffers and collected before consequently entering the coolers of the TCs. The larger part of the entering water goes to the gas cooler, where the two parts mix again before entering the recovery heat exchanger, where the resulting fume from the combustion process are cooled.

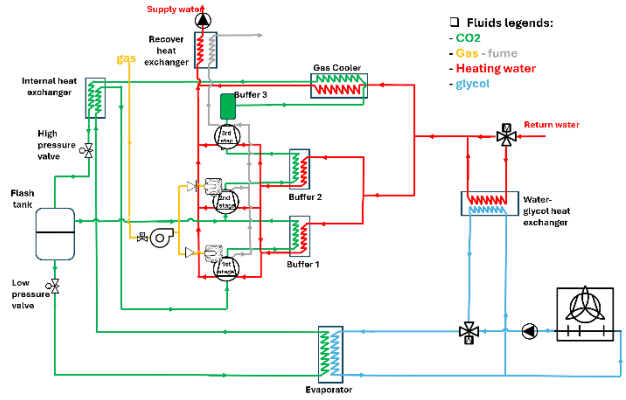


Figure 1: Schematic representation of the TCHP.

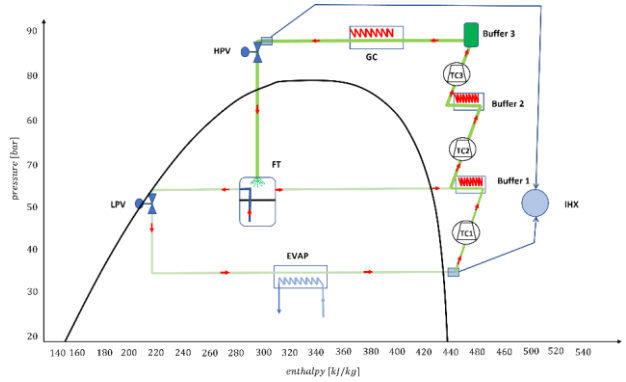


Figure 2: p-h diagram of CO2 in the TCHP cycle.

2.2 COP.

On the gas burning side, the first two TCs are directly heated with burned gas, while the third one is heated with their exhaust gas, before recovering the remaining by water. The heating of the water occurs in several places, in gas cooler which is the main one, that we need to optimize, and the recovered heat in coolers 1,2, and 3 and buffers 1 and 2. Since the

primary source of a TDHP is heat and not electricity, the used COP is a thermal one defined as the released heat energy over the consumed heat. The range of total heating COP as reported in several applications is between 1-1.7 [7]. So, the total COP resulting from the output heat over the input heat can be written as follows:

$$COP_t = \frac{\dot{Q}_c + \dot{Q}_{cooler1,2,3} + \dot{Q}_{buffer1,2} + \dot{Q}_{rec}}{\dot{Q}_{comb}} \quad (1)$$

Where $\dot{Q}_c, \dot{Q}_{cooler1,2,3}, \dot{Q}_{buffer1,2}, \dot{Q}_{rec}$ are the heat recovered from the gas cooler, coolers 1, 2 and 3, the two buffers and the recovery heat exchanger, respectively. $\dot{Q}_{comb}$ is the gas power provided to the cycle. In this heat pump application, optimal performance is defined by maximizing heat rejection in the gas cooler rather than maximizing heat recovery in the other heat exchangers. This being said, the COP term in this work is reduced to be:

$$COP = \frac{\dot{Q}_c}{\dot{Q}_{comb}} \quad (2)$$

Where:

$$\dot{Q}_c = \dot{m}_c\left(h_{c,in} - h_{c,out}\right) \quad (3)$$

Knowing that $h_{c,out}$ is computed from a previously derived and validated dynamic model for the gas cooler. And the combustion power is calculated as function of the methane gas (CH_4) flow rate and the lower heating value (LHV):

$$\dot{Q}_{comb} = \dot{m}_{CH4} LHV \quad (4)$$

2.3 TC Empirical Models.

In this section, we give an insight about the most important component of our cycle which is a TC. In our previous work we have developed simple empirical models for the main thermal compressor performance indicators, such as the mass flow rate and discharge temperature. These models were developed based on collected experimental data from a thermal compressor in a basic single stage heat pump cycle. The derived empirical models in [15] were used to find the TC performance indicators represented in figure 3.

Figure 3 (a) shows that the mass flow rate decreases as pressure ratio increases, while it increases when the speed of motor increases. In the other hand, the discharge temperature increases harmonically with the increase of both motor speed and pressure ratio, as seen in Figure 3 (b). In both plots, a constant temperature ratio is considered: $T_r = 3.2$. It is important to note out that these figures better represent the first two TCs as they are directly heated by gas, while the third TC is heated by the resulting fume from the first two. For this reason and for the sake of simplicity we consider that mass flow rate and the discharge temperature of the third thermal compressor to depend on the total pressure ratio and burner fan speed regulating the amount of gas being burned. The following empirical models are derived from fitting the whole cycle data found in [3] into a polynomial regression type model. The inlet temperature of the gas cooler and the mass flow rate are modeled empirically as follow:

$$\dot{m} = 0.013\omega_b + 13P_{rt} - 0.0044\omega_b P_{rt} - 29.7 \text{ [g/s]} \quad (5)$$

$$T_{c,in} = 0.023\omega_b + 7.4P_{rt} + 0.00076\omega_b P_{rt} + 17 \text{ [°C]} \quad (6)$$

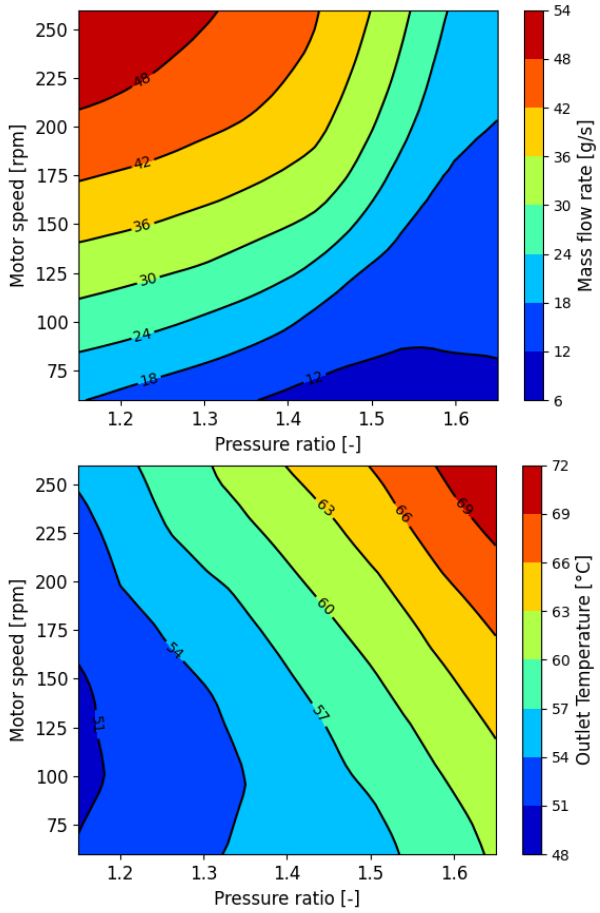


Figure 3: Performance indicators of a single thermal compressor demonstrated by (a) mass flow rate and (b) discharge temperature as function of pressure ratio and motor speed.

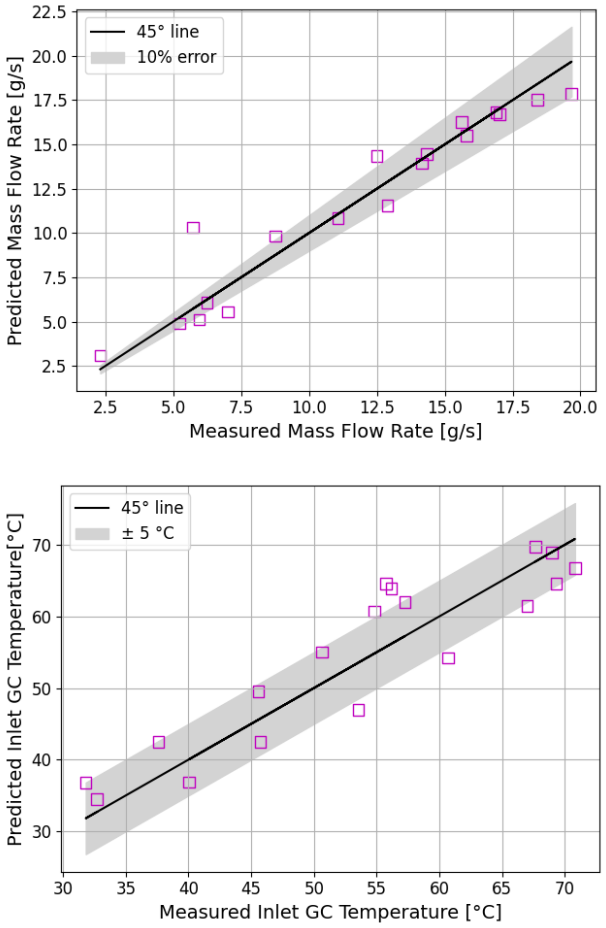


Figure 4: Parity plots between the predicted and measured values of the (a) mass flow rate and (b) inlet temperature of the gas cooler.

Where the total pressure ratio $P_{r_t} = \frac{p_c}{p_e}$, the temperature ratio of the third TC. The combustion power can be presented as function of combustion power:

$$\dot{Q}_{comb} = 1.2\omega_b - 1420.4\,[\mathrm{W}] \qquad (7)$$

Figure 4 demonstrates that the empirical correlations for mass flow rate and gas cooler inlet temperature predict the observed data with a good accuracy, thus reliable for our model-based parameters analysis.

3 Results And Discussions

In this work we consider the return water temperature instead of the gas cooler outlet temperature as it will be more relevant when having two-phase flow at the exit of the gas cooler, which makes it more relevant to consider the return water temperature instead. A parametric study is carried out to show the effect of several parameters on the heating COP. The range of the gas cooler pressure is varied from 58 to 88 bar, the return water temperature (T_w) between 15 and 40 °C, the evaporation temperature (T_e) is varied from -15 °C to 10 °C, and the burner fan speed (ω_b) is between 2000 and 7000 rpm.

3.1 Analysis.

Figures 5, 6, and 7 show the variation of the COP as function of high-pressure values at different evaporation temperatures, with (a) and (b) being top and bottom figures respectively. In figure 5 the return water temperature is fixed at 30 °C and burner fan speed at 4500 rpm. (a) shows that the COP slightly varies as evaporation temperature varies, while (b) shows that at different evaporation temperatures the optimal high-pressure value (characterized by the curve peak) is constant (80 bar). Figure 6 shows the impact of varying the high-pressure and burner fan speed on the COP, while the evaporation temperature is kept constant 0 °C. The figure also shows a slight change in the COP as the burner fan speed varies. Figure 7 shows the impact of varying the return water and high-pressure on the COP. It is seen that varying the return water temperature leads to distinct optimal

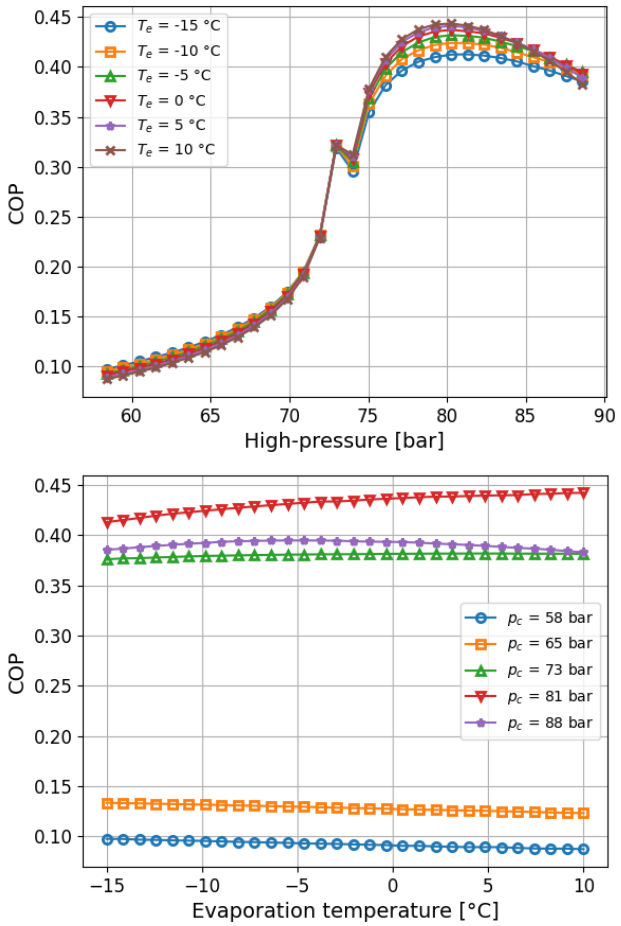


Figure 5: The impact of varying evaporation temperature (high-pressure) on the COP at different high-pressure (evaporation temperature).

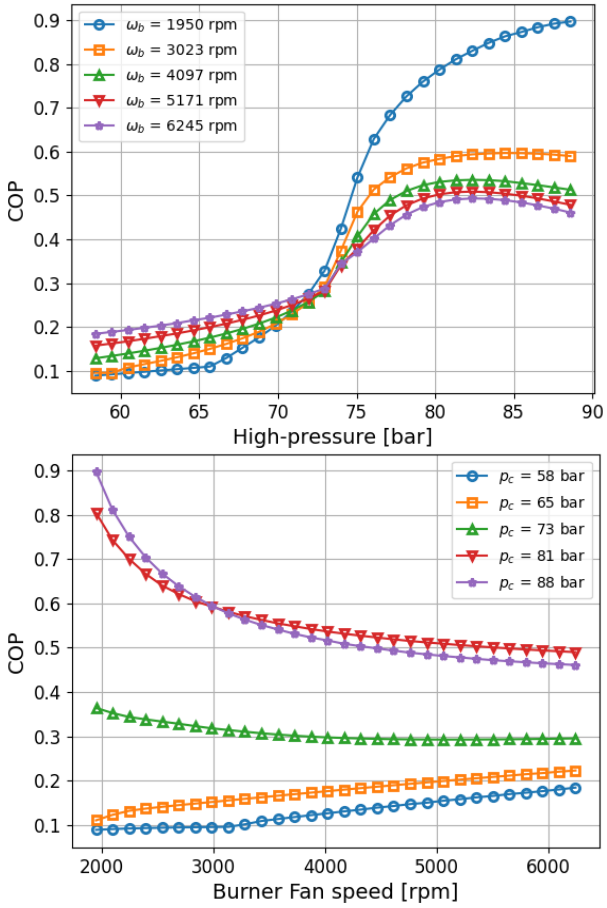


Figure 6: The impact of varying burner fan speed (high-pressure) on the COP at different high-pressure (burner fan speeds).

high-pressure values. As the return water temperature increases (increase of heat load), the COP seems to decrease and the optimal high-pressure increases. It is then concluded that the return water temperature has the highest influence on the COP and the variation of the optimal high-pressure values.

3.2 Optimal High-Pressure.

In this section we aim to find the optimal high-pressure correlation that induces highest COP based on our model, as function of return water temperature which have shown to be the most significant parameter. By simulating the model at different range of return water temperature values, the following optimal high-pressure correlation is obtained:

$$p_{c,new} = 3.3T_w - 0.03T_w^2 + 6.7 \text{ [bar]} \quad (8)$$

To validate the derived correlation, we apply it on real data and compare it with other correlations.

We use the data from [3], where the TCHP is experimented when the outdoor temperature is between -10 and 12 °C, at water supply temperatures of 55 °C (W55). At each outdoor temperature the machine is automated to deliver the demanded water supply temperature by varying the operating conditions by the TCs. The previous optimal high-pressure correlation was solely and linearly dependent on the return water temperature described as follows:

$$p_{c,old} = 1.47T_w + 31.53 \text{ [bar]} \quad (9)$$

The derived new correlation, the old one and Liao correlations are compared with the simulated optimal pressure at different outdoor temperatures for W55 in Figure 7. The figure shows the best fit is obtained by the new correlation (absolute average deviation of 2%), followed by 4.5 % deviation by the old one, then Liao's correlation which shows a significant deviation.

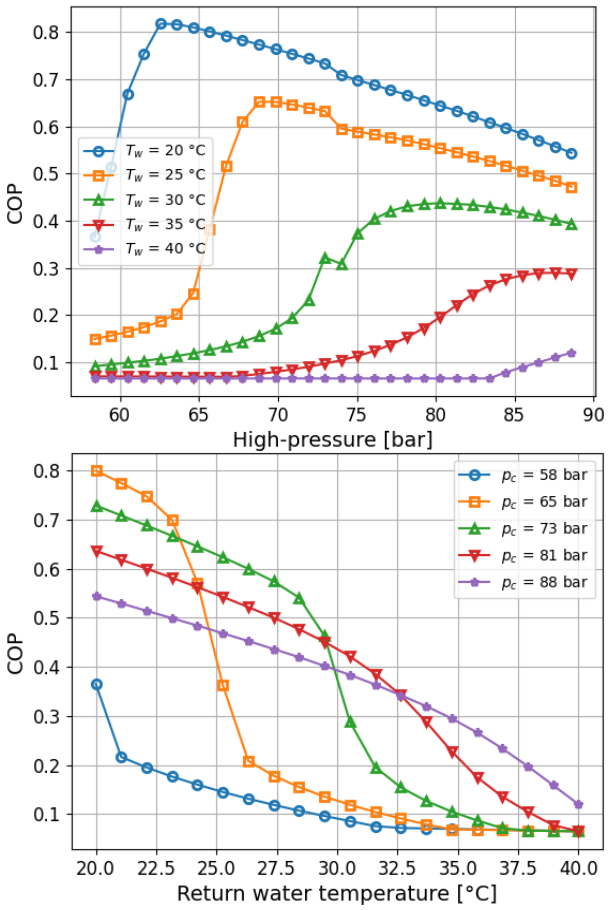


Figure 7: The impact of varying return water temperature (high-pressure) on the COP at different high-pressure (return water temperature).

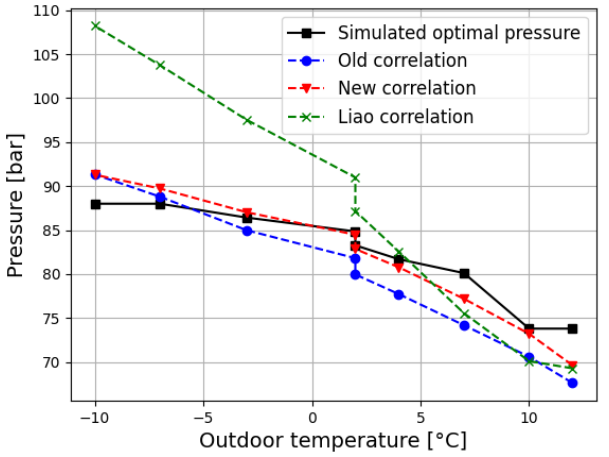


Figure 8: Comparison between different optimal high-pressure correlations with the simulated one.

4 Conclusion

Although TDHPs are not as attractive as electrically driven heat pumps, it remains interesting when it comes to valorising waste heat. As a conventional CO2 heat pump, the high-pressure plays a crucial role in obtaining the optimal COP. We studied the effect of varying the evaporation, burner fan speed, and return water temperatures on the COP, which showed the former two parameters have a neglected effect compared to the latter one. Therefore, based on carried simulations, we derived an optimal high-pressure correlation as function of return water temperature and compare it with other existing correlations. This correlation can be imposed as an optimal high-pressure setpoint for future control and optimization attempts.

Acknowledgement

The French ministry of higher education and research is acknowledged for the financial support of this CIFRE PhD thesis 2022-0549.

References

[1] Bell, I.H., Wronski, J., Quoilin, S., Lemort, V., 2014, Pure and Pseudo-pure Fluid Thermophysical Property Evaluation and the Open-Source Thermophysical Property Library CoolProp, *Ind. Eng. Chem. Res.*, 53(6), p. 2498-2508.

[2] Chen, Y., & Gu, J. (2005). The optimum high pressure for CO2 transcritical refrigeration systems with internal heat exchangers. International Journal of Refrigeration, 28, 1238-1249.

[3] H. Fallahsohi, Energy analysis of the heat pump operating with supercritical CO2 driven by thermal compression. American Journal of Engineering Research (AJER), Volume-12, Issue-11, pp: 61-74, 2023.

[4] R. Ibsaine et al., Modelling of a new thermal compressor for supercritical CO2 heat pump, *Energy*, Volume 117, Part 2, p. 530-539.

[5] H. Inokuty, Graphical method of ending compression pressure of CO2 refrigerating machine for maximum coefficient of performance, in: Proceedings of the 5th International Congress Refrigeration, Rome, pp. 185-192, 1928.

[6] F. Kauf Determination of the optimum high pressure for transcritical CO2-refrigeration cycles. International Journal of Thermal Sciences, 38, 325-330, 1999.

[7] A. Kühn, Thermally Driven Heat Pumps for Heating and Cooling, 2013.

[8] S. M. Liao et al., A correlation of optimal heat rejection pressures in transcritical carbon dioxide cycles. Applied Thermal Engineering, 20, 831-841, 2000.

[9] G. Lorentzen, Revival of carbon dioxide as a refrigerant. International Journal of Refrigeration, 17, 292-301, 1994.

[10] P. Neksa, CO2 heat pump systems, Int J Refrig 25, p. 421–427, 2002.

[11] P. Neksa et al., CO2-heat pump water heater: characteristics, system design and experimental results, Int J Refrig 21 (3), p. 172–179, 1998.

[12] A. Okasha and N. Müller. Simulation and Performance Correlation for Transcritical CO2 Heat Pump Cycle, 2018.

[13] J. Pettersen and G. Skaugen, Operation of trans-critical CO2 vapour compression circuits in vehicle air conditioning, in: Proceedings of the New Applications of Natural Working Fluids in Refrigeration and Air Conditioning, Hannover, Germany, pp. 495-505, 1994.

[14] P. C. Qi et al., Experimental investigation of the optimal heat rejection pressure for a transcritical CO2 heat pump water heater, Applied Thermal Engineering, 56, 120-125, 2013.

[15] A. Salame et al., An Empirical Model for a CO2 Thermal Compressor Based on Experimental Data. International Compressor

Engineering Conference. Paper 2868., 2024.

[16] J. Sarkar et al., Optimization of a transcritical CO2 heat pump cycle for simultaneous cooling and heating applications. International Journal of Refrigeration, 27, 830-838, 2004.

[17] M. G. Yarral et al., Performance of a transcritical CO2 heat pump for simultaneous refrigeration and water heating. In: XX Int. Congress of Refrigeration, Sydney, Paper 651, 1999.

ANALYSIS OF HEAT PUMP PERFORMANCE IN A TUMBLE DRYER BASED ON DRYING AIR PROPERTIES

Marko Hočevar[1]*, Lovrenc Novak[1], Aleš Malneršič[1], Janez Lupše[2], and Emir Mujagić[3]

[1] University of Ljubljana, Faculty of Mechanical Engineering, Chair of Energy Engineering, Aškerčeva 6, 1000 Ljubljana, Slovenia

[2] Gorenje, Partizanska cesta 12, 3320 Velenje, Slovenia

[3] Sonce Energija, Šmartinska cesta 130, 1000 Ljubljana, Slovenia

** Corresponding Author: marko.hocevar@fs.uni-lj.si*

Abstract. Tumble dryers are white appliances used for drying clothes. During the operation, they consume high amounts of electric energy and because of a tumbling motion, fibres are generated from clothes and released into the environment. In this work, the efficiency of the tumble dryer operation was assessed and the interaction of the moist air and heat pump circuits was discussed. The analysis has shown that the specific enthalpy of the drying air at the entrance to the heat pump significantly affects the operation of the system; a specific enthalpy enables a greater transfer of energy to the heat pump. In addition, the thermodynamic properties of the refrigerant are crucial for optimizing the efficiency of the heat pump. It has been found that the highest coefficient of performance values is achieved when the heat pump operates at low pressures. These findings are key to further optimizing the operation of tumble dryers and contribute to better energy efficiency of the entire system.

Keywords. Tumble dryer, Heat pump, Fibres.

Nomenclature

h	Specific enthalpy (J/kg)
p	Pressure (Pa)
RH	Relative humidity (%)
T	Temperature (°C)

1 Introduction

An increasingly fast-paced lifestyle and a lack of time and space for drying clothes increase the use of household tumble dryers today. As with other household devices, the community also strives for more efficient, energy-saving, and environmentally friendly solutions in tumble dryers. However, research has in recent years drifted away from solely optimising energy use [1], several authors report on damage to clothes and fibres generated during the drying process [2].

One key component in a tumble dryer is the heat pump (later referred to as HP). Simply understanding the operation of the HP is not enough; it is necessary to connect its role with the entire dryer system. Therefore, in this work, we will describe in more detail the interaction and interdependence between the HP circuit and the air-drying circuit. Our goal is to determine how one system influences the other, identify visible shortcomings, and explore possible improvements to achieve better results.

2 Measurements

The measuring station is arranged around a household tumble dryer with a heat pump with a nominal drying capacity of 8 kg of dry laundry. The system is composed of two circuits. The first circuit is the aerodynamic circuit (shown by the solid black line in the Fig. 1) through which the air flows. The second circuit (shown by the dashed black line) is the heat pump circuit, through which R290 refrigerant flows in our case.

To describe the operation of the heat pump in the dryer system, we measured all the variables in the circuit of the heat pump, which allowed us to plot the operation of the log(*p*)-*h* diagram throughout the drying cycle. In addition, we performed functional tests covering all variables in the aerodynamic part.

The tumble dryer operation and measuring station schematics are shown in Figure 1.

2.1 Sensing equipment

The following sensing equipment was used in the experiment. Differential pressure on the heat pump and fan in the air circuit was measured using Endress Hauser PMD235 pressure transmitters. The heat

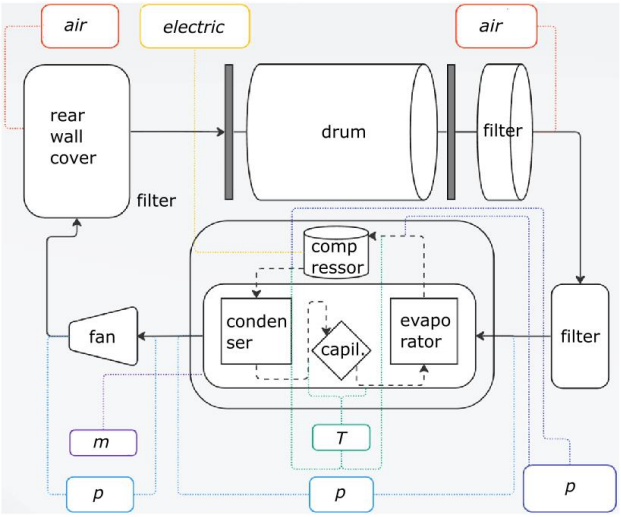


Figure 1: Tumble dryer schematics with location of measured variables (in *italic*).

pump fluid pressure was measured using Honeywell, MIPAN pressure transmitters. The temperature and relative humidity in the air circuit were measured using DeltaOhm HD48T sensors. The temperature inside the heat pump condenser and evaporator was measured using thermocouples Flukem TypeK and Agilent 34970A data logger instrument. The mass of the condensate was measured using Kerm FKB15KO 0.5A scale and the mass of the entire machine was measured using Tedea Huntleigh model 1042 load cells with a 50 kg range. All electrical variables of the fan and heat pump compressor were measured using Norma 4000 power analyser. Data acquisition was performed using National Instruments CompactDAQ 9147 chassis with National Instruments CompactDAQ 9205 16-bit (250 kHz) 32-channel analog module. For data acquisition, we used the National Instruments Labview software package.

Pressure tappings were implemented as follows. To measure pressure changes in the air circuit for the heat pump, we constructed pressure taps as follows: (1) at the filter cover at the heat pump inlet two pressure taps were connected to the same port of the differential pressure transducer, allowing for aerodynamic averaging of the measured pressures and (2) at the outlet of the heat pump, the method of aerodynamic pressure averaging was also used.

To measure differential pressure in the air circuit on the fan, pressure tappings were implemented in the rear wall cover and in the side chamber at the inlet to the fan chamber. Here, small holes were made, allowing for pressure equalization with the flow tract and ensuring accurate measurement of the static pressure on the cover wall. In the fan inlet channel, we also used the method of aerodynamic pressure averaging.

2.2 Experimental procedure

To establish the operation of the heat pump during laundry drying, we performed laundry drying functional tests. Measurements were performed using a standard drying program with loads of 4, 6, and 8 kg of 60% moistened cotton laundry, in accordance with the BS EN 61121:2013 standard [3]. The standard specifies standard-sized laundry, consisting of sheets, pillowcases, and cloths. Based on the load weight, the number of items for each type of laundry is determined, as shown in Table 1.

The laundry was placed in the dryer following the internal laboratory procedure, which specifies the method and order of loading. This arrangement has proved in the past to reduce the likelihood of excessive tangling and help ensure the measurement results were comparable. Finally, the standard drying program was started. This also means that no fan and heat pump control were used and the fan and compressor of the heat pump were on for the entire duration of the experiment.

Table 1: Number of sheets, pillows, and clothes used for each loading setting.

Laundry mass	Sheets	Pillows	Cloths
[kg]	[-]	[-]	[-]
4	2	4	14
6	2	8	24
8	2	12	27

Before each experiment, all filters were thoroughly cleaned, dry laundry mass was measured, and laundry was wetted to 60 % ± 1 % mass water content and loaded into the drum according to the procedure. Later, the measurements data acquisition was initiated, and the drying process was started. After the measurements, the mass of dry clothes was weighted. The measurements were valid if the final mass of the clothes was ± 3 % of the initial mass of dry clothes.

3 Experimental results

The experimental results were evaluated for both heat pump and air circuits. The circuits are not working

independently, so we will compare them to draw conclusions on the operation of the tumble dryer.

3.1 Heat pump

As shown in Table 1, we analyzed the operation of the heat pump (HP) in a tumble dryer at three different load conditions. The analysis is based on the log(*p*)-*h* diagram shown in Figure 2. We monitored performance over time, observing changes in variables such as refrigerant pressures at the compressor inlet and outlet, changes in refrigerant mass flow rate, specific enthalpy variations at the evaporator and condenser, cooling and heating capacities, and COP within a given time interval.

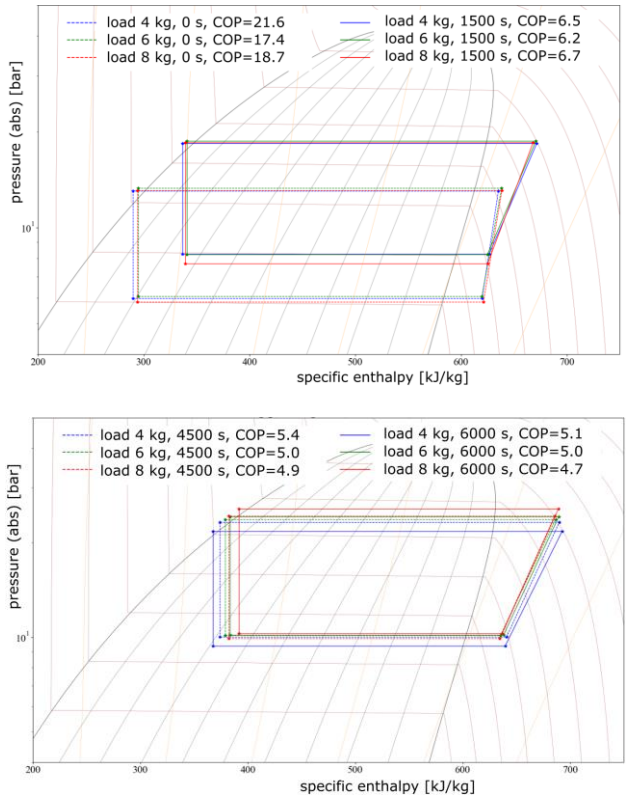


Figure 2: Heat pump operation for a selected time interval.

Results from Fig. 2 show that as the cycle in the log(*p*)-*h* diagram moves higher in pressure, smaller changes in the specific enthalpies *h* of the refrigerant at the evaporator and condenser are achieved. This phenomenon is attributed to the thermodynamic properties of the refrigerant. For all three loads, the cycle moved upward in pressure until approximately 80% of the cycle duration, after which it began to gradually move downward.

Additionally, as the cycle moved upward in pressure, the pressure difference across the compressor and the refrigerant mass flow rate increased. Conversely, when the cycle moved downward in pressure, the pressure difference across the compressor decreased, and the refrigerant mass flow rate dropped. Based on our observations, the cycle can be divided into three phases as follows.

In the **initial phase**, in the log(*p*)-*h* diagram, the cycle moves upward along the pressure axis. Due to the thermodynamic properties of the refrigerant, the change in specific enthalpy of the refrigerant decreases at both the evaporator and the condenser. At the same time, the pressure difference between the compressor inlet and outlet increases, along with the refrigerant mass flow rate. In this phase, both heating and cooling capacities increase, with the refrigerant mass flow rate rising faster than the decrease in specific enthalpy change at the evaporator and condenser. The increased cooling capacity is achieved due to the higher refrigerant mass flow rate, which is directly linked to increased compressor power. Consequently, the COP decreases during this phase.

In the **stable phase**, the cycle operates at relatively constant variable values. During this time, there is no significant movement of the cycle in the log(*p*)-*h* diagram.

In the **final phase**, the cycle begins to move downward along the pressure axis in the log(*p*)-*h* diagram. Due to the properties of the refrigerant, the change in specific enthalpy increases at both the condenser and the evaporator. At the same time, the pressure difference across the compressor decreases, leading to a reduction in refrigerant mass flow rate and, consequently, compressor power. Despite the increase in specific enthalpy change, the cooling and heating capacities decrease due to the more significant impact of the drop in refrigerant mass flow rate. The cooling capacity declines, as do the pressure difference across the compressor and refrigerant mass flow rate, which dictate the compressor's power. The COP increases during this phase. This can be attributed to the refrigerant properties, as larger changes in specific enthalpy are achieved at lower positions in the log(*p*)-*h* diagram.

3.2 Air

To better understand the operation of the HP, it is necessary to measure what is happening on the side of the drying air. The temperatures and relative humidity at the exit from the drum, a location from the thermodynamic point of view is the same as the entrance to the heat pump evaporator. Results are shown in Fig. 3. It is important to be aware that the evaporator can only absorb as much energy as the

drying air can provide, and vice versa for the condenser.

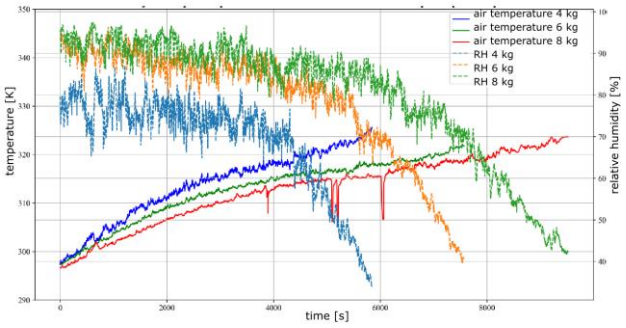


Figure 3: Changes in temperature and relative humidity during the entire dying cycle at the location of the entrance to the heat pump.

3.3 Discussion

Within the drum, the temperature of the air decreases, while the humidity increases due to the evaporation of water from clothes. At the drum exit, the relative humidity may reach values higher than 90 % at the beginning of the drying cycle. The specific internal energy of the drying air at the entrance to the HP is closely related to the operation of the HP. The higher specific internal energy of the drying air at the inlet means that more energy is available for transfer from the drying air to the HP, which leads to an increase in the refrigerant pressure difference across the compressor. This in turn causes an increase in temperatures, refrigerant mass flows, and compressor power, which increases the cooling capacity and thus the amount of energy transferred from the drying air to the refrigerant. It is also important to be aware of the influence of volume flow or mass flow of drying air, which can be dictated by the mass of laundry or the rotation frequency of the fan.

We want to achieve the largest possible mass flow of drying air with the highest possible specific internal energy, to achieve the high heat flow between the drying air and the coolant. This can be achieved by properly setting the fan frequency or by choosing the optimal mass of clothes, which enables maximum moisture transfer from the laundry with minimal heat transfer in the shortest possible time. Thus, we increase the specific internal energy of the air and the mass flow of the drying air at the entrance to the HP.

Higher COP values are achieved where the mass flow rate of the refrigerant is lower, where we have lower temperatures, lower pressure of the refrigerant, and, with all of this, lower compressor power. When we have lower values of pressures and temperatures of the refrigerant, we are located lower on the log(p)-h diagram, which in turn leads to greater changes in the specific enthalpy of the refrigerant. Larger changes in the specific enthalpy of the refrigerant at lower compressor power mean higher COP values.

The higher the mass of the laundry, the more moisture needs to be removed from the laundry, which lengthens the cycle. A longer cycle means that the system heats up more, which means that we are located higher on the log(p)-h diagram. The higher we are on the log(p)-h diagram, the lower the ratio between the input power of the compressor and the obtained cooling power (COP value). This happens mainly on the calculation of the material properties of the coolant or smaller changes in specific enthalpy at higher temperatures and pressures of the coolant in the system.

4 Conclusions

Results and analysis have shown the following:

- optimisation of the HP domestic tumble dryer should start with energy consumption,
- the most important parameter in the design is the enthalpy of the air entering the heat pump,
- set of variables available for control of the drying process is limited, among them are rotational frequencies of the drum (changing laundry surface exposed to energy transfer) and fan (velocity of air around clothes and through the HP)
- future and improved domestic clothes dryers should in the optimisation procedure consider also damage to the laundry and emissions of particles from it.

Acknowledgment

The authors acknowledge the project “Hybrid technologies of factories of the future for the green transition (Greentech), TN-02-0782” was financially supported by the ARIS National Research Agency.

References

[1] A. M. Bassily et al., Performance Analysis of an Electric Clothes Dryer. Drying Technol. 2003, vol. 21, 499–524.

[2] L. Novak et al., “Quantification of fiber shedding from cotton fabrics during drying in a domestic heat pump tumble dryer”, Journal of Natural Fibers, vol. 21, no. 1, pp. 1-23, 2024.

[3] IEC. 2012. IEC 61121: Tumble Dryers for Household Use - Methods for Measuring the Performance. Geneva, Switzerland: Int. Electrotechnical Commission (IEC).

SIMULATION OF A DISTRICT HEATING NETWORK WITH INTEGRATED HIGH TEMPERATURE STORAGE SYSTEM POWERED BY RENEWABLE ENERGY

Spiros Alexopoulos[1]*, Pascal Schmitz[1], Daniel Högemann[2], Georgios Panaras[3], Georgios Makris[4]

[1] FH Aachen University of Applied Sciences, Solar-Institut Jülich, Germany

[2] Kraftanlagen Energies & Services SE, Germany

[3] University of Western Macedonia, Greece

[4] Zeus Helios Electricity Company, Cyprus

* *Corresponding Author: alexopoulos@sij.fh-aachen.de*

Abstract. District heating (DH) networks supply residential and commercial buildings with low-temperature heat for space heating and water heating on a large scale. These large heating networks often utilize waste heat from power plants or heat-intensive industrial processes and incorporate backup heat generators to buffer temporary peak loads. This paper examines the integration of a renewably powered high-temperature thermal storage system with power generation unit into an existing heating network in the city of Kozani (Greece), which is powered by waste heat from a lignite-fired power plant and fossil-fired backup boilers. The authors of this paper present the simulation model of a demonstrator-scale setup for the new energy concept that aims to substitute a part of the fossil thermal and electric energy supply of the DH network. Annual simulations of the entire system are performed with an appropriate software tool and it is analysed how much of the thermal energy supply by power plant and backup boilers can be substituted by the new energy concept. The results indicate that the energy system demonstrator can cover a maximum of about 2.6 % of the total thermal demand of the DH network and in turn, the CO_2 emissions are decreased by 1971 tons CO_2 per year.

Keywords. Simulation, Thermal storage, District heating, Renewable energy, High temperature

1 Introduction

In the city of Kozani, located in the Northern part of Greece, a district heating (DH) network is in operation since 1993. The DH network covers the main heating and hot water demand of the city buildings and infrastructure. The DH network is supplied with heat from the nearby lignite-powered "Agios Dimitrios power plant", which is located about 20 km away from the city. The thermal energy is transferred to the city through a hot water piping network and fossil-fired boilers are operated intermittently to cover a part of the thermal demand in times it reaches temporary spikes. The backup boilers are located in a boiler house on the outskirts of the city of Kozani.

As part of the EU-funded research project NEUTRON ("Net-zero Energy fUture through the identification of innovative Technologies under a circulaR, sustainable, and inclusive just transitiON") an innovative energy system with power generation unit and thermal energy storage, the so-called Green Heat Module (GHM), is developed for the integration into the existing district heating network in Kozani. The aim is to reduce the use of fossil fuels and fossil electricity for the operation of the DH network.

The sensible thermal energy storage is based on a ceramic storage material and allows high operating temperatures of up to 1000 °C. The achievable high discharging temperatures enable the operation of conventional power cycles, e.g. a Water-Steam-Cycle or Organic Rankine Cycle (ORC). The power cycle provides electricity on demand as well as waste heat for the supply of the district heating network (cogeneration), acting as a combined heat and electricity storage. The concept of a ceramic-based high temperature storage with ORC unit was built and demonstrated within two research projects funded by the German Federal Ministry of Economic Affairs and Climate Action. The project was realised by Solar-Institut Jülich, Kraftanlagen Energies & Services SE and additional industry partners with the construction of the so-called multiTESS facility located in Jülich. [1]

Two different system variants are considered within the NEUTRON project: On the one hand, a

smaller-sized "demo plant" utilizing an Organic Rankine Cycle (ORC) as power generation unit to showcase the technology and on the other hand, a large-scale installation utilizing a larger thermal energy storage and a conventional water-steam cycle as power generation unit. In addition, several system variations are investigated, which use different renewable energy systems (RES). Within the scope of this paper, the focus is on the simulation of the smaller-sized demo plant powered by a local photovoltaic (PV) plant. In the following chapters, the simulated energy system is referred to as "demo plant".

In the NEUTRON project, a technical and economic analysis is carried out to evaluate the performance of the district heating system with integrated thermal energy storage and power generation unit. Annual simulations with hourly resolution are conducted in order to calculate the performance of the plant and reveal how much of the thermal and electric energy of the current DH system can be substituted by retrofitting the DH network with the proposed system.

In the chapters below, the structure and components of the simulation model are described and preliminary simulation results are presented. The model is currently still in the process of ongoing optimisation and refinement.

2 Simulation Model Setup

2.1 Layout of demo plant simulation model

The software tool TOP-Energy is used for the modelling and simulation of the demo plant. TOP-Energy contains a built-in library with a set of technical components. The component blocks can be arranged and connected in a visual simulation scheme. The specification and dimensioning of the technical components is done through a graphical user interface. In addition to the components contained in the library, user-defined components can be programmed from scratch.

In Figure 1, the layout of the demo plant is shown. Each block represents a component and the input and output nodes are connected to other blocks with lines, enabling the exchange of economic, ecological and technical data (e.g. energy flows) between them. The main system components are highlighted with dashed boxes and labels and a short description of each one is given below:

- **Heat supply power plant**: Fossil district heating supplier (lignite-fired power plant) and price tariff for the supplied heat.
- **Backup boiler(s)**: Fossil-fired backup boiler with price tariff for the supplied heat
- **Green Heat Module (GHM)**: Contains power-to-heat (P2H) unit and sensible high temperature energy storage.
- **PV plant**: Consists of a solar radiation block providing data to a PV field block. The PV electricity powers the GHM and/or covers the demand of electric devices within the scope of the DH network (e.g. circulation pumps).
- **ORC unit**: The Organic Rankine Cycle provides electricity and thermal energy for the DH network operation. A separate heat exchanger allows the direct pass-through of heat from GHM to the DH network, effectively bypassing the ORC.
- **Public electricity grid**: Public grid connection and price tariff for the public electricity supply.

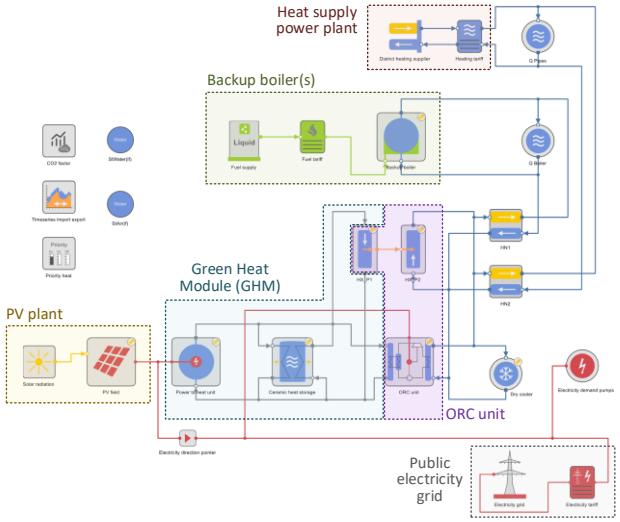


Figure 1: Layout of demo plant simulation model

2.2 Remarks on the model structure and simulation settings

The demo plant model contains thermal and electric demand blocks, which represent the energy demands required for the operation of the DH network. These blocks contain the hourly power demand over the course of a full year. The demands are based on historic measurement data of the DH network. The DH network itself is not fully included on a component-level in the simulation model, but only its required energy demands and the conventional DH suppliers, namely power plant and backup boilers, are part of the model.

For the thermal demands, two separate blocks are used: One block named "Q_pipes" contains the

historic annual thermal power curve that was provided to the DH network by the power plant in a given year. The block named "Q_boiler" contains the historic annual thermal power curve provided by the fossil backup boilers to the DH network. In addition to these two thermal demands, the red circular block with lightning symbol "Electricity demand pumps" contains the corresponding electric demand of the water circulation pumps in the DH network (compare Figure 1).

In the simulation, the thermal demands are covered by a combination of the conventional district heat suppliers, the power plant and the backup boilers, as well as by the thermal energy contribution of the retrofitted demo plant system. The electric demand of the water circulation pumps is covered by a combination of electricity supplied by the public grid and by the demo plant through direct supply from PV and through operation of the ORC unit from stored energy. The simulation results then show how much thermal and electric energy is provided by the demo plant and in turn how much energy of the conventional district heating suppliers can be substituted.

3 Exemplary simulation case

3.1 Operation strategy and optimisation procedure

The operation strategy for the energy system simulated in TOP-Energy can be adjusted based on different settings. One option is the use of integrated optimisation functions that aim to achieve a minimum or maximum for a value of interest. For example, the solver can aim to minimise the annual operation costs or the annual CO_2 emissions of a simulated energy system. Another option is the definition of switch-on sequences for the system components. As an example, the switch-on sequence can specify that PV electricity is supplied to the P2H unit with first priority and to other components with second priority.

An additional setting influencing the operation strategy for the energy system is the so-called "look ahead time". The look ahead time determines how many hours in the future are used as a prognosis to calculate the optimal operation strategy for a given time step in the simulation. For simulation models containing renewable energy producers and energy storages, this prognosis allows the optimisation of the charging and discharging cycles of the energy storage.

For the simulation model of the DH network and demo plant covered in this paper, an optimisation function for the minimisation of operation costs is used in conjunction with a look ahead time of 24 hours. In a first simulation case, the thermal energy supply of the demo plant sent to the DH network is prioritised over its electricity output to supply circulation pumps. The prioritisation is chosen, in order to calculate the maximum achievable thermal energy supply from the demo plant to the DH network. In a second case, the thermal energy supply to the DH network is not prioritised over the electricity output to supply circulation pumps and the optimisation function predicts the distribution of the energy streams to achieve a minimum for the overall operation costs.

3.2 Simulation case boundary conditions

The system components in the simulation scheme shown in Figure 1 above are dimensioned inside separate submenus for each component where the technical, economic and ecological characteristics are specified. In the current version of the model, economic parameters are only specified in form of operation costs for the conventional district heating suppliers and for the public electricity supply. Capital costs are not considered within the annual simulation, as they have no impact on the operation regime. CO_2 emission factors are set for the conventional district heating suppliers, namely power plant and backup boilers, and for the public electricity supply. Currently, only direct CO_2 emissions occurring during the operation of the plant are considered, but no CO_2 emissions occurring within the full life cycle of each component are considered.

The main technical parameters of the components, which are part of the demo plant, are listed below:

- **PV plant**: South-oriented fixed PV installation with a module elevation angle of 30 ° and a nominal electric output power of 12.5 MW. Solar radiation data for the city of Kozani is used from the PVGIS database.
- **P2H unit**: E-heater heating up air with a nominal thermal power of 8 MW and an efficiency of 97 %.
- **Thermal storage**: Sensible thermal energy storage based on a ceramic storage material. The thermal storage capacity is 48 MWh and the charging and discharging power is limited to 8 MW and 5.25 MW respectively. The daily relative thermal losses are 5 % of the energy stored.
- **ORC unit**: The nominal electric output power is 1 MW and the thermal to electric

efficiency is around 20 %. The efficiency of the bypass heat exchanger is set to 90 %.

3.3 Brief summary of first simulation results

The annual simulation was conducted with the historic energy demand curves of the DH network for the year 2022.

Simulation case 1:

For the first simulation case with prioritisation of the thermal energy supply to the DH network, the results indicate that about 2.6 % of the total thermal energy demand of the DH network can be covered by the demo plant installation. Separated into the covered backup boiler and power plant energy, about 22.4 % of the backup boiler demand and 1.8 % of the power plant demand is supplied by the demo plant. The electric demand of the circulation pumps is covered by a share of 2.2 %.

The substitution rate of 22.4 % of the thermal energy previously provided by the backup boilers of the DH network has a strong impact on the reduction of operation costs, as the specific operation costs for the backup boilers are several magnitudes higher compared to the specific operation costs of the power plant district heating supplier.

During the heating period of the DH network from October to May, the PV plant supplies most of the electricity to the P2H unit of the demo plant. Only a small share is available to supply the circulation pumps (coverage of 2.2 %). During summer time, between May and September, the DH network is not in operation and in this period the PV plant supplies approximately 8.1 GWh of electricity, which is available for other electric devices.

The avoided CO_2 emissions due to substituted fossil thermal energy in the DH network account to a total of 1971 tons CO_2 per year and respectively to 82.4 tons CO_2 per year for the replaced grid electricity.

Simulation case 2:

For the second simulation case without prioritisation of the thermal energy supply to the DH network, about 1.6 % of the total thermal energy demand of the DH network can be covered by the demo plant installation. The substituted energies amount to 15.3 % for the backup boiler and to 1 % for the power plant energy. 41.4 % of the electric demand of the pumps is supplied by the demo plant.

The annual CO_2 emission reduction on the thermal side of the DH network amounts to 1230 tons CO_2 and to 1563 tons CO_2 on the electric side for replaced grid electricity. A CO_2 emission factor of 376.67 g CO_2 per kWh was set for the electricity mix in Greece. [2]

4 Conclusions

In this short paper, the approach of modelling and simulating a renewably powered high temperature energy storage system and ORC unit integrated into an existing district heating network in Kozani (Greece) was presented. First annual simulation results show the potential of the demo plant system to provide thermal energy to the existing DH network in Kozani. Depending on the boundary conditions, the thermal supply to the existing DH network can be maximised or the focus can be placed on the co-supply of the circulation pumps with electricity. The simulation model is in its early development phase and will be further developed to build the base for a detailed economic assessment of the demo plant system. In future simulations, the utilisation of the thermal storage to store and release electricity during the summer months to profit from variable electricity market prices will be investigated. In addition, a large-scale plant will be developed based on the current simulation model and deliver insight into the performance of a large-scale system with a higher potential for cost reductions and CO_2 emission reductions.

Acknowledgement

The authors would like to thank the company DEYAK for their cooperation within the NEUTRON project and the provision of operation data of the district heating network in Kozani which was used for the presented simulation.

References

[1] “multiTESS-Anlage in Jülich”, FH Aachen, https://www.fh-aachen.de/forschung/institute/sij/forschungsprojekte/multitess-anlage-in-juelich (accessed on 15th November 2024)

[2] Carbon intensity of the power sector in Greece from 2000 to 2023 (in grams of CO_2 per kilowatt-hour) [Graph], Ember, July 3, 2024. [Online]. Available: https://www.statista.com/statistics/1290229/carbon-intensity-power-sector-greece/

LABOTHAPPY: DEVELOPMENT OF AN OPEN-SOURCE PYTHON LIBRARY FOR THERMODYNAMIC SYSTEM MODELLING AND SIMULATION

Elise Neven[1]*, Basile Chaudoir[1]*, Vincent Lemort[1]

[1] Thermodynamics Laboratory, University of Liege, Liege, Belgium

* *Corresponding Author:* elise.neven@uliege.be

Corresponding Author: basile.chaudoir@uliege.be

Abstract. Modelling and simulation are essential in the design, optimization, and control of thermodynamic systems, yet developing reliable models can be time-consuming, and recreating similar models across different platforms or code versions is redundant and inefficient. To address this challenge, researchers at the University of Liege have developed *LaboThapPy*, an open-source Python library designed to gather a wide range of thermodynamic models accumulated over years of research. By using Python's Object-Oriented Programming (OOP) capabilities, *LaboThapPy* offers a modular and flexible toolkit for simulating thermodynamic systems. The library can support a variety of applications, such as, Organic Rankine Cycle (ORC) systems, Brayton cycle systems, and Heat Pump (HP) systems, and can simulate part-load behaviour. This paper presents an overview of *LaboThapPy*'s architecture, capabilities, and applications, demonstrating its potential as a resource for thermodynamic research and engineering.

Keywords. Python library, Thermodynamic system modelling, Open-source software, Object-Oriented Programming

Nomenclature

$\dot{m}$	Mass flow rate (kg/s)
h	Specific enthalpy (J/kg)
$\dot{Q}$	Transferred heat power (W)
$\dot{W}$	Transferred work power (W)

1 Introduction

Over years of research, numerous thermodynamic models have been developed to simulate individual components and entire systems, allowing the design, optimization, and control of thermodynamic systems. At the Thermodynamics Laboratory of the University of Liege, researchers observed a recurring issue: identical or similar models were being recreated repeatedly over different software or codes, while others were lost as researchers departed, resulting in lost time and efficiency for new team members. This challenge underscored the need for a standardized, accessible repository that would gather these models, fostering continuity and productivity across research projects.

The *LaboThapPy* library emerged as a solution to this problem, establishing a common framework for modelling thermodynamic components and enabling users to assemble these components into larger systems. Designed as a flexible and modular toolkit, *LaboThapPy* offers researchers a platform to build and simulate complex thermodynamic systems. Python was chosen as the development language due to its Object-Oriented Programming (OOP) capabilities, which enhance modularity and extensibility, its wide adoption in scientific research and its free availability. Furthermore, *LaboThapPy* is available as an open-source library on GitHub, encouraging collaboration and open-science practices that are becoming increasingly important in energy system modelling [1].

Although a range of thermodynamic modelling libraries exist (e.g., ASPEN [2], Thermocycle [3], TESPy [4], and oemof [5]), *LaboThapPy* distinguishes itself with its focus on detailed component-level modelling, an aspect often less emphasized by other platforms. This paper presents an overview of *LaboThapPy*, its architecture, capabilities, and contributions, demonstrating its potential as a resource for the thermodynamics research and engineering community.

2 Scope and content

The *LaboThapPy* library currently encompasses a range of steady-state models and sizing models for thermodynamic components, with plans to

incorporate dynamic models in future versions. Its component models span from basic models (for example a constant isentropic efficiency model for compressors), to more complex models (for example semi-empirical models for compressors), offering flexibility to accommodate various levels of model complexity depending on the user's needs.

In addition to core component models, *LaboThapPy* provides tools that extend the modelling process, including functions for generating pressure-enthalpy (p-h) diagrams, model calibration codes, and post-processing utilities for data analysis.

With respect to thermodynamic system models, *LaboThapPy* includes basic templates for standard cycles such as simple Organic Rankine Cycle (ORC) systems and Heat Pump (HP) systems, along with solvers for these straightforward cycle simulations. For more complex configurations, the library offers a flexible structural framework, enabling users to assemble component models into larger systems. However, cycle-specific solvers for advanced configurations are currently left to the user to implement, as the primary focus of *LaboThapPy* remains on component-level model development rather than system-level cycle-solving.

3 Architecture

LaboThapPy is built using an object-oriented programming approach, resulting in a highly modular and adaptable codebase. This modularity provides users with the flexibility to configure various thermodynamic cycles and to select specific model types for each component based on the requirements of their simulation. The architecture of *LaboThapPy* is inspired from established thermodynamic simulation libraries (e.g., Thermocycle [2]).

At the core of *LaboThapPy* are three primary modules:

- **Connector:** Allows the linking of components through energy transfers that occur between them.
- **Components:** Serves as the fundamental building blocks, representing individual parts of a system, such as compressors, turbines, and heat exchangers.
- **Machine:** Acts as a container for each simulation, representing entire systems and organizing the assembly of components and connections into cohesive models.

3.1 Connectors

Connectors are the elements that link different components in the system, representing the transfer of energy between them. Energy flows are represented by three types of connectors:

- **Mass Connector** carries energy through mass flow, defined as $\dot{m} \cdot h$ (mass flow rate multiplied by specific enthalpy). It computes thermodynamic properties at each point using two thermodynamic properties as inputs. The library relies on CoolProp [6] to obtain these thermodynamic properties. Currently, fluid mixtures are not implemented
- **Heat Connector** represents the transfer of thermal energy, defined as $\dot{Q}$ (rate of heat flow), to account for heat energy transfer between components or with the ambient.
- **Work Connector** represents the transfer of mechanical energy, defined as $\dot{W}$ (rate of work), allowing the modelling of power-related interaction within the system.

3.2 Components

Component models are the fundamental building blocks for simulating thermodynamic systems. Representing individual components under steady-state conditions, they can be connected using connectors to form complex system models. Each component model is implemented as a class defined by specific parameters, inputs, outputs and connectors. All component classes inherit from a parent class, *`BaseComponent`*, which provides shared methods and ensures uniformity across models. This structure allows coders to focus only on the specifics of each component model, streamlining collaboration and model development.

Components can be defined in two main ways:

1. **Connectors:** Inputs are set via connectors, enabling components to directly exchange energy with other components within a system. This approach is ideal for full-system simulations.
2. **Direct Inputs/Outputs:** Inputs and outputs are set directly within each component, useful for standalone use of component models.

Currently, the library supports only steady-state models, while future expansions may include dynamic modelling capabilities.

3.3 *Machines*

The *Machine* module acts a container for each simulation, organizing the assembly of components into functional circuits and systems. Individual components can be linked to form circuits, which may be either open or closed loops, and each circuit is characterized by a single working fluid. Multiple circuits can then be combined to construct entire systems.

Circuits within a machine can also connect to *sources* and *sinks* for mass, heat, or work. Sources are defined as hypothetical reservoirs that can supply an unlimited amount of mass, heat, or work, while sinks represent theoretical outlets capable of absorbing these flows. Users can also define *`sub-machines`*, which group components to function as single units within larger systems, enhancing modularity.

Similar to the *`BaseComponent`* class, which standardizes component-level models, the *`Circuit`* class serves as a parent class containing essential methods shared across different circuit types, simplifying circuit creation.

The library uses a causal-recursive approach to solve systems, prioritizing robustness and reliability, particularly for complex thermodynamic models. While this method may be slower and less flexible, it simplifies debugging. Conversely, an acausal approach offers more readable models but makes debugging harder and less robust [7].

4 Method of Implementation

The modelling process for simulating a specific thermodynamic system involves several structured steps, illustrated here using the example system in Figure 1. This system comprises an Organic Rankine Cycle (ORC) with R1233zd(E) as the working fluid, as well as a hot and a cold water loop. The latter features an air mass source and sink. This example will be soon available in the library.

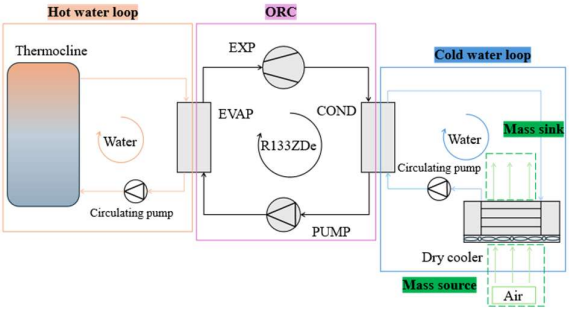


Figure 1: Example of a thermodynamic system.

1. **System Initialization**: The simulation begins by creating an empty machine class, which serves as a container for all system components and initial parameters. Each main loop in the system, such as the ORC, hot water, and cold water loops, is represented by a corresponding circuit object to help organize the components within each section.

2. **Component Instantiation**: Within each circuit, individual components are instantiated with their specific parameters. For instance, the ORC circuit includes a pump, heat exchangers, and an expander; the hot water loop includes a pump and a thermal storage; and the cold water loop contains a dry cooler and a pump.

3. **Component Connection**: Components within each circuit are connected through connectors, which facilitate the flow of energy between them. In this example, mass connectors link components within the ORC, hot water, and cold water loops, enabling continuous energy and mass flow through each part of the system.

4. **Initialization of Guesses**: After the circuits and components are configured, initial guesses for the solution process are provided either by the user or through a pre-conditioner. These initial guesses serve as a foundation for the subsequent recursive solution process.

5. **Recursive Solution Process**: The solution process involves traversing each circuit recursively. As the process advances, each component model is solved based on its inputs, parameters, and initial guesses. This recursive process updates and refines the solution iteratively until the system reaches convergence on a stable and accurate solution.

5 Documentation

Comprehensive documentation is essential for an open-source project like *LaboThapPy*, which aims to support collaboration among multiple contributors and users. To facilitate ease of use and ensure consistency, a standardized nomenclature is implemented throughout the code. The documentation is organized in four different levels:

1. **In-Code Comments**: Comments to clarify complex or less intuitive parts of the code.

2. **Docstrings**: Each model and function is documented with docstrings that describe its purpose, underlying assumptions, and key parameters.

3. **Usage Examples**: Practical usage examples demonstrate how to apply models within the library.

4. **Related Articles/Reports**: For certain models, detailed articles and reports are available, offering in-depth explanations.

Additionally, a *Read the Docs* site [8] has been implemented to provide centralized, accessible documentation. This online resource lists all component models currently available in the library, with descriptions and usage guidelines. The LaboThapPy GitHub repository [9] hosts the code, facilitates collaboration, and includes bug tracking, creating a transparent and collaborative platform for development.

6 Work in Progress

LaboThapPy is an evolving project with active development aimed at expanding its model library and capabilities. Current goals include adding new component models, system applications, test units, charge-sensitive models, and dynamic models. An interesting future feature could be integrating existing frameworks for solving model equations, which could enhance the library's ability to handle dynamic simulations more efficiently.

7 Conclusion

LaboThapPy is a flexible and modular open-source Python library for thermodynamic modelling, developed from models based on years of research at the University of Liege. By offering standardized, object-oriented component models, the library reduces coding redundancy and promotes collaboration across projects. With its structured framework of connectors, components, and machine models, *LaboThapPy* supports the simulation of various thermodynamic systems, including Organic Rankine Cycles (ORC), heat pumps, and other thermodynamic system applications. To ensure accessibility, *LaboThapPy* features layered documentation and is hosted on GitHub, where users can contribute to its development, report issues, and suggest enhancements. This open-source approach not only facilitates research and engineering applications but also encourages ongoing improvement and innovation within the thermodynamic modelling community.

Acknowledgement

Many thanks to all contributors.

References

[1] S. Pfenninger, J. DeCarolis, L. Hirth, S. Quoilin, and I. Staffell, 'The importance of open data and software: Is energy research lagging behind?', *Energy Policy*, vol. 101, pp. 211–215, Feb. 2017, doi: 10.1016/j.enpol.2016.11.046.

[2] Aspen Technology, Inc. *ASPEN Plus.* Bedford, MA, USA: Aspen Technology, 2023.

[3] S. Quoilin, A. Desideri, J. Wronski, I. Bell, and V. Lemort, 'ThermoCycle: A Modelica library for the simulation of thermodynamic systems', presented at the the 10th International Modelica Conference, March 10-12, 2014, Lund, Sweden, Mar. 2014, pp. 683–692. doi: 10.3384/ecp14096683.

[4] F. Witte and I. Tuschy, 'TESPy: Thermal Engineering Systems in Python', *JOSS*, vol. 5, no. 49, p. 2178, May 2020, doi: 10.21105/joss.02178.

[5] S. Hilpert, C. Kaldemeyer, U. Krien, S. Günther, C. Wingenbach, and G. Plessmann, 'The Open Energy Modelling Framework (oemof) - A new approach to facilitate open science in energy system modelling', *Energy Strategy Reviews*, vol. 22, pp. 16–25, Nov. 2018, doi: 10.1016/j.esr.2018.07.001.

[6] I. H. Bell, J. Wronski, S. Quoilin, and V. Lemort, 'Pure and Pseudo-pure Fluid Thermophysical Property Evaluation and the Open-Source Thermophysical Property Library CoolProp', *Ind. Eng. Chem. Res.*, vol. 53, no. 6, pp. 2498–2508, Feb. 2014, doi: 10.1021/ie4033999.

[7] G. Schweiger, H. Nilsson, J. Schoeggl, W. Birk, and A. Posch, 'Modeling and simulation of large-scale Systems: a systematic comparison of modeling paradigms', Sep. 01, 2019, *arXiv*: arXiv:1909.00484. doi: 10.48550/arXiv.1909.00484.

[8] "LaboThapPy documentation" [Online] Available: labothappy.readthedocs.io (2024)

[9] "LaboThapPy repository" [Online]. Available: https://github.com/PyLaboThap/LaboThapPy (2024)

UNDERSTANDING THERMODYNAMIC NON-EQUILIBRIUM EXPANSION

Xander van Heule[1,*], Michel De Paepe[1,2,3], Steven Lecompte[1,2]

[1] Ghent University, Department or Electromechanical, systems and Metal Engineering, Sint-Pietersnieuwstraat 41, Ghent, 9000, Belgium

[2] FlandersMake@UGent – Core lab MIRO, Ghent, 9000, Belgium

[3] Department of Mechanical Engineering, University of Cape Town, Private Bag X3, Rondebosch 7701, South Africa

** Corresponding Author: xander.vanheule@ugent.be*

Abstract. Most of the primary burned fuel is lost as low-temperature residual heat. This low-temperature heat is classified at temperatures of 100 °C or lower. There are currently no widely used technologies that are capable of effectively utilizing these heat streams. However, some technologies have been proposed. One proposed technology is the trilateral flash cycle which operates similarly to the basic organic Rankine cycle, but with saturated liquid at the expander inlet. This requires an expander capable of expanding two-phase conditions. Additionally, during rapid decompression of a liquid, it has been shown that thermodynamic non-equilibrium effects occur. This has also been shown to occur within the trilateral cycle. This research presents a model to predict the degree of these thermodynamic non-equilibrium effects, the impact on the expansion process, and the cycle. Additionally, an experimental setup is described that is used to validate the previous model.

Keywords. Two-phase, Expander, Non-equilibrium, ORC

1 Introduction

The available residual heat equals around half of the primary burned energy. Additionally, around two-thirds of this residual heat is within the low-temperature region of below 100°C [1].

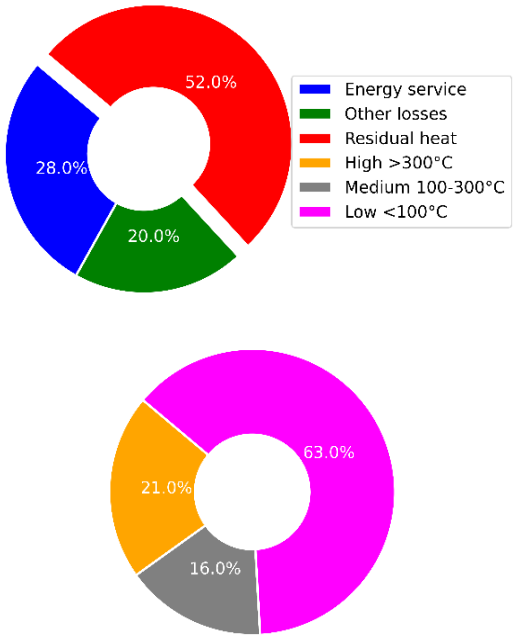


Figure 1: Estimated global ratios of available residual heat and their temperature levels [1].

Technologies to effectively reuse these heat streams have been studied [2]. However, they are often not as effective for the low-temperature sources. One technology applicable to this region is the organic Rankine cycle (ORC) or alternatives from it. A promising alternative is the trilateral cycle (TLC) or the partially evaporating ORC (PEORC). In these cycles, the working fluid is no longer fully evaporated as is the case in the ORC. Instead, the working fluid is partially evaporated in the evaporator. This results in better temperature profile matching, resulting in greater second-law efficiencies [3]. The TLC is a PEORC where there is no evaporation, thus a saturated liquid exits the evaporator. For both cycles, the expander operates within the two-phase region. This process occurs sufficiently fast for non-equilibrium effects, metastable superheated liquid, to occur [4], similar to phenomena that occur during static flashing [5]. These non-equilibrium effects have not been implemented within a model for a volumetric expander. The goal of this research was to construct a predictive model for a free linear reciprocating two-phase expander that takes into account the non-equilibrium phenomena measured [6]. Secondly, to compare the results with other predictive models which apply standard equilibrium thermodynamics [7]. Lastly, to compare the predicted expansion behaviour with experimental measurements.

2 Expansion model

Here the expansion model will be shortly elaborated. Secondly, the implementation within a cycle is explained.

2.1 Expansion chamber

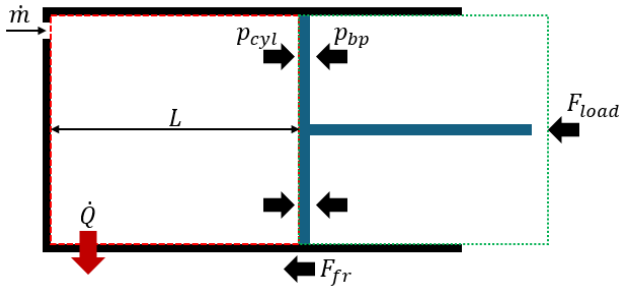


Figure 2: Illustration of the working chamber of a free linear reciprocating expander.

Newton's second law is applied to the green dashed-dotted line in Figure 2 to determine the acceleration of the piston. The friction force is determined based on the modified LuGre model [8].

2.2 Non-equilibrium model

The expansion model is adapted from a homogeneous relaxation model [9] and elaborated in a previous work [6]. Here an extra relaxation equation, Equation (1), is added to the conservation equations of the red dotted volume in Figure 2. The equations of Woschni [10] are applied for the heat loss within the conservation of energy.

$$\frac{\Gamma_g}{\rho} = -\frac{x - \bar{x}}{\Theta} \tag{1}$$

Where Γ_g is the volumetric vapour generation rate, ρ the density, x the vapour quality, $\bar{x}$ vapour quality that would be achieved at thermodynamic equilibrium conditions, and Θ the relaxation time. This equation is the simplest linear expression, but it has been used effectively in past research [9]. The relaxation time, Θ, is defined based on the dimensionless pressure, ψ, and the void fraction, ϵ, as defined in Equation (2).

$$\Theta = \Theta_0 \cdot \epsilon^a \cdot \psi^b \tag{2}$$

The coefficients Θ_0, a, and b are empirically determined based on relevant experimental data related to working fluid, process, and dimensions. For this application, the best available data was based on the experiments of Kanno and Shikazono [11] and the found values are listed in Table 1.

Table 1: Empirical coefficients for the relaxation time of Equation (2)

Θ_0	a	b
$4.71 \cdot 10^{-3} s$	-0.224	-2.998

2.3 Partially evaporating ORC

The expansion model, which incorporates the thermal non-equilibrium effects, is applied in a PEORC. The set conditions of the cycle and the free linear expansion device are listed in Table 2. The vapour quality at the inlet of the expander and the amount of expansion cycles (intake, expansion, exhaust, recompression) per minute can be varied. For each chosen vapour quality, the model will look for the matching cycle speed such that the working fluid mass flow rate in the evaporator and the expansion device are the same.

Table 2: Empirical coefficients for the relaxation time of Equation (2)

Condensing temperature	$20°C$
Evaporating temperature	$100°C$
Working fluid	R1233ZD(E)
Heat source	Air
Heat source temperature	110°C
Heat source mass flow rate	0.2 kg/s
Subcooling pump inlet	5°C
Pinch point temperature difference	5°C
Isentropic pump efficiency	0.7
Expander diameter	0.09 m
Expander clearance length	0.003 m
Cut-off ratio	25 %

3 Simulation results

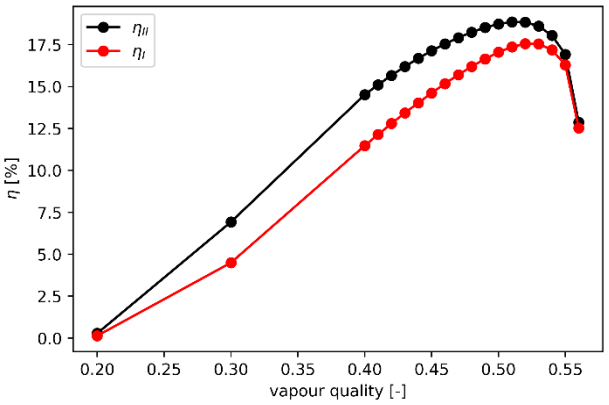


Figure 3: First (red) and second (black) law efficiency of the PEORC in Table 2 in function of vapour quality at the expander inlet.

Figure 3 presents the first and second law efficiency of the PEORC with the parameters listed in Table 2 in function of the vapour quality at the inlet of the expander. The first law efficiency is the net recovered power divided by the heat transferred in the evaporator, while the second law efficiency is the net recovered power divided by the incoming exergy flow of the heat source. As the heat source inlet is taken as a constant flow rate and temperature, the inlet exergy flow is also constant. Therefore, the second law efficiency follows linearly with the net recovered power. For very low vapour qualities, the required cycle speed of the expander increases significantly. Resulting in a behaviour more similar to a valve than an expander. This results in net power recoveries nearing zero, or going negative when the required pumping power becomes greater. For increasing vapour quality, the efficiencies increase. Up until a certain point, after which they decrease again. This is likely due to the pinch point condition. For increasing vapour qualities, the transferred heat in the evaporator will decrease for the same pinch point temperature difference. Resulting in possible lower net recovered power. Additionally, for greater vapour qualities, the simulation fails to find a viable solution. The required cycle speed becomes too low, and too long strokes are needed. This is a result of the chosen geometry. This indicates the importance of designing the expander based on the application.

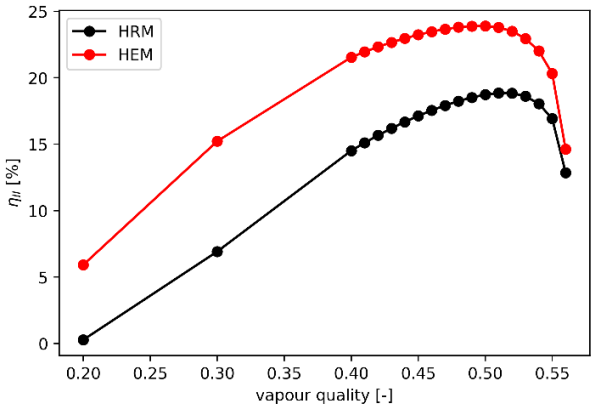


Figure 4: Comparison between the second law efficiency of the PEORC in Table 2 for non-equilibrium (black) and equilibrium (red) expansion.

The second law efficiency for the PEORC with non - equilibrium (HRM) expansion is plotted in Figure 4 together with the second law efficiency of the same cycle, but with equilibrium expansion (HEM) [12]. The results show a reduction of the net recovered power by around 20%. These are significant losses related to the non-equilibrium expansion which are not present in most studies. However, this difference is less than the benefit gained when comparing the PEORC to the basic ORC [13]. It can be assumed that therefore the PEORC is still beneficial compared to the basic ORC for low-temperature heat sources, but to a lesser extent than originally derived.

4 Experimental setup

To validate the results of the simulations and obtain better related experimental data for a more accurate fit of the empirical parameters, an experimental setup has been designed and constructed as presented in Figure 5.

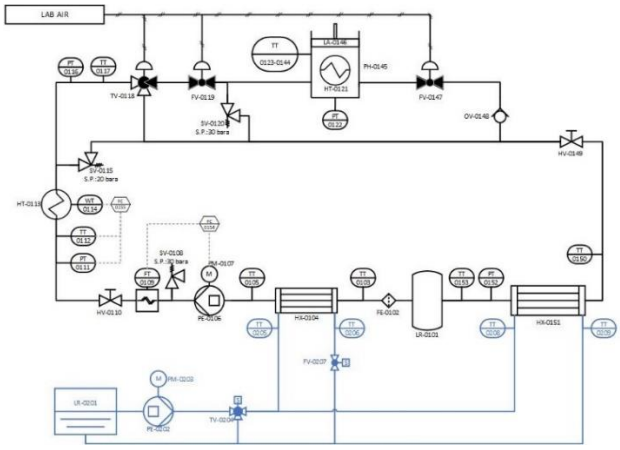


Figure 5: P&ID of the experimental setup with the blue chiller loop and the black refrigerant loop.

The goal of the setup is to quantify the degree of metastability or, in other words, the amount of superheat at the instantaneous pressure within the expansion chamber. The setup is capable of expanding a preconditioned mixture with a predefined movement profile set by the linear actuator. The first task to achieve this is to precondition the refrigerant to the desired thermodynamic state for the measurement. This can be achieved by altering the pump frequency and the manual valve until the desired pressure level is reached. The vapour quality can be controlled by setting the power within the heating element. During this preconditioning, the setup runs in by-pass as indicated by the white parts of the three-way valve in Figure 5. Once the refrigerant is conditioned, the setup is ready for an expansion experiment. All three valves are powered. This results in the expansion chamber now being a part of the flow path for the refrigerant. The expansion chamber is isolated by removing the power to the three valves again, returning the flow to the by-pass with the three-way valve. With the loaded expansion chamber now isolated, an experiment can be performed. This is achieved by running any preloaded movement profile

with the linear actuator. After the expansion, the heating element around the piston is used to evaporate all the refrigerant in case there is some liquid left. All liquid will be assumed evaporated if every thermocouple measures a temperature five degrees above the saturation temperature. With the thermodynamic state in a stable vapour, the density of the expanded mass can be determined which can be used to determine the expanded mass as well. The expansion test of the setup has been validated to show [14] that it is capable of measuring the temperature and pressure profiles sufficiently fast.

5 Conclusions

This work shortly introduces the results of a research project about volumetric two-phase expansion devices. Initially, the expansion itself has been modelled with the implementation of an adapted homogeneous relaxation model. This expansion model takes into account the thermal non-equilibrium phenomena occurring within the expansion chamber. This non-equilibrium expansion model was secondly implemented within a free linear reciprocating expander model, that was in turn implemented within a partially evaporating organic Rankine cycle model. The simulations predict that this cycle performance will be reduced with around 20% due to the incorporation of the non-equilibrium losses. However, based on literature, this cycle would still show a benefit compared to the basic organic Rankine cycle, even with this extra reduction included. Lastly, an experimental setup was designed and build to validate the simulation results of the constructed models.

Acknowledgement

I would like to thank the Research Foundation-Flanders for their financial support through FWO-Flanders grants (1SD9723N).

References

[1] C. Forman et al., “Estimating the waste heat potential”, Renewable and Sustainable Energy Reviews, no. 57, pp. 1568-1579, 2016.

[2] E. Garofalo et al., “ Waste heat to power: Technologies, current applications, and future potential”, Energy Technology, no. 8, 2020.

[3] S. Lecompte et al., “Thermodynamic analysis of the partially evaporating trilateral cycle”, in Proceedings of ORC 2013 – 2nd International Seminar on ORC Power Systems, Rotterdam, Netherlands.

[4] H. Kanno et al., “Experimental study on two-phase adiabatic expansion in a reciprocating expander with intake and exhaust processes”, Int. Journal of Heat and Mass Transfer, no. 102, pp. 1004-1011, 2016.

[5] L. Friedel et al., “Phase distribution in vessels during depressurization”, Int. Journal of heat and fluid flow, no. 5, pp. 229-234, 1984.

[6] X. van Heule et al., “Modelling of two-phase expansion in a reciprocating expander”, Applies Thermal Engineering, no. 218, pp. 119224, 2023.

[7] X. van Heule et al., “Optimization of a partially evaporating organic Rankine cycle with thermal non-equilibrium expansion”, in Proceedings of ORC 2023 – 7th International Seminar on ORC Power Systems, Sevilla, Spain.

[8] X. B. Tran et al., « Dynamic friction behaviors of pneumatic cylinders”, Intelligent control and automation, no. 4, PP. 65-75, 2012.

[9] P. D. Zapolski et al., The non-equilibrium relaxation model for one-dimensional flashing liquid flow”, Int. Journal of multiphase flow, no. 3, pp. 473-483, 1996.

[10] G. Woschni, “A universally applicable equation for the instantaneous heat transfer coefficient in the internal combustion engine”, SAE technical papers, 1967.

[11] H. Kanno et al., “Modeling study on two-phase adiabatic expansion in a reciprocating expander”, Int, Journal of Heat and Mass Transfer, no. 104,pp. 142-148, 2017.

[12] S. Lecompte et al., “Design of an optical-access expansion chamber for two-phase expansion”, in Proceedings of ECOS 2017 – 30th Environmental conference on efficiency, cost, optimization, simulation and environmental impact of energy systems, San Diego, USA.

[13] F. Dawo et al., “Experimental assessment of an organic Rankine cycle with a partially evaporated working fluid”, Applied Thermal Engineering, no. 221, 2023.

[14] X. van Heule et al., “Experimental setup for measuring the thermal non-equilibrium effects within two-phase expansion”, in Proceedings of ExHFT10 – 10th World conference on experimental heat transfer, fluid mechanics and thermodynamics, Rodes, Greece.

HEAT PUMP MONITORING THROUGH DIGITAL TWINS VIA NEURAL NETWORKS

Maarten Evens[1,2]*, Alessia Arteconi[1,2,3]

[1] KU Leuven, Department of Mechanical Engineering, Leuven, Belgium

[2] EnergyVille, Genk, Belgium

[3] Università Politecnica delle Marche, Dipartimento di Ingegneria Industriale e Scienze Matematiche, Ancona, Italy

* *Corresponding Author: maarten.evens@kuleuven.be*

Abstract. Heat pumps are recognised as a key technology to reach net zero emissions by 2050, while they can also support the energy grid through the provision of energy flexibility. Regarding the latter aspect, smart energy management systems require accurate insights in the real heat pump behaviour when composing an operational schedule. These operational insights could be delivered through a digital twin, i.e. a real-time running model which is updated with the latest information of the real system and aims to predict the real heat pump behaviour and performance. To limit the modelling effort, while maximising the potential for model generalisation, this work proposes an artificial neural network that can be used to predict the performance and behaviour of the heat pump. In contrast to frequently adopted timesteps of one hour in literature, this work uses a fifteen minutes time step to better incorporate the internal control logics already implemented by heat pump manufacturers. A feedforward neural network architecture using a total number of five inputs and one output is proposed, for which the hyperparameters are tuned via a grid search approach. The model predicts the electricity consumption with a 2.01 % error. Finally, a critical analysis lists the required modifications for a future work aimed at predicting the entire heat pump behaviour.

Keywords. Heat pump – Digital twin – Artificial neural network – Energy flexibility.

Nomenclature

ANN	Artificial neural network
COP	Coefficient-of-performance (-)
$CV(RMSE)$	Coefficient of variation of the root mean squared error (%)
E	Energy (kWh)
HP	Heat pump
$SCOP$	Seasonal coefficient-of-performance (-)
Subscripts	
$elec$	At the electrical side
$load$	At the heat load side

1 Introduction

Heat pumps (HPs) are key in reaching net zero emissions by 2050, while they can also support the energy grid by providing energy flexibility services [1]. However, obtaining insights in the operational HP behaviour and performance is crucial for smart energy management systems. Indeed, manufacturers also implement internal control strategies to ensure the HP safety and reliability. The internal HP control in this work refers to the operational control to cover heating services, but does not refer to fault detection at very small time steps. The envisioned internal controls include compressor ramping rates, minimum on/off times, pump control, etc. The impact of these strategies on the operational HP behaviour and the need for incorporation to achieve accurate HP control was already highlighted in several works [2]–[4].

Real-time insights in the HP behaviour can be obtained through a digital twin of the HP, i.e. a real-time running model which is updated with the latest information of the system and aims to predict the HP behaviour. Such a digital twin can be built using white, grey or black box models. While white box models require many HP system details and can be computationally complex, black box models using machine learning have large potential for model generalisation. Recent works on HPs already showed the potential of artificial intelligence [5], [6] in which artificial neural networks (ANNs) are predominant.

Exploring available HP models shows that a variety of inputs is used, ranging from a few inlet and outlet

temperatures [7] until the weather data and electricity consumption [8], [9]. The outputs are the electrical power or coefficient-of-performance (COP) with coefficient-of-variation of the root mean squared errors ($CV(RMSE)$) around 5 %. However, using hourly time steps neglects the internal control effects.

It becomes clear that the available black box models for HPs cannot be used by an energy management system as the internal HP control is neglected due to using an hourly time step. Accurate HP performance predictions can thus not be achieved, while they are necessary to determine the cost related to the energy flexibility. In addition, the available models do not predict the flow rates nor the outlet temperatures. Hence, it is assumed that the HP system will exactly meet its setpoint temperature, while the flow rates are considered to be constant or are controlled externally.

As a first step to bridge these gaps of incorporating the internal HP control in a black box HP model, this paper proposes an ANN model with a fifteen minutes time step to better match the needs of an energy management system. The aim is to evaluate if and how similar prediction errors as in the case of using hourly time steps can be reached. An analysis on the hyperparameters of the ANN will be performed. Our model is focussed on the compressor control and is not yet aimed to predict the entire HP behaviour such as the circulation pump and back-up heater controls. However, the required changes to fully replicate the electrical and thermal HP behaviour will be analysed.

2 Methodology

2.1 Experimental data collection and case study

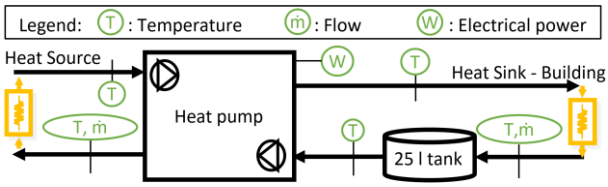


Figure 1: Hardware-in-the-loop set-up.

This work uses experimental data from a hardware-in-the-loop set-up. The set-up was already described in a previous work [10] where a relative measuring error of 1.661 % on the COP at nominal conditions was found. Figure 1 shows a simplified hydraulic lay-out. The heat source and sink are emulated by heat exchangers. A water/water HP from the Daikin type EGSAX06DA9W [11] is used and has a nominal thermal capacity of 7.98 kW and electricity consumption of 1.79 kW at B0/W35 conditions. A 25 l tank is used to fulfil the thermal inertia constraints set by the HP manufacturer. The evaporator pump and condenser pump are controlled by the HP unit.

As a case study, a residential single-family building with a nominal heat loss of 9.4 kW was modelled in Modelica [12]. Three datasets were collected. The coldest and warmest week in a Belgian winter for training and validation, where 5.5 days of each week are used for training and 1.5 day for validation. For testing, a typical winter week [13] is used. Dataset normalisation via the minimum and maximum values is applied. The experimental data is measured every fifteen seconds and averaged over fifteen minutes.

2.2 Neural network model for energy monitoring

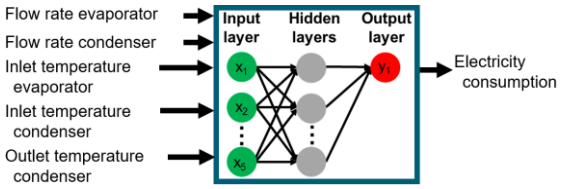


Figure 2: Model architecture: input/output overview.

Aiming to monitor the HP performance, a starting point is to define the ANN model requirements. To correctly determine the thermal capacity, the flow rate accompanied by the entering and leaving water temperatures at the condenser side are required. The outlet temperature can be estimated at the setpoint value when assuming that the HP will quickly reach its setpoint or as done in this work by taking the average temperature over the last interval of fifteen minutes. The evaporator inlet temperature is also crucial in correctly predicting the HP performance. Given that a previous work on the adopted HP [10] showed the dependency of the evaporator flow rate on the actual compressor speed, this study also uses the evaporator flow rate as an input to the model. The model then predicts the electrical power drawn from the grid. Figure 2 overviews the model architecture. The models are built via the Tensorflow package in Python [14] and use feedforward neural networks.

A first analysis showed that the Adam optimiser is preferred over RMS or SGD, while using the ReLU activation function led to better results than using Sigmoid or Tanh. For the remaining, most relevant hyperparameters of an ANN model, a grid search approach was used and the evaluated values were [5, 20, 35, 50, 65, 80, 95, 110, 125, 140, 155, 170, 185, 200] for the number of neurons and [1, 2, 3, 4, 5, 6, 7, 8, 9, 10] for the number of hidden layers. The number of epochs was varied in the range [25, 50, 100, 200, 400]. Given that the model was not improving above 200 epochs, 200 epochs were used.

The performance of the models is evaluated through the $CV(RMSE)$ errors on the electricity consumption. The seasonal coefficient-of-performance ($SCOP$) and total electricity consumption (E_{elec}) for the testing dataset, i.e. a typical winter week, are also evaluated. Equation (1) determines the $SCOP$, in which E_{load} holds the total thermal energy supplied to the load.

$$SCOP = \frac{E_{load}}{E_{elec}} \quad (1)$$

3 Results

3.1 Hyperparameter evaluation

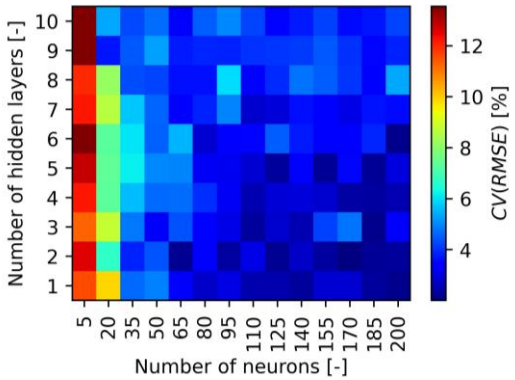


Figure 3: Hyperparameter grid search for the number of hidden layers and neurons: $CV(RMSE)$.

Figure 3 shows the results from a grid search on the number of hidden layers and number of neurons. It becomes clear that an optimal performance is reached when opting for a high number of neurons and a low number of hidden layers. An optimum is found when using 170 neurons and 2 hidden layers and reaches a $CV(RMSE)$ of 2.01 % on the electrical power. Figure 4 compares the electrical HP power predicted by the model to the testing dataset and shows the capability of the model for variable capacity HPs. Electrical powers below 100 W refer to a compressor off-status.

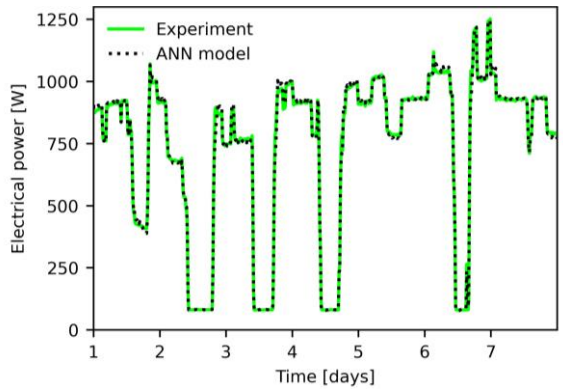


Figure 4: Electrical HP power: comparison of the ANN model predictions to the experimental data.

3.2 Evaluation of the total energy consumption

Table 1: Comparison of the energy performance between the experimental set-up and ANN model.

Indicator	Experiment	ANN model
E_{load}	836.5 kWh_{th}	
E_{elec}	124.2 kWh_e	124.4 kWh_e
$SCOP$	6.7337	6.7233

Table 1 shows the energy performance over the testing dataset of seven days. Taking into account that the temperatures and flow rates at the heat sink serve as inputs to the ANN model, E_{load} is already known and thus identical for the experimental set-up and ANN model. The results presented in Table 1 over the entire testing dataset and the instantaneous COP values shown in Figure 5 over one full day in the testing dataset indicate the potential of the ANN model to well estimate the HP behaviour over time.

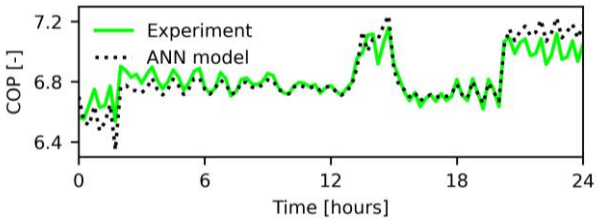


Figure 5: Instantaneous COP comparison between experimental data and ANN model for an entire day.

3.3 Critical evaluation of the model architecture

Reviewing the model architecture of Figure 2 against the role of the internal HP control indicates a major limitation of this work. Indeed, the model predicts the electricity consumption when the thermal response is already fully known. In fact, the evaporator and condenser flow rates and also the condenser outlet temperature serve as inputs to the model. Regarding the pump controls, variable capacity HPs can be equipped with variable speed pumps to adjust the pump speed as a function of the thermal load and the effects on the HP behaviour were shown in literature [10], [15]. While the model is tested under variable loads (Figure 4), the flow rates should not only be a model input, but should also be predicted for the next time step to fully replicate the HP system. Supplying the actual condenser outlet temperature as an input to the model also neglects the role of the compressor speed control in which the HP control compares the actual outlet temperature to its setpoint value when regulating the compressor speed. Given these limitations, a future work should focus on adjusting the model architecture in order to predict both the electrical and thermal HP behaviour under a variety

of conditions and both for energy monitoring and for behaviour predictions with a high time resolution.

Conclusions

This work presents a neural network architecture for a water/water heat pump, able to partially incorporate the internal control and to predict the electrical power. A grid search approach was used to optimise the hyperparameters. An optimal performance with a 2.01 % error on the electrical power was found when using 170 neurons and 2 hidden layers. The ability of the neural network to correctly predict the electrical power over time was also shown. While the model can be used to predict the heat pump performance for a given set of conditions, future work is needed to evaluate (1) how well the model can be used to predict the heat pump behaviour multiple time steps ahead in future, (2) if and how the architecture should change to also incorporate the internal control strategies acting on auxiliary components such as circulation pumps and (3) how the architecture should be adapted to cover the heat pump behaviour on both its electrical and thermal connections.

Acknowledgement

We gratefully acknowledge the financial support of the Flemish Government and Flanders Innovation Entrepreneurship (VLAIO) through the Moonshot project Upheat-INES (HBC.2020.2616).

References

[1] IEA, "The Future of Heat Pumps," 2022. [Online]. Available: www.iea.org.

[2] J. Clauß and L. Georges, "Model complexity of heat pump systems to investigate the building energy flexibility and guidelines for model implementation," *Appl. Energy*, vol. 255, no. 113847, 2019.

[3] M. Evens and A. Arteconi, "Design energy flexibility within a Comfort and Climate Box – An experimental evaluation of the internal heat pump control effects," *Appl. Therm. Eng.*, vol. 254, no. 123842, pp. 1–17, 2024.

[4] T. Pean, R. Costa-Castello, E. Fuentes, and J. Salom, "Experimental Testing of Variable Speed Heat Pump Control Strategies for Enhancing Energy Flexibility in Buildings," *IEEE Access*, vol. 7, pp. 37071–37087, 2019.

[5] S. Noye, R. Mulero, L. Carnieletto, and M. De Carli, "A review of advanced ground source heat pump control : Artificial intelligence for autonomous and adaptive control," *Renew. Sustain. Energy Rev.*, vol. 153, no. 111685, 2022.

[6] T. Ahmad, H. Chen, Y. Guo, and J. Wang, "A comprehensive overview on the data driven and large scale based approaches for forecasting of building energy demand: A review," *Energy Build.*, vol. 165, pp. 301–320, 2018.

[7] J. H. Shin and Y. H. Cho, "Machine-learning-based coefficient of performance prediction model for heat pump systems," *Appl. Sci.*, vol. 12, no. 362, 2022.

[8] A. Najib, A. Hussain, and S. Krishnamoorthy, "Machine-learning-based models for predicting the performance of ground-source heat pumps using experimental data from a residential smart home in California," in *IGSHPA Research Track*, 2022, pp. 256–263.

[9] L. Yan *et al.*, "The performance prediction of ground source heat pump system based on monitoring data and data mining technology," *Energy Build.*, vol. 127, pp. 1085–1095, 2016.

[10] M. Evens and A. Arteconi, "Hardware-in-the-loop heat pump model validation for flexibility evaluations," in *Proceedings of the 14th REHVA HVAC World Congress*, 2022.

[11] "Technical Data EGSAH/X Daikin," 2020. [Online]. Available: https://www.daikin.eu.

[12] F. Jorissen, G. Reynders, R. Baetens, D. Picard, D. Saelens, and L. Helsen, "Implementation and verification of the IDEAS building energy simulation library," *J. Build. Perform. Simul.*, vol. 11, no. 6, pp. 669–688, 2018.

[13] M. Evens and A. Arteconi, "Representative cycle for heat pump energy flexibility evaluations – A comparative simulation study of existing day selection procedures to a new consecutive day procedure," *Energy Build.*, vol. 297, pp. 1–17, 2023.

[14] Abadi et al., "TensorFlow: Large-scale machine learning on heterogeneous systems." 2015, [Online]. Available: https://www.tensorflow.org.

[15] M. Evens and A. Arteconi, "Influence of Internal Control Simplifications in Heat Pump System Modelling for Energy Flexibility Evaluations," in *Proceedings of 17th Building Simulation Conference of IBPSA*, 2021.

REHP-4-TUNE: RENEWABLE ELECTRIC HIGH-TEMPERATURE HEAT PUMPS FOR THERMAL USERS IN NEUTRAL CO2 ENVIRONMENTS

Matteo Ametta[1], Lisa Branchini[2], Andrea De Pascale[2], Lorenzo Ferrari[3], Guido Francesco Frate[3], Alessandra Ghilardi[3], Chiara Poletto[2]*, Alessio Sapienza[1], Salvatore Vasta[1]

[1] Consiglio Nazionale delle Ricerche, Messina, Italy

[2] Università di Bologna, Bologna, Italy

[3] Università di Pisa, Pisa, Italy

* *Corresponding Author: chiara.poletto3@unibo.it*

Abstract. REHP-4-TUNE is a national research project focused on exploring the feasibility and performance of integrating Power-to-Heat and Power-to-Heat-to-Power technologies to decarbonize energy-intensive industrial sectors. The aim is to provide sustainable and flexible solutions exploiting renewables overgeneration and reusing industrial waste heat to meet processes' energy demand. The ceramic industry, particularly energy-intensive and involving processes requiring heat at different temperature levels, is selected as the primary case study for this project. The methodology combines advanced numerical modelling with experimental and commercial data, to simulate and evaluate the optimal design and operation of different energy-recovery configurations in real-world industrial environments. Expected outcomes include the identification of optimal thermodynamic arrangements, a thorough evaluation of the potential for heat recovery and storage, and the overall performance of the system in reducing carbon emissions and costs. The project's results will offer a comprehensive techno-economic analysis of the integrated system in various industrial scenarios, and guidelines for the optimal design and operation of energy-recovery systems tailored to specific requirements of industrial users.

Keywords. Power-to-Heat-to-Power; High-Temperature Heat Pump; Organic Rankine Cycle; Ceramic Industrial Sector; Waste Heat Recovery.

1 Introduction

Energy-intensive industries (EIIs) heavily rely on fossil fuels for high-temperature processes. The ceramic industry, as a subset of EIIs, is responsible for 19 million tons of CO_2 emissions yearly [1]. Among emission-reduction technologies, energy efficiency strategies, such as kiln waste heat recovery (WHR), are the most immediately feasible [2].

Delpech et al. [3] investigated heat-pipe-based heat exchangers (HPHE) for kiln WHR, showing savings in fuel consumption and CO_2 emissions. Notable savings and return on investment using HPHEs are reported also by Jouhara et al. [4]. Milani et al. [5] developed a model to test kiln and burner design options, achieving 10 % fuel and CO_2 emissions savings. Venturelli et al. [6] validated the efficiency of HPHE in real facilities. Furthermore, Organic Rankine Cycles (ORCs) demonstrated potential for converting waste heat into electricity, reducing fossil fuel dependence [7]. These studies pave the way for further investigations on sustainable energy practices in the ceramic industry.

1.1 Contribution of this project

The REHP-4-TUNE project aims to investigate Power-to-Heat (P2H) and Power-to-Heat-to-Power (P2H2P) systems to boost EIIs decarbonization. The project is going to evaluate technical, environmental and economic performance of multiple energy recovery solutions to diminish ceramic industry reliance on fossil fuels. Numerical modelling, supported by experimental and commercial data, is being employed to simulate different configurations under real industrial conditions. Key outcomes will include a full assessment of effective heat-recovery systems' potential in emissions reduction, a detailed techno-economic evaluation, and guidelines for optimal design and operation of P2H and P2H2P systems tailored to diverse industrial scenarios.

2 High-Temperature Heat Pump market share

High-Temperature Heat Pumps (HTHP), if powered by renewable, can lower reliance on fossil fuel boilers, reducing energy costs and emissions in

industrial processes. Despite integration challenges, there is a notable rise in HTHP applications. According to data available in Annex 58 [9], commercial HTHP solutions suitable for ceramic industry applications include over 30 manufacturers and approximately 40 technologies, encompassing commercial and near-commercialization systems. Sink outlet temperature values up to 230 °C are reached (Figure 3.1), with temperature lifts up to 196 K. The most suitable options for ceramic applications feature configurations, such as reverse Stirling, mechanical vapor recompression, and hybrid compression-absorption cycles. Specific investment costs range around 650 €/kW on average (Figure 3.2).

3 Ceramic tiles energy recovery system

In the ceramic tiles manufacturing (Figure 3.3), waste heat is generated in spray drying, drying, firing, and cooling stages. The general concept for the WHR system analysed in this project, illustrated in Figure 3.3, includes alternative configurations combining a HTHP, an ORC, and a Thermal Energy Storage (TES), to simulate different P2H, H2P, and P2H2P systems.

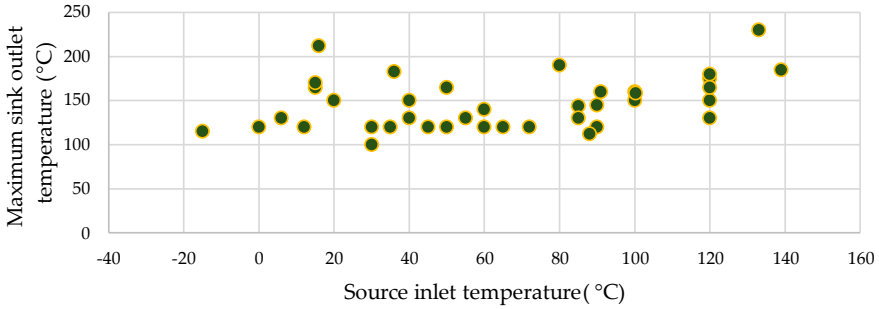


Figure 3.1: Sink outlet temperature versus source inlet temperature for HTHPs on the market [9].

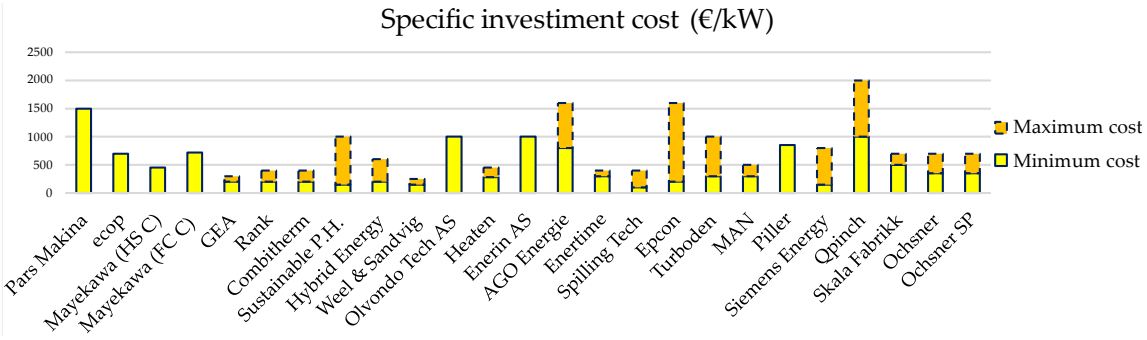


Figure 3.2: Specific investment cost of the HTHP technologies on the market [9].

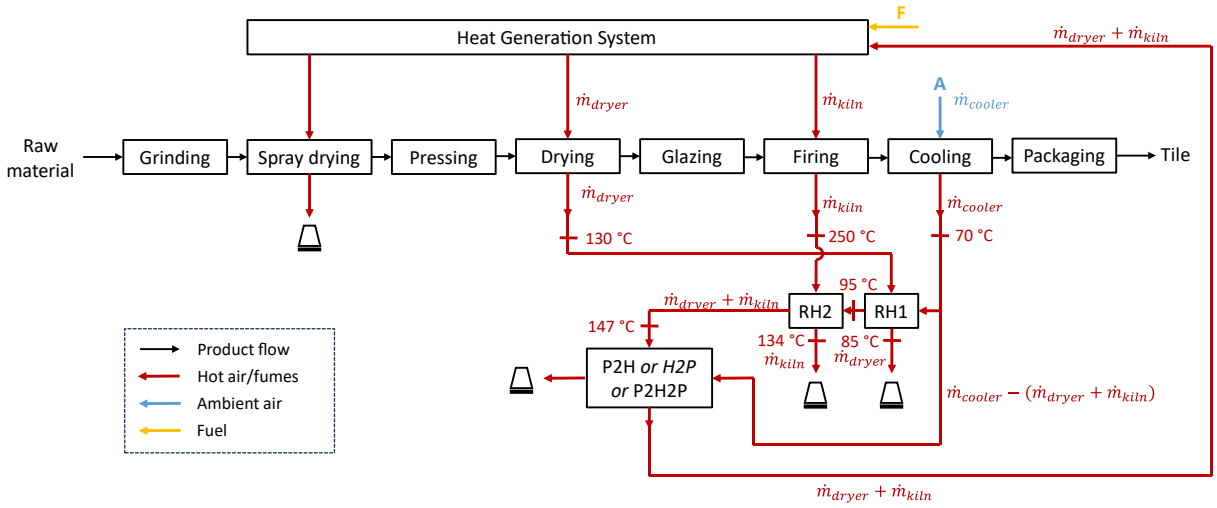


Figure 3.3: Ceramic tiles manufacturing process and energy recovery system scheme.

3.1 *Simulated scenarios*

Supposing a photovoltaic power as renewable energy source (RES), several layouts are simulated by considering different combinations (i) of technologies (HTHP, ORC, and TES), and (ii) of variable boundary conditions, such as electricity and Natural Gas (NG) prices, and electric and thermal demand profiles. A summary of the simulated layouts and boundary conditions is provided in Table 3.1. The presence of variable RES production, prices, and demand leads to the necessity of implementing a management paradigm. The latter can be trivial for simple layouts - e.g., stand-alone ORC - or complex enough to require dedicated optimization algorithms, as described in Table 3.1.

3.2 *Methods*

Figure 3.4 shows the methods. The optimization process simultaneously minimizes operational expenditures (OPEX) and CO_2 emissions. A two-level optimization procedure is used, as done for comparable problems [10]. The outer level, based on Non-Linear Programming (NLP) algorithm, searches for the optimal size of the involved technologies; the inner level, based on Mixed Integer Linear Programming (MILP) algorithm, finds the optimal management for each combination of technologies and sizes. Results are iteratively used at the outer level until the minimum value of the objective function is achieved. As final result, the trade-off between OPEX and CO_2 emissions is explored, building the Pareto front.

Table 3.1: Simulated layouts and variable inputs. For each combination, it is reported whether the layout management is optimized (✓) or not (✗).

Simulated layouts	**HTHP**	**HTHP + TES**	**ORC**	**ORC + TES**	**HP + ORC + TES**
Variable Inputs	**Optimized management**				
RES output	✓	✓	✗	N/A	✓
RES output + Energy Price	✓	✓	✗	N/A	✓
RES output + Energy Price + El./Th. Demand	✓	✓	✗	✓	✓

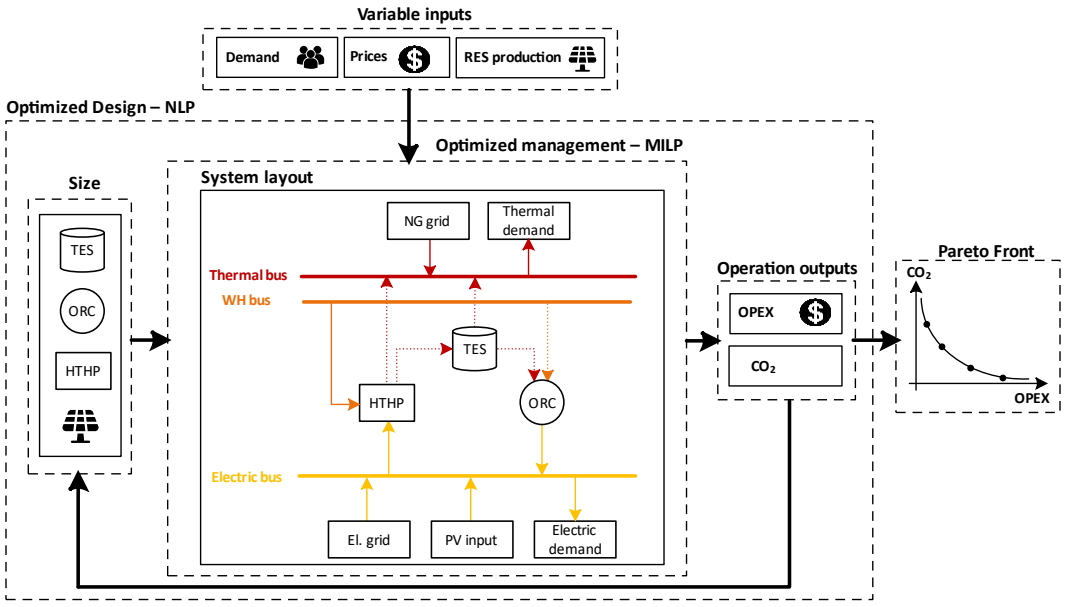


Figure 3.4: Two-level multi-objective optimization procedure to explore the trade-off between OPEX and CO_2 emissions. Dashed arrows refer to the interactions among HTHP, TES, ORC, thermal and electric busses.

4 Conclusions

The REHP-4-TUNE project provides a framework for integrating Power-to-Heat and Power-to-Heat-to-Power technologies to support decarbonization in energy-intensive industries, with a focus on the ceramic sector. This paper outlines the project's methodology, which combines numerical modelling with experimental and commercial data to assess various configurations for WHR and energy management. By applying HTHP and ORC systems, the project aims to reduce reliance on fossil fuels and minimize CO_2 emissions.

The proposed multi-objective optimization approach will identify optimal configurations and management strategies that balance operational costs with emission reductions, supporting the development of flexible, renewable-based solutions tailored to industrial needs. As the project progresses, findings are expected to provide valuable insights for designing efficient energy recovery systems applicable across diverse energy-intensive sectors, aligning with the EU's climate goals.

Acknowledgement

We acknowledge financial support under the National Recovery and Resilience Plan (NRRP), Mission 4, Component 2, Investment 1.1, Call for tender No. 104 published on 2.2.2022 by the Italian Ministry of University and Research (MUR), funded by the European Union – NextGenerationEU– Project Title *REHP-4-TUNE: Renewable Electric High-temperature Heat Pumps For Thermal Users in Neutral CO2 Environments* – CUP J53D23002060006 - Grant Assignment Decree No. 961 adopted on the 30th of June 2023 by the Italian Ministry of Ministry of University and Research (MUR).

References

[1] D. D. Furszyfer Del Rio *et al.*, "Decarbonizing the ceramics industry: A systematic and critical review of policy options, developments and sociotechnical systems," *Renewable and Sustainable Energy Reviews*, vol. 157, p. 112081, Apr. 2022, doi: 10.1016/j.rser.2022.112081.

[2] "Policy Department for Economic, Scientific and Quality of Life Policies Directorate-General for Internal Policies, Energy-intensive industries - Challenges and opportunities in energy transition, PE 652.717–July 2020, available at: Highlights | Supporting analyses | Committees | European Parliament (europa.eu)."

[3] B. Delpech *et al.*, "Energy efficiency enhancement and waste heat recovery in industrial processes by means of the heat pipe technology: Case of the ceramic industry," *Energy*, vol. 158, pp. 656–665, Sep. 2018, doi: 10.1016/j.energy.2018.06.041.

[4] H. Jouhara *et al.*, "Investigation on a full-scale heat pipe heat exchanger in the ceramics industry for waste heat recovery," *Energy*, vol. 223, p. 120037, May 2021, doi: 10.1016/j.energy.2021.120037.

[5] M. Milani, L. Montorsi, M. Stefani, R. Saponelli, and M. Lizzano, "Numerical analysis of an entire ceramic kiln under actual operating conditions for the energy efficiency improvement," *Journal of Environmental Management*, vol. 203, pp. 1026–1037, Dec. 2017, doi: 10.1016/j.jenvman.2017.03.076.

[6] M. Venturelli, D. Brough, M. Milani, L. Montorsi, and H. Jouhara, "Comprehensive numerical model for the analysis of potential heat recovery solutions in a ceramic industry," *International Journal of Thermofluids*, vol. 10, p. 100080, May 2021, doi: 10.1016/j.ijft.2021.100080.

[7] B. Peris, J. Navarro-Esbrí, F. Molés, and A. Mota-Babiloni, "Experimental study of an ORC (organic Rankine cycle) for low grade waste heat recovery in a ceramic industry," *Energy*, vol. 85, pp. 534–542, Jun. 2015, doi: 10.1016/j.energy.2015.03.065.

[8] K.-M. Adamson *et al.*, "High-temperature and transcritical heat pump cycles and advancements: A review," *Renewable and Sustainable Energy Reviews*, vol. 167, p. 112798, Oct. 2022, doi: 10.1016/j.rser.2022.112798.

[9] B. Zühlsdorf, Annex 58. Accessed: Oct. 29, 2024. [Online]. Available: https://heatpumpingtechnologies.org/annex58/

[10] C. Elsido, A. Bischi, P. Silva, and E. Martelli, "Two-stage MINLP algorithm for the optimal synthesis and design of networks of CHP units," *Energy*, vol. 121, pp. 403–426, Feb. 2017, doi: 10.1016/j.energy.2017.01.014.

OPTIMAL INTEGRATION OF A HIGH-TEMPERATURE HEAT PUMP IN A CO_2 CAPTURE PILOT PLANT

Brieuc Beguin*, Théo Van Lierop, Grégoire Léonard

University of Liège, Department of Chemical Engineering, Liège, Belgium

* *Corresponding Author: brieuc.beguin@uliege.be*

Abstract. This study investigates the integration of a high-temperature heat pump into a CO_2 capture process within a 1-tonne-per-day carbon capture pilot plant, designed to separate CO_2 from the flue gases of an industrial biomass boiler by the means of an absorption-regeneration solvent loop. The operating pressure of the solvent regeneration unit (stripping column) was optimised as a trade-off between the increased reboiler heat duty and the decreased temperature lift as pressure decreased. A single-stage heat pump was initially tested and, although it could not totally replace the reboiler, it reduced total electricity consumption. A two-stage configuration was then explored, with the intermediate evaporator optimised to recover heat from the stripper overhead condenser at an optimal temperature. Final results showed that the best achievable reduction in electricity consumption reached 73%, but stagnated below 80 kPa due to increased CO_2 compressor consumption. These findings suggest that a fully electrified CO_2 capture process is feasible and should ideally operate at or below atmospheric pressure for optimal energy efficiency.

Keywords. CO_2 capture, High-temperature heat pump, Heat integration

1 Introduction

Over the past two decades, CO_2 capture has gained momentum as a tool both for carbon dioxide removal (CDR) and for the mitigation of hard-to-abate emissions. Amine-based chemical absorption stands out as the most mature technology, with large-scale industrial applications already in operation [1].

This process relies on the selective absorption of CO_2 from gaseous streams by a chemical solvent, most commonly 30 wt-% monoethanolamine (MEA) in water. At first, the gaseous stream and the aqueous solvent are brought in contact with each other in an absorption column and the solvent becomes loaded with CO_2 as it is removed from the gaseous stream. The loaded solvent is then regenerated in a stripping column using thermal energy. This heat consumption remains the largest challenge of the technology. To limit its burden, researchers are developing alternative solvents, process modifications, and heat integration techniques.

The source of thermal energy varies depending on the host process, with steam extraction preferred when feasible. In cases where on-site steam is unavailable, electricity may be an alternative carrier, particularly for pilot plants where versatility and simplicity are essential. Heat pumping is a sensible way to electrify the process and many configurations based on a heat pumping effect are proposed in the scientific literature [2]. However, the sole dependency on a heat pump to sustain the energy consumption of the whole system is a more recent research area. Jensen *et al.* [3] have proposed using a high-temperature heat pump in such scenarios, applying their electrification approach to a biogas upgrading plant.

Within the MEA-based CO_2 capture process, operating parameters can be adjusted to minimise energy requirements. One of these variables is the stripper pressure: higher pressures reduce the specific reboiler heat duty (SRD) [4]. The marginal gains tend to decrease, and a techno-economic optimum can be found, accounting for additional equipment and pumping costs. However, higher stripper pressures have a side effect that conflicts with heat pump integration: as pressure rises, so does the reboiler temperature. This increases the temperature lift that the heat pump must achieve, thereby reducing its performance.

This study extends the proposed methodology by Jensen *et al.* [3] to another case study, analysing both the optimal stripper pressure and the optimal waste heat temperature level. Basic heat pump architectures are tested, and total electricity consumption is compared.

2 Case study

A 1-tonne-per-day carbon capture pilot plant currently in development at the University of Liège, Belgium, is used as the case study. It separates CO_2 from the flue gases of an industrial biomass cogeneration plant. Because it is designed to be mobile, the pilot's heat requirements are met by electric heaters and waste heat can only be recovered from within the capture process. The challenge is therefore to minimise the electricity consumption by efficient internal heat recovery.

The pilot is modelled in Aspen Plus V14, with the base design setting the stripper pressure at 200 kPa (absolute). The corresponding energy requirement amounts to 3.28 MJ/kgCO_2, or 37.94 kW. Waste heat is available at different temperature levels, with most of it at 40°C. However, the stripper overhead condenser (SOC), which condenses water vapour to separate it from CO_2 at the top of the stripper, operates at a higher temperature, releasing 8.37 kW as it cools the stream from 94°C to 40°C. As illustrated in Figure 1, this partial condenser has a concave temperature-enthalpy (T-Q) diagram, allowing the recovery of a larger amount of waste heat at any temperature level compared to the linear T-Q curve of a conventional heat exchanger.

Regarding the heat pump, preliminary studies have identified R1233zd(E) as the heat pump working fluid for its safety, its critical temperature (165.5°C), and its low environmental impact [5].

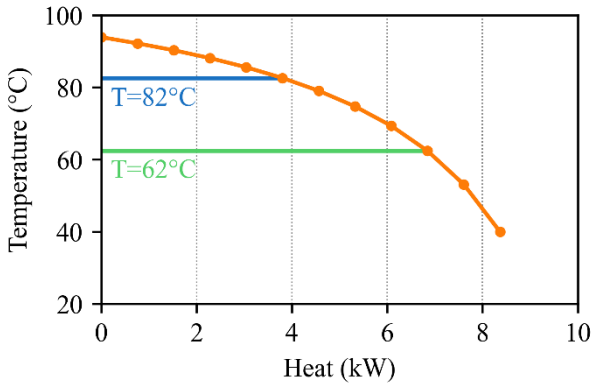


Figure 1: T-Q curve of the SOC at 200 kPa. The blue and green lines are examples of waste heat recovery potentials at two different temperatures.

3 Methodology

The Aspen Plus model is sized to achieve the target capture capacity of 1 tonne CO_2 per day. Simulations are conducted for 18 stripper pressure levels ranging from 30 kPa to 500 kPa. In every simulation, the captured CO_2 is compressed to 500 kPa to allow for a fair comparison. For each pressure level, temperature profiles, reboiler duty, and T-Q curves are generated and saved as inputs for the heat pump model.

The heat pump is modelled in Engineering Equation Solver (EES). Compressor power consumption is calculated with an assumed isentropic efficiency of 0.85 and a motor efficiency of 0.8. Heat exchangers are set with a pinch point temperature difference of 5 K.

At first, a single-stage architecture is simulated. The heat pump draws all available heat from the SOC to relieve the electric reboiler. This option ensures compacity, low complexity and low costs, which are all relevant for a pilot plant.

Then, a two-stage architecture is implemented. The electric reboiler is entirely replaced by the heat pump condenser while two evaporators are used to recover waste heat. The first evaporator draws heat from the SOC and individual simulations based on a 12-point discretisation of the T-Q curve are performed to identify the optimal operating temperature. Figure 1 illustrates two example points, showing the heat recovery potential when the stripper pressure is set to 200 kPa. The second evaporator supplies the remaining required power by extracting heat from an unlimited source at 40°C, representing the aggregate of other waste heat sources within the process. This lowest temperature is a strict constraint to which all streams are cooled as they leave the system to maintain the water balance. Limitations on the amount of heat that can be extracted from this low-temperature source are discussed in the next section. Total power consumption of the coupled CO_2 capture and heat pump system is then compared across all simulations.

4 Results and discussion

Figure 2 shows the influence of stripper pressure on both reboiler heat duty and temperature. The opposing trends in these variables appear clearly. On a side note, it is interesting to note that reboiler temperature impacts solvent degradation, with higher temperatures leading to increased degradation [6], [7]. Future works could extend the capture model to account for this phenomenon, and degradation product concentrations could be monitored for each pressure level.

Simulations results from the single-stage heat pump show that for any stripper pressure, waste heat

availability in the SOC alone is insufficient to replace the reboiler, regardless of the waste heat temperature level. An electric boiler is still required for a fraction of the power. Therefore, the minimum electricity consumption is achieved when the heat pump operates at the lowest possible waste heat temperature (40°C) as it allows for the recovery of the largest amount of heat.

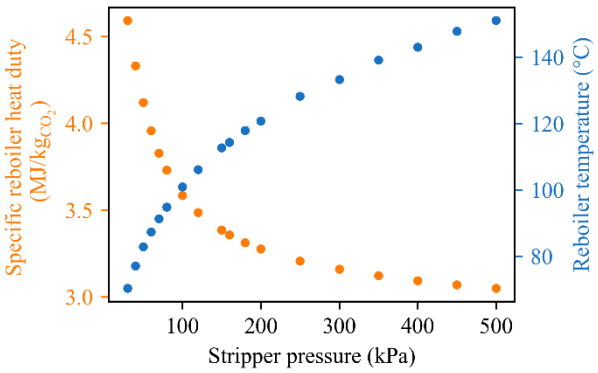


Figure 2: Influence of the stripper pressure on the reboiler heat duty and the reboiler temperature.

In the two-stage configuration, electricity consumption reaches a minimum at an intermediate waste heat temperature level in the SOC, as illustrated in Figure 3. This entails that this intermediate temperature achieves a higher COP, even though not all available waste heat is extracted. While the SOC temperature range varies with pressure, the optimal temperature appears to lie consistently a few degrees below the midpoint of the range. Further studies could provide insights into this trend.

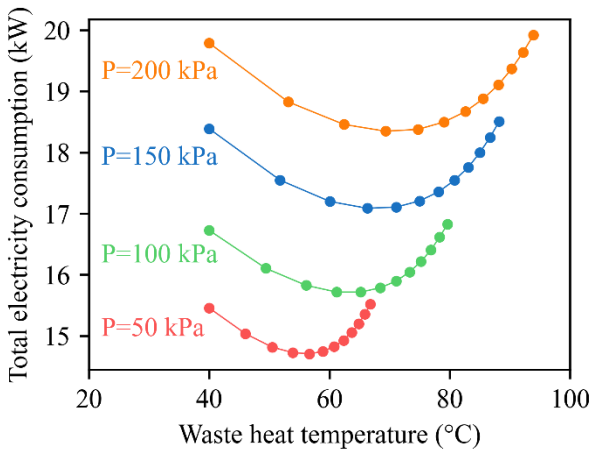


Figure 3: Optimal waste heat temperature.

Figure 4 depicts the total energy consumption for each of the 18 stripper pressure levels. The blue dot represents the base case consumption, *i.e.* before heat pump integration when electric heaters supplied the heat. For all investigated pressures, integrating the heat pump reduces the total electricity consumption. The savings range from 23% of the initial electricity consumption to a maximum of 73%.

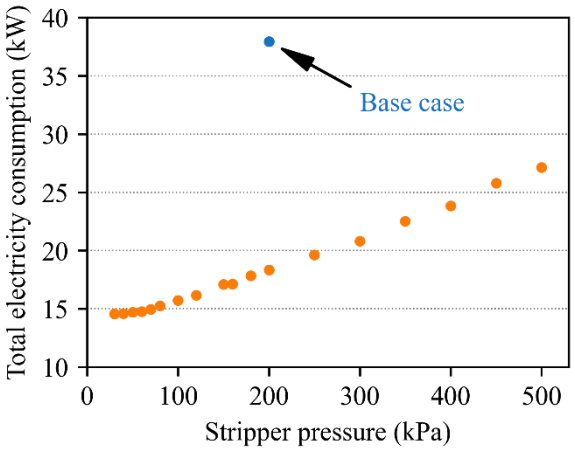


Figure 4: Total electricity consumption of the pilot plant for different stripper pressures.

The benefits of a lower temperature lift outweigh the increase in reboiler heat duty. High-pressure strippers, in addition to the increased risk of solvent degradation [6], appear suboptimal for integrated electrified CO_2 capture systems.

Given the scale of the pilot plant, solvent pumping is a negligeable contribution to the total electricity consumption. Instead, the electricity consumption is divided between the heat pump and the CO_2 compressor, with the compressor accounting for under 1% at 450 kPa, 5% at 200 kPa, 13% at 100 kPa, and 34% at 30 kPa. As the stripper pressure decreases, the compressor's electricity consumption increases, causing the benefits of a low temperature lift start to fade at lower pressures as the total electricity consumption stagnates from around 80 kPa. The consumption increase at the lowest pressures identified by Jensen *et al.* [3] does not appear in the present results. This implies that vacuum-operated strippers (VOS) may only bring marginal benefits and that operating the stripper at atmospheric pressure could be a satisfying balance. A finer analysis is necessary to clarify the total consumption behaviour in vacuum-operated strippers.

Lastly, the lack of constraints on the second evaporator (the unlimited, low-temperature heat

source at 40°C) has not compromised the results, as the extracted heat remains below the total available waste heat at the respective temperature across all simulations.

5 Conclusions

A high-temperature heat pump was modelled and integrated into a CO_2 capture pilot plant.

Initially, a single-stage configuration was tested to extract waste heat from the stripper overhead condenser, which is the nearest available source. Results indicated that while this configuration could not fully replace the reboiler, it did reduce the overall electricity consumption.

Next, a two-stage heat pump was evaluated. The intermediate evaporator extracted heat from a source with a large temperature glide (94°C to 40°C) and the second drew heat from an additional source at 40°C. The temperature level of the intermediate evaporator was optimised according to heat availability. With an increasing CO_2 compressor consumption at lower pressure levels, the reduction of total consumption stalled from 80 kPa downwards with an energy saving of 73% compared to the base case.

Integrating a high-temperature heat pump to electrify the CO_2 capture process is possible and leads to a substantial reduction in electricity consumption. To maximise these benefits, it is advised to go against the high-pressure stripper trend and instead design atmospheric or vacuum-operated strippers.

The present work was conducted on a small-scale pilot plant. However, there is no indication that these conclusions would degrade if the system were scaled up. In fact, applying the methodology to a full-scale plant, along with its host process, could reveal additional opportunities for heat integration as more waste heat sources would be available.

Exploring alternative heat pump configuration beyond the basic two-stage heat pump architecture could further expand the integration analysis. Introducing internal heat exchangers, flash tanks, vapour injection, and other components could bring down the energy consumption, at the expense of complexity. Testing alternative refrigerants could also be valuable.

It should also be noted that a closed-loop heat pump may not be the most optimal way to integrate a vapour compression system into the carbon capture process. A more comprehensive analysis of the entire system's heat integration is needed. A pinch analysis would be an essential first step in that direction.

Finally, because heat pump performance decreases under part-load conditions, it would be relevant to extend the present work to an hourly study of the system. This would allow for the study of transient operation and the resulting heat pump performance. Relying solely on nominal power simulation results may be unrealistic and may yield overly optimistic performance estimates.

Acknowledgement

This publication is supported by the Walloon Region through a FRIA grant.

References

[1] M. Bui et al., 'Carbon capture and storage (CCS): the way forward', Energy Environ. Sci., vol. 11, no. 5, pp. 1062–1176, 2018.

[2] Y. Le Moullec et al., 'Process modifications for solvent-based post-combustion CO_2 capture', Int. J. Greenh. Gas Control, vol. 31, pp. 96–112, 2014.

[3] E. H. Jensen et al., 'Electrification of amine-based CO_2 capture utilizing heat pumps', Carbon Capture Sci. Technol., vol. 10, p. 100154, 2024.

[4] G. Léonard, et al., 'Influence of process operating conditions on solvent thermal and oxidative degradation in post-combustion CO_2 capture', Comput. Chem. Eng., vol. 83, pp. 121–130, 2015.

[5] C. Arpagaus et al., 'High temperature heat pump using HFO and HCFO refrigerants - System design, simulation, and first experimental results', International Refrigeration and Air Conditioning Conference, Purdue, USA, 2018.

[6] S. S. Warudkar et al., 'Influence of stripper operating parameters on the performance of amine absorption systems for post-combustion carbon capture: Part I. High pressure strippers', Int. J. Greenh. Gas Control, vol. 16, pp. 342–350, 2013.

[7] J. Davis and G. Rochelle, 'Thermal degradation of monoethanolamine at stripper conditions', Energy Procedia, vol. 1, no. 1, pp. 327–333, 2009.

HEAT TRANSFER DURING THE DOMINANT CONVECTION MELTING REGIME IN RECTANGULAR ENCLOSURES HEATED FROM THE SIDE

Maité Goderis[1,2]*, Wim Beyne[1,2], Michel De Paepe[1,2,3]

[1] Ghent University, Department of Electromechanical, Systems and Metal Engineering, Sint-Pietersnieuwstraat 41, Ghent, 9000, Belgium

[2] FlandersMake@UGent – Core lab MIRO, Ghent, 9000, Belgium

[3] University of Cape Town, Department of Mechanical Engineering, Private Bag X3, Rondebosch 7701, South Africa

* *Corresponding Author: maite.goderis@ugent.be*

Abstract. Latent thermal energy storage (LTES) systems using phase change materials (PCMs) are key for managing the variability of renewable energy sources. This study examines heat transfer during the melting process in rectangular PCM enclosures heated from one side at a constant temperature, with a focus on the convection-dominated regime. Existing correlations for the Nusselt number in this regime are often limited to specific conditions, so multiple data sets were combined to derive a more generalized correlation. The analysis identified the Rayleigh number as the dominant factor in heat transfer, aligning with theoretical expectations based on boundary-layer convection theory. While the obtained correlation showed strong agreement with the data, with lower mean and maximum relative errors compared to correlations from literature. Future research will focus on investigating the transitions between the regimes, and the less understood solid shrinking regime. These findings aim to enhance the predictive models for heat transfer in LTES systems.

Keywords. Thermal energy storage, melting, heat transfer

Nomenclature

AR	Aspect Ratio (-)
H	Height of enclosure (m)
LTES	Latent Thermal Energy Storage
Nu	Nusselt number (-)
PCM	Phase Change Material
Pr	Prandtl number (-)
Ra_H	Rayleigh number based on height (-)
Ste	Stefan number (-)
W	Width of enclosure (m)

1 Introduction

Latent thermal energy storage (LTES) systems, utilizing phase change materials (PCMs), offer a solution for the intermittent nature of renewable energy sources. Rectangular configurations are a common geometry for LTES systems due to their simplicity, ease of construction, and versatility [1].

A key aspect in the design and analysis of LTES systems involves the boundary conditions applied to the PCM. Typically, two common boundary conditions are considered: constant temperature or constant heat flux [1]. This study focuses on solid-liquid phase change in rectangular LTES systems, with a constant temperature boundary applied to one side wall, while the remaining walls are considered adiabatic.

In such systems, heat transfer during solidification is primarily governed by conduction. However, the melting process is more complex due to the significant influence of natural convection, which becomes the dominant heat transfer mechanism as melting progresses. The heat transfer behavior is inherently influenced by the thermophysical properties of the PCM, the boundary conditions, and the geometry of the enclosure [1].

Jany and Bejan [2] were the first to identify the distinct melting regimes that occur throughout the melting process of PCMs (see Figure 1). During the initial stage of melting, conduction is the dominant heat transfer mode, with the phase change front advancing parallel to the heated wall. As the melting process continues and more liquid forms, convective heat transfer comes into play and becomes the dominant heat transfer mechanism. When the phase change front reaches the wall opposite to the heated

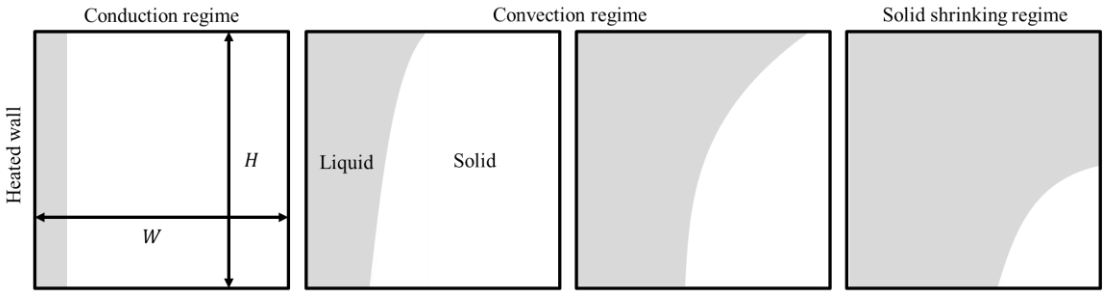


Figure 1: Schematic of different melting regimes.

boundary, the final regime, known as the solid shrinking regime, begins. During this stage, the remaining solid PCM gradually diminishes in height until complete melting is achieved.

Several numerical and experimental studies have verified these melting regimes, observing both the shape of the melting front and the evolution of the Nusselt number as key indicators. During the initial conduction-dominated stage, the Nusselt number decreases rapidly, consistent with the solution to the classical Stefan problem. As the process transitions to the convection-dominated regime, the Nusselt number reaches a relatively constant value, reflecting the steady convective heat transfer [2], [3]. Finally, during the solid shrinking regime, the Nusselt number decreases as the remaining solid phase diminishes. However, comprehensive understanding of the heat transfer dynamics during this final regime remains limited.

To characterize the heat transfer during melting, multiple authors have developed correlations for the Nusselt number, as it directly relates to the heat transfer rate and thus to the melting rate [4]. These correlations are often derived without accounting for the distinct transitions between different melting regimes, resulting in a single expression across the entire melting process. This can lead to inaccuracies, as each regime is governed by different heat transfer mechanisms.

To address this limitation, a distinction between the different melting regimes has to be made: each melting regime, and the transitions between them, has to be studied separately. This approach was used by Wang et al. [5], who conducted a numerical study validated with experimental data of Shokouhmand and Kamari [6] on a rectangular enclosure filled with lauric acid. Wang et al. performed simulations with variable wall temperature, initial temperature, and enclosure dimensions. They derived separate correlations for the heat transfer coefficient and liquid fraction evolution for each melting regime. However, their correlations are complex and limited to specific boundary and geometrical conditions and are only valid for one specific PCM material. Furthermore, the correlations are not derived based on fundamental heat transfer theory, but are obtained through fitting. From heat transfer theory, transition liquid fractions, linked to specific phase change front shapes, might be more meaningful then transition times.

In this study, the focus is specifically on the dominant-convection regime, where the Nusselt number is assumed to be constant. The other melting regimes are beyond the scope of this study, as the conduction regime is considered well-understood, and the solid shrinking regime lacks qualitative data in literature.

Some authors already investigated the heat transfer behavior during the dominant-convection regime. For example, Yanxia et al. [7] executed experiments with an enthanolamine-water mixture as PCM (high Prandtl). A correlation was obtained for the constant Nusselt number during the convection regime, incorporating factors such as Stefan, Rayleigh and Prandtl. However, this correlation suffers from limited applicability.

Duan et al. [8] numerically studied the melting of ice. Initially, the expected conductive behavior was observed, followed by the typical scaling law between Nusselt and Rayleigh during the convective regime. One correlation was developed for the position-averaged Nusselt number as a function of aspect ratio, Rayleigh, Stefan and Fourier number. No distinction was made between the different regimes, despite the clearly observed conduction and convection regimes.

This work aims to address these limitations by consolidating literature data from various studies to develop a generalized correlation for heat transfer during the convection-dominated melting regime. The proposed correlation is intended to be applicable across a range of PCM materials, enclosure dimensions, and boundary conditions.

2 Dominant-convection regime

During the dominant-convection regime of the melting process, the liquid phase of the PCM fills the entire height of the enclosure, leading to a deformation of the phase change front. Unlike in the initial conduction-dominated stage, the phase change front is thus no longer parallel to the heated wall.

Based on the scale analysis of Jany and Bejan [2], during the convection regime, the Nusselt number scales with the Rayleigh number, according to the boundary-layer convection theory (Equation (1)).

$$Nu \sim Ra_H^{0.25} \quad (1)$$

The Rayleigh number is based on the height H of the enclosure.

To develop a more generalized correlation for the Nusselt number during the convection-dominated regime, the data sets from the studies mentioned in the introduction were combined and analysed using dimensionless numbers. Table 1 summarizes the relevant data used for fitting the correlation.

Table 1: Overview of data sets.

Ref.	Pr	AR	Ra	Ste
Wang et al. [5]	100	$1 - 8.4$	$3.02 \cdot 10^8$ $- 3.24 \cdot 10^{10}$	0.128 $- 0.31$
Yanxia et al. [7]	693	0.71	$3.56 \cdot 10^7$ $- 5.56 \cdot 10^8$	0.091
Duan et al. [8]	6.722	$0.5 - 2$	$8.14 \cdot 10^4$ $- 6.5 \cdot 10^5$	0.864

The fitting led to Equation (2) for the Nusselt number during the dominant-convection melting regime.

$$Nu = 0.359 \cdot AR^{-0.037} \cdot Ra_H^{0.247} \cdot Ste^{0.059} \quad (2)$$

The fitting results are visually represented in Figure 2, where the proposed correlation is compared against the data from different studies. The correlation achieved an R^2 value of 0.998, indicating a strong agreement between the fitted model and the data. The mean relative error of the correlation was found to be 5.54%, with the largest deviations occurring in the data from Duan et al., where a maximum relative error of 26.02% was observed. The maximum absolute error across the entire data set was 2.3.

The correlation provides valuable insights into the heat transfer behavior during the dominant-convection regime. Equation (2) highlights the Rayleigh number as the most influential parameter

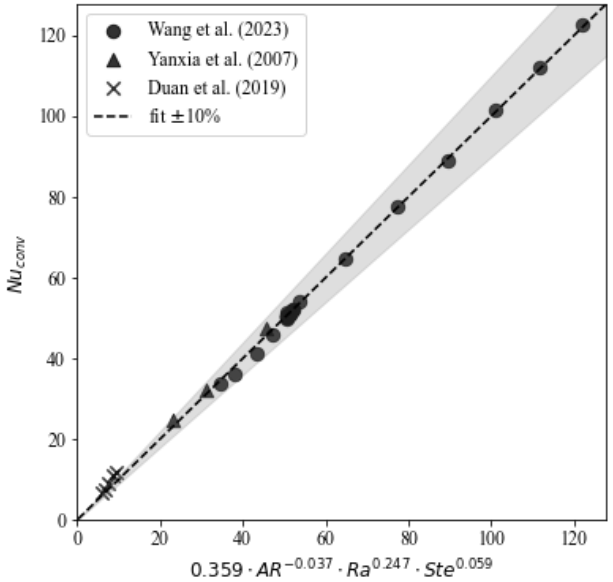


Figure 2: Fitting of Nusselt number.

affecting the Nusselt number during this phase of melting. The Rayleigh number depends on fluid properties (i.e. Prandtl number), the boundary condition (wall temperature), and geometry (height). The power of Rayleigh corresponds to what can be expected following from the scaling theory in Equation (1).

This analysis suggests that previous studies have performed overfitting by including a lot of parameters or introducing complex correlations. For a generalized relationship applicable across different PCM materials and geometries, the Rayleigh number emerges as the most critical parameter to consider.

2.1 Comparison to Nusselt correlations from literature

Yanxia et al. [7] had previously proposed a correlation for the constant Nusselt number during the convection regime. While their correlation performs well for their own data, it exhibits significant errors when applied to the data from Wang et al. [5] and Duan et al. [8].

Similarly, Duan et al. [8] proposed a time-dependent correlation for the Nusselt number over the entire melting process. To evaluate its performance, the average of this predicted Nusselt is calculated during the convection regime. The start and end of the convection regime are determined based on the shape of the numerically obtained Nusselt curve.

Table 2 highlights the performance of the in this work developed correlation compared to those from Yanxia et al. [7] and Duan et al. [8]. The proposed correlation shows significantly lower mean and maximum relative errors across all datasets, demonstrating its generalized applicability. The improved accuracy arises from combining and fitting

to multiple datasets, capturing a wider range of conditions than the correlations derived from individual datasets.

Table 2: Overview of errors with various Nusselt correlations.

Ref.	Mean rel. error	Max. rel. error
Eq. (2)	6%	26%
Yanxia et al. [7]	14%	54%
Duan et al. [8]	45%	87%

3 Conclusions and future work

Existing literature provides correlations for the Nusselt number during melting in rectangular PCM enclosures heated from one side at constant temperature. Often, the different melting regimes are not taken into account, despite their fundamental different heat transfer behaviour. Furthermore, these correlations are often limited by their specific boundary conditions, geometrical parameters, and PCM properties. However, to develop a general design method for these systems, distinct correlations are required for each regime, and the correlations should be generally applicable.

In this study is focussed on characterising the value of the Nusselt number during the dominant convection melting regime. Multiple data sets from prior research were combined, allowing for the development of a more generalized correlation for the Nusselt number.

The analysis conducted in this work highlights the dominant role of the Rayleigh number in determining heat transfer during the convection regime. The relationship between the Nusselt and Rayleigh numbers aligns with theoretical predictions derived from scale analysis and fundamental principles of convective heat transfer. This finding underscores the importance of the Rayleigh number as a critical parameter in the characterization of melting behavior in PCM systems. Furthermore, the developed correlation shows significantly lower errors, compared to correlations from literature.

Future work will focus on determining the Nusselt correlations for the other regimes, as well as predicting the transitions between the different regimes. In particular, the solid shrinking regime remains poorly understood, and developing a more comprehensive understanding of this phase is a priority for advancing the accuracy of PCM heat transfer models.

Acknowledgement

This research was funded by an FWO grant (1SHBC24N) for strategic basic research.

References

[1] S. Huang *et al.*, “Experimental study on the influence of PCM container height on heat transfer characteristics under constant heat flux condition,” *Appl Therm Eng*, vol. 172, May 2020, doi: 10.1016/j.applthermaleng.2020.115159.

[2] P. Jany and A. Bejan, “Scaling theory of melting with natural convection in an enclosure,” 1988.

[3] D. Gobin and C. Bénard, “Melting of Metals Driven by Natural Convection in the Melt: Influence of Prandtl and Rayleigh numbers,” *J Heat Transfer*, vol. 144, pp. 521–524, 1992.

[4] B. W. Webb and R. Viskanta, “ON THE CHARACTERISTIC LENGTH SCALE FOR CORRELATING MELTING HEAT TRANSFER DATA,” 1985.

[5] Z. Wang, Y. Li, Y. Wang, and A. Li, “Stagewise melting heat transfer characteristics of phase change material in a vertically placed rectangular enclosure,” *J Energy Storage*, vol. 62, Jun. 2023, doi: 10.1016/j.est.2023.106917.

[6] H. Shokouhmand and B. Kamkari, “Experimental investigation on melting heat transfer characteristics of lauric acid in a rectangular thermal storage unit,” *Exp Therm Fluid Sci*, vol. 50, pp. 201–212, 2013, doi: 10.1016/j.expthermflusci.2013.06.010.

[7] D. Yanxia, Y. Yanping, J. Daiyong, C. Baoyi, and M. Jinfeng, “Experimental investigation on melting characteristics of ethanolamine-water binary mixture used as PCM,” *International Communications in Heat and Mass Transfer*, vol. 34, no. 9–10, pp. 1056–1063, Nov. 2007, doi: 10.1016/j.icheatmasstransfer.2007.07.002.

[8] J. Duan, Y. Xiong, and D. Yang, “On the melting process of the phase change material in horizontal rectangular enclosures,” *Energies (Basel)*, vol. 12, no. 16, Aug. 2019, doi: 10.3390/en12163100.

DEVELOPMENT OF A HEAT TRANSFER CORRELATION FOR HORIZONTAL FLOW OF SUPERCRITICAL REFRIGERANTS UNDER HEATING CONDITIONS

Jera Van Nieuwenhuyse[1]*, Steven Lecompte[1,2], Michel De Paepe[1,2,3]

[1] Ghent University, Department or Electromechanical, Systems and Metal Engineering, Ghent, Belgium

[2] Flanders Make – Core lab MIRO, Ghent, Belgium

[3] University of Cape Town, Department of Mechanical Engineering, Rondebosch, South Africa

** Corresponding Author: jera.vannieuwenhuyse@ugent.be*

Abstract. Supercritical heat transfer correlations applicable to refrigerants are required in order to design the heat exchangers of supercritical systems (e.g. vapor generators in transcritical organic Rankine cycle systems). Existing correlations that have been developed for horizontal flow of specific supercritical refrigerants, lack accuracy when applied to other refrigerants. In addition, directives when to apply which correlation are also missing. In this work, a generally applicable heat transfer correlation for supercritical refrigerants flowing horizontally under heating conditions is proposed. First, based on data available in literature and data from an in-house performed experimental campaign, existing correlations are evaluated. Especially at the top of the tube, the existing correlations from literature have a low prediction capability. Next, the prediction capability of several correction factors commonly applied to heat transfer correlations for supercritical flows is investigated. Finally, two new more generally applicable heat transfer correlations based on this analysis are proposed, i.e. for the top and bottom separately. These new correlations incorporate a viscosity-based correction factor to take into account the radial property variations and a correction factor to account for pseudo-boiling effects. The prediction capability of the heat transfer on the bottom is comparable to the best performing correlation from literature, but the prediction of the heat transfer on the top can be significantly improved when using the newly developed correlation. For the bottom of the tube, 90% of the data can be predicted within a relative error below 30%. For the top, this is 92%.

Keywords. Supercritical, Heat transfer correlation, Refrigerants, Horizontal, Convection

1 Introduction

In order to design the heat exchangers of supercritical systems (e.g. vapor generators in transcritical organic Rankine cycle systems), it is important to accurately predict the heat transfer. For this purpose, heat transfer correlations are developed. They should be specific enough to handle the exact geometry and fluid properties. Yet, even correlations that have been developed for horizontal flow of specific supercritical refrigerants, lack accuracy when applied to other refrigerants. This is because of the strong property variations that occur when a fluid passes the pseudocritical temperature, resulting in secondary phenomena such as buoyancy and pseudo-boiling (similar to subcritical boiling). For horizontal tubes, this can result in large temperature differences between the top and bottom of the tube. Directives when to apply which correlation are also missing [1].

Therefore, based on data available in literature and data from an in-house performed experimental campaign, a new more generally applicable heat transfer correlation is proposed for horizontal flow of supercritical refrigerants under heating conditions.

2 Evaluation of existing supercritical correlations

2.1 Selection of heat transfer correlations for supercritical fluids

As already mentioned, several heat transfer correlations have been developed over the years to predict the heat transfer to supercritical fluids. Here, the prediction capabilities of some of these correlations, which have been developed for horizontal flows (based on either water or R134a data), are compared. The selected correlations are these from (with d_i or d_h the investigated inner diameter or hydraulic diameter of the tube, respectively): Tian et al. [2] (R134a, d_i = 10.3 mm, smooth tube), Huang et al. [3] (water, d_i = 26 mm, smooth tube), Yu et al. [4] (water, d_i = 26 mm, smooth tube), and Wang et al. [5] (R134a, d_h = 15.5 mm, internally ribbed tube).

All these correlations are modifications of the well-known Dittus-Boelter correlation, and contain one or more correction factors to take the heat transfer characteristics under supercritical conditions into account. This is also why, in most works, two correlations are developed: one for the bottom and one for the top of the tube. This is because in horizontal flow, the buoyancy force can have a significant impact on the heat transfer, resulting in a different heat transfer performance as function of the circumferential position in the tube. Only Huang et al. [3] did not define separate correlations depending on the radial position in the tube.

2.2 Selection of heat transfer correlations for supercritical fluids

The correlations mentioned in the previous section are evaluated based on how accurately they predict the heat transfer of supercritical refrigerants flowing horizontally under heating conditions. Therefore, the data series summarized in Table 1 have been selected for the evaluation. All the selected papers from literature contain experimental heat transfer data on refrigerants flowing in a horizontal smooth tube. The fluid under investigation and the inner diameter of the tube are tabulated.

Table 1: Selected supercritical data series.

Data series	Author	Fluid	d_i (mm)
1	Tian et al. [6]	R134a	10.3; 16
2	Wang et al. [7]	R134a	10.3
3	Tian et al. [2]	R134a	10.3
4	Tian et al. [8]	R1234yf	10.3
5	Cui et al. [9]	R134a	8
6	Van Nieuwenhuyse et al. [10]	R1234ze(E)	22.9

2.3 Prediction capability of existing heat transfer correlations

The correlations are evaluated by comparing the calculated Nusselt number from the correlation (Nu_{calc}) to the measured Nusselt number (Nu_{exp}), where the measured Nusselt numbers are the ones based on measurements presented in literature. In Table 2, the prediction capability of the correlations is tabulated based on the relative error RE, which is defined as $|Nu_{exp} - Nu_{calc}|/Nu_{exp}$. The refrigerant properties are calculated with REFPROP v10.0.

For, the bottom of the tube, only $Nu_{Tian,bottom}$ can adequately predict the experimental values, with 87% of the data predicted within RE < 30%, and with a mean relative error of 15%. The prediction capabilities of all the other correlations are far worse.

Table 2: Prediction capability of heat transfer correlations from literature.

Correlation	% of data with RE<30%	Mean RE [%]	Max RE [%]
Tian,bottom	87	15	149
Huang,bottom	23	111	403
Yu,bottom	39	58	274
Wang,bottom	54	35	238
Tian,top	81	19	116
Huang,top	12	129	515
Yu,top	73	22	112
Wang,top	5	53	87

Also for the top surface, the correlation developed by Tian et al. [2] outperforms the other correlations as all parameters determining the prediction capability are a lot higher. However, it should be mentioned that the data used to develop these correlations is also included in the data series used to evaluate the prediction capability of the correlations (data series 3), so these results might be biased. The prediction capability of the other correlations is not satisfactory. In Figure 1, the prediction capability of this best performing correlation from literature is illustrated for top of the tube. The solid black lines indicate an interval of +30% to -30% w.r.t. Nu_{exp}. The different colours correspond to the different data series listed in Table 1.

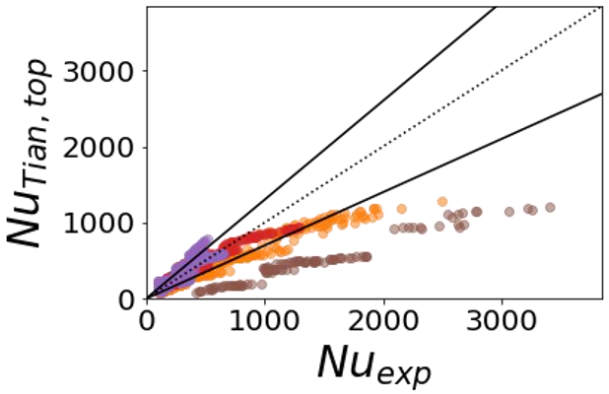


Figure 1: Prediction capability of the correlation of Tian et al. [2] for the top of the tube.

From Figure 1, it is clear that the data of data series 6 is not well predicted by the correlation, as all of these datapoints are largely underestimated. Therefore, a new heat transfer correlation for supercritical refrigerants is proposed to better fit the data from literature.

3 Development of a new heat transfer correlations

3.1 General form of the heat transfer correlation

In this section, it is evaluated which correction factors are best suited to predict the heat transfer phenomena under supercritical conditions. For this, the prediction capability of several newly generated heat transfer correlations for supercritical refrigerants are compared to identify the most important factors (based on the data from Table 1). All the developed heat transfer correlations are of the general form:

$$Nu = C_0 \cdot Re_b^{n_1} \cdot \overline{Pr_b}^{n_2} \cdot CF_1^{n_3} \cdot CF_2^{n_4} \qquad (1)$$

CF_1 and CF_2 are the correction factors taking into account the heat transfer characteristics under supercritical conditions. Together with the Reynolds number at the bulk Re_b and the Prandtl number at the bulk $\overline{Pr_b}$ (based on the cross sectional averaged isobaric specific heat capacity), they are the independent variables. n_1 to n_4 are the exponents of the independent variables and C_0 is a scaling factor. These parameters are optimized by performing a linear regression (using the least squares approach) on the natural logarithm of Equation (1).

In theory, a large amount of correction factors can be added to the correlation. However, in order to avoid overfitting and to keep the complexity of the correlation low, the decision was made to limit the amount of correction factors to two. In order to take the property variation between the fluid at the wall (w) and the bulk (b) of the flow into account, the following correction factors are considered: the dynamic viscosity based correction factor ($\frac{\mu_w}{\mu_b}$) and the isobaric specific heat capacity based correction factor ($\frac{\overline{c_p}}{c_{p,b}}$). The effect of buoyancy on the heat transfer is accounted for by ($\frac{Gr_b}{Re_b^2}$) (Gr is the Grashof number). The analogy with subcritical boiling is expressed by the supercritical boiling number SBO ($\frac{q}{G \cdot h_{pc}}$) of Zhu et al. [11], which is a reformulation of the subcritical boiling number (with q the heat flux, G the mass flux and h_{pc} the specific enthalpy at the pseudocritical temperature), equal to the ratio of mass of vapor generated per unit area of heat transfer surface to the mass flow rate per unit of flow cross-sectional area.

3.2 Influence of correction factors on prediction capability

The results of the linear regression are tabulated in Table 3, showing the applied correction factors and the prediction capabilities of the different correlations based on the relative error.

Table 3: Prediction capability of newly developed heat transfer correlations.

Correlation	CF_1	CF_2	% of data with RE<30%	Mean RE [%]	Max RE [%]
0,bottom	-	-	83	18	109
1,bottom	$\frac{\mu_w}{\mu_b}$	-	86	16	107
2,bottom	$\frac{\overline{c_p}}{c_{p,b}}$	-	83	18	109
3,bottom	$\frac{\mu_w}{\mu_b}$	$\frac{Gr_b}{Re_b^2}$	91	15	119
4,bottom	$\frac{\mu_w}{\mu_b}$	SBO	90	14	80
0,top	-	-	73	23	76
1,top	$\frac{\mu_w}{\mu_b}$	-	78	20	77
2,top	$\frac{\overline{c_p}}{c_{p,b}}$	-	73	23	79
3,top	$\frac{\mu_w}{\mu_b}$	$\frac{Gr_b}{Re_b^2}$	87	16	87
4,top	$\frac{\mu_w}{\mu_b}$	SBO	92	13	64

From this table, it is clear that adding an isobaric specific heat capacity correction factor does not lead to an improvement, but incorporating the viscosity based correction factor does lead to a better prediction capability. For the bottom of the tube, additionally adding SBO or $\frac{Gr_b}{Re_b^2}$ gives similar results, however, on average, SBO captures the data better (reduction of the mean RE and max RE). Figure 2 graphically shows the results for the bottom of the tube for case 4. For the top, the influence is more outspoken and incorporating the pseudo-boiling effects results in a significant improvement. This is because data series 6 is well-captured by the SBO number. This is illustrated in Figure 3. Incorporating $\frac{Gr_b}{Re_b^2}$ leads to a similar separation in data sets as shown in Figure 1.

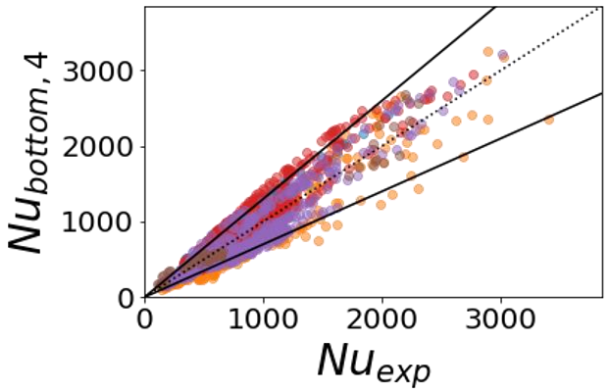


Figure 2: Prediction capability of the correlation incorporating $\frac{\mu_w}{\mu_b}$ and SBO for the bottom of the tube.

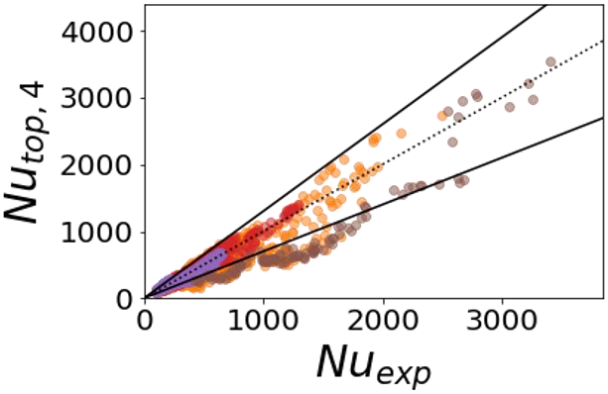


Figure 3: Prediction capability of the correlation incorporating $\frac{\mu_w}{\mu_b}$ and SBO for the top of the tube.

3.3 New heat transfer correlations

Based on the considerations above, the following heat transfer correlations are devised for the bottom and the top of the tube, respectively (corresponding to case 4):

$$Nu_{bottom} = 0.5985 \cdot Re_b^{0.81301} \cdot \overline{Pr_b}^{1.22519} \cdot \left(\frac{\mu_w}{\mu_b}\right)^{0.88356} \cdot SBO^{0.44736} \quad (3)$$

$$Nu_{top} = 2.69259 \cdot Re_b^{0.82849} \cdot \overline{Pr_b}^{1.48734} \cdot \left(\frac{\mu_w}{\mu_b}\right)^{1.18861} \cdot SBO^{0.67369} \quad (4)$$

For the bottom of the tube, 90% of the data can be predicted within RE < 30%, and the average RE is 14%. For the top of the tube, 92% of the data can be predicted within RE < 30%, and the average RE is 13%.

These correlations can be used in the design of supercritical vapor generators consisting of horizontal tubes, by splitting up the tube to be sized in a top and bottom half. Using two correlations (instead of one representing the average heat transfer coefficient) increases complexity of the design calculations. However, this way, locations where severe deteriorated heat transfer occurs, resulting in high wall temperatures (usually at the top of the horizontal tube and depending on the operating conditions), can be identified, ensuring that the heat exchanger is designed to operate under safe conditions.

4 Conclusions

Reliable heat transfer correlations for supercritical refrigerants are key in designing vapor generators of supercritical systems. In this work, existing correlations from literature are evaluated, and a new heat transfer correlation for the bottom and top of a horizontal tube is proposed.

- For both sides of the tube, the correlation developed by Tian et al. [2] performs best. All the other correlations from literature perform inadequately, especially at the top.
- Two new heat transfer correlations are put forward, incorporating a viscosity based correction factor and a correction factor for the pseudo-boiling effects. The prediction of the heat transfer on the top can be significantly improved when using the newly developed correlation. For the top of the tube, 92% of the data can be predicted within RE < 30%. For the bottom, this is 90%.

Acknowledgement

This paper is partly funded by an FWO - Flanders grant (1SA3720N) for strategic basic research.

References

[1] J. Van Nieuwenhuyse et al., “Current status of the thermohydraulic behavior of supercritical refrigerants: A review”, Applied Thermal Engineering, no. 218, 119201, 2023.

[2] R. Tian et al., “Experimental study of the heat transfer characteristics of supercritical pressure r134a in a horizontal tube”, Experimental Thermal and Fluid Science, no. 100, pp. 49-61, 2019.

[3] X. Huang et al., “Heat transfer characteristics of supercritical water in a horizontal tube considering local temperature fields”,

International Journal of Heat and Mass Transfer, no. 198, 123404, 2022.

[4] S. Yu et al., “Experimental investigation on heat transfer characteristics of supercritical pressure water in a horizontal tube”, Experimental Thermal and Fluid Science, no. 50, pp. 213-221, 2013.

[5] D. Wang et al., “Heat transfer investigation of supercritical r134a for transcritical organic Rankine cycle system”, Energy, no. 169, pp. 542-557, 2019.

[6] R. Tian et al., “Experimental study of buoyancy effect and its criteria for heat transfer of supercritical r134a in horizontal tubes”, International Journal of Heat and Mass Transfer, no. 127, pp. 555-567, 2018.

[7] D. Wang et al., “Experimental comparison of the heat transfer of supercritical r134a in a micro-fin tube and a smooth tube”, International Journal of Heat and Mass Transfer, no. 129, pp. 1194-1205, 2019.

[8] R. Tian et al., “Mixed convection heat transfer of supercritical pressure r1234yf in horizontal flow: Comparison study as alternative to r134a in organic Rankine cycles”, Energy, no. 205, 118061, 2020.

[9] Y.L. Cui. et al., “Experimental and numerical studies on convective heat transfer of supercritical r-134a in a horizontal tube”, International Journal of Heat and Mass Transfer, no. 136, pp. 34-45, 2019.

[10] J. Van Nieuwenhuyse et al., “Determination of the supercritical heat transfer of the low GWP refrigerant R1234ze(E)”, in 10th World Conference on Experimental Heat Transfer, Fluid Mechanics and Thermodynamics, Rhodes, Athens, 2024.

[11] B. Zhu. et al., “The general supercritical heat transfer correlation for vertical up-flow tubes: K number correlation”, International Journal of Heat and Mass Transfer, no. 148, 119080, 2020.

EXPERIMENTAL EVALUATION OF A THERMAL LOAD SIMULATION MODEL OF A LIVESTOCK FARM

Manon Everaert[1,2*], Jarissa Maselyne[1], Steven Lecompte[2]

[1] EV ILVO, Belgium

[2] University of Ghent, Belgium

** Corresponding Author: manon.everaert@ilvo.vlaanderen.be*

Abstract. Livestock farms exhibit a wide range of annual energy use, ranging between 15 and 839 kWh/m². With deterministic Building Energy Simulation (BES) models, that can accurately simulate the energy use patterns, innovative renewable energy integration schemes can be evaluated. As such, a transition to a more environmentally friendly farming can be made. While BES models are extensively available for residential and commercial buildings, there are few documented cases reported for the livestock sector with its specific needs.

In a first effort, a preliminary BES model was developed that estimated the thermal load of a pig farm in Belgium. Although the model successfully predicts a correct order of magnitude and trends on a monthly basis, it is not able to predict correct trends on an hourly basis (outliers up to 700 %). These disagreements may arise from factors such as neglection of the farm's thermal inertia, incorrect boundary conditions for certain heating systems, inaccuracies in the measurements, or manual interventions by the farm manager.

This work presents a comparison between the modelling results and experimental data. The deviations and their underlying causes are identified and potential solutions are proposed. A first analyses indicates that manual interventions during summer, the strong dependence of the model outside temperature, and neglecting domestic hot water, could explain these outliers.

Keywords. Pig farm, Building simulation, Energy.

AGGREGATING RESIDENTIAL ELECTRICAL WATER HEATERS INTO A VIRTUAL POWER PLANT TO PROVIDE SERVICES TO THE GRID.

David Rojas Plana[1]*, Ray Antonio Rojas Candia[1], Nicolas Leclercq[2], Sylvain Quoilin[1]

[1] Thermodynamics Laboratory, Integrated & Sustainable Energy Systems, University of Liège, Sart Tilman, 4000, Liège, Belgium

[2] Thermodynamics Laboratory, Thermal Energy Systems, University of Liège, Sart Tilman, 4000, Liège, Belgium

* *Corresponding Author: drplana @uliege.be*

Abstract. This work proposed a methodology for developing a virtual power plant (VPP) used to aggregate electric water heaters (EWHs) and heat pump water heaters. The main objective is to quantify the flexibility services these can offer to the grid in terms of volume and cost. For a fleet of 1000 EWHs, with an average capacity of 195 L, a maximum power of 2500 kW was obtained for the VPP, for an equivalent storage capacity of 15 MWh. The greatest potential for flexible demand is found between 7 and 10 a.m., representing 34 % of the total capacity of the VPP. The results show how EWHs can provide positive and negative regulation to the grid for different activation times. It is observed that the VPP has higher potential in terms of positive regulation than negative, but that this potential is tightly linked to the chosen control strategy. The VPP flexibility evaluation is finally validated using a digital twin of the water heaters portfolio with a simplified control strategy. Results demonstrate the suitability of the proposed model, but further work is required to accurately quantify the ancillary services to be provided to the grid.

Keywords. Virtual power plant, Demand response, Thermostatically controlled loads, Electric water heaters

Nomenclature

VPP	Virtual Power Plant
EWHs	Electric Water Heaters
$e_{e,t}$	State of charge of each of the EWH e, at time t
$\overline{E}_{e,t}$	Upper bound of the energy stored in EWH e, at time t (kWh)
$\underline{E}_{e,t}$	Lower bound of the energy stored in EWH e, at time t (kWh)
$\overline{D}_{e,t}$	Maximum power capacity of each EWH (W)
$d_{e,t}^{flex}$	Power consumed in each time step by each EWH (W)
$D_{e,t}$	Term for accounting thermal losses through the tank walls and water withdrawals (W)
$\overline{P}_{VPP,t}$	Maximum power in the VPP at time t (kW)
$\underline{P}_{VPP,t}$	Minimum power in the VPP at time t (kW)
$P_{VPP,t}$	Power consumption in the VPP at time t (kW)
$\overline{E}_{VPP,t}$	Upper bound in the VPP, at time t (MWh)
$\underline{E}_{VPP,t}$	Lower bound in the VPP, at time t (MWh)
$E_{VPP,t}$	Energy content in the VPP, at time t (MWh)
$\overline{D_t^{flex}}$	Power available for upward regulation at time t
$\underline{D_t^{flex}}$	Power available for downward regulation at time t
$E_{e,t}^{Up}$	Energy available for upward regulation from the VPP at time t
$E_{e,t}^{Down}$	Energy available for downward regulation from the VPP at time t

Subscripts

e	Electric water heater
t	time

1 Introduction

The current deployment of variable renewable energy sources into the grids has increased the need for regulation reserves in the electric power system. This growing need for system flexibility has coincided with the rise of smart grids, which can potentially manage electric loads with precision similar to supply-side resources. **Thermostatically controlled loads** (TCLs), such as electric water heaters and

HVAC systems, are particularly promising because they can provide flexibility without compromising user comfort [1, 2, 3]. These loads can provide grid services such as **demand response** (DR), reducing reliance on expensive reserves during peak demand periods and enhancing grid stability. By aggregating TCLs into a **virtual power plan**t (VPP), utilities can optimize energy use and support the integration of renewables while providing essential services such as frequency regulation [4, 5].

Authors in [3] developed a method to quantify the power flexibility of thermostatically controlled loads (TCLs) under different scenarios, controller types, and load profiles. They observed that EWHs tend to synchronize their operation due to their hysteresis control, which can result in simultaneous activation or deactivation of devices following a flexibility activation. This synchronisation leads to significant rebound effects causing voltage, congestion and frequency problems. The authors proposed a control algorithm to mitigate this issue.

[6] focuses on characterizing the flexibility activation potential of **electric water heaters** (EWHs) in Norway, where a set of key parameters are proposed, including rebound percentage, ramp rates, and temperature deviation, to quantify flexibility. The authors simulated a population of 1000 households with one EWH in each household. Each EWH has a rated power of 2000 W and a capacity of 200 L. The temperature threshold limits in their study are $\underline{T} = 70°C$ and $\overline{T} = 75°C$, where $\underline{T}$ is the minimum temperature and $\overline{T}$ indicates the maximum temperature.

This work presents a methodology to aggregate a fleet of EWHs and Heat Pump Water Heaters (HPWHs) into a VPP. The focus is on harnessing these TCLs as decentralized energy storage and demand response resources to enhance grid flexibility. The proposed approach defines the key parameters and variables required for integrating EWHs and HPWHs into the VPP framework, assessing their potential to support the power system. The study quantifies their flexibility and evaluates how these technologies can improve grid performance.

2 Methods

2.1 Virtual power plant formulation

The formulation for modelling storage facilities is found in [7] in its most general form. In our case, some modifications were made to adjust them to our study, such as the non-use of binary variables. These are used to prevent unintended storage cycling when using renewable energy targets [8]. The approach used in this work is inspired by [9] which was applied to explore the potential of electric vehicles as a flexible resource within the power system of the Netherlands.

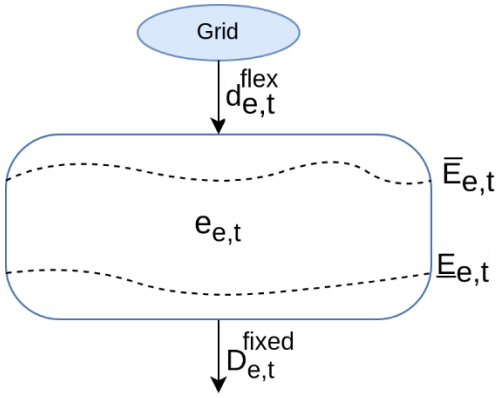


Figure 1 Energy balance for an individual EWH.

Figure 1 shows the main parameters of one individual energy storage unit. As can be seen, the unit takes energy from the grid where the parameter $d_{e,t}^{flex}$ represents the power consumed during each time step (t) by each unit (e). In this case, since they are electric heaters, the balance shows that energy can only be transferred in one direction. Another important parameter is the **state of charge** represented by $e_{e,t}$ which is limited by the minimum energy stored $\underline{E}_{e,t}$ and the maximum energy stored $\overline{E}_{e,t}$. The term $D_{e,t}^{fixed}$ is used to account for energy losses, which in this case are related to thermal losses through the tank walls and the water withdrawals made by the user at each time step. Finally, $d_{e,t}^{flex}$ is constrained by the maximum power of each unit denoted by $\overline{D}_{e,t}$. All of this is summarized in equations 1 to 3.

$$e_{e,t} = e_{e,t-1} + \Delta t \cdot (d_{e,t}^{flex} - D_{e,t}^{fixed}) \quad (1)$$

$$\underline{E}_{e,t} \leq e_{e,t} \leq \overline{E}_{e,t} \; \forall e \in EWH \; \forall t \in Time \quad (2)$$

$$0 \leq d_{e,t}^{flex} \leq \overline{D}_{e,t} \quad (3)$$

Once we stablished our equations to describe the general behaviour of each of heater, it is proceeded to formulate the equations that define the VPP. Equations 4 and 5 determine the maximum minimum power of the VPP at each time step. Eq. 6 then calculates the actual power being used by the VPP. In

a similar way we determine the maximum, minimum and the actual energy of the VPP through equations 7-8. Once all the above parameters have been obtained, we can estimate the flexibility services that our VPP can offer at each time step using equations 10-13.

$$\overline{P}_{VPP,t} = \sum_{e} \overline{D}_{e} \; \forall e \in EWH \forall t \in Time \tag{4}$$

$$\underline{P}_{VPP,t} = 0 \tag{5}$$

$$P_{VPP,t} = \sum_{e} d_{e,t}^{flex} \tag{6}$$

$$\overline{E}_{VPP,t} = \sum_{e} \overline{E}_{e,t} \; \forall e \in EWH \forall tTime \tag{7}$$

$$\underline{E}_{VPP,t} = \sum_{e} \underline{E}_{e,t} \; \forall e \in EWH \forall tTime \tag{8}$$

$$E_{VPP,t} = \sum_{e} e_{e,t} \; \forall e \in EWH \forall tTime \tag{9}$$

$$\overline{D_t^{flex}} = min\left(P_{vpp,t} - \underline{P}_{vpp,t}; \frac{E_{e,t}^{Up}}{\Delta t}\right) \tag{10}$$

$$\underline{D_t^{flex}} = min\left(\overline{P}_{vpp,t} - P_{vpp,t}; \frac{E_{e,t}^{Down}}{\Delta t}\right) \tag{11}$$

$$E_{e,t}^{Down} = \overline{E}_{vpp,t} - E_{vpp,t} \tag{12}$$

$$E_{e,t}^{Up} = E_{vpp,t} - \underline{E}_{vpp,t} \tag{13}$$

With the foundational equations stablished, we examine two additional key concepts: i) **positive regulation** (downward regulation) and ii) **negative regulation** (upward regulation). Generating more or consuming less energy is known as upward regulation. On the other hand, downward regulation refers either to a decrease in generation or an increase in consumption [6]. According to Elia, when an imbalance is caused by an excess of power in the grid, the company activates the downward regulation service. The opposite case would be an activation of upward regulation when the imbalance is the result of a power deficit in the grid [10].

By aggregating the contributions of individual components, we can evaluate the system's capability to supply energy during peak demand periods and support services like frequency regulation. The connection between individual components and the overall energy capacity of the VPP highlights the necessity for effective monitoring and management of these components to enhance the overall performance of the virtual power plant.

3 Case study and results

3.1 General assumptions and characteristics of the EWHs pool.

Our study focuses on a pool of 1000 EWHs in Belgium. The pool is generated by using a library developed in [11] and available in a dedicated repository[1]. This library allows to create a pool of EWHs or HPWHs, each with distinct characteristics such as power, volume, temperature, stochastic hot water consumption profiles and others.

In the absence of external signal, the EWHs are controlled by a hysteresis with a set point of 55 ± 3° C. The inlet water temperature and the maximum temperature was set as 14 and 80 °C respectively. The average volume of the pool is 196 L, ranging from a minimum of 120 L to 290 L. Their nominal powers are distributed between 2000 W and 3000 W, resulting in an average power of 2485 W.

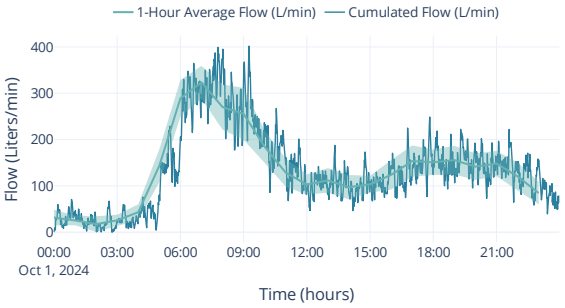


Figure 2 Aggregated water consumption profile over time.

In Figure 2 the aggregated how water consumption is depicted across a 24-hours period for a typical weekday. The curve shows that from 5:00 to 8:00 AM the demand is increased to an average value of 320 L/min approximately. After 9:00AM, the demand gradually declines until it reaches a value of 100 ± 30 L/min and remains fairly constant for the rest of the day. The results were compared to the ones presented in [6] for the Norwegian case, and they look similar between 6 to 10 AM. However, their study shows that there are two additional periods of increased demand, between 4:00-5:00 PM, and 7:00-

[1] https://github.com/NLeclercq27/Water-Heater

9:00 PM, which slightly differs from our results. The consumption pattern for the weekends is different, as users' routines usually vary compared to weekdays.

3.2 Results of VPP methodology simulation and flexibility quantification.

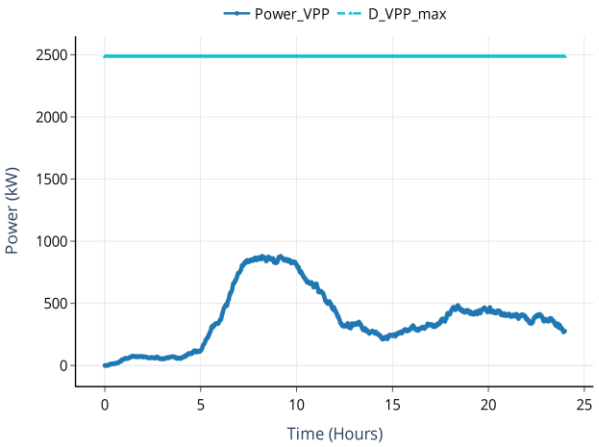


Figure 3 Available power for up and down regulation in the VPP.

For the simulation involving 1000 EWHs, over a 24-hour period, the execution time was approximately 10 minutes, but this will depend on factors such as the number of heaters and layers selected for each, the simulation period, time step and also the specific characteristics of the computer [11]. Then, by applying the methodology outlined in the previous section, **Figure 3** was confectioned.

The "Power_VPP" curve is the power consumed at each time step by the EWHs pool. Therefore, this also represents the amount of power that can be switched off to provide upward regulation, and the subtraction of the two curves is the maximum power available for downward regulation. The peak active power occurs between 7:00-10:00 AM, where the consumption slightly exceeds 800 kW.

Similarly, **Figure 4** shows the energy boundaries of the VPP. The upper line with a value of 15 MWh represents the energy that can be stored between the inlet temperature (14°C) and its maximum temperature of 80°C for safety reasons. The minimum state of charge (7.7 MWh) corresponds to a minimum temperature of 48°C.

With the previous parameters established, we can proceed to the next step, which is to determine the flexibility we can offer to the system for different activation periods. This is done using equations 10-13. The results of this calculation are shown in Figure 5. As illustrated, it covers activation windows of 15, 30, 60, 120, 180, and 240 minutes. These curves highlight the limitation of in terms of available flexibility for longer activation lengths (typically higher than 60 min): the power is limited by the fact that longer activations can lead to a violation of the minimum or maximum state of charge constraint.

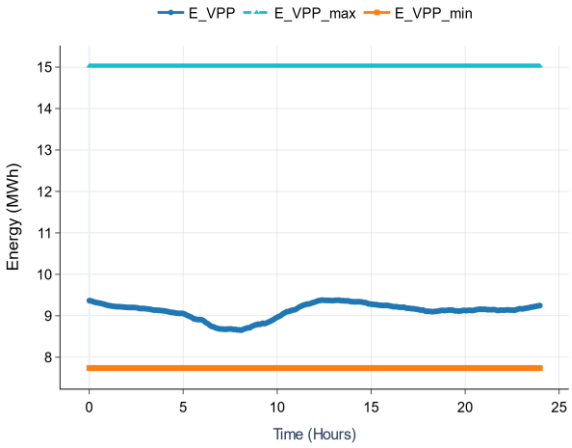


Figure 4 Available energy for up and down regulation in the VPP.

It is also worthwhile to note that the VPP has more capacity for downward regulation than upward regulation. This is due to the fact that, on average, less than 50% of the electrical heaters are active.

Additionally, it can be seen how for activation times longer than 60 minutes, the power is considerably reduced.

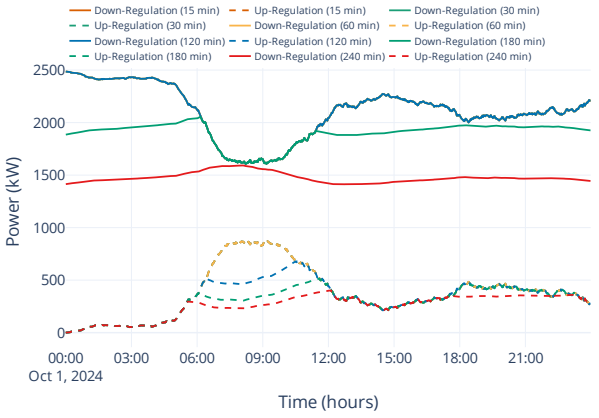


Figure 5 Available flexibility for up and down regulation for different activation periods of time.

3.3 Implementing a control strategy to flexibility activation

In this section, a new control strategy implemented in the library is presented, which allows turning on or off several heaters, thus overriding their own internal control strategy. The number of heaters to switch

on/off is determined by the flexibility previously calculated and shown in **Figure 5.**

To that aim, a priority list is built, where the heaters are sorted from the lowest to the highest temperature in case a downward regulation is desired (switch on heaters). This guarantees that the heaters with the lowest state of charge are switched first. In the opposite case, they are ordered from highest to lowest to turn them off, starting with those exhibiting the highest temperature.

Another important aspect in the control strategy is to ensure that, when activating the available flexibility, the temperature limits of each electric water heater and the energy limits of our VPP are not exceeded. If the temperature goes above the maximum, the activation is stopped for that particular heater, thus reducing the aggregated power of the VPP.

For testing purposes four simulations are run:

1. 1800 kW of downward regulation from 12:00 to 15:00, when the maximum of solar penetration occurs [12], and it also could be considered as a critical point due to the fact that many water heaters have reached their maximum set point temperature.
2. 1900 kW of downward regulation from 3:00 to 5:00 AM, it is made to investigate how much the power we will change during the maximum water consumption hours.
3. 800 kW of upward regulation from 7:30 – 8:30 AM.
4. increase the set point temperature to 70 °C.

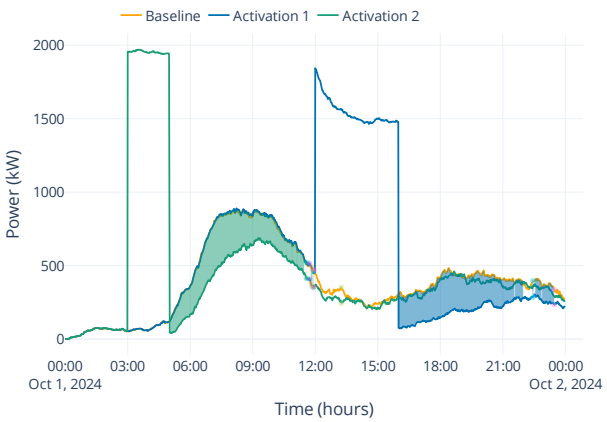


Figure 6 VPP power consumption for 1800 kW downward flexibility activations.

Figure 6 shows that during the activation periods, the power gradually decreases. This occurs because, as some heaters reach the maximum temperature set by the automatic control, they switch off, leading to a drop in power. To avoid this phenomenon, one could implement another control strategy which keeps the heaters that were already on at the beginning of the activation period. However, for this particular activation, this decrease can be leveraged, as PV generation also begins to decline following its peak around noon. Regarding activation 2, an interesting aspect is the reduction of power demand during the biggest demand for hot water, as some of the heaters do not need to be turned on at that moment to satisfy user requirements.

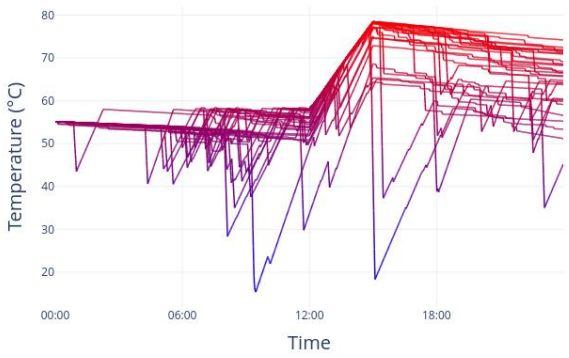


Figure 7 Impact of flexibility activation on temperatures of every electrical heater (activation 1).

Additionally, it can be observed that after the activation period, power decreases nearly to one-third of its value when compared to base case. This is known as the rebound effect and goes in the opposite direction from the activation.

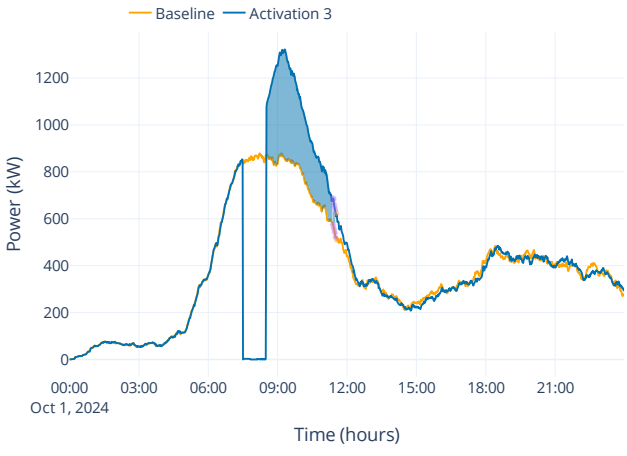


Figure 8 VPP power consumption for 800 kW upward flexibility activation.

Figure 7 illustrates the temperature behavior over time for some of them and none exceed the established maximum temperature, although some came close to reaching it. This analysis was also made for other flexibilities and the maximum temperature was never exceeded. This indicates a

priori that the sized flexibility (Eqs. **10** and **11**) is realistic and achievable.

In activation 3 the opposite direction is carried out, where 800 kW are switched off for one hour. As in the previous case, **Figure 8** highlights the rebound effect in the blue area, which causes the power to surge to a maximum of 1300 kW after the activation period. This can directly impact the quality of energy in the grid. Therefore, for such flexibility activations, more advanced strategies should be implemented to mitigate this effect.

Another question explored was the impact of increasing the set point temperature to 75 °C. The results indicate a 30 % increase in power availability for providing upward regulation during longer activation periods. On the contrary, the capacity to provide positive regulation services from the VPP decreases by 400 kW and is limited to only one-third of the activation time compared to activation 1. Additionally, one disadvantage is that setting a higher set point temperature increases of heat transfer losses and therefore the overall electricity consumption. These findings highlight the potential for further study to determine the optimal set point temperature or maybe having a combination of water heaters with different set points, depending on the specific regulation service to be provided.

4 Conclusions

In this work, a methodology for parametrizing a VPP providing services to the electric grid was presented. The two key parameters to be determined are $\overline{D_t^{flex}}$ and $\underline{D_t^{flex}}$ which allows determining the amount of flexible power that can be activated for different periods of time.

The proposed control strategy, although relatively simple, demonstrates to be solid as none of the heaters exceed their maximum temperature. In scenarios where these limits are overpassed it could be implemented a security margin in the methodology to overcome that issue.

Although this VPP was developed specifically for EWHs, the same methodology can be applied HPWHs, allowing for similar benefits in terms of grid flexibility.

The setpoint temperature plays a fundamental role in determining the flexibility services that can be provided. When it is set at 55°C, it is favorable for positive regulation, whereas for negative regulation, values like 75°C are better.

Further research will focus on the rebound effect, on the additional electricity consumption linked to flexibility provision, and on the integration of the VPP into a power system model.

Acknowledgement

This work was performed in the scope of the "Unleash" Belgian Energy Transition Fund project.

References

[1] L. Brouyaux, S. Iacovella, and G. Deconinck, "Practical Comparison of Aggregate Control Algorithms for Demand Response with Residential Thermostatically Controlled Loads," in *2020 6th IEEE International Energy Conference (ENERGYCon)*, Sep. 2020, pp. 870–875. doi: 10.1109/ENERGYCon48941.2020.9236437.

[2] S. Koch, J. Mathieu, and D. Callaway, "Modeling and Control of Aggregated Heterogeneous Thermostatically Controlled Loads for Ancillary Services," presented at the Proc. PSCC, Aug. 2011.

[3] M. V. Gasca, F. Ibáñez, and D. Pozo, "Flexibility quantification of thermostatically controlled loads for demand response applications," *Electr. Power Syst. Res.*, vol. 202, p. 107592, Jan. 2022, doi: 10.1016/j.epsr.2021.107592.

[4] M. Bahloul, L. Breathnach, J. Cotter, M. Daoud, A. Saif, and S. Khadem, "Role of Aggregator in Coordinating Residential Virtual Power Plant in 'StoreNet' : A Pilot Project Case Study," *IEEE Trans. Sustain. Energy*, vol. 13, no. 4, pp. 2148–2158, Oct. 2022, doi: 10.1109/TSTE.2022.3187217.

[5] I. Arafat, H. Shokouhinejad, E. Castillo Guerra, J. Meng, and J. L. Cardenas-Barrera, "Maximum Reserved Capacity of Aggregated Electric Water Heaters Virtual Battery for Peak Management," *IEEE Access*, vol. 12, pp. 67574–67588, 2024, doi: 10.1109/ACCESS.2024.3391298.

[6] V. Lakshmanan, H. Sæle, and M. Z. Degefa, "Electric water heater flexibility potential and activation impact in system operator perspective – Norwegian scenario case study," *Energy*, vol. 236, p. 121490, Dec. 2021, doi: 10.1016/j.energy.2021.121490.

[7] L. Baringo and M. Rahimiyan, *Virtual Power Plants and Electricity Markets: Decision Making Under Uncertainty*. Cham: Springer International Publishing, 2020. doi: 10.1007/978-3-030-47602-1.

[8] M. Kittel and W.-P. Schill, “Renewable energy targets and unintended storage cycling: Implications for energy modeling,” *iScience*, vol. 25, no. 4, p. 104002, Apr. 2022, doi: 10.1016/j.isci.2022.104002.

[9] A. Beltramo, A. Julea, N. Refa, Y. Drossinos, C. Thiel, and S. Quoilin, “Using electric vehicles as flexible resource in power systems: A case study in the Netherlands,” in *2017 14th International Conference on the European Energy Market (EEM)*, Dresden, Germany: IEEE, Jun. 2017, pp. 1–6. doi: 10.1109/EEM.2017.7982006.

[10] Elia, “Belgian Electricity Market: Final Implementation Plan CRM (22062020),” Federal Public Service (FPS) Economy, S.M.E.s, Self-employed, and Energy, Belgium, Jun. 2020. [Online]. Available: https://economie.fgov.be/sites/default/files/Files/Energy/Belgian-electricity-market-Final-implementation-plan-CRM-22062020.pdf

[11] N. Leclercq, S. Marichal, S. Quoilin, and V. Lemort, “DYNAMIC MODELING AND EXPERIMENTAL VALIDATION OF AN ELECTRICAL WATER HEATER WITH A DOUBLE STORAGE TANK CONFIGURATION,” 2024.

[12] “Solar-PV power generation data.” Accessed: Nov. 18, 2024. [Online]. Available: https://www.elia.be/en/grid-data/generation-data/solar-pv-power-generation-data

DESIGN AND OPTIMIZATION OF A HEAT PUMP COUPLED WITH A STORAGE SYSTEM FOR DISTRICT HEATING

Michael Khairallah[1]*, Assaad Zoughaib[1], Patrick Havil[2], Maxime Frerejacque[2]

[1] Center Energy, Environment, Processes (CEEP), Mines Paris - PSL, Palaiseau, France

[2] Total Energies, R&D Power Hybrid & Storage, Paris La Défense Cedex, France.

** Corresponding Author: michaelkhairallah@hotmail.com*

Abstract. This paper presents a methodology for integrating a heat pump (HP) with a thermal energy storage (TES) system for district heating applications. The proposed system aims to enhance energy efficiency, reduce operational costs, and improve the flexibility of urban heating network. A linear programming (LP) model is developed to optimize the design and operation of the HP-TES system. The model reduces the annual heating demand into four representative days to reduce computational complexity. Results demonstrate that integrating TES with a properly sized HP reduces both capital and operating expenses compared to a system without storage, making it a viable solution for sustainable urban heating.

Keywords. District Heating, Heat Pumps, Thermal Energy Storage, Optimization, Energy Efficiency.

Nomenclature

$\dot{m}$	Mass flow rate (kg/s)
$\dot{W}$	Electric power (W)
$\dot{Q}$	Heat transfer rate (W)
C	Cost (€)
C_p	Specific heat capacity (J/kg·K)
N	Number of years
h	Specific enthalpy (J/kg)
T	Temperature (°C)
t	Time (s)
V	Volume (m^3)
w	Weight
Special characters	
ρ	Density (kg/m^3)
Abbreviations	
TES	Thermal Energy Storage
HP	Heat Pump

1 Introduction

District heating systems are vital for delivering efficient and sustainable heating solutions in urban environments. They distribute heat generated from centralized sources through a network of insulated pipes to residential and commercial buildings, resulting in reduced energy consumption and lower carbon emissions compared to individual heating units. Integrating renewable energy sources into these systems has become increasingly important to enhance efficiency however this requires improving their flexibility. Heat pumps (HPs) play a significant role in modern district heating by utilizing low-temperature heat sources such as ambient air, groundwater, or waste heat. However, fluctuations in electricity prices and the intermittent nature of renewable energy pose challenges to the operational efficiency and cost-effectiveness of HPs. Thermal energy storage (TES) systems address these challenges by decoupling heat generation from demand. By storing excess thermal energy during periods of low demand or low electricity prices, TES enables HPs to operate more efficiently and economically. This integration enhances energy flexibility, smooths out demand peaks, and allows for better utilization of renewable energy sources.

This paper presents a methodology that integrates a HP with a TES system for district heating applications. The proposed approach involves designing an optimized system configuration and developing an operational strategy that minimizes total costs while meeting heating demand requirements.

2 Heat Pump and Thermal Energy Storage System Description

2.1 District Heating and Heat Demand

The district heating network in this study supplies heat to office buildings over a period from October to

April. The heating demand varies daily, with two prominent peaks occurring in the early morning and late afternoon (Figure 1). This pattern corresponds to typical office occupancy hours.

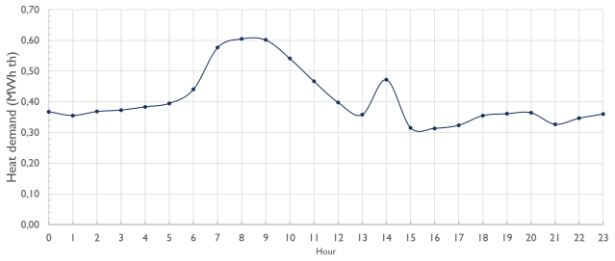


Figure 1: Heat demand profile for a typical day.

The hot water supply temperature is regulated according to the outdoor temperature, following a predefined 'law of water' (Figure 2). As the outside temperature decreases, the required supply temperature increases to maintain indoor comfort levels.

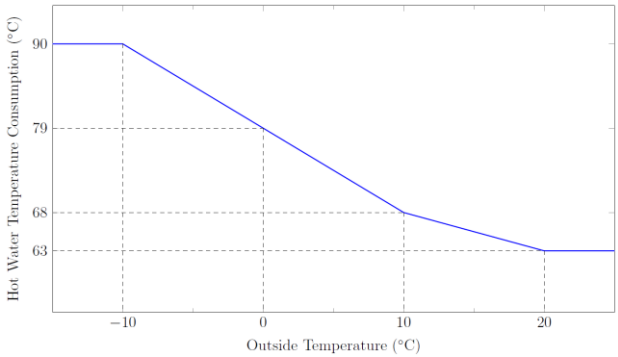


Figure 2: Hot water supply temperature as a function of the outside temperature.

2.2 Heat Pump Selection

Before starting the optimization process, we must select the architecture of the heat pump based on its coefficient of performance. Two architectures were chosen to be studied: simple heat pump, and a heat pump with internal heat exchanger.

After defining the evaporation and condenser temperature depending on the source of heat and the hot water supply, and trying two different working fluids (Propane and R-1234ze(E)), and using simplified model of each pump architecture, we found that the optimal COP for the maximum day can reach a maximum value of 2.61 for a heat pump with internal heat exchanger, $T_{evap} = 8$°C, $T_{cond} = 88$°C, and R-1234ze(E) as working fluids.

2.3 Thermal Energy Storage

In the context of energy markets, the fluctuation of the electrical demand and the price, make it possible to study economic opportunities for storage systems.

Thermal Energy Storage (TES) is a technology that stocks thermal energy by heating or cooling a storage medium so that the stored energy can be used later for heating and cooling applications and power generation. There are several types of TES systems, including: sensible heat storage, latent heat storage, thermochemical storage [1] [2]. Among these, water-based sensible heat storage is the most common and cost-effective option for building and district heating applications.

Stratified water tanks are a crucial component in TES systems, particularly when coupled with heat pumps for efficient heating and cooling applications. The principle of operation is based on buoyancy-driven thermal stratification, where hot water, being less dense, rises to the top of the tank, while cooler water settles at the bottom. This natural separation creates distinct temperature zones within the tank, allowing for simultaneous storage of water at different temperatures [3]. In this study, we model the stratified storage tank using a perfect thermocline model. This simplified model assumes that there is a sharp interface between the hot and cold water layers, with no mixing between them.

Optimization of a heat pump system with a stratified water tank involves careful consideration of several factors. Tank sizing must balance the heating load profile, heat pump capacity, and desired autonomy period. Charging and discharging flow rates must be carefully controlled to preserve stratification while meeting demand requirements [4].

2.4 Proposed Architecture for the system

The proposed system integrates the HP with a stratified TES tank, supplying the district heating network as shown in Figure 3. The HP operates continuously or during off-peak electricity periods to charge the TES, which then meets the variable heating demand [5].

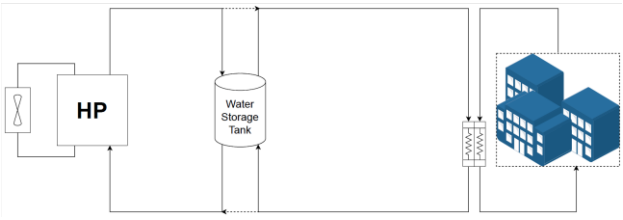


Figure 3: HP + TES architecture.

This configuration allows for a reduced HP size: by leveraging TES, the HP can be sized closer to the average load rather than peak demand, reducing capital costs. Also, it can achieve load shifting: The system can operate the HP during times of lower electricity prices, storing heat for use during peak demand periods. Moreover, efficiency is enhanced because operating the HP at steady conditions improves its COP and extends equipment life.

3 Optimization Methodology

3.1 Modelling of the system

The mass flow rate of hot water entering the heating network of the residential buildings can be computed by $\dot{Q}_{load} = \dot{m}_{net} C_p (T_{start} - T_{end})$. Moreover, the electric power consumed by the HP to produce $\dot{Q}_{load}$ are related by the coefficient of performance (COP). The variation of the hot and cold-water volume inside the tank are modelled using the following equations:

$$V_{hot}(t+1) = V_{hot}(t) + \frac{\dot{m}_{hot}}{\rho} \times \Delta t \qquad (1)$$

$$V_{cold}(t+1) = V_{storage} - V_{hot}(t+1) \qquad (2)$$

The mass flow of water flowing from and to the HP is the sum of both the mass flow of the storage and the network mass flow. An economic assessment of a project involves evaluating both Capital Expenditures (CAPEX) and Operational Expenditures (OPEX) to determine the overall financial viability. The CAPEX cost is calculated by adding the cost of the heat pump and the cost of the storage tank. The latter depends on the volume of the storage tank, and the former on the maximum electric power consumed by the HP. Both are optimized to reduce the CAPEX while ensuring constant supply of the required hot water temperature. For the OPEX, it depends on the hourly electric power $\dot{W}_{HP}$ and the price of electricity, which is assumed to be 71€/MWh for off-peak hours (from 10 PM until 5 AM) and 100€/MWh for peak hours (from 6 AM until 9 PM). With a discount rate of 8%, the total cost to be optimized in this project over N_{years} is compute using Eq. 3:

$$C_{total} = C_{CAPEX} + \sum_{i=1}^{N_{years}} \frac{C_{OPEX}}{(1+r)^i} \qquad (3)$$

The levelized cost of heat produced is a key economic parameter when evaluating heating systems and it is defined by Eq. 4:

$$C_{heat} = \frac{C_{total}}{\dot{Q}_{total-heat} \times N_{years}} \qquad (4)$$

The optimized variables are the sizing of the HP and the storage and the hourly operation.

3.2 Necessity for a reduced model

In our model, we have around 200 days between October and April. If we must consider each 24 hour per day, we end up with 4944 values of $\dot{W}_{HP}$ to be optimized; and this without adding the volume profiles that should be also optimized simultaneously. The high number of variables to be optimized complicates finding the best solution. To mitigate this, reduced models simplify the problem by decreasing decision variables without significantly compromising solution quality. Specifically, we use a reduced model based on four typical days, effectively balancing computational tractability and system behaviour representation.

Having the average temperature of each day, we can classify it based on three intervals. We find that 122 days are classified as “Interval 2”, so they have an average outside temperature falling in the interval [5; 15]°C. “Interval 1” [-5;5]°C includes 60 days, and the third interval [15;25]°C has 25 days. We group all the hours having the same label together and do the average of the heating load at this specific hour. This is done subsequently for the remaining hours of the day to get a 24-hours profile for each interval. The interval 3 has a zero-heating load supply needed, which is obvious for its high average temperature interval. Adding the two extreme cases: the first one corresponds to the day in which the heating demand is the highest, and the second one corresponds to the lowest non-zero demand. Having these two days and their corresponding hourly demand profile, we can add them to the calculated profiles of Interval 1 & Interval 2 on the same plot shown below:

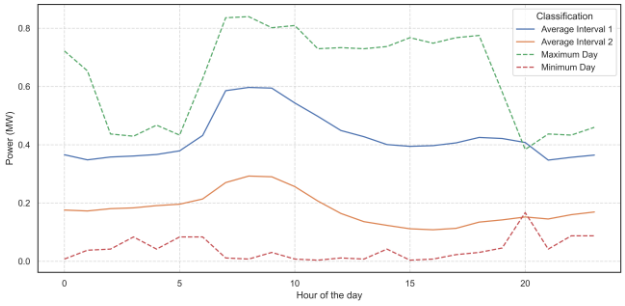


Figure 4: Heat demand for the four typical days.

To keep our optimization model linear, each typical day is assigned a constant COP calculated in a similar way to the one of the Maximum Day done previously for this architecture by adjusting T_{cond} based on the water law (Figure 2). As a result, we find: $COP_{MaxDay} = 2.61$; $COP_{Int1} = 3.13$; $COP_{Int2} = 3.75$; $COP_{MinDay} = 4.13$.

4 Optimization Results

Linear Programming (LP) is employed to determine the optimal design and operation strategy that minimizes total capital and operating costs while meeting all system constraints. The reduced optimization problem now consists on calculating the 53 decision variables: 48 electric power consumed by HP (24 in each typical day); 4 initial hot water volumes in the TES; total volume of the tank. A reference case is considered where only heat pump is considered without TES. Economic assessment for the reference case is shown in Table 1.

The CAPEX will reflect only the cost of the HP in this reference case; the size of the HP is determined by the maximum electrical load that occurs obviously in the maximum day. The inclusion of TES is expected to optimize the system's operation by levelling the heating load fluctuations, enabling the heat pump to function more efficiently at steadier, lower capacities. This not only has the potential to reduce the CAPEX by allowing for a smaller heat pump size but also to decrease the OPEX through improved energy management and exploitation of off-peak electricity tariffs. The optimization results, shown in Table 2, provide valuable insights into the benefits of TES integration for district heating applications.

Table 1: Results summary of both cases.

Parameter	Case without storage	Case with storage	
		$C_{storage} = 750$€/m³	$C_{storage} = 1125$€/m³
Storage volume	-	38.36 m³	13.12 m³
Maximum electric power HP	0.32 MW	0.246 MW	0.278 MW
OPEX (one year)	33.94 k€	32.11 k€	32.91 k€
CAPEX	583.53 k€	563 k€	570.19 k€
Total Cost ($N_{years} = 10$)	829.5 k€	778.49 k€	791.05 k€
Heat Cost ($N_{years} = 10$)	40.9 €/MWh	67.5 €/MWh	68.59 €/MWh

The analysis reveals that incorporating TES allows for a reduction in the installed power of the heat pump. In scenarios where storage costs are lower, the heat pump's installed power is reduced by 80 kW. Even with more expensive storage, the heat pump remains 40 kW smaller than in systems without storage. This reduction in size leads to lower capital expenditures (CAPEX), making the combined system more cost-effective than a standalone heat pump. The OPEX also benefit from TES integration. The annual electricity bill is reduced by approximately 2000 euros due to the ability to exploit off-peak electricity tariffs.

5 Conclusion

This paper presents the design and optimization of a HP integrated with a TES system for a district heating network. By incorporating a stratified water tank, the system effectively manages load variations, reduces peak demand, and enhances overall efficiency. The simplified modelling approach using four typical days captures the essential performance characteristics while reducing computational complexity. The integration of TES allows for a smaller HP size, leading to reduced capital expenditures, and enables the exploitation of off-peak electricity rates, lowering operational costs. The optimized HP + TES system demonstrates significant economic benefits and improved operational behaviour compared to a system without storage, making it a viable and sustainable solution for urban heating needs.

References

[1] I. Sarbu and C. Sebarchievici, "A Comprehensive Review of Thermal Energy Storage," *Sustainability*, vol. 10, no. 1, p. 191, Jan. 2018.

[2] A. Arteconi, N. J. Hewitt, and F. Polonara, "State of the art of thermal storage for demand-side management," *Applied Energy*, vol. 93, pp. 371–389, May 2012.

[3] Q. Li *et al.*, "Thermocline dynamics in a thermally stratified water tank under different operation modes," *Applied Thermal Engineering*, vol. 212, p. 118560, Jul. 2022.

[4] A. Campos Celador, M. Odriozola, and J. M. Sala, "Implications of the modelling of stratified hot water storage tanks in the simulation of CHP plants," *Energy Conversion and Management*, vol. 52, no. 8–9, pp. 3018–3026, Aug. 2011.

[5] K. Turunen, "Energy efficiency improvement potential in a paper mill by means of heat load balancing," Aalto University, School of Engineering, 2017.

EVALUATING SPACE COOLING STRATEGIES IN FULLY INTEGRATED, OPTIMALLY CONTROLLED MICRO ENERGY COMMUNITIES

Lucas Verleyen[1*], Lieve Helsen[1]

[1] KU Leuven, Belgium

** Corresponding Author: lucas.verleyen@kuleuven.be*

Abstract. Micro energy communities (MECs) are an appealing solution for decarbonising energy supply in suburban areas with lower heating and cooling demand densities, where large-scale district heating networks are less cost-effective. This work compares the performance and the CO2 emission reduction potential of air-source heat pumps (ASHPs) with ground-source heat pumps (GSHPs) in a tiny residential cluster of three single-family houses with moderate building envelope qualities, located in Belgium. Three energy system scenarios for delivering all domestic energy services, i.e. space heating, space cooling, domestic hot water and electricity, are investigated. The energy system scenarios can be classified as one individual scenario, i.e. no energy sharing, and two MEC scenarios, i.e. (i) sharing only electricity, and (ii) sharing heat, cold and electricity. All layouts are modelled in Modelica using a non-linear physics-based approach to fully exploit the inherent system flexibility and the synergies between multiple energy carriers. Detailed building models, proper hydraulic and electrical connections between all components, and optimal control as a system integrator are combined to have workable solutions and evaluate system performance through dynamic simulations. The non-linear white-box optimal controller accounts for the dynamic electricity tariff and the dynamic CO2 emission intensity of the Belgian distribution grid and targets the cost of CO2 emission reduction as key performance indicator. Previous work investigated the aforementioned energy system scenarios but only considered ASHPs and excluded space cooling. The results showed that the second MEC scenario, i.e. the full energy community scenario in which heat and electricity are shared, performed best. This scenario achieved the greatest reduction in CO2 emissions at the lowest cost of 179 EUR per ton of CO2 abated, compared to a reference scenario with individual gas boilers. Given the significant space cooling demand of the houses during summer and the direct cooling capabilities of the geothermal source, further improvements are expected when replacing the collective ASHP with a GSHP. Preliminary results confirm that a collective GSHP maximally reduces CO2 emissions in fully integrated and optimally controlled MECs.

Keywords. Micro energy communities, Thermal and electrical district energy systems, Optimal control, System integration, CO2 emission reduction.

THERMODYNAMIC AND ECONOMIC ANALYSIS OF A LIQUID AIR ENERGY STORAGE SYSTEM WITH THERMAL INTEGRATION

Márcio Santos[1*], José Mota[1], Bernardo Almeida[1], Joel Morgado[1] and José B. Ribeiro[1]

[1] Univ Coimbra, ADAI, Department of Mechanical Engineering, Rua Luís Reis Santos, Pólo II, 3030-788 Coimbra, Portugal

** Corresponding Author: marcio.santos@dem.uc.pt*

Abstract. Liquid Air Energy Storage (LAES) has emerged as a promising technology for large-scale energy storage, offering a potential solution to the key challenges currently facing the integration of renewable energy sources, including intermittency and grid stability. By employing cryogenic processes, LAES stores energy in the form of liquid air, which is then regasified and expanded in turbines to generate electricity during periods of high demand. Liquid Air Energy Storage (LAES) offers significant advantages over traditional Compressed Air Energy Storage (CAES) systems, particularly in terms of reduced storage volume due to the liquefaction of air, which makes it suitable for urban and grid-scale applications. This paper presents a preliminary technical and economic analysis of a cascade air compression system integrated with waste heat recovery, with the objective of enhancing the LAES charging process. This study examines the thermodynamic advantages of employing waste heat to enhance system efficiency and reduce operational costs. It encompasses key performance metrics, such as round-trip efficiency and storage capacity, and economic factors, including capital and operating expenses. The findings of this investigation underscore the potential of LAES as a viable and cost-effective solution for long-duration energy storage, offering valuable insights for future grid energy management and renewable energy integration endeavors.

Keywords. Energy Storage, Liquid air energy storage, Thermodynamic analysis.

ANALYSIS OF A WATER-AMMONIA HIGH-TEMPERATURE HEAT PUMP WITH A LIQUID-INJECTED TWIN-SCREW COMPRESSOR

Jari Raeymackers[1]*, Elias Vieren[1], Kenny Couvreur[1], Michel De Paepe[1,2,3], Steven Lecompte[1,2]

[1] Ghent University, Department of Electromechanical, Systems and Metal Engineering, Gent, Belgium

[2] FlandersMake@UGent – Core lab MIRO, Ghent, 9000, Belgium

[3] Department of Mechanical Engineering, University of Cape Town, Private Bag X3, Rondebosch 7701, South Africa

** Corresponding Author: jari.raeymackers@ugent.be*

Abstract. High-temperature heat pumps (HTHPs) provide a crucial solution for bridging the gap between low-temperature residual heat (<100 °C) and industrial process heat requirements at temperatures between 100°C and 200°C. Heat pumps can significantly reduce CO_2 emissions by lowering primary energy use, and by shifting from fossil fuels to electricity. In this research, a HTHP, using a water-ammonia mixture as the working fluid, is developed. The HTHP design makes use of a twin-screw compressor, known for its wide range of flow rates, high compression ratio per stage, and tolerance to liquid carryover. The water-ammonia mixture is selected for its low global warming potential, cost-effectiveness, availability, and non-flammable characteristics. However, water-ammonia has certain drawbacks including high pressure ratios, a low volumetric heating capacity, and elevated discharge temperatures. These elevated temperatures can cause issues within the compressor, including increased thermal stresses and thermal expansion. This requires larger tolerances, leading to higher losses, the need for high-temperature-resistant materials, and an increased risk of screw clogging. To address this issue, an innovative technique is applied to the twin-screw compressor: liquid injection combined with hydrodynamic lubrication, thereby enabling true oil-free operation. This study focuses on the thermodynamic effect of the liquid injection and the leakage path from the bearing lubrication to the compression process. Furthermore, this research aims to enhance the understanding of phenomena during compression and develop a more accurate compressor model, by incorporating non-equilibrium effects and to optimize the liquid injection rate and water-ammonia mixture composition. To achieve these objectives, a dedicated test rig is being developed for experimental evaluation, supported by a comprehensive thermodynamic model using Dymola software and the TIL-library. This test rig demonstrates proof of concept and will map steady-state operation, off-design performance, and dynamic operating conditions. While the dynamic model intends to characterize the heat pump's behaviour for applications outside the test conditions, such as higher power capacities, mixtures with increased ammonia content, and steam production with the HTHP.

Keywords. High-temperature heat pumps, Twin-screw compressors, Liquid injection, Water-ammonia mixture, oil-free compressor

1 Introduction

In the European union, the industry sector accounts for 25.1% of the final energy consumption, which makes it the third largest consumer, after transport (31.0%) and households (26.9%) [1]. When taking a closer look at the purpose of the industrial energy in the EU, a vast majority of this industrial energy is used for process heating as seen in Figure 1, with space heating accounting for an additional 11%.

The majority of process heat (77%) is generated from fossil fuels, with biomass at 11%, district heating at 8%, and electricity at just 3% [1]. Biomass's environmental impact is debated, and district heating often depends on fossil-based waste heat, highlighting the energy-intensive and fossil-fuel-reliant nature of industrial process heating.

This process heating energy is demanded at different temperatures, as can be seen in Figure 1. Although a majority of the heat is demanded at temperatures above 200°C, a significant 26% of the total demand is for heat within the 100 °C to 200 °C range. This range offers significant potential for the implementation of high-temperature heat pumps (HTHPs). These HTHPs operate using low-temperature waste heat as a heat source, which is

widely present in industry. HTHPs offer substantial energy efficiency gains by reducing primary energy demand, reusing waste heat, and by electrifying process heat. Their potential emission reductions are even greater when powered by renewable electricity, theoretically enabling carbon-free process heating for a wide range of applications.

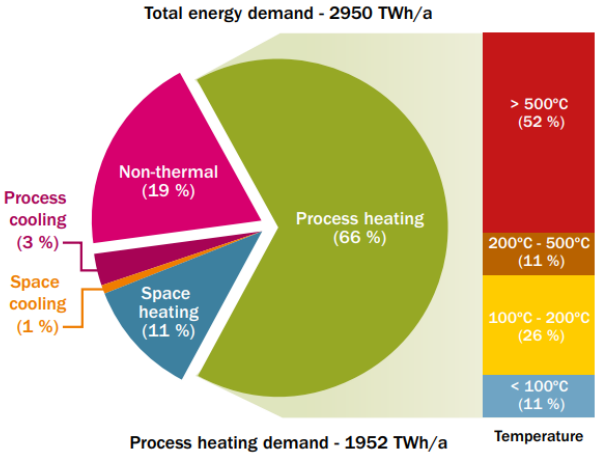


Figure 1: Breakdown of final energy demand in European industry by broad application and temperature level [2].

1.1 Market and technology overview

The International Energy Agency (IEA) Heat Pumping Technologies (HPT) Annex 58 – Task 1 provides a comprehensive overview of the state-of-the-art in HTHPs, classifying them as systems capable of supplying heat at temperatures above 100°C. According to this framework, vapor compression heat pumps with maximum supply temperatures up to 120°C are currently being commercially deployed [3]. Technologies capable of supplying heat between 120°C and 160°C are in the demonstration phase, while heat pumps exceeding 160°C are still in the prototype stage. The refrigerants used in these systems include synthetic options such as R-245fa, R-1234ze(E), R-1233zd(E), and R-1336mzz(Z), as well as natural refrigerants like R-744 (carbon dioxide), R-600 (butane), and R-601 (pentane) [3]. Open-loop water vapor compressors are also under development. Capacities of HTHPs range from 0.03 MW to several tens of MW. Closed-loop systems are typically single-stage or cascaded cycles, with or without internal heat exchangers. Piston compressors are most commonly used for heating capacities below 1 MW, while screw compressors are typically used for capacities up to 10 MW and centrifugal compressors are preferred for capacities above 10 MW [3]. In the range of 1 MW to 10 MW, both screw and centrifugal compressors are employed. Nearly all compressors used in closed-loop systems are oil-lubricated.

1.2 Working fluid selection

Proper working fluid selection is one of the main research areas for HTHPs. No single pure working fluid is considered ideal, as each has one or more of the following drawbacks: poor thermodynamic performance, toxicity, flammability, unacceptable environmental properties, very high or sub-atmospheric operating pressures or chemical instability [4]. Therefore, working fluids are often mixed to attenuate the negative properties while maintaining the positive properties. Furthermore, by using a zeotropic mixture, it is possible to provide a flexible match with many secondary heat streams due to its non-isothermal phase change. This effectively decreases the irreversibilities in the heat exchanger and thus increases the thermodynamic performance of the cycle.

In the pursuit of optimal working fluids, natural refrigerants stand out as highly promising candidates for future HTHP applications, largely due to their low global warming potential and minimal environmental impact. A thermodynamic simulation and optimization framework of pure working fluids and zeotropic mixtures in vapor compression heat pumps and chillers, where 134 pure working fluids and over 1000 binary mixtures were screened, for use in HTHPs has shown that water-ammonia is a highly efficient working fluid for use in HTHPs [5]. Besides the improved COP of water-ammonia compared to water, adding of ammonia allows for a reduction in compression pressure ratio up to 25% and a heating capacity up to 25% [6][7].

1.3 Technical challenges

Mainstream adoption of heat pump technology has traditionally been driven by ensuring high compressor performance and reliability. This was achieved by minimizing leakage paths, reducing wear, optimizing inlet and outlet flow paths (such as valves, ports, and nozzles), and lowering both ambient and friction losses. However, scaling this technology to operate at higher temperatures (>150°C) introduces several new challenges, primarily due to the limitations of current compressor technology [8].

The use of oil has many advantages and serves multiple functions inside the compressor: improving compression and volumetric efficiency, reducing leakage paths inside the compressor, thereby also allowing looser tolerances, cooling and protecting the moving components against wear. However, in

HTHPs, higher heat sink temperatures require higher pressure ratios, which, combined with higher heat source temperatures, lead to higher discharge temperatures. This causes dissociation of lubricating oil and thus restricts proper operation of the compressor [9]. Therefore, oil-free designs are preferred for high-temperature applications. To compensate for the advantages of the oil during compression, liquid injection of refrigerant can be used . When using liquid injection in conventional 'oil-free' designs, the compressors require an expensive and complicated sealing system in order to prevent oil-leakage from the bearings into the working chamber or vice versa, both being highly undesirable.

1.4 Solutions

An innovative solution to address the compression challenges in HTHPs is to employ the refrigerant itself for both liquid injection and lubrication within the compressor, enabling completely oil-free operation. This approach has several advantages: it eliminates the risk of cross-contamination, and any leakage from the bearings helps cooling during the compression. This cooling effect also allows for tighter tolerances, reducing the need for costly seals and simplifying overall operation. However, combining oil-free operation with liquid injection is achievable in only a few technical designs, the most prominent being the twin-screw compressor. Twin-screw compressors are more tolerant to liquid carryover than reciprocating and centrifugal machines, making them ideal for this approach [10]. Another key advantage is their lack of valves or delicate blades, which enhances durability and reliability. Additionally, twin-screw compressors offer a broad application range by allowing high volume flow rates and they are characterized by high compression ratios which enable substantial temperature lifts per compression stage.

1.5 Research gaps and questions

While some research has explored water-injected compressors and water lubrication in air compressors [11][12][13], there remains a significant knowledge gap regarding the use of refrigerants as both a bearing lubricant and for liquid injection to achieve true oil-free operation. In particular, there is no available data or open research on liquid injection in high-temperature applications (up to 200°C) and for refrigerants other than pure water. Additionally, no studies have examined the effects of hydrostatic bearings fed with liquid refrigerant, leaving key factors, such as discharge temperature impacts, volumetric and energy efficiency changes, as well as optimal injection pressures and mass flow rates, largely unknown.

Therefore, this study investigates the potential of liquid injection in a twin-screw compressor for HTHPs using a water-ammonia mixture. Specifically, it aims to address the following research questions:

- What is the effect of liquid injection on cooling and leakage paths?
- How can the bearing leakage paths be quantified, and what is their thermodynamic effect on compression?
- What is the optimal water-ammonia composition?
- What is the ideal liquid injection rate for various operating conditions?

2 Methodology

To achieve the objectives, a two-folded methodology is employed, involving both theoretical modelling and an experimental investigation. To support this research, a new HTHP test rig is currently being constructed. This rig is designed to provide heating up to 200°C and thermal capacities of up to 100 kW. A detailed summary of the operational performance specifications is provided in Table 1. The compressor utilizes hydrostatic/dynamic bearings supplied with liquid refrigerant, integrated with a liquid injection system.

Table 1: Specifications and operational conditions of the HTHP system

Heat sink temperature	160-200°C
Heat source temperature	100°C
Max temperature lift	100°C
COP (100°C lift)	2.5
Electrical power	30kW
Thermal power	60-100kW

The piping and instrumentation diagram of the experimental rig is presented in Figure 2 (see Appendix). The black section represents the main circuit, the actual HTHP system where testing is conducted and performance is evaluated. The blue, red, and yellow circuits serve as auxiliary systems that simulate realistic heat sources and sinks but are also carefully measured. By adjusting parameters such as mass flow rate, input power, or heat

exchanger fan speed, these auxiliary circuits replicate the behaviour of industrial heat sources and sinks.

2.1 Thermodynamic compressor and HTHP model

The first step of this approach involves a theoretical assessment of a HTHP with liquid injection, specifically developing a thermodynamic model of the compressor. Liquid injection introduces a complex interaction between the existing gas and liquid, and since compression occurs rapidly compared to the phase change rate, non-equilibrium thermodynamic states arise. Additionally, phase change behaviour must be accurately modelled, and for this, a homogeneous relaxation time model will be applied to approach the non-equilibrium conditions.

The second step is the development of a dynamic model of the heat pump cycle, which includes the bearing lubrication loop and secondary circuits surrounding the compressor model created in the first step. Each sub-model will be based on the physical parameters and geometries of the selected heat pump components. This model will be built with Dymola software (using the Modelica programming language,) and the TIL library. This approach enables both steady-state and dynamic simulations, with the dynamic model serving as a tool for initial tuning of control parameters during heat pump commissioning. The dynamic model will also provide a test matrix for the experimental campaign to investigate the impact of factors such as heat source/supply profiles, compressor speed, bearing conditions, and injection rates/pressures.

2.2 Experimental campaign

The second part of the research focuses on the experimental investigation. After commissioning the setup, testing will begin with pure water as a refrigerant for several reasons. First of all, it provides a benchmark for comparing future measurements of the water and ammonia mixture. Additionally, any initial leakage will be confined to water before ammonia is introduced, preventing any potential toxicity issues. Subsequently, testing will progress to a water-ammonia mixture, gradually increasing ammonia mass fractions. Each water-ammonia composition will be tested under various operational conditions outlined in a testing matrix. For each operating point, key parameters such as COP, heating capacity, and compressor discharge temperature will be measured, while defining the most efficient operating conditions for each scenario. The experimental data will be used refine the theoretical model developed earlier.

2.3 Performance evaluation

The final task involves comparing the theoretical model to the experimental results. Since the theoretical model is based on semi-empirical correlations, calibration and fitting values will be evaluated. An iterative calibration procedure will be carried out to replicate the heat pump's behaviour as accurately as possible, enabling the virtual performance of a new experimental campaign. This task will be followed by a sensitivity analysis of design and operational parameters, as well as an exploration of alternative cycle configurations. The calibrated theoretical model will then be applied to a case study from industry, where process heat demand, temperature levels, and heat availability will be gathered. The ability of the heat pump to meet changing demand will be assessed, and electricity usage and financial considerations will be accurately determined.

3 Conclusion

As industrial heating remains heavily reliant on fossil fuels during growing energy demands, transitioning to more sustainable alternatives is critical. High temperature heat pumps (HTHPs) offer a promising solution by utilizing waste heat to meet low-temperature process heat needs (<200°C), thereby reducing primary energy demand and carbon emissions. However, challenges remain in the compressor, particularly in limiting discharge temperature for higher-temperature applications. This research aims to reduce discharge temperature by exploring an innovative approach that combines liquid injection with working-fluid-lubricated hydrostatic bearings, using a water-ammonia mixture as the working fluid. Through the development of a theoretical model and a dedicated experimental test rig, the study aims to close key knowledge gaps, optimize compressor performance, and gain insight into complex interactions inside the compressor working chamber. The results of this work could greatly accelerate the adoption of HTHPs in industry, providing more energy-efficient and environmentally sustainable heating solutions.

4 Appendix

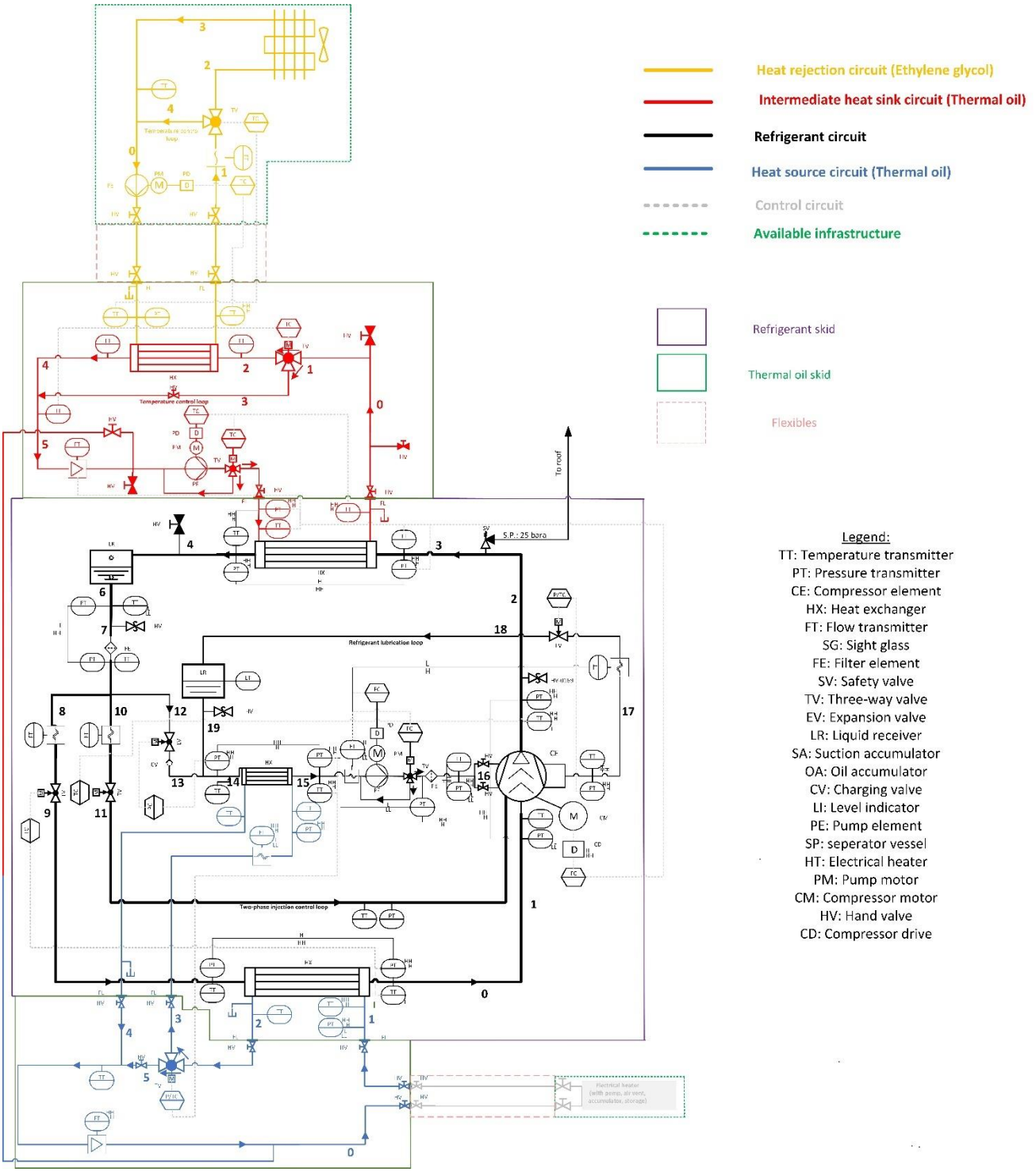


Figure 2: P&ID of high temperature heat pump setup

References

[1] European Commission, "Final energy consumption in industry - detailed statistics," Eurostat, 27-Oct-2023. Available: https://ec.europa.eu/eurostat/statistics-explained/index.php?title=Final_energy_consumption_in_industry_-_detailed_statistics. [Accessed: 04-Nov-2024].

[2] de Boer R et al. (2020). *Strengthening Industrial Heat Pump Innovation: Decarbonizing Industrial Heat*.

[3] B. Zühlsdorf *et al.*, *IEA HPT Annex 58: High-Temperature Heat Pumps. Task 1 report: Technologies*, English, Aug. 2023

[4] M. O. McLinden, et al., "A thermodynamic analysis of refrigerants: Possibilities and tradeoffs for low-GWP refrigerants," *International Journal of Refrigeration*, vol. 38, pp. 80-92, 2014. doi: 10.1016/j.ijrefrig.2013.09.032.

[5] H. Abedini et al. , "A comprehensive analysis of binary mixtures as working fluid in high temperature heat pumps," *Energy Conversion and Management*, vol. 277, p. 116652, 2023, doi: 10.1016/j.enconman.2022.116652.

[6] E. Vieren *et al.*, "Optimal temperature matching in high-temperature heat pumps," in *3rd High-Temperature Heat Pump Symposium 2022 : book of presentations*, Kongens Lyngby, Denmark, 2022, pp. 225–229.

[7] E. Vieren, K. Couvreur, M. De Paepe, and S. Lecompte, "Design of a high-temperature heat pump providing heat up to 200 °C," in *16th IIR-Gustav Lorentzen Conference on Natural Refrigerants*, College Park, Maryland, USA, 2024.

[8] J. Gómez-Hernández *et al.*, "Carbon dioxide and acetone mixtures as refrigerants for industry heat pumps to supply temperature in the range 150–220 °C," *Energy*, vol. 269, p. 126821, 2023

[9] G. F. Frate, L. Ferrari, and U. Desideri, "Analysis of suitability ranges of high temperature heat pump working fluids," *Appl. Therm. Eng.*, vol. 150, Mar. 2019

[10] C. Huang, *"New Twin Screw Compressor Design by Deviation Function Method,"* Ph.D. dissertation, Dept. Mech. Eng., Univ. California, Los Angeles, CA, USA, 2015

[11] M. Chamoun, et al., "Experimental and numerical investigations of a new high temperature heat pump for industrial heat recovery using water as refrigerant," *Int. J. Refrig.*, vol. 44, pp. 177–188, 2014, doi: 10.1016/j.ijrefrig.2014.04.019.

[12] Y. Tian et al. , "Investigation on water injection characteristics and its influence on the performance of twin-screw steam compressor," *Energy*, vol. 259, 124886, 2022, doi: 10.1016/j.energy.2022.124886.

[13] C. Wang et al. , "Development of an oil free water-lubricated twin-screw air compressor," *Appl. Therm. Eng.*, vol. 143, pp. 396–402, 2018, doi: 10.1016/j.applthermaleng.2018.07.119.

GEOCOOLING FOR SUMMER COMFORT IN EUROPEAN DWELLINGS

Nathan Guilbaud[1]*, Antoine Fabre[1], Pascal Stabat[1]

[1] Mines Paris, PSL University, Centre for Energy Environment Processes (CEEP), 75006 Paris, France

* *Corresponding Author:* nathan.guilbaud@minesparis.psl.eu

Abstract. Geothermal heat pumps are one of the most efficient solutions for heating buildings. Although the technology is mature, it is struggling to develop due to high investment costs and a lack of qualified professionals, such as drillers. However, geothermal probes can provide another service that is rarely exploited due to unawareness: geocooling, which is a free, high-performance solution for summer thermal comfort.

The proposed study aims to investigate the potential of geocooling to cool dwellings in different climates. Two emitter options are being studied, one involving the use of an underfloor heating system for cooling, with condensation constraints limiting the cooling capacity, and the other involving the addition of fan coil units dedicated to cooling. The study approach is based on dynamic modelling of the building using EnergyPlus, coupled with system modelling using Modelica via the Spawn of EnergyPlus module developed by the LNBL.

The results show the extent to which geocooling can ensure thermal comfort in European climates. Concerning underfloor heating, even if its available cooling capacity is limited, thermal discomfort is low in most climates, except in the warmest European regions, where the cooling demand is much greater than the heating demand. Regarding fan coil units, since they use all the ground cooling capacity, they improve comfort, but they are still not sufficient to avoid overheating periods for warmest climates. The EERs of Geocooling range from 16 to 58, as the system only requires a probe circulation pump.

Keywords. Free cooling, Borehole, Residential, Distribution system, Thermal comfort

1 Introduction

Geothermal heat pumps (GHPs) are an effective means of heating buildings. A geothermal heat pump circulates a fluid through the ground to extract heat. From just a few meters deep, the ground maintains a stable temperature, enabling the heat pump to operate very efficiently throughout the year, unlike air-to-air and air-to-water heat pumps, whose performance is highly sensitive to weather conditions.

Although geothermal heat pumps are recognized for their heating efficiency, their free cooling potential is often unknown. It is possible to use the ground as a natural cooling source, thus removing heat from buildings without relying on the heat pump compressor. This free cooling method, also known as geocooling, is one of the most effective cooling technologies, requiring only the electrical power of a circulation pump to operate.

Despite the great interest shown by the profession, in practice, few such systems have been installed for summer use. It is important to understand more about the cooling power that this system can provide, the comfort level achieved, and the energy consumed. However, the subject has received little attention in the literature.

Few studies based on the analysis of in-situ data [1, 2, 3, 4] have provided information on the performance of geocooling. Lachal & Hollmuler [1] analysed the performance of geocooling in a few commercial buildings with borehole fields. They assessed average specific cooling capacities by geocooling ranging from 10 to 30 W/m of borehole. In 2011, the Federal Office of Energy (OFEN) published a geocooling handbook [2], presenting a detailed methodology for sizing geocooling installations, primarily for large tertiary buildings. Based on field data, OFEN estimates a maximum geocooling capacity for a ground conductivity of 2

W/(m·K), ranging from 30 to 50 W/m of borehole. In the case study of a 5700 m² multi-family building in Switzerland, equipped with 13 probes, each 200 meters deep, Belliardi [3] determined a maximum specific cooling capacity of 12 W/m and an average specific capacity of 9 W/m. Geocooling successfully maintained the room temperature between 22 and 24°C. The low specific cooling capacities correspond simply to an oversized probe field for geocooling, with the probes being sized for heating. In 2009, the European project GROUND-MED [4] assessed the seasonal performance of geocooling on two sites.

These studies show several promising cases, but do not provide a comprehensive overview of the geocooling performance as a function of climate in residential sector. The aim of this study is to carry out a parametric study to assess potential and limits of geocooling for single-family houses in Europe.

2 Methodology

The study is based on dynamic simulations of both the building and its heating and cooling systems, from the ground up to the emitters. The building model is created using the reference software EnergyPlus, while the systems are modeled with Modelica. These two simulation tools are coupled through Spawn of EnergyPlus, developed by LBNL [5]. The heating system is sized in accordance with European standards.

2.1 Building Modeling

The building studied is a representative archetype of single-family homes in France from 1948 to 1974. The house features a single floor of 100 m², with three bedrooms, a kitchen, a living room, and a bathroom. The house is built on a crawl space and has an unconverted attic, with a sloped roof. Two variants of the house have been defined to represent different insulation levels:

- An “old house” with poor insulation compliant with the French building code RT74 [6].
- A “new house” with good insulation compliant with the French building code RT2012 [7].

Each room in the building represents a thermal zone in the model. The meteorological data comes from Meteonorm 8.

2.2 System Modeling

A Modelica model of a geocooling system has been developed based on the Buildings library [8]. This model integrates a geothermal probe model as well as its heat exchange with the ground, using the undisturbed ground temperature as an input parameter. Inside the probe, an antifreeze fluid circulates. During the heating season, this fluid passes through the heat pump's evaporator, which produces water at a temperature between 24 and 35°C, supplying underfloor heating systems located in different rooms of the house.

During the cooling season, the antifreeze fluid no longer passes through the heat pump but through a heat exchanger to cool the return water from the underfloor heating. To prevent condensation on the surface of the floors, a three-way valve regulates the flow rates in the heat exchanger, to maintaining the temperature of the water feeding the floors above 18°C (Figure 1).

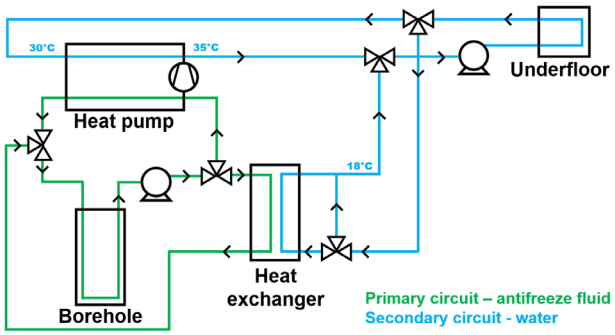


Figure 1: Representation of the geocooling model

Different methods for sizing a geothermal probe have been compared. The NF X10-970 method [9] is chosen to size the probe length, showing results in line with the average of all the methods in all case studies.

The Modelica *Borefields.TwoUTubes* model has been selected for this study. The borehole characteristics are based on CARTODIM [10].

The base case is adapted for the three main climate types in Europe. The study is aligned with the EN 14825 standard [11], which evaluates heat pump performance based on three cities: Helsinki (cold climate), Strasbourg (average climate), and Athens (warm climate). From this standard, the setpoint air temperature is set at 27°C in summer.

2.3 Parametric study

A parametric study is conducted to evaluate the influence of different parameters on the geocooling potential.

The **type of ground** directly affects the heat exchange with the probe. The selected sizing method reduces the probe length to account for better thermal exchange. Clay ground (base case) is compared with a granite variant, known for its good thermal conductivity.

The **heat pump's COP** indirectly impacts the cooling capacity by influencing the design of the probe length. A higher COP requires greater extraction to achieve the capacity needed at the condenser. Keymark [12] is used to obtain certificates for geothermal heat pumps. It is observed that COPs at -7°C cover a wide range of values from 3.50 to 5.25, with most falling between 4.25 and 4.90, across all SCOP ranges. A high-performance heat pump with a COP of 4.80 (base case) is tested alongside another with a COP of 4.00.

A sizing of GHP including **domestic hot water** (DHW) production is added, which may affect the ground recharge ratio and the probe size in the case of the warm climate.

Then, the impact of **improved insulation** is assessed using a house complying with French building code of 2012.

Next, two types of **emitters** are examined. The first one is an underfloor heating used for cooling, considering condensation constraints with a minimum inlet temperature of 18°C. The second is a fan coil unit (FCU) sized on cooling needs.

Additionally, the **impact of climate change** is evaluated using a 2050 climate scenario based on the IPCC RCP 8.5.

3 Results

3.1 Discomfort degree hours

Figure 2 shows the reduction of summer discomfort assessed through the degree hours (DDH) over 27°C by using geocooling. Geocooling is effective in the cold and average climates but unsuitable in the warm climate due to a small probe size, very low underfloor flow rates, and high ground temperatures.

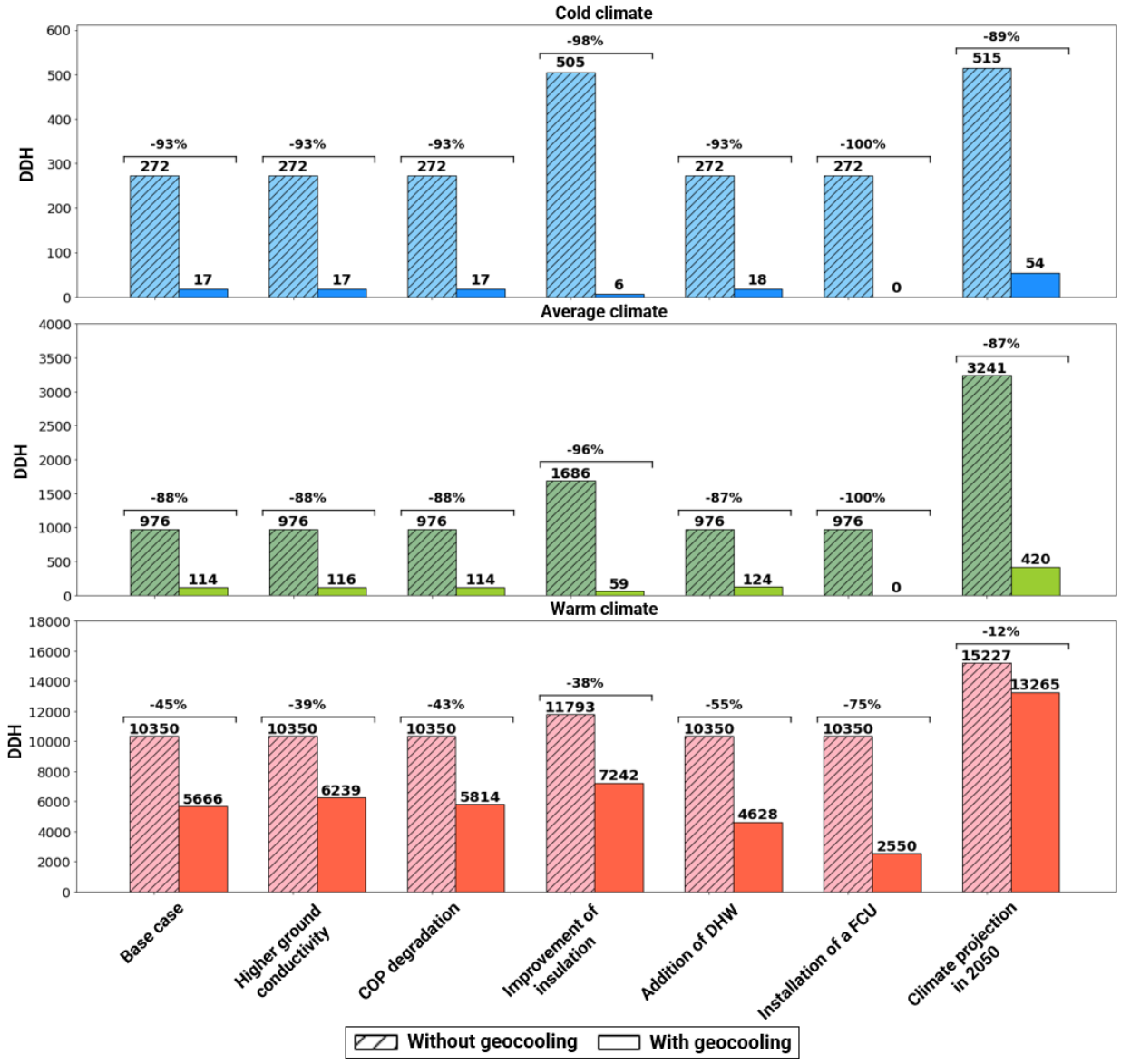


Figure 2: Summer discomfort degree hours

If the nominal COP of the heat pump decreases from 4.8 to 4.0, the power needed to extract energy from the ground is reduced, and consequently, the probe length is slightly shortened. While the impact on comfort is low in cold and average climates, in a warm climate, where geocooling was already struggling to cool the house, the slight reduction in probe length worsens the situation.

If the thermal insulation is upgraded, the heating needs are reduced, leading to a halving of the probe length. Discomfort significantly increases without geocooling, as the heat is trapped inside the house in the absence of natural ventilation. However, with geocooling, discomfort hours are further reduced compared to the base case, except in the warm climate, where the cooling capacity is too limited.

The integration of domestic hot water (DHW) into the system allows the heat pump to produce 200 L of water at 55°C each day between midnight and 2 AM. To meet this demand, a heat pump with a minimum capacity of 4 kW is required. This requirement leads to an increase in probe length in a warm climate only, which improves summer comfort.

If FCUs are installed and sized for cooling, the cooling capacity of the ground can be fully exploited since the condensation constraint of underflow does not exist anymore. There is no more discomfort in cold and average climates, but in the warm climate, comfort is not always achieved, as the probe size and the high ground temperatures still limit the available cooling capacity power.

3.2 Cooling capacity and SEER

Figure 3 shows the cooling capacity and SEER. The cooling capacity is defined as the maximum power delivered by the emitter under the summer period.

The cooling capacity is similar in cold and average climates in the base case, which is attributed to an identical supply temperature of 18°C.

If the conductivity of the ground is better, the length of the probe is shorter, but the cooling capacity relative to the total probe length remains comparable to that of the base case.

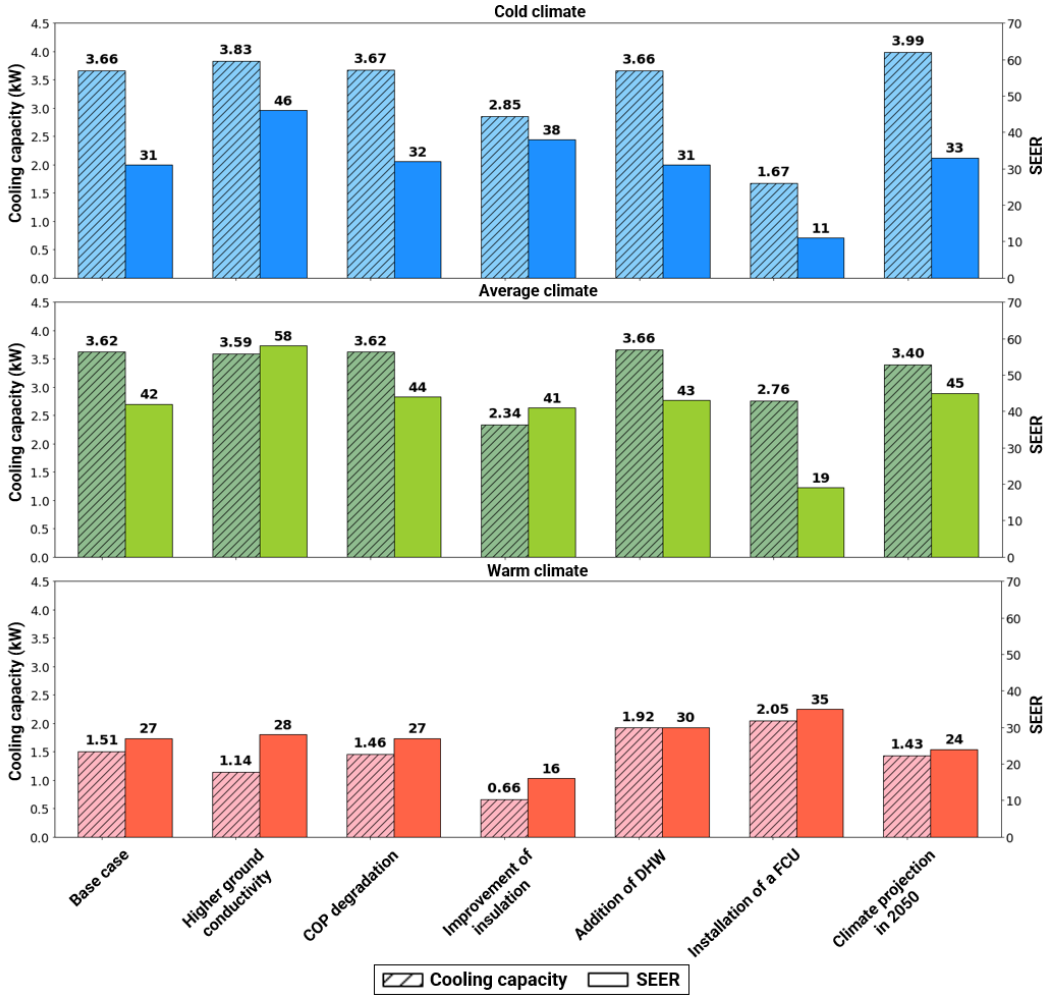


Figure 3: Cooling capacities and SEER for all cases

As expected, the improvement of the insulation implies a reduction of the probe length and of the cooling capacity.

Contrary to underfloor heating, the FCU is an emitter without thermal inertia and by convective transfer exclusively. Consequently, the maximum delivered cooling power is lower in cold and average climates, but it precisely meets the building's peak cooling requirements in both climates. However, in the warm climate, as the FCU can exploit all the cooling potential from the ground, the maximum delivered capacity is higher than with underfloor emitter. In warm climate, the presence of domestic hot water production allows for an increase of cooling capacity.

The climate change induces an increase of cooling demand. As shown on figure 2, the geocooling is still an efficient solution for summer comfort in cold and average climates.

When required cooling power surpasses required heating power, it becomes more logical to size the probes and emitters according to the cooling requirements. This is particularly relevant in the context of climate change, which is expected to reduce heating needs and increase cooling needs over time.

The SEER range between 11 and 58. Only the geothermal fluid circulation pump is taken into account in the calculation of the SEER. The main factor influencing the SEER is the ground's conductivity: the more conductive the ground, the shorter the probe can be for the same cooling capacity, reducing the pressure drops.

4 Conclusions

A Modelica model representing a geocooling system has been developed for this study. All characteristics of the model's components, as well as their sizing, are fully based on existing standards or studies.

The simulations have shown that geocooling is an effective means of cooling homes in cold and average climates, although its potential is not fully exploited in these regions. The SEER is high in both climates, with the best performance observed in the average climate. In contrast, the geocooling potential is more limited in warm climate due to limitations, including a too-short probe sized for heating and higher ground temperatures.

A parametric study revealed that the presence of domestic hot water production or a sizing on required cooling power enhances geocooling performance in warm climate. Additionally, the FCU was found to be more efficient than the cooling underfloor, particularly due to the absence of condensation constraints. Significant differences were observed between the underfloor and the FCU, making direct comparisons difficult. While the underfloor cools both the air and the walls, requiring more power, it improves occupant comfort, although this does not always translate to a reduction in discomfort hours based on air temperature.

Acknowledgement

This research was supported by ADEME and NIBE. The authors would also like to express their gratitude to BRGM and EDF for their valuable advice.

References

[1] P. Hollmuller, B. Lachal, and D. Pahud, "Rafraîchissement par geocooling : Bases pour un manuel de dimensionnement". 2005.

[2] OFEN, "Geocooling Handbook - Cooling of Buildings using Vertical Borehole Heat Exchangers", 2011.

[3] M. Belliardi, "Applied analysis of geocooling technology for a residential building", BRENET 20° Status-Seminar, 5-6 September 2018, ETH-Zurich 2018.

[4] Ground Med, "Demonstration of Ground Source Heat Pumps on Mediterranean Climate", EU Project, 2014.

[5] M. Wetter, "Software Architecture and Implementation of Modelica Buildings Library Coupling for Spawn of EnergyPlus", 2021.

[6] MTE, "RT 1974", 1974.

[7] MTE, "RT 2012", 2012.

[8] LNBL, "Modelica Buildings Library" [Online]. Available: https://simulationresearch.lbl.gov/modelica/ [Accessed June 2024]

[9] NF X10-970, " Forage d'eau et de géothermie - Sonde géothermique verticale - Réalisation, mise en oeuvre, entretien, abandon", 2011.

[10] BRGM, "Outil de dimensionnement CARTODIM", [Online]. Available: https://plateforme-geothermie.brgm.fr/fr/outil-de-dimensionnement [Accessed June 2024]

[11] NF EN 14825, 2022.

[12] KEYMARK, "Heat Pump KEYMARK Certificates", [Online]. Available: https://keymark.eu/en/products/heatpumps/certified-products [Accessed June 2024]/

MODELS AND METHODOLOGY FOR THE DESIGN AND CONTROL OF THERMAL ENERGY STORAGE IN RESIDENTIAL DISTRICT HEATING SYSTEMS

Alixe Degelin[1,2]*, Ilya T'Jollyn[2], Michel De Paepe[1,3,4]

[1] Department of Electromechanical, Systems and Metal Engineering, Ghent University, Sint-Pietersnieuwstraat 41, 9000 Ghent, Belgium

[2] EMIB, Faculty of Applied Engineering, University of Antwerp, Groenenborgerlaan 171, 2020 Antwerp, Belgium

[3] FlandersMake@UGent– Core lab MIRO, Ghent, 9000, Belgium

[4] Department of Mechanical Engineering, University of Cape Town, Private Bag X3, Rondebosch 7701, South Africa

* *Corresponding Author: alixe.degelin@ugent.be*

Abstract. District heating networks for building applications will need integrated thermal energy storage systems to be able to include more renewable energy into their operation. Thermal energy storage models currently require too much calculation time to use them for district heating network topology optimization. They show the same deficiencies when control during operation is considered. This paper presents the ongoing research on the development of a model for sensible and latent thermal energy storage system, aimed at reducing the calculation time while maintaining high accuracy and reliability. The proposed correlation is based on the charging time energy fraction method and predicts the outlet temperature of the heat transfer fluid based on the heat transfer fluid inlet conditions and thermal energy storage capacity. The ultimate goal is to implement and validate the use of this correlation in commonly used simulation software for the design of district heating networks. Secondly, an heuristic topology optimization method which will allow to design quickly and reliably a district heating network with thermal energy storage will be developed. Finally, the models will be used to define control strategies for thermal storage systems by simulation in Modelica.

Keywords. Thermal storage systems, charging time energy fraction method, district heating

Nomenclature

c_p	Specific heat capacity (J/kg.K)
HTF	Heat transfer fluid
J	Stored thermal energy (J)
$\dot{m}$	Mass flow rate (kg/s)
Q	Heat transfer rate (W)
t	Time (s)
T	Temperature (°C)
TES	Thermal energy storage
U	Internal energy (J)

Special characters

α	Energy fraction (-)

Subscripts

c	Charging
in	Inlet
out	Outlet
ref	Reference
0	Start

1 Introduction

Increasing the share of renewable energy up to 45 % of all used energy by 2030, as set by the European Commission, means doubling the share of renewable energy of 2022 in the coming years [1]. Energy storage will be an important enabler for this energy transition as it provides flexibility in the energy system by storing excess renewable energy and as such increasing the usability of the available sources [2]. Therefore, the importance of thermal energy storage systems can not be neglected as heat accounted for almost half of the global energy use in 2022 [3].

Thermal energy storage (TES) systems can be classified based on their working principle into three categories: sensible, latent and thermochemical storage. Sensible storage systems, in which the temperature of the storage medium is elevated to charge the system, are most often used. A well-known principle is the water tank, used in district heating networks, industrial sites and residential building [4]. Latent thermal energy storage systems store or release heat during solidification of melting of a phase change material. An important advantage is their operation at relatively constant temperatures

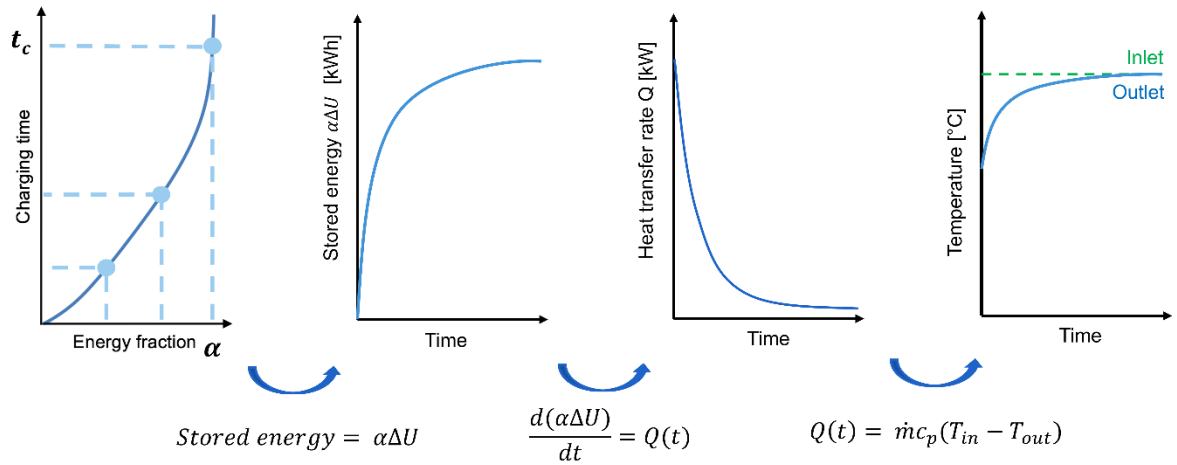


Figure 1: Use of the charging time energy fraction method to predict the stored energy, heat transfer rate and HTF outlet temperature during a charging cycle.

and their high storage density [5]. Thermochemical energy storage make use of an reversable chemical reaction for the storage of heat [5]. Thermochemical energy storage is out of scope of this paper.

Dynamic models of TES systems are crucial for the design, sizing, control of large-scale energy systems with integrated thermal storage. Most popular for the simulation of water tanks are 1D stratified tank multi-node models [6]. With these models, the tank is divided into multiple horizontal layers with a central node. The temperature of the layers is calculated at the location of the nodes based on mass and energy conservation. Compared to 3D CFD models, a good accuracy and reasonable calculation time is obtained. However, for the simulation and optimization of large-scale energy systems with multiple water tanks, multi-node models appear to require too much calculation time [7]. The modelling of latent TES systems is mainly focussed on the enhancement design and the heat transfer of the system [8]. As a result, for the simulation of latent TES systems, CFD models are often used which are unsuitable for system optimization [9].

Another way to accelerate the modelling of TES is by defining empirical correlations from experimental or numerical measurements predicting their transient behavior. The charging time energy fraction method, recently defined by Beyne et al. [10], is a method to relate the fraction α to the required charging time t_c during a charging cycle, as can be seen in Figure 1. The correlation allows to calculate the stored energy during the cycle $J(t)$, the heat transfer rate $Q(t)$ from the heat transfer fluid (HTF) to the tank and the outlet temperature T_{out} of the HTF, based on Eq. (1) to (3) at any moment in the charging cycle.

$$J(t) = \alpha\Delta U, \quad with\ \Delta U = U(T_{in}) - U(T_{ref}) \tag{1}$$

$$Q(t) = \frac{d(J(t))}{dt} \tag{2}$$

$$Q(t) = \dot{m}c_p(T_{in} - T_{out}) \tag{3}$$

With U the internal energy [J], T_{ref} the temperature of the storage tank at the start [°C], $\dot{m}$ the HTF mass flow rate [kg/s], c_p the HTF specific heat capacity, and T_{in} the HTF inlet temperature [°C]. A correlation for the charging time t_c for sensible (Eq. (4)) and latent (Eq. (5)) thermal energy storage systems has been proposed by Degelin et al. [11] and Beyne et al. [10] and validated for a full charging cycle against experimental data.

Sensible:

$$t_c(\alpha) = C(\alpha) + \frac{D(\alpha)}{\dot{m}} \tag{4}$$

Latent:

$$t_c(\alpha) = \left(A(\alpha) + \frac{B(\alpha)}{\dot{m}}\right)\frac{1}{\Delta T} + \left(C(\alpha) + \frac{D(\alpha)}{\dot{m}}\right) \tag{5}$$

With $A, B\ C$ and D fitting coefficients as a function of the energy fraction α, and ΔT the temperature difference between the HTF inlet and the phase change material. Although the correlation has been proven able to predict the outlet temperature of the heat transfer fluid during a full charging cycle with constant inlet conditions, the use of this correlation in system simulations with varying inlet conditions has not been demonstrated yet. This paper presents the ongoing research into the potential of this correlation for the development of a TES model for system simulations.

2 Method for the use of the charging time correlation with dynamic inlet conditions

The charging time correlation describes how the energy fraction changes with constant HTF mass flow rate and inlet temperature. With this empirical correlation the dynamic behaviour of the storage tank is captured for certain constant boundary conditions. In order to use the charging time correlation as a basis for a dynamic thermal storage model, a method for the use of this charging time correlation with varying inlet conditions is required.

An explicit calculation procedure to predict the HTF outlet state with varying inlet conditions is proposed in Figure 2. At the start of the simulation t_0, the total amount of stored energy is equal to zero and the reference temperature T_{ref} is equal to the initial tank temperature. The energy fraction α is given an initial value. At the start of a charging cycle, the energy fraction equals zero, and one at the start of a discharging cycle. After this initialisation stage, the procedure is repeated for every timestep t_i. First, the energy fraction is calculated based on the previously stored energy in the tank and the maximum possible stored energy ΔU (Eq.(1)). This maximum possible stored energy varies with varying inlet temperatures. The energy fraction is thus rescaled at the beginning of the procedure based on the previously stored energy $J(t_i)$ and the inlet temperature $T_{in,i}$. In the next step, the change in energy fraction, which is $\alpha_{i+1} - \alpha_i$, is predicted by approximating the charging time correlation for the HTF mass flow rate $\dot{m}_i$ by its tangent in α_i. This step is visualized in Figure 3. The calculation of the heat transfer $Q_{i,i+1}$ between timesteps t_i and t_{i+1} is based on Eq. (2) and the calculation of the outlet temperature $T_{out,i}$ at t_i based on Eq. (3). Lastly, the heat transfer rate $Q_{i,i+1}$ is added to the total stored energy $J(t_i)$. This procedure is then repeated for time instance t_{i+1} with HTF mass flow rate $\dot{m}_{i+1}$ and inlet temperature $T_{in,i+1}$. Important in this procedure is that the fitting coefficients resulting from the characterization of the TES tank form a polynomial such that their derivative exists.

With this method, it is assumed that the energy fraction can be rescaled when in the HTF inlet temperature varies. Additionally, it is expected that the actual energy fraction can be a composed of parts of the charging time correlation with constant inlet mass flow rate.

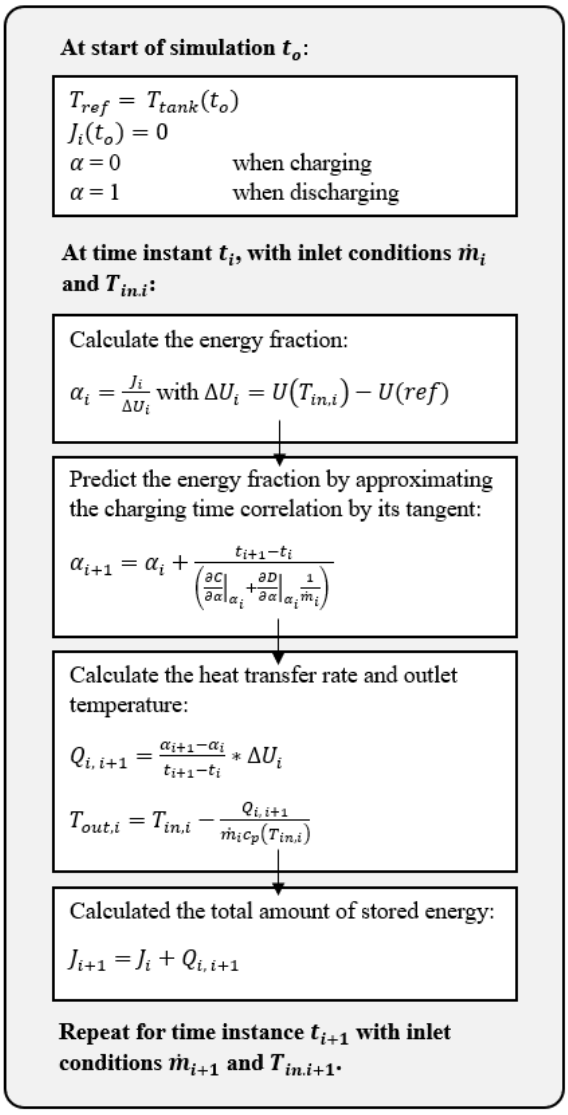


Figure 2: Calculation procedure for the use of the charging time correlation with dynamic inlet conditions.

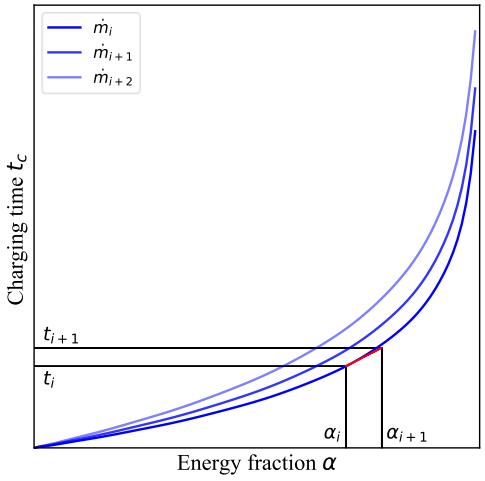


Figure 3: Example prediction of the change in energy fraction.

3 Future work

The accuracy off this method as well as the computational efficiency requires validation with experimental measurements and comparison with other modelling techniques. The aim of this research project is to validate the proposed procedure with varying HTF inlet conditions and compare its ability to predict the HTF outlet conditions to currently available stratified tank model. Once validated, the principle will be implemented in Dymola, a well-known software for dynamic system simulations to test its computational efficiency.

The availability of fast and dynamic models for thermal energy storage will enable the simulation of large-scale energy systems including these TES storages. Currently, design and optimization tools disregard the implementation of TES systems as the calculation time is drastically increased with the use of thermal storage models. The ultimate goal of this research project is to prove the use of the proposed model for sensible and latent storage in the design and optimization of a district heating network lay-out and in the development of a control strategy of the thermal storage systems in the network.

4 Conclusions

In this paper, the ongoing research into the development of a fast, accurate and dynamic model for sensible and latent thermal storage systems is discussed. The model is based empirical correlations which describe the charging time as a function of the energy fraction based on the heat transfer fluid inlet conditions during a charging cycle. These correlations are obtained using the charging time energy fraction method. In this work, an explicit procedure is proposed to use the charging time correlations with varying boundary conditions, such that the accuracy of the modelling principle can be validated and compared to existing modelling techniques. Once the explicit procedure is validated, the goal is to develop a thermal energy storage model in Dymola, a well-known software for dynamic systems simulations. The computational time of this model will be evaluated, in order to assess its potential for the design and optimization of district heating networks and the development of control strategies.

Acknowledgement

This work was funded by a FWO–Flanders, Belgium grant (1SHDE24N) for strategic basic research of the Research Foundation Flanders. The financial support is gratefully acknowledged.

References

[1] “Renewable energy targets - European Commission.” Accessed: Jul. 03, 2024.

[2] “Why Energy Storage?,” EASE Storage. Accessed: Jul. 03, 2024.

[3] “Heat – Renewables 2023 – Analysis,” IEA. Accessed: Jul. 03, 2024.

[4] S. Danehkar and H. Yousefi, “A comprehensive overview on water-based energy storage systems for solar applications,” *Energy Rep.*, vol. 8, pp. 8777–8797, Nov. 2022

[5] L. F. Cabeza, I. Martorell, L. Miró, A. I. Fernández, and C. Barreneche, “1 - Introduction to thermal energy storage (TES) systems,” in *Advances in Thermal Energy Storage Systems* 2015.

[6] F. Karg Bulnes, K. R. Gluesenkamp, and J. Rendall, “Comparison of Plug Flow and Multi-Node Stratified Tank Modeling Approaches Regarding Computational Efficiency and Accuracy,” 2021

[7] T. Boeykens, “Comparison of stratified tank modelling techniques in a district heating network based on computational complexity and performance.”

[8] R. Waser *et al.*, “Fast and experimentally validated model of a latent thermal energy storage device for system level simulations,” *Appl. Energy*, vol. 231, pp. 116–126, Dec. 2018.

[9] K. Couvreur, M. Goderis, W. Beyne, and M. D. Paepe, “An improved charging time energy fraction model for latent thermal storage heat exchangers,” presented at the International Heat Transfer Conference 17, 2023..

[10] W. Beyne, K. Couvreur, I. T’ Jollyn, R. Tassenoy, S. Lecompte, and M. De Paepe, “A charging time energy fraction method for evaluating the performance of a latent thermal energy storage heat exchanger,” *Appl. Therm. Eng.*, vol. 195, p. 117068, Aug. 2021.

[11] A. Degelin *et al.*, “Experimental characterization of a solar boiler as a sensible thermal energy storage system,” in *10th World Conference on Experimental Heat Transfer, Fluid Mechanics and Thermodynamics*, 2024.

DEVELOPMENT OF AN EXPERIMENTAL SETUP FOR SELF-CONSUMPTION AND GRID SERVICES PROVISION AT THE RESIDENTIAL LEVEL

Simon Marichal[1]*, Nicolas Leclercq[1], Sylvain Quoilin[1], Vincent Lemort[1]

[1] Thermodynamics Laboratory, University of Liège, Sart Tilman, 4000, Liège, Belgium

* *Corresponding Author: smarichal@uliege.be*

Abstract. The current energy transition and energy efficiency requirements involve integrating smart operation techniques and developing new control strategies for different home appliances. The aim is to maximise self-consumption of local renewable energy sources, but also to provide services to the grid such as frequency containment reserve or automatic frequency restauration reserve. Through this approach, research aims to balance energy consumption, enhance system efficiency, and promote sustainable energy practices in residential buildings. This study will present the development and implementation of a control strategy for a typical photovoltaics (PV) household installation, with two storage devices, a 60 L double cylindrical electrical water heater and two 3.2 kWh batteries. The study will be conducted experimentally in the Thermodynamics laboratory of the University of Liege, where a 6.45 kWp of PV installation is installed on the roof. The control system will be developed in LabView. Tests will be carried on for one week, and the data will be recorded each 15 minutes. Results shall demonstrate the effectiveness of the control strategy, which could significantly increase self-consumption while responding to external activation or shut-down signals.

Keywords. Virtual power plant, Self-consumption, Demand response, thermostatically controlled loads

1 Introduction

Integrating an increasing amount of renewable generation into the system will require more flexibility and a continued focus on adequacy. To maintain a reliable energy system, significant investments must be realised by 2025, with an extremely tight schedule.

An efficient way of addressing the increase in volume and volatility of power flows is to harness the potential of all technologies that can contribute to adequacy and flexibility as soon as possible.

Such technologies include decentralised resources such as battery storage, electric vehicles, electric water heaters and heat pumps. To ensure reliable operations of the power grid under these fundamental changes, an increasing amount of flexibility is required: Elia, the Belgian Transmission System Operator (TSO) foresees that the total need for upward flexibility (increase production or decrease demand) will increase by 64% in the coming decade, whereas the need for

downward flexibility (decrease production or increase demand) will increase by 54% [1]. In the past year, over 200.000 residential electric storage water heaters (ESWHs) have been sold in Belgium, with a total installed base of over 400.000 units with a storage capacity exceeding 80 litres. These appliances are geographically evenly distributed across Belgium and have individual power and energy specifications exceeding 2kW and 4kWh, respectively, totalling over 1GW of flexible capacity.

At the same time, an increasing number of households is equipped with a PV system in Belgium. Since 2024, the net metering scheme has been abolished in the three Belgian regions, which constitutes a strong incentive to increase self-consumption (i.e. minimizing the power sold to the grid and maximizing the PV power directly consumed in the household) [2] .This can be achieved by the use of residential home batteries and/or by the load shifting capabilities of home appliances and in particular of thermostatically controlled loads [3].

Prosumers are therefore facing multiple possible objectives (self-consumption vs. services to the grid) and multiple possible technologies (load shifting vs home battery storage), which pose challenges in terms of optimal control strategy.

The goal of this paper is to design a laboratory test bench capturing the above trade-offs and challenges

for a realistic residential application. A representative PV system including a battery is installed on the university campus and tested together with a realistic electrical household consumption profile. Load shifting capabilities are also experimentally tested with a domestic hot water installation coupled to stochastic domestic hot water demand profile.

2 Experimental setup

2.1 Domestic hot water installation

A preliminary experimental campaign has been carried out for the thermal characterisation of electrical water heaters. This test bench was used to validate a non-linear dynamic model of the water heater [4] and is now available to experimentally characterize the activation of flexibility services to the grid. The characteristics of the tested device are provided in Table 1 and Figure 1 shows the experimental installation.

Table 1: Specifications of the Ariston Velis Evo dry boiler

Technical Data	Values
Volume	2X 30 L cylindre
Height	930 mm
Number of heating element	2X 1350 W
Maximum Température	80 °C



Figure 1: Testing installation for Water heaters characterisation located in the climatic chamber of the thermodynamic laboratory of the university of Liege.

Figure 2 shows the experimental validation of the numerical model proposed in [4], with an excellent agreement between the measured axial temperature profile and the simulated nodal temperatures.

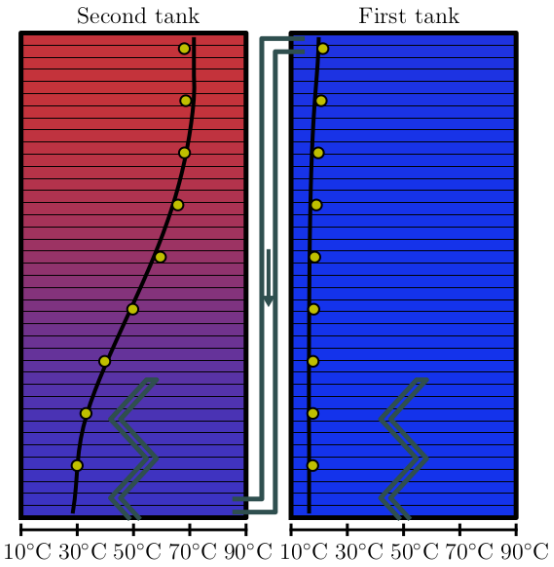


Figure 2: Temperature profile validation of the Velis boiler [4].

2.2 Residential PV and battery installation

A typical residential PV installation was installed during the summer 2024 on the roof of the thermodynamic laboratory of the University of Liège to reproduce realistic operating conditions.

Its characteristics are provided in Table 2.

Table 2: Technical specifications of the Key components in the Hybrid Solar energy system.

Material	Technical Data	Values
PV panels (15x Trina Solar 430 dual glass mono N-type)	Peak Power Watts	430 Wp/panel
	Maximum Power Voltage	43,6 V/panel
	Maximum Power Current	9,87 A/panel
SMA Hybrid Inverter (STP5.0-3SE-40)		
Input (PV DC)	Max. PV array power	7500 Wp
	Rated input voltage	600 V
	Max. usable input current at input A / input B	12.5 A / 12.5 A

.

Battery connection	Max. charging current / max. discharging current	30 A / 30 A
	Max. charging power / max. discharging power	7500 W / 6000 W
AC connection	Max. apparent AC power	5 KVA
	Rated output current	3 x 7.3 A
SMA Home Storage (2 x HS-BM-3.28-10)	Usable energy capacity	6.56 kWh
	Nominal voltage	192 V
	Max. charging / discharging current	36 A

2.3 Stochastic demand profiles

To capture the stochasticity of a typical household demand profile, a bottom-up model is used considering all appliance in the house. Base load, tumble dryer, dishwasher, washing machine, heating, and electric vehicle charging are all accounted for and can be included or excluded from the model depending on the desired profile configuration.

Furthermore, the water draw-off profile is also obtained stochastically.

These profiles are defined for a whole year with 1 min time resolution for both the electrical demand and water draw-off.

The electrical demand profile is directly provided to the control system to mimic the measurements provided by a residential smart meter.

The water draw-off profile is used to control an electro valve as indicate in the scheme provided in Figure 3.

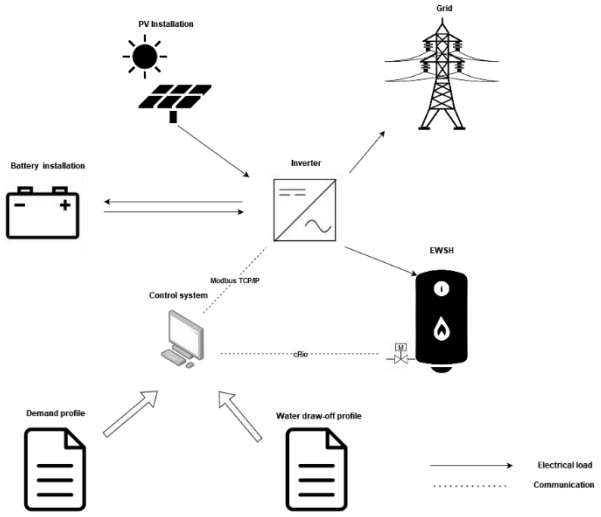


Figure 3: System architecture of the Hybrid solar energy system with Battery and water storage.

3 Control system

3.1 Modbus communication with the inverter

SMA hybrid inverters are provided with a Modbus interface allowing to access all electrical measurement, but also to control some key operational parameters such as the maximum injection to the grid. In the scope of this work, communication is established through relevant registers as described in Table 3.

Table 3: Measured parameters and corresponding Modbus register addresses for the hybrid Solar energy system.

Measured values and parameters	**Modbus Register Adress**
PV Power generation (W)	30775
PV Daily yield (Wh)	30535
Battery state of Charge (Wh)	30845
Battery Discharge (W)	31395
Battery Charge (W)	31393
Grid power absorption (W)	30865
Battery activation control (-)	40151
Battery Discharging control (%)	40073
Battery charging control (%)	40723

3.2 LabView interface

The whole experimental setup is controlled using a user-friendly LabVIEW interface, allowing researchers and students to implement and test different control strategies.

Measurements are collected using the following devices: a Gossen MetraWatt A200 for power measurement, a Sfere DGN951C for flow rate measurement, and Type T thermocouples for temperature monitoring. All these devices are connected to a CompactRIO (cRIO) system for seamless data acquisition.

Control signals are transmitted using the Modbus TCP/IP protocol for components managing current flow, including the battery, inverter, photovoltaic panels, boiler, and grid. Whereas signals for the wired electro valve are managed via an analog output module (NI 9265) integrated within the cRIO system.

Both data acquisition and data logging are setup with a 1s sampling rate within the system. A TDMS file containing every required data is generated at the end of each test run for further analysis.

4 Conclusions

This short paper describes the design and construction of an experimental setup to test active demand response strategies at the residential level, and their trade-offs with self-consumption strategies. The two sources of flexibility are the thermal storage capacity brought by typical household electrical water heaters, and from PV-coupled home batteries.

The test bench will be used to evaluate in real life the impacts of participating into a Virtual Power Plant providing services to the TSO in the Belgian grids. In particular, the consequence of flexibility activation up and down (originating from the participation in ancillary markets) will be evaluated in terms of:

- Potential overconsumption, e.g. due to increased thermal losses
- economic impacts, e.g., due to the competition with the self-consumption targets.

Future works will concentrate on the design of an optimal control strategy maximizing the economic benefits from the prosumer perspective. This control will be tailored to different scenarios in terms or retail price structure, dynamic pricing schemes, and weather conditions.

5 Acknowledgement

This work was performed in the scope of the “Unleash” Energy Transition Fund project.

6 References

[1] E. Van Wanrooij, F. Nobel, B. Hebb, and J. Voet, “Design of a harmonised reactive balancing market with cross zonal optimisation of frequency restoration between LFC Blocks.” 2014.

[2] S. Quoilin, K. Kavvadias, A. Mercier, I. Pappone, and A. Zucker, “Quantifying self-consumption linked to solar home battery systems: Statistical analysis and economic assessment,” *Appl. Energy*, vol. 182, pp. 58–67, Nov. 2016, doi: 10.1016/j.apenergy.2016.08.077.

[3] P. Lubello, I. Bensana-Tournier, C. Carcasci, and S. Quoilin, “Estimation of load shifting impact on energy expenses and self-consumption in the residential sector”.

[4] N. Leclercq, S. Marichal, S. Quoilin, and V. Lemort, “DYNAMIC MODELING AND EXPERIMENTAL VALIDATION OF AN ELECTRICAL WATER HEATER WITH A DOUBLE STORAGE TANK CONFIGURATION,” in *37th International Conference on Efficiency, Cost, Optimization, Simulation and Environmental Impact of Energy Systems (ECOS 2024)*, Rhodes, Greece: ECOS 2024, 2024, pp. 168–179. doi: 10.52202/077185-0015.

WHAT ARE STUDENTS' ALTERNATIVE CONCEPTIONS OF ENTROPY AND THE SECOND LAW OF THERMODYNAMICS?

Vincent Natalis[1,2*], Bernard Leyh[1,2]

[1] Department of Chemistry, University of Liège, Belgium

[2] DIDACTIfen Research Unit, University of Liège, Belgium

** Corresponding Author: vincent.natalis@uliege.be*

Abstract. Entropy and the second law of thermodynamics have long been identified as major difficulties in the physical chemistry curriculum at undergraduate level, and several alternative conceptions (AC) have been identified, many of them attributable to the misfit disorder metaphor. In this study, we observe and critically discuss these ACs and reveal new ones thanks to a supplemented and modified multiple-choice questionnaire with written justification based on the literature. The test was undertaken by N = 581 scientific and engineering undergraduates following a classical macroscopic thermodynamics course and completed by N = 20 interviews of chemistry undergraduates. Our results support multiple ACs identified in the literature and report 7 new ones, backed by their presence in erroneous answers in multiple chemical contexts in the written answers and the interviews. The pre/post design data around the classical macroscopic course revealed little to no conceptual change. This novel evidence also lays ground for a teaching proposal involving a systematic microscopic comparison of the relative magnitudes of internal degrees of freedom contributions on entropy to tackle these ACs.

Keywords. Second law of thermodynamics, Thermodynamics education, Alternative conceptions.

Part III

Thermodynamics and the Energy Transition

ENERGY TRANSITION IN MARITIME TRANSPORT: TOWARDS CLIMATE NEUTRALITY

Pablo Yánez-Rosales[1*], Beatriz del Río-Gamero[1], Julieta Schallenberg-Rodriguez[1]

[1] Industrial and Civil Engineering School, Universidad de Las Palmas de Gran Canaria, Spain.

* *Corresponding Author: pablo.yanez@ulpgc.es*

Abstract. Maritime transport is one of the world's biggest consumers of fossil fuels, even more so in island and isolated systems, where most goods arrive by sea and it is the main means of communication between the islands. The objective of this study is to analyse the technical feasibility of achieving carbon neutrality in maritime trade routes. To this end, the methodology presented analyses the possible alternative fuels that could lead the technological transition in the maritime transport sector: hydrogen, ammonia, methanol and synthetic methane. One of the main novelties of the study lies in the fact that all the proposed alternatives are produced from renewable sources, as well as CO2 capture. Another novelty is that it compares the production of e-fuels from renewable surpluses in the electricity mix with the installation of a renewable energy park dedicated to the production of these e-fuels. Due to the seasonal nature of renewable sources in the Canary Islands, the needs of e-fuel storage would increase significantly if they were produced from surpluses, since most of them are produced during the summer, which would increase the cost of storing the e-fuels. The results show that to achieve climate neutrality in inter-island shipping in Tenerife (the region under study), around 19 000 tonnes of hydrogen, 133 000 tonnes of e-Ammonia, 110 000 tonnes of e- methanol, and just over 42 500 tonnes of LSG would be needed.

Keywords. Maritime Transport, Energy Transition, Alternative Fuels, Canary Islands.

EXERGY EFFICIENCY FOR DESALINATION PROCESSES

Nenna Arakcheeva El Kori[1]*, Ana M. Blanco-Marigorta[1], Noemi Melián-Martel[1]

[1] Department of Process Engineering. University of Las Palmas de Gran Canaria, Spain

* *Corresponding Author:* nenna.elkori@ulpgc.es

Abstract. Water desalination has positioned itself as an essential alternative source of freshwater that allows to reduce the gap between the availability of freshwater and its continuously rising demand. Nowadays desalination plants provide nearly 95 million m^3/day of desalinated water, supplying over 300 million people worldwide. Reverse Osmosis (RO), which uses a semipermeable membrane for the separation of salts, is the most predominant by producing 69% of desalinated water. About 25% of desalinated water is produced by thermal desalination systems, such as Multi-Effect Distillation (MED) and Multi-Stage Flash Distillation (MSF), based on the phase separation of water. The continuous pursuit of improvement in the efficiency of desalination processes has led to the appearance of so-called "emerging" desalination technologies. Membrane distillation (MD) is one of the most promising emerging technologies in improving the efficiency of desalination systems due to the independence of energy consumption of this process from feedwater salinity. From the thermodynamic point of view, different definitions for exergy efficiency have been proposed in order to assess the performance of desalination processes but often ambiguously and confusingly, which hinders its standardization and practical use. In the context of the desalination units, the conceptualization of exergy efficiency in the literature provides in some cases contradictory results when comparing the exergy efficiency values for the overall processes. The definition of fuel exergy and product exergy plays a fundamental role in the estimation of the efficiency of desalination units, where the consideration of chemical exergy, acts as a key element due to the separation of salts. The purpose of this work is to provide clear definitions of exergy efficiency for desalination units of the main conventional and emerging desalination technologies, in order that these can be used consistently and without confusion.

Keywords. Desalination, Exergy efficiency, Thermal Desalination, Membrane Desalination.

1 Introduction

Freshwater demand is continuously rising, exacerbated by population growth, economic development which cause shifts in consumption patterns, and climate change. The situation is specially concerning for areas where natural water resources are scarce or non-existent. By 2030, a global water deficit is expected to reach 40% and 5.7 billion people are presumed to live in areas susceptible to water scarcity by 2050. This suggests that the number regions which conventional water sources such as lakes, rivers or aquifers are no longer able to meet the water demand, is increasing. [1]

Securing the availability of freshwater has become a primary global challenge, included in the Sustainable Development Goal (SDG) 6, one of the 17 goals established in 2015 by the United Nations General Assembly [2]. Since 97.5% of surface water is saline, desalination processes have established themselves as a high-valuable solution for freshwater production particularly in regions where natural water resources are not capable of meeting water demand [3].

Over the past 20 years, the number of desalination plants and projects has grown exponentially, with an annual growth rate between 5 and 6 % since 2010, with several water-stressed regions relying exclusively on desalination technologies for freshwater production [4]. The number of desalination plants surpassed the 18.000 in the last years, producing over 87 million m^3/day [5]. Thermal processes dominated desalinated water production since 1980s, until 2000s when membrane processes specifically Reverse Osmosis rise exponentially accounting nowadays for 84% of all operational desalination plants. However, thermal processes mainly Multi-Effect Distillation and Multi-Stage Distillation technologies are still predominant in the Middle East with over half of all the desalination plants operating in the region[4].

The developing of desalination technologies has been always accompanied with several challenges, where high electrical and thermal energy consumption, environmental impact and low water recovery are the most significant in terms of water production cost [6].

Efforts to find desalination technologies to address these issues have led to the development of so-called *emerging technologies* such as Membrane Distillation, which unifies membrane-based and thermal-based technologies within a single process [7]. The optimization of well-established desalination systems has been also consistently pursued [8]. Approaching the thermodynamic limit of desalination processes leads to greater efforts to improve their efficiency [9]. Thus, identifying and comprehending the sources of major energy consumption in the desalination technologies becomes a fundamental aspect of addressing its energy requirements [10].

Exergy analysis is a well-established analytical tool for characterization and efficiency assessment of energy-intensive processes, such as desalination technologies. In the early 1980s, exergy analysis was first introduced for the thermodynamic analysis of desalination systems [11]. The interest in its application for the analysis of desalination technologies has continued to grow as it provides a more comprehensive analysis of system efficiency than energetic analyses and its simplicity in comparison with the traditional application of Second Law [12].

However, exergy efficiency approaches are often not well defined for desalination systems, especially for desalination units, which turn out to be the limiting factor in the performance of these processes.

The purpose of this paper is to propose clear definitions of fuel efficiency and product efficiency of desalination units for the main desalination processes, Reverse Osmosis, Multi-Stage Flash Distillation, Multi-Effect Distillation and Membrane Distillation, so that they can be used without ambiguity.

2 Exergy analysis and exergy efficiency

Exergy analysis is a globally recognized tool used to assess the thermodynamic performance (development, evaluation, and improvement) of an energy-dependent system, by identifying the location, cause and estimation of thermodynamic inefficiencies. It's practical application in the industry grows slowly, due in part to a lack of standardization of definitions, leading to results difficult to interpret [13].

Several definitions of exergy efficiency can be found in the literature [12-17], which can be classified into two main categories: a) Total exergy efficiency or input-output and b) fuel-product exergy efficiency. Brodyansky et al. [16] offered a deep analysis of the terminology issue and how these terms can lead to different results and formulations for exergy efficiency, by using different examples. Sciubba et al. [20] categorized the exergy efficiencies into three general definitions. Lior and Zhang [21] classified and made distinctions between different definitions for energy, exergy and second law efficiencies. They referred to the input-output efficiency as the total or overall efficiency and suggested its use for processes where a major part of the output is "useful". Cornelissen [22] made a comparison between three exergy efficiency definitions. The terms product exergy and fuel or consumption exergy, have been extensively used in the literature by several authors with slight differences [14-17, 23, 24] often indicated as the most appropriate definition for exergy efficiency.

Szargut et al. [17] and Tsatsaronis [19] proposed to take into account those exergy transfers, which were used in the production of the desired exergy from the driving exergy of the system, being necessary a coherence between the purpose of the system and its exergy analysis, giving rise to the concepts of fuel exergy and product exergy. In addition, Lazzaretto and Tsatsaronis [25], proposed a systematic procedure for the definition of the exergy efficiency for process components.

The exergy supplied to the system is either delivered in the outputs or destroyed inside the system. This balance can also be expressed in terms of exergy of the fuel, (the exergy related to the resources), E_F, exergy of the product (the desired exergy output), E_P, exergy loss (with effluents), E_L, or exergy destructed (within the system due to irreversibilities), E_D:

$$\dot{E}_F = \dot{E}_P + \dot{E}_L + \dot{E}_D \qquad (1)$$

Exergy efficiency is the ratio between the desired exergy at the system outlet or product exergy and the exergy required to drive the system or fuel exergy [24]:

$$\eta_e = \frac{desired\ output\ exergy}{input\ exergy\ required} = \frac{\dot{E}_P}{\dot{E}_F} \qquad (2)$$

.

The total exergy of a system can be divided into four main components: physical, chemical, kinetic and potential exergy. Being an extensive property, the specific exergy can be defined as [18]

$$e = e_{ph} + e_{ch} + e_{kn} + e_{pt} \qquad (3)$$

Under conditions of rest of the system with respect to the environment, the terms of kinetic exergy and potential exergy are zero $e_{kn}=e_{pt}=0$, the exergy of the system is given by the physical exergy e_{ph}, as the maximum theoretical work of a system when changing from an initial state with temperature T and pressure p to a restricted dead state or thermomechanical state with temperature T_0 and pressure p_0, and chemical exergy e_{ch}, as the maximum theoretical work of a system when changing its state from the restricted dead state or thermomechanical state to the dead state or state in complete equilibrium with the environment.

The exergy balance of a system arises from the first and second thermodynamic laws. That is, from the combination of the energy and entropy balances. For the case of a system in a steady state, the balance expression is the following [16, 22]

$$0 = \sum_j \dot{E}_Q - \dot{E}_W + \sum_i \dot{E}_i - \sum_i \dot{E}_e - \dot{E}_D \qquad (3)$$

The exergy associated with the exergy transfer of the flows of matter considering rest conditions:

$$\dot{e}_i = \left[(h_i - h_{i0}) - T_0(s_i - s_{i0}) + e_i^{ch}\right] \qquad (4)$$

Where h_i and s_i represent the specific enthalpy and entropy of the stream, while h_{i0} and s_{i0} represent the specific enthalpy and entropy of the stream in the restricted dead state. e^{ch} represents the chemical exergy associated with the stream and m_i is the mass flow.

3 Exergy definitions in Desalination systems

3.1 Reverse Osmosis

In reverse osmosis processes, salt separation takes place thanks to a semi-permeable membrane. Although it needs high pressures to overcome the osmotic pressure particularly for seawater desalination, it operates at ambient temperature and therefore, outperforms thermal processes in terms of efficiency, by using only electrical energy[10].

A schematic of the RO module is shown in Fig. 1.

The dead state is defined considering the feed water conditions, in order to obtain a null exergy value of the feed water stream[26].

At the desalination unit level, the membrane module causes a variation in the chemical composition of the feed water, which leads to an increase in chemical exergy between the outlet and inlet streams. This makes the chemical exergy the real product of the desalination unit.

$$\dot{E}_P = \left(\dot{E}^{CH}_{permeate} + \dot{E}^{CH}_{brine}\right) - \dot{E}^{CH}_{feed\ water} \qquad (5)$$

The physical exergy, mainly related to the operating pressure, decreases between the inlet stream and the outlet streams. It is therefore consumed to give rise to the increase in chemical exergy, converting it into fuel exergy.

$$\dot{E}_F = \dot{E}^{PH}_{feed\ water} - \left(\dot{E}^{PH}_{permeate} + \dot{E}^{PH}_{brine}\right) \qquad (6)$$

The definition of both fuel exergy and product exergy is thus in line with the proposal of Lazzaretto and Tsatsaronis [25] which pursues consistency between the real purpose of the components of a process and their thermodynamic behavior.

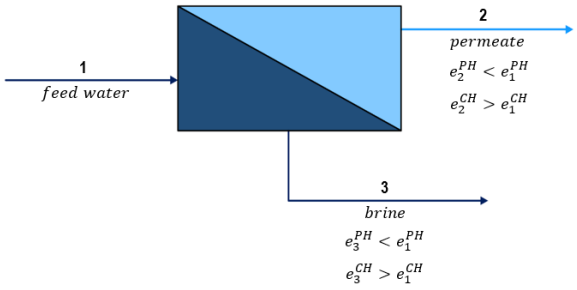


Figure 1: Reverse Osmosis module

Qureshi and Zubair [27] provided a comparison of two approaches to exergy efficiency of RO plants. It presents a similar definition of dead state, with the purpose of nullifying the exergy value of the input stream. The authors lean towards an approach more consistent with the aim of the process, which allows the definition of fuel and product exergy. However, it does not distinguish between exergy types, considering the value of the exergy streams in their entirety for efficiency assessment.

Beni et al. [28] applies the ingoings-outgoings approach to exergy efficiency estimation, where the input and output streams of the desalination unit are treated equally, regardless of the purpose of each. For the product exergy, the authors propose to calculate

the minimum energy of a hypothetical thermodynamically reversible process through a mass balance approach.

Likewise, Yargholi et al. [29] and Khanmohammdi et al. [30] propose a similar definition to the previous study for fuel and product exergies with slight differences. In the first case, the product exergy is defined as the difference between the output exergies (brine and permeate) and the input water. While in the second case, the product exergy is assumed to be the sum of the output streams. This may be due to different considerations in the dead state.

3.2 Multi-Stage Flash Distillation

Multi-stage flash distillation is a thermal desalination process, characterised by the separation of salts through the evaporation of water using thermal energy. It was the first desalination technology to be commercialised and for years remained the industry leader. This process is characterised by operating temperatures often exceeding 100°C and pressures maintained slightly below the saturation point of the water vapor in the distillation units, which are in turn placed in successive stages [28, 29].

A schematic of the MSF module is shown in Fig. 2.

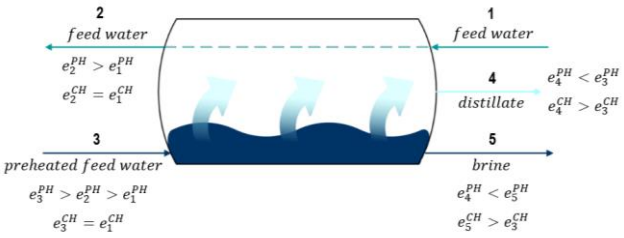


Figure 2: Multi-Stage Flash Distillation module

The same assumptions have been used for the definition of the dead state as those mentioned in the reverse osmosis analysis. In this case, two types of product must be taken into account. In the first case, the feed water is preheated as it passes through the distillation unit, allowing condensation of the water vapour generated. In the second case, the preheated feed water is evaporated by flash distillation, resulting in distillate and brine streams. The product exergy would therefore be composed of the increase in physical exergy associated with the heating of the input stream, and the increase in chemical exergy as a result of the separation of salts.

$$\dot{E}_P = \dot{E}_d^{CH} + \dot{E}_b^{CH} + \left(\dot{E}_{f,out} - \dot{E}_{f,in}\right) - \dot{E}_{hf}^{CH} \qquad (7)$$

hf Preheated feed water,

b Brine,

f Feed water,

d Distillate.

Fuel exergy is reflected in the reduction of the physical exergy of the distillate and brine streams relative to the preheated water stream.

$$\dot{E}_F = \dot{E}_{hf}^{PH} - \left(\dot{E}_b^{PH} + \dot{E}_d^{PH}\right) \qquad (8)$$

Unlike reverse osmosis technology, the exergy consumed is mainly associated with thermal energy, to give rise to the chemical exergy associated with the change in salinity.

Al-Weshahi et al. [33], Nafey et al. [34]and Almerri et al. [35] used the same input-output approach for desalination units without differentiating the types of exergy involved in the process and their role in the process. All three obtained efficiency values exceeding 90% for some of the stages, while the overall process efficiency values barely exceeded 1% in some of the cases. The huge difference between overall process and desalination unit efficiency results is not consistent considering that distillation units are a limiting factor for thermal desalination processes.

3.3 Multi-Effect Distillation

As with multi-stage flash distillation, multi-effect distillation primarily uses thermal energy to produce the separation of salts. In this case, vapor is generated by heat transfer between the steam passing through the tubes of the distillation unit and the feed water that is sprayed onto them [31]. In addition, this technology allows the use of slightly lower operating temperatures than those used in MSF, allowing the exergy efficiency of the process to be increased.

A schematic of the MED module is shown in Fig. 3.

The dead state conditions for this case are associated, as in the previous approaches, with the state of the feed water.

The chemical exergy of the distillate and brine streams is increased compared to the feed water. Therefore, they are associated with the product exergy.

$$\dot{E}_P = \dot{E}_b^{CH} + \dot{E}_d^{CH} - \dot{E}_f^{CH} \qquad (9)$$

st Steam,

$cond$ Condensate,

b Brine,

f Feed water,

d Distillate.

On the other hand, the inlet steam passes through the condensation tubes changing phase and giving off heat in order to generate the distilled vapor of the unit. Taking into account that this process causes a decrease in the physical exergy of said stream, this proves its main role as fuel exergy within the distillation unit.

$$\dot{E}_F = \dot{E}_f^{PH} + \left(\dot{E}_{st} - \dot{E}_{cond}\right) - \left(\dot{E}_d^{PH} + \dot{E}_b^{PH}\right) \quad (10)$$

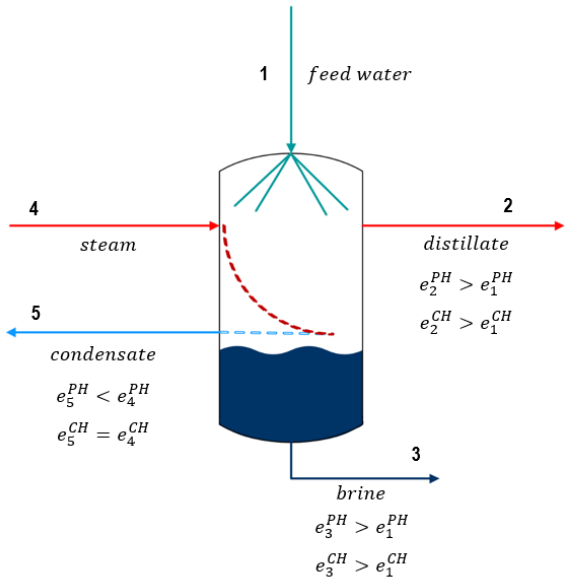


Figure 3: Multi-Effect Distillation module

Although there are several studies that apply exergy analysis to MED processes [33-36] similar approaches have been found in all of them for desalination units. Piacentino et al. [40] compares two exergy efficiency approaches applied to a process effect. The input-output approach and a more rational approach, according to the authors, based on useful product exergy and consumed exergy. As a result, it was found that the first definition kept the exergy efficiency of the effects above 88%, while the second approach gave values below 10% for each effect. The authors suggested that in the first case, the exergy efficiency completely lacks "productive purpose" in its definition. Whereas the second definition reflects the actual useful purpose of the effects, which is the separation of salts. Therefore, the low efficiency values reflect the actual performance of the desalination units in producing very little chemical exergy, compared to the amount of thermal exergy required for this to take place.

3.4 Membrane Distillation

Membrane distillation is a hybrid process, involving both a thermal driving force and the presence of a selective membrane for water desalination. Unlike conventional thermal processes, it operates at mild temperature conditions and, unlike conventional membrane processes, uses nearly ambient pressures. Nevertheless, its output is not comparable to previous processes [7,41].

A schematic of the MD module is shown in Fig. 4.

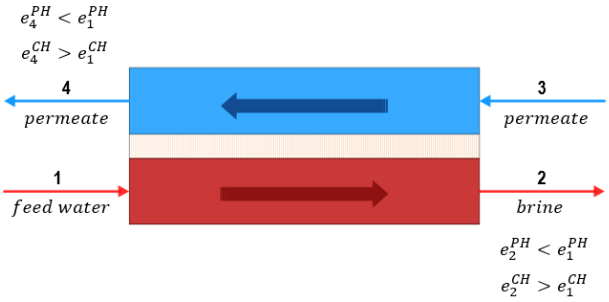


Figure 4: Membrane Distillation module

As defined in the above processes, the dead state is defined by considering the conditions of the feed water.

The Membrane Distillation module presents two countercurrent currents. The temperature gradient between the two streams causes the water transfer to the permeate stream. As a result, the permeate stream undergoes an increase in flow rate, while the feed water stream is concentrated, giving rise to brine.

The chemical exergy of the permeate streams increases compared to the chemical exergy of the feed water. However, the product in this case is the increase in the flow rate of the permeate stream as it is in recirculation. Likewise, the increase in the chemical exergy of the brine is also considered.

$$\dot{E}_P = \left(\dot{E}_{p,out} - \dot{E}_{p,in}\right) + \left(\dot{E}_b^{CH} - \dot{E}_{fw}^{CH}\right) \quad (11)$$

p, out Permeate output,

p, in Permeate input,

b brine,

f feed water.

The physical exergy, mainly related to the temperature as a driving force of the process, decreases between the feed water and the brine streams. In this way, the thermal exergy acts as the fuel being consumed to generate the water vapor that

is incorporated into the permeate stream, thus transforming the thermal exergy into chemical exergy.

$$\dot{E}_F = \left(\dot{E}_b^{PH} - \dot{E}_{fw}^{PH}\right) \quad (12)$$

b brine,

f feed water.

As in the previous cases, the aim is to preserve the coherence between the purpose of the process and its thermodynamic behaviour.

Ali et al. [42] compared both the outgoing-ingoing approach and the fuel product approach but taking into account each stream entirely. The authors pointed out that the fuel product approach provides more appropriate and consistent information on the process. This conclusion can also be obtained from the work of Okati et al. [43]. The outgoing-ingoing approach is applied, the outputs and the inputs are equally considered regardless of what they are being used for. The results presented are unusually high for this type of processes with efficiency values above 50%.

Conclusions

In this work, an analysis of the definitions of exergy efficiency for the desalination units of the 4 main desalination processes has been performed. The following summary is the overall conclusions of this work.

- Contradictory results have been found in the literature due to the use of the input-output approach as the majority approach found in the reviewed works. Values above 90% efficiency were reported for the desalination units, while the exergy efficiency of the overall process remained very low. This approach has proven to be inconsistent with the purpose of desalination units and does not correctly describe the thermodynamic behaviour of desalination units.
- No approaches have been observed in the literature that distinguish between exergy types according to their behaviour in the process.
- A clear definition has been proposed for fuel and product exergies from desalination units. The proposed approach aims to pursue consistency between the actual purpose of the components of a process and their thermodynamic behaviour.
- The increase of chemical exergy within desalination units has been observed to be mainly responsible for product exergy. Physical exergy, on the other hand, showed a general decrease in all the processes analysed, being mainly associated with fuel exergy. This shows that desalination processes are characterised by the conversion of mechanical exergy into chemical exergy.

Nomenclature

E	Exergy (kW)
e	Specific exergy (kJ/kg)
η_e	Exergy efficiency (%)
h	Specific enthalpy (kJ/kg)
s	Specific entropy (kJ/kg)
T	Temperature (°C)

Subscripts

F	Fuel
P	Product
P	Product
D	Destruction
i	Related to chemical species
0	Dead state
s	Salt, saline water
W	Work
Q	Heat
i	inlets
e	outlets

Superscripts

ch	Chemical
kn	Kinetical
ph	Physical
pt	Potential

References

[1] UNESCO, "United Nations World Water Development Report 2021:The Value of Water.," Paris, 2021. [Online]. Available: www.unwater.org.

[2] UNESCO, "United Nations World Water Development Report 2020: Water and Climate Change," París, 2020. [Online]. Available: www.unesco.org/open-access/

[3] A. Najim, "A review of advances in freeze desalination and future prospects," *NPJ Clean*

Water, vol. 5, no. 1, Dec. 2022, doi: 10.1038/s41545-022-00158-1.

[4] E. Jones, M. Qadir, M. T. H. van Vliet, V. Smakhtin, and S. mu Kang, "The state of desalination and brine production: A global outlook," *Science of the Total Environment*, vol. 657, pp. 1343–1356, Mar. 2019, doi: 10.1016/j.scitotenv.2018.12.076.

[5] World Bank, "The Role of Desalination in an Increasingly Water-Scarce World," Washington, DC, Mar. 2019. [Online]. Available: www.worldbank.org/gwsp

[6] M. Al-Obaidi *et al.*, "Hybrid membrane and thermal seawater desalination processes powered by fossil fuels: A comprehensive review, future challenges and prospects," Aug. 19, 2024, *Elsevier B.V.* doi: 10.1016/j.desal.2024.117694.

[7] V. G. Gude, "Use of exergy tools in renewable energy driven desalination systems," *Thermal Science and Engineering Progress*, vol. 8, pp. 154–170, Dec. 2018, doi: 10.1016/j.tsep.2018.08.012.

[8] M. N. Soliman, F. Z. Guen, S. A. Ahmed, H. Saleem, M. J. Khalil, and S. J. Zaidi, "Energy consumption and environmental impact assessment of desalination plants and brine disposal strategies," *Process Safety and Environmental Protection*, vol. 147, pp. 589–608, Mar. 2021, doi: 10.1016/j.psep.2020.12.038.

[9] A. Pistocchi *et al.*, "Can seawater desalination be a win-win fix to our water cycle?," Sep. 01, 2020, *Elsevier Ltd.* doi: 10.1016/j.watres.2020.115906.

[10] H. Nassrullah, S. F. Anis, R. Hashaikeh, and N. Hilal, "Energy for desalination: A state-of-the-art review," Oct. 01, 2020, *Elsevier B.V.* doi: 10.1016/j.desal.2020.114569.

[11] A. M. Blanco-Marigorta, A. Lozano-Medina, and J. D. Marcos, "A Critical Review of Definitions for Exergetic Efficiency in Reverse Osmosis Desalination Plants," *Energy*, vol. 137.

[12] F. Macedonio and E. Drioli, "An exergetic analysis of a membrane desalination system," *Desalination*, vol. 261, no. 3, pp. 293–299, 2010, doi: 10.1016/j.desal.2010.06.070.

[13] M. A. Rosen, "Benefits of exergy and needs for increased education and public understanding and applications in industry and policy - Part II: Needs," *International Journal of Exergy*, vol. 3, no. 2, p. 219, 2006, doi: 10.1504/IJEX.2006.009046.

[14] P. Grassmann, "Zur allgemeinen Definition des Wirkungsgrades," *Chemie Ingenieur Technik - CIT*, vol. 22, no. 4, pp. 77–80, Feb. 1950, doi: 10.1002/cite.330220402.

[15] H. Baehr, "Zur Defintion Exergeticshe Wirkuksgrader (to the Definition of Exergetic Efficencies," *Brennstoff-Wärme-Kraft*, vol. 20, pp. 197–244, 1968.

[16] V. Brodyansky, M. Sorin, and P. Le Goff, *The Efficiency of Industrial Processes: Exergy Analysis and Optimization*. Amsterdam: Elsevier, 1994.

[17] J. Szargut, D. Morris, and F. Steward, *Exergy Analysis of Thermal, Chemical, and Metallurgical Processes*. New York: Hemisphere Publishing Corporation, 1988.

[18] A. Bejan, G. (George) Tsatsaronis, and M. J. Moran, *Thermal design and optimization*. Wiley, 1996.

[19] G. Tsatsaronis, "Thermoeconomic analysis and optimization of energy systems," *Prog Energy Combust Sci*, vol. 19, no. 3, pp. 227–257, Jan. 1993, doi: 10.1016/0360-1285(93)90016-8.

[20] E. Sciubba and G. Wall, "A brief Commented History of Exergy From the Beginnings to 2004," *Int. J. of Thermodynamics*, vol. 10, no. 1, pp. 1–26, 2007, doi: 10.5541/ijot.184.

[21] N. Lior and N. Zhang, "Energy, exergy, and Second Law performance criteria," *Energy*, vol. 32, no. 4, pp. 281–296, 2007, doi: 10.1016/j.energy.2006.01.019.

[22] R. L. Cornelissen, *Thermodynamics and sustainable development : The use of exergy analysis and the reduction of irreversibility*. Enschede: Febodruk, 1997.

[23] R. A. Gaggioli, "The concept of available energy," *Chem Eng Sci*, vol. 16, no. 1–2, pp. 87–96, Dec. 1961, doi: 10.1016/0009-2509(61)87010-3.

[24] G. Tsatsaronis, "Definitions and nomenclature in exergy analysis and exergoeconomics," *Energy*, vol. 32, no. 4, pp. 249–253, 2007, doi: 10.1016/j.energy.2006.07.002.

[25] A. Lazzaretto and G. Tsatsaronis, “SPECO: A systematic and general methodology for calculating efficiencies and costs in thermal systems,” *Energy*, vol. 31, no. 8–9, pp. 1257–1289, 2006, doi: 10.1016/j.energy.2005.03.011.

[26] M. H. Sharqawy, J. H. Lienhard V, and S. M. Zubair, “On exergy calculations of seawater with applications in desalination systems,” *International Journal of Thermal Sciences*, vol. 50, no. 2, pp. 187–196, Feb. 2011, doi: 10.1016/j.ijthermalsci.2010.09.013.

[27] B. A. Qureshi and S. M. Zubair, “Exergetic efficiency of NF, RO and EDR desalination plants,” *Desalination*, vol. 378, pp. 92–99, Jan. 2016, doi: 10.1016/j.desal.2015.09.027.

[28] A. N. Beni, I. Ghofrani, and A. Moosavi, “On comparison of three multi-feed osmotic-mediation-based configurations for brine management: Techno-economic optimization and exergy analysis,” *Desalination*, vol. 525, Mar. 2022, doi: 10.1016/j.desal.2021.115517.

[29] R. Yargholi, H. Kariman, S. Hoseinzadeh, M. Bidi, and A. Naseri, “Modeling and advanced exergy analysis of integrated reverse osmosis desalination with geothermal energy,” *Water Supply*, vol. 20, no. 3, pp. 984–996, May 2020, doi: 10.2166/ws.2020.021.

[30] S. Khanmohammdi, F. Musharavati, and M. Sheykhmohammadi, “Energy and exergy examinations of a PVT based hybrid system for power, heating and potable water production: Transient modeling,” *Renew Energy*, vol. 195, pp. 540–553, Aug. 2022, doi: 10.1016/j.renene.2022.05.114.

[31] N. Voutchkov, “Energy use for membrane seawater desalination – current status and trends,” *Desalination*, vol. 431, pp. 2–14, Apr. 2018, doi: 10.1016/j.desal.2017.10.033.

[32] V. G. Gude, “Energy storage for desalination processes powered by renewable energy and waste heat sources,” *Appl Energy*, vol. 137, pp. 877–898, Jan. 2015, doi: 10.1016/j.apenergy.2014.06.061.

[33] M. A. Al-Weshahi, A. Anderson, and G. Tian, “Exergy efficiency enhancement of MSF desalination by heat recovery from hot distillate water stages,” *Appl Therm Eng*, vol. 53, no. 2, pp. 226–233, May 2013, doi: 10.1016/j.applthermaleng.2012.02.013.

[34] A. A. Mabrouk, A. S. Nafey, and H. E. S. Fath, “Analysis of a new design of a multi-stage flash-mechanical vapor compression desalination process,” *Desalination*, vol. 204, no. 1-3 SPEC. ISS., pp. 482–500, Feb. 2007, doi: 10.1016/j.desal.2006.02.046.

[35] A. H. ; Almerri, A. A. R. ; Al-Obaidi, A. H. Almerri, M. A. Al-Obaidi, S. Alsadaie, and I. M. Mujtaba, “Modelling and simulation of industrial multistage flash desalination process with exergetic and thermodynamic analysis. A case study of Azzour seawater desalination plant,” *Chemical Product and Process Modeling*, 2023, [Online]. Available: http://hdl.handle.net/10454/18926

[36] A. Khouya, “Performance evaluation of a MED-MVC desalination plant driven by a concentrated photovoltaic thermal system and an organic Rankine cycle,” *Energy Convers Manag*, vol. 274, Dec. 2022, doi: 10.1016/j.enconman.2022.116428.

[37] A. Farsi and I. Dincer, “Development and evaluation of an integrated MED/membrane desalination system,” *Desalination*, vol. 463, pp. 55–68, Aug. 2019, doi: 10.1016/j.desal.2019.02.015.

[38] Z. Fergani *et al.*, “Analysis of Desalination Performance with a Thermal Vapor Compression System,” *Water (Switzerland)*, vol. 15, no. 6, Mar. 2023, doi: 10.3390/w15061225.

[39] H. Cao *et al.*, “Thermal-exergy efficiency trade-off optimization of pressure retarded membrane distillation based on TOPSIS model,” *Desalination*, vol. 523, Feb. 2022, doi: 10.1016/j.desal.2021.115446.

[40] A. Piacentino, “Application of advanced thermodynamics, thermoeconomics and exergy costing to a Multiple Effect Distillation plant: In-depth analysis of cost formation process,” *Desalination*, vol. 371, pp. 88–103, Sep. 2015, doi: 10.1016/j.desal.2015.06.008.

[41] A. Alkhudhiri, N. Darwish, and N. Hilal, “Membrane distillation: A comprehensive review,” Nov. 15, 2012. doi: 10.1016/j.desal.2011.08.027.

[42] E. Ali, J. Orfi, and A. Najib, “Assessing the Thermal Efficiency of Brackish Water Desalination by Membrane Distillation Using Exergy Analysis,” *Arab J Sci Eng*, vol. 43, no.

5, pp. 2413–2424, May 2018, doi: 10.1007/s13369-017-2831-5.

[43] V. Okati, A. J. Moghadam, M. Farzaneh-Gord, and M. Moein-Jahromi, “Thermo-economical and environmental analyses of a Direct Contact Membrane Distillation (DCMD) performance,” *J Clean Prod*, vol. 340, Mar. 2022, doi: 10.1016/j.jclepro.2022.130613.

OPTIMIZING HYBRID OFF-GRID ENERGY SYSTEMS AND REVERSE OSMOSIS DESALINATION WITH CARNOT BATTERY TECHNOLOGY AND MODEL PREDICTIVE CONTROL

Mario Petrollese[1], Mostafa Esmaeili Shayan[1]*

[1] University of Cagliari, Department of Mechanical, Chemical and Materials Engineering, Cagliari, Italy

* *Corresponding Author:* mostafa.esmaeili@unica.it

Abstract. This research introduces the Renewable Energy Source-Pumped Thermal Energy Storage (RES-PTES) system as a cost-efficient and performance-optimizing solution for off-grid agricultural applications. The study, conducted at a farm in Ben Guerir, Morocco, integrates a Reverse Osmosis (RO) desalination plant with the RES-PTES system to meet energy demands and provide a reliable water supply. The integration of an optimization framework that combines Model Predictive Control (MPC) with machine learning-based predictive strategies results in substantial decreases in the Levelized Cost of Storage (LCOS). Integrating MPC with a 20% load curtailment strategy results in a 69.4% reduction in the LCOS, bringing it to $106.26/MWh, with an optimal RO plant capacity of 3.6 kW. The LCOS across all configurations is $177.60/MWh, highlighting the economic feasibility of the optimized RES-PTES. The findings highlight the necessity of aligning reverse osmosis plant capacity with system design and energy supply, illustrating the capability of innovative control systems to enhance renewable energy use and decrease reliance for conventional grid electricity. The integrated RES-PTES approach offers a cost-effective and sustainable solution for economically feasible off-grid agriculture procedures.

Keywords. Renewable Energy, Thermal Energy Storage, Reverse Osmosis, Energy Demands, Model Predictive Control.

1 Introduction

Renewable energy sources (RES) are transforming the global energy landscape, reducing carbon emissions and addressing basic energy needs like food spoilage and irrigation [1]. Achieving a sustainable future necessitates the reconfiguration and optimization of the energy production sector to reduce CO2 emissions, diminish dependency on fossil fuels, and satisfy energy demands through the utilization of renewable and locally sourced energy [2]. However, the intermittent nature of RES presents significant challenges for developing efficient and reliable energy storage solutions. In this context, Pumped thermal energy storage (PTES) technology emerges as a compelling solution, offering advantages such as low costs, extended cycle life, scalability, and adaptable power ratings for large-scale electrical energy storage [3]. PTES works by converting electrical energy into thermal energy, typically by heating a medium, which can later be converted back to electricity when needed. Recently, interest in PTES systems has grown significantly, as demonstrated by the various studies presented in the literature. For instance, Hadelu et al. analyzed the performance of PTES systems, reporting a roundtrip efficiency of 63.4% and a storage cost of 0.143 USD/kWh, though these systems have limitations in terms of expandability and local energy source utilization [4]. In another study aimed at addressing the uncertainty within the PTES system and seawater energy storage source, the Monte Carlo method's uncertainty analysis was employed in conjunction with geothermal resources to optimize the system [5]. Further advancements include the thermal coupling between PTES and other systems. In this regard, Frate et al. proposed a novel PTES system with thermal integration to improve the heat pump's COP and overall roundtrip efficiency by lowering operating temperature differences [6]. In a recent study, a reductive control model was applied to optimize an Energy Management System (EMS) for a stratified thermal energy storage system, with validation through experimental data [7]. Kurşun et al. investigated an integrated PTES system coupled with a concentrated photovoltaic thermal system, demonstrating a round-trip efficiency ranging from 48% to 81%. Additionally, the system exhibited a reduced levelized cost of storage (LCOS) [8]. Ökten et al. further demonstrated that the integration of a

PTES with an absorption refrigerator could yield a LCOS of 242 USD/MWh [9].

The objective of this research is to optimize a PTES system within a renewable energy-based off-grid framework, thereby addressing intermittency issues and maximizing energy yield while concurrently minimizing costs through the employment of an integrated modeling approach.

2 Materials and Methods

Figure 1 illustrates the proposed architecture of the RES-PTES system, which integrates renewable energy sources (RES) and non-renewable sources including diesel generators (DG) or grid connections. The PTES system consists of a heat pump (HP) and a heat engine (HE) operating in tandem with a thermal energy storage (TES) unit comprising a hot tank (HT) and a cold tank (CT). During the charging phase, electrical energy drives the HP to transfer heat from the CT to the HT, effectively storing thermal energy. During the discharging phase, the HE utilizes the thermal energy stored in the HT to generate electricity. Additionally, a concentrated solar thermal (CST) system can also supply heat to the HT. The TES unit can also be designed to meet heat and cold loads, if required. Inverters and battery energy storage systems (BESS) are incorporated to manage electrical load demands and power generation.

A Matlab-GAMS optimization tool using mixed-integer linear programming (MILP) has been developed for the design and performance evaluation of the proposed system across various scenarios. Figure 2 shows the optimization process for the RES-PTES system design, involving data preparation, weather data acquisition, and the definition of cold, heat, and electricity demand profiles.

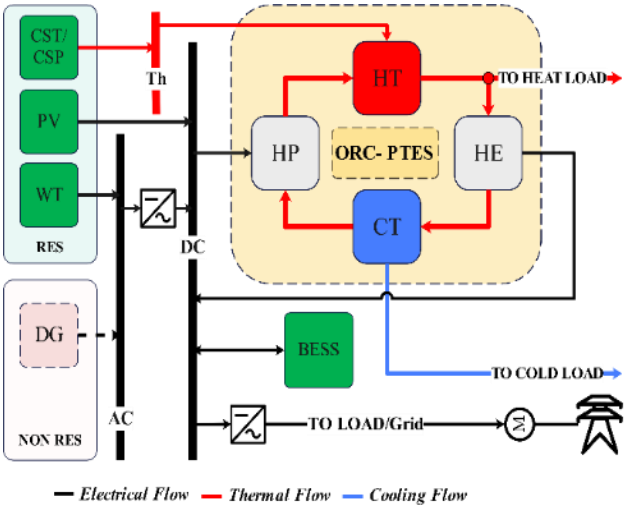


Figure 1: RES-PTES system's block diagram.

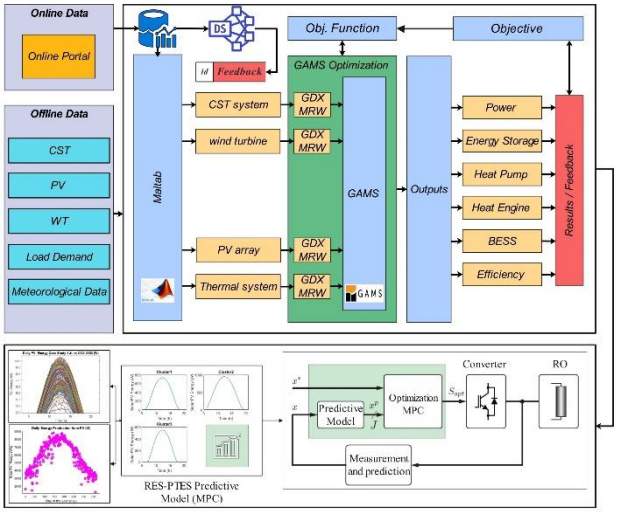


Figure 2: The framework of MPC integrated to RES-PTES.

The objective function of the optimization tool, as depicted in Equation (1), is designed to minimize the initial system cost required to satisfy a specified energy demand by optimizing a set of design parameters. These factors include the number of PV arrays (n_{PV}), the number of wind turbines (n_{WT}), the area of the CST heliostat field (A_{CST}), the storage capacity of the hot tank ($Q_{HT,n}$) and of the cold tank ($Q_{CT,n}$), and the battery energy storage capacity ($E_{B,n}$). The objective function excludes the rated powers of the heat pump and heat engine to maintain a linear problem formulation:

$$\begin{aligned} \text{Cost}_{min} = & \underbrace{c_{PV} \cdot n_{PV}}_{\text{PV Cost}} + \underbrace{c_{WT} \cdot n_{WT}}_{\text{WT Cost}} \\ & + \underbrace{c_{CST} \cdot A_{CST}}_{\text{CST cost}} \\ & + \underbrace{c_{TES} \cdot \left(Q_{HT,n} + Q_{CT,n}\right)}_{\text{TES Cost}} \\ & + \underbrace{c_B \cdot E_{B,n}}_{\text{BESS Cost}} + \underbrace{c_{RO} \cdot E_{RO,n}}_{\text{RO Cost}} \end{aligned} \quad (1)$$

The costs for PV, WT, CST, TES, and BESS are denoted by c_{PV}, c_{WT}, c_{CST}, c_{TES}, and c_B, respectively. The optimization is constrained by component performance criteria

An advanced control system based on MPC for the RES-PTES system has been developed to enhance system efficiency and improve the utilization of RES output by considering local meteorological conditions. The algorithm, depicted in Figure 3, governs controlled variables (such as the power ratings of the PTES system and batteries or the timing of deferrable loads) based on measured data and evaluates the projected renewable energy state variables across various potential states to optimize system performance.

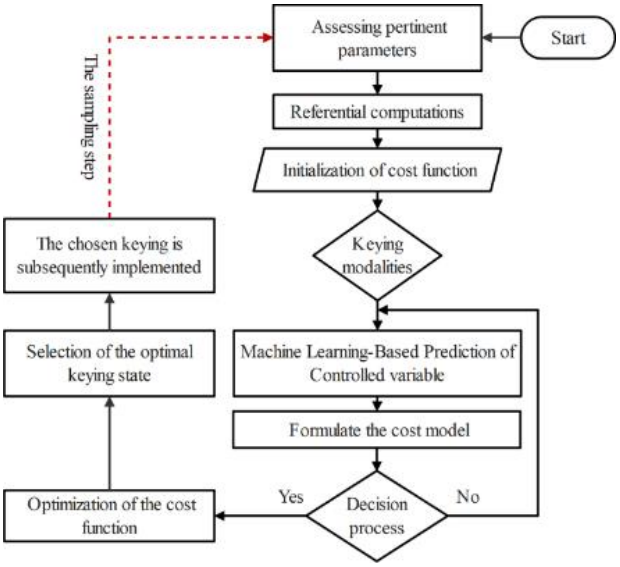


Figure 3: The model predictive control algorithm of the controlled unit in RES-PTES system.

Specifically, the MPC approach uses predicted system behaviour to optimize the control inputs, $u(k)$, by minimizing a cost function that considers both the predicted state variables and the desired setpoints. The optimization problem within the MPC framework can be formulated as shown in Equation (2), with the associated constraints outlined thereafter.

$$\min_{u(k),u(k+1),\ldots,u(k+N)} J = \sum_{i=0}^{N} \left[\left\| x(k+i) - x_{ref}(k+i) \right\|_Q^2 + \left\| u(k+i) \right\|_R^2 \right] \quad (2)$$

$$x(k+i+1) = g(x(k+i), u(k+i), \theta)\ ;\ u_{min} \le u(k+i) \le u_{max}\ ;\ x_{min} \le x(k+i) \le x_{max}$$

where $x(k+i)$ represents the predicted state at time step $k+i$, $X_{ref}(K+i)$ is the reference setpoint for the state at the same time step, g is the system dynamics function, θ denotes the model parameters, and Q and R are weight matrices that balance the relative importance of state tracking and control effort in the cost function. The constraints ensure that both the control inputs $u(k+i)$ and the states $x(k+i)$ remain within predefined bounds.

2.1 Case study

The performance of the RES-PTES system was evaluated using a case study based on a farm located in Ben Guerir, Morocco. The system is designed to meet the electrical and fresh water demands of agricultural operations in off-grid scenarios. The PTES system features a Rankine-cycle heat pump with a COP of 2.7 and an ORC unit with a 26.7 kW nominal power and an efficiency of 6.2%. The RES-PTES system is integrated with a multi-layered Load Profile and Energy System Optimization approach, utilizing machine learning to respond to farm energy demand. The latter is introduced to reduce the feed water electrical conductivity (EC) from 3.8 mS/cm to 1.5 mS/cm, which is an optimal value for the crops cultivated on the farm. Figure 5 illustrate the proposed RO plant. The system includes a water mixing tank to blend the fresh water produced by the RO process with groundwater at a 2:1 ratio.

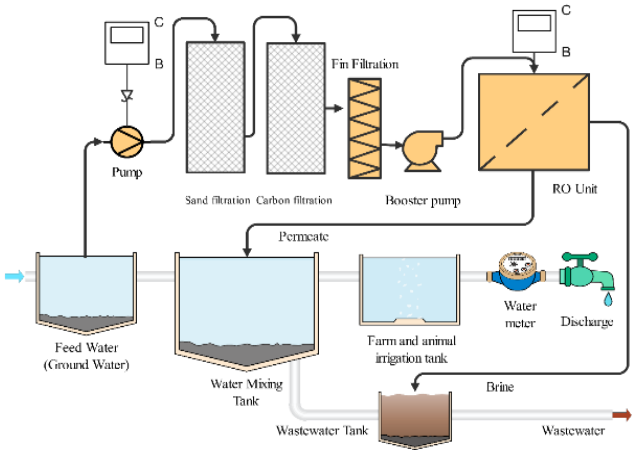


Figure 4: Block diagram of fresh water production plant with reverse osmosis method.

According to Ref [10], the power consumption of the RO (P_{RO}) can be estimated using the Equation (3):

$$P_{RO} = \frac{\dot{Q} \cdot \Delta p \cdot \sigma}{\eta_{RO} \cdot R_m} \quad (3)$$

Where, $\dot{Q}$ is the water flow rate, Δp indicates the pressure drop across the RO membrane (assumed equal to 20 bars), σ denotes the electrical conductivity of the feed water, η_{RO} the efficiency of the RO system (60%) and R_m indicates the specific resistance of the RO membrane (assumed equal to 1012 Ω·cm^2). Since higher water flow rates increase power consumption but reduce the daily operational time of the RO system, a parametric analysis of P_{RO} was conducted. Moreover, the integrated system employs MPC with a machine learning optimization framework to align energy demand with the availability of renewable resources. The MPC optimizes the demand profile by aligning peak electricity demand with the greatest possible capacity of solar energy and RO desalination. This is accomplished without decreasing the supply of water by only shifting the demand profile. Figure 5

illustrates the preliminary and enhanced demand profiles of the farm subsequent to the implementation of the machine learning-based optimization method. The irrigation pumps are scheduled; nevertheless, best irrigation of occurs at night when surface evaporation is minimal and right after sunset when the demand for the storage system is minimized.

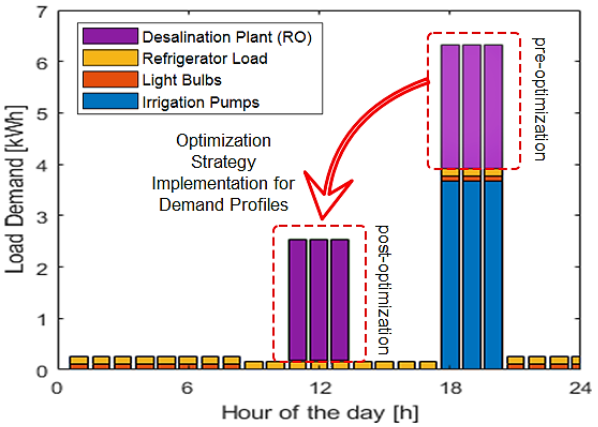


Figure 5: Comparison of Farm Demand Profiles Before and After Optimization Strategy.

Finally to assess the expected performance of RES generators, the meteorological data were analyzed and classified using machine learning techniques. Figure 6 presents the classification results for solar and wind energy availability. The MPC algorithm was assigned for three operation modes, accounting for 102 days (27.95%), 102 days (27.95%), and 161 days (44.11%) annually, based on the data's relevance to solar and wind energy. Meteorological data shows a daily average global sun irradiance of 5.73 kWh/m², average wind speed of 2.42 m/s, and ambient temperature of 20.1°C.

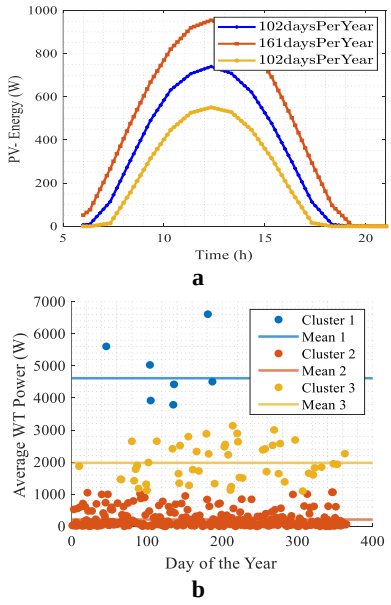


Figure 6: Classification of Solar and Wind Energy Using Machine Learning.

3 Results and Discussion

The optimal design of the RES+PTES system for the given case study and the corresponding expected LCOE/LCOS are presented in function of the percentage of the load that can be curtailed (X_{curt}) and for different RO rated power. The variations in RO power size do not indicate a restricted response to water output. If a smaller RO system requires periodic recharging (consistent with renewable energy production potential), the necessity for storage will diminish during periods of unavailability of renewable energy sources. Consequently, water storage tanks might serve as a buffer, supplying the farm with water in both optimal amount and quality for the plants' requirements. Figure 7 shows the distribution of electrical load demand by varying X_{curt} and for two values of P_{RO}. As can be observed, the introduction of MPC for the control of RO introduces an increase of the direct use of PV to load but the presence of storage systems (PTES+Batteries) is required to cover the loads demands during the evening (for irrigation). The use of HE is preferred to batteries if a percentage of Load curtailment is allowed. Moreover, the increase in sizing of the RO plant led to a reduction in battery penetration and an increase in heat engine (HE) utilization. Figure 8 shows the LCOE and LCOS for various configurations of the RES-PTES system. The integrated system reduced LCOS by up to 69.4% using a 20% load curtailment strategy. The study emphasizes the importance of synchronizing the power rating of a RO plant with the system design and energy availability. Increasing RO capacity can increase water production but may lead to elevated LCOS if not properly regulated. The ideal configuration yields the lowest LCOS of 106.25 USD/MWh, with an average LCOS of 177.60 USD/MWh.

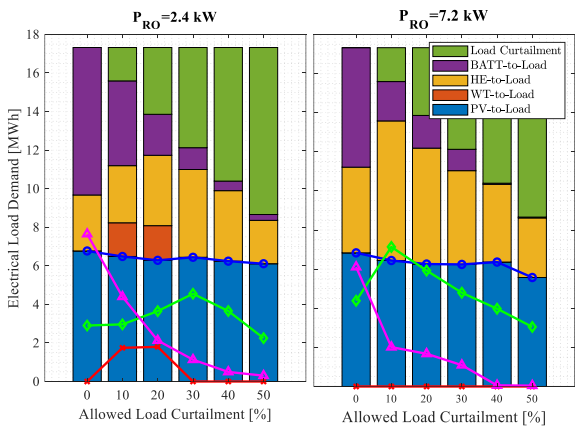


Figure 7: Electrical Load Demand Distribution for different allowed load curtailment and RO rated power.

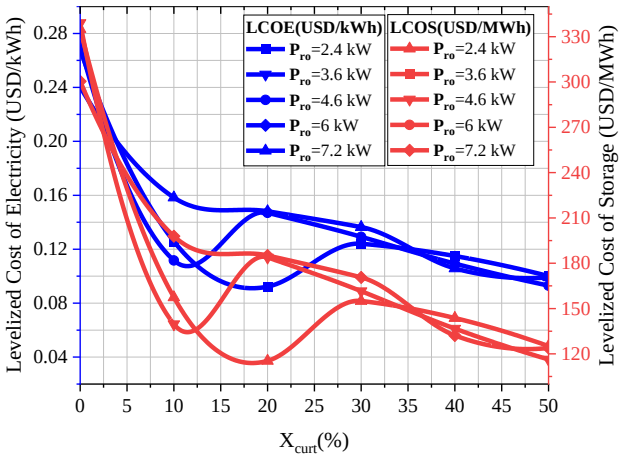


Figure 8: The LCOE and LCOS of the RES-PTES System.

4 Conclusion

In a case study of an agricultural farm's energy demand network, we developed an optimal energy demand response system, synchronized with consumer subsystems through a control system employing an advanced machine learning algorithm with day-ahead prediction. The use of RES-PTES in off-grid agriculture has significantly lowered the LCOE and LCOS, enhancing sustainability and efficiency. The results demonstrate that the integration of RES-PTES with MPC and machine learning enhances off-grid agricultural energy systems, resulting in a 69.4% decrease in LCOS to an average of 177.60 USD/MWh. Synchronizing RO plant capacity with system design and renewable energy availability is essential for affordable and sustainable farming activities.

Acknowledgement

This work was supported by the project "*REPTES - Renewable Plants Integrated with Pumped Thermal Energy Storage for Sustainable Satisfaction of Energy and Agricultural Needs of African Communities*" under the LEAP-RE programme. The LEAP-RE programme has received funding from the European Union's Horizon 2020 Research and Innovation Program under Grant Agreement No. 963530.

References

[1] A. Jain, S. Yamujala, A. Gaur, P. Das, R. Bhakar, J. Mathur, Power sector decarbonization planning considering renewable resource variability and system operational constraints, Appl. Energy. 331 (2023) 120404. https://doi.org/10.1016/J.APENERGY.2022.120404.

[2] Y. Shang, S. Sang, A.K. Tiwari, S. Khan, X. Zhao, Impacts of renewable energy on climate risk: A global perspective for energy transition in a climate adaptation framework, Appl. Energy. 362 (2024) 122994. https://doi.org/10.1016/J.APENERGY.2024.122994.

[3] C. Poletto, O. Dumont, A. De Pascale, V. Lemort, S. Ottaviano, O. Thomé, Control strategy and performance of a small-size thermally integrated Carnot battery based on a Rankine cycle and combined with district heating, Energy Convers. Manag. 302 (2024) 118111. https://doi.org/10.1016/J.ENCONMAN.2024.118111

[4] L.M. Hadelu, A. Noorpoor, F.A. Boyaghchi, Assessment and multi-objective dragonfly optimization of utilizing flash tank vapor injection cycle in a new geothermal assisted-pumped thermal energy storage system based on transcritical CO2 cycle, J. Energy Storage. 88 (2024) 111628. https://doi.org/10.1016/J.EST.2024.111628.

[5] Y. Zhang, J. Liu, Z. Liu, Thermo-economic examination of ocean heat-assisted pumped thermal energy storage system using transcritical CO2 cycles, Appl. Therm. Eng. 255 (2024) 123992. https://doi.org/10.1016/J.APPLTHERMALENG.2024.123992.

[6] G.F. Frate, L. Ferrari, U. Desideri, Multi-criteria investigation of a pumped thermal electricity storage (PTES) system with thermal integration and sensible heat storage, Energy Convers. Manag. 208 (2020) 112530. https://doi.org/10.1016/J.ENCONMAN.2020.112530.

[7] D. Zinsmeister, P. Tzscheutschler, V.S. Perić, C. Goebel, Stratified thermal energy storage model with constant layer volume for predictive control — Formulation, comparison, and empirical validation, Renew. Energy. 219 (2023) 119511. https://doi.org/10.1016/J.RENENE.2023.119511.

[8] B. Kurşun, K. Ökten, Comprehensive energy, exergy, and economic analysis of the scenario of supplementing pumped thermal energy storage (PTES) with a concentrated photovoltaic thermal system, Energy Convers. Manag. 260 (2022) 115592. https://doi.org/10.1016/J.ENCONMAN.2022.115592

[9] K. Ökten, B. Kurşun, Thermo-economic assessment of a thermally integrated pumped thermal energy storage (TI-PTES) system combined with an absorption refrigeration cycle driven by low-grade heat source, J. Energy Storage. 51 (2022) 104486. https://doi.org/10.1016/J.EST.2022.104486.

[10] DuPont™, Water solutions: FilmTec™ Reverse Osmosis Membranes Technical Manual, Costa Brava Region, Spain, 2020. https://www.dupont.com/content/dam/dupont/amer/us/en/water-solutions/public/documents/en/RO-NF-FilmTec-Manual-45-D01504-en.pdf.

NUMERICAL MODELLING OF A 50 KWE REVERSIBLE CARNOT BATTERY COUPLED WITH WASTE HEAT

Aitor Cendoya[1]*, Frederic Ransy[1], Vincent Lemort[1], Olivier Dumont[1],Bentao Guo[1] and Pierre Dewallef[1]

[1] Thermodynamics Laboratory, Faculty of Applied Sciences, University of Liege, Liege, Belgium

** Corresponding Author: acendoya@uliege.be*

Abstract. The full integration of renewables into the electricity grid has become one of the biggest challenges to support the full migration to a non-fossil fuel energy mix. Intermittency and randomness of Renewable Energy Sources (RES) are some of the aspects that constrain grid integration. Energy storage is a key factor in connecting RES to the grid. Among energy storage, Carnot battery technology provides great benefits due to the easy integration of various heat sources and improved flexibility. Nowadays, this technology is mainly developed on a laboratory scale, and finding commercial components is difficult and expensive. This article presents the modelling of a reversible Carnot battery coupled to a sensitive energy storage. The numerical modelling of the system has been presented and validated against manufacturer data. The integration of the components was implemented in Python, obtaining as a result the refrigerant charge and the operation map for charging and discharging modes. The presented design achieves a round-trip efficiency of up to 49.5%, at design conditions, and a charge difference ratio of 3 between Organic Rankine and heat pump modes. This difference highlights the necessity of a charge management system, such as a liquid receiver, to ensure proper operation across modes.

Keywords. Reversible HP/ORC, Energy transition, Waste heat, Refrigerant charge

Nomenclature

h	Specific enthalpy (J/kg)
M	Mass (kg)
$\dot{M}$	Mass flow rate (kg/s)
P	Pressure (Pa)
$\dot{Q}$	Heat Power (kW)
r	Ratio
T	Temperature (°C)
V	Volume (m^3)
$\dot{W}$	Electrical Power (kW)
x	Quality (-)

Special characters

ε	Effectiveness (-)
η	Efficiency (-)
Δ	Difference (-)
ρ	Density (kg/m^3)

Subscripts

cd	Condenser
cp	Compressor
ev	Evaporator
ex	Exhaust
exp	Expander
HP	Heat pump
hx	Heat exchanger
ORC	Organic Rankine cycle
pp	Pump
pre	Preheater
r	Refrigerant
sat	Saturation
sc	Subcooling
sh	superheating
su	Supply
tp	Two-Phase
v	Volumetric
void	Void
w	Water
zi	Zone

1 Introduction

Currently, RES constitute approximately 30.24% of the global energy mix [1]. Nevertheless, the RES are inherently variable and subject to fluctuations, leading to frequent mismatches between energy production and consumption [2]. Therefore, to integrate more RES into the energy mix, energy storage systems are essential, acting as a buffer between supply and demand [3].

Storage technologies are generally classified into six main categories: mechanical, electrochemical, electrical, thermochemical, chemical, and thermal storage systems [4]. One technology that does not suffer from geographical constraints presents a long life cycle, and high energy density depending on the storage medium corresponds to Carnot Batteries (CBs) [5].

CBs have the potential to integrate different types of energy sources. This type of system is often referred to as Thermally Integrated Pumped Thermal Energy Storage (TI-PTES), and it has attracted significant interest, particularly in applications connected with District Heating Networks (DHN) [6]. TI-PTES systems can significantly improve overall performance and offer the added advantage of enabling seasonal energy storage for multi-energy dispatch [7], such as heating, cooling and electricity based on the user's demand.

Among CB systems, the reversible design offers notable advantages due to its compact configuration, allowing it to operate as both a Heat Pump (HP) and an Organic Rankine Cycle (ORC) system using the same set of components [8]. This design reduces the Levelized Cost of Storage (LCOS) [9], as the shared use of major components substantially lowers initial investment costs compared to other types of CB systems [10].

Several prototypes have been proposed, and different challenges identified such as charge management, pressure drops for 4-way valves, oil management, reversible operation, overheating in the components, etc [11], [12]. This paper focuses on maximizing component reuse within Rankine-CB systems to enhance affordability while streamlining production and facilitating broader deployment of CB technology. This encourages the transition from fossil fuel energy production to RES, increasing the participation of energy storage in the energy mix. The main objective and novelty of this work is the application of reversible CB integrating low-grade waste heat, as the design considered to avoid the problems reported by researchers. This is achieved by numerical modelling of the different components used in the presented CB, which are validated against selected shell components. The operation maps and critical design considerations are obtained.

2 Methodology

The methodology presents the boundary and design conditions to reach the target power of 50 kW_e in ORC mode and 400 kW_{th} in HP mode. Secondly, the modelling and model validation of each component is presented. Finally, the integration of each model is carried out in Python by a modular approach.

2.1 Design conditions

The reversible CB system is designed to operate in two modes: as a HP for converting electricity into heat and as an ORC for generating electricity from stored heat. The storage medium is pressurised water at 4 bars, selected to maintain operational temperatures below 135°C, aiming to avoid any risk of oil degradation. The CB shares core components across both modes, including heat exchangers (HXs), a volumetric machine, a liquid receiver, refrigerant and water piping. Here, a 4-way valve arrangement on the water loops is considered to always guarantee a counterflow in the HXs.

The system is designed to operate under different conditions for each mode. In ORC mode, the nominal conditions include a water supply temperature of 90°C at the evaporator and 15°C at the condenser. Whereas, in HP mode, the system is configured for a water supply temperature of 90°C at the condenser and 55°C at the evaporator. Additionally, low-temperature Waste Heat (WH) at 70°C is integrated into the ORC's preheater. The WH temperature considered represents the average temperature of several processes. Moreover, this temperature can also be found in geothermal sources or DHN or the integration within solar sources [6]. Figure 1 presents the integration of the system within their typical operational temperature scheme. The design conditions were selected to achieve a target electrical output of approximately 50 kW_e in ORC mode and a thermal output of 400 kW_{th} in HP mode. These values are selected to be integrated with different energy sources from flooded abandoned mines in the city of Martelange in the south of Belgium. The idea is to connect the system to the different temperature levels of the mines, as well as to the system on the surface, which has a DHN and a low-temperature waste heat network from a thermal photovoltaic plant.

The working fluid selected for this system corresponds to R1233zd(E). Several reasons are

taken into account as its low Global Warming Potential (GWP) and high performance in CB applications for the considered range of temperatures [13]. The selected components correspond to the HSEL8591 screw expander from Bitzer, chosen for its dual functionality in both ORC and HP modes. Braze Plate Heat Exchangers (BPHXs) from Alfa Laval were selected due to their high efficiency and low-pressure drops. KSB vertical centrifugal pump was chosen for its low Net Positive Suction Head (NPSH) requirements and high efficiency. The pump is used exclusively during the ORC mode. Additionally, an expansion valve is incorporated to operate exclusively in HP mode.

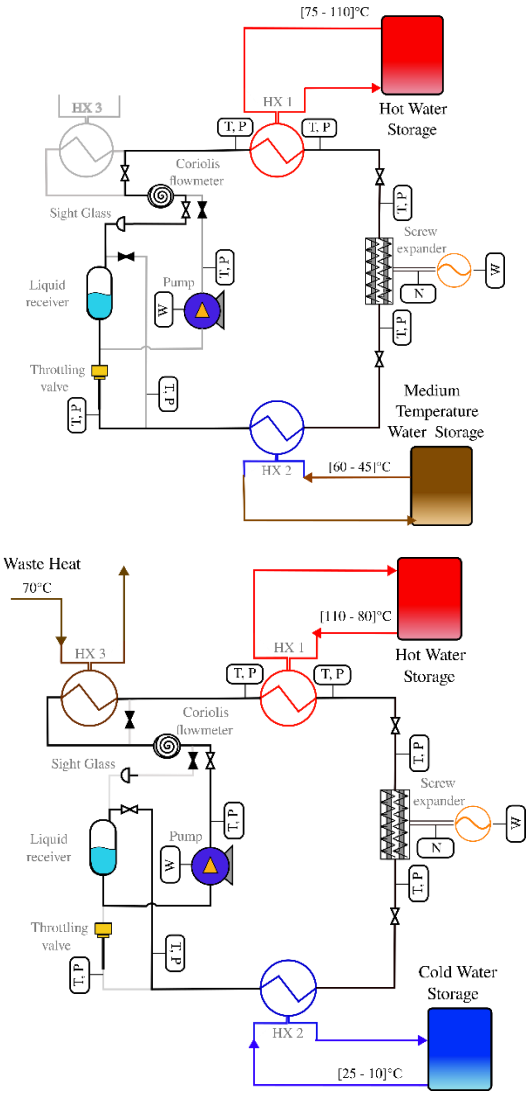


Figure 1: Boundary conditions of the reversible machine HP mode (top) and ORC mode (bottom).

2.2 Components modelling

2.2.1 Condenser: For this type of heat exchanger, the heat is transferred from the refrigerant (working fluid (wf)) to the secondary fluid (sf). Usually, the sf could vary between oil, water or brine. The heat transfer process is discretized in three zones from the wf to the sf. We can identify three important zones (zi), the superheated (sh), the two-phase (tp) and the subcooled (sc) zone. In each of these zones heat and energy balance are computed according to the methodology presented by Cuevas et al. [14]. The energy balance for the water (sf) side is presented in Equation 1 and the heat transfer process in Equation 2. A counterflow configuration is considered in the plates of the BPHX.

$$\dot{Q}_{zi,cd} = \dot{M}_w \cdot \left(h_{w,ex,zi,cd} - h_{w,su,zi,cd}\right) \quad (1)$$

$$\dot{Q}_{zi,cd} = \varepsilon_{zi,cd} \cdot \dot{C}_{min,zi,cd} \cdot \left(t_{r,su,zi,cd} - t_{w,su,zi,cd}\right) \quad (2)$$

2.2.2 Evaporator: The evaporator model follows the same methodology as the condenser, with the difference that the process is inverse. Now the secondary fluid transfers heat to the refrigerant, so instead of condensing the refrigerant now starts to boil. In the case of the HP, the evaporators work in two zones (two-phase and superheating). In ORC mode could operate in also two zones but normally operates in three (subcooling, two-phase and superheating), because the subcooling after the pump normally is larger.

2.2.3 Preheater: In the case of the preheater now there is the possibility depending on the source and temperature that there is refrigerant evaporation. However, normally the preheater is used to remove a large part of the liquid zone of the refrigerant before entering the evaporator. This aims to increase the heat transfer performance between the large part of the subcooling and the evaporation process.

2.2.4 Expander: The expander model is based on the methodology presented by Lemort et al. [15] for a scroll expander, which applies to semi-hermetic machines like the selected expander. This model is preferred because it can represent not only the real performance as polynomials but also the physical effects inside the machine. The model includes a calibration phase, requiring manufacturer data or experimental information to fine-tune the model and identify the parameters. This methodology has already been implemented in reversible machines, as demonstrated by Mateu-Royo et al. [16], who presented the performance map of an innovative reversible machine using this approach, and Pezo et al.[17] for the compression part of the reversible machine.

This model relies on several parameters which must identified during the calibration process between the model and the data provided by the manufacturer or experimentally. The expander parameters are determined from the operational points provided by Bitzer for the expander HSEL8591. The parameters are obtained by calibrating the model within 17 operation points.

2.2.5 Compressor: For the screw machine in compressor mode it was not possible to obtain operating points or data to replicate the compressor semi-empirical model. For that reason, and following the discussion with the manufacturer first, the performance of the screw should be similar to the expander mode as long as the compressor works in the envelope of the machine, which is limited by the generator/motor and operational speed chosen.

To represent the same screw machine, the volumetric ratio and swept volume at constant speed are obtained from Bitzer manufacturer. With that and through equation 3, it is possible to compute the compression swept volume as depends on the volume ratio [18]. During this process the isentropic efficiency ($\varepsilon_{s,cp}$) and volumetric efficiency ($\varepsilon_{v,cp}$), are obtained from the expander model.

$$V_{s,cp} = V_{s,exp} \cdot r_{v,exp} \tag{3}$$

2.2.6 Pump: The operation of the pump is modelled using a set of dimensionless factors: the pressure factor (ψ), the flow factor (ϕ), and the power factor (λ) [19]. These factors depend on the geometry and performance curves of the pump. The selected pump is a vertical centrifugal model, specifically the KSB Movitec V F010/11, which will be used in ORC mode.

2.2.7 Charge, Heat Transfer Coefficients (HTC) and Pressure Drop Correlations (PDC): Different correlations were employed depending on the operational regime of the fluid. Table 1 presents the specific correlations applied and for which regime.

The refrigerant charge for the different conditions is divided into 2 types. The first one corresponds when there is a single refrigerant phase, where Equation 4 presents the procedure to obtain the charge. The second case corresponds to a two-phase state, where the charge is calculated using the correlation of Cioncolini and Thome (2012) [20] for annular two-flow, presented in Equation 5, for which a discretisation of 100 steps is considered between the supply and output quality.

$$M_{r,zi} = V_{zi} \cdot (\rho_{su_{zi}} + \rho_{ex,zi})/2 \tag{4}$$

$$M_{r,tp} = \int_{x_{su}}^{x_{ex}} V_{tp}/\Delta x \cdot \rho_{void}(x)\, dx \tag{5}$$

Table 1: HTC and PD Correlations

Fluid	Regime	HTC	PDC
(r)	Single phase	Holger M. (2010) [21]	
	Condensation	Shah et al. (2021) [22]	Longo G.A (2010) [23]
	Boiling	Amalfi et al. (2016) [24], [25]	
(w)	Single phase	Holger M. (2010) [21]	

2.3 Model validation

The model validation is made through data comparison within manufacturing, where the main variables are compared. For the expander the data is compared within the Bitzer manufacturer, the main outputs; refrigerant mass flow rate, expander power and the exhaust temperature of the expander present errors lower than ±5%, ±5% and ±5K, respectively.

The brazed plate heat exchangers are validated against the Alfa Laval manufacturer data for the nominal operation point in both modes. The performance of the model is presented in Table 2 for the different BPHXs. These values are obtained at the nominal operation design, as usually the manufacturer does not provide partial operation.

Table 2: BPHX validation within manufacturer data.

BPHX Model	Mode	Heat Power	Pressure drops	Temperature difference
CB410-200M	Condenser	± 0.41%	±3.2%	±1.12 °C
	Evaporator	± 2.98%	±5.9%	±1.51 °C
CBH210-170AH	Evaporator	± 1.76%	±0.05%	±0.2 °C
	Condenser	± 0.57%	±0.4%	±1.22 °C
CB210-60AM	Preheater	± 3.31%	±7.7%	±0.1 °C

The curve fit of the pump presents a R^2 of 99.5% and 97.6% for the ϕ and λ, respectively. The pump curve fits the non-dimensional factors based on the ψ. Moreover, as the models are validated stand-alone, is assumed that during the integration the whole system will be validated as well.

2.4 Model integration

The model integrations are carried out according to the scheme presented in Figure 2, which shows the inputs and outputs of the models. Here a modular

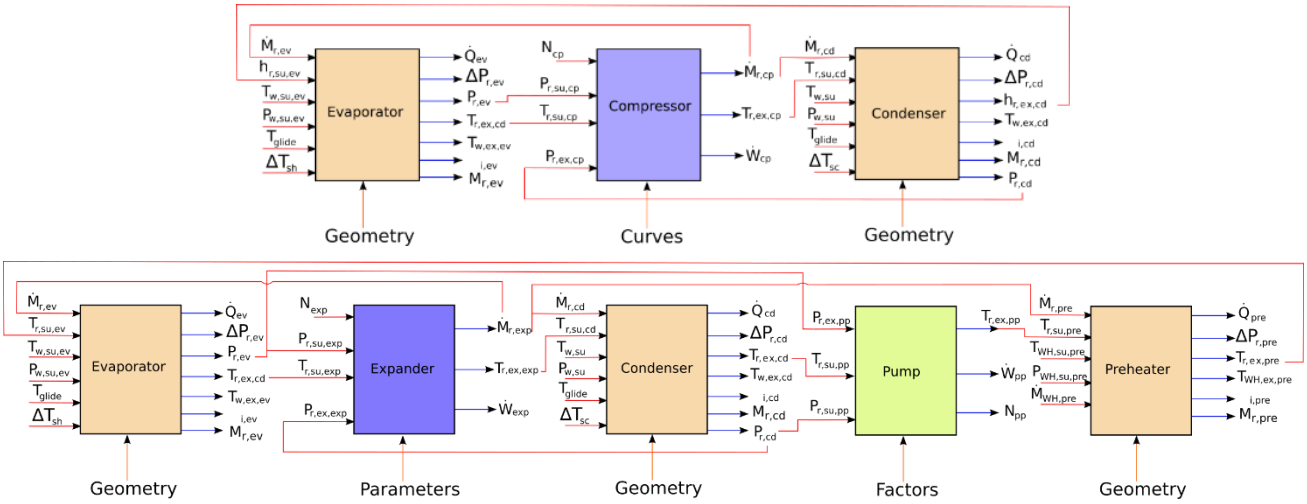


Figure 2: Sub-models interaction HP mode (top) and ORC mode (bottom).

approach of the models was carried out in Python, where the thermodynamic properties were obtained from CoolProp and the numerical method to find the root of the system while operating for the different boundary conditions was extracted from SciPy. Moreover, each module is developed with modularity to allow for easy integration.

The expansion valve is integrated assuming that can keep a constant evaporator's overheating. Moreover, the liquid receiver can store the entire refrigerant charge and maintain the same pressure as the condenser in HP and ORC modes.

In this approach, the operational pressure is imposed by the geometry of the heat exchangers and the boundary conditions. The models iterate within 7 variables in HP mode:

- CD: $P_{r,sat,cd,HP}$ $\Delta P_{sh,cd,HP}, \Delta P_{tp,cd,HP}, \Delta P_{sc,cd,HP}$
- EV: $P_{r,sat,ev,HP}, \Delta P_{tp,ev,HP}, \Delta P_{sh,ev,HP}$

Whereas in ORC mode iterates within 9 variables:

- CD: $P_{r,sat,cd,ORC}, \Delta P_{sh,cd,ORC}, \Delta P_{tp,cd,ORC}, \Delta P_{sc,cd,ORC}$
- EV: $P_{r,sat,ev,ORC}, \Delta P_{sc,ev,ORC}, \Delta P_{tp,ev,ORC,}$ $\Delta P_{sh,ev,ORC}$
- PRE: $h_{w,ex,pre,ORC}, \Delta P_{pre,ORC}$

The system iterates until finds a solution when the residual of each variable is lower than $1 \cdot 10^{-6}$. Once, the system reaches these residuals in each variable, is assumed that the operational point is found.

3 Results and analysis

This section will present the performance operation and discuss the results between both modes of operation; discharging mode (ORC) and charge mode (HP). As mentioned only the machine is limited to the operational envelope provided by the manufacturer at 50 Hz and within the chosen generator. This envelope will limit the operation for both modes and all the presented results will be limited for the envelope.

3.1 ORC Mode

In ORC mode, a low-temperature WH source at 70°C is integrated, represented by water at 4 bars, with a steady supply to the BPHX preheater at a fixed mass flow rate of 14.3 kg s^{-1}. A constant temperature glide of 5 K on the evaporator and 7 K on the condenser is achieved by adjusting the water volume flow rate via variable-speed pumps to maintain thermal efficiency. Those values were selected to have good heat transfer and not large pressure drops on the selected BPHXs.

Figure 3 illustrates the required source fluid (sf) temperatures to reach the different saturation temperatures within the ORC. Here, the hot heat exchanger corresponds to the evaporator and the cold to the condenser.

Importantly, as the evaporator saturation temperature rises, the temperature difference between the refrigerant and the sf increases. Additionally, the condenser saturation temperature is influenced by both water temperatures as the exhaust of the expander directly supplies the condenser, so any changes in the evaporator temperature will affect the condenser.

The electricity power produced by the expander is presented in Figure 4. For the different operational conditions, it is important to note that the maximum expander outpower can reach up to 77 kW. This is constrained by the maximum torque on the generator/motor. In contrast, the minimum outpower corresponds to 28 kW. Note that different speeds or different generator models will generate different expander envelopes.

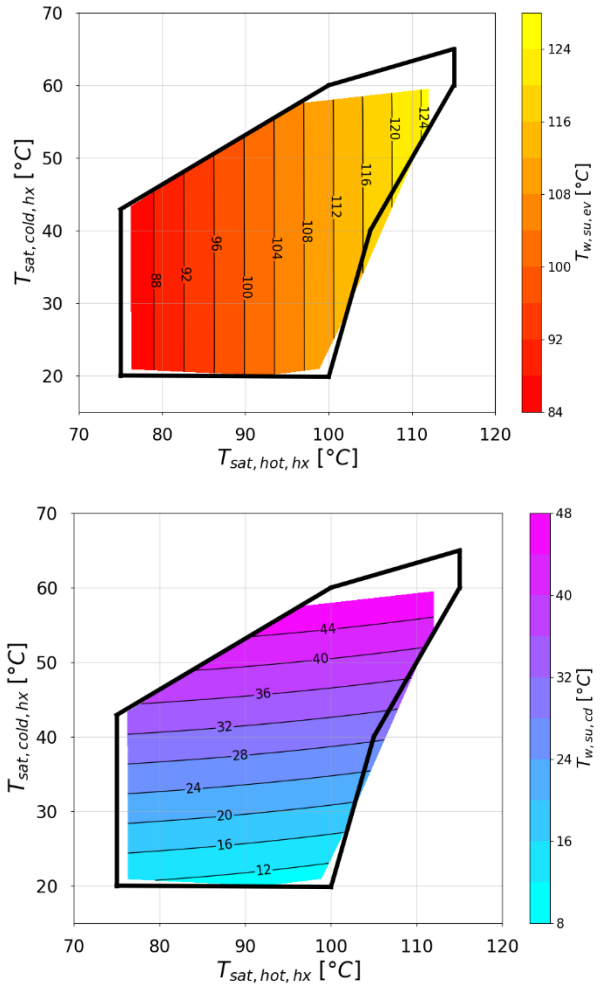


Figure 3: Required temperatures in ORC mode, evaporator (top) and condenser (bottom).

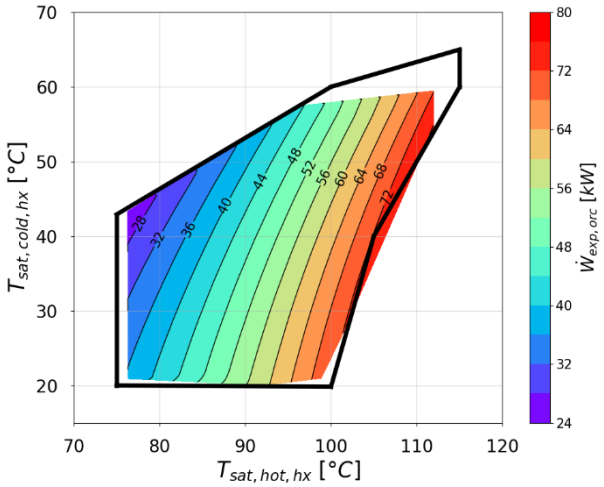


Figure 4: Electricity production of the expander.

The total electricity production must account for the consumption of the pump which, according to simulation, achieves an efficiency up to 70%. This corresponds to a significant performance, as pumps in previous test benches often encountered issues due to low efficiency. This result aligns with the findings of Dumont et al. [8], who indicated that centrifugal pumps are optimal for reversible machines.

The performance of the ORC in reversible machines typically does not reach optimal values due to various operational issues, such as charge management, larger pressure drops, and the lack of suitable volumetric machines on the market. However, "high-performance" values can be achieved here thanks to the integration of WH, which serves as a free energy source. Equation 6 is employed to compute the ORC performance for the entire operational envelope. This equation excludes the sf fluid pump energy consumption.

$$\eta_{ORC} = (\dot{W}_{exp,orc} - \dot{W}_{pp,orc})/\dot{Q}_{ev,orc} \quad (6)$$

The performance map is presented in Figure 5. Here, the maximum performance of the ORC is achieved under the design conditions, (sf supply temperature of 90°C at the evaporator and 15°C at the condenser). The performance of the ORC appears to be independent of the evaporator temperature. However, it begins to change as the condenser temperature varies. This suggests that the ORC efficiency can remain the same under different water supply conditions to the evaporator. Further analysis reveals that these same performances in two evaporator temperatures are driven by the increases in the pressure drops in the BPHXs and decreased expander performance because the refrigerant must be driven at a higher pressure ratio.

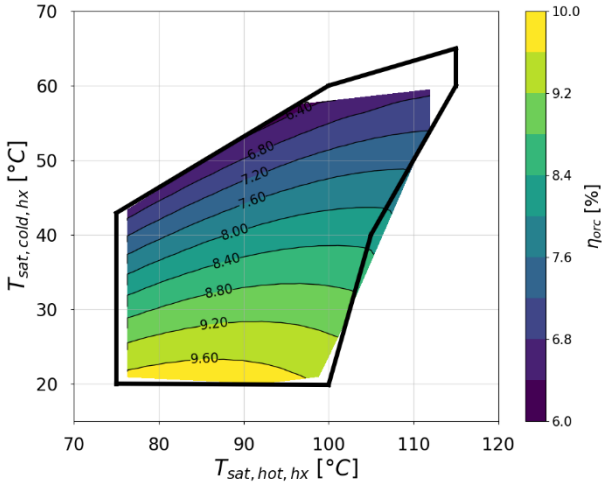


Figure 5: ORC efficiency map.

3.2 HP performance

For the HP mode, a medium temperature source was considered supplied to the evaporator, which can represent a DHN or a geothermal source. Ideally, this hot source is used in the cold sink of the heat pump to improve the Coefficient of Performance (COP)

while operating at high temperatures in the HP condenser. The condenser is in charge of charging the sensible storage, which is later used for ORC operation. The water temperatures are obtained with fixed sf mass flow rates, for the condenser and evaporator the values correspond to 14.3 and 22 kg s^{-1}, respectively. It is important to highlight that these values are the mass flow rates used in ORC mode under design conditions. This approach was chosen to prevent low heat transfer coefficients on the waterside and ensure better performance. Additionally, this consideration results in a smaller temperature difference between the fluids compared to ORC mode. Figure 6 presents the required water temperatures for different operational conditions, where the cold heat exchanger corresponds to the evaporator and the hot one to the condenser.

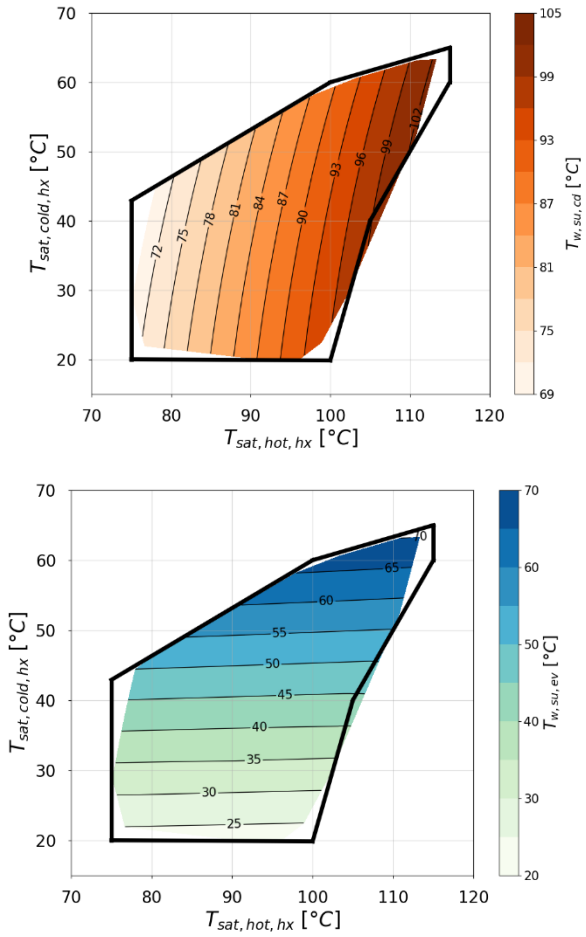


Figure 6: Required temperatures in HP mode, condenser (top) and evaporator (bottom).

The heat power transfer from the refrigerant to the water is depicted in Figure 7. This heat capacity is influenced by the supply temperatures. The required heat output (400 kW) in HP)mode is achieved under the design conditions of 55°C in the evaporator and 90°C in the condenser. It is also important to observe that the heat transfer fluctuates significantly across the operating envelope. This variability can be attributed to the changes in the COP, as shown in Figure 8. The COP values exhibit a wide range, varying from 3 to 7.5 throughout the envelope.

The observed variation in the COP is expected, as a lower temperature lift between the two heat exchangers typically results in higher performance. The equation used to calculate the COP is given by Equation 7. It is important to note that the energy consumption of the water circulation pumps (sf pumps) is excluded in this analysis.

$$COP_{HP} = \dot{Q}_{cd,HP}/\dot{W}_{cp,HP} \quad (7)$$

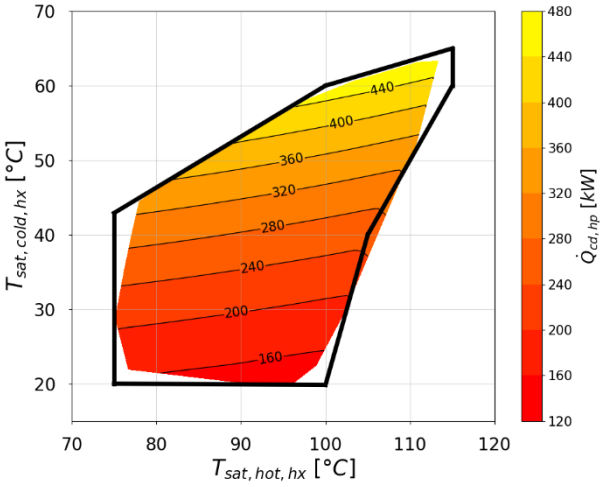


Figure 7: Heat power capacity in HP mode.

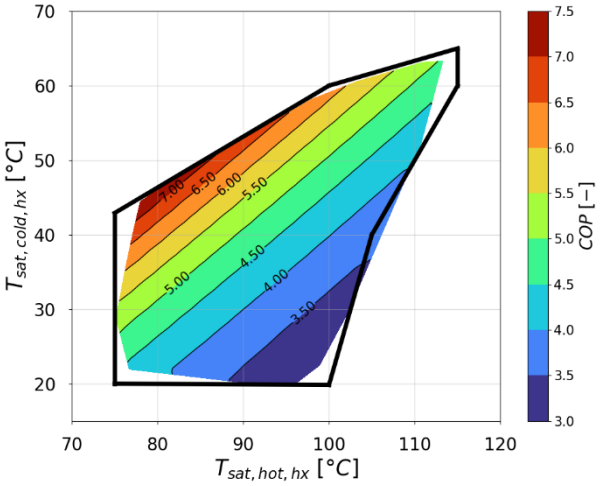


Figure 8: Coefficient of Performance of the HP.

3.3 Reversible operation

The charge difference between both modes is one of the main challenges in the reversible integration of volumetric machines into CBs. To achieve a decent performance of the machine in both HP and ORC modes, it has been suggested to adjust the Reynolds

number ratio [8]. However, this adjustment is difficult to implement when only a single volumetric machine is used. The operating envelope constraints for reversible machines limit the capacity to manage the charge smoothly and flexibly between modes.

Charge management is crucial in the design of a reversible machine to prevent issues such as excessive subcooling at the condenser exhaust, which can negatively impact ORC performance [21]. Moreover, improper charge management can lead to the failure of components, such as the ORC pump, due to vapour generation at the pump's suction, potentially causing cavitation [11]. These problems can significantly compromise both the efficiency and the reliability of the system

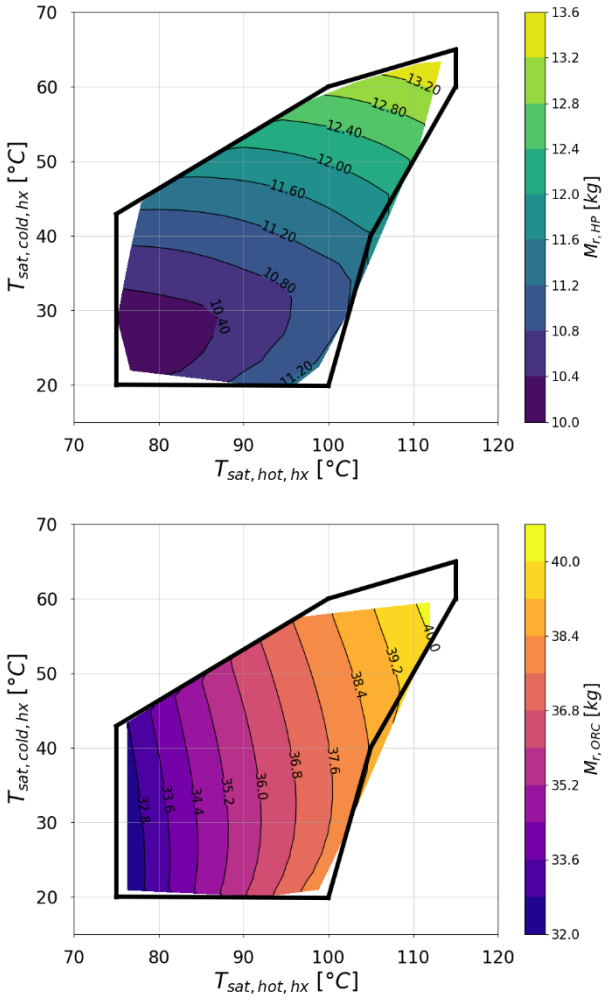


Figure 9: Refrigerant charges in the CB, for the HP (top) and for the ORC (bottom).

Figures 9a and 9b compare the charge values for the HP and ORC modes, highlighting the challenges in charge management. On one hand, the ORC can reach charge values of up to 40 kg of refrigerant, while the HP mode requires only 13.2 kg, resulting in a charge ratio of approximately 3. This difference is expected, as the ORC system has a larger liquid refrigerant zone between the pump and the evaporator.

There are two potential methods to manage this charge difference. The first approach involves increasing the subcooling in the HP condenser, although this will result in a reduction in the HP performance. The second option is to incorporate a liquid receiver capable of operating in both HP and ORC modes. This would allow for the storage of excess charge from one mode, which can then be used to meet the charge requirements of the other mode without compromising performance. However, the integration of the liquid receiver must be done carefully. At the exhaust of the liquid receiver, the refrigerant is in a saturated liquid state, so enough height must be considered in the design, to meet the NPSH required by the pump to avoid cavitation problems. In the present paper, Figure 1 presents the integration of the liquid receiver in the scheme of the machine, able to operate in HP and ORC modes. This configuration will allow for storage of the excess charge during ORC mode, ensuring that the system can operate effectively in HP mode. Similarly, the liquid receiver will allow it to operate optimally throughout the entire operational envelope in ORC mode, even when the machine is operating outside of the design point

The charge distribution at the design conditions is presented in Table 3. The different charge in the heat exchanger is compared as along the pipes the same amount of refrigerant will be. The difference between modes is made by the preheater, where the large part of the liquid zone of the refrigerant takes place.

Table 3: BPHX charge distribution for the design conditions.

BPHX Model	Zone	ORC [kg]	HP [kg]
	sc	3.22	1.59
CB410-200M	*tp*	5.58	6.60
	sh	0.06	0.06
	sc	5.00	-
CBH210-170AH	*tp*	4.92	3.63
	sh	0.07	0.07
CB210-60AM	*sc*	14.62	-
Total		33.47	11.95

The charge distribution under design conditions is presented in Table 2. The different charges in the heat exchangers are compared. Here, it is clear that the primary difference between the modes occurs in the preheater, where the majority of the refrigerant's liquid phase takes place. The percentage of charge

that is present in this heat exchanger corresponds to 43.7% of the total ORC charge.

4 Conclusions

This paper presents some of the key findings from the design process of a reversible Carnot Battery. Numerical models have been developed in Python, and validation was conducted using manufacturer data. The high accuracy of the models for the expander, heat exchangers, and pump ensures that the system can effectively capture the physical phenomena occurring during the processes.

The performance map of the reversible machine integrating waste heat has been presented, demonstrating promising results. The ORC performance can reach values of up to 9.7% (Water at: 90°C (ev), 12.5°C (cd) and 70°C (pre)) which is attributed to the efficient operation of both the heat exchanger and the pump. In contrast to previous test benches in the literature, where the pump is typically an exergy destructor, the pump in this system operates efficiently. On the other hand, the HP COP can achieve high values, reaching approximately 5.1 (Water at: 90°C (cd) and 55°C (ev)), thanks to its integration with a geothermal source. This results in a RTE efficiency of 49.5%. This implies that variability in the electricity price of at least a factor of 2 is necessary to derive benefits from reversible storage.

Several operational conditions were analysed, and one of the major challenges of reversible machine integration is also discussed. Charge management was examined, highlighting that achieving the same refrigerant charge within the same machine is difficult. In this context, the liquid receiver plays a key role in charge management. However, the pump Net Positive Suction Head must be carefully considered during the design process to avoid cavitation problems, as the refrigerant will reach a saturated liquid state.

Acknowledgement

The project that produced the results presented in this paper has received funding from the European Union's Horizon Research and Innovation programme under grant agreement No. 10112355, in the framework of the WeForming project. The authors would also like to acknowledge the funding provided by the Walloon Region of Belgium in the framework of the ARDNrgy project.

References

[1] H. Ritchie, P. Rosado, and M. Roser, 'Electricity mix', *Our World in Data*, 2024, Accessed: Nov. 03, 2024. [Online]. Available: https://ourworldindata.org/electricity-mix

[2] B.-M. Hodge, C. Brancucci Martinez-Anido, Q. Wang, E. Chartan, A. Florita, and J. Kiviluoma, 'The combined value of wind and solar power forecasting improvements and electricity storage', *Applied Energy*, vol. 214, pp. 1–15, Mar. 2018, doi: 10.1016/j.apenergy.2017.12.120.

[3] A. Vecchi *et al.*, 'Carnot Battery development: A review on system performance, applications and commercial state-of-the-art', *Journal of Energy Storage*, vol. 55, p. 105782, Nov. 2022, doi: 10.1016/j.est.2022.105782.

[4] X. Luo, J. Wang, M. Dooner, and J. Clarke, 'Overview of current development in electrical energy storage technologies and the application potential in power system operation', *Applied Energy*, vol. 137, pp. 511–536, Jan. 2015, doi: 10.1016/j.apenergy.2014.09.081.

[5] G. F. Frate, L. Ferrari, and U. Desideri, 'Multi-Criteria Economic Analysis of a Pumped Thermal Electricity Storage (PTES) With Thermal Integration', *Front. Energy Res.*, vol. 8, p. 53, Apr. 2020, doi: 10.3389/fenrg.2020.00053.

[6] C. Poletto, O. Dumont, A. De Pascale, V. Lemort, S. Ottaviano, and O. Thomé, 'Control strategy and performance of a small-size thermally integrated Carnot battery based on a Rankine cycle and combined with district heating', *Energy Conversion and Management*, vol. 302, p. 118111, Feb. 2024, doi: 10.1016/j.enconman.2024.118111.

[7] A. Cendoya, F. Ransy, V. Lemort, A. Hernandez, P.-H. Gresse, and J. Windeshausen, 'Modelling and Simulation of a Carnot Battery Coupled to Seasonal Underground Stratified Thermal Energy Storage for Heating, Cooling and Electricity Generation', in *International High Performance Buildings Conference*, West-Lafayette, United States - Indiana: University of Purdue, 2024, p. 10. [Online]. Available: https://docs.lib.purdue.edu/ihpbc/472/

[8] O. Dumont, 'Investigation of a heat pump reversible in an organic Rankine cycle and its

application in the building sector', ULiège - Université de Liège, Liège, 2017. [Online]. Available: https://orbi.uliege.be/handle/2268/218181

[9] X. Yu, H. Qiao, B. Yang, and H. Zhang, 'Thermal-economic and sensitivity analysis of different Rankine-based Carnot battery configurations for energy storage', *Energy Conversion and Management*, vol. 283, p. 116959, May 2023, doi: 10.1016/j.enconman.2023.116959.

[10] S. Daniarta, P. Kolasiński, and A. R. Imre, 'Performance map and theoretical analysis of Carnot battery technology via novel reversible Rankine-based cycle', *Energy Reports*, vol. 11, pp. 4500–4514, Jun. 2024, doi: 10.1016/j.egyr.2024.04.024.

[11] M. Weitzer, D. Müller, and J. Karl, 'Reversible Heat Pump-ORC Pilot Plant – Experimental Results and Fluid Charge Optimization', in *Proceedings of the 7th International Seminar on ORC Power System (ORC 2023)*, 2024th ed., Editorial Universidad de Sevilla, 2023, pp. 430–438. doi: 10.12795/9788447227457_72.

[12] O. Dumont, A. Charalampidis, and V. Lemort, 'Experimental Investigation Of A Thermally Integrated Carnot Battery Using A Reversible Heat Pump/Organic Rankine Cycle', in *International Refrigeration and Air Conditioning Conference*, West-Lafayette, United States - Indiana: University of Purdue, 2021, p. 14. [Online]. Available: https://docs.lib.purdue.edu/iracc/2085

[13] O. Dumont and V. Lemort, 'Mapping of performance of pumped thermal energy storage (Carnot battery) using waste heat recovery', *Energy*, vol. 211, p. 118963, Nov. 2020, doi: 10.1016/j.energy.2020.118963.

[14] C. Cuevas, J. Lebrun, V. Lemort, and P. Ngendakumana, 'Development and validation of a condenser three zones model', *Applied Thermal Engineering*, vol. 29, no. 17–18, pp. 3542–3551, Dec. 2009, doi: 10.1016/j.applthermaleng.2009.06.007.

[15] V. Lemort, S. Declaye, and S. Quoilin, 'Experimental characterization of a hermetic scroll expander for use in a micro-scale Rankine cycle', *Proceedings of the Institution of Mechanical Engineers, Part A: Journal of Power and Energy*, vol. 226, no. 1, pp. 126–136, Feb. 2012, doi: 10.1177/0957650911413840.

[16] C. Mateu-Royo, A. Mota-Babiloni, J. Navarro-Esbrí, B. Peris, F. Molés, and M. Amat-Albuixech, 'Multi-objective optimization of a novel reversible High-Temperature Heat Pump-Organic Rankine Cycle (HTHP-ORC) for industrial low-grade waste heat recovery', *Energy Conversion and Management*, vol. 197, p. 111908, Oct. 2019, doi: 10.1016/j.enconman.2019.111908.

[17] M. Pezo, C. Cuevas, E. Wagemann, and A. Cendoya, 'Net Zero Energy Building technologies – Reversible Heat Pump/Organic Rankine Cycle coupled with Solar Collectors and combined Heat Pump/Photovoltaics – Case study of a Chilean mid-rise residential building', *Applied Thermal Engineering*, vol. 252, p. 123683, Sep. 2024, doi: 10.1016/j.applthermaleng.2024.123683.

[18] V. Lemort, S. Quoilin, C. Cuevas, and J. Lebrun, 'Testing and modeling a scroll expander integrated into an Organic Rankine Cycle', *Applied Thermal Engineering*, vol. 29, no. 14–15, pp. 3094–3102, Oct. 2009, doi: 10.1016/j.applthermaleng.2009.04.013.

[19] B. Eck and B. Eck, *Fans: design and operation of centrifugal, axial-flow and cross-flow fans*, 1. engl. ed. Oxford: Pergamon Pr, 1973.

[20] A. Cioncolini and J. R. Thome, 'Void fraction prediction in annular two-phase flow', *International Journal of Multiphase Flow*, vol. 43, pp. 72–84, Jul. 2012, doi: 10.1016/j.ijmultiphaseflow.2012.03.003.

[21] Holger Martin, Ed., 'N6: Pressure Drop and Heat Transfer in Plate Heat Exchangers', in *VDI HeatAtlas: Chapter*, Berlin, Heidelberg: Springer Berlin Heidelberg, 2010. doi: 10.1007/978-3-540-77877-6.

[22] M. M. Shah, 'Heat transfer during condensation in corrugated plate heat exchangers', *International Journal of Refrigeration*, vol. 127, pp. 180–193, Jul. 2021, doi: 10.1016/j.ijrefrig.2021.02.011.

[23] G. A. Longo, 'Heat transfer and pressure drop during HFC refrigerant saturated vapour condensation inside a brazed plate heat exchanger', *International Journal of Heat and Mass Transfer*, vol. 53, no. 5–6, pp. 1079–

1087, Feb. 2010, doi: 10.1016/j.ijheatmasstransfer.2009.11.003.

[24] R. L. Amalfi, F. Vakili-Farahani, and J. R. Thome, ‘Flow boiling and frictional pressure gradients in plate heat exchangers. Part 1: Review and experimental database’, *International Journal of Refrigeration*, vol. 61, pp. 166–184, Jan. 2016, doi: 10.1016/j.ijrefrig.2015.07.010.

[25] R. L. Amalfi, F. Vakili-Farahani, and J. R. Thome, ‘Flow boiling and frictional pressure gradients in plate heat exchangers. Part 2: Comparison of literature methods to database and new prediction methods’, *International Journal of Refrigeration*, vol. 61, pp. 185–203, Jan. 2016, doi: 10.1016/j.ijrefrig.2015.07.009.

THEORETICAL APPLICABILITY EVALUATION OF CARNOT BATTERIES FOR AGRICULTURAL ENERGY DEMANDS IN FARMS

Bentao Guo[1]*, Aitor Cendoya[1], Vincent Lemort[1]

[1] Thermodynamics Laboratory, University of Liege, 4000 Liege, Belgium

* *Corresponding Author: Bentao.Guo@uliege.be*

Abstract. With the rapid growth of variable renewable energy (VRE) technologies, their high dependence on weather conditions results in significant intermittency. Carnot battery (CB) is considered a promising energy storage technology to enhance their resilience and be applied in residential buildings, communities, and power plants. The potential of CBs applied for agricultural activities in farms is investigated, and their demands differ from those of the above sectors. Two generic systems are studied with a heat pump (HP) to cover power/cooling demands or an electrical heater (EH) to only cover power demands. The indicator *gain* is proposed to evaluate their economic gain with various hot storage temperatures (T_h), grid reliability, the ratio of the diesel and grid price, the proportion of the solar energy after curtailment (e), the proportion used for load directly (u), and specific investment cost of VRE and CBs (c_{PV}, c_{CB}). The *gain* value in the system with an HP is higher, and the condition to get positive *gain* for the system only supplying power is harder. In the system with an HP, when e = 1, c_{PV} = 0.15 € / kWh, c_{CB} = 0.40 € / kWh, and T_h = 373 K, the *gain* is with 1.5 ~ 5.8 with u from 0.1 to 0.9. The gain is only within 0.15 ~ 2.5 for another system with c_{CB} = 0.25 € / kWh and T_h = 1473 K. The results can be a reference for determining and designing a proper energy solution for farms.

Keywords. Pumped thermal energy storage, Techno-economic evaluation, Heat pump, Heat engine, Electrical heater.

Nomenclature

C	Cost (€)
c	Specific cost (€/kWh)
COP	Coefficient of performance (-)
g	Efficiency with respect to ideal cycles
gain	Economic gain ratio (-)
PV	Photovoltaic
P2P	Power-to-power efficiency (-)
Q	Thermal/cooling energy (kWh)
R	Reliability of grid (-)
RTE	Round-trip-efficiency (-)
r	Ratio (-)
T	Temperature (K)
W	Work (kWh)

Special characters

η	Efficiency (-)
Δ	Difference of temperature (K)

Subscripts

a	Annual, air
c	Cold, cooling
Carnot	Carnot efficiency
diesel	Diesel generator
EH	Electrical heater
grid	National grid
h	Hot
HP	Heat pump
HE	Heat engine
inv	Investment
PV2l	From PV to loads
req	Required by demands
1	Generic systems with an HP
2	Generic systems with an EH

1 Introduction

It is a challenge to keep on track to meet either 1.5℃ or 2℃ climate targets [1] and some urgent actions must be undertaken to reduce global CO_2 emissions [2], with solar and wind energy playing a key role. Pumped thermal energy storage (Carnot battery, CB) is a technology that stores electricity as thermal energy by heat pump (HP) or electrical heater (EH) and transforms it back to power by heat engines (HE) when it is needed [2, 3]. CBs have been developed sharply, acting as a supplement to renewable energy resources [4], and they are mainly focused on those sectors: residential buildings, power plants, and industry [3-8], neglecting the agricultural sector. However, there are about 570 million farms in the world at present [9], illustrating the importance of farms and agricultural activities in energy research and CO_2 emission targets. Farms are facing plenty of energy problems, for instance, many farms are off-grid, or the national grid is intermittent, thus they use diesel/petrol generators for power generation when the grid is not available [10, 11]. This is neither economical nor environment-friendly, meaning those farms need a new energy solution. Hence, CBs combined with renewable energy are ideal energy solutions for farms, especially if the power demand peaks mismatch the power production peaks, for instance, the irrigation activity is conducted during the night when photovoltaic (PV) does not work.

Farms have electricity demand for irrigation pumps and cooling demand for food preservation, and they might also have electricity demand for the desalination process as the irrigation water is too salty in many farms, which is not good for the growth of crops. If there is a cooling demand for food preservation, the required temperature range is about 0-5 ℃, which is lower than the cooling requirement of residential buildings [10]. As a result, whether there is some techno-economic potential to apply CBs in farms should be studied.

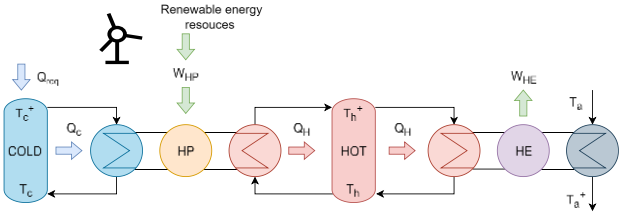
This study investigates the potential of two generic CB configurations, replacing the national grid and diesel generators to cover power/cooling demands in farms. The variety of grid reliability, grid/diesel price, specific cost of PV and CB, and effective percentage of renewable energy used for loads are considered. The second section is the description of the studied systems, and the third section is the techno-economic evaluation model for generic systems. In Section 4, the economic potential in generic systems is presented under various e, u, c_{PV}, c_{CB} and R and r_c, and the techno-economic comparison of the two proposed systems is also given.

2 Carnot battery description

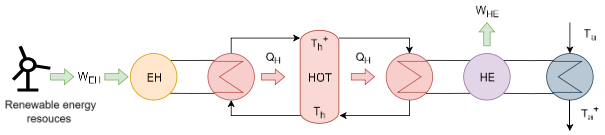
This study assumes that there is power demand for agricultural activities (irrigation or desalination), and cooling demands for food preservation, whose temperature range is 0-5 ℃ [10]. The ambient air is 27 ℃. Renewable energy resources are represented by solar energy, which is PV here. The maximum temperature of the hot storage and HE is 1200 ℃ [12-15].

2.1 Generic system without EH

This configuration shown in Figure 1(a) is proposed by Guo and Lemort [10] and modified to be more generic here. The HP is charged by PV, and it charges hot/cold storage, and the HP/cold storage can supply cooling capacity to the farm's cooling demands. On the other hand, the HE discharges hot storage and produces power.



(a). Generic system with HP



(b). Generic system with an EH

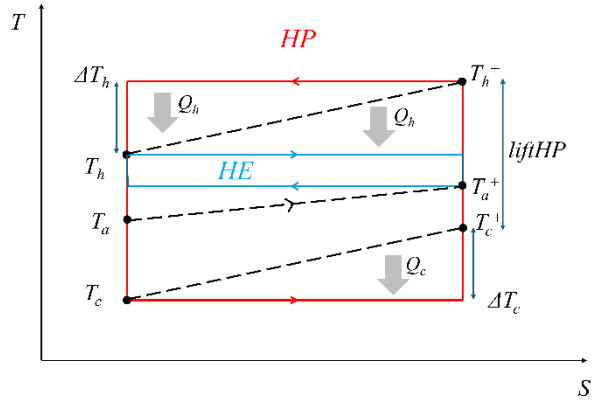
Figure 1. Configurations of generic systems

2.2 Generic system with an EH

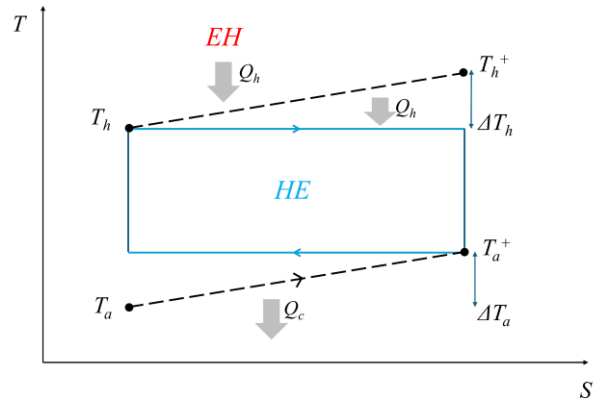
This configuration is also investigated because it can reach a higher hot storage temperature, and it is shown in Figure 1(b). An EH is used to replace HP for charging the hot storage, and the farm's cooling demands are still covered by the existing cold rooms or refrigerators. Hence, the hot storage can reach higher temperatures without the limitations of HP ability and the CB here only supplies power for the farms. More technical details of these two generic systems can be found in Section 3.

2.3 Carnot cycles in HP/HE

The HP and HE are both working in an ideal Carnot cycle [14] in the two above systems, but an efficiency g is introduced with respect to the ideal cycles, considering the inevitable irreversibility. The detail of their efficiency is described in section 3.1. Their ideal Carnot cycles are shown in Figure 2.



(a). Carnot cycle with an HP



(b). Carnot cycle with an EH

Figure 2. Ideal Carnot cycles of generic systems

3 Methodology

3.1 Generic system without EH

These parameters are introduced to evaluate HP/HE performance:

$$\Delta T_c = T_c^+ - T_c \quad (1)$$

$$liftHP = T_h^+ - T_c^+ \quad (2)$$

$$\Delta T_h = T_h^+ - T_h \quad (3)$$

The maximum *liftHP* is set as 120 K [16], so the maximum T_h^+ is 398 K. Thus, Carnot efficiency of HP / HE (*COP*, η) can be expressed as:

$$COP_{Carnot} = \frac{T_h^+}{T_h^+ - T_c} = \frac{T_c^+ + liftHP}{liftHP + \Delta T_c} \quad (4)$$

$$\eta_{Carnot} = 1 - \frac{T_a^+}{T_h} = 1 - \frac{T_a^+}{T_c^+ + liftHP - \Delta T_h} \quad (5)$$

Considering the actual cycles are not ideal, the real *COP*, η and *P2P* are:

$$COP = COP_{Carnot} \times g \quad (6)$$

$$\eta = \eta_{Carnot} \times g \quad (7)$$

$$P2P = COP \times \eta \quad (8)$$

The efficiency of the hot storage is assumed to be 100 %, and thus the energy connection of HP/ HE is:

$$Q_h = COP \times W_{HP} = \frac{W_{HE}}{\eta} \quad (9)$$

For maximum efficiency, $\Delta T_h = 0$, $\Delta T_c = 0$, yielding max.$P2P = g^2$. For PV, e represents the percentage of effective energy for HP charging and loads [17, 18] after the curtailment (1 - e), and u is the effective energy percentage only for loads:

$$e \times W_{PV} = W_{HP} + W_{PV2l} \quad (10)$$

$$u = \frac{W_{PV2l}}{e \times W_{PV}} \quad (11)$$

Thus, the relationship of W_{HP}, W_{HE} and W_{PV} is:

$$W_{HP} = (1 - u) \times e \times W_{PV} \quad (12)$$

$$\frac{W_{PV}}{W_{HE}} = \frac{1}{COP \times \eta \times e \times (1-u)} \quad (13)$$

Regarding the cold storage side, it supplies cooling capacity for cooling demands:

$$Q_c = W_{HP} \times (COP - 1) \quad (14)$$

$$\frac{Q_{req}}{Q_c} = k \leq 1 \quad (15)$$

Regarding the power demand, the relationship of W_{HE} and W_{PV2l} is:

$$W_{req} = W_{HE} + W_{PV2l} \quad (16)$$

As the electricity demand is covered by HE and PV in the generic system, an evaluation criterion is proposed in equation (17), where if *gain* > 0, the Carnot battery makes profits:

$$gain = \frac{C_{a,grid} + C_{a,diesel} - C_{a,inv}}{C_{a,inv}} \quad (17)$$

The annual cost of the system is simplified as the sum of PV annual cost and CB annual cost:

$$C_{a,inv} = c_{PV} \times W_{PV} + c_{CB} \times (W_{HE} + \frac{Q_c}{EER}) \quad (18)$$

As the discount rate is not considered here for simple evaluation, the above parameter c_{CB} is higher than the levelized cost of energy of the corresponding type of Carnot battery and it is assumed to be within the range of 0.1 ~ 0.7 € / kWh [4, 19]. The c_{PV} is assumed as 0.15 € / kWh [20]. The grid reliability (R) is the proportion of hours in one year when the grid is available. The total electricity of the grid and diesel generators includes the required electricity demand and electricity consumption of the refrigerators used

at present in the farm, which is Q_{req} divided by *EER*, so the annual costs of the grid and diesel are:

$$C_{a,grid} = c_{grid} \times R \times (W_{req} + \frac{Q_{req}}{EER}) \quad (19)$$

$$C_{a,diesel} = c_{diesel} \times (1 - R) \times (W_{req} + \frac{Q_{req}}{EER}) \quad (20)$$

EER represents the energy efficiency ratio of the refrigerators in farms. As the fluctuation of the diesel price is larger than the grid price [21-23], c_{grid} is assumed constant and a ratio of diesel to grid price is defined:

$$r_c = \frac{c_{diesel}}{c_{grid}} \quad (21)$$

Substitute the above formula into the definition formula of *gain*, it can also be expressed as:

$$gain = c_{grid} \times [R + r_c \times (1 - R)] \times \frac{1+e\times u+k\times e/EER\times(1-u)\times(COP-1)}{c_{PV}+c_{CB}\times[P2P\times e\times(1-u)+e/EER\times(1-u)\times(COP-1)]} - 1 \quad (22)$$

The *gain* will be impacted by *R*, r_c, and *u*, c_{PV} and c_{CB} if the CB performance is fixed. When the parameter $k = 1$ (the HP cooling capacity has no loss), the *gain* can reach the maximum value, so *k* is set as 1.

The CB round-trip-efficiency is defined [10] as:

$$RTE = \frac{W_{HE}+\frac{Qreq}{EER}}{W_{HP}} = P2P + \frac{k\times(COP-1)}{EER} \quad (23)$$

The electricity saved by the HP cooling capacity that replaces the existing refrigerators for food preservation is also included in the definition of the *RTE*, as the energy output of the system.

3.2 Generic system with an EH

For this system, the Carnot efficiency of HE can be expressed as:

$$\eta_{Carnot} = 1 - \frac{T_a^+}{T_h} \quad (24)$$

The real η are also defined as the ideal value multiplied by *g*. As the EH replaces HP for charging the hot storage, assuming the heating efficiency of the EH is also 100%, the energy relationship between EH and HE is:

$$Q_h = W_{EH} = \frac{W_{HE}}{\eta} \quad (25)$$

Regarding the PV, as the EH is also charged by renewable energy, the relationship among them is:

$$e \times W_{PV} = W_{EH} + W_{PV2l} \quad (26)$$

According to equations (16) (26), the W_{req} / W_{HE} and W_{PV} / W_{HE} can be gained:

$$\frac{W_{req}}{W_{HE}} = 1 + \frac{u}{(1-u)\times\eta} \quad (27)$$

$$\frac{W_{PV}}{W_{HE}} = \frac{1}{e\times(1-u)\times\eta} \quad (28)$$

The annual cost of this system:

$$C_{a,inv} = c_{PV} \times W_{PV} + c_{CB} \times W_{HE} \quad (29)$$

For the CB layout of an EH and HE, its specific cost is lower than that with an HP [3, 24, 25], so the c_{CB} in this system is assumed within 0.10 ~ 0.40 € / kWh. In this system, only the solution for power demands is replaced, and the cost for cooling demands is not changed, so the annual costs of grid and diesel are:

$$C_{a,grid} = c_{grid} \times R \times W_{req} \quad (30)$$

$$C_{a,diesel} = c_{diesel} \times (1 - R) \times W_{req} \quad (31)$$

At last, in this system, the *gain* can be expressed as:

$$gain = \frac{c_{grid}\times[R+r_c\times(1-R)]\times[e\times(1-u)\times\eta+e\times u]}{c_{PV}+c_{CB}\times e\times(1-u)\times\eta} - 1 \quad (32)$$

Regarding the studied application, ambient air temperature (T_a) is assumed to be 300 K. For η, T_h should be as high as possible until reaching its maximum limit (1473 K), when max $\eta = 0.8147 \times g$ is achieved. Hence, the *gain* will be also impacted by *R*, r_c, and *u*, c_{PV} and c_{CB} with the constant η.

The round-trip-efficiency in this system is defined as:

$$RTE = \frac{W_{HE}}{W_{EH}} = \eta \quad (33)$$

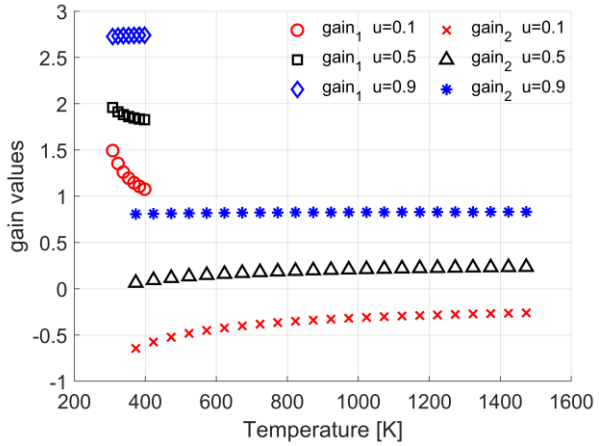
In both systems, the value of *g* is assumed to be 0.5 [14]. The value of the *EER* is set to be 2.73 [10, 11]. Only the grid purchase is considered without selling electricity to the grid. Grid price is assumed to be fixed to be 0.20 € / kWh [26].

4 Results

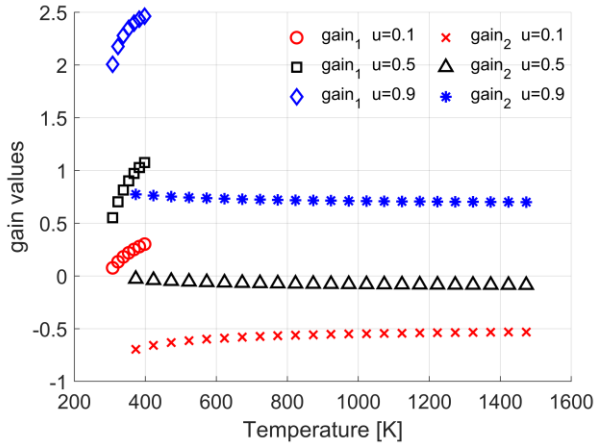
4.1 Impact of hot storage temperature

Figure 3 presents the variation of $gain_1$ and $gian_2$ values with T_h, under different conditions (a. $c_{PV} / c_{CB} > 1$; b. $c_{PV} / c_{CB} < 1$). For $gain_1$, the $T_{h,1}$ will influence the *COP* and η simultaneously, and the trending of the $gain_1$ is impacted by the trade-off of the W_{PV}, W_{HE}, and Q_c in equation (22). When $c_{PV} / c_{CB} > 1$, $gain_1$ decreases with the rising of $T_{h,1}$, and when $c_{PV} / c_{CB} < 1$, $gain_1$ increases with the rising of $T_{h,1}$. In equation (32), when $c_{PV} / c_{CB} \geq 1$, $gain_2$ always increases with the rising of η and $T_{h,2}$. When $c_{PV} / c_{CB} < 1$, if $u < e \times c_{PV} / c_{CB}$, $gain_2$ will increase with η, and if $u > e \times c_{PV}$

/ c_{CB}, $gain_2$ will decrease with η. This is the trade-off result of the costs of PV and CB, because W_{PV} and W_{HE} will decrease and increase with η, respectively, under two above conditions. Hence, the value of c_{PV} / c_{CB} will affect the trending of $gain_2$ at various u.



(a). $c_{CB,1} = c_{CB,2} = 0.1$ € / kWh



(b). $c_{CB,1} = c_{CB,2} = 0.4$ € / kWh

Figure 3. *gain* values against T_h

Regarding the *RTE* values of both systems, the utilization of HP increases the RTE_1 in the system with an HP, compared to another one, as shown in Figure 4. With the T_h increasing, RTE_1 is reduced because the *COP* of HP drops significantly, from 4.40 to 1.59, and RTE_2 is lifted by the enhanced η. In conclusion, a lower $T_{h,1}$ is good for the technical performance but reduces the economic gain when $c_{CB,1}$ is high, and a higher $T_{h,2}$ contributes to better technical performance and economic gain as it varies little with $T_{h,2}$. The value of RTE_1 can exceed 1 as the electricity saved by the cooling of HP is included.

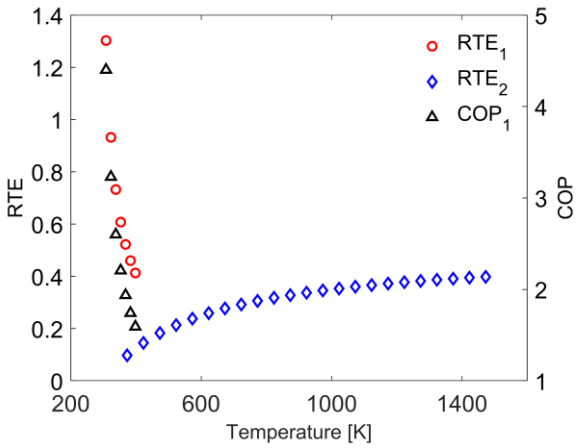


Figure 4. *RTE* values against T_h

4.2 *Impact of cooling loss*

The $T_{h,1}$ is set to be 373 K with $COP_1 = 1.87$ and $\eta_1 = 10$ %, and $T_{h,2}$ is set to be 1473 K with $\eta_2 = 40$ % in the following calculation. Figure 5 presents the $gain_1$ variation with parameter k when $R = 0.5$ and $r_c = 2$, which can represent the effective proportion of the cooling capacity, and $(1 - k)$ means the percentage of the colling energy loss. The $gain_1$ is increased slightly with the growth of k, and the incline is larger at $c_{CB,1} = 0.1$ € / kWh than that at $c_{CB,1} = 0.7$ € / kWh when c_{PV} is fixed at 0.15 € / kWh.

When k is low, the required cooling demand is relatively low and HP cooling capacity has a lot of overage, because the HP is sized large to get a huge Q_h and W_{HE} for high power demands. Compared to the existing energy solution, where the $C_{a,grid}$ and $C_{a,diesel}$ is expensed for high power and low cooling demands, the proposed system with an HP needs a high investment and annualized cost for high power demands and by-produced high cooling capacity, leading to a low $gain_1$ value. When k is higher, higher cooling demands make full use of the by-produced cooling capacity in the system with an HP, but in the present energy solution, the consumption of the grid/diesel should be increased, resulting in a higher $gain_1$ by the proposed system. As the HP cooling capacity is related to the $c_{CB,1}$, if $c_{CB,1}$ is lower, the difference between the grid/diesel annualized cost and PV/CB annualized cost is enlarged when k is growing, so the $gain_1$ rises more significantly. What's more, the incline of the $gain_1$ is becoming smaller from $u = 0.1$ to $u = 0.9$, because the proportion of the cooling demands in all the power/cooling demands drops. As the variation of $gain_1$ is not significant as shown in Figure 5, the value of k is set as 1 in the following calculation.

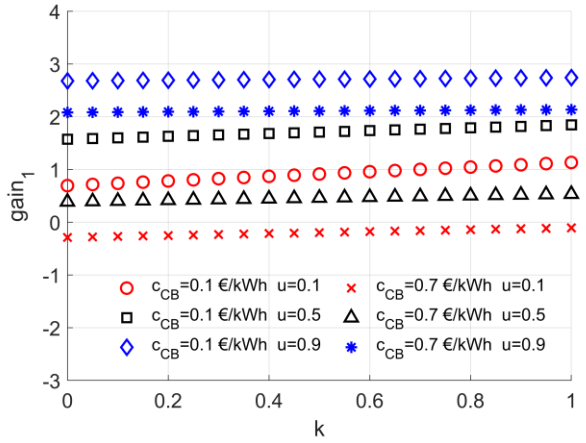


Figure 5. $gain_1$ values against k

4.3 *Impact of R and r_c*

Figure 6 presents the variation of the criterion $gain_1$ in the generic system with HP for various R, u, r_c, and $c_{CB,1}$. The lower R and higher r_c lead to better $gain_1$ values, as the total cost of grid and diesel is high. When r_c is about 1, the impact of R is less compared to r_c, and when R is about 1, the impact of r_c is less. In the system with an EH, Figure 7 illustrates the impact of R and r_c on the criterion $gain_2$ at various $c_{CB,2}$. The overall trending of $gain_2$ value with R and r_c is the same as in the system with an HP. If $c_{CB,2}$ is above 0.25 € / kWh and u = 0.1, it is hard to get a positive $gain_2$, because of high values of both W_{HE} and $c_{CB,2}$.

Even $c_{CB,1} > c_{CB,2}$, the system with an HP performs better in economic gain, illustrating the advantage of the integration of power and cooling solution by CB with HP/HE.

4.4 *Impact of specific cost of PV/CB*

Figure 8 presents the variation of $gain_1$ and $gain_2$ with c_{PV} and c_{CB}, when R = 0.5, and r_c = 2 and the T_h values keep the same as in Section 4.2. Lower PV and CB costs contribute to higher *gain* values in both systems. For the system with an EH and without cooling capacity, lower c_{PV} and c_{CB} are needed to get a positive $gain_2$ value than those in the system with an HP. With the u increasing, the c_{PV} has more effect than c_{CB}, due to the smaller value of W_{HE}. This is more obvious in the system with an EH because it cannot supply cooling capacity and more sensitive to the change of W_{HE}.

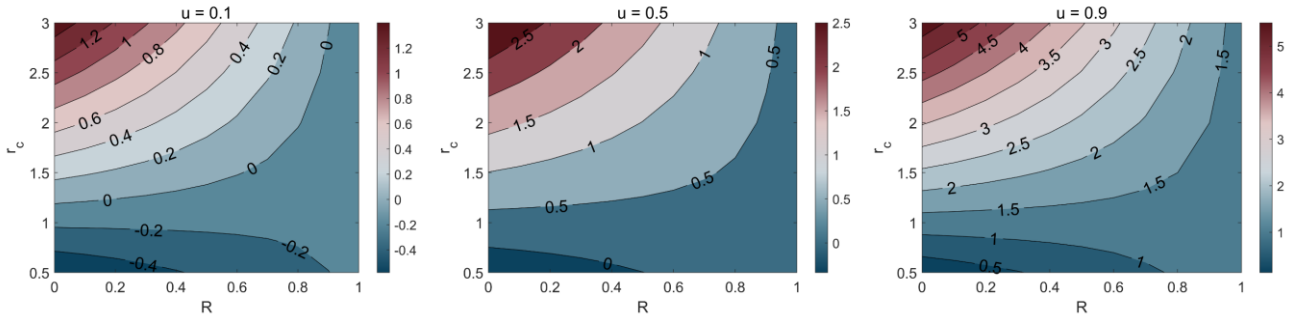


Figure 6. Relative *gain* with HP (c_{CB} = 0.40 € / kWh)

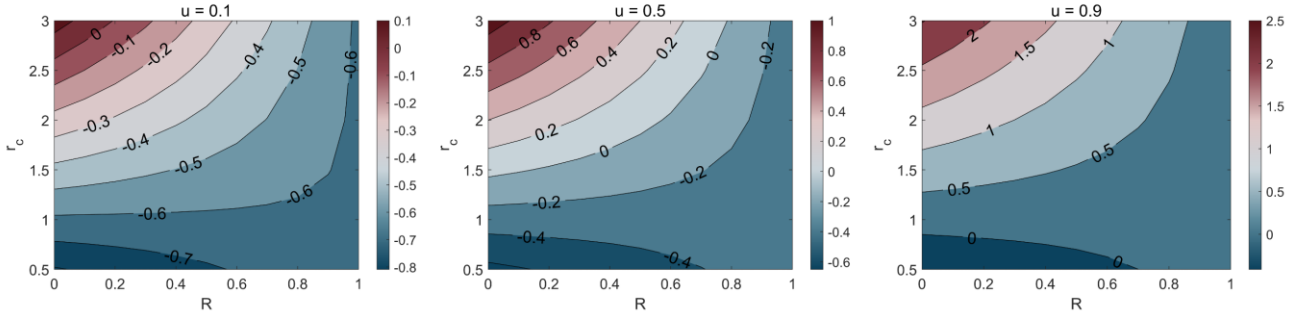


Figure 7. Relative *gain* with an EH (c_{CB} = 0.25 € / kWh)

4.5 *Impact of PV curtailment and parameter u*

In the above sections, e is fixed as 1 in the assumption that there is no curtailment of PV output, but it is ideal, so the effect of e is studied in Figure 9 ($c_{CB,1}$ = 0.40 € / kWh, $c_{CB,2}$ = 0.25 € / kWh).

In the system with an HP, when u < 0.5, more PV output is used for HP consumption than that for the power load directly, illustrating the ratio of W_{HE} and

W_{PV2l} is high, and thus the lifted CB cost is higher than the reduced PV cost with the growth of e, so higher e leads to lower $gain_1$. If $c_{CB,1} < 0.15$ € / kWh, this situation will not happen. In the system with an EH, increasing the e value means more W_{PV2l} and less W_{HE}, so the $gain_2$ grows with e. When $u < 0.5$, it is impossible to get positive $gain_2$ until $e = 1$ (no PV curtailment) at $c_{CB,2} = 0.25$ € / kWh.

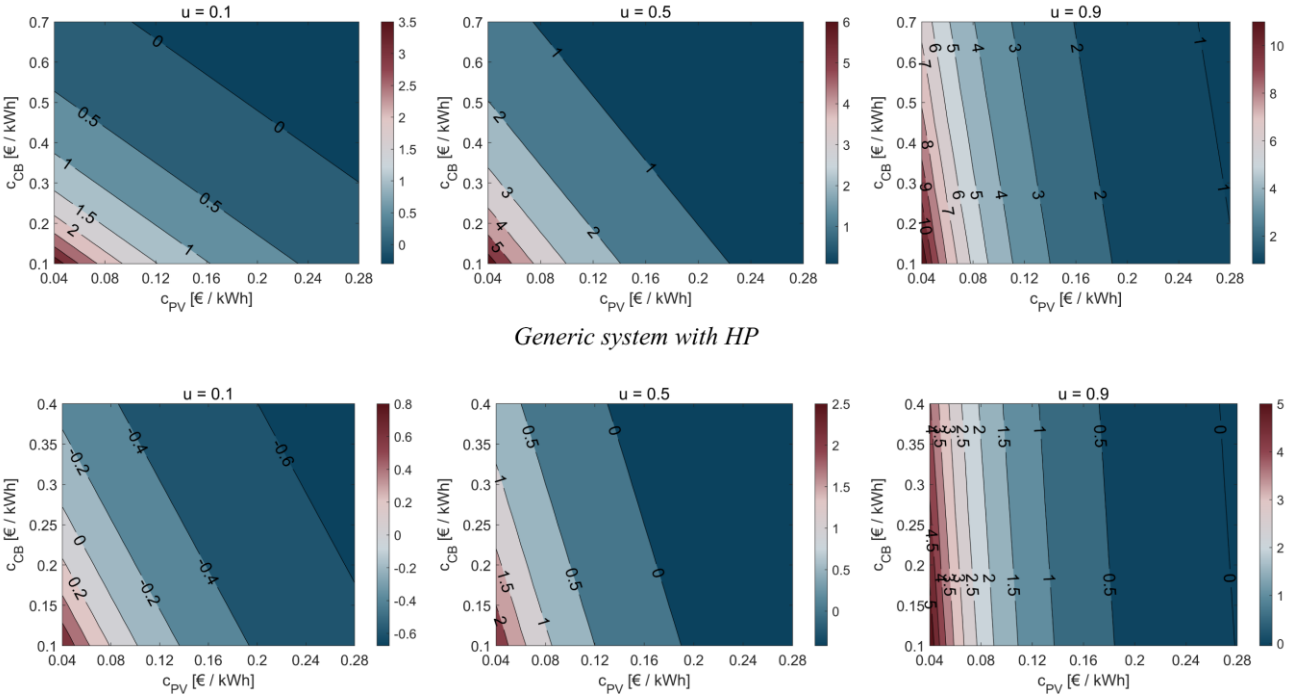


Figure 8. *gain* values with c_{PV} and c_{CB}

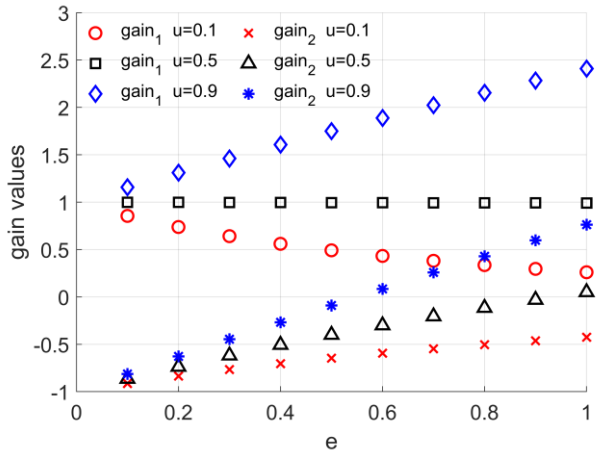


Figure 9. *gain* with e and u

The *gain* improves with the u increasing. In the system with an HP, a higher u means a higher value of W_{PV} / W_{HE} according to equation (13), and regarding the variation of the W_{PV}, there are 2 cases. If W_{PV} is decreasing or constant, W_{HE} cannot be rising because of their increasing ratio above. In the second case, if W_{PV} is rising, and u is also rising, W_{PV2l} will increase more, and thus W_{HE} will decrease a lot, because of their relationship in equation (17). In conclusion, in any case, W_{HE} and Q_c will decrease with u, and when the grid and diesel prices (c_{grid}, c_{diesel}) are fixed, the $gain_1$ is higher. In the system with an EH, the impact of u is weaker than that with a HP, because the value of W_{PV} / W_{HE} is smaller.

5 Conclusions

Two generic Carnot battery systems for the energy demands in farms are proposed and their techno-economic potential evaluation is conducted. A new evaluation criteria *gain* is proposed and its values in two systems are presented and analysed with various grid reliability (R), the effective percentage of solar energy (e), the proportion of the solar energy used for load directly after its curtailment (u), the ratio of the diesel price to grid price (r_c), and the specific investment cost of the Carnot battery (c_{inv}). The main conclusion is listed here:

- In the system with a HE for power demands and HP for cooling demands ($T_{h,1}$ = 373 K), the defined $gain_1$ value can reach 1.5 to 5.8 with u from 0.1 to 0.9 at various R and r_c values, when $c_{CB,1}$ = 0.4 € / kWh.
- For the generic systems with an EH ($T_{h,2}$ = 1473 K), it only supplies power, and the farm's cooling demands is covered by existing refrigerators. Its $gain_2$ value can reach 0.15 to 2.5 when $c_{CB,2}$ = 0.25 € / kWh, and u ranges from 0.1 to 0.9.
- The hot storage temperature has more effect in the system with an HP than in that with an EH, and $gain_2$ is not sensitive to $T_{h,2}$. The system with an HP can get a higher *gain* value than another system, illustrating the advantage of the solution with integrated HP and HE for power and cooling demands, respectively.
- The $gain_1$ in the system with an HP varies slightly with the proportion of the cold energy loss. When $c_{CB,1}$ is lower, the $gain_1$ growth is more significant.
- Lower R and higher r_c contribute to higher *gain* values in both systems. In the system with an EH, $gain_2$ is more sensitive to c_{PV} than $c_{CB,2}$ at each u, and $gain_1$ is more sensitive to $c_{CB,1}$ than c_{PV} at u = 0.1.
- The system with an HP is more sensitive to u than another system without cooling capacity. The $gain_2$ grows with e, but when $c_{CB,1}$ > 0.15 € / kWh, $gain_1$ decreases at a low level of u (u < 0.5) with the growth of e.

In this study, the HP/HE cycles are based on the Carnot cycle as limited by pages, so in future studies, the Lorenz-cycle-based potential evaluation will be investigated to provide a more comprehensive reference for energy solution design in agriculture. The impact of parameter g is not presented in this study due to the page limitation, which should be studied in future work.

Acknowledgment

The authors would like to acknowledge the support of the project "REPTES - Renewable plants integrated with pumped thermal energy storage for sustainable satisfaction of energy and agricultural needs of African communities" under LEAP-RE programme, which has received funding from the European Union's Horizon 2020 Research and Innovation Program under Grant Agreement 963530. This work was also supported by the Fonds de la Recherche Scientifique - FNRS under Grant(s) n° R.8003.23.

References

[1] I. P. o. C. Change. "Global Warming of 1.5ºC." https://www.ipcc.ch/sr15/ (accessed October 3, 2024).

[2] M. U. Tareen, S. Quoilin, A. Laterre, S. Meyer, P. Thiran, and A. Hernandez, "Modeling the impact of energy sufficiency on European integrated energy systems," in *37th International Conference on Efficiency, Cost, Optimization, Simulation and Environmental Impact of Energy Systems 2024*, 2024: ECOS, Rhodes, Greece.

[3] O. Dumont, G. F. Frate, A. Pillai, S. Lecompte, and V. Lemort, "Carnot battery technology: A state-of-the-art review," *Journal of Energy Storage*, vol. 32, p. 101756, 2020.

[4] A. Vecchi *et al.*, "Carnot Battery development: A review on system performance, applications and commercial state-of-the-art," *Journal of Energy Storage*, vol. 55, p. 105782, 2022.

[5] V. Novotny, V. Basta, P. Smola, and J. Spale, "Review of carnot battery technology commercial development," *Energies*, vol. 15, no. 2, p. 647, 2022.

[6] A. Cendoya *et al.*, "Modelling And Simulation Of A Carnot Battery Coupled To Seasonal Underground Stratified Thermal Energy Storage For Heating, Cooling And Electricity Generation," 2024.

[7] S. Hu, Z. Yang, J. Li, and Y. Duan, "Thermo-economic analysis of the pumped thermal energy storage with thermal integration in different application scenarios," *Energy Conversion and Management*, vol. 236, p. 114072, 2021.

[8] A. Basta, V. Basta, J. Spale, T. Dlouhy, and V. Novotny, "Conversion of combined heat and power coal-fired plants to Carnot batteries-Prospective sites for early grid-scale applications," *Journal of Energy Storage*, vol. 55, p. 105548, 2022.

[9] S. K. Lowder, J. Skoet, and T. Raney, "The number, size, and distribution of farms, smallholder farms, and family farms worldwide," *World development*, vol. 87, pp. 16-29, 2016.

[10] B. Guo and V. Lemort, "Designing of an Off-Grid Reversible Heat Pump/Organic

Rankine Cycle System for Electricity and Cooling Demands of a Nigerian Family Farm," in *37th International Conference on Efficiency, Cost, Optimization, Simulation and Environmental Impact of Energy Systems*, Rhodes, Greece, 2024: ECOS2024.

[11] B. Guo and V. Lemort, "Comparison of control strategies of an off-grid Carnot battery combined with renewable energy resources: Priority of electrical and Carnot battery," in *4th International Workshop on Carnot Batteries*, 2024.

[12] A. Gil *et al.*, "State of the art on high temperature thermal energy storage for power generation. Part 1—Concepts, materials and modellization," *Renewable and sustainable energy reviews,* vol. 14, no. 1, pp. 31-55, 2010.

[13] J. Gasia, L. Miró, and L. F. Cabeza, "Review on system and materials requirements for high temperature thermal energy storage. Part 1: General requirements," *Renewable and Sustainable Energy Reviews,* vol. 75, pp. 1320-1338, 2017.

[14] O. Thome, O. Dumont, and V. Lemort, "Potential evaluation of Carnot battery integrating waste heat recovery in industry," in *36th International Conference on Efficiency, Cost, Optimization, Simulation and Environmental Impact of Energy Systems (ECOS 2023)*, 2023: International Conference on Efficiency, Cost, Optimization, Simulation and ….

[15] T. Liang *et al.*, "Key components for Carnot Battery: Technology review, technical barriers and selection criteria," *Renewable and Sustainable Energy Reviews,* vol. 163, p. 112478, 2022.

[16] J. Jiang, B. Hu, R. Wang, N. Deng, F. Cao, and C.-C. Wang, "A review and perspective on industry high-temperature heat pumps," *Renewable and sustainable energy reviews,* vol. 161, p. 112106, 2022.

[17] L. Bird *et al.*, "Wind and solar energy curtailment: A review of international experience," *Renewable and Sustainable Energy Reviews,* vol. 65, pp. 577-586, 2016.

[18] E. O'Shaughnessy, J. R. Cruce, and K. Xu, "Too much of a good thing? Global trends in the curtailment of solar PV," *Solar Energy,* vol. 208, pp. 1068-1077, 2020.

[19] P. Sorknæs, J. Z. Thellufsen, K. Knobloch, K. Engelbrecht, and M. Yuan, "Economic potentials of carnot batteries in 100% renewable energy systems," *Energy,* vol. 282, p. 128837, 2023.

[20] S. Joshi, S. Mittal, P. Holloway, P. R. Shukla, B. Ó Gallachóir, and J. Glynn, "High resolution global spatiotemporal assessment of rooftop solar photovoltaics potential for renewable electricity generation," *Nature communications,* vol. 12, no. 1, pp. 1-15, 2021.

[21] Y. Cheng, "Forecasting the delayed impact of energy price fluctuations on China's general prices based on a temporal input-output approach," *Energy Strategy Reviews,* vol. 52, p. 101340, 2024.

[22] F. Gkatzoglou, T. Papadimitriou, and P. Gogas, "Fuel Price Networks in the EU," *Economies,* vol. 12, no. 5, p. 102, 2024.

[23] I.-C. Tsai, "Fossil energy risk exposure of the UK electricity system: The moderating role of electricity generation mix and energy source," *Energy Policy,* vol. 188, p. 114065, 2024.

[24] D. Pardillos-Pobo, P. González-Gómez, M. Laporte-Azcué, and D. Santana, "Thermo-economic design of an electric heater to store renewable curtailment in solar power tower plants," *Energy Conversion and Management,* vol. 297, p. 117710, 2023.

[25] F. Nitsch, M. Wetzel, H. C. Gils, and K. Nienhaus, "The future role of Carnot batteries in Central Europe: Combining energy system and market perspective," *Journal of Energy Storage,* vol. 85, p. 110959, 2024.

[26] B. A. M. Nouadje, P. T. Kapen, V. Chegnimonhan, and R. Tchinda, "Techno-economic analysis of a grid/fuel cell/PV/electrolyzer system for hydrogen and electricity production in the countries of African and Malagasy council for higher education (CAMES)," *Energy Strategy Reviews,* vol. 53, p. 101392, 2024.

ACCURATE ESTIMATION OF IGNITION DELAY IN DUAL-FUEL MARINE ENGINES USING METHANOL OR HYDROGEN

Somayeh Parsa*[1], Sebastian Verhelst[1,2]

[1] Ghent University, Department Of Electromechanical, Systems And Metal Engineering, Ghent, Belgium

[2] Lund University, Department of Energy Science, Lund, Sweden

* *Corresponding Author: Somayeh.parsa@ugent.be*

Abstract. Maritime transport accounted for 2.9% of global anthropogenic CO_2 emissions in 2018, releasing 1,076 million tons of CO_2. To mitigate greenhouse gas emissions from maritime transport, one viable approach is the use of renewable fuels, such as hydrogen and methanol, in marine engines. Due to their unique combustion characteristics, these fuels can serve as primary energy sources in internal combustion (IC) engines. However, their high autoignition temperatures necessitate an external ignition source to initiate combustion in compression ignition (CI) engines. The dual fuel approach presents an efficient solution for integrating these fuels. Given the time-consuming and costly nature of marine engine development, simulation plays a crucial role in the process. Accurate estimation of ignition delay (ID) time is essential for modelling dual-fuel combustion effectively. This study focuses on the precise estimation of the ignition delay time in methanol/diesel and hydrogen/diesel dual-fuel marine engines under real-world conditions, paving the way for accurate modelling of dual-fuel combustion in maritime applications. A constant volume batch reactor model within the open-source Cantera code is initially used to examine the impact of premixed fuels on the ignition delay of the pilot fuel. The findings show that premixed hydrogen has a minimal effect on the ID of the pilot fuel, except when hydrogen constitutes a very high proportion of the premixed fuel. However, premixed methanol significantly influences the ID of the pilot fuel. Following this, two methodologies—an artificial neural network (ANN) and a lookup table approach—are introduced to estimate the ignition delay within a multi-zone thermodynamic combustion model in GT-Power under real operating conditions. Additionally, a correlation is employed to calculate ignition delay in the dual-fuel multi-zone combustion model. The numerical results are then compared with experimental data from a dual-fuel medium-speed engine to evaluate the accuracy of each method under real-world conditions and determine the most accurate approach. The neural network method demonstrates superior accuracy in predicting ignition delay compared to both the correlation and lookup table methods.

Keywords. Ignition delay, ANN, Lookup table, Dual fuel, Methanol, Hydrogen

1 Introduction

Maritime transport is regarded as one of the most energy-efficient forms of transportation. However, it is also a significant and growing contributor to greenhouse gas emissions. In Europe, maritime transport is responsible for 3 to 4% of the EU's total CO_2 emissions, amounting to over 124 million tonnes of CO_2 in 2021. These emissions are expected to increase to 130% of their 2008 levels by 2050 [1, 2]. To address this issue, the European Union has set targets to reduce emissions by 6% by 2030 and by 80% by 2050 [3-5]. With a ban on internal combustion engines set for 2035, light-duty road transport has transitioned to electrification. However, sectors like marine navigation, heavy-duty road transport, and long-distance trucking present significant challenges for electrification due to their high power and autonomy demands. As a result, replacing fossil fuels with alternative options like hydrogen, methanol, and ammonia, produced sustainably from renewable electricity, with methanol specifically using recycled CO_2, is seen as the most promising solution for powering ship engines [6-8]. Although these alternative fuels can function as primary energy sources in internal combustion engines, their high autoignition temperatures require an external ignition source to start combustion in compression ignition engines. The Dual Fuel (DF) approach provides an effective

* Corresponding author: somayeh.parsa@ugent.be

method for incorporating these fuels. In dual fuel applications, there are different types based on how the main fuel is injected. It can either be injected into the intake manifold at low pressure or injected along with the diesel fuel at high pressure [2, 8, 9]. The port fuel injection (PFI) method, which involves low-pressure injection, is commonly used when converting a compression ignition (CI) engine to dual fuel mode because it doesn't present significant challenges when retrofitting the engine. In this work, PFI type is considered. Although port fuel injection (PFI) is considered an efficient method, certain challenges arise when developing PFI dual fuel engines that run on methanol or hydrogen [10-12]. Hydrogen presents several challenges when used with port fuel injection (PFI), including pre-ignition, knocking, and backfiring. These issues arise from hydrogen's broad flammability range, low minimum ignition energy, and limited quenching distance [13]. Moreover, hydrogen's presence in the intake system displaces air, which can reduce the engine's power density. On the other hand, methanol can be effectively utilized in dual-fuel applications through fumigation. However, it also has its challenges. The low cetane number of methanol may cause severe knocking under high-load conditions. Additionally, the high heat of vaporization of alcohols makes ignition difficult during cold starts, warm-up periods, and low-load situations, Furthermore, using these fuels can increase the levels of carbon monoxide (CO) and total hydrocarbon (THC) emissions [14, 15]. In PFI dual-fuel applications, diesel fuel is injected into a premixed fuel-air mixture, as shown in Figure 1. This results in a non-homogeneous mixture within the cylinder, creating various zones with differing equivalence ratios, ranging from lean to rich [16]. The areas surrounding the pilot injection are rich in diesel fuel, while the regions farther away are lean, containing little or no diesel fuel. Consequently, these varying zones exhibit different behaviors, which must be considered when calculating ignition delay (ID) and laminar burning velocity (LBV) in dual-fuel combustion simulations.

Since developing marine engines is both time-consuming and expensive, simulations are essential in this process. For precise modelling of dual fuel combustion, it is crucial to accurately estimate certain parameters, one of the most important being the ignition delay time (ID) of the pilot diesel.

Some numerical and experimental studies have investigated the ignition delay of hydrogen-diesel and methanol-diesel mixtures.

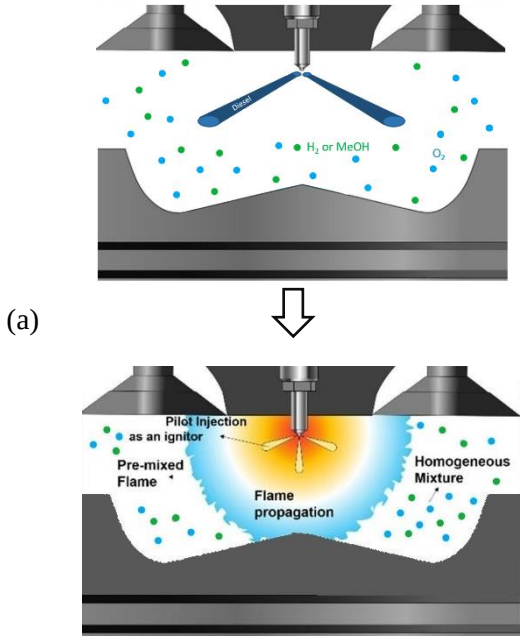


Figure 1 The schematic of in-cylinder mixture in dual fuel application before (a) and after (b) ignition

Aggarwal et al. [17] conducted a numerical study on the ignition of hydrogen/n-heptane and methane/n-heptane blends using CHEMKIN software to simulate combustion in a closed, homogeneous reactor. They applied three different mechanisms to estimate the ignition delay at 30 and 55 atm, for three different equivalence ratios, and across a high-temperature range of 800-1400 K. Frolov et al. [18] numerically investigated the effect of hydrogen addition on the autoignition of homogeneous hydrocarbon/air mixtures through numerical simulations. They observed that at temperatures below 1050 K, the ignition delay increased with higher hydrogen content, whereas it decreased at temperatures above 1050 K. Comandini et al. [19] studied the combustion characteristics of hydrogen/n-heptane mixtures. They experimentally determined the laminar flame speeds of various hydrogen/n-heptane/air mixtures at 294 K and 1 bar using the spherical bomb technique. Additionally, they measured the ignition delay for different hydrogen-n-heptane combinations at 20 bar using the reflected shock tube technique. Their results showed that adding 25% and 50% hydrogen increased the burning velocity by 3% and 10%, respectively. They also found that hydrogen enrichment had minimal impact on the ignition delay at high temperatures. Wenjing Qu et al. [20] proposed a skeletal mechanism for hydrogen/PRF (Primary Reference

Fuel) blends and measured ignition delay times for various hydrogen/n-heptane mixtures in a shock tube at high temperatures and 1.25 atm. They validated their proposed mechanism against experimental data and demonstrated that blends with higher hydrogen percentages and lower equivalence ratios exhibited shorter ignition delays. Liu et al. [21] proposed a skeletal kinetic mechanism for methanol-n-heptane mixtures. Their findings showed that adding methanol shifted the Negative Temperature Coefficient (NTC) regime toward the lower temperature range. Furthermore, the NTC regime disappeared when high percentages of methanol were added to the blend. Zang et al. [22] used the chemical kinetic model developed by Xu et al. [23] simulations to analyse combustion and emissions in a diesel/methanol dual-fuel engine. Decan et al. [24] also employed tabulated ignition delays generated by detailed chemical schemes to model dual-fuel methanol/diesel combustion.

Few studies have investigated the ignition delay in hydrogen/diesel and methanol/diesel dual-fuel engines under actual operating conditions. Dhole et al. [25] conducted an experimental study focusing on the combustion duration and ignition delay of a dual-fuel diesel engine using hydrogen, producer gas, and various mixtures of these gases with diesel as the pilot fuel. The experiments were carried out on a 4-cylinder turbocharged and intercooled diesel engine, part of a 62.5 kW generator set, operating at a constant speed of 1500 rpm. The results indicated that under low load conditions, replacing 30% of the diesel fuel (by mass) with hydrogen increased the combustion duration by 2.5° crank angle (CA) and extended the ignition delay by 2° CA. At 80% load, with 50% hydrogen substitution, the combustion duration decreased by up to 5° CA, and the ignition delay was reduced. The study also revealed that the ignition delay in dual-fuel engines is influenced not only by the type and concentration of the gaseous fuels but also by factors such as charge temperature, pressure, and oxygen concentration.

Some correlations also have been proposed to estimate the ignition delay for methanol/diesel and hydrogen/diesel dual-fuel combustion. A correlation was proposed by Dierickx et al. [26] to calculate ignition delays in dual-fuel engines using hydrogen or methanol in a medium-speed single-cylinder engine. The newly developed methanol dual-fuel correlation accounts for the inhibition effect by using the methanol-air equivalence ratio. In the case of hydrogen dual-fuel operation, the study found that the measured ignition delay was only slightly affected by increasing the hydrogen energy fraction.

According to the literature review which shows, in particular, the important impact of the presence of methanol on the ignition delay of the pilot fuel, there is a need for a more accurate estimation of ignition delay in dual-fuel engines, particularly for marine applications operating under high-temperature and high-pressure conditions. This study first examined how the ignition delay (ID) of a diesel pilot fuel was affected by the presence of either premixed hydrogen or methanol. To achieve this, several chemical kinetic mechanisms were first assessed against experimental data from the literature to identify the most suitable schemes. Next, ignition delay was calculated under various engine-like conditions to determine how it would be influenced by factors such as different percentages of hydrogen and methanol and varying air-to-fuel equivalence ratios. In the next step, the study incorporated ignition delay data from chemical kinetic mechanisms, calculated with Cantera across a broad range of operating conditions, into a dual-fuel multi-zone combustion model, employing two different methodologies: machine learning and look-up tables. Additionally, the correlation developed by Dierickx et al. [26] was used to calculate ignition delay times. The accuracy of these methodologies was then assessed by comparing them to experimental data from a medium-speed marine engine. The aim was to determine the most accurate methodology for estimating ignition delay times in methanol/diesel and hydrogen/diesel dual-fuel engines, regardless of engine type and specifications. This work summarizes the process of developing an accurate method for calculating ignition delay, suitable for use across all engine types.

1 Evaluation of the chemical kinetics schemes

1.1 Methodology

Numerical estimation of the ignition delay time provides valuable insight into autoignition parameters, which is essential for accurate modelling of CI engine combustion. Chemical kinetics are particularly useful for precisely predicting ignition delay times. In this investigation, a constant volume batch reactor is used in the open-source Cantera code to predict the ignition delay time of the mixture at various initial temperatures and pressures. Ignition time can be defined in various ways both experimentally and numerically. In this work, the ignition delay time is described as the time when the concentration of OH species reaches its maximum [27]. The study evaluates various chemical kinetic schemes for calculating ignition delay using experimental data across different pressure ranges.

The objective is to identify accurate schemes for predicting the ignition delay of hydrogen-diesel and methanol-diesel mixtures. The subsequent sections present the evaluation results for pure n-heptane, hydrogen/n-heptane, and methanol/n-heptane mixtures.

1.1.1 Pure n-heptane

Various schemes are employed to calculate the ignition delay of pure n-heptane at high pressures ranging from 50 to 60 bar and temperatures between 900 and 1150 K. The results are then compared with experimental data from the literature [28]. Figure 2 illustrates that the chemical kinetic schemes developed by Andrae et al. (2009), Zhang et al. (2016), Cai et al. (2019), Xu et al. (2023), and Zhisong et al. (2023) predict the ignition delay of pure n-heptane with higher accuracy than other schemes, showing a relative error of less than 30%. Moreover, as the temperature increases (from right to left in the figure), all schemes show improved accuracy in predicting ignition delay.

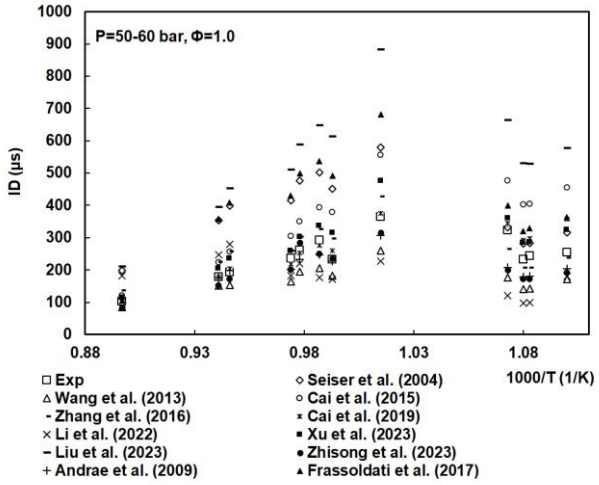


Figure 2 Comparison of ID estimated by various chemical kinetics schemes (Seiser et al. (2004) [29], Andrae et al. (2009) [30], Wang et al. (2013) [31], Cai et al. (2015) [32], Zhang et al. (2016) [33], Frassoldati et al. (2017) [34], Cai et al. (2019) [35], Li et al.(2022) [36], Xu et al. (2023) [37], Liu at al. (2023) [21], Zhisong et al. (2023) [38] for pure n-heptane with experimental data [28]

1.1.2 Hydrogen/n-heptane blend

The ignition delay of various hydrogen/n-heptane mixtures are calculated using the selected schemes that demonstrated good accuracy for pure n-heptane at high pressures. The results are then compared with experimental data at 20 bar. Figure 3 shows a comparison of the calculation results for mixtures containing 75% hydrogen and 25% n-heptane. As illustrated in Figure 2, the schemes developed by Andrae et al. (2009), Cai et al. (2015) and Zhang et al. (2016) accurately predict the ignition delay for hydrogen/n-heptane mixtures.

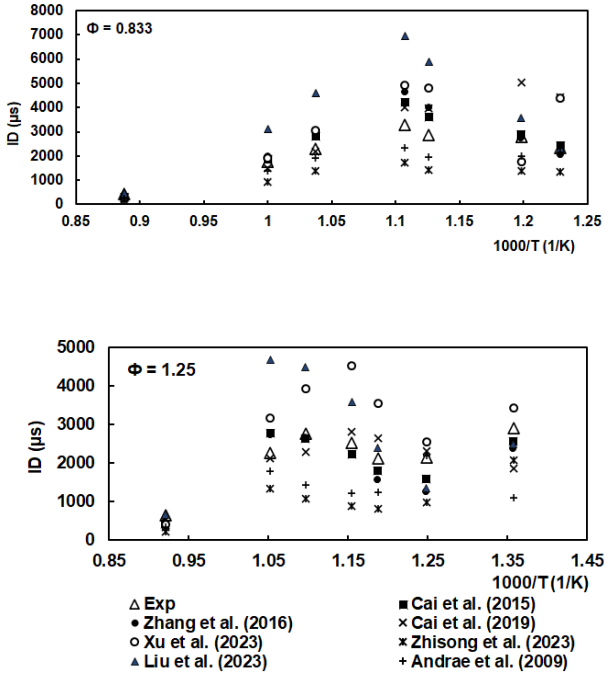


Figure 3 Comparison of ignition delay predictions from various chemical kinetic schemes for a 75% hydrogen and 25% n-heptane blend against experimental data at 20 bar and two different equivalence ratios [19]

1.1.3 Methanol/n-heptane blend

In this section, seven different schemes are applied to estimate the ignition delay of methanol/n-heptane mixtures. Figure 3 demonstrates that the schemes proposed by Andrae et al. (2009), Cai et al. (2019), Zhang et al. (2016), and Liu et al. (2023) exhibit good agreement with the experimental data.

1.2 The effect of premixed fuel on the ID of the pilot diesel

In the following section, schemes that have demonstrated high accuracy in calculating ignition delay (ID) for methanol/n-heptane and hydrogen/n-heptane mixtures are applied to examine how different combinations of hydrogen/n-heptane and methanol/n-heptane affect ID under various high-pressure conditions and equivalence ratios. This section aims to explore how ID in these different zones are influenced by varying conditions in dual-fuel operation.

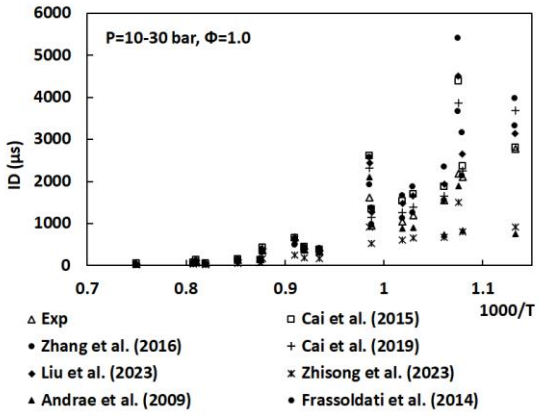


Figure 4 Comparison of ID calculated by various chemical schemes for the blend of 78.9% methanol and 21.1% n-heptane with experimental data [39]

1.2.1 Hydrogen/n-heptane blend

The scheme proposed by Cai et al. (2015) is employed to estimate the ignition delay of hydrogen/n-heptane blends. Figure 4 illustrates the impact of varying hydrogen content on the ignition delay of hydrogen/n-heptane mixtures at 70 bar and four different equivalence ratios. The figure indicates that both rich and lean mixtures show similar behaviour. Increasing hydrogen content from 0% to 75% has little effect on the ID across different equivalence ratios. However, when hydrogen content rises from 75% to 95%, the ID increases by approximately 2.5 times in the lower temperature range (T < ~1100 K). Conversely, at temperatures above 1100 K, the ID decreases by up to 50% as hydrogen content reaches 95%.

1.2.2 Methanol/n-heptane blend

Figure 5 demonstrates how the ignition delay (ID) of methanol/n-heptane mixtures varies with increasing methanol content in the premix. The scheme proposed by Cai et al. (2019) is used to calculate the ignition delay. The findings show different patterns for rich and lean mixtures in the high-temperature range (T > ~1250 K). As depicted in Figure 5, ID rises as the methanol percentage increases up to 1250 K. Specifically, ID increases by 70%, by a factor of two, and by a factor of thirteen when methanol content goes from 0% to 50%, 75%, and 95%, respectively, at 900 K (Φ = 1.0). However, at temperatures above 1250 K, ID decreases as the blends become richer.

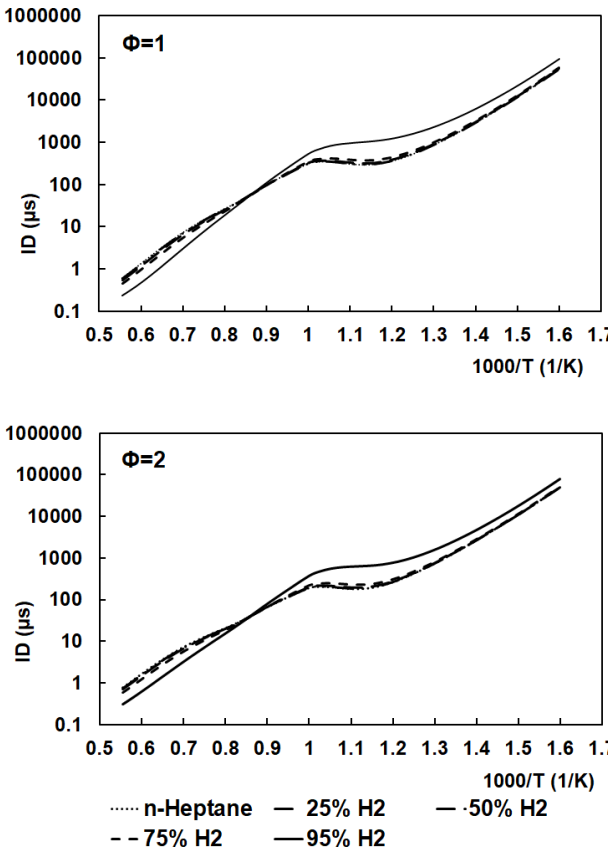
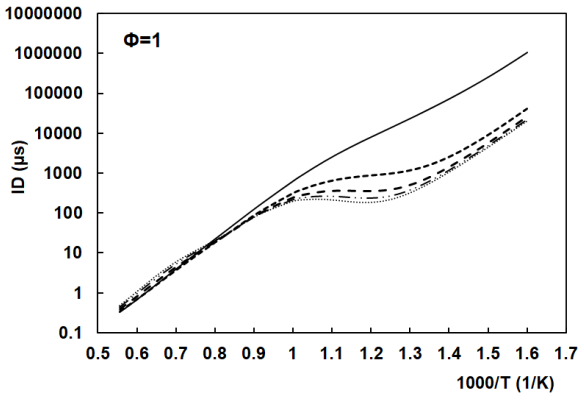


Figure 5 The effect of premixed hydrogen content on ID of hydrogen/n-heptane mixtures at 70 bar and different equivalence ratios



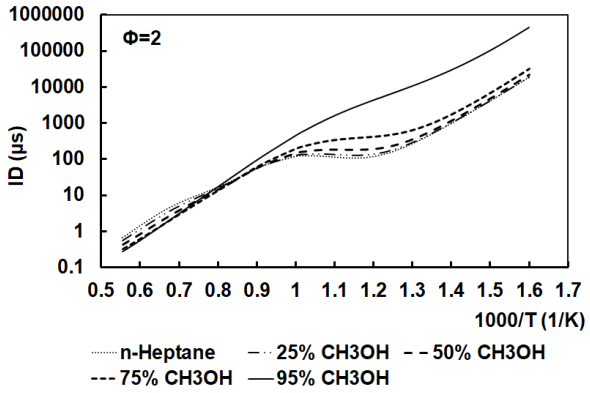


Figure 6 The effect of methanol content in the premixed fuel on the ignition delay of methanol/n-heptane mixtures at 70 bar and various equivalence ratios

More detailed results can be found in the literature [40].

After evaluating the various schemes, the most accurate ones are used to generate datasets for different operating conditions in Cantera. These datasets are then utilized in methodologies such as machine learning and lookup tables within a multi-zone combustion model to predict ignition delay under real-world engine conditions. The predictions are subsequently compared with those from the correlation developed by Dierickx et al. [26]. The following section provides a detailed explanation of this process.

2 Different methodologies for calculating the ignition delay

The selected schemes are used to generate datasets under real-world engine-like conditions, with pressure ranging from 40 to 130 bar, temperatures between 625 K and 1800 K, overall equivalence ratios from 0.5 to 3.5, and methanol or hydrogen molar percentages varying from 0% to 95%. These data are then applied to a multi-zone dual fuel combustion model with various methods. The following sections provide a detailed explanation of the methodologies used.

2.1 Multi-zone dual fuel thermodynamic combustion model in Gt-Power

In this study, the predictive dual fuel multi-zone combustion model in GT-SUITE is used to model a medium-speed dual fuel engine. This model has been previously applied by researchers to simulate the dual fuel combustion of methane and diesel [41, 42]. The multi-zone model incorporates three main components: the spray combustion model (EngCylCombDIPulse), the transition function from spray to flame combustion, and the flame combustion model (SITurb). The DIPulse model accurately predicts the combustion rate and associated emissions for direct-injection diesel engines, considering both single and multiple injection pulse scenarios. The fundamental approach of this model involves tracking the fuel through its injection, evaporation, mixing with surrounding gases, and subsequent combustion. The DIPulse model simulates the key physical processes during injection and combustion by employing several sub-models. These sub-models calculate spray entrainment, ignition delay, premixed combustion, and diffusion combustion. The model divides the cylinder into three different thermodynamic zones, each with its own temperature and composition. The main unburned zone contains the entire cylinder mass at intake valve closing (IVC), the spray unburned zone includes the injected fuel and entrained gases, and the spray burned zone consists of the combustion products. Each individual injection event is considered as an injection pulse, tracked separately from all other pulses, with no inherent difference between pilot, main, or post-injection pulses. The ignition delay of the mixture in each pulse (τ_{ign}) is modelled using an Arrhenius equation as below:

$$\tau_{ign} = C_{ign}\rho^{-1.5}\exp\left(\frac{3500}{T}\right)[O_2]^{-0.5} \quad (1)$$

ρ pulse gas density

$[O_2]$ oxygen concentration

T pulse temperature

The equation 1 can be adjusted by using the ignition delay multiplier of C_{ign}. The Livengood-Wu integral [43] is a widely used method for modelling ignition delay. It is based on the principle of delay conservation, which asserts that the total ignition delay can be determined by summing the instantaneous ignition delays from the moment of injection. Ignition occurs when the time integral equals one, as described in Equation 2.

$$\int_{t_{SOI}}^{t_{SOC}} \frac{1}{\tau_{ign}(t)} = 1 \quad (2)$$

t_{SOI} time of start of injection

t_{SOC} time of start of combustion

2.2 Experimental set up

In this study, data from a single-cylinder engine (SCE) is utilized. The engine specifications are outlined in Table 1. It is important to note that the SCE, developed in collaboration with Anglo Belgian Corporation, is located at the WTZ Roßlau laboratory. Experimental data were collected from two engines, one with a bore size of 240 mm and the other with a bore size of 256 mm. A detailed explanation of the experimental setup and the study cases can be found in the literature [10].

Table 1 The engine specifications

Engine model name	FM24
Cylinders	1
Compression ratio	12.1:1
Bore × stroke	240 × 290 mm (SCE1) 256 × 290 mm (SCE2)
Displacement volume	13.1 l (SCE1) & 14.9 l (SCE2)
Diesel injection system	Cam-driven Single Injection Pumps
Nominal power	200 kW (SCE1), 224 kW (SCE2)
Nominal speed	1000 rpm

2.3 Machine learning method

In this study, an Artificial Neural Network (ANN) is employed to train the model.

Initially, the chemical kinetic mechanisms proposed by Andrae et al. [30] and Liu et al. [21] are applied in Cantera to generate datasets under a range of operating conditions. The datasets are based on four input parameters: pressure (P), temperature (T), overall equivalence ratio (φ), and the molar fraction of methanol or hydrogen in the fuel mixture.

The following sections explain the machine learning method employed in this study.

2.3.1 Artificial Neural Network (ANN)

Artificial Neural Networks (ANNs), inspired by the human brain, are used for tasks such as classification and regression. In this study, the ANN model is designed with an input layer of 10 neurons, a hidden layer of 12 neurons, and an output layer. The Artificial Neural Network (ANN) model uses four key input parameters: pressure (P), temperature (T), overall equivalence ratio (φ), and the molar percentage of methanol or hydrogen in the mixture. Based on these inputs, the model predicts the ignition delay as the output. The model is trained using the Levenberg–Marquardt algorithm, with performance measured by mean squared error (MSE). Random data division is applied to split the dataset into training, validation, and testing subsets, ensuring a more reliable and generalizable model. The data is randomly divided into three subsets: 70% for training, 15% for testing, and 15% for validation. The results show R^2 values exceeding 99% in both methanol/diesel and hydrogen/diesel, demonstrating excellent performance.

2.3.2 Incorporating ANN into the Multi-Zone Dual-Fuel Combustion Model in GT-Power

After training the Artificial Neural Network (ANN), the high-performance model is integrated into the dual-fuel multi-zone combustion model in GT-Power. The ANN network, once trained, can be expressed mathematically using its weights, biases, and transfer functions [44]. To ensure accurate and balanced input contributions, four inputs including pressure, temperature, overall equivalence ratio, and the molar percentage of methanol or hydrogen are normalized. This normalization, achieved using the "*mapminmax*" method, scales data between -1 and 1 or 0 and 1, which improves algorithm performance and accelerates convergence during training. To obtain the actual output, the scaled output must be de-normalized.

GT-Power software allows for developing ignition delay and flame speed models using user-defined codes. The DIPulse code, described earlier, accesses pulse conditions like temperature, pressure, and composition to estimate ignition delay. This study implements a trained neural network through the user code to calculate ignition delay based on pulse conditions such as pressure, temperature, equivalence ratio, and fuel composition.

2.4 Look-up table method

An alternative way to incorporate ignition delay data from Cantera into the multi-zone combustion model is by using a look-up table. This involves initially generating a table that covers a wide range of operating conditions to account for all possible scenarios during the pulse. Afterward, specific commands are added to the DIPulse user code to

retrieve τ(t), according to equation 2, from the look-up table.

2.5 Correlation method

In this study, the phenomenological correlation proposed by Dierickx et al. [26] is also used to estimate ignition delay. This correlation was specifically developed for dual-fuel operation with hydrogen or methanol in a medium-speed, single-cylinder engine.

2.6 Comparison of different methods

The described methods are applied to predict ignition delay within a multi-zone combustion model, and the results are compared with experimental data from a medium-speed dual-fuel engine.

Results from all methods demonstrate that the ignition delay of the pilot diesel is significantly affected by the increase in methanol percentage in the premixed fuel under real engine conditions, aligning well with previous works [40]. However, the ignition delay of pilot diesel is not considerably influenced by the hydrogen percentage in the premixed fuel under real-world engine conditions [40].

For the SCE1 methanol/diesel cases, the average relative errors are 13% for the ANN method, 17% for the correlation method, and 23% for the lookup table method. In the SCE2 methanol/diesel cases, the ANN method achieves an average relative error of approximately 14%, which is lower than the 15% and 18.17% errors observed with the correlation and lookup table methods, respectively. Additionally, in the SCE2 hydrogen/diesel cases, both the ANN and correlation methods show an average relative error of about 10.9%.

Therefore, the ANN results provide significantly more accurate predictions of ignition delay compared to other methods. Additionally, both the ANN and correlation methods demonstrate faster runtime.

3 Conclusions

Accurately estimating the ignition delay time of pilot diesel is crucial for simulating methanol/diesel and hydrogen/diesel dual-fuel combustion. However, there has been limited research on calculating ignition delay for these fuels under real engine conditions. This study aimed to compare various methods for estimating ignition delay times in methanol/diesel and hydrogen/diesel dual-fuel engines under real-world conditions, identifying the most accurate approach among them. It can be concluded that:

- Premixed methanol significantly affects the ID of the pilot fuel.
- Premixed hydrogen has little impact on the ID of the pilot fuel, unless the hydrogen proportion is very high.
- The proposed ANN method shows greater accuracy in predicting ignition delay in methanol/diesel dual-fuel marine engines compared to both lookup table and correlation methods.

Acknowledgment

The research received funding from the Flemish Agency for Innovation (VLAIO) through the inter cluster Strategic Basic Research project (cSBO) titled CHyPS (Clean Hydrogen-based Propulsion of Ships). The authors sincerely appreciate this financial support.

References

[1] G. Dnv, "Maritime Forecast to 2050, Energy Transition Outlook 2019," *DNV GL, Høvik, Norway*, 2019.

[2] J. Dierickx, J. Verbiest, T. Janvier, J. Peeters, L. Sileghem, and S. Verhelst, "Retrofitting a high-speed marine engine to dual-fuel methanol-diesel operation: A comparison of multiple and single point methanol port injection," *Fuel Communications*, vol. 7, p. 100010, 2021.

[3] J. Faber *et al.*, "Reduction of GHG emissions from ships—Fourth IMO GHG study 2020—Final report," *IMO MEPC*, vol. 75, no. 7, p. 15, 2020.

[4] C. Fetting, "The European green deal," *ESDN Report, December*, vol. 2, no. 9, 2020.

[5] A. Hedberg, "The European Green Deal: How to turn ambition into action. EPC Discussion Paper 04 November 2021," 2021.

[6] S. Verhelst, J. W. Turner, L. Sileghem, and J. Vancoillie, "Methanol as a fuel for internal combustion engines," *Progress in Energy and Combustion Science*, vol. 70, pp. 43-88, 2019.

[7] S. Verhelst, T. Wallner, and R. Sierens, "Hydrogen-Fueled internal combustion engines," *Handbook of hydrogen energy*, pp. 821-902, 2014.

[8] S. H. Hosseini *et al.*, "Use of hydrogen in dual-fuel diesel engines," *Progress in*

Energy and Combustion Science, vol. 98, p. 101100, 2023.

[9] S. Parsa, S. Jafarmadar, E. Neshat, and N. Javani, "Thermodynamic analysis of a novel biomass-driven trigeneration system using different biomass resources," *Biomass Conversion and Biorefinery*, vol. 14, no. 5, pp. 6591-6607, 2024.

[10] H. Havemann, M. Rao, A. Natarajan, and T. Narasimhan, "Alcohol in diesel engines," *Journal of the Indian Institute of Science*, vol. 88, no. 3&4, p. 820, 2008.

[11] C. Yao, W. Pan, and A. Yao, "Methanol fumigation in compression-ignition engines: a critical review of recent academic and technological developments," *Fuel*, vol. 209, pp. 713-732, 2017.

[12] J. Dierickx, "Study of the Combustion of Hydrogen and Methanol in Dual-Fuel Engines," Ghent University, 2023.

[13] H. Fayaz, R. Saidur, N. Razali, F. S. Anuar, A. Saleman, and M. Islam, "An overview of hydrogen as a vehicle fuel," *Renewable and Sustainable Energy Reviews*, vol. 16, no. 8, pp. 5511-5528, 2012.

[14] A. Imran, M. Varman, H. H. Masjuki, and M. A. Kalam, "Review on alcohol fumigation on diesel engine: a viable alternative dual fuel technology for satisfactory engine performance and reduction of environment concerning emission," *Renewable and Sustainable Energy Reviews*, vol. 26, pp. 739-751, 2013.

[15] Z. Zhang, K. Tsang, C. S. Cheung, T. L. Chan, and C. Yao, "Effect of fumigation methanol and ethanol on the gaseous and particulate emissions of a direct-injection diesel engine," *Atmospheric Environment*, vol. 45, no. 11, pp. 2001-2008, 2011.

[16] P. Sharma and A. Dhar, "Compression ratio influence on combustion and emissions characteristic of hydrogen diesel dual fuel CI engine: Numerical Study," *Fuel*, vol. 222, pp. 852-858, 2018.

[17] A. K. Agarwal, H. Valera, M. Pexa, and J. Čedík, *Methanol: A Sustainable Transport Fuel for CI Engines*. Springer Nature, 2021.

[18] S. Frolov, S. Medvedev, V. Y. Basevich, and F. Frolov, "Self-ignition of hydrocarbon–hydrogen–air mixtures," *international journal of hydrogen energy*, vol. 38, no. 10, pp. 4177-4184, 2013.

[19] A. Comandini, N. Chaumeix, J. Maclean, and G. Ciccarelli, "Combustion properties of n-heptane/hydrogen mixtures," *International Journal of Hydrogen Energy*, vol. 44, no. 3, pp. 2039-2052, 2019.

[20] W. Qu *et al.*, "Hydrogen/PRF skeletal mechanism study based on shock tube experiments and kinetic analysis," *Fuel*, vol. 333, p. 126342, 2023.

[21] S. Liu, T. Sun, L. Zhou, M. Jia, W. Zhao, and H. Wei, "A new skeletal kinetic model for methanol/n-heptane dual fuels under engine-like conditions," *Energy*, vol. 263, p. 125648, 2023.

[22] R. Zang and C. Yao, "Numerical study of combustion and emission characteristics of a diesel/methanol dual fuel (DMDF) engine," *Energy & Fuels*, vol. 29, no. 6, pp. 3963-3971, 2015.

[23] H. Xu, C. Yao, and G. Xu, "Chemical kinetic mechanism and a skeletal model for oxidation of n-heptane/methanol fuel blends," *Fuel*, vol. 93, pp. 625-631, 2012.

[24] G. Decan, T. Lucchini, G. D'Errico, and S. Verhelst, "A novel technique for detailed and time-efficient combustion modeling of fumigated dual-fuel internal combustion engines," *Applied Thermal Engineering*, vol. 174, p. 115224, 2020.

[25] A. Dhole, R. Yarasu, and D. Lata, "Investigations on the combustion duration and ignition delay period of a dual fuel diesel engine with hydrogen and producer gas as secondary fuels," *Applied Thermal Engineering*, vol. 107, pp. 524-532, 2016.

[26] J. Dierickx, L. Mattheeuws, K. Christianen, K. Stenzel, and S. Verhelst, "Evaluation and extension of ignition delay correlations for dual-fuel operation with hydrogen or methanol in a medium speed single cylinder engine," *Fuel*, vol. 345, p. 128254, 2023.

[27] D. Healy *et al.*, "n-Butane: Ignition delay measurements at high pressure and detailed chemical kinetic simulations," *Combustion and Flame*, vol. 157, no. 8, pp. 1526-1539, 2010.

[28] B. Gauthier, D. F. Davidson, and R. K. Hanson, "Shock tube determination of

ignition delay times in full-blend and surrogate fuel mixtures," *Combustion and Flame,* vol. 139, no. 4, pp. 300-311, 2004.

[29] R. Seiser, H. Pitsch, K. Seshadri, W. Pitz, and H. Gurran, "Extinction and autoignition of n-heptane in counterflow configuration," *Proceedings of the Combustion Institute,* vol. 28, no. 2, pp. 2029-2037, 2000.

[30] J. C. Andrae and R. Head, "HCCI experiments with gasoline surrogate fuels modeled by a semidetailed chemical kinetic model," *Combustion and flame,* vol. 156, no. 4, pp. 842-851, 2009.

[31] H. Wang, R. D. Reitz, M. Yao, B. Yang, Q. Jiao, and L. Qiu, "Development of an n-heptane-n-butanol-PAH mechanism and its application for combustion and soot prediction," *Combustion and Flame,* vol. 160, no. 3, pp. 504-519, 2013.

[32] L. Cai and H. Pitsch, "Optimized chemical mechanism for combustion of gasoline surrogate fuels," *Combustion and flame,* vol. 162, no. 5, pp. 1623-1637, 2015.

[33] K. Zhang *et al.*, "An updated experimental and kinetic modeling study of n-heptane oxidation," *Combustion and Flame,* vol. 172, pp. 116-135, 2016.

[34] A. Frassoldati, A. Cuoci, A. Stagni, T. Faravelli, and E. Ranzi, "Skeletal kinetic mechanism for diesel combustion," *Combustion Theory and Modelling,* vol. 21, no. 1, pp. 79-92, 2017.

[35] L. Cai, A. Ramalingam, H. Minwegen, K. A. Heufer, and H. Pitsch, "Impact of exhaust gas recirculation on ignition delay times of gasoline fuel: An experimental and modeling study," *Proceedings of the Combustion Institute,* vol. 37, no. 1, pp. 639-647, 2019.

[36] S. Li, C. Huang, J. Liu, and T. Zhang, "Development of a reduced n-heptane/toluene/tetrahydrofuran mechanism for dual-fuel engine combustion prediction," *Fuel,* vol. 326, p. 124914, 2022.

[37] L. Xu, Y. Chang, M. Treacy, Y. Zhou, M. Jia, and X.-S. Bai, "A skeletal chemical kinetic mechanism for ammonia/n-heptane combustion," *Fuel,* vol. 331, p. 125830, 2023.

[38] Z. Zhang, H. Wang, H. Feng, R. Ma, and X. Zhong, "Development of a reduced kinetic chemical mechanism of gasoline surrogate containing alcohols and pentenes," *Fuel,* vol. 338, p. 127181, 2023.

[39] Y. Wu *et al.*, "Understanding the antagonistic effect of methanol as a component in surrogate fuel models: A case study of methanol/n-heptane mixtures," *Combustion and Flame,* vol. 226, pp. 229-242, 2021.

[40] S. Parsa and S. Verhelst, "Numerical Investigation of the Ignition Delay and Laminar Flame Speed for Pilot-Ignited Dual Fuel Engine Operation with Hydrogen or Methanol," SAE Technical Paper, 0148-7191, 2023.

[41] M. Wenig, K. Roggendorf, and N. Fogla, "Towards predictive dual-fuel combustion and prechamber modeling for large two-stroke engines in the scope of 0D/1D simulation," in *Proceedings of the 29th CIMAC world congress on combustion engine technology, Vancouver, BC, Canada,* 2019, pp. 10-14.

[42] F. Millo, F. Accurso, A. Piano, G. Caputo, A. Cafari, and J. Hyvönen, "Experimental and numerical investigation of the ignition process in a large bore dual fuel engine," *Fuel,* vol. 290, p. 120073, 2021.

[43] J. Livengood and W. PC, "Correlation of autoignition phenomena in internal combustion engines and rapid compression machines," 1955.

[44] A. I. Lawal, "An artificial neural network-based mathematical model for the prediction of blast-induced ground vibration in granite quarries in Ibadan, Oyo State, Nigeria," *Scientific African,* vol. 8, p. e00413, 2020.

DESIGN STUDY OF THE MONIKA ORC-TURBINE AND COMPARISON WITH EXPERIMENTAL RESULTS

H.-J. Wiemer[1]*, C.L. Niño Avella[1], T. Schulenberg[1]

[1] Karlsruhe Institute of Technology, Institute of thermal energy and safety, Karlsruhe, BW, Germany

* *Corresponding Author: wiemer@kit.edu*

Abstract. This study presents the development, verification, and validation of a MATLAB code for conducting a mean-line analysis of a four-stage Organic Rankine Cycle (ORC) turbine with a power output of around 100 kW, operated with supercritical propane at the Karlsruhe Institute of Technology (KIT). Typically, a mean-line analysis is performed for an envisaged design point during the initial phase of turbomachinery design. In this study, it is used to analyse the performance and efficiency of a turbine at different operating conditions. Accuracy checks were carried out to validate the applied loss correlations. The ORC turbine was installed in the MONIKA test facility, a modular geothermal power plant, which was tested here using a simulated heat source instead. Propane at a design pressure of 5.5 MPa and a temperature of 390 K, undergoes expansion to an outlet pressure of 1.1 MPa. During the tests, however, the test conditions deviated significantly from the original design, and nitrogen leakage into the propane cycle could not be prevented from the turbine sealing system. The mean-line analysis confirms that the developed code can still predict the ORC turbine's performance and attributes with reasonable accuracy. Additionally, the software can analyse the impact of different design alterations on the thermodynamic properties of the fluid at the inlet and outlet, as well as on the performance of the turbine.

Keywords. Supercritical-Organic-Rankine-Cycle, Turbine-Design, Mean-line-analysis.

Nomenclature (if relevant)

An	Area of cross section $[m^2]$
At	Throat area of vanes $[m^2]$
ca	Vane/Blade chord length $[m]$
dq	Specific energy losses $[J/kg]$
F	Fraction of aperture
h	Specific enthalpy (J/kg)
Hb	Blade height [m]
s	Specific entropy [J/kgK]
tvp	Throat of a vane passage [m]
T	Temperature (K)
M	Mass flow [kg/s]
Mv	Vane mass flow [kg/s]
Ml	Leakage mass flow [kg/s]
P	Pressure (kPa)
PR	Pressure ratio
Pturb	Turbine power [W]
PV	Ventilation power [w]
qFE	Spec. filling/emptying losses [J/kg]
qV	Spec. energy by ventilation [J/kg]
R	Radius [m]
U	Blade velocity [m/s]
V	Abs. Velocity [m/s]
W	Relative Velocity [m/s]
zl	Number of labyrinth tips

Special characters

α	Outlet angle vanes $[rad]$
β	Outlet angle blades $[rad]$
ε	Deflection angle $[rad]$
ζ	Soderberg loss coefficient [-]
ρ	Density $[kg/m^3]$
ω	Angular velocity $[rad/s]$
Ω	Aperture angle $[rad]$
η_{turb}	Turbine efficiency [-]

Subscripts

ax	Axial
u	Circumferential
n	Cross section number

1 Introduction

A usual technology for thermal energy sources with a temperature in the range of 100°C to 260°C is the Organic Rankine Cycle (ORC). These sources include geothermal reservoirs and industrial waste heat. In this cycle, organic liquids are used as working fluids instead of steam to extract electrical energy from low-temperature heat sources more efficiently.

The globally installed capacity of ORCs in renewable energy and waste heat plants has grown rapidly in recent years. It is estimated that there is now about 2000 MW of installed capacity in plants using ORC cycles [1].

The focus of this paper is on the turbine of the MONIKA (Modular Low Temperature Cycle Karlsruhe) project, a facility of the Institute for Thermal Energy and Safety (ITES) at the Karlsruhe Institute of Technology (KIT). The MONIKA plant consists of an ORC cycle with supercritical live steam parameters and propane as working fluid. As MONIKA is an experimental facility, an artificial heat source is producing hot water, which has been adjusted to a temperature of 150°C for the experiments.

The work focuses on the study of MONIKA's axial 4-stage impulse turbine, which is one of the main components of the system along with the pump, evaporator and condenser, as it is responsible for converting the enthalpy of the fluid into mechanical energy through expansion.

In order to analyse the behaviour of the MONIKA ORC turbine, this work deals with the calculation of the stage parameters based on a mean line analysis in steady-state operation. The results obtained are compared with the characteristics provided by the manufacturer [3] and with experimental data of Perez [2], which showed the behaviour of the turbine under different operating conditions.

The aim of this study was to develop a MATLAB code utilizing balance equations and loss correlations for axial turbines. The code can predict the thermodynamic properties, power, and efficiency of a turbine-based a given geometry of the turbine and its inlet/outlet conditions. The results are validated using measured data. More details can be found in [4].

The essential geometric features, such as cross sections, blade exit angles, and labyrinths, are taken from CAD data provided by the turbine manufacturer [3].

With the developed code, we are able to predict the behaviour of the turbine under different operating conditions, varying characteristics such as pressure or temperature at the inlet and the pressure at the outlet of the turbine. In addition, we can examine the influence of impurities of the working fluid on the turbine parameters.

2 Materials and Methods

The After compression, a supercritical Rankine cycle heats the working fluid to pressures and temperatures above its critical point. Unlike superheated, subcritical cycles, this cycle facilitates a smooth transition from subcooled liquid to superheated vapor above the critical point during the heat exchange phase. Evaporation occurs gradually, and all properties change continuously during the heating process. In organic Rankine cycles, working fluids have lower critical pressures and temperatures than water. This makes it easier for them to reach supercritical conditions, resulting in better heating performance.

This is especially advantageous when the temperature of the heat source is limited. By selecting the appropriate working fluid, one can find a heating curve that matches approximately the cool-down curve of the heat source. This reduces the logarithmic mean temperature difference and, consequently, exergy losses [5].

2.1 The MoNiKa facility

The MONIKA power plant is a facility located in the Karlsruhe Institute of Technology, Campus Nord. It consists of a generic steam cycle like a geothermal power plant. The cycle is modular and offers unique opportunities for the study of low-temperature electricity generation.

The different components of the facility are presented in Figure 1. The red line represents the cycle when the turbine is running under normal operation conditions, while the dashed line indicates the turbine bypass. The major components of the power plant are the turbine, condenser, propane tank, heat exchanger and pumps.

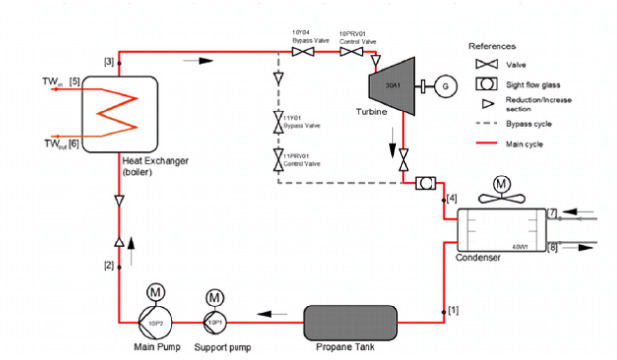


Figure 1: MONIKA POWER PLANT

2.2 ORC-Turbine

The 4-stage axial impulse turbine GT 120 – 4 (Fig. 2) manufactured by M+M Turbinen-Technik GmbH, is positioned between the heat exchanger and the condenser. The turbine table, which contains the gearbox and the 4-pole synchronous generator, is installed on vibration dampers in a 10 feet sea container. The turbine maintains a constant blade cross-section while running at a nominal speed of 9960 rpm. A unique feature of this turbine is the partial admission of the guide vanes for all stages (Figure 3). This design differs from the usual standard, where only the first row of guide vanes is partially admitted. The turbine operates at an inlet pressure of 5.5 MPa and an inlet temperature of 117°C according to the design data. It is expected to produce a power output of 139 kW.

Table 1: Design data of the ORC Turbine [3]

GT 120 – 4	
Propane mass flow	2.9 kg/s
Rotor speed	9960 rpm
Turbine inlet pressure (abs)	5.5 MPa
Turbine outlet pressure (abs)	1.1 MPa
Turbine inlet temperature	117 °C (390 K)
Power (Calculated)	139 kW



Figure 2: Monika ORC-Turbine and gearbox without isolation.

For operation, nitrogen is used as a sealing gas, which prevents propane leakage through the casing to the environment. Unfortunately, there was a residual amount of N_2 inside the working fluid during operation, which has to be taken into account in the validation analyses.

As shown in Figure 3, there are three labyrinth tips each inside the vane discs 2 to 4, which produce a leakage mass flow to be taken into account.

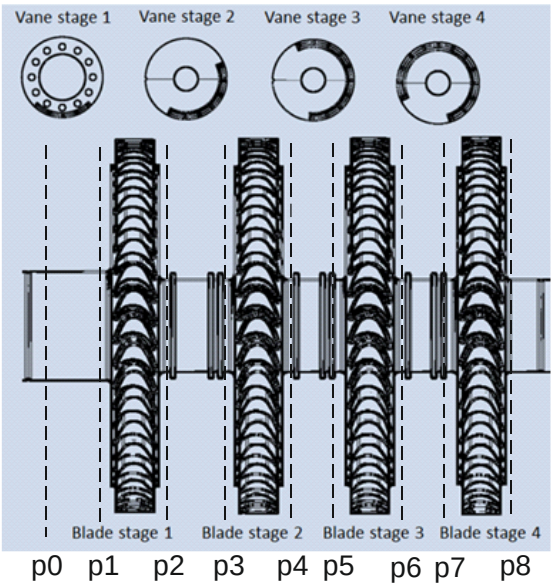


Figure 3: Rotor design and open vane passages

Equation 1 shows how the outlet angle α of the vane can be determined from the throat area At and the cross-section area An of a vane. Here, tvp is the throat of a vane passage, hb the vane height, ovp the number of open vane passages, R_e the outer radius of the vane, R_i the inner radius of the vane and Ω the aperture angle of the vane cross section.

$$\sin(\alpha) = \frac{At}{An} = \frac{2*tvp*hb*ovp}{\Omega({R_e}^2-{R_i}^2)} \qquad (1)$$

The blade outlet angle b is measured at the mean radius by extending the pressure side of the blade.

The chord length "ca" is used instead of the axial width, as shown in Figure 4 for vanes on the left and blades on the right-hand side. This approach conservatively increases the losses using the Soderberg correlations [9].

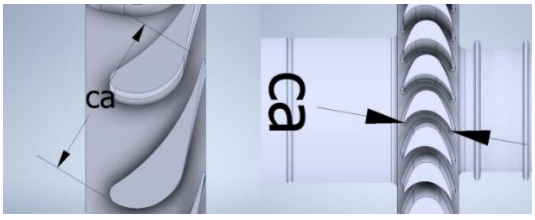


Figure 4: Chord length of vanes and blades

2.3 Measured experimental data

The facility has pressure and temperature sensors at the turbine inlet and outlet, as indicted in Fig 1. The mass flow sensor is situated behind the main pump. These sensors continuously transmit data to the control unit, which are averaged for the analysis of each run. To ensure consistent results, only steady-state conditions are selected, when the bypass valve is entirely closed. These measurements were extracted from a previous work of Perez [2], which details the pressure, temperature, mass flow of the fluid, and power output under varying conditions, Table 2. The measurements were taken on the first day of the study, 8 November 2021, and on the second day, 9 November 2021.

The turbine outlet pressure is observed to range from 1035 to 1128 kPa, with the former value corresponding to smaller mass flows and the latter to larger mass flows.

Table 2: Measured data from test runs [2]

Day/ Run	Mass Flow [kg/s]	Valve Inlet Temp. [K] (2p)	Valve Inlet Pressure [kPa] (2p)	Turb. Power [kW]
1/4.	2.2	381.3	5189.7	96.0
1/6.	1.9	383.1	5190.4	83.7
2/3.	2.6	383.6	5627.1	102.2
2/4.	2.6	382.5	5499.3	102.6
2/5.	2.6	382.1	5427.7	103.4
2/6.	2.6	380.8	5295.3	103.1
2/7.	2.6	379.9	5196.9	103.8
2/8.	2.6	379.2	5131.0	103.6
2/9.	2.7	379.9	5219.9	104.4

2.4 Reference data base Refprop

The thermodynamic properties of pure propane and propane-nitrogen mixtures have been determined with REFPROP 9.1 [7]. REFPROP uses the Kunz and Wagner model for hydrocarbon mixtures [8], to calculate the thermodynamic properties of the propane-nitrogen mixture. From the experimental data, we determined the nitrogen content using the measured pressure and temperature at the turbine outlet to 1.6 %mass.

2.5 Turbine inlet conditions

The stagnation conditions at turbine inlet are determined from the measured data upstream the turbine inlet valves (marked as '2p' in Fig. 1). Under supercritical conditions, the measured pressure and temperature determine the enthalpy h, entropy s and density ρ there. Knowing the heat losses h1loss between these two points, the enthalpy at turbine inlet (1p) is determined then as:

$$h_{1p} = h_{2p} - h_{1loss} \tag{2}$$

With the measured pressure in (1p), the calculated enthalpy h_{1p} determines all other mixture properties there. Finally, the static pressure at turbine inlet (0p) is determined from these data at (1p) assuming an adiabatic acceleration of an incompressible flow.

2.6 Turbine mean line analysis

A mean line analysis is considering a 3D flow through a turbine, which is averaged in radial and circumferential direction as well as in time. In this particular case of an axial turbine, the radial velocity component is even considered to be zero [9]. Pressures, enthalpies and velocities are determined only for each axial cross section at the inlets and outlets of turbine vanes and blades, indicated as p0 to p8 in Fig. 3 and numbered by n = 0 to 8, while the details of flow inside these stages are taken into account by empirical loss correlations. The balance equations for these axial cross sections are: The conservation of mass, Eq. (3), Euler's equation (4) (shown exemplarily for blade 1), and conservation of energy, Eq. (5). Here, the mass flow is denoted by *M*, the axial cross-section by *An*, the speed in the absolute system by *V* and in the rotating system by *W*, the rotor speed by *U*, the specific turbine work by *dA*, and the energy losses by *dq* [6].

$$M = \rho A n V_{ax} = constant \tag{3}$$

$$dA = \frac{{U_1}^2 - {U_2}^2}{2} + \frac{{V_1}^2 - {V_2}^2}{2} - \frac{{W_1}^2 - {W_2}^2}{2} \tag{4}$$

$$d\left(h + \frac{1}{2}V^2\right) = dA + dq \tag{5}$$

Unlike conventional methods, where the enthalpies in these cross sections are taken as input to determine the required flow angles of vanes and blades, the outlet flow angles are taken from the given design, as described in section 2.2. The balance equations are solved iteratively, starting from an initial guess of the pressure distribution, such that mass flows, velocities and enthalpies can be determined for each stage. The pressure distribution is iterated then until the mass flow of each stage becomes identical. This uniform

mass flow, as well as the predicted turbine power, can be compared then with the measured ones for validation. The method is outlined by Traupel [6]. The energy losses in Eq. (5) are determined by a loss correlation of Soderberg as recommended by Dixon [10].

It's important to note that the empirical correlations used to determine losses within the turbine were derived only for gases or steam. If the fluid entering the turbine has a high liquid fraction, bubbles will form in the first stage of the blades, resulting in cavitation similar to that of a pump. As such, the fluid is beyond the scope of the correlations that are to be used. Only vapor qualities greater than 0.8 are considered to be correct.

2.7 Initial pressure distribution

To enable comparison of the mean line analysis with measure data, the inlet and outlet pressures as given in Tab. 3 are taken as boundary conditions. They are used also to determine the initial pressure distribution at different cross sections for the iterative procedure.

This initial guess of the pressure distribution is assuming the same pressure ratio for each stage as the total pressure ratio PR of the entire turbine. With $P_0 =$ inlet pressure and $P_8 =$ outlet pressure, we get:

$$PR = \frac{P_0}{P_8} \tag{6}$$

Consequently, we obtain the pressure at each vane outlet as

$$P_{2m-1} = \frac{P_{2m-2}}{PR^{1/4}} \tag{7}$$

with m=1 to 4 as the stage number.

In case of an ideal impulse turbine, like in our case, an initial guess of the pressure at blade outlets is:

$$P_{2m} = P_{2m-1} \tag{8}$$

2.8 Velocity of the blades

In a mean line analysis, the circumferential component Uu of the rotor velocity equals the mean radius Rm times the angular velocity ω. In the particular case of the MONIKA turbine, the mean radius is constant and consequently the blade velocity. Therefore, we get for each cross-section n =1 to 8

$$\omega = 2\pi f \tag{9}$$

$$U_{ax,n} = 0 \tag{10}$$

$$U_{u,n} = R_{m,n}\omega \tag{11}$$

In Eq. (9), *f* is the rotor frequency.

2.9 Calculation for a vane row

The index *n* at vane outlets is 1, 3, 5, or 7. The following procedure is repeated for each vane outlet.

The first step is to find the isentropic enthalpy $h_{s,n}$ by using the entropy s_{n-1} from the previous step and the prescribed pressure P_n for this step. If n = 1, the entropy used corresponds to the inlet entropy s_0 of the turbine.

$$h_{s,n} = h(P_n, s_{n-1}) \tag{12}$$

To determine the energy losses, we used the Soderberg loss correlation [10] to derive the loss coefficient ζ_n'. In Eq. (13), ε_n is representing the blade deflection angle that results from the difference between the inlet angle α_{n-1} and the outlet angle α_n. With the loss coefficient given by Eq. (13), the chord length ca_n and the blade height hb_n, we can calculate the overall loss of each blade row ζ_n as shown in Eq. (15).

$$\zeta_n' = 0.04 + 0.06 * \left(\frac{\varepsilon_n}{100}\right)^2 \tag{13}$$

$$\varepsilon_n = \alpha_n - \alpha_{n-1} \tag{14}$$

$$\zeta_n = (1 + \zeta_n') * \left(0.993 + 0.021 * \frac{ca_n}{hb_n}\right) - 1 \tag{15}$$

The vane efficiency η be expressed as function of the losses, as:

$$\eta_n = 1 - \zeta_n \tag{16}$$

With the vane efficiency and the isotropic enthalpy, we calculate the actual enthalpy at vane outlet as:

$$h_n = h_{n-1} - \eta_n(h_{n-1} - h_{s,n}) \tag{17}$$

Using REFPROP, we can determine the following properties of the fluid from the given enthalpy and pressure in each cross-section n.

$$s_n = s(h_n, P_n)$$

$$\rho_n = \rho(h_n, P_n)$$

$$T_n = T(h_n, P_n)$$

From the energy balance, we can express the change in enthalpy as a change in kinetic energy using Eq. (18). Here, V represents the absolute velocity at the vane inlet *(n-1)* and outlet *(n)*.

$$\frac{{V_n}^2}{2} - \frac{{V_{n-1}}^2}{2} = h_{n-1} - h_n \tag{18}$$

The mass flow Mv_n through the vane channels correlates with the fluid velocity and density, as:

$$V_n = \frac{Mv_n}{\rho_n An_n sin\alpha_n} \tag{19}$$

$$V_{n-1} = \frac{Mv_n}{\rho_{n-1} An_{n-1} sin\alpha_{n-1}}$$

Since the mass flow at the inlet and outlet of the vane is constant, we can combine Eqs. (18) and (19) to yield:

$$Mv_n = \sqrt{2 * (h_{n-1} - h_n)} * \sqrt{\left(\frac{1}{(\rho_n An_n sin\alpha_n)^2} - \frac{1}{(\rho_{n-1} An_{n-1} sin\alpha_{n-1})^2}\right)} \tag{20}$$

After calculating the mass flow through the vanes, we determine the velocity component V_{ax} and V_u in the absolute system as:

$$V_{ax,n} = \frac{Mv_n}{\rho_n An_n} and\ V_{u,n} = \frac{V_{ax,n}}{tan\ \alpha_n} \tag{21}$$

$$|V_n| = \sqrt{{V_{ax,n}}^2 + {V_{u,n}}^2} \tag{22}$$

As previously stated, the mass flow rate *Mv* only relates to the flow through the vane passages. For a more precise calculation, the leakage mass flow rate through the labyrinth tips *Ml* must be taken into account as well. This is affected by the labyrinth's geometry, fluid density, number of tips *z1*, and pressure ratio upstream and downstream the tips [11]. With the labyrinth's tip diameter *(DL)* and the distance *(HL)* between the tips, we can determine the leakage mass flow as:

$$Ml1_n = 0.8 * \pi * DL * HL * \sqrt{\rho_{n-1} P_{n-1}} \tag{23}$$

$$Ml_n = ML1_n * \sqrt{\frac{1 - \left(\frac{P_n}{P_{n-1}}\right)^2}{z1 + \ln\left(\frac{P_{n-1}}{P_n}\right)}} \tag{24}$$

Finally, the mass flow *M* through the stage equals the total vane mass flow as:

$$M_n = Mv_n + Ml_n \tag{25}$$

This mass flow is taken as well for the blade row of each stage, such that

$$M_{n+1} = M_n \tag{26}$$

2.10 Calculation for a blade row

Once the stage mass flow has been determined, we can continue with the blade outlet at cross sections n=2, 4, 6, 8. The velocity at blade inlet equals the vector sum

$$\vec{W}_{n-1} = \vec{V}_{n-1} - \vec{U}_{n-1} \tag{27}$$

which defines the inlet flow angle β_{n-1}:

$$\beta_{n-1} = \text{atan}\left(\frac{W_{ax,n-1}}{W_{u,n-1}}\right) \tag{28}$$

The blade outlet angle β_n is taken from the CAD data as described in section 2.2. Thus, we get the blade outlet velocity *W* in the rotating system as

$$W_{ax,n} = \frac{M_n}{\rho_n An_{n-1}} and\ W_{u,n} = \frac{W_{ax,n}}{tan\ \beta_n} \tag{29}$$

Here, however, the density ρ_n at blade outlet must be iterated. As an initial guess, we assume that the density remains constant.

The density is a function of enthalpy and pressure at blade outlet. The blade outlet enthalpy can be determined by the energy equation (5), as will be described next.

The Soderberg correlation is once again taken to calculate the internal blade losses. It should be noted that the expression used for the blades differs slightly from that of the vanes [10]:

$$\zeta_n{}' = 0.04 + 0.06 * \left(\frac{\varepsilon_n}{100}\right)^2 \tag{30}$$

The blade deflection angle ε_n is determined by the inlet and outlet angles β_{n-1} and β_n of the blades as:

$$\varepsilon_n = \beta_n - \beta_{n-1} \tag{31}$$

With the Soderberg's loss coefficient,

$$\zeta_n = (1 + \zeta_n{}') * \left(0.975 + 0.075 * \frac{ca_n}{hb_n}\right) - 1 \tag{32}$$

we determine the blade efficiency as:

$$\eta_n = 1 - \zeta_n \tag{33}$$

The energy balance is giving us the enthalpy at blade outlet as:

$$h_n = h_{n-1} + \tfrac{1}{2}(|W_{n-1}|^2 - |W_n|^2 - |U_{n-1}|^2 + |U_n|^2) \tag{34}$$

Together with Eq. (17), we can use this energy balance to determine the isentropic enthalpy $h_{s,n}$ at blade outlet as:

$$h_{s,n} = h_{n-1} - \left(\frac{|W_n|^2}{2\eta_n}\right) + \frac{1}{2}(|W_{n-1}|^2 - |U_{n-1}|^2 + |U_n|^2) \tag{35}$$

Now, the pressure at blade outlet can be calculated with REFPROP from the entropy at blade inlet and the isentropic enthalpy at blade outlet as $P_n = P(h_{s,n}, s_{n-1})$. For turbines with partially open vane channels, known as partial admission, the blades are running temporarily through stagnant regions, causing ventilation losses. According to Traupel [6], the ventilation power, PV, can be predicted as:

$$PV_n = \pi C_n (1 - F_{n-1}) \rho_n 2R_{m,n} hb * {U_{u,n}}^3 \tag{36}$$

with the aperture fraction $F = \Omega/(2\pi)$. The ventilation coefficient C_n varies depends on the structural arrangement and on the direction of turbine rotation. For the MONIKA turbine, the expression is given in [5] for wreath wrapped, forward directed flow as:

$$C_n = 0.0095 + 0.55 * \left(0.125 + \frac{hb_n}{2R_m}\right)^2 \tag{37}$$

The ventilation power and mass flow rate determine the ventilation losses qV_n as:

$$qV_n = \frac{PV_n}{M_n} \tag{38}$$

An additional effect of partial admission results near the active zone due to the inflow from the admission into the blade section (filling) and outflow from the rotor out of the blade section (emptying). These losses are directly proportional to the blade's circumferential velocity $U_{u,n}$ [12].

$$qFE_n = \frac{0.21 ca_n U_{u,n} \sqrt{h_{n-1} - h_{s,n}}}{F_{n-1} 2R_{m,n}} \tag{39}$$

Including these ventilation losses, filling losses, and emptying losses, we get the enthalpy at blade outlet as:

$$h'_n = h_n + qV_n + qFE_n \tag{40}$$

This corrected blade outlet enthalpy and the blade outlet pressure allow now to iterate the outlet density as $\rho_n = \rho(h'_n, P_n)$. Having determined the velocity W_n in the rotating system, we get the velocity V_n in the absolute system at the inlet of the next vane as:

$$\vec{V}_n = \vec{W}_n + \vec{U}_n \tag{41}$$

2.11 Convergence of the method

This method is predicting so far, a different mass flow for each turbine stage. Therefore, the pressures at vane outlets with n=*1, 3, 5* must be iterated until the mass flows through all turbine stages become identical. We know from Stodola's law that the mass flow through a turbine stage is approximately proportional to the pressure at its inlet. Thus, the pressure P_1 is proportional to the mass flow through the second stage, P_3 is proportional to the mass flow through the third stage, etc. The relative mass flow error of the second and higher stage, compared with the inlet mass flow M_0, is:

$$dM_n = \frac{M_n}{M_0} - 1 \tag{42}$$

With this mass flow error, a pressure correction dP_n is calculated for *n=1, 3, 5* as:

$$dP_n = -P_n * dM_{n+2} \quad (43)$$

For each iteration, the new pressure distribution $P_{n,new}$ is then:

$$P_{n,new} = P_n + dP_n * FR \quad (44)$$

An under-relaxation factor *FR* has been included here to avoid negative pressures during iterations. With the new pressure distribution, the mean line analysis described above is iterated until the mass flow error becomes negligible.

After all variables have converged, the turbine power P_{turb}, the turbine efficiency η_{turb} and turbine mass flow can be predicted.

With *M* as the turbine mass flow after convergence, we get the turbine power as:

$$Pturb = M(h_0 - h_8) \quad (45)$$

With REFPROP, we determine the isentropic enthalpy hs,8 at turbine outlet as: $h_{s,8} = h(P_8, s_0)$ From this, we get the turbine efficiency as:

$$\eta_{turb} = \frac{h_0 - h_8}{h_0 - h_{s,8}} \quad (46)$$

2.12 Verification under design conditions

These equations were programmed in a MATLAB code, which was verified by comparison with the design data, Tab. 1. Ideal conditions were assumed, with pure propane as the working fluid. An under-relaxation factor *FR=0.5* has been chosen to reach best conversion. According to the design point, the inlet conditions were supercritical and the outlet pressure was set at 1100 kPa for this calculation.

Table 3: Results and deviation from design data

Item	Unit	Design	Calc	Err
Turbine Power	kW	139	137.	1%
Turbine effic.	%	-	78	-
Mass flow	kg/s	2.9	2.84	2%

Table 3 shows good agreement with the design data. The error is in the order of 1 to 2 %. We can conclude that the loss correlations, i.e., the blade and vane efficiency calculated through the Soderberg correlation, ventilation losses, filling and emptying losses, and labyrinth losses, that account for bypass mass flow via the seals, are appropriate for this application. More convincing, however, will be a comparison with measured data, as will be described next.

3 RESULTS AND DISCUSSION

The method described in Chapter 2.6 was used to determine the properties at the turbine inlet, using the data listed in Table 2 as input data. The achieved results are presented in Table 4. It is important to note that these results reflect the average of steady-state measurements taken under conditions with the bypass valve being completely closed. The nitrogen content in the propane was 1.6 %mass. The critical pressure in this case is 4791.4 kPa and the critical temperature is 371.34 K.

According to the results obtained, the fluid that entered the turbine was sometimes subcritical, but always superheated.

Table 4: Inlet properties of the turbine

Run		Enthalpy [kJ/kg]	Entropy [kJ/kgK]	Pressure [kPa]	Temp. [K]
Day 1	4th	623.159	2.322	4288.47	369.22
	6th	634.859	2.364	3876.54	365.07
Day 2	3rd	606.421	2.268	4793.05	374.31
	4th	608.484	2.273	4798.66	374.60
	5th	611.477	2.281	4811.32	375.10
	6th	612.920	2.285	4804.55	375.17
	7th	615.636	2.292	4825.04	375.77
	8th	615.677	2.292	4822.86	375.74
	9th	612.825	2.283	4909.43	376.53

Following the procedure described in Chapter 2, the properties for each turbine cross section were calculated and iterated. The measured pressures at the turbine inlet and outlet were used to determine the initial pressure distribution for each case. A relaxation factor of FR=0.5 was assumed for this analysis. Fig. 5 show the enthalpy entropy (h-s)-diagram of the predicted turbine expansion. The critical point is at the left end of the saturation line. These results are typical for an impulse turbine with almost constant pressure across the blades.

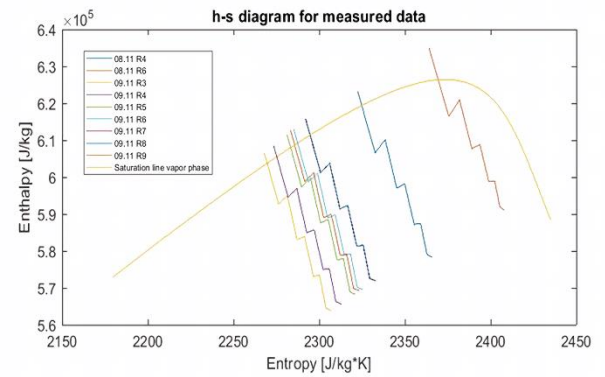


Figure 5: h-s Diagram for measured data

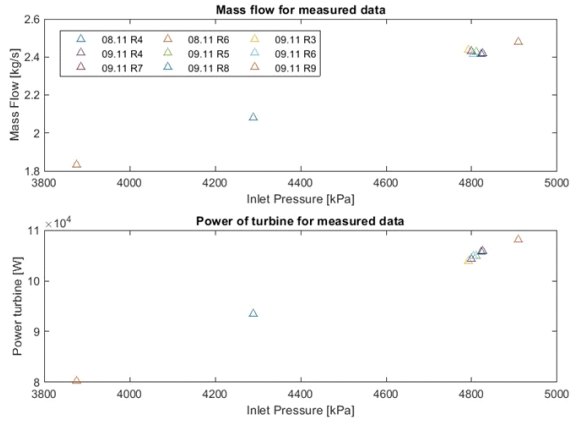


Figure 6: Mass flow and power output calculated with measured data

The fluid's inlet pressure and temperature significantly impact the power generated by the turbine. On days, when the fluid does not reach the supercritical conditions at the turbine inlet, the generated power is lower. Although these values are lower than those at design conditions, the turbine's overall efficiency is not significantly affected. This is because the reduction in generated power is directly related to the reduction in mass flow, and the enthalpy drop in the various stages of the turbine is similar in all cases.

Table 5: Mass flow, power output, efficiency and the error in regard to Measured values

	Run	Calculated M [kg/s]	Power [kW]	Eff.	Error M	Power
Day 1	4th	2.08	93.420	0.77	5%	3%
	6th	1.83	80.174	0.77	4%	4%
Day 2	3rd	2.43	103.812	0.78	6%	-2%
	4th	2.43	104.228	0.78	7%	-2%
	5th	2.42	104.922	0.78	7%	-1%
	6th	2.41	104.802	0.78	7%	-2%
	7th	2.41	105.819	0.78	7%	-2%
	8th	2.41	105.698	0.78	7%	-2%
	9th	2.47	108.138	0.78	8%	-4%

Table 5 shows the predicted turbine performance in comparison with measured results. A positive sign of the error indicates that a higher value was measured. The predicted power agrees reasonably well with the measured ones, whereas the mass flow turned out to be underpredicted by 4 to 8 %. This might be caused by slight modifications in the vane outlet angles, either due to our analysis or caused by manufacturing, which can heavily impact the turbine mass flow. Additionally, discrepancies in calculating the bypass flow through the seals could further contribute to the observed deviations.

In summary, it can be concluded that the difference between the implemented calculation method and measured data for generated power ranges from -4% to 4%, and for mass flow rate it ranges from 4% to 8%. We considered this result to be accurate enough for validation and the method can be used to predict the turbine performance under different operating conditions.

4 SENSITIVITY STUDY

The benefit of this mean line analysis shall be illustrated with an exemplary result of our sensitivity analyses, for which the turbine inlet temperature was kept constant at the design temperature of 390 K, while the pressure at turbine inlet was decreased in steps of 162 kPa, between P_{max} = 5500 kPa, the design pressure, decreasing to P_{min} = 3877 kPa, the minimum pressure recorded on day 1. The outlet pressure was fixed at 1000 kPa for all cases. The fluid was assumed to be pure propane, which has a critical pressure of 4251 kPa and a critical temperature of 369.8 K

Figure 7 depicts that the enthalpy drop in the first turbine stage will increase with decreasing turbine inlet pressure, and the fluid will be still be superheated at turbine outlet if the inlet pressure is less than 5200 kPa. Accordingly, power and mass flow of the turbine are decreasing with decreasing turbine inlet pressure. Such studies can be important to optimize an ORC power plant for given heat source conditions.

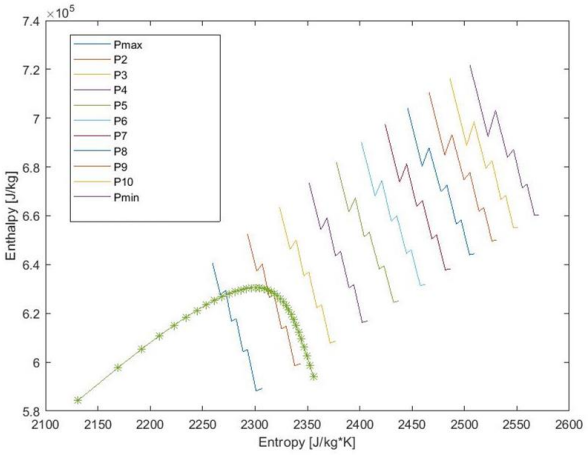


Figure 7: h-s diagram for varying turbine inlet pressure

5 CONCLUSION

A mean line analysis is a powerful tool not only to design a turbine, but also to study its behaviour under varying operating conditions. The method described here can be applied to any given turbine even in case that the working fluid is contaminated with non-condensable gases. The loss correlations, which we implemented here, are typical for multistage, axial impulse turbines with partial admission in the first stage or even, like in the case discussed here, in all turbine stages. The good agreement with measured data is encouraging us to use these loss correlations for future design of ORC turbines for low temperature applications.

References

[1] P. Colonna, E. Casati, C. Trapp, T. Mathijssen, J. Larjola, T. Turunen-Saaresti and A. Uusitalo, "Organic Rankine Cycle Power Systems: From the Concept to Current Technology, Application, and an Outlook to the Future," vol. 137, no. 10, pp. 100801-1-100801-19, 2015.

[2] J. M. Perez, "Experimental examination of the MONIKA-ORC-Turbine and comparison of the results with thermodynamical calculation," Master Thesis, ITES, Karlsruhe Institut für Technologie, Karlsruhe, 2022.

[3] M.TURBINE-TECHNIK, "Turbinenanlage Propan- expander: Project 1 15 3514 0 2018".

[4] C.L. Niño Avella, Design study of the MONIKA-ORC-Turbine and comparison with experimental results, Master Thesis, ITES, Karlsruhe Institut für Technologie, Karlsruhe, 2023, https://doi.org/10.5445/IR/1000170045

[5] E. Macchi, M. Astolfi, Organic Rankine Cycle (ORC) Power Systems Technologies and Applications ISBN: 978-0-08-100510-1, Elsevier, 2017.

[6] W. Traupel, Thermische Turbomaschinen Thermo- dynamisch-strömungstechnische Berechnung, ISBN : 978-3-642-62102-4, Verlag Berlin Heidelberg: Springer, 2001.

[7] Eric Lemmon, Ian H. Bell, Marcia L. Huber, and Mark O. McLinden. NIST Standard Reference Database 23: Reference Fluid Thermodynamic and Transport Properties-REFPROP, Version 9.1, National Institute of Standards and Technology, 2018. Available https://www.nist.gov/srd/refprop. [Accessed 12 January 2023]

[8] W. Wagner, O. Kunz, R. Klimeck and M. Jaeschke, Wide-Range Equation of State for Natural Gases and Other Mixtures, ISBN 978-3-18-355706-6, Düsseldorf: GERG, 2007.

[9] E. Dick, Fundamentals of Turbomachines ISBN 978-94-017-9627-9, Dordrecht: Springer, 2015

[10] S. L. Dixon, Fluid Mechanics, Thermodynamics of Turbomachinery ISBN 0 7506 7059 2, Oxford, UK: Butterworth-Heinemann, 1998.

[11] H. K. Müller and B. S. Nau, "www.fachwissen-dichtungstechnik.de," 2003. [Online]. Available: www.fachwissen-dichtungstechnik.de/Kapitelseiten/Kapitel17.html. [Accessed 12 January 2023].

[12] A.Berger, T. Polklas, O.Brunn and F. Joos, "Experimental investigation on performance of a control stage turbine under partial admission Paper ID ETC2019-135," Helmut Schmidt University, Hamburg, 2019.

SIMULATION MODEL FOR AUTONOMOUS ENERGY PLANNING FOR OTHONI ISLAND

Spiros Alexopoulos[1]*, Proyank Alpesjkumar[2], Daryn Slyamov[2] and Dhrumit Suthar[2]

1 Solar-Institut Jülich of the FH Aachen University of Applied Sciences, Germany, Jülich (Germany)

2 FH Aachen University of Applied Sciences, Jülich (Germany)

* *Corresponding Author: alexopoulos@sij.fh-aachen.de*

Abstract. A new project to generate electricity on a selected remote Greek island with a population of less than 1,000 inhabitants has been developed, using only renewable energy sources (RES) and energy storage systems.

This new energy plan was made taking into account the framework of the clean energy transition for islands, for the island of Othoni in the Northern Ionian Sea and compared with the current energy coverage. The electricity demand coverage needs on this island are met by using conventional fuels with the operation of diesel engines.

Appropriate software was selected and used for the optimisation and creation of energy systems. For the energy study of the island, integrated simulation models were created both for the current total energy supply and for different scenarios of the newly developed energy planning.

Keywords. Energy transition, Clean energy, Energy planning, Remote island, Simulation model, Renewable energy system (RES), Energy storage system.

1 Introduction

In Greece, there are a considerable number of remote islands, most of which are not interconnected with the mainland electricity grid of Greece. It is very common that such remote places with high potential for usage of renewable energy systems aren't being fully taken advantage of. On the contrary, the Public Power Corporation (PPC) uses autonomous thermal power plants to meet the needs of the Aegean and Ionian islands [1]. These plants require large quantities of either light (diesel) or heavy (fuel oil) oil to operate, with correspondingly high carbon dioxide emissions.

The vast majority of the remote islands of Greece are characterized by a very high solar, but also a remarkable wind potential. In addition to the Aegean there is one remote island in the Ionian Sea, the Othoni, with a moderate solar and wind potential compared to the Aegean.

A new project to generate electricity on the selected remote Greek island Othoni with a population of less than 1,000 inhabitants has been developed, using only renewable energy sources (RES) and energy storage systems. This article describes this new concept for an energy system for Othoni island in Greece and the simulations which ran with an software application. The simulations results are then compared with the current supply of energy in the island.

2 Description of current situation

According to [2] the majority of the island's energy is provided by diesel generators and imported electricity via underwater cables from Independent Power Transmission Operator (IPTO). The Public Power Corporation (see [1]) uses according to [3] autonomous thermal power plants (CHPs) to meet the needs of the Aegean and Ionian islands.

The main source being used are the diesel generators which provide a consistent source of power, but they are costly to operate and maintain, and their emissions contribute to air pollution and climate change.

Table 1 shows a list of the available and running

diesel generators on Othoni Island.

Table 1: List of diesel generators on Othoni Island as described in [4].

No.	Generator	Capacity [kW]	Efficiency [%]
1	G3	80	85.0
2	G4	80	85.0
3	G5	80	85.0
4	G7	180	93.7
5	G8	200	93.7

It is important to note that the five generators with a total capacity of 0.62 kW can produce more than the required demand of the island. These generators are switched on and off according to the real-time electricity demand.

Figure 1 shows the current energy system model in Othoni island.

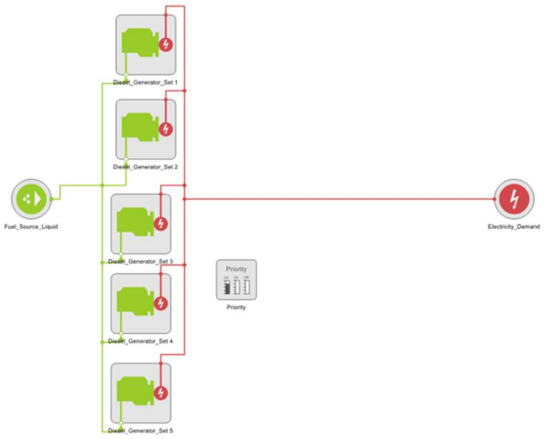


Figure 1: Current energy system model in the island of Othoni.

This model was created by selecting the required components from the component library of the software tool and linking every input and output accordingly. Each of the components in the model can be configured with the respective technical data. In Othoni, all of the electricity comes from the diesel generators.

3 New concept for energy production in Othoni

It is important to describe first the potential of renewable energy sources. This is followed by the new energy planning with the aim of 100% renewable energy use and modelling with appropriate software

3.1 Renewable energy potential

It is a fact that the vast majority of the remote Aegean and Ionian islands are characterised by a very high solar, but also a remarkable wind potential. The choice of renewable energy technologies is illustrated by a potential analysis which focuses on the location of the island.

Regarding the solar potential Othoni receives enough of sunlight throughout the year, making it a promising location for the installation of solar panels [5].

Figure 2 shows according to [6] the solar and wind energy potential for Greece. As can be derived from this figure the solar potential for Othoni is not so high in Greece with annual solar radiation values of 1450 kWh/m² and annual mean wind speed at 30 m of less than 3 m/s [6].

The average annual global horizontal solar irradiance in Othoni Island varies depending on the exact location, but it is generally around 1,700 kWh/m²/a [7].

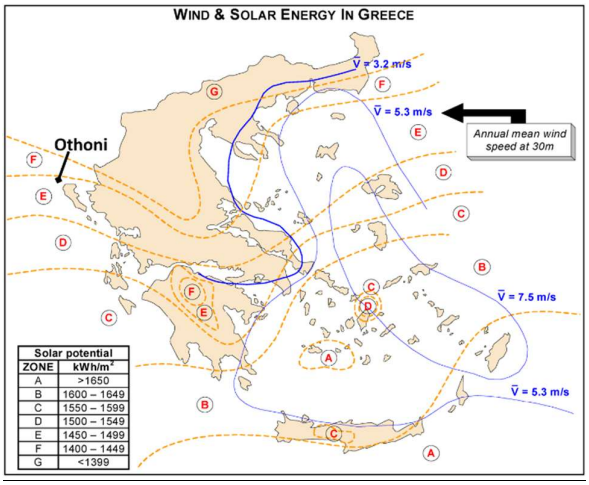


Figure 2: Solar and wind energy potential for Greece, according to [6].

The average wind speed on Othoni Island is around 6-8 m/s, with maximum wind speeds reaching up to 10 m/s at 50 m [8]. Othoni is exposed to strong and steady winds due to its exposed position in the Ionian Sea. These features generate average wind speeds and turbulence, making wind energy generation possible.

3.2 New concept

Taking into account the pressing need to meet the island's energy needs without further use of conventional and therefore polluting fuels, the

prospects for the development of a new energy system on the island, based mainly on the exploitation of the available solar and wind potential and the use of energy storage systems, are proposed and explored.

The main difficulty in drawing up an energy plan is that renewable energy production is always linked to storage, as it fluctuates throughout the day and the seasons. Generating electricity with photovoltaic and wind power systems is a way to make up for the use of conventional forms of energy in the long term.

The new concept envisages a combination of these two types of energy production technologies, as they work well together. In winter, wind speeds are high, so more electricity is produced than solar power, and in summer, solar power is high while wind power is lower, so the two are balanced throughout the year. For energy security, storage is also added to ensure that energy is available during the dark phase or in case of problems with the systems.

3.3 Simulation model development

Appropriate software was selected and used for the optimisation and creation of energy systems. For the energy study of the island, integrated simulation models were created both for the current total energy supply and for different scenarios of the newly developed energy planning.

The authors used the TOP Energy software, as it has a number of advanced features, which are mentioned in [9]:

- the possibility of carrying out economic and ecological evaluation
- the freedom to design and test new ideas
- the integration of solvers that help to find the right economic, ecological and energy optimum

Figure 3 shows the concept with new PV arrays, wind turbines and a battery for Othoni island.

The new energy concept includes PV arrays with an installed capacity of 400 kW and a small wind turbine with an installed capacity of 100 kW. The battery was chosen to have a capacity of 20 MWh, which was not yet optimized. The priority is also configured so that the renewable energy sources are set as the main source of electricity.

The energy comparison is carried out using real data describing hourly step by hour the production of the renewable energy plants for a full year of operation.

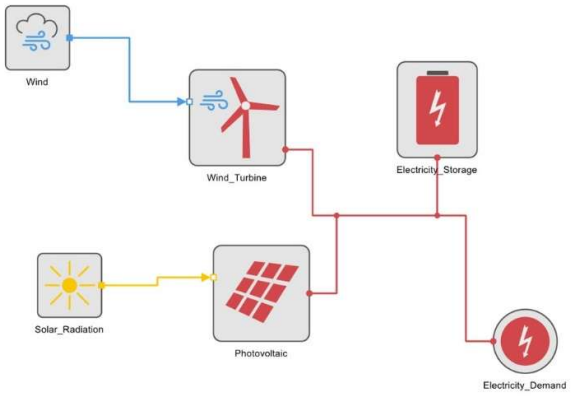


Figure 3: Model of new energy concept for Othoni Island.

The climate impact is presented on the basis of a CO_2 balance and taking into account the reduction of fuel requirements.

4 Simulation results

Figure 4 shows the power production from wind and PV for the new energy concept. According to this chart most of the energy production comes from the new PV and the stored energy with the battery. In the early morning hours and in the afternoon the PV and wind installation as well as the battery provide enough power to cover the electricity demand. During daytime, the extra electricity production from RES is stored in the battery.

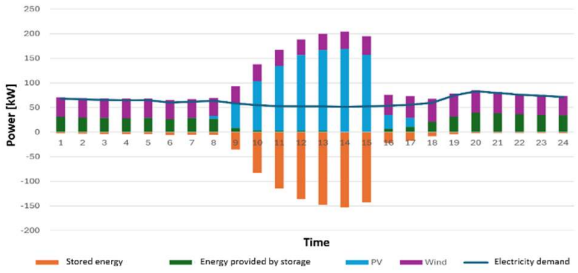


Figure 4: Overview of the simulation results for a characteristic winter day in Othoni [10].

The yearly electricity production as shown in [10] was around 0.9 GWh.

Figure 5 further shows the power production from wind and PV for the new energy concept for a characteristic summer day. The demand curve in summer is higher than in winter, because cooling demand is rising, through air conditioning. Similar to

the characteristic winter day the PV and wind installation together with the battery system are providing the electricity to cover the electricity demand of the Othoni island.

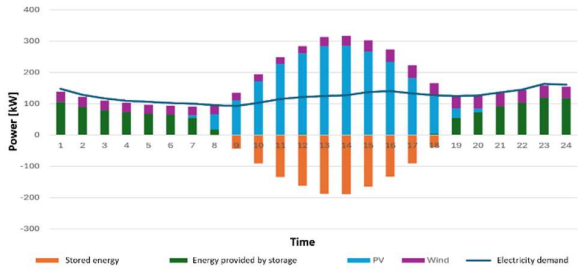


Figure 5: Overview of the simulation results for a characteristic summer day in Othoni.

The main objective when implementing renewable energy sources is to lower the emissions of carbon dioxide. The currents sources of energy in Othoni island still include diesel as a source, which has a high CO_2-emission factor of 1.1. With the simulations, it was possible to eliminate in a high amount the usage of diesel and replace it with sustainable sources. The simulation results provided that an amount of more than 450 t CO_2/a can be saved, when the new concept is implemented [10] [11].

The self-sufficiency rate for the new concept is around 95%. This means that the planned renewable energy sources can almost fully cover the electricity demand for the Othoni island.

5 Conclusions and future steps

A new energy concept for the production of electricity on a selected remote Greek island with a population of less than 1,000 inhabitants has been developed for Othoni in the Ionian Sea, using only renewable energy sources (RES).

The electricity demand coverage needs on Othoni are so far covered by the use of conventional fuels with the operation of diesel engines. Taking into account the pressing need to meet the energy needs of Othoni without further use of polluting fuels, the prospects of developing a new energy system on the island, based mainly on the exploitation of the available solar and wind potential and the use of energy storage systems, were explored.

Acknowledgement

The authors would like to thank at this point the TOP Energy team for their assistance and software support. The main author would like to thank Prof. J. K. Kaldellis for his scientific contributions in form of publications in the field of remote island energy planning for Greece, which provided very useful basic information about the RES potential and the energy concepts in this paper.

References

[1] Public Power Coorporation Detailed Map of the Stations, available at: https://www.dei.gr/, [Accessed January 2021].

[2] Interconnection of Cyclades Phase D Santorini-Folegandros-Milos-Serifos. [online] IPTO. Available: https://www.admie.gr [Accessed 22 Apr. 2023].

[3] Kaldellis J.K., Zafirakis D., 2007. Present Situation and Future Prospects of Electricity Generation in Aegean Archipelago Islands, Energy Policy Journal, Vol.35 (9), pp.4623-4639

[4] Publication of NII Daily Energy Planning Data. [online] Available: https://deddie.gr/en/ [Accessed 22 Apr. 2023].

[5] Geography of Othoni island |Greeka 2024. [online] Greekacom. Available at: https://www.greeka.com/ionian/corfu/sightseeing/othonoi-island/ [Accessed 29 Jul. 2024]

[6] Kaldelis J.K., 2021. Supporting the Clean Electrification for Remote Islands: The Case of the Greek Tilos Island Energies 2021, 14, 1336

[7] Global Solar Atlas Web Application. [online] Available at: https://globalsolaratlas.info/en/ [Accessed 29 Jul. 2024]

[8] Global Wind Atlas Web Application. [online] Available at: https://globalwindatlas.info/en/ [Accessed 29 Jul. 2024]

[9] Schwarzkopf I., 2022. Autarke Energie- und Klimaschutzkonzepte für ausgewählte kleine deutsche und griechische Inseln Bachelorarbeit FH Aachen University of Applied Sciences 2022

[10] Suthar D., 2024. Entwicklung eines Autarkiekonzepts für Othonoi, Griechenland Project work FH Aachen University of Applied Sciences 2024

[11] Pathel P., Slyamov D., 2024. Othonoi Insel, Neues Konzept, Project work FH Aachen University of Applied Sciences 2024

INTEGRATING CARNOT BATTERIES IN THE ELECTRICAL GRID: A MATTER OF UNDERSTANDING SYSTEM DYNAMICS?

Robin Tassenoy[1]*, Michel De Paepe[1,2,3], Steven Lecompte[1,2]

[1] Ghent University, Department of Electromechanical, Systems and Metal Engineering, Ghent, Belgium

[2] FlandersMake@UGent, Core lab MIRO, Ghent, Belgium

[3]University of Cape Town, Department of Mechanical Engineering, Rondebosch, South Africa

* *Corresponding Author:* Robin.Tassenoy@UGent.be

Abstract. This short paper explains which dynamic characteristics of pumped thermal energy storage are important for their successful integration within the energy system. Based on literature examples, it summarizes the current state-of-the-art on the topic. Finally, an outlook for further research is provided.

Keywords. Carnot battery, PTES, Grid services, System Dynamics, Review

1 Introduction

Renewable energy sources (RES) made up 41 % of all electricity use in the EU in 2022. Variable renewable energy (VRE), like wind and solar, accounted for almost 56 % of this renewable electricity [1]. The intermittency of this VRE challenges the stability of the electrical grid. Ensuring stable and secure energy supply requires additional power system flexibility, which is the extend to which a power system can scale electricity production or consumption in response to variability, expected or otherwise [2]. Technical grid requirements typically drive very short-term flexibility needs (sub-second to minutes), while short- to very long-term flexibility is required to ensure sufficient generation capacity to meet electricity demand at hourly, daily, up to seasonal timescales [2]. Energy storage is considered one of the main solutions providing the flexibility required to decarbonize the electricity grid [3].

Carnot batteries (CB) are an emerging storage concept that might contribute to grid flexibility. They store electricity in thermal energy storage systems (TES). During the charge process, electricity is converted into heat and kept in the heat storage. During the discharge process, the stored heat is converted back into electricity [4]. Pumped thermal energy storage (PTES) is one of the Carnot battery's subsets in which an electrically driven heat pump (HP) elevates the temperature of heat coming from a cold source and delivers it to a TES at higher temperature [5]. Within this subset, systems based on the Brayton-cycle and Rankine-cycle can be distinguished [6]. So far, studies focused mainly on the steady-state performance and optimization to determine the obtainable round-trip efficiencies [6]. More recently, techno-economic evaluations gained interest as well [7]. The literature reveals that Carnot batteries have mainly been considered for load-shifting and arbitraging services. Considering these services alone, creating a positive business case is often challenging. These systems could thus benefit from a portfolio of revenue streams.

A full discussion on all grid related services is not possible here. This short paper aims to illustrate why understanding of the system dynamics is crucial for successful integration of PTES within the electrical grid. Then, the state-of-the-art is illustrated based on literature examples. Finally, some suggestions for further research are formulated.

2 Dynamic EES characteristics to support the electricity grid

Within this short paper, a non-exhaustive overview of grid services and their technical requirements is given. For a comprehensive overview the reader is referred to Schmidt and Staffell [2]. Based on their overview, it can be understood that a full dynamic characterization for PTES integration within the grid involves:

- Cyclic operation
- Startup and shutdown behaviour
- Power modulation capability

The importance of the cyclic operation can be understood by the structure of the day-ahead market, typically used for arbitraging. This market is based

on 1h – energy bids. This means an accurate prediction of the power uptake or delivery for each hour of operation is essential. For some PTES-concepts, this power depends on the variable state-of-charge (SOC) of the TES as will be illustrated in the next section. Even during consecutive nominal charge- and discharge processes, the instantaneous power uptake or production and system efficiency will thus vary. Understanding of this cyclic behaviour is essential to make an accurate performance prediction for real operation. Moreover, this relationship between SOC and power uptake and/or delivery is important with respect to the offered capacity in shorter-term markets.

While the startup and shutdown procedures of the charge- and discharge cycle are often assumed negligible to assess the average system performance, they still determine the flexibility of the system to be quickly activated or shut down, or to switch between operating modes. Therefore, understanding them is relevant for determining realistic operating schedules. Depending on the response times, activation or shutdown in response to grid balancing signals might be an option too. Finally, detailed understanding of these processes might support cycle optimization for real operating scenarios and highlight technical limitations or mechanical considerations related to the start-stop behaviour and system lifetime.

Finally, power modulation during the charge- and discharge period is important for load-following of VRE production or variable demand, grid balancing services in the transmission grid or even behind-the-meter optimization of different assets. Understanding the system dynamics and control allows to assess the compatibility between the PTES and the variation of VRE. Moreover, the technical requirements for grid-balancing services can be verified. In the central European grid, the offered capacity should be activated within 30 s, 5 min and 12.5 min for primary, secondary and tertiary reserve, respectively. Taking these dynamic considerations into account allows to further optimize them, potentially opening up additional revenue streams.

3 PTES dynamics: literature examples

Linked to the discussion above, this section aims to illustrate the state-of-the-art regarding PTES dynamics based on the literature. While this overview is not exhaustive, it highlights some important aspects and gives a qualitative understanding of the dynamic behaviour of PTES.

3.1 Cyclic operation

Wang et al. [8] assessed the cyclic behaviour of a 10 MW / 4 h (charge and discharge) Brayton-based PTES with packed bed storage. An argon- and helium based system were assessed. The results clearly show that the storage outlet temperatures vary during the charge- and discharge process. Consequently, the system power and efficiency are variable as well. During the 4 hour discharge process, the output power decreases 71 % for the argon based, and 45.9 % for the helium based system compared to its initial value. This variation is thus definitely not negligible when scheduling the system. Moreover, the authors also discuss the influence of storage geometry and cycle design on this dynamic variation. It highlights the importance of optimizing the system behaviour in the design stage for the whole cyclic process, rather than for the nominal design condition only.

An example for Rankine-based systems can be found in the work of Tafone et al. [9]. This work compares the cyclic behaviour of a conventional CHEST-concept using sensible two-tank water storage and a latent packed bed PCM storage to an alternative concept using a cascaded PCM packed bed with 3 PCMs having different melting temperatures. For both, a 1 MW / 3 h (discharge) system is considered. Again, the work illustrates the variation in performance of the charge- and discharge cycle due to the variation of inlet and outlet TES-temperatures. It shows that the proposed cascaded storage could partially mitigate the decreasing thermal power during the discharge phase enhancing the total electricity production. Moreover, the adapted design achieves a better match of the TES and heat transfer fluid temperature profiles during the full cycle. This leads to a higher efficiency of the HP and organic Rankine cycle (ORC) during the full charge- and discharge process – improving the effective round-trip efficiency of the system when evaluated during the full cycle.

The studies above clearly illustrate a variation of system performance during the charge- and discharge process that would be neglected based on steady-state analysis only. Although this difference in operation is illustrated, the overall performance loss when designing the system based on the nominal point rather than on the full cyclic process is not quantified. This would be interesting to identify to what extent the design optimization problem could be simplified to not require simulation of the full charge- and discharge process and what the impact of such a simplification on the optimal design would be.

Noticeably, the transient behaviour in the studies above is dominated by a packed bed storage, either directly integrated in the cycle or connected with an intermediate heat transfer loop. Packed bed storage does not allow to control the heat transfer medium on the secondary side. While no detailed studies have been found, this effect might thus be less important for indirect two-tank liquid storage where the temperature profile of the storage tank could be kept more constant by controlling the storage medium's mass flow rate. It is thus worth investigating this dynamic behaviour for different TES-types. From a modelling perspective, it can be noted that only the TES is modelled dynamically, while the thermal cycles are considered quasi-steady state. This thus implies that the impact of varying TES conditions on the cycle is considered, but transient effects within the cycle are neglected. Moreover, their startup and shutdown procedure itself is considered negligible compared to the duration of the full cycle.

3.2 Startup and shutdown

While the startup and shutdown process might be negligible to assess the average performance during consecutive full cycles, they are relevant from a scheduling and flexibility perspective as explained above.

Lu et al. [10] analyzed the startup process of a 1.5 MW (discharge) Brayton-based PTES using two-tank liquid storage during charging and discharging. Assuming the two-tank storage can be controlled to maintain constant inlet- and outlet temperatures, the TES is not modelled in detail. Instead, constant water temperatures are imposed as boundary conditions. Moreover, the thermal machines and heat exchangers are both modelled quasi-steady and the dynamic mass- and energy balance are considered for the inventory reservoir only. Additionally, the dynamic momentum balance of the rotor axis is included. The authors discuss the effect of different initial working fluid charge conditions and axis acceleration rates on the startup time. The initial system pressure does not affect the steady-state pressure ratio, but does affect the absolute values of these pressures and thus the steady-state power uptake or production. The variation in flow rate during both cycle startups effectively follows the variation of the rotational speed of the shaft. For the charge process, the steady, nominal conditions can be reached in about 4000 s (1.1 h) after starting the shaft rotation, while it takes about 500 s (8.3 min) to reach these steady values for the discharge process. A more recent analogous study by An et al. [11] performed by the same research group for a 1.715 MW (discharge) system with similar topology reached the steady-state values in about 1400 s (0.4 h) for both the charge- and discharge process. While there is no clear explanation for this difference, it seems related to the allowable compressor ramping rate and speed control, and the cavity volume of the inventory tank. The model description in both studies is rather vague and shutdown behavior is not considered. This highlights the significant uncertainty on the values mentioned and the need for additional analysis.

No study of the startup or shutdown procedure of large-scale Rankine PTES has been found. Knowledge on these processes in open literature is currently limited to few experimental studies on kW-scale demonstration plants. Even in these studies, it is mostly not the focus. As an example, the procedures for startup and shutdown of the 10 kW CHEST demonstrator developed within the H2020 CHESTER-project were described in [12]. Startup of the HP was demonstrated in less than 15 min (reaching nominal compressor speed and charge conditions), while the full cold-start procedure of the ORC took approximately 40 min, including preheating of the circuit and gradual ramping of the pump and expander speed to their nominal values. Shutdown of the HP when practical operation could no longer be sustained took approximately 6 min, while for the ORC it took less than 10 min. While the procedure is instructive, these times are expected to change with scale and further optimization of the procedures. During these experimental tests, conservative ramping rates were applied to protect the experimental equipment. It would be interesting to evaluate the response times and additional mechanical considerations of more aggressive procedures, like instantaneously switching off the heat pump compressor or bypassing the ORC expander before partially decreasing its rotational speed first.

3.3 Power modulation

For power modulation of Brayton PTES, inventory control seems to be mostly favoured, which implies controlling the amount of mass contained in the closed cycle volume to vary the system net power output (discharge phase) or net power input (charge phase) [13]. The potential of this approach is shown by Frate et al. [13] for a 10 MW (charge and discharge) PTES with two-tank liquid storage. Using inventory control a +10 % power step was estimated to take around 21 s and 20 s during charge and discharge, respectively. However, the authors stress that the methodology introduced some simplifying assumptions meaning these values are indicative for

the potential and provide meaningful qualitative results, but should be upgraded for more detailed estimations.

In Rankine-based systems, variable-speed control for power regulation seems to be mainly implemented. As an indication, Tassenoy et al. [14] analysed a 1.5 MW variable-speed vapour compression HP based on a volumetric twin-screw compressor for application in a PTES with two-tank liquid storage and found that a 50 % power step was taken within 1 % of the nominal power in 15 s and 17 s for a downward and upward step, respectively. Moreover, they demonstrated the suitability of the system for secondary and tertiary reserves. Despite promising dynamic responses, primary reserve was currently not possible as the allowable tolerance was exceeded for the Belgian prequalification test. For another system based on two-tank storage, they showed that the ORC (based on turbomachines) could qualify for secondary and tertiary reserves as well [15].

4 Conclusion and outlook

This short paper discusses the importance of dynamic system behaviour for integration of PTES in the energy system. The few available studies on the topic illustrate that this is still an emerging field. To drive this field forward, it would be valuable to:

- Define a clear set of KPIs and common test profiles, based on the requirements of the energy system. This would allow to compare different topologies, explore trade-offs between different KPIs and help to derive simplified dynamic parameters that can be included in grid planning and techno-economic studies.
- Evaluate and discuss these KPIs and test results for different topologies, capacities and use cases. As such, systems cannot only be designed for nominal conditions but also for their actual operating schedules.
- Experimentally validate all these dynamics – especially at medium and large capacities. This could provide additional confidence in the model strategies currently used, which then allows to further optimize the dynamic behaviour numerically.

References

[1] "Electricity from renewable sources up to 41% in 2022", [Online]. Available: https://ec.europa.eu/eurostat/web/products-eurostat-news/w/ddn-20240221-1. [Accessed 31 October 2024].

[2] O. Schmidt and I. Staffell, “Monetizing Energy Storage: A Toolkit to Assess Future Cost and Value”, 1st edition. Oxford University Press , 2023.

[3] "Study on energy storage: contribution to the security of the electricity supply in Europe", [Online]. Available: https://data.europa.eu/doi/10.2833/077257. [Accessed 31 October 2024].

[4] A. Vandersickel et al., “Task 36 Carnot Batteries Final Report”, German Aerospace Center (DLR), 2023.

[5] J. D. McTigue et al., “Techno-economic analysis of recuperated Joule-Brayton pumped thermal energy storage”, Energy Conversion and Management, no. 252, pp. 115016, 2022.

[6] O. Dumont et al., “Carnot battery technology: A state-of-the-art review”, Journal of Energy Storage, no. 32, pp. 101756, 2020.

[7] A. Vecchi et al., “Carnot Battery development: A review on system performance, applications and commercial state-of-the-art”, Journal of Energy Storage, no. 55, pp. 105782, 2022.

[8] L. Wang et al., “Cyclic transient behavior of the Joule–Brayton based pumped heat electricity storage: Modeling and analysis”, Renewable and Sustainable Energy Reviews, no. 111, pp. 523-534, 2019.

[9] A. Tafone et al., “Dynamic modelling of a compressed heat energy storage (CHEST) system integrated with a cascaded phase change materials thermal energy storage”, Applied Thermal Engineering, no. 226, pp. 120256, 2023.

[10] C. Lu et al., “Dynamic modeling and numerical investigation of novel pumped thermal electricity storage system during startup process”, Journal of Energy Storage, no. 55, pp. 105409, 2022.

[11] X. An et al., “Physical modeling and dynamic characteristics of pumped thermal energy storage system”, Energy, no. 290, pp. 130144, 2024.

[12] K. Theologou et al., “CHESTER: Experimental prototype of a compressed heat energy storage and management system for energy from renewable sources”, Energy

Conversion and Management, no. 311, pp. 118519, 2024.

[13] G. F. Frate et al., “Dynamic modelling of a Brayton PTES system”, in ASME Turbo Expo 2022 Turbomachinery Technical conference and Exposition (GT2022), Rotterdam, The Netherlands.

[14] R. Tassenoy et al., “Assessing the influence of compressor inertia on the dynamic performance of large-scale vapor compression heat pumps for Carnot batteries”, Journal of Energy Storage, no. 101, pp. 113948, 2024.

[15] R. Tassenoy et al., “Performance analysis of a 1.5 MW organic Rankine cycle in a Carnot battery system for grid balancing services”, in 7th International Seminar on O.R.C. Power Systems, Seville, Spain.

EXPERIMENTAL PRE-VERIFICATION OF A 7 KW_{EL}/3,000 RPM RADIAL RE-ENTRY TURBINE FOR SMALL ORGANIC RANKINE CYCLE (ORC) PLANTS

Andreas P. Weiß[1*], Philipp Streit[1,2], Jan Špale[2,3], Václav Novotný[2,3] and Michal Kolovratník[3]

[1] Centre of Excellence for Cogeneration Technologies, East Bavarian Technical University of Applied Sciences Amberg-Weiden, Kaiser-Wilhelm-Ring 23, 92224 Amberg, Germany

[2] University Centre for Energy Efficient Buildings (UCEEB), Czech Technical University in Prague, Třinecká 1024,Buštěhrad 273 43, Czech Republic

[3] Department of Energy Engineering, Faculty of Mechanical Engineering, Czech Technical University in Prague, Technická 1902/4, Prague 160 00, Czech Republic

* *Corresponding Author: a.weiss@oth-aw.de*

Abstract. Experimentally determined efficiency characteristics of an uncommon velocity compounded radial four-fold re-entry turbine are discussed in this short paper. The small 7 kW turbine was designed to drive a 3,000-rpm standard-generator in a small ORC plant operating with hexamethyldisiloxane (MM). It was pre-investigated numerically and experimentally with compressed air as working fluid to check the overall functionality and to learn about complex flow phenomena. Due to the "off-design" working fluid, maximum total-to-static isentropic efficiency of only 27 % was achieved. However, the uncommon small turbine has the potential to substitute an existing standard axial impulse turbine with a similar rating which must work at 24,000 rpm driving an expensive high-speed generator.

Keywords. Radial re-entry turbine**,** Velocity compounded**,** Organic Rankine Cycle (ORC).

1 Introduction

Organic Rankine Cycles (ORC) are a well-established solution to recover low temperature waste heat in industry [1]. Most turbine driven systems work with power ratings from some 100 kilowatts to a few megawatts. Below 100 kW_{el}, volumetric expanders dominate because they are cheaply available as derivates of mass-produced refrigeration compressors [2]. However, turbines provide several advantages: they do not need any lubrication within the working fluid, they experience almost no wear, and they can be easily adjusted to different fluids and boundary conditions. The main disadvantage of those small (< 100 kW_{el}) turbines is the fact that they must work at rotational speeds of several 10^4 rpm [3]**.** Therefore, an expensive high-speed generator must be installed instead of a 3,000 rpm off-the-shelf generator along with the need for high-speed bearings, precision manufacturing and balancing. This drawback can be overcome by using a velocity compounded radial multi-fold re-entry turbine – a so-called Elektra turbine [4]. Figure 1 displays the architecture of the designed Elektra turbine: a convergent-divergent nozzle accelerates the fluid, then, the supersonic jet passes the wheel, four times in our case, at almost constant pressure. The velocity or kinetic energy of the jet is reduced from wheel pass to wheel pass (1st WP: 45%, 2nd WP: 30%, 3rd WP: 19%, 4th WP: 6%). This approach is called velocity compounding. Whereas for a simple impulse turbine, the optimal circumferential speed of the wheel would be half of the jet velocity, for the Elektra it is only one-eighth. Thus, the rotational speed can be reduced to 25 % compared to the impulse stage. In the discussed application, the Elektra wheel diameter was furthermore doubled compared to the existing 24,000 rpm axial impulse turbine. Thus, the necessary rotational speed could be reduced from 24,000 rpm to 3,000 rpm for the same duty [5].

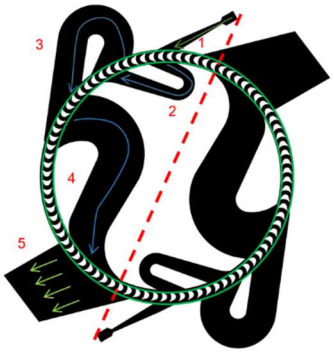


Figure 1: Architecture and flow path of the velocity compounded radial four-fold re-entry turbine (Elektra): 1 con-di-nozzle, 2 first deflection channel, 3 second deflection channel, 4 third deflection channel, 5 outlet. Two sets of nozzles and two sets of deflection channels are installed which are used in parallel with the same wheel. (red dotted line shows the symmetry plane).

2 Results and discussion

The preliminary efficiency characteristics of the 3,000 rpm Elektra turbine, designed for MM, were experimentally determined with compressed air at different pressure ratios and compared to computational fluid dynamics (CFD) results. Table 1 lists the MM turbine design data in comparison with the air pre-verification data. The compressed air test facility is described in [6].

Table 1: Turbine MM design and air pre-verification data

Parameter	Unit	Design	Pre-verification
Fluid	-	MM	air
Mass flow rate	kg/s	0.30	0.15
Inlet pressure	bar	6.50	6.00
Inlet temperature	°C	190	20
Outlet pressure	bar	0.55	≈1

First, Figure 2 compares the calculated absolute Mach number distributions for the given boundary conditions (Table 1) for MM (top, see [5]) and for air (bottom, see [7]). The simulation approach is explained in detail in [5]. The MM flow in the nozzles continuously accelerates to an outlet Mach number of about 2. The air flow accelerates even to higher Mach number but a strong normal shock within the nozzles leads to transonic flow at their outlets. The MM flow utilizes the cross-section of the deflection channels more effectively while the air flow forms rather singular jets. The overall Mach number level in the deflection channels with MM is significantly higher than with air. This clearly shows that the expansion of the air flow does not match the geometry of the MM turbine. Ultimately, this is also reflected in the calculated expansion efficiency, which is approx. 50 % for MM and approx. 34 % for air.

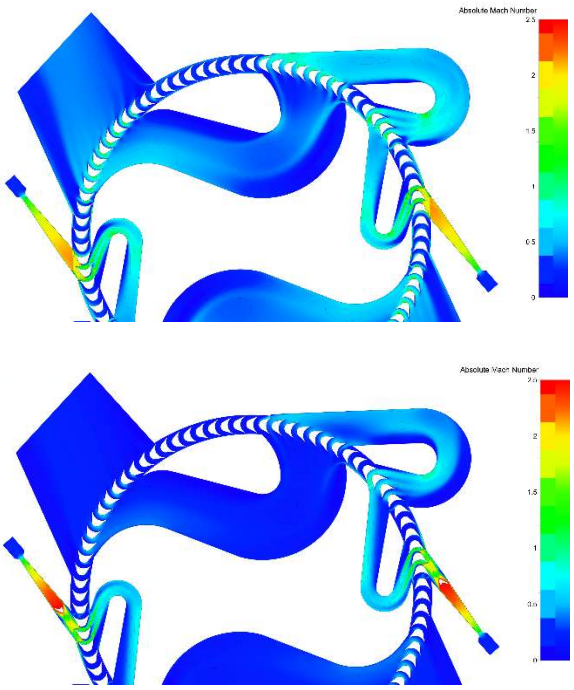


Figure 2: Absolute Mach number distributions at mid span for MM (top, [5]) and air (bottom, [7]).

The experimentally determined total-to-static isentropic efficiencies as function of rotational speed are depicted in Fig. 3. The maximum achieved efficiency for maximum PR = 6 was about 27 %, which is relatively low. Firstly, this is due to the wrong fluid – air instead of hexamethyldisiloxane (MM). The second adverse effect is the too small pressure ratio. The design pressure ratio with MM is PR = 13 (compare Table 1). On the compressed air test rig, PR = 6 was the maximal achievable pressure ratio. Finally, this is the tribute of the velocity compounding. A supersonic jet impinges on the wheel at very high relative velocity and is re-deflected three times (see Figure 2). These flow physics reduce efficiency significantly.

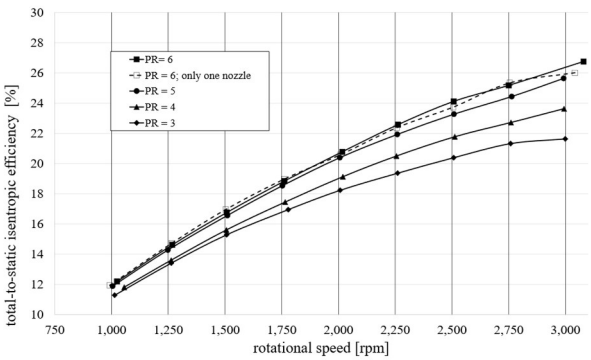


Figure 3: Total-to-static isentropic efficiency of the Elektra turbine for air at different pressure ratios (PR) as a function of rotational speed [7].

It is interesting that for PR = 3, maximum efficiency is achieved at 3,000 rpm. This is the design rotational speed for MM. For the higher-pressure ratios, maximum efficiency will be achieved at higher rpm which could not be tested due to limitations of the brake. At PR = 3 the enthalpy drop of compressed air is about 65 kJ/kg which is close to the MM design enthalpy drop (PR = 13) of 54 kJ/kg. With the increasing air pressure ratio, the enthalpy drops increases as well and achieves about 117 kJ/kg for PR = 6. The optimum rotational speed of a turbine is a function of the enthalpy drop. Because the enthalpy drop with air at PR = 6 is about twice the enthalpy with MM at PR = 13, the optimum rotational speed with air (PR = 6) is theoretically √2 times higher than that with MM. Finally, the dashed curve in Fig 3. displays efficiency with only one of the two nozzles open i.e. with only 50 % of the mass flow rate. Interestingly, efficiency is almost the same, what shows, that ventilations losses of the half non-admitted arc of the wheel are obviously very small at 3,000 rpm.

Fig. 4 displays the comparison of streamwise static pressure distribution – measurements versus computational fluid dynamics (CFD).

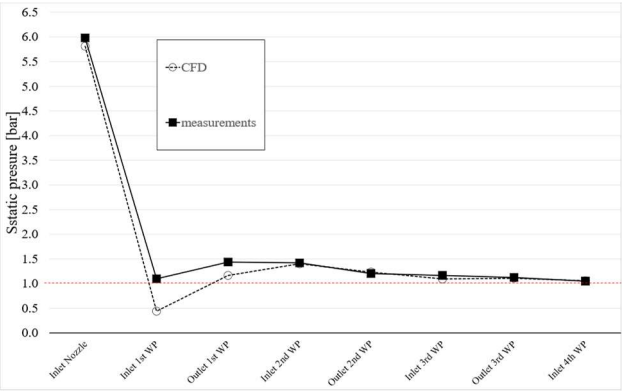


Figure 4: Streamwise static pressure distribution for air: measurement (full squares) versus computational fluid dynamics (CFD, open circles).

The qualitative shapes with a strong expansion over the con-di-nozzle, a pressure increase over the first wheel pass (WP) and an almost constant pressure distribution further downstream are the same. However, in the simulation (CFD), the nozzle expands to 0.5 bar, whereas the measurement shows about 1.0 bar nozzle exit pressure. Furthermore, static pressure is still higher at the outlet of the first wheel pass in the measurement. It cannot be excluded that these discrepancies are just due to the positions of the specific pressure taps in the measurement.

Finally, Fig. 5 compares total-to-static isentropic efficiencies as function of total-to-static pressure ratio (PR). As expected, the simplified frozen rotor CFD-simulation (see [7]), neglecting tip leakages and disc friction, shows about 5 p.p. higher efficiencies compared to measurements. Efficiency is rising with pressure ratio (PR) because the nozzle or the turbine is operated far below the design pressure ratio (PR_{Design} = 13).

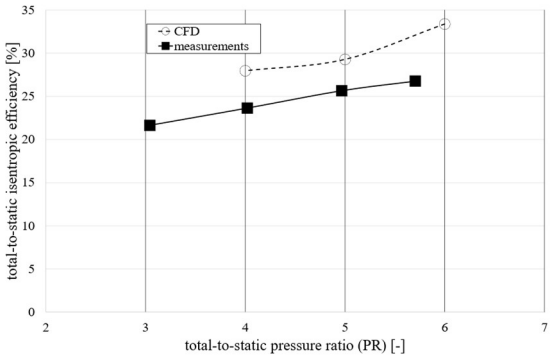


Figure 5: Total-to-static isentropic efficiency for air as a function of pressure ratio: measurement (full squares) versus computational fluid dynamics (CFD, open circles) [7].

3 Summary and conclusions

The short paper discusses the compressed air pre-verification of a small MM Elektra turbine. Of course, the gathered results can only give a tendency because the properties of the chosen test working fluid air differ significantly from those of the design working fluid hexamethyldisiloxane. However, this approach helped the authors to understand the flow phenomena of the Elektra turbine better and to develop and adjust their design approach.

The 50% isentropic expansion efficiency, forecasted by CFD, would be quite competitive with regard to volumetric expanders with similar power ratings [2]. Imran *et al.* 2015 lists many measured efficiencies of small 3,000 rpm ORC expanders. The mentioned maximum efficiencies vary from 30 % to 70 % for rotary vane, 10 % to 75 % for piston, 22 % to 84 % for scroll and 45 % to 80 % for screw expanders. All these positive displacement expanders need lubrication in the working fluid because they suffer from mechanical wear. Furthermore, some expander parts must be regularly replaced due to wear (e.g. vanes, gaskets etc.). They are prone to vibrations and noisy operation. All these disadvantages could be avoided by an Elektra turbine.

In 2025, the Elektra will be finally tested in an operational MM ORC plant [8] at UCEEB in Prague. There, it will substitute a 3,000 rpm rotary vane expander which is achieving about 56% expansion efficiency.

Acknowledgement

The research leading to these results has received funding from the EEA Grants and the Technology Agency of the Czech Republic within the KAPPA Programme. Project code TO01000160. Furthermore, the material is also based upon work supported by the Grant Agency of the Czech Technical University in Prague, grant No. SGS24/087/OHK2/2T/12

References

[1] Tartière T, Astolfi M. A World Overview of the Organic Rankine Cycle Market. Energy Procedia 2017;129:2–9. https://doi.org/10.1016/j.egypro.2017.09.159.

[2] Imran M, Usman M, Park B-S, Lee D-H. Volumetric expanders for low grade heat and waste heat recovery applications. Renewable and Sustainable Energy Reviews 2016;57:1090–109. https://doi.org/10.1016/j.rser.2015.12.139.

[3] Weiß AP. Volumetric expander versus turbine - which is the better choice for small ORC plants? In: University of Liège and Ghent University, editor. ASME-ORC2015: Proceedings of the 3rd International Seminar on ORC Power Systems; 2015.

[4] Stodola A. Die Dampfturbinen. 3rd ed. Berlin, Heidelberg, Germany: Springer; 1905.

[5] Streit P, Weiß AP, Stümpfl D, Špale J, Anderson LB, Novotný V et al. Concept and Design of a Velocity Compounded Radial Four-Fold Re-Entry Turbine for Organic Rankine Cycle (ORC) Applications. Energies 2024;17(5):1185. https://doi.org/10.3390/en17051185.

[6] Weiß AP, Stümpfl D, Streit P, Shoemaker P, Hildebrandt T. Numerical and Experimental Investigation of a Velocity Compounded Radial Re-Entry Turbine for Small-Scale Waste Heat Recovery. Energies 2022;15(1):245. https://doi.org/10.3390/en15010245.

[7] Schulze Julian. Numerische und experimentelle Untersuchung einer radialen Vierfach-Wiedereintrittsturbine: Bachelor Thesis. Amberg; 2024.

[8] Mascuch J, Novotny V, Spale J, Vodicka V, Zeleny Z. Experience from set-up and pilot operation of an in-house developed biomass-fired ORC microcogeneration unit. Renewable Energy 2021;165:251–60. https://doi.org/10.1016/j.renene.2020.11.021.

EXPERIMENTAL AND NUMERICAL INVESTIGATION OF A RETROFITTED ORGANIC RANKINE CYCLE TOWARDS ITS INTEGRATION INTO A CARNOT BATTERY

Mattéo Hauglustaine[1,2]*, Antoine Laterre[1,3], Benjamin Berger[4], Francesco Contino[1]

[1] Catholic University of Louvain (UCLouvain), Institute of Mechanics, Materials and Civil engineering (iMMC), Louvain-la-Neuve, Belgium

[2] University of Mons (UMons), Thermal Engineering and Combustion Unit, Mons, Belgium

[3] University of Liège (ULiège), Thermodynamics Laboratory, Liège, Belgium

[4] ECAM Brussels Engineering School, Mechanical and Thermal Engineering Unit, Brussels, Belgium

* *Corresponding Author: matteo.hauglustaine@uclouvain.be*

Abstract. The transition towards sustainable energy systems requires innovative solutions for energy storage and conversion. Among these, Carnot batteries are emerging as a promising technology for integrating variable renewable energy sources into the electrical grid and for coupling heat and electricity. They operate on the basic principles of thermodynamics to store excess electrical energy as heat, which can then be converted back into electricity. A key component in low-temperature Carnot batteries is the Organic Rankine Cycle (ORC), efficient in converting thermal energy from low to moderate heat sources into useful work. This paper presents an experimental and numerical study of a low temperature ORC, aiming to assess its compatibility and performance within a Carnot battery system. The numerical model is designed to predict the ORC performance under various operational states, providing necessary insights for effective experimental characterization. In parallel with numerical efforts, the paper conducts a series of experimental tests to evaluate the ORC under off-design conditions. Such conditions are essential for understanding practical challenges and behaviours of the ORC when integrated into a Carnot battery, where variable heat sources are envisaged. Furthermore, the experimental component enriches the model with empirical data, crucial for refining and enhancing its predictive accuracy. By addressing both theoretical and practical aspects of the ORC within a Carnot battery context, this research contributes to the technological development of the machine and its subsequent optimization for improved integration of ORC technology into future energy storage solutions. The findings of this work could thus inform the design and operation of more efficient Carnot batteries, supporting a smoother transition towards renewable energy infrastructures.

Keywords. Organic Rankine Cycle, Carnot Battery, Retrofit, Off-design, Experimental

1 Introduction

Carnot batteries (CB) stand out as a Long Duration Energy Storage (LDES) for their cheap cost, low impact on critical resources, scalability and lifetime. They rely on heat as storage medium to store the excess energy produced and deliver it when needed [1]. They are composed of three main steps: (i) the charging phase – a heat pump converts excess electricity from the grid into heat, (ii) the storage phase – a Thermal Energy Storage (TES) stores the energy under the form of heat for a few hours to several days, (iii) the discharge phase – a heat engine turns the heat back to electricity when needed.

Among other power cycles, the Organic Rankine Cycle (ORC) is a suitable candidate for the discharge phase of the CB for its abilities to efficiently exploit low temperature heat (< 300 °C) and turn it into heat. It is composed of a pump, an evaporator, an expander and a condenser. During the Carnot Battery operation, for example as the TES discharges or the power output demand differs from the nominal power, the ORC may be brought to off-design working points – i.e. points that are away from the nominal, designed, working point. These operating conditions negatively impact the efficiency of the cycle and by extend, the efficiency of the CB. Therefore, the efficiency of the ORC should be studied to quantify its evolution throughout the operational conditions. This study investigates a commercial micro-scale ORC (< 1 kW) to evaluate the potential of a Carnot Battery for a domestic

application. The ORC is retrofitted to operate at a lower temperature than which it was designed for, and the machine is characterized under off-design conditions.

2 Research gap addressed in this paper

In this paper, the interest of a domestic scale Carnot Battery is investigated. For this purpose and to meet acceptable investment costs, the use of a low temperature water sensible heat storage is envisioned. The use of water is justified by the fact that it is a cheap and abundant material. It might also be combined with other cheap and locally abundant materials such as sand and rocks to increase the storage density of the tank. The goal is to utilize a storage temperature of maximum 100°C not to pressurize the tank. Indeed, at atmospheric pressure, water brought at ≈ 100°C would start to boil and be detrimental for the components. A solution would be to pressurize the tanks to reach higher storage temperatures and increase the efficiency of the system. But this pressurization comes with financial costs that are undesired.

Therefore, the goal is to investigate the use of a low temperature storage (< 100°C) tank in the CB. To this end, the behaviour of Organic Rankine Cycles at such low temperature needs to be assessed. This paper represents a first step in the assessment of an ultra-low temperature ORC. The main objective is to experimentally operate and characterize the performance of an ORC in off-design conditions.

Method

To achieve this objective, a numerical *off-design* model of the ORC is constructed. At first, the model will allow to select a new working fluid by simulating the cycle in new working conditions. Moreover, the model will be used to highlight the most influencing parameters on the total efficiency of the machine by means of a Monte Carlo simulation. The experimental campaign will be design consequently and optimized in time and resources by only focusing on the most crucial quantities.

2.1 Numerical model

A steady-state and *off-design* model of the ORC is required because the purpose of the study is to characterize the ORC performance all along its operation range. This means that the machine is likely to operate in conditions that are away from the nominal operating point. Also, during the experimental campaign, the ORC will always be brought to a constant working point before acquiring the measures. Therefore, a steady state model is considered sufficient in this work.

The main feature that will negatively impact the ORC efficiency in off-design conditions is the over and under-expansion losses in the expander. As the expander is a volumetric machine (a scroll expander), losses occur when the volumetric ratio that the expander witnesses deviates from the one it was designed for. No matter what the operational conditions are, the fluid will be expanded by a ratio equal to the Built in Volume Ratio (BVR), bringing the working fluid at the exhaust pocket of the scroll at a certain pressure. Any difference (positive or negative) between the pressure of the fluid at the exhaust pocket and the pressure in the discharge pipe (i.e. the condensation pressure) is then perceived as a loss. The pressure of the fluid at the exhaust chamber of the scroll is derived from to the specific volume imposed by the expander at the same location. This pressure is called the adapted pressure. If the exhaust pipe pressure is lower than the adapted pressure, an instantaneous isochoric expansion is considered, for the exhaust fluid state to match the fluid state in the downstream pipe. The refrigerant thus underwent *under-expansion*. On the other hand, if the exhaust pipe pressure is greater than the adapted pressure, an instantaneous compression is considered to match the downstream state. It is called an *over-expansion.*

2.2 Selection of a new working fluid

The ORC unit is a commercial product. It was designed to operate between approximately 110°C (heat source) and 50°C (heat sink). Those temperatures where estimated based on the nameplate of the machine. The refrigerant that was initially present in the machine, R601a (iso-pentane), suits this temperature duet. But as the unit will operate under lower temperatures (i.e. maximum 70°C at the source and approximately 15°C at the sink), another working fluid must be selected. Otherwise, the maximum performance of the components cannot be harvested. For instance, the volume ratio must be similar to the one the scroll expander was designed for in order not to undergo too much over or under-expansion losses [2]. Likewise, the volume coefficient VC strongly depends on the fluid density at the expander inlet. It will have a negative impact on the output work if the density decreases, as the volumetric flow remains constant in a volumetric expander. The selected refrigerant is R600a or iso-butane. The R600a presents a low GWP value of 3, which impacts global warming in a minor way in case of leaks to the ambient during operation or maintenance. It is highly

flammable and non-toxic. The most ideal charge of refrigerant in the machine was determined empirically. The goal was to charge enough fluid for the ORC to run at the maximum thermal power provided by the bench while keeping a superheating of approximately 5K maximum. Indeed, the more thermal power available at the heat source for a constant temperature, the higher the refrigerant flow rate must be. Otherwise, it would result in an exaggerated superheating, leading to a decrease in thermal efficiency. The reason for that is the decrease in evaporating pressure imposed by the pinch point that is located at the expander inlet. Since the pressure is lower, the density for an equivalent temperature is diminished. The lower the density of the refrigerant at the inlet port of the expander, the lower is the resulting mass flow rate. The expander volume flow rate being constant for a fixed speed, the work that it produces is decreased. Therefore, the procedure to add charge to the circuit is to start by filling a low amount of refrigerant. Then, the cycle is operated with the heat source and sink brought to their maximum power and the superheating is measured. Refrigerant charge is added accordingly until an appropriate degree of superheating is observed (≈ 4 K). The total charge present in the ORC is worth 600g.

2.3 Identification of the influencing parameters

To ensure the reliability of the numerical model and the optimization of the experiments, two sensitivity analyses are performed. The first analysis assesses the impact of uncertain parameters on the efficiency of the Organic Rankine Cycle. It will be referred to from now on as: *technological sensitivity analysis*. Firstly, this analysis will highlight which parameter inherent to the components has the most impact on the global performance. Secondly, as those parameters were unknown to the author and were fixed based on the literature, the technological analysis will help to focus the experimental data analysis on the relevant parameters. For instance, if the technological sensitivity analysis highlights that the built-in volume ratio of the expander is highly correlated to the ORC performance, the experimental investigation can then focus on accurately measuring this parameter to precisely identifying it afterwards and adapting the model parameters accordingly. The second analysis aims to assess the key control variables (e.g. temperature of heat source supply, source glide, flow rates) that have the greatest influence on cycle performance. It will be referred to from now on as: *operational sensitivity analysis*. This analysis will be useful when designing the experimental campaigns. Indeed, to map the performance of the ORC machine, each control quantity has to be experimented in its operating range. With the increasing number of quantities, the number of operating points necessary to characterize each of these quantities grows exponentially. Thus, the operational analysis will help to adapt the number of operating points of each quantity depending on their influence. The experimental campaign should then be better optimized by minimizing time and resource constraints. The methodology employed in both studies is based on Monte Carlo simulation, using the *Monaco* library [3] for *Python*. This approach enables a comprehensive analysis of the sensitivity of the system based on statistical deductions, which better reflects the real-world variability than only considering extrema.

The operational sensitivity analysis revealed that three quantities influence the most the total ORC efficiency: the source supply temperature, the source glide and the sink glide. The former being the most influential of the three. Moreover, the operational sensitivity analysis showed that the contribution of the expander speed (linked to its volumetric efficiency) and the pump speed (controlling the superheating) were less significant. However, the technological sensitivity analysis highlighted that the expander characteristics (i.e. its built-in volume ratio, isentropic and volumetric efficiencies) are the main component parameters that influence the total efficiency of the cycle. It is thus interesting to evaluate them at best.

2.4 Experimental campaign

The results from the sensitivity analyses are exploited to optimize the campaign in terms of time and human resources: each parameter (called *factor* in Design of Experiment) will be tested on a number of levels depending on its influence on the total efficiency. The main goal of the experimental study is to map the performance of the ORC unit and quantify its key component parameters (e.g. expander efficiency and built-in volume ratio, heat exchanger effectivenesses). Because of time constraints, only one campaign is conducted for both objectives. This is not ideal since some working points necessary to catch every subtlety will be missed. An alternative would have been to conduct a campaign dedicated on the analysis of the performance of one component at a time, in addition to the global performance mapping of the ORC. Future work may consist in studying isolated components in more depth. The design employed in the current work is the Generalized Subset Design (GSD) [4]. It is a generalized version of the fractional factorial design.

3 Results

The results presented are the main results of the experimental study. The others are not discussed in the current paper.

3.1 Uncertainties propagation and sensors accuracy

Since the measures are taken at steady state, the working fluid mass flow rate is constant through every component of the cycle. Both values should therefore be equal. The working fluid flow rate computed at the evaporator can then be compared to the result at the condenser to verify redundancy. See Figure 1. A decent parity of ±15 % is observed for the

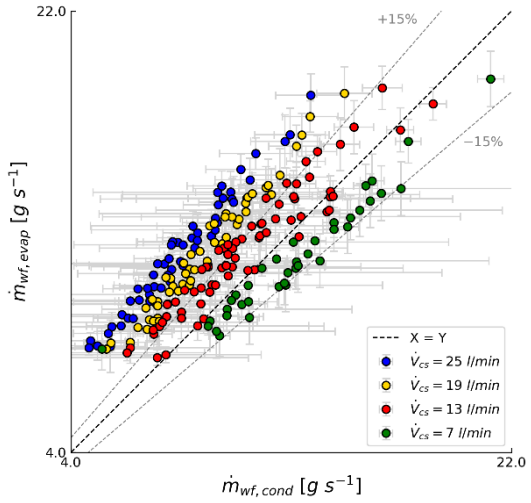


Figure 1: Parity plot of the working fluid mass flow computed via an energy balance at the evaporator ($\dot{m}_{wf,evap}$) and at the condenser ($\dot{m}_{wf,cond}$). A horizontal deviation proportional to the sink fluid flow rate is observed.

two lowest source flow rates. Nevertheless, a systematic error depending on the source flow rate is noted. The higher the source flow rate, the bigger the deviation is, underestimating the refrigerant mass flow rate calculated at the condenser. The uncertainty of the latter is large, allowing the error bars to lay in the ±15 % parity range. But such large uncertainties are not observed for greater values. In fact, they are induced by the high variation of enthalpy calculated by *CoolProp* [5] for the state corresponding to the condenser inlet and the recuperator outlet. This point lays at the boundary between superheated steam and dry saturated vapor. As mentioned earlier in this section, high variations of enthalpy are witnessed in this region, leading to an amplification of the uncertainties. Another source of error may be the heat losses to the ambient. Indeed, if all the heat exchanged by the working fluid is not received by the cold sink fluid but is rather lost to the surroundings, the calculation underestimates the working fluid mass flow rate. However, a similar observation would be made at the evaporator, which is not the case. Since the error is correlated to the cold sink flow, the most likely phenomenon occurring in this measuring process is a bad calibration or placement of the cold source fluid flow meter. For instance, when the volume flow rate increases, the speed of the fluid also increases and can lead to measuring errors due to the stream being more turbulent. For this reason, manufacturers recommend a minimum length of straight piping upstream and downstream of the flow meter in order to ensure fluid stability at the measure location. A correct calibration of the flow sensor is to be made for the entire range to check for a potential bad installation. In the next analyses, quantities that depend on the working fluid flow rate are computed with the averaged values calculated via the condenser and evaporator energy balances.

3.2 Technological parameters identification

This section focuses on identifying the inherent parameters of the key components of the ORC, i.e.: the pump, the expander, the recuperator as well as the condenser and evaporator. However, in this paper, only the expander parameters are discussed. Figure 2 highlights the effects of the under- and over-expansions losses.

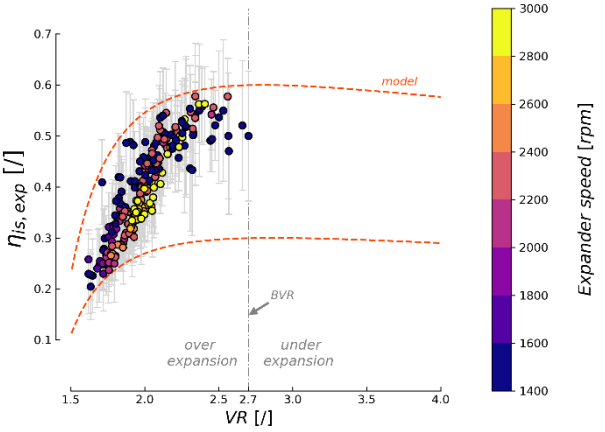


Figure 2: Expander isentropic efficiency ($\eta_{is,\mathrm{exp}}$) versus the imposed volume ratio (VR). The bounding curves simulated by the model are displayed in dashed lines.

The peak efficiency is expected to be observed at an imposed volume ratio corresponding to the built-in volume ratio of the expander. For volume ratios deviating from the built-in volume ratio, under- and over-expansion decrease the performance of the

machine. Over-expansion losses being more detrimental than under-expansion losses. The measured data is compared to the results of the expander model for a built-in volume fixed to 2.7. One can suggest that the actual machine has a similar built-in volume ratio. However, this value does not make sense. The simulated volume ratio for the nominal conditions of the ORC unit is 2.1. It means that at nominal regime, the expander would constantly operate below its BVR. Yet, the desired nominal volume ratio witnessed by the expander should be greater that its BVR, in order to undergo under-expansion losses which less degrade its efficiency than over-expansion losses. The available data appears to map only the over-expansion region of the machine. Therefore, to actually measure the expander BVR, a future experimental campaign should focus on operating the ORC with larger volume ratios. To do this, the specific volume at the expander inlet must be reduced. One way to achieve this is to increase the evaporation pressure of the refrigerant. In practice, this is done by increasing the supply temperature of the heat source.

The expander rotational speed affects the expander efficiency as well. At low speeds (< 1600 rpm), the internal leakages are increased, degrading the efficiency. At high speeds (> 3000 rpm), the efficiency is also decreased because of larger mechanical friction losses. A moderate speed of approximately 2300 rpm is found to be a good trade-off for optimal performance of the expander. A maximum efficiency of 58% is observed. Comparable results are identified in expanders with similar output power ratings ([6][7][2]).

3.3 ORC unit off-design performance

This section aims at mapping the performance of the ORC unit in off-design conditions with a new working fluid. The efficiency is expected to decrease as it moves away from the nominal working point, but the goal is to highlight the limits of operation and the rate of degradation of the total efficiency.

At part load regimes (less than the full capacity), the global energetic efficiency maintains a maximum value of ≈ 4% and a global exergetic efficiency of ≈ 28% (cf. Figure 3). However, from 150W power production and below, both efficiencies start to degrade rapidly. At 40W power production, a value of maximum 0% efficiency is observed. Two phenomena induce this degradation of efficiencies. Firstly, the thermodynamic potential available decreases with the source temperature. The Carnot efficiency diminishes and the irreversibilities have a relative larger impact. Moreover, at lower sink and source flow rates, heat transfers are less effective. It is translated by a rise in the pinch points values at the evaporator and the condenser. Thus, the exergetic potential available for the working fluid at the evaporator is lowered. Secondly, as the power produced declines, constant losses such as mechanical losses in the expander and the pump become predominant and affects the total efficiency until negative efficiencies are witnessed.

4 Conclusion and perspectives

To conclude, this paper presents a first step in the assessment of a low temperature domestic application of Carnot Batteries. A commercial ORC is characterized, and its off-design performance is evaluated: a maximum energetic and exergetic total efficiency of 4.4% and 29% respectively, and a maximum output power of 331.8W. Future work will consist in studying the coupling of the ORC with a low temperature sensible water thermal storage and its control along the discharge process of the storage.

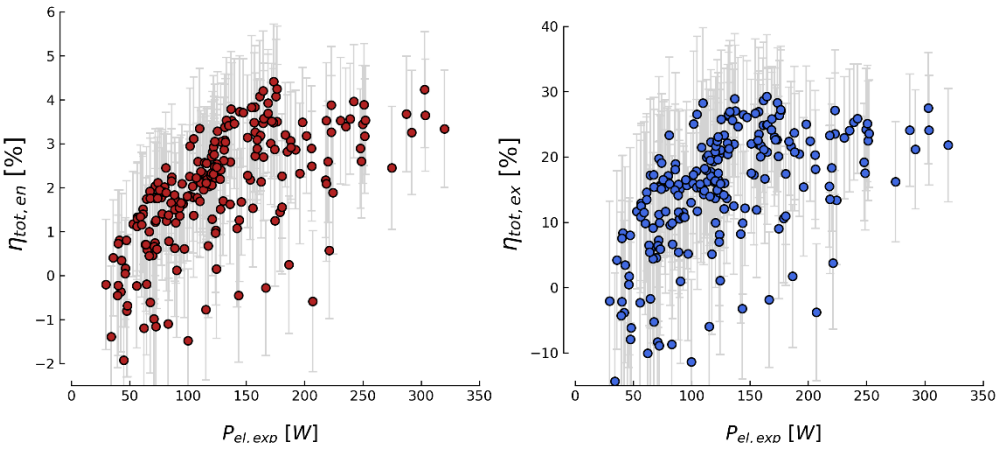


Figure 3: ORC net energetic and exergetic conversion efficiencies ($\eta_{tot,en}$ and $\eta_{tot,ex}$) as a function of the expander electrical power output ($P_{el,exp}$).

Some improvements of the test bench are also envisioned: a proper calibration of the cold sink flow meter and the replacement of the cycle temperature probes for improved precision.

Acknowledgements

The first author acknowledges the SPW Research for the funding, the ECAM Brussels Engineering School and the University of Liège (ULiège) for the collaboration, and the technicians of the CREDEM platform from UCLouvain for their contribution to the experimental work.

References

[1] O. Dumont, G. F. Frate, A. Pillai, S. Lecompte, M. De Paepe, and V. Lemort, "Carnot battery technology: A state-of-the-art review," Journal of Energy Storage, vol. 32, p. 101756, 2020.

[2] S. Quoilin, Sustainable energy conversion through the use of Organic Rankine Cycles for waste heat recovery and solar applications. PhD thesis, ULiège - Université de Liège, 04 October 2011.

[3] W. S. Shambaugh, "Monaco: A Monte Carlo library for performing uncertainty and sensitivity analyses," in Proceedings of the 21st Python in Science Conference (M. Agarwal, C. Calloway, D. Niederhut, and D. Shupe, eds.), pp. 202 – 208, 2022.

[4] I. Surowiec, L. Vikström, G. Hector, E. Johansson, C. Vikström, and J. Trygg, "Generalized subset designs in analytical chemistry," Analytical Chemistry, vol. 89, May 2017.

[5] H. Bell, J. Wronski, S. Quoilin, and V. Lemort, "Pure and pseudo-pure fluid thermophysical property evaluation and the open-source thermophysical property library Coolprop," Industrial & Engineering Chemistry Research, vol. 53, no. 6, pp. 2498–2508, 2014.

[6] R. Taccani, J. B. Obi, M. De Lucia, D. Micheli, and G. Toniato, "Development and experimental characterization of a small scale solar powered Organic Rankine Cycle (ORC)," Energy Procedia, vol. 101, pp. 504–511, 2016. ATI 2016 - 71st Conference of the Italian Thermal Machines Engineering Association.

[7] R. Dickes, Charge-sensitive methods for the off-design performance characterization of organic Rankine cycle (ORC) power systems. PhD thesis, ULiège, June 2019.

DECARBONIZING PROCESS STEAM SUPPLY – A FRAMEWORK TO ASSESS PATHWAYS FOR INDUSTRY RETROFITTING

Francesco Witte[1]*, Niklas Kießling[2], Mathias Hofmann[3]

[1] German Aerospace Center (DLR), Institute of Networked Energy Systems, Oldenburg, Germany

[2] TU Berlin, Chair of Energy Engineering and Climate Protection, Berlin, Germany

[3] TU Berlin, Chair of Energy Process Engineering and Conversion Technologies for Renewable Energies, Berlin, Germany

* *Corresponding Author: francesco.witte@dlr.de*

Abstract. While the integration of renewable energy sources is increasing in the power sector, process steam supplies in the industry often rely on fossil fuels as a source of energy. In the light of EU decarbonization goals and with the rise of new technologies, e.g. high-temperature heat pumps combined with storage or hydrogen-ready gas turbines, plant operators need to plan the retrofitting of their steam supply systems while securing continuous production and economic competitiveness. This research aims to facilitate this decision-making by developing an open source software framework that enables users to assess various decarbonization technology options for power and heat supply at different temperature levels in process chains. The framework allows users to define a site-specific energy system including heat and power demands and select the technology options to be considered. Based on the specifications, the properties of the technologies are calculated using a thermodynamic model. The results are passed to a mixed-integer linear program, which optimises dispatch and capacity planning. As a first step, a proof-of-concept model has been built to establish the basic architecture for the framework.

Keywords. Open source, Process steam supply, Thermo-economic assessment

1 Introduction

The supply of process heat in the German industrial sector is a relevant proportion (approx. 20%) of the total final energy consumption [1,2]. It is currently mainly supplied from fossil fuels [1,3]. If decarbonization approaches are adopted, industrial sites will become more dependent on the availability of variable renewable energy and the resulting green electricity (electrification of steam supply using high-temperature heat pumps) and green hydrogen (hydrogen-ready gas turbines). In addition, the potential decarbonization options depend on the respective temperature level of the required process steam.

If it is intended to suggest and optimise potential solutions under the boundary conditions (availability, economic efficiency, sustainability, and environmental impact), both a thermodynamic analysis of the local energy system and a systemic analysis of the technically feasible options must be carried out.

After all, without knowing the thermodynamics of the process steam, it is impossible to make a decarbonization proposal, and consequently to carry out a systemic analysis, because I cannot determine the actual delta CO2 or delta € or delta flexibility at all. At the same time, it must be checked whether the requirements of the technology option (electricity, H2) can be provided systemically at all and, conversely, what effects this will have on the overall system. To this end, it is necessary to map both the technical process and the process steam supply with sufficient accuracy (saturated steam pressure level) and to make it possible to determine interaction with the overarching (regional or national) energy system. A possible way to study this interaction with a focus on a plant specific steam supply is to pass time-variable prices of commodities from the overarching system simulation to the plant-level transformation planning model.

A variety of frameworks have been implemented to optimise energy supply in such a context, among many others, the open source frameworks COMANDO, which provides functionality to optimise low temperature heating supply structures and also to carry out optimization of power plant designs [4]. Or SecMOD, which combines economic assessment with life cycle assessment for multi-objective decision making. It however does not specifically target a single steam supply system [5]. In the context of industrial steam supply systems, the

proprietary tool TOP ENERGY [6] is available. Another implementation from this context has been proposed by [7], but it only features a single case study for demonstration regarding the by-product portfolio of a pulp mill. Formulations for mixed-integer modelling of CHP plants in context of district heating supply systems have been developed by [8] and integrated in oemof-solph [9].

A common ground of most of these frameworks is that the user has to parametrize the optimization problem based on calculations made before, which depend e.g. on temperature or pressure levels of the materials involved or technology specific attributes (compressor efficiency). Meaning, thermodynamic calculations have to be carried out in preparation of the optimization.

With this in mind, the aim of this work is to facilitate the transfer of such information from the thermodynamic modelling of the steam supply to a decision support tool for the investment in retrofits or new technologies in order to meet the energy demands at minimum cost. This should be accomplished through an open source framework, which builds on and extends existing solutions. The development is at an early stage, the envisioned workflow as well as a proof of concept model are presented in this paper.

2 Methods

The overall concept is based on an optimization of dispatch and the capacities of a variety of supply options in order to provide the steam and power demands of an industrial site at minimum cost. For that, information from thermodynamic modelling of the supply options are automatically transferred to a mixed-integer linear model by linearising the conversion factors between the material and energy flows. The assessment can be carried out based on variable boundary conditions of the surrounding energy system, for example, electricity or gas prices.

2.1 Toolchain

The abstract toolchain is shown in figure 1. A scenario is set up in the problem definition by providing the buses and components of the system as well as input time series, such as electricity prices or time variable demand. The buses represent the commodities (materials and energy) of the system. The available technologies for conversion between the different buses or energy storage, sources and sinks of commodities are provided as the system's components.

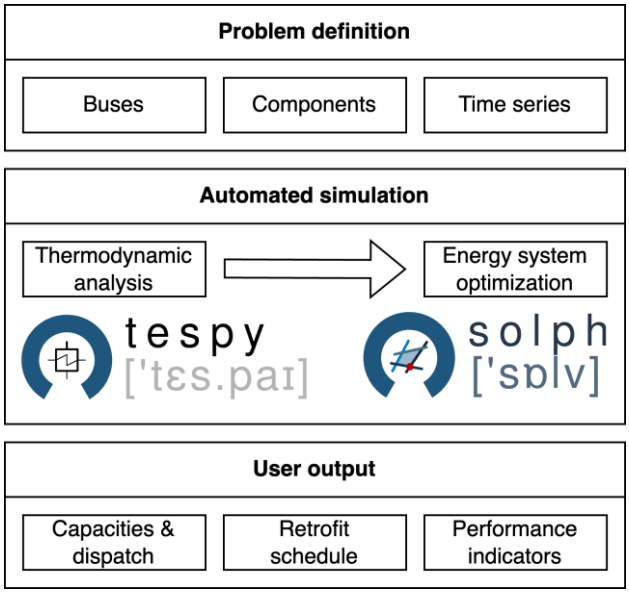


Figure 1: Toolchain implemented in the framework.

With the definition of the buses and the converters, the thermodynamic simulation automatically calculates the technology-specific conversion factors between the different buses. The buses can have user-specified pressure (and temperature) levels. The resulting conversion factors are linearised and merged with the capacity information for every technology, i.e. electrical power of a steam turbine or storage capacity. This information is provided to the energy system optimization model, which at the current state optimises the dispatch of the available technologies in order to meet the demand at minimum cost.

As a result, the operation schedule can be derived in the current state of the work. From that it is possible to derive various performance indicators, e.g. to assess the role of different technologies within the scenario. At a later stage the capacities of the technologies as well as the timeplan for retrofitting and capacity expansion will be available as well.

2.2 Thermodynamic model

Within the context of the process heat supply various technological options are available. These options include extraction-condensing steam turbines, heat pumps, gas and electric boilers, or high temperature storage, e.g., in the context of Pumped Thermal Storage (PTES) [10]. The conversion processes are influenced by pressure and temperature levels of the steam demand or temperature level of the district heating system. The underlying processes of the conversion options are not necessarily single component processes. For example, a heat pump is built from four components at a minimum, or a steam turbine may integrate an inlet control valve and steam

conditioning with feed water injection at the outlet to match the desired temperature and pressure level of the respective steam line.

The thermodynamic model uses the open-source software tespy [11], which is based on the CoolProp [12] fluid property engine. In tespy the simulation of the thermal energy conversion processes is carried out on component level based on the thermodynamic properties of the different material flows, e.g. pressure, temperature, quality, and properties of the components, e.g. isentropic efficiency or pressure loss.

In the proposed framework the technology options are available as separate predefined tespy models. The user can select from the catalogue and connect an instance of a technology to the required input and output buses. Then, based on the properties of the connected buses, the tespy model will calculate the conversion factors between the buses. The result is exported to serve as an input for the dispatch model. At the moment, the calculation is carried out in design conditions only. Table 1 shows an example of the linear conversion factors for a high pressure and a low-pressure turbine. It is planned to include an estimation of part-load operation. For this lookup tables can be passed to tespy, e.g. in order to connect the mass flow through a turbine to its isentropic efficiency and to respect Stodola's cone law.

2.3 Dispatch and capacity optimization model

Once the conversion factors between energy and material flows per technology option have been determined the optimization problem is formulated. At the current state a linear dispatch optimization model is implemented, which can work with constant conversion factors as outlined in the previous section. To model part-load efficiency a mixed-integer formulation will be implemented at a later point in time. The goal of the unit-commitment optimization is to dispatch the available technologies in order to meet the steam demand at minimal cost. The framework will make use of the open-source software oemof-solph [9] to implement the optimization.

In oemof-solph the energy system formulation is built on 4 basic types: Converters, sources, sinks and storages. To the energy conversion technologies nominal installed capacity, minimal part load as well as specific investment, fixed and variable cost of operation are required next to the conversion factors. In the linear model, the following equation is implemented, relating the input to the output material and energy streams $\dot{E}_k(t)$ for every time step via the linear conversion factors $\eta_{k,t}$, where k denotes an inlet or an outlet and t is the time-step within the optimization horizon.

$$\dot{E}_o(t) \cdot \eta_{i,t} = \dot{E}_i(t) \cdot \eta_{o,t}$$

With the extension of the model to respect part-load dependent efficiency, additional information is required. In this case the relationships are described by a slope m relative to a reference stream (ref) and an offset b. These can be determined through linearization of the part-load characteristics provided by the technology models. The binary variable $y_{ref}(t)$ determines the on/off status of the component.

$$\dot{E}_k(t) = \dot{E}_{ref}(t) \cdot m_{k,t} + b_{k,t} \cdot y_{ref}(t)$$

The sinks are used to represent demand for energy or material flows, or to represent the opportunity of selling electricity to the power system. Every demand comes in the form of a time series, which the optimization model is constrained to deliver. The opportunity of selling electricity to the power grid is coupled to a variable price time series. Similarly, buying electricity from the grid is modelled with a source connected to an own price time series. A PV plant installed at the location can also be represented with a source component. Here the availability of the energy source is constrained by the solar irradiance time series.

In a later step of the framework, a multi-period investment model is formulated, that will determine the capacities to be invested into for every selected technology option as well as the points in time when the investment should happen.

3 Proof of concept

As a first proof of concept example, a single steam demand supply system is selected as illustrated in figure 2.

The system consists of a (time-variable) steam demand at 4 bar and 160 °C (SD) as well as a power demand (PD). A natural gas-fired boiler (GB) can generate high-pressure steam at 90 bar and 510 °C. The high-pressure steam can be expanded to low-pressure steam through a turbine (HP ST) or a throttle valve (HP VA). In order to match the steam demand temperature, feedwater injection is required in both cases. Instead of exclusively using the low-pressure steam exiting the high-pressure turbine to satisfy the demand, a condensing turbine (LP ST) allows additional generation of power. A second scenario integrates a thermal energy storage charged via direct

resistance heating (DRH) and discharged by a heat exchanger (HX) generating high-pressure steam.

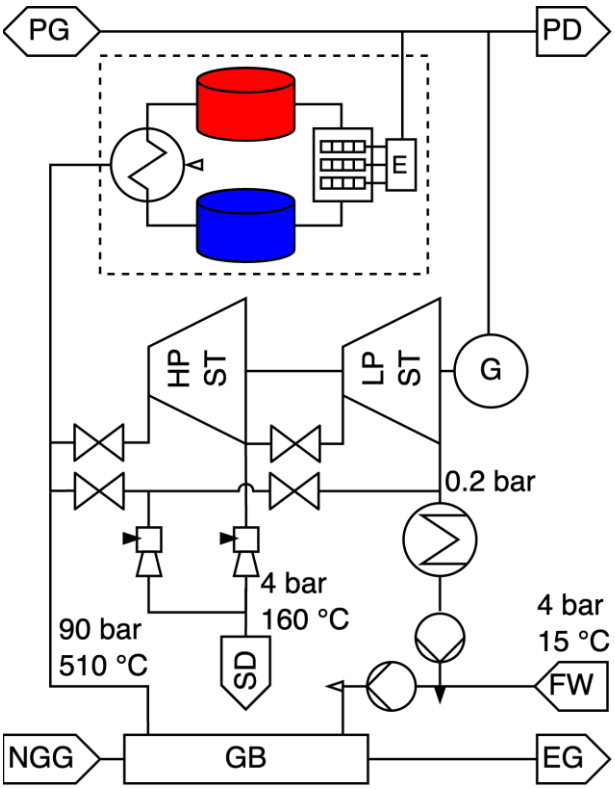


Figure 2: Flowsheet of the steam supply system.

A second scenario integrates a thermal energy storage charged via direct resistance heating (DRH) and discharged by a heat exchanger (HX) generating high-pressure steam. The table 1 gives an overview on the assumptions for the installed capacities in the considered scenarios.

Table 1: Available technologies and installed capacities per scenario.

scenario	technology	capacity	
Status quo	HP ST	8.0	MWel
	LP ST	4.0	MWel
	GB	60.0	t/h
	Throttles	-	t/h
Retrofit	DRH	7.5	MWel
	Storage	50.0	t
	HX	3	t/h

The plant is operating at the spot market, electricity can be bought from or sold to the power grid (PG), natural gas can be bought from the natural gas grid (NGG). The variability of the prices determines the plant dispatch. The capacities of the different components are fixed and the dispatch model is formulated as a pure linear problem.

4 Results

In this section we will present the results of the two different scenarios in the proof of concept example. Note that the presented results heavily depend on the assumptions on gas and electricity prices as well as available capacities. In table 2, the results of the thermodynamic model of the steam turbines and the throttle valve are displayed, i.e. the conversion factors for the given input and output buses.

Table 2: Exemplary conversion factors of a high-pressure steam turbine.

label	consumption		production	
HP ST	HP steam	6.50 t/h	LP steam	6.50 t/h
			power	1.00 MW
LP ST	LP steam	9.94 t/h	wet steam	9.94 t/h
			power	1.00 MW
HP VA	HP steam	0.81 t/h	SD	1.00 t/h
	feed-water	0.19 t/h		

The high-pressure steam turbine is obviously more efficient at generating electricity than the low-pressure turbine. On top of that, the high-pressure throttle valve (unsurprisingly) allows to generate the largest amount of steam at demand conditions, since it adds more feedwater to the high-pressure steam and is unconstrained in capacity. This means, when electricity production is not attractive economically, the throttle will come into place instead of the high temperature turbine.

Based on the calculated conversion factors of all components, prices for gas and electricity as well as the fixed steam and electricity demands, the cost-minimal dispatch of the system is calculated. Figure 3 shows the results of the status-quo system. In this case, five possible modes of operation are observed:

- The electricity prices are at a very high level. Both turbines are operated. In order to maximise the availability of steam for the low-pressure turbine, additional high-pressure steam is reduced with the throttle valve to fulfil the demand. Overproduction of electricity is sold to the grid.
- The electricity prices are at a high level. Both steam turbines are operated and the steam demand is fully supplied by steam extraction from the high-pressure steam turbine outlet. Overproduction of electricity is sold to the grid.
- The electricity prices are at a medium level. Both steam turbines are operated and the steam demand is fully supplied by steam extraction from the high-pressure steam turbine outlet. Electricity production meets the power demand.
- The electricity prices are at a low level. Only the high-pressure steam turbine is dispatched and the steam production is supplied by extracting all steam at its outlet. The gap in supplying the power demand is provided by the grid.
- The electricity prices are at a very low level, so it is economically more attractive to buy electricity from the grid to supply the electricity demand and to satisfy the steam demand by dispatching the throttle valve.

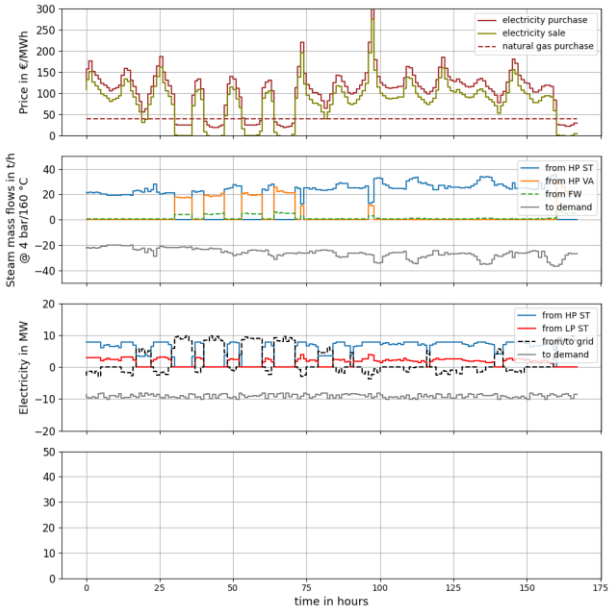


Figure 3: Example dispatch the status-quo system.

In the second scenario, a TES is added to the system. Similar behaviour can be observed in principle, the utilisation of the storage is triggered by (very) low electricity prices (see figure 4):

- On top of the provision of the steam demand from the throttle valve, the DRH is dispatched to charge the storage (note, that on rare occasions the storage is bypassed). The storage is then discharged in the directly following time steps.
- Due to the inherent standing energy loss of the storage, the storage level is usually not kept at a high level but discharged immediately after charging it. The only exception is triggered by the maximum in electricity price just before the time-step 100.

Comparing both scenarios in the selected period of operation, the total import of electricity is about 50 % higher when including the PTES and DRH while the electricity exports are nearly identical in both scenarios. At the same time the utilisation of natural gas is reduced by only 3.8 %. Note, that this is driven by the fact that more than 5700 MWh of gas are imported compared to only about 400 MWh of electricity in the status-quo system. Overall, a reduction of the total operational cost of only about 1.5 % is achieved. As mentioned before, the dispatch strategy is highly sensitive not only to conversion efficiencies, but also prices and will therefore be subject of extensive future research.

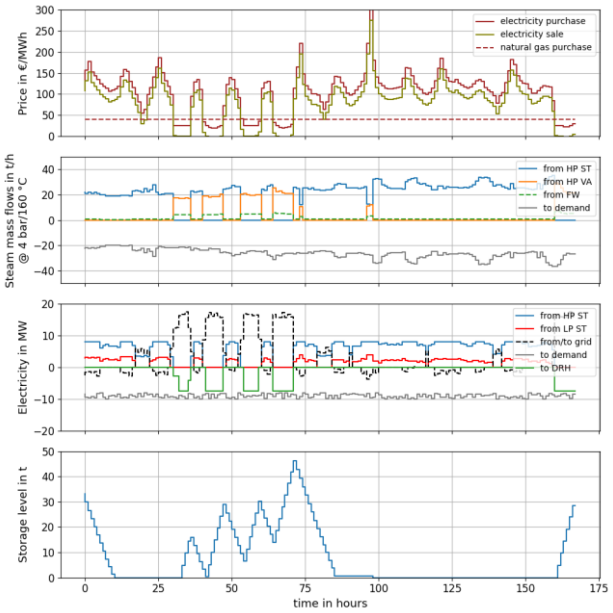


Figure 4: Example dispatch of a system including a PTES as storage option.

5 Outlook

In the current state a simplified version of the framework is available that allows LP dispatch optimisation. In the next step it is planned to extend the capabilities of the components to mixed-integer modelling in order to constrain operation, e.g., minimum load, part load efficiency or uptime and downtime constraints. On top of that, capacity expansion for a single period will be integrated. In the

final step it is planned to integrate multi-period modelling. The goal of this is to facilitate the simulation of a step-by-step retrofit of the industrial heat supply.

Apart from the thermo-economic assessment other indicators might be relevant for decision makers or within the political framework, e.g. indicators from a life cycle analysis. Results of the LCA could be integrated by a pareto-optimisation approach, which simultaneously optimises the component sizing for minimal cost of heat as well as minimal emissions or other indicators.

In the context of capacity expansion and multi-objective decision making, heuristic optimization methods, e.g. as provided by the pagmo framework [14] can be explored. This allows to integrate non-linear cost- or objective functions and pareto-optimization.

Finally, instead of modelling material and energy flows, using exergy flows in context of the dispatch optimisation is a possible option, which has rarely been explored.

Acknowledgement

This work was funded by the German Federal Ministry for Economic Affairs and Climate Action (BMWK) in the project SecöndLife (grant number 03EI1076A).

References

[1] AG Energiebilanzen, Endenergieverbrauch nach Energieträgern und Anwendungszwecken, 2023 https://ag-energiebilanzen.de/wp-content/uploads/2023/01/AGEB_22p2_rev-1.pdf

[2] R. de Boer et al., Strengthening Industrial Heat Pump Innovation: Decarbonizing Industrial Heat, 2020

[3] Fleiter at al., CO2-neutrale Prozesswärme-erzeugung - Umbau des industriellen Anlagen-parks im Rahmen der Energiewende: Ermittlung des aktuellen SdT und des weiteren Handlungs-bedarfs zum Einsatz strombasierter Prozess-wärmeanlagen (Endbericht), 2023

[4] M. Langiu et al., "COMANDO: A Next-Generation Open-Source Framework for Energy Systems Optimization", Comput. Chem. Eng., (152), no. 107366, 2021, 10.1016/j.compchemeng.2021.107366

[5] C. Reinert et al., "Design of low-carbon multi-energy systems in the SecMOD framework by combining MILP optimization and life-cycle assessment", Comput. Chem. Eng., (172), no. 108176, 2023, 10.1016/j.compchemeng.2023.108176

[6] T. Bauer et al., "Ideal-Typical Utility Infrastructure at Chemical Sites – Definition, Operation and Defossilization", Chem. Ing. Tech., (94), pp. 840-851, 2022, 10.1002/cite.202100164

[7] E. Svensson et al.,"Assessing the value of a diversified by-product portfolio to allow for increased production flexibility in pulp mills" Nord. Pulp Pap. Res. J., (35), no. 4, pp. 533-558, 2020, 10.1515/npprj-2020-0034

[8] E. Mollenhauer et al., "Evaluation of an energy- and exergy-based generic modeling approach of combined heat and power plants", Int. J. Energy Environ. Eng. (7), pp. 167–176, 2016, 10.1007/s40095-016-0204-6

[9] U. Krien et al., "oemof.solph-A model generator for linear and mixed-integer linear optimisation of energy systems", Software Impacts, no. 6, 2020, 10.1016/j.simpa.2020.100028.

[10] A. Vandersickel et al., "Task 36 Carnot Batteries Final Report", 2024.

[11] F. Witte and I. Tuschy, "TESPy: Thermal Engineering Systems in Python", J. Open Source Software, no. 5, 2020, 10.21105/joss.02178.

[12] I. Bell et al., "Pure and Pseudo-pure Fluid Thermophysical Property Evaluation and the Open-Source Thermophysical Property Library CoolProp", Ind. Eng. Chem. Res., no. 6, pp. 2498-2509, 2014, 10.1021/ie4033999.

[13] W. Hart et al., "Pyomo: modeling and solving mathematical programs in Python", Math. Program. Comput., no. 3, pp. 219-260, 2011, 10.1007/s12532-011-0026-8

[14] F. Biscani and D. Izzo, "A parallel global multiobjective framework for optimization: pagmo", J. Open Source Software, no. 5, 2020, 10.21105/joss.02338

STEAM-ASSISTED MILD-POX: A FLEXIBLE PROCESS FOR THE PRODUCTION OF HYDROGEN

Marco Lubrano Lavadera[1,2]*, Axel Coussement[1,2], Alessandro Parente[1,2,3]

[1] Aero-Thermo-Mechanics Department, Université Libre de Bruxelles, 1050 Bruxelles, Belgium.

[2] Brussels Institute for Thermal-Fluid Systems and Clean Energy (BRITE), Université Libre de Bruxelles and Vrije Universiteit Brussel, Brussels, Belgium.

[3] WEL Research Institute, Avenue Pasteur, 6, 1300, Wavre, Belgium.

* *Corresponding Author:* marco.lubrano.lavadera@ulb.be

Abstract. The aim of the present work is to propose an alternative hydrogen production process using water and sustainable feedstocks to promote the utilisation of cheap and renewable raw materials on a large scale by increasing flexibility, efficiency, and eco-compatibility of existing technologies without sacrificing their reliability and affordability. The idea to accomplish this aim is to combine non-catalytic Partial Oxidation and Moderate or Intense Low-oxygen Dilution combustion technologies by adding water. Thermodynamic equilibrium calculations, accompanied by kinetic modelling, are used to assess and interpret the general behaviour of a potential unit that uses the interaction of these two technologies and to compare the performances over a range of operating conditions of interest. The presented results show that thermochemical production of H_2 using the proposed process is theoretically feasible and has the potential to offer many advantages over standard processes. The immediate advantage of such an approach is that a very high H_2/CO ratio can be obtained that could eliminate the water gas shift conversion stages, making the reactor more compact and simple than conventional reformers. Moreover, water vapour addition limits the formation of soot precursors due to a "leaning" effect from releasing hydroxyl radicals.

Keywords. MILD combustion; Non-catalytic partial oxidation; Hydrogen production; Chemical kinetics; Water dilution.

1 Introduction

Numerous research programs recently funded by the International Energy Agency promote hydrogen (H_2) utilisation as a clean energy carrier to make the inevitable transition toward renewable energy and transport systems feasible [1]. At present, approximately 96% of H_2 is globally produced using fossil fuels as feedstock; *i.e.*, ~48% from natural gas, ~30% from petroleum, and ~18% from coal, which makes the current cost of H_2 more than twice as much as that of conventional fuels [2, 3]. Only 3.9% of H_2 is produced from water (H_2O) and merely 0.1% from biomass. In these cases, even if renewable raw materials are used, the required energy input driving the process to extract H_2 from the feedstock is still derived from fossil fuels [4]. Therefore, despite H_2 being commonly perceived as an environmentally friendly energy carrier at the point of utilisation (direct combustion or use in fuel cells), it shifts the carbon footprint concern to its production stage. The transition toward a secure and sustainable H_2 economy is feasible only if the proportion of H_2 produced from cheap, renewable, locally available, and carbon-neutral raw materials/energy sources is significantly increased. Promising candidates include H_2O, the most abundant and inexhaustible H_2-containing raw material on earth, and bio-resources, which can be classified as carbon-neutral. Therefore, the overall purpose of the present work is to propose and assess an alternative prospective process to produce H_2 using H_2O and gaseous/liquid bio-resources as raw materials.

The proposed research idea combines conventional non-catalytic partial oxidation (POX) for the H_2 production and innovative Moderate or Intense Low-oxygen Dilution (MILD) [5] technologies by adding H_2O. This approach allows to benefit from the main advantages of POX while minimising its emissions. The low-temperature increase of the MILD-POX enables low hazardous pollutant emissions like NO_x and soot without gas after-treatment, which avoids adding costs, complexity, and space. Moreover, the requirement of the inlet temperature (T_{in}) in the combustion chamber higher than the self-ignition temperature (T_{ign}) enables the stable conversion of

Low Calorific Value (LCV) feedstocks, such as gaseous and liquid biofuels. This aspect may offer more advantages over the standard techniques.

2 Thermodynamic and kinetic analysis

This section aims to use the CRECK reaction scheme [6] to theoretically define, assess, and interpret the general behaviour of a potential unit that uses the steam-assisted MILD-POX route of methane (CH_4) for syngas production and to compare the performances over a range of different operating conditions of interest. The H_2O/CH_4 feeding ratio is selected as the primary variable for the parametric study as dilution variation through internal or external recirculation is the most suitable way to achieve MILD conditions and thus control the process. The H_2O/CH_4 ratio is also essential in industrial Steam Reforming (SR) and POX to prevent carbon deposits. However, while traditional SR and POX generally employ ratios of 3-5 and 0-3, respectively, MILD-POX conditions require this ratio to be from ~5 up to 500, which makes the proposed process significantly different from the conventional ones. The H_2O/CH_4 ratio is restricted at its lower end by the MILD combustion definition; namely, the adiabatic temperature increase must be lower than the T_{ign}. The upper limit of H_2O admixing employed here has been set to have a minimum temperature increase of 10 K, the criterion commonly used for defining the ignition delay time in MILD combustion [7]. Other aspects that may be relevant in practical systems, such as the geometry of the reactor, fluid dynamics, heat transfer, *etc.*, will not be considered in this study.

First, a thermodynamic analysis employing Gibbs free energy minimisation has been performed with mixtures of CH_4 and O_2, highly diluted in H_2O, at atmospheric pressure and T_{in}=900 K, to investigate the potential of the proposed process by examining the equilibrium conversion limits and product gas yield and composition as a function of process parameters. All 159 species included in the CRECK model were considered in the calculations.

Figure 1 shows the effect of the H_2O/CH_4 inlet mole ratio on the reformed gas's equilibrium composition at the adiabatic temperature for three defined CH_4/O_2 inlet mole ratios under MILD-POX conditions, thus $T_{in}>T_{ign}$, fuel-rich and highly diluted mixtures. As shown in Fig. 1, different H_2O/CH_4 limits exist for any CH_4/O_2 ratio due to different adiabatic temperatures.

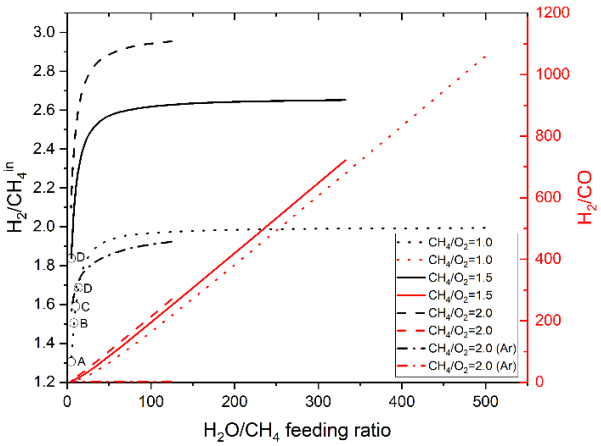


Figure 1: Effect of H_2O/CH_4 feeding ratio on the H_2/CH_4^{input} ratio (black lines, left axis) and H_2/CO ratio (red lines, right axis) for $CH_4/O_2/H_2O$ mixtures at equilibrium, T_{in}=900 K, and p=1.0 atm for three CH_4/O_2 feeding ratios. Dotted lines: CH_4/O_2=1.0. Solid lines: CH_4/O_2=1.5. Dashed lines: CH_4/O_2=2.0. Dash-dotted lines: CH_4/O_2=2.0 with H_2O replaced by Ar. Open circles: A-B: τ^{90}<10 s; B-C: 10<τ^{90}<100 s; C-D: 100< τ^{90}<1000 s. Where no circles are reported τ^{90}>1000 s.

The first interesting result, not displayed in Fig. 1, is that the conversion is always complete for the explored H_2O/CH_4 and CH_4/O_2 ratios. In addition, no free carbon is present, and the expected products are, independent of the operating conditions, only H_2, carbon oxides, and residual H_2O. Therefore, for all the equilibrium results, the product composition is unambiguously presented in terms of H_2/CH_4^{input} and H_2/CO since the main interest is the efficient conversion of CH_4 to H_2. Calculations show that the main trends strongly depend on H_2O addition; in particular, it can be seen that the H_2/CH_4^{input} yield (left axis) first significantly grows with increasing H_2O/CH_4 ratio and then reaches a plateau for values higher than ~50, independent on the CH_4/O_2 ratio. At the same time, the quantitative values of H_2/CH_4^{input} strongly grow with CH_4/O_2 ratio starting from about 1.3-2.0 at CH_4/O_2=1.0 to 2.1-2.95 at CH_4/O_2=2.0. Note that for CH_4/O_2 ratios of 1.5 and 2.0, the H_2/CH_4^{input} ranges from the one typical of POX (~2.0) to the one of SR (~3.0). It must be recalled that the SR reaction is strongly endothermic, with the heat for driving the reaction supplied by firing additional CH_4. Thus, if this amount of CH_4 is also included, SR's H_2/CH_4^{input} yield is lower than 3.0. A further increase of the CH_4/O_2 ratio above 2.0 (not reported in Fig. 1) does not lead to significant improvements in terms of performance. In addition, at CH_4/O_2>2.0, the process begins to lose the characteristic self-

sustaining regime, and the CH_4 conversion ratio shifts to values lower than 1.0, independent of the amount of H_2O.

On the other hand, the H_2/CO ratio (right axis) increases quasi-linearly with the addition of H_2O, and the improvement may be considerable. Note that an increase in the H_2/CO ratio corresponds to a decrease in the H_2/CO_2 ratio. In this case, increasing the CH_4/O_2 ratio does not have a significant influence for a fixed H_2O/CH_4 ratio, but lower CH_4/O_2 ratios can be beneficial because they would allow extending the H_2O/CH_4 range. Surprisingly, the synthesis gas composition in terms of H_2/CO ratio, ranging from 3.0 to 1060, is always significantly higher than that obtainable with conventional processes (1-2 for POX and ~3.0 for SR), which is beneficial for H_2 production. In fact, the next phase of SR and POX usually involves the water gas shift reaction, where the CO from the initial step is further reacted with additional steam in two catalytic reactors (high- and low-temperature) to form H_2 and CO_2, with small amounts of residual CO. The very high H_2/CO ratio obtained from the steam-assisted MILD-POX could reduce the number of unit processes and the complexity of the operation by eliminating the shift conversion.

Low temperature favour the H_2 yield and selectivity; thus, from the analysis, it needs to be clarified if the changes in process performances with the addition of H_2O are influenced by a decrease in the adiabatic temperature or by the presence of steam itself. Therefore, an additional case has been investigated at CH_4/O_2=2.0 with argon dilution instead of H_2O (dash-dotted lines). Thermodynamic calculations suggest that the nonlinear increasing trend of H_2/CH_4^{input} is very similar in the case of dilution by an inert gas, which is therefore explained by the fact that the diluent addition to the mixture shifts the adiabatic temperature to lower values. However, the H_2/CH_4^{input} yield drops by a factor of 1.36-1.54, and the conversion is never complete, but ranges from 95 to 97%. On the other hand, increasing the Ar/CH_4 ratio does not influence the H_2/CO ratio, which is ~2.0 in the entire explored range. It confirms that the steam-assisted MILD-POX process extracts H_2 from the hydrocarbon feedstock and H_2O. Indeed, 27-35% of the H_2 produced comes from the steam when CH_4 is used as a feedstock, as seen from the difference between solid lines and dash-dotted lines. This contrasts with some numerical studies [8-10] in which no significant effect of the H_2O/CH_4 ratio on H_2 yield was observed, probably because of the too-low H_2O/CH_4 ratio used in the calculations. In addition, steam is the only cause for the enhanced H_2/CO ratio. This result justifies using surplus H_2O that increases the syngas yield, the H_2/CO ratio, and the CH_4 conversion.

This analysis aims to show process flexibility rather than find optimal thermodynamic conditions. As shown in Fig. 1, the comparison of the raw synthesis gas produced by steam-assisted MILD-POX can be adjusted as desired by changing the proportion of reactants. Providing an extremely tunable H_2/CO ratio is essential not only for H_2 production but also for many industrial applications such as ammonia, methanol, and oxo syntheses, oil refining, iron ore reduction, *etc*.

The description based on thermodynamic analysis is approximate because it can only suggest the potential product composition. However, it does not provide any information on reactor residence times required to achieve proper CH_4 conversion in real systems; thus, calculations must include reaction kinetics. Therefore, zero-dimensional, adiabatic simulations have been carried out over the entire range of conditions reported in Fig. 1 employing the Perfectly Stirred Reactor (PSR) code of the ANSYS Chemkin-Pro 2021® software, implementing the CRECK reaction mechanism and setting the residence time to 10, 100, and 1000 s. In Fig. 1, the conditions that allow a CH_4 conversion of more than 90% (τ^{90}) at the reactor outlet, thus a product gas composition close to equilibrium, are shown with open circles. For CH_4/O_2 ratios higher than 1.0, reactions need more than 1000 s to reach equilibrium in the whole H_2O/CH_4 range, which is impractical. Indeed, in the conditions explored, the adiabatic gas temperature is lower than 1300 K for CH_4/O_2=1.5 and lower than 1100 K for CH_4/O_2=2.0. A conversion higher than 90% is attained for τ<1000 s only at CH_4/O_2=1.0 and H_2O/CH_4<16 where the adiabatic temperature ranges from 1300 to 1750 K. These very long residence times are not related to the use of H_2O, because also in the case of dilution with Argon the results are similar. At CH_4/O_2=2.0, τ90<10 s only if H_2O/ or Ar/CH_4=0 (not shown in Fig. 1). As a matter of fact, the non-catalytic POX of hydrocarbons is controlled by reaction kinetics, which, despite being faster than SR, is intrinsically much slower than conventional flame burners, and even an approximation to equilibrium can only be achieved by accepting very high temperatures (1500<T<3000 K), where chemical reactions are sufficiently rapid. Below 1500 K, catalysts are typically added to the POX system to enhance reaction kinetics and approach an acceptable conversion. However, the objective of the present work is to propose a process that can be realised within residence times typical of non-catalytic POX,

i.e., τ<~50 s, and adiabatic temperatures typical of MILD combustion, *i.e.*, 1000-1500 K. The influence of parameters that enhance chemical kinetics, namely T_{in} and p, on the equilibrium composition and characteristic times will be discussed at the conference.

3 Conclusions

The goal of the present work was to propose the combination of non-catalytic POX and MILD combustion technologies with the addition of H_2O and assess its potential for the efficient generation of H_2 from any sustainable gaseous or liquid feedstock, leaving a minimal environmental footprint.

Thermodynamic equilibrium calculations, accompanied by kinetic modelling, were used to interpret and assess the general behaviour of a potential unit that uses the steam-assisted MILD-POX route of CH_4 for syngas production and to compare the performances over a range of operating conditions of interest. In particular, the effects of H_2O/CH_4 and CH_4/O_2 ratios, inlet temperature, and pressure on CH_4 conversion, H_2 yield, and product gas composition were computationally investigated. Particular emphasis was devoted to the effect of H_2O on gas-phase chemistry. The presented results demonstrate that thermo-chemical production of H_2 using the proposed process is theoretically feasible and can be accomplished without a catalyst, making the process highly feedstock-flexible and impurity tolerant. The achieved performances can be even better than those of the existing technologies over a wide range of process parameters, subject to the constraints of characteristic times. In particular, equilibrium favours the formation of H_2 and CO_2 at low adiabatic temperatures and high H_2O/CH_4 and CH_4/O_2 ratios in the input gas. At the same time, reaction kinetics are faster at elevated temperatures and pressures and low H_2O/CH_4 and CH_4/O_2 ratios. Therefore, a compromise must be made among these parameters to maximise performance. The immediate advantage of such an approach is that a very high H_2/CO ratio can be obtained that could eliminate the water gas shift conversion stages, making the reactor more compact and simple than conventional reformers. Moreover, water vapour addition limits the formation of soot precursors due to a "leaning" effect from the release of OH radicals. Technically, excess water vapour can be eliminated efficiently from the produced gas by condensation and re-used as a feed by recirculation, retrieving the sensible heat of the outgoing hot products to vaporise and preheat the incoming H_2O, for example, by using recuperative burners. In this way, the gas following the MILD-POX unit can be treated like the product gas from existing processes.

Acknowledgement

The authors acknowledge research funding from "Le Fonds de la Recherche Scientifique – FNRS" awarded to Marco Lubrano Lavadera (Research Associate).

References

[1] IEA (2022), Hydrogen, IEA, Paris https://www.iea.org/reports/hydrogen, License : CC BY 4.0.

[2] B. Zhang et al., "Progress and prospects of hydrogen production: opportunities and challenges", J. Electron. Sci. Technol., no. 19, pp. 100080, 2021.

[3] I. Rosyadi et al., "Producing hydrogen-rich syngas via microwave heating and co-gasification: a systematic review", Biofuel Res. J., no. 33, pp. 1573-91, 2022.

[4] A. Al-Qahtani et al., "Uncovering the true cost of hydrogen production routes using life cycle monetisation", Appl. Energy, no. 281, pp. 115958, 2021.

[5] A. Cavaliere, M. de Joannon, "Mild combustion", Prog. Energy Combust. Sci., no. 30, pp. 329-66, 2004.

[6] G. Bagheri et al., "Comprehensive kinetic study of combustion technologies for low environmental impact: MILD and OXY-fuel combustion of methane", Combust. Flame, no. 212, pp. 142-55, 2020.

[7] M. de Joannon et al., "Dependence of autoignition delay on oxygen concentration in mild combustion of high molecular weight paraffin", Proc. Combust. Inst., no. 29, pp. 1139-46, 2002.

[8] MS. Benilov, GV. Naidis, "Modeling of hydrogen-rich gas production by plasma reforming of hydrocarbon fuels", Int. J. Hydrogen Energy, no. 31, pp. 769-74, 2006.

[9] KV. Dobrego et al., "Partial oxidation of methane in a reverse flow porous media reactor. Water admixing optimization", Int. J. Hydrogen Energy, no. 33, pp. 5535-44, 2008.

[10] S. Kumar et al., "Hydrogen production by partial oxidation of methane: Modeling and simulation", Int. J. Hydrogen Energy, no. 34.

FIRST EXPERIMENTAL INSIGHTS ON A REVERSIBLE ORC TEST RIG FOR GEOTHERMAL CHP APPLICATIONS

Jannik von Zabienski[1,*], Florian Kaufmann[1], Hartmut Spliethoff[1], Christopher Schifflechner[1]

[1] *Chair of Energy Systems, Technical University of Munich, Boltzmannstraße 15, 85748, Garching, Germany*

* Corresponding Author: jannik.zabienski@tum.de

Abstract. Reversible Organic Rankine Cycles (rev. ORC) offer promising flexibility for geothermal combined heat and power (CHP) applications by supplying heat to district heating networks (DHN) during peak demand and generating electricity when heat demand is low. As a key technology in the European project *FlexGeo*, rev. ORC systems aim to advance flexible geothermal energy use through innovative configurations, with the construction of a 200 kW_{el} demonstrator underway in close collaboration with industry. This work presents initial experimental data from a 20 kW_{el} rev. ORC test rig at the Technical University of Munich (TUM), which uses a 200 kW_{th} hot water circuit as its heat source, a closed-loop cooling system to simulate DHN conditions and the low-GWP refrigerant R1233zd(E) as working fluid. First test data indicate stable operation with observed COP values of 3.0 to 6.4 in high-temperature heat pump (HTHP) mode and thermal efficiencies between 1% to 6% in ORC mode. Technical challenges could be identified, including high pressure losses in the oil separator, insufficient lubrication and limitations from the current working fluid pump. This first analysis offers insights into both the test rig's performance and specific areas for design optimization, underscoring the potential of rev. ORC technology to enhance the versatility of geothermal CHP systems.

Keywords. High temperature heat pump, Organic Rankine Cycle, Reversible, Combined Heat and Power Generation, Deep Geothermal Energy, Operation

1 Introduction

In recent years, reversible Organic Rankine Cycles (rev. ORC) have gained increasing interest in both academia and industry for their ability to flexibly supply heat or electricity. While their applications in Carnot batteries and domestic systems have been widely studied [1,2], their potential in geothermal energy systems has received less attention. In geothermal combined heat and power (CHP) plants, rev. ORCs enhance flexibility by supplying additional heat to district heating networks (DHN) during peak-load times, working as high temperature heat pumps (HTHP) by utilizing medium- and low-temperature heat from geothermal brine as previously examined by Kaufmann et al. [3]. Conversely, during periods of low heat demand, medium- and high-temperature geothermal heat can be used to generate electricity in the ORC mode by reversibly operating the same volumetric machine. In the absence of a standard definition for reversible ORCs in terms of configuration and functionality, this work uses the term to describe systems that operate in both ORC and HTHP modes, as is common in the field. In previous publications these systems were also referred to as reversible HTHP [4].

Experimental research on this topic is notably limited, which led Kaufmann et al. to recently construct a reversible ORC test rig for geothermal applications at the Technical University of Munich (TUM) starting its initial operation in April 2024 [5]. This same test rig was utilized for a detailed experimental analysis previously published by the authors [4]. For a more comprehensive understanding of the processes discussed here, the reader is encouraged to refer to the aforementioned publications, which also detail the plant layout, main cycle components and include a simplified P&ID of the rev. ORC test rig. Thus, a comprehensive analysis and characterisation of the test rig as well as a detailed error analysis are beyond the scope of this work and are instead referenced in the cited study. This paper serves solely to present some first experimental raw data and outline the insights gained from it. Additionally, the limitations of the current design are identified and briefly discussed. The presented work is part of the European project *FlexGeo*, starting in June 2024, where the rev. ORC, as a key technology, contributes to the flexible use of geothermal energy through innovative system concepts. A central objective of the project is the construction of a 200 kW_{el} demonstrator in collaboration

with industry partner Orcan Energy AG, paving the way for the market entry of rev. ORCs.

2 Material and Methods

2.1 Test rig description

The test rig is supplied by a 200 kW_{th} hot water heating circuit, serving as the heat source, and incorporates a fully reversible 20 kW_{el} twin-screw machine. A closed-loop intermediate cooling circuit allows the simulation of a DHN with varying temperature levels and mass flows during HTHP operation. The heat source temperature (T_{HS}) for ORC operation spans a range between 90°C and 140°C. Conversely, the heat sink temperature ranges from 80°C to 120°C in HTHP mode, using heat source temperatures between 40°C and 95°C. The low-GWP refrigerant R1233zd(E) is used as working fluid. To get a detailed description of the whole process, the reader is again invited to read the publication by Kaufmann et al., which is why no further description is given in this paper [4].

Figure 1 shows a picture of the rev. ORC test rig at TUM with insulation on the significant components and pipework. The reversible compressor unit with motor can be seen at the top left and heating and cooling supply at the bottom.

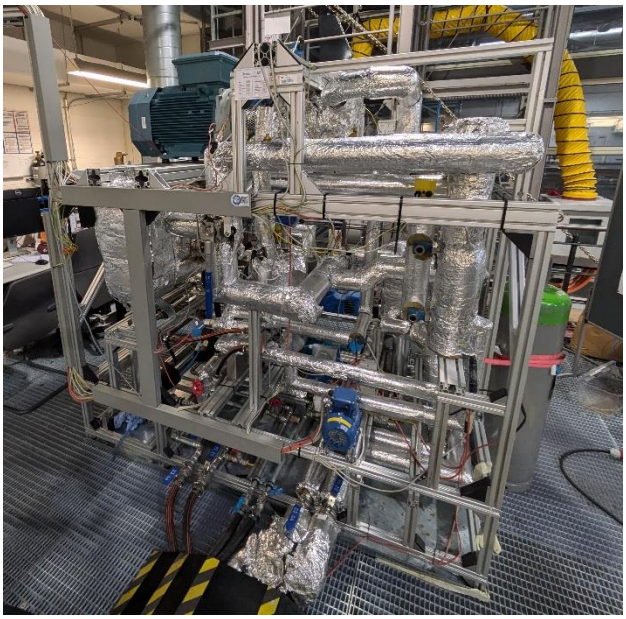


Figure 1: Picture of the rev. ORC test rig at TUM.

2.2 Methodology

To assess the performance of the rev. ORC system, several parameters were varied in the entire study based on real application scenarios [4]. For the HTHP mode the hot water mass flow rate was set at a constant 2.0 kg/s, while the supply temperature was set at three different levels: 55°C, 75°C, and 95°C. The DHN mass flow was adjusted across three values (0.5 kg/s, 1.0 kg/s, and 1.5 kg/s) accompanied by DHN return temperatures of 50°C, 70°C and 90°C. Additionally, the temperature spread in the DHN was adjusted at two levels, 20 K and 30 K. The compressor inlet superheating was consistently maintained at 20 K throughout the tests.

However, in most heat pump applications, lower-temperature heat sources are more accessible and cost-effective, while heat sink temperatures remain application-specific. Therefore, high temperature lifts with efficient COP are ideal, making lift-dependent COP at different heat duties a key measure for HTHP performance. For this reason, this paper focuses exclusively on this approach. Here, temperature lift is defined as the difference in working fluid saturation temperatures before and after compression. For the specific temperature lift variations, a constant 10 K spread in the DHN is maintained.

For the ORC analysis, several operational parameters were adjusted. The hot water mass flow rate was varied between 0.5 kg/s, 1.0 kg/s, and 1.5 kg/s, while the hot water supply temperature was set at either 110°C or 130°C. The evaporation pressure (p_{evap}) was tested at five levels: 7, 8, 9, 10, and 11 bar, with a constant condensation pressure of 2.5 bar. Additionally, the pump inlet subcooling was maintained at 15 K, and the working fluid pump speed was varied at 25%, 35%, and 45%.

During the test campaigns, steady-state conditions were considered achieved when key parameters such as fluid temperatures and pressures remained stable for a duration of five minutes. To ensure more accurate statistical evaluation, an additional five minutes was allowed for the data to stabilise, resulting in a total period of 10 min for averaging. In this paper, only raw data are presented, with steady-state points appearing only toward the end of each plateau in the curves of the diagrams shown in the following section.

To evaluate the overall system performance in both operational modes, several performance indicators can be defined based on common metrics. For heat pumps, the Coefficient of performance (COP) is widely used to assess system efficiency, relating the heat transferred from the working fluid to the DHN to the electrical power consumed by the compressor. For ORC systems, the net electric thermal efficiency ($\eta_{th,el,net}$) provides a measure of performance by calculating the ratio between the net electrical power output, accounting for the working fluid pump's

power consumption and the heat transferred from the geothermal brine to the working fluid. This work assumes that the reader is familiar with these performance indicators.

To align with the scope of the present work, only a small selection of operational data and thus, only one testing day per operating mode is presented in the following section. In HTHP mode it is focused on the operational points of a T_{HS} of 75°C at the mentioned DHN mass flows, over a range of attainable temperature lifts. In ORC mode, the results are presented for operational points with a hot water mass flow rate of 1.0 kg/s, setting the specified pump capacities, p_{evap} and T_{HS}.

3 First experimental results

3.1 HTHP operation results

Figure 2 shows the operation in HTHP mode at the testing day, which lasted around 5 h. The curves display the behaviour of COP and the corresponding temperature lift over time. Specific operating points become visible when focusing on the plateaus of each curve. Here, the DHN mass flow was varied from 0.5 (0 – 6500 s) over 1.0 (6500 – 12500 s) to 1.5 kg/s (12500 – 18000 s). It becomes evident that for every selected DHN mass flow rate, the COP progressively declines as the temperature lift increases. This behaviour is expected given the COP definition, as greater electrical power is required to meet higher heating duties by compressing the working fluid to a higher pressure and increasing its mass flow $\dot{m}_{wf}$.

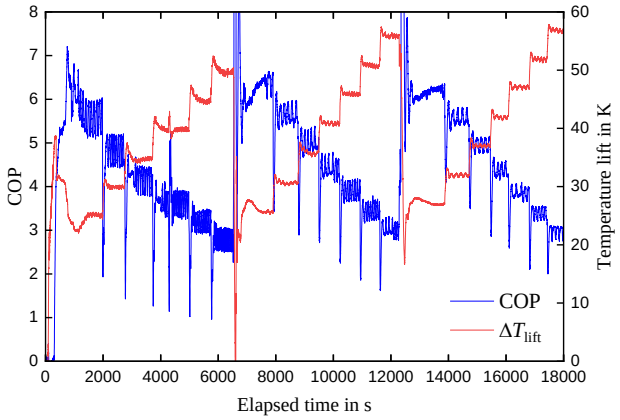


Figure 2: COP and Temperature lift over time.

Figure 3 shows the working fluid mass flow and compressor speed (n_{comp}) as well as the pressure loss across the oil separator (Δp_{OS}) over time. Compressor speed and mass flow are increasing progressively over time. Between seconds 8000 and 11000 the mass flow decreases, showing an unusual behaviour. This effect can be attributed to various compressor performance metrics, such as volumetric efficiencies. However, the relationships involved are rather complex and beyond the scope of this paper. Further details can be found in the comprehensive publication [4].

Overall, the initial test campaigns yielded promising results, achieving steady-state COPs between approximately 3.0 and 6.4, depending on the required temperature lift, ranging from 25 to 57 K. Higher lifts were not feasible for this T_{HS} due to temperature limitations in the primary cooling water line.

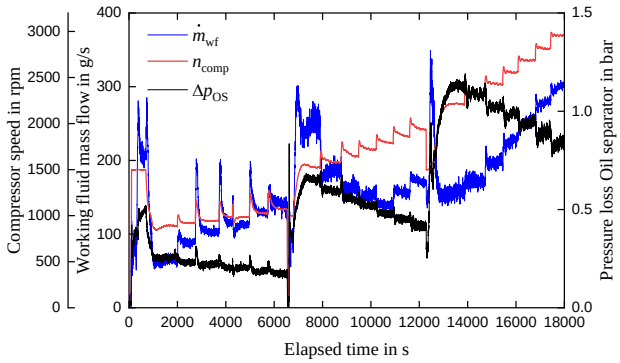


Figure 3: Compressor speed, working fluid mass flow and pressure loss of the oil separator over time.

However, other limitations were also identified during the tests. To ensure proper lubrication of the reversible compressor, oil is directly introduced into the machine and directed towards the bearings and the rotor profiles. After compression and prior to expansion in ORC mode, the oil is separated from the working fluid in the oil separator. As shown in Figure 3, unexpectedly high values for Δp_{OS} were notable. This was observed early on during the commissioning phase. Particularly at lower temperature lifts and high heat duties, the highest values for Δp_{OS} occurred, reaching over 1 bar in the 13000 to 18000 s range. These instances involved relatively low working fluid densities, resulting in high volumetric flows at high $\dot{m}_{wf}$ and n_{comp}. The manufacturer further specifies that the pressure loss in the oil separator should not exceed 0.8 bar. This, along with other effects such as liquid oil in the outlet gas stream, suggests inadequate separation, likely indicating an undersized oil separator. In this context, low volumetric efficiencies were also observed, which suggests insufficient lubrication, although this is not specified further here.

3.2 ORC operation results

For ORC mode Figure 4 shows the net electrical thermal efficiency as well as the generated electric power for the given operational points over time. On

this testing day, operations ran for up to 8 h. From 1000 to 20000 s, all operational points with a T_{HS} of 110°C were tested, while the points for 130°C appear from 20000 to 30000 s. Between 10000 and 15000 s, the plant was inactive, indicated by near zero generator power output and inaccurate thermal efficiency values.

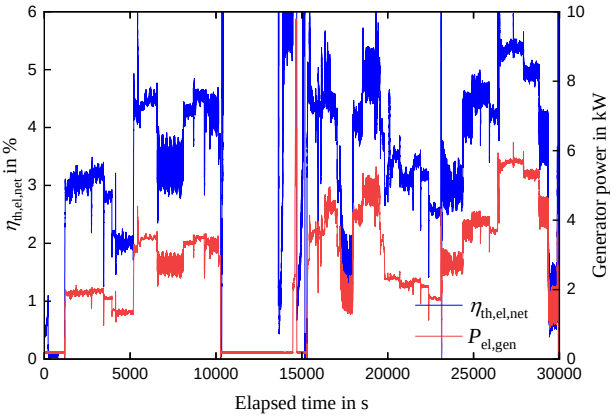


Figure 4: Net electric thermal efficiency and Electrical generator power over time.

Figure 5 shows individual parameter levels and operational points, depicting expander speed (n_{exp}), $\dot{m}_{wf}$ and p_{evap} over time. It becomes clear that notably higher speeds were achieved, particularly at lower p_{evap}. With values around 4000 rpm, the operational limits of the expander were approached. Furthermore, Figure 4 illustrates that thermal efficiencies increase with higher T_{HS} and $\dot{m}_{wf}$.

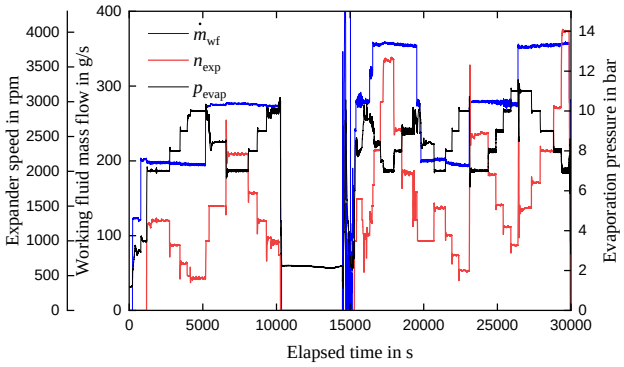


Figure 5: Expander speed, working fluid mass flow and evaporation pressure over time.

Generally speaking, thermal efficiencies ranging from 1% to 6% were achieved, with the highest values occurring at a T_{HS} of 130°C and maximum $\dot{m}_{wf}$ at intermediate p_{evap} around 8 bar. These pressure levels align well with the built-in volume ratio of the expander of 3.1, indicating an adapted expansion. Under these conditions, generated power peaked at approximately 6 kW. It should also be noted that high thermal efficiency can result from limited heat source utilisation, as this raises the average evaporation temperature and thereby increases Carnot efficiency. This aspect is explored in further detail in the publication focused on experimental characterization [4].

In ORC mode, relatively high pressure losses were also observed across the oil separator. Due to the specific configuration, oil circulation times are longer in this mode compared to HTHP mode, leading to a rapid emptying of the oil separator. As a result, only minimal oil flows could be maintained, which were just enough to ensure lubrication and preventing damage to the rev. compressor. This finding supports the assumption that the oil separator is undersized and will need replacement in future configurations. Furthermore, a limited pump capacity restricted operations to only 50% of its full capacity, as higher pump speed levels caused strong vibrations. This limitation prevented the necessary increase in mass flow required to control superheating of the working fluid, particularly at high heat source mass flows and low p_{evap}. Installing a working fluid pump with a larger capacity would address this issue, also enabling further cooling of the heat source. Additionally, at high p_{evap} and low $\dot{m}_{wf}$, the expander speed dropped below 500 rpm, thereby preventing efficient operation.

In general, favorable expander efficiencies were observed for ORC mode. However, the overall machine efficiency is anticipated to improve with increased oil supply and a larger oil separator, which would also enhance part-load efficiency of the test rig.

4 Conclusions

This study presents the first experimental data from a reversible ORC test rig designed for geothermal CHP applications. Initial tests demonstrate stable operation in both HTHP and ORC mode, with COP values of 3.0 to 6.4 and net electric thermal efficiencies up to 6% under optimal conditions. Key challenges identified include high pressure losses across the oil separator, inadequate lubrication and capacity limitations in the current working fluid pump, highlighting areas for future optimization. These findings lay the groundwork for enhancing reversible ORC technology, supporting its integration into flexible, geothermal-based energy systems.

Acknowledgement

Funding from the Bavarian State Ministry of Education, Science and the Arts in the framework of the project Geothermal-Alliance Bavaria and from the European Union's Horizon Europe research and innovation programme under grant agreement No. 101147576 (*FlexGeo*) is gratefully acknowledged.

References

[1] G.F. Frate et al., "A novel Pumped Thermal Electricity Storage (PTES) system with thermal integration", Applied Thermal Engineering 121 (2017) 1051–1058. https://doi.org/10.1016/j.applthermaleng.2017.04.127.

[2] O. Dumont et al., "Experimental investigation of a reversible heat pump/organic Rankine cycle unit designed to be coupled with a passive house to get a Net Zero Energy Building", International Journal of Refrigeration 54 (2015) 190–203. https://doi.org/10.1016/j.ijrefrig.2015.03.008.

[3] F. Kaufmann et al., "Techno-Economic Evaluation of reversible Organic Rankine Cycles in geothermal combined Heat and Power Plants", Proceedings of ECOS 2022 - 35th International Conference on Efficiency, Cost, Optimization, Simulation and Environmental Impact of Energy Systems (2022) 197–208.

[4] F. Kaufmann et al., "Experimental Analysis of a Reversible High-Temperature Heat Pump/Orc Test Rig for Geothermal CHP Applications", Preprint (2024). https://doi.org/10.2139/ssrn.5013851.

[5] F. Kaufmann et al., "Design and Construction of a Reversible ORC Test Rig for Geothermal CHP Applications", Proceedings of the 7th International Seminar on ORC Power Systems (2023) 81–90.

HIGH TEMPERATURE RECUPERATOR FOR MICRO GAS TURBINE

Joseph Jojomon[1*], Danish Rehman[1], Michel Delanaye[1]

[1] MITIS, Belgium

** Corresponding Author: joseph.jojomon@mitis.be*

Abstract. Decentralised energy systems are being revolutionized by micro-combined Heat and Power systems (mCHP), which provide heat and electricity simultaneously with lower emissions. Recuperated mCHP consists of a compressor that pressurizes air to an appropriate pressure ratio, then passes into the recuperators, where it gets preheated. The preheated air enters the combustors, where it raises the temperature for the turbine inlet that extracts required power for the generator. After the turbine expansion, it enters the low pressure (LP) side of the recuperator, where the heat is recuperated to the HP side of the recuperator for preheating. The remaining heat from the recuperator exit is extracted based on the application. However, the recuperator enhances the recuperator cycle efficiency by nearly 8–10%. The high temperature recuperator (> 650 C) must have a thermal effectiveness greater than 90 percent by accepting 4 percent pressure losses (on both the HP and LP sides).

This work investigates MITIS patented recuperators consisting of complex wire-net microchannels and collectors by using a computational fluid dynamics (CFD) approach. The turbine exhaust flow enters the primary collector, where the flow is distributed into secondary collectors and then into microchannels. Three levels of flow maldistribution and its influence on global thermal efficiency and pressure losses are presented in this work. Conducting a complete conjugate heat transfer (CHT) study requires a large amount of processing power due to the hundreds of parallel microchannels with secondary and primary collectors. In order to assess the performance of the heat exchanger as a whole, a novel method is proposed in this work. It is based on a reduced model (RM), in which the microchannels are represented as porous media with a compressible gas acting as the working fluid.

As a first step, a three-dimensional CFD analysis of conjugate heat transfer for a microchannel section was performed to calculate the inertial and viscous coefficients of the porous medium model based on the Darcy-Forchheimer law. High temperature variations and compressibility effects were accounted for in this analysis. Axial wall conduction losses influence on various microchannel parameters will be presented in this work. Besides, a detailed investigation of the wire-net flow physics was made using a higher order Reynolds stress turbulence model to obtain the full velocity gradient tensor. This could detail the effect of anisotropic flow physics in the isotropic wire-net microchannels. Furthermore, the analysis of the turbulence production terms provided a deeper insight into flow attachment and detachment near the wire-net intersections. It was shown that shifting the critical Reynolds number to lower values using perturbators decreases the pressure losses and enhances the thermal efficiency and that there is an optimum mass flow where the thermal efficiency reaches maximum. Using the RM approach, investigation of collectors with different microchannel configurations (s-shaped, wire-net and plane channels) showed that mass flow rate deviation decreases with an increase in microchannel resistance. The recirculation zones in the cylindrical collectors also changed the maldistribution pattern. It was also shown that there is a substantial drop in thermal effectiveness at low microchannel inlet mass flow rates due to axial wall conduction losses and high flow maldistribution.

Keywords. Micro CHP, Porous model, Conjugate heat transfer, Wall conduction, Microchannel heat transfer.

OPTIMIZING A BLUE HYDROGEN-FUELLED GAS TURBINE COMBINED CYCLE

Maria Jose Mendoza Morales[1,2]*, Julien Blondeau[2], Ward De Paepe[1]

[1] UMONS, Thermal engineering and combustion research unit, Mons, Belgium

[2] VUB, Thermo and fluid dynamics (FLOW), Brussels, Belgium

* *Corresponding Author: mariajose.mendozamorales@umons.ac.be*

Abstract. Hydrogen has gained significant momentum in recent years due to its versatility in addressing various challenges within the energy system. As the electricity sector evolves with increased integration of renewable sources and a growing need to limit CO_2 emissions, the utilization of hydrogen as fuel in technologies such as gas turbines has gained considerable attention. However, the current production of green hydrogen remains limited. According to the International Energy Agency (IEA), hydrogen production is estimated to have generated approximately 920 million tons of CO_2 emissions in 2023, with only about 1% of global hydrogen classified as low carbon. A promising solution for this transitional period is "blue hydrogen," which combines traditional steam methane reforming (SMR) with carbon capture technology to mitigate the impact of hydrogen production. The reforming process is highly endothermic, requiring the combustion of natural gas to provide heat, while the carbon capture unit also consumes significant energy for solvent regeneration, making both processes highly energy-intensive. This highlights the critical need for effective process integration to limit their impact on the environment. In this short paper, we focus on the first step in optimizing the integration of a gas turbine combined cycle powered by blue hydrogen, which involves performing a sensitivity analysis to evaluate the impact of the parameters in the flue gases of the SMR. The analysis will be done by employing Aspen Plus models for each system. Additionally, pinch analysis, a well-established method for energy integration, is utilized to improve system efficiency. As a result of this analysis, key parameters impacting the performance of the system are identified. To facilitate the integration of hydrogen into the energy system, multiple factors must be addressed, and this work evaluates and addresses one of the alternatives.

Keywords. Blue hydrogen, Steam Methane Reforming, Gas Turbines, Thermodynamic Performance.

1 Introduction

In 2022, the International Renewable Energy Agency (IRENA) estimated that hydrogen and its derivatives would contribute to 10% of total CO_2 emission reductions under the 1.5°C scenario by 2050 [1], driven by commitments made under the Paris Agreement [2]. The demand for low-carbon hydrogen is expected to grow significantly regardless of the scenario and the sector [3]. Particularly in the energy sector, hydrogen has gained importance as efforts intensify to reduce CO_2 emissions due to its long-term energy storage potential and the variety of technologies that can utilize it without emitting CO_2.

However, the current production of green hydrogen remains limited. A promising solution for this transitional period is "blue hydrogen," which combines traditional steam methane reforming (SMR) with carbon capture technology to mitigate the impact of hydrogen production. There are four blue-hydrogen facilities in the world, including Port Arthur in the United States, Quest in Canada, and Port Jerome in France [4]. These facilities employ pre-combustion carbon capture, a method that offers several advantages. While post-combustion capture is also a viable option, the preference for pre-combustion capture highlights its superior technical benefits in these operations.

CO_2 can be captured at three distinct stages of the SMR process: (1) before the separation process, (2) after the separation process, or (3) at the flue gas outlet [5]. For this study, we have selected to capture CO_2 at the flue gas outlet, as it represents the total amount of CO_2 produced by the system. The most suitable technology for this stream is an absorption process using monoethanolamine (MEA) process. However, this method is energy-intensive, and its efficiency is influenced by factors such as the CO_2

partial pressure in the gases being treated. Along with the highly endothermic process that SMR is, the optimization of the blue hydrogen process is critical for the deployment of this solution.

Gas turbine-based systems will remain essential in future energy systems to enable operators to effectively match fluctuating energy demand. However, these systems are traditionally powered by natural gas. Despite their relatively high efficiency, operating such units may become economically challenging in a future energy landscape where CO_2 emissions are likely to incur increasing penalties due to rising carbon prices [6]. To address these challenges, the industry is exploring two main solutions: transitioning to hydrogen as fuel or integrating carbon capture technologies. While carbon capture is a promising option, its feasibility depends on the partial pressure of CO_2 in the treated gas, which is particularly low in GTs. This limitation, combined with the cyclic operation of GTs—affecting the performance of carbon capture systems—and the uncertainty surrounding their ability to maintain high capture rate efficiency during transient load phases, makes hydrogen fuel adoption a potentially more straightforward and practical solution for deployment.

The use of blue hydrogen as fuel in GTs offers operators a viable solution to maintain grid stability while mitigating financial penalties associated with rising carbon capture prices. In this approach, the carbon capture unit operates in conjunction with hydrogen production, capturing CO_2 emission at the source. The produced hydrogen can then be stored, sold, or used directly in GTs to generate electricity, providing flexibility and supporting a low-carbon energy system.

With this investigation, we aim to assess the potential of these options by optimizing and integrating a system comprising hydrogen production by steam methane reforming with carbon capture, a gas turbine, and a steam cycle. This short paper's objective is to perform a preliminary assessment to examine how the operational conditions of the SMR impact the properties and state of the exhaust gases, as these factors directly affect the reboiler duty of the carbon capture unit.

2 Methodology

The simulations have been done in Aspen Plus v12 [7], a software for process simulation widely used in industry. The whole process consists of a traditional steam methane reforming (SMR), an amine-based (MEA) carbon a capture (CC) unit, a heavy-duty gas turbine and a three-pressure level (HRSG), shown in Figure 1.

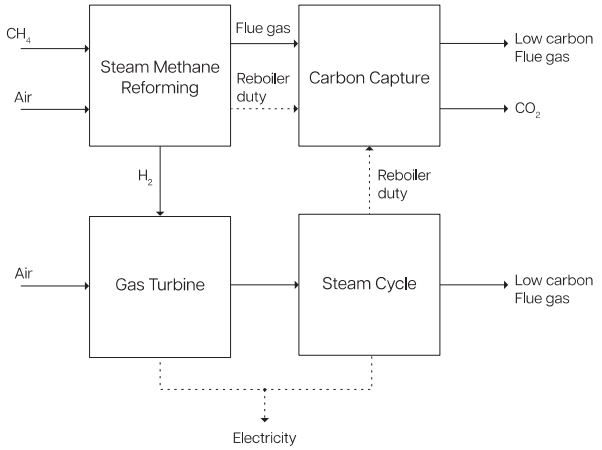


Figure 1: Blue hydrogen CCGT system integration.**Figure 1:** Blue hydrogen CCGT system integration.

The steam methane reforming (SMR) process follows a conventional configuration. It is based on the models by Soltani [5] and Molburg [8]. However, some of the parameters are adapted to allow flexibility. The carbon capture unit is a conventional amine-based absorption-regeneration process. Two columns representing the absorber and the stripper, the pumps and the associated heat exchange units make up the system. Our research group has studied this process, and it is available in detail [9].

For the GT, the model is based on the performance characteristics of the GE 7HA.02 [10] and has been adapted to simulate off-design operational conditions. This adaptation accounts for the different properties of hydrogen, compared to methane, which necessitates modifications to the model. A comprehensive explanation of the model can be found in [11]. Similarly, the steam cycle model is based on a state-of-the-art, three-pressure-level HRSG with reheat, which is the standard in combined cycle gas turbine systems and described in [11].

As shown in Figure 1, the SMR process requires natural gas, steam, and air inputs. The hydrogen produced in the SMR process can be utilized as fuel for the GT. The exhaust gases from the GT, which exit at high temperatures, are directed to the steam cycle, where they contribute to additional electricity generation. In the SMR, the flue gases are routed to the carbon capture unit to mitigate carbon emissions. As previously discussed, both SMR and carbon capture are highly energy-intensive processes.

Consequently, utility inputs are essential to sustain the system's operation. For the SMR process, a furnace supplies the substantial heat required for reforming, given the high temperature required for the reaction. The carbon capture system demands significant heat to regenerate the solvent, which can be sourced either from the residual heat of the SMR or the steam cycle.

The potential of this low-carbon approach can be assessed by the application of pinch analysis for heat integration optimization and the use of advanced optimization tools to identify the most effective system configuration. In this study, as we conducted it in an academic context, the primary objective is to maximize the overall energy efficiency of the system. To facilitate the optimization, the parameters influencing the system's performance must be evaluated and their impact assessed. Consequently, a sensitivity analysis is performed to identify the parameters with the greatest influence on system outcomes.

3 Results and discussion

As shown in one of the preliminary pinch analysis results in Figure 2, the extended plateau at approximately 130°C corresponds to the reboiler duty, underscoring its critical role in the overall energy balance. The process utility demands are evident at both ends—on the cooling and heating sides—representing a typical pinch analysis problem. In this scenario, the goal is to eliminate the need for external heating utilities, ensuring that the system is self-sufficient in meeting its thermal requirements. Such a situation is referred to as a "threshold problem," where utility demand is required only on one end of the system.

The parameters we initially evaluated for the sensitivity analysis are the pressure of the methane compressor and water pump, the temperature of the reformer, the steam-to-carbon ratio, the temperature of the furnace air, and the temperature of exhaust gases of the furnace. The cases shown in Figure 3 correspond to the base case model while maintaining a ~10% excess air and no extra fuel for the furnace. The parameters all impact the properties and state of the exhaust gases, as shown in Figure 3. In almost all cases, an inverse relationship is observed between the CO_2 fraction and the mass flow rate. Ideally, achieving a lower mass flow rate and a higher CO_2 fraction is preferable to minimize the reboiler duty.

The temperature of the reformer, system pressure, and steam-to-carbon ratio influence the methane conversion rate. Higher pressures generally reduce methane conversion due to the volumetric expansion of the reaction, as the number of moles on the product side exceeds those on the reactant side. However, elevated pressures enhance the permeation rate, a phenomenon observed in experimental studies [12]. A higher S/C and reformer temperature both increase the conversion rate, for this reason less CO_2 is obtained in the flue gases. Regarding air temperature, only the inlet air changes to maintain constant excess air. Higher air temperatures enhance combustion efficiency, reducing both the air mass flow rate and CO_2 fraction.

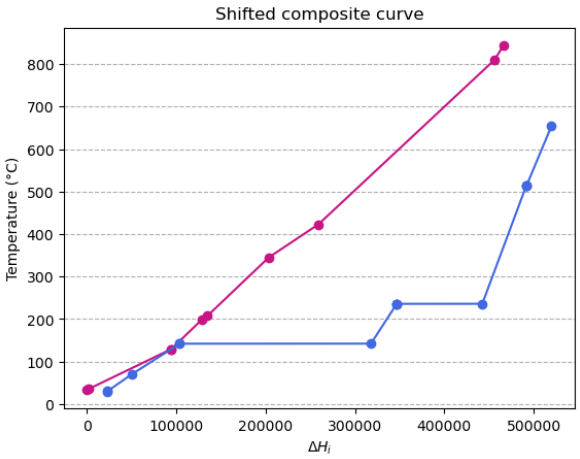


Figure 2. Preliminary shifted composite curve for pinch analysis of the base case, incorporating reboiler duty.

4 Conclusions

The operational parameters significantly influence the properties and state of the SMR flue gases, thereby also affecting the specific reboiler duty. Highlighting the need to optimize the system. Once the key parameters and optimization objectives are identified, the system is optimized using RHEIA [12], an open-source computational framework developed by the research group for robust optimization. RHEIA enables the determination of parameter values that achieve the defined optimization goals.

In future work, other performance metrics, such as minimizing CO_2 emissions, enhancing flexibility, or maximizing return on investment (ROI), will be taken into consideration.

5 Acknowledgment

This research is part of the BE-HyFE project, which is a Belgian academic collaboration project funded by the federal Energy Transition Fund by FPS Economy. More information on www.behyfe.be.

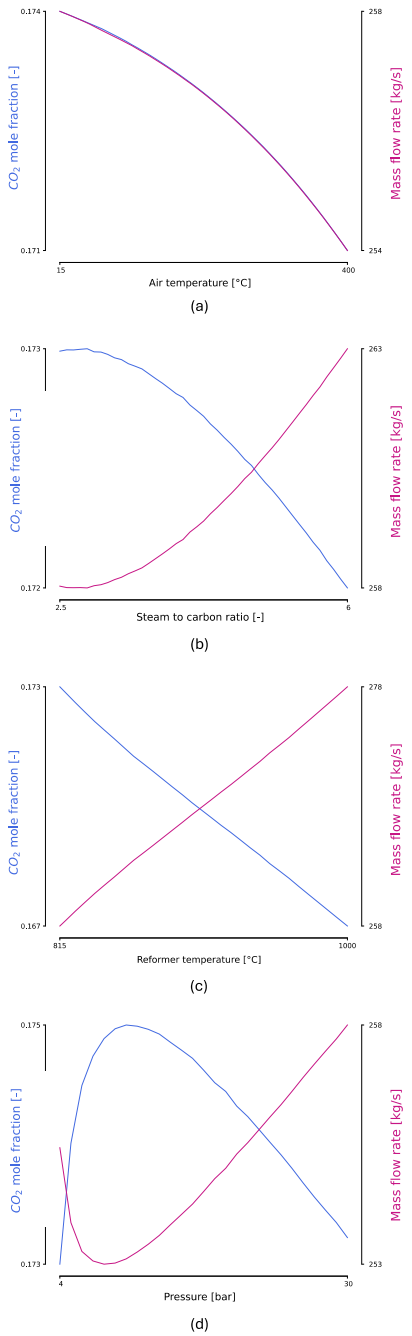


Figure 3. Results from the sensitivity analysis

References

[1] IRENA, "World Energy Transitions Outlook 2022: 1.5◦C Pathway," Abu Dhabi, 2022.

[2] UNTC XXVII 7.d., *Paris Agreement*, Paris, 2016.

[3] C. Gulli, B. Heid, J. Noffsinger, M. Waardenburg and M. Wilthaner, *Global Energy Perspective 2023: Hydrogen outlook*, McKinsey, 2023.

[4] IEAGHG, "Low-Carbon hydrogen from Natural Gas: Global Roadmap," 2022.

[5] R. Soltani, M. Rosen and I. Dincer, "Assessment of CO2 capture options from various points in steam methane reforming for hydrogen production," *International Journal of Hydrogen Energy*, vol. 39, no. 35, pp. 20266-20275, 2014.

[6] S. Öberg, M. Odemberger and F. Johnsson, "Exploring the competitiveness of hydrogen-fueled gas turbines in fututе energy systems," *International Journal of Hydrogen Energy*, vol. 47, no. 1, pp. 624-644, 2022.

[7] Aspen Plus v12, Aspen Tech.

[8] M. John and D. Richard, "Hydrogen from Steam-Methane Reforming with CO2 Capture," in *20th Annual International Pittsburgh Coal Conference*, Pittsburgh, 2003.

[9] A. Verhaeghe, L. Dubois, L. Bricteux, D. Thomas, J. Blondeau and W. De Paepe, "Carbon Capture Performance Assessment Applied to Combined Cycle Gas Turbine Under Part-Load Operation," *Journal of Engineering for Gas Turbines and Power*, vol. 145, no. 4, 2023.

[10] GE Vernova, "LM2500 aeroderivative gas turbine," [Online]. Available: https://www.gevernova.com/gas-power/products/gas-turbines/lm2500. [Accessed 14 11 2024].

[11] M. J. Mendoza Morales, A. Verhaeghe, L. Bricteux, J. Blondeau and W. De Paepe, "Is Blue Hydrogen a Better Alternative Than Post-Combustion Carbon Capture for Combined Cycle Gas Turbines? A Thermodynamic Point of View," in *ASME Turbo Expo 2023: Turbomachinery Technical Conference and Exposition*, Boston, 2023.

[12] D. Coppitters, P. Tsirikoglou, W. De Paepe, K. Kyprianidis, A. Kalfas and F. Contino, "RHEIA: Robust design optimization of renewable Hydrogen and dErIved energy cArrier systems," *The Journal of Open Source Software*, vol. 7, no. 75, 2022.

[13] IRENA., *World Energy Transitions Outlook 2023: 1.5◦C Pathway,* Abu Dhabi, 2023.

CARNOT BATTERY INTEGRATION IN A GEOTHERMAL POWER PLANT: STUDY CASE OF ZORLU ENERJI

Aitor Cendoya [1]*, Basile Chaudoir [1]*, Titouan Janod [1]*, Tuğrul Hazar [2], Ural Halaçoğlu [2], Vincent Lemort [1]

[1] University of Liège, Thermodynamics Laboratory, Liège, Belgium

[2] Zorlu Enerji, Istanbul, Türkiye

* *Aitor Cendoya: acendoya@uliege.be*

* *Basile Chaudoir: Basile.Chaudoir@uliege.be*

* *Titouan Janod: Titouan.Janod@uliege.be*

Abstract. Waste heat generated by the industrial sector is a major source of unused energy. Integrating technologies into this process improves energy efficiency and contributes to the reduction of greenhouse gas emissions. In this scope, the SEHRENE project presents a novel approach to industrial waste heat recovery, increasing process flexibility and efficiency. The concept integrates an Electro-Thermal Energy Storage (ETES) system, including a High-Temperature Heat Pump (HTHP), a Phase Change Material (PCM) storage and an Organic Rankine Cycle (ORC). This study evaluates the optimal integration of an ETES in the largest Geothermal Power Plant (GPP) in Türkiye. The 80 MWe Kızıldere-2 GPP belongs to the Zorlu Enerji group. This plant is composed of a triple flash-binary (ORC) combined GPP. Several ETES architectures and refrigerants are analysed, to select the optimal configuration. This paper presents the results of this study case including system performance and a sensitivity analysis of various system parameters. These were then chosen to get the best design out of the trade-off between the potential performance and industrial feasibility of the machine. The main findings indicate that cyclopentane is the optimal working fluid for the given operating temperatures, where with different system architectures the round-trip efficiency (RTE) can reach values higher than 80%. Also, the performance sensitivity of the varied parameters was assessed. The most impactful varied parameters were the PCM melting temperature and the turbine isentropic efficiency. These results show the promising integration of ETES in geothermal power plants and all other processes with usable low and medium-temperature waste heat.

Keywords. High Temperature Heat Pump, Organic Rankine Cycle, Thermal Integration, Geothermal energy, ETES

Nomenclature

A	Heat transfer area (m²)
$\dot{C}$	Heat capacity rate (W/K)
E	Energy (J)
F	LMTD correction factor (-)
h	Specific enthalpy (J/kg), Heat Transfer Coefficient (W/m²·K)
$\dot{m}$	Mass flow rate (kg/s)
$\dot{Q}$	Heat duty (kW)
t	Time (h)
T	Temperature (°C or K)
U	Overall heat transfer coefficient (W/m²·K)
v	Specific volume (m³/kg)
$\dot{V}$	Volumetric flow rate (m³/s)

Special characters

η	Efficiency (-)
Π_r	Pressure ratio (-)
Δ	Difference (-)

Acronyms

COP	Coefficient Of Performance
ETES	Electro-Thermal Energy Storage
GWP	Global Warming Potential
(HT)HP	(High Temperature) Heat Pump
IWH	Industrial Waste Heat
KPI	Key Performance Indicators
LMTD	Log Mean Temperature Difference (K)
ORC	Organic Rankine Cycle
PCM	Phase Change Material
RTE	Round-Trip Efficiency
VHC	Volumetric Heat Capacity (J/K·m²)

Subscripts	
cd	Condenser
cp	Compressor
ev	Evaporator
ex	Exhaust
HX	Heat Exchanger
pp	Pump, Pinch point
s	Isentropic
sf	Secondary fluid
su	Supply
sto	Storage
tu	Turbine
wf	Working fluid
x1	Vapor quality of 1

1 Introduction

Research on Electro-Thermal Energy Storage (ETES) has gained increasing interest because of the recent need for electricity storage to damp renewable energies' intermittent production [1]. This specific storage solution depends less on geographical conditions [2] and on rare earth elements [3] and thus could be a suitable long-term solution. However, the complexity of these machines and the recency of the research interest are barriers to overcome. The SERHENE project aims to contribute to this field by presenting and deeply assessing novel thermally integrated designs. These designs contain High Temperature Heat Pumps (HTHP), Organic Rankine Cycles (ORC) and novel Phase Change Material (PCM) heat storages. They are also studied as to be integrated into real test cases, the one focused on here is the largest Geothermal Power Plant (GPP) in Türkiye from Zorlu Enerji. The Kızıldere-2 (KZD II) GPP has an installed capacity of 80 MWe and is composed of a triple flash-binary (ORC) combined GPP. This paper will be led as the following:

- Introduction of the case study and of the reference topology.
- Presentation of the thermodynamic model.
- Selection of the refrigerant and the topology.
- For the final topology, refinement of the parameters thanks to a sensitivity study.
- Pre-sizing of the components of the system.

2 Reference Case Definition

2.1 Case study description and reference topology

The reference Carnot battery design is depicted on Figure 1. Its HTHP contains an internal heat exchanger and its ORC includes a recuperator.

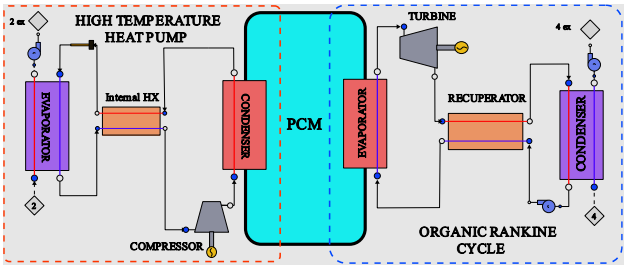


Figure 1: ETES reference configuration.

According to the information provided by Zorlu Enerji regarding the Kilzideri II three-flash plant with a Binary cycle, various energetic vectors can be recovered or utilized for potential integration into the ETES system. Table 1 presents the properties of the different vectors that could be integrated into the ETES. Based on this data, the low-pressure separator brine point will be considered as the Industrial Waste Heat (IWH) for the HTHP evaporator. Using the fluid coming from KZD II wells would have been on option but it also would have decreased the energy produced by the current system. Meanwhile, the cooling water supply to the binary cycle will be used as the cold source for the ORC condenser.

Table 1: Available residual heat sources from KZD-II GPP.

Point	T [°C]	P [bar]	$\dot{m}$[ton/h]	Fluid
From KZD II wells (1)	178.1	10.65	2678.5	97% steam/brine
Low-pressure separator brine (2)	113.1	1.59	3088.6	100% steam/brine
Condensate from binary Plant (3)	50.6	3	283.9	99.9% steam/brine
Cooling water supply to the binary plant (4)	24.1	3.63	9000	100% steam/brine

2.2 Thermodynamic Modelling

Various components are employed and modelled, in this first stage as a thermodynamic model based on different assumptions. These hypotheses are represented for each component involved in the possible configuration of each case study. The modelling of individual components is conducted using EES 2024 (Engineering Equation Solver).

2.2.1 Heat exchangers with phase change (Evaporator and Condenser): In these components the heat transfer process involves two fluids or mediums. In the evaporator, the refrigerant or working fluid (wf) undergoes a phase change from liquid (or two-phase) to saturated, or even superheated vapour, or even to superheated vapour. Conversely, in the condenser, the refrigerant transitions from vapour (or two-phase) to liquid

through condensation. The energy balance between the refrigerant and the secondary fluid (sf) is presented in Equation 1. This relation corresponds to the condenser, nevertheless, for the evaporator it is the same in the reverse way.

$$\dot{m}_{wf,cd} \cdot \left(h_{wf,ex,cd} - h_{wf,su,cd}\right) = \dot{Q}_{cd}, \qquad (1)$$
$$\dot{Q}_{cd} = \dot{m}_{sf,cd} \cdot \left(h_{sf,su,cd} - h_{sf,ex,cd}\right)$$

The saturation temperature is computed as the mean temperature between the one at the beginning and the one at the end of the two-phase zone. The equations of the pinch-point ($PPTD$) for the HP condenser are presented in Equations 2 and 3. These equations allow to determine by iteration of the pinch-point in the heat exchanger and set to determine the saturation state.

$$\dot{Q}_{pp,cd} = \dot{m}_{sf} \cdot \left(h_{sf,pp,cd} - h_{sf,su,cd}\right), \qquad (2)$$
$$\dot{Q}_{pp,cd} = \dot{m}_{wf} \cdot \left(h_{wf,x1,cd} - h_{wf,ex,cd}\right)$$

$$\Delta T_{pp,cd} = T_{wf,x1,cd} - T_{sf,pp,cd} \qquad (3)$$

2.2.2 Sensible heat exchangers (recuperator, preheater and superheater): These heat exchanger models only transfer sensible heat between two fluids. The recuperator transfers heat from the turbine exhaust to the pump exhaust (ORC), and after the condenser with the exhaust of the evaporator (HTHP). The preheater preheats the fluid upstream of the ORC evaporator. The superheater serves to increase the gaseous temperature at the exhaust of the ORC evaporator. The assumption for modelling these components corresponds to considering an isobaric process, then no pressure drops. A counterflow heat transfer process is considered. Finally, energy and mass are conserved in both fluids. The same energy balances are considered as in the phase change heat exchanger, adding the heat transfer equation, which is presented in Equation (4).

$$\dot{Q}_{hx} = \dot{C}_{min,hx} \cdot \eta_{HX} \cdot \left(T_{hot,su,HX} - T_{cold,su,HX}\right) \qquad (4)$$

2.2.3 Compressor: This component is employed in the HTHP to raise the pressure from the evaporator to the condenser. To avoid any kind of problem, superheating of the compressor suction due to refrigerant droplets must be ensured. The isentropic and volumetric efficiencies are presented in Table 2. The first is used to compute the machine real work. The second is used to compute the swept volume of the volumetric machines. The energy balance for computing the input energy for the compressor is presented in Equation 5, whereas the calculation of the swept volume is presented in Equation 6.

$$\dot{W}_{cp} = \dot{m}_{wf} \cdot \left(h_{wf,s,ex,cp} - h_{wf,su,cp}\right)/\eta_{s,cp} \qquad (5)$$

$$V_{cp} = \frac{\dot{m}_{wf}}{\eta_{v,cp} \cdot N_{cp} \cdot \rho_{wf}} \qquad (6)$$

2.2.4 Turbine: This component is the machine used in the ORC to convert the fluid internal energy into electricity. This component and model can be considered identical to the compressor but with the energy transfer taking place in the opposite direction. The energy balance to compute the energy taken from fluid in the turbine corresponds to Equation 6.

$$\dot{W}_{tu} = \dot{m}_{wf} \cdot \eta_{s,tu} \cdot \left(h_{wf,su,tu} - h_{wf,s,ex,tu}\right) \qquad (7)$$

2.2.5 Pump: The pump is the drive component in the ORC, which increases the pressure in the working fluid from the lower (condenser) to the upper pressure (evaporator). This component also consumes energy and to avoid any cavitation problems the working fluid is subcooled. The assumption for modelling these components corresponds to an isentropic process driving the fluid from the supply to the exhaust, where an efficiency of 65% was considered. The power required for the pump is computed according to Equation 7.

$$\dot{W}_{pp} = \dot{m}_{wf} \cdot \left(v_{wf,su,pp} \cdot \frac{\left(P_{wf,ex,pp} - P_{wf,su,pp}\right)}{\eta_{s,pp}}\right) \qquad (8)$$

2.2.6 Phase Change Storage: PCM heat storage is the key component for the ETES which stores the energy from the HTHP and releases it in the ORC for producing electricity. The material has not been yet defined. The project's Key Performance Indicators (KPIs) require a PCM storage with an energy density corresponding to $90\,kWh/m^3$. It is assumed that PCM can release a constant energy flow rate corresponding to the total energy storage divided by the discharging time. The energy storage in the PCM is computed according to Equation 8.

$$E_{sto,\,PCM} = \int_{t_{initial}}^{t_{final}} \dot{Q}_{cd,\,HP}\, dt \qquad (9)$$

2.2.7 Expansion valve: This component considers an isenthalpic process which connects the HTHP condenser with the HTHP evaporator. It is considered that this component can maintain a constant evaporator superheating.

Table 2 summarises the pinch point and efficiencies mentioned in the equations 3 to 8.

Table 2: Assumed parameters for the reference case

Parameter	$Value$	Unit
$\Delta T_{pp,cd}$, $\Delta T_{pp,ev}$	3	K
η_{HX}	0.8	-
$\eta_{s,cp}$, $\eta_{s,tu}$, $\eta_{s,pp}$	0.65	-
$\eta_{v,cp}$, $\eta_{v,pp}$	0.95	-
T_{PCM}	160	°C
t_{charge}	4	h
$t_{discharge}$	2	h
V_{PCM}	322.22	m^3

2.3 Refrigerant Selection

This section focuses on selecting refrigerants suitable for use in the ETES system. A PCM temperature of 160°C is considered in this evaluation. For HTHPs, refrigerants such as R1233zd(E), R1234(Z), R600, R601, R1336mzz(Z) and R1224yd(Z) are considered promising candidates for this application [4]. Additionally, R1234ze(Z) and R1234ze(E) are highlighted as viable options for high-temperature applications [5, 6], along with hydrocarbon-based refrigerants [7].

A comprehensive study by Frate et al. [8] has assessed 27 potential refrigerants with a Global Warming Potential (GWP) lower than 1000, identifying options that achieve critical temperatures above 125°C and maintain a saturation pressure above 0.05 bar at 40°C. Furthermore, zeotropic refrigerant mixtures have been thermodynamically evaluated, demonstrating performance improvements of up to 46% [9].

The working fluids selected for potential integration in the ETES system include Acetone, Benzene, Cyclopentane, Cyclohexane, Ethanol, Isopentane, Isohexane, Methanol, n-pentane, R1233zd(E), R1234ze(Z), R245fa, R600, and Toluene. These fluids are evaluated based on two key performance metrics for HTHP: the Coefficient of Performance (COP) and the Volumetric Heat Capacity (VHC) [9]. In ORC, the fluids are assessed based on the cycle efficiency (η_{orc}). Additionally, for ETES, the Round-Trip Efficiency (RTE) is also considered, calculated as the product of the HTHP COP and the ORC cycle efficiency.

At first glance, refrigerants like R1234ze(Z), R245fa, and R600 are not suitable for operation at temperatures above 150°C due to limitations imposed by their critical pressures. Similarly, R1233zd(E) has a critical pressure near this threshold, which can cause operational challenges when PCM temperatures exceed 160°C. Additionally, fluids such as ethanol, methanol, cyclohexane, and toluene exhibit pressures below 0.1 bar at 20°C, which extremely increases the risk of air leakage into the ORC condenser. These refrigerants are assessed in the configuration presented in Figure 1, which integrates the reference configuration for the HTHP [4] and ORC.

The main simulation results are summarized in Table 3, where refrigerants are evaluated at a HTHP heat capacity of 7 MW_{th}, and times of charge and discharge of 4 and 2 hours, respectively. The compressor and turbine are considered at a fixed speed of 50 Hz.

Table 3: Results from the simulation of the reference configuration of the pre-selected refrigerants

Fluid	COP	η_{orc}	RTE	VHC
Acetone	4.27	0.156	0.667	3.625
Benzene	4.47	0.165	0.739	1.92
Cyclopentane	4.28	0.163	0.699	3.57
IsoPentane	3.83	0.156	0.597	4.81
IsoHexane	4.173	0.163	0.682	2.63
n-pentane	3.93	0.158	0.620	4.29

Among the fluids tested, benzene achieves the highest RTE, exceeding 70%. However, benzene's low VHC necessitates larger components, resulting in higher investment costs compared to isopentane and n-pentane, which exhibit VHC values above 4. Acetone and cyclopentane emerge as optimal fluids, offering a balanced trade-off between RTE and VHC. Notably, cyclopentane achieves a 3.2% higher RTE and a 1.5% lower VHC compared to acetone. In conclusion, with the considered PCM temperature and the evaluated parameters, cyclopentane is determined to be the most suitable choice for the ETES system.

2.4 Architecture Selection

Since the HTHP and the ORC will never work at the same time, it is possible to imagine architectures where the IWH is used during the ETES discharge. The different possible configurations analysed correspond to:

- HP/ORC: Reference case (Figure 1).
- HP/ORC + PRE: Reference case with integration of preheater fed with IWH.
- HP/ORC + SUP: Reference case with integration of IWH to feed the evaporator and where the PCM HX is a superheater.

- HP/ORC + 2 stages: Reference case with integration of a 2-stages ORC. The high-pressure turbine is supplied by the PCM HX and the low-pressure turbine by IWH.
- ORC standalone: Only ORC, directly in contact with the IWH.

For the architecture selection, a PCM temperature of 150°C is considered while all the other parameters remain the same as in Table 2. The results of the different assessed configurations are presented in Table 4. The better RTE corresponds to configuration 1, which can produce 2.168 MW_e during the discharging time. Another interesting option is configuration 3, which has lower RTE performance and higher electricity output. An important remark on this configuration corresponds to the required size of the ORC is 18 and 14 times higher than cases 1 and 2, respectively.

Table 4: Simulation results architecture selection.

Variables	HP/ ORC	HP/ORC + PRE	HP/ORC + SUP	HP/ORC + 2stages	ORC stand-alone
η_{orc}	15.9	15.7	10.9	12.5	12.2
COP	5.5	5.5	5.5	5.5	-
RTE	0.87	0.86	0.60	0.68	-
$\dot{W}_{cp}$ $[MW]$	1.23	1.23	1.23	1.23	-
$\dot{W}_{tu}$ $[MW]$	2.17	2.62	8.36	2.14	2

The best trade-off between the RTE and output power corresponds to configuration HP/ORC + PRE, which has a RTE lower of 1.15%, but the power output increases by 20.8%. For this reason, configuration HP/ORC + PRE is highlighted as the better configuration with the given pre-design conditions. In configuration HP/ORC + SUP, the ORC efficiency is the lowest due to the fact that the ORC working fluid mass flow rate is very high in order to satisfy the discharge time as the specific heat transfer is lower. This high mass flow rate results in a drop of secondary fluid temperature in the evaporator, lowering the saturation temperature. This decreases the pressure ratio, and thus the efficiency of the ORC. The representation of the chosen architecture is presented in Figure 2. This is the selected pre-design for the Zorlu use case, this will be further analysed in the parametric section. The idea is to get the optimal values for this configuration.

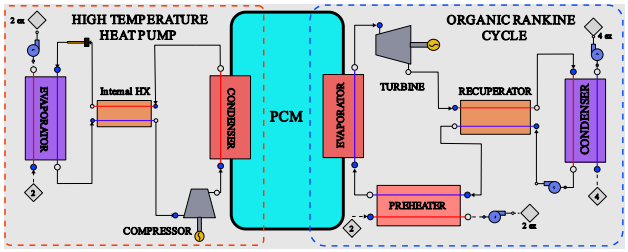


Figure 2: Zorlu configuration HP-ORC(Preheater)

3 Reference Case Refinement

Different constraints shall be added to give a more realistic view of the ETES performance potential. These constraints and the machine parameters shall then be varied to determine which ones are the most performance sensitive and then chosen/optimized in consequence. As shown in Figure 2, the heat pump and the ORC can be studied separately except for the integrated PCM heat exchanger. Note that the impact of each parameter variation was evaluated by only considering one variation at a time.

3.1 Constraints Addition

Many constraints are to be added, which are:

- Constraints on heat exchanger pinch point temperature differences (PPTD).
- Heat exchanger pressure drops.
- Secondary fluids and their auxiliaries.

First, varying **heat exchanger PPTD** has an impact on their working fluid saturation temperatures. This in turn impacts the saturation pressures, leading to higher/lower pressure ratios of the machine. Increasing PPTDs of HP heat exchangers increases its pressure ratio for a given condenser power, leading to lower COP. Increasing PPTDs of ORC heat exchangers decreases its pressure ratio for a given evaporator power, leading to lower efficiency. For example, the novel PCM-integrated heat exchanger still has to undergo experiments to determine its performance, a PPTD of 10K is therefore chosen as a first safety value.

Secondly, **heat exchanger pressure drops** lower the performance of Carnot Batteries. However, some are more important than others. For the heat pump, pressure drops in the high-pressure part show little impact on its performance as the valve does not recover any work. However, the low-pressure side pressure drops tend to increase the heat pump pressure ratio, leading to higher compressor work lowering the COP. The conclusions are similar for the ORC. The pressure drops in the low-pressure side lead to a higher pressure at the outlet of the turbine,

as the condensing pressure is constrained to be higher than a threshold value of 0.5 bar to prevent leakages. This decreases the pressure ratio of the machine, leading to lower work production and lower ORC efficiency. The high-pressure HX pressure drops still remove useful work but this impact is lower compared to the phenomenon explained above. Depending on their importance, the allowable pressure drops assumed in heat exchangers are listed in Table 5.

Table 5: HX assumed pressure drops [kPa].

Importance	Liquid	Gas	Evaporating	Condensing
Low	50	20	50	50
High	30	10	15	15

Finally, **secondary fluid auxiliary consumptions** need to be considered since they decrease the ETES performance as they impact the heat pump COP and the ORC efficiency as follows:

$$\eta_{ORC} = \frac{\dot{W}_{exp,orc} - \dot{W}_{pp,orc} - \dot{W}_{pp,sf}}{\dot{Q}_{ev,orc}} \quad (10)$$

$$COP_{HP} = \frac{\dot{Q}_{cd,HP}}{\dot{W}_{cp,HP} + \dot{W}_{pp,sf}} \quad (11)$$

However, this negative impact can be reduced through an optimization of the secondary fluid flowrate. The optimization can be determined in this case through the tradeoff between pump consumption and the efficiency of the heat exchanger.

3.2 Heat pump parameter choice

Considering the HP, the first parameters to set are the **allowable heat exchanger pressure drops**. These are set according to values in Table 4 and the discussion above it.

Another parameter to vary is the **PCM heat exchanger PPTD**. From discussions with manufacturers, it was decided to fix it first to a value of 10K instead of the 3K one that was first considered. However, note that this specific heat exchanger shall be shared between the two machines. This implies that the areas computed in Section 4.1 for these two virtually independent heat exchangers (heat pump condenser and ORC evaporator) shall be similar. The biggest area is then selected because it is the most restrictive and the other PPTD is then adjusted to fit a similar area value. The PPTD for the heat pump condenser is thus adjusted from 10 K to 5 K.

In addition, the **heat pump secondary fluid at the evaporator** has been considered. From a sensitivity study on the COP with respect to its flowrate, a value of 500 kg/s (previously 858 kg/s) was determined as optimal and set.

Finally, the last parameter to consider is the **PCM temperature**. Lowering the PCM temperature allows the heat pump COP to increase but the ORC efficiency to decrease. In this case, the impact on the HP COP is dominant on the global system performance. Decreasing the PCM temperature increases the RTE. It was decided to vary it from 150 (in section 2.4) to 141°C. This is the lowest fusion temperature among the PCM selected for this study.

Figure 3 shows the effect of the parameter variations on the heat pump COP. It can be concluded that the PCM melting temperature change has by far the most impact on performance. This is to be expected as it has a direct impact on the pressure ratio, leading to a change of compressor work and COP. The second most important factor is the increase of the PPTD at the integrated-PCM heat exchanger as it counteracts the lowering of the PCM temperature. Thirdly, the secondary fluid pump work shows a non-negligible impact on performance as it englobes the flowrate and the pressure drop effects. Finally, as already mentioned in Section 3.1, the impact of heat exchanger pressure drops highly depends on the working fluid and the pressure level that the heat exchanger is working on. The low-pressure side is the most sensitive.

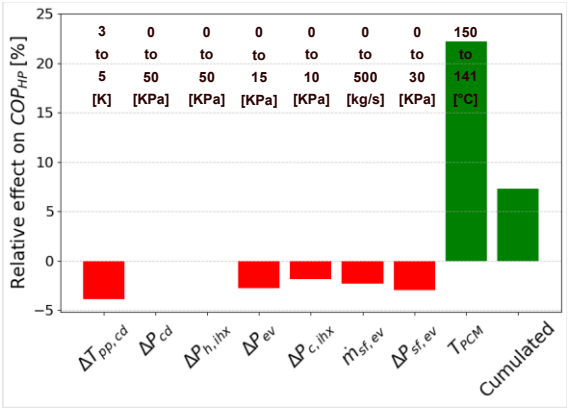


Figure 3: Relative effect of parameter variation on Heat Pump Performance.

In conclusion, the change in parameters had a positive cumulated impact on heat pump performance thanks to the lowering of the PCM temperature. The COP of the HP improved by 0.4 (+7.3% from the previous value).

3.3 *ORC parameter choice*

For the ORC, the same hypotheses as for the heat pump were considered for **allowable heat exchanger pressure drops.**

Concerning the **PCM heat exchanger PPTD**, the value of 10K mentioned by manufacturers was considered.

In addition, there are two secondary fluid related heat exchangers for this ORC architecture. For the sake of completeness, both of them shall be considered. The **preheater secondary fluid** flowrate and related pressure drop have been respectively to 60 kg/s and 50 kPa. Concerning the **condenser secondary fluid**, it was chosen to set its flowrate to 900 kg/s and its pressure drop to 30 kPa. These values result from a sensitivity study on ORC performance.

The **PCM melting temperature** shall be identical to the heat pump's one. The positive impact on the heat pump COP is higher than the negative one on the ORC efficiency when lowering the PCM temperature. Even though the ORC efficiency will suffer from it, the PCM temperature is set to 141°C.

Other parameters have to be considered specifically for the ORC. First, the **ORC condenser PPTD** shall be varied to maintain the pressure before the pump above 50 kPa. Its value was set to 5K. Secondly, as active charge management is meant to be studied in the project, the **ORC condenser subcooling** was changed from 3K to 1K to get closer to a system with a liquid receiver. Finally, the ORC features a 2MWe turbomachine. The value of 65% for its isentropic efficiency seems underestimated. It was then decided to fix it to 80%, which is closer to what can be seen in the industry while not being too optimistic.

Figure 4 shows the effect of the parameter variations on the ORC efficiency. It can be concluded that the most impactful change was to increase the turbine isentropic efficiency as it increases the net generated work significantly for the same turbine inlet conditions. In the ORC case, the second most impactful varied parameter type is the refrigerant heat exchanger pressure drops (again the low-pressure side ones) as they impact directly the pressure ratio of the turbine, reducing its output work. The PCM temperatures and heat exchanger PPTD had similar impacts on the ORC performance. These parameters reduce the cycle temperature difference, lowering the pressure ratio and thus, the efficiency. The difference in relative importance is mainly due to the change in Kelvins. Finally, the impact of secondary fluids is lower in the case of the ORC (especially for the preheater since the flowrate is very low).

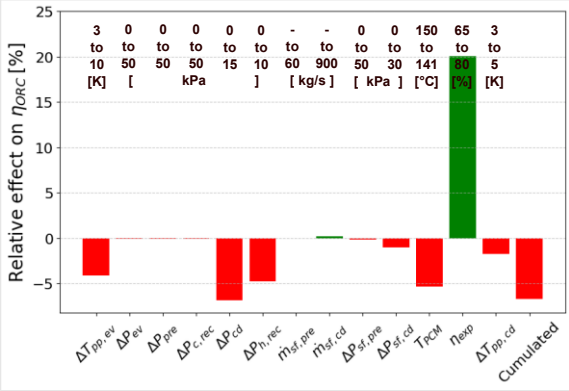


Figure 4: Relative effect of parameter variation on ORC Performance.

In conclusion, the change in parameters had a negative cumulated impact on ORC performance because of low-pressure side heat exchanger pressure drop and the lowering of PCM melting temperature. The ORC efficiency dropped by 1.04 [%] (-6.72% relative to the previous value).

3.4 *Global system performance*

To sum up, many sources of losses were added to the ETES to refine the study case. Their effects were first analysed through a sensitivity analysis together with some previously set parameters. Then, values were set (or re-set) for all these parameters. Most added parameters have a negative impact on ETES performance as they are sources of irreversibility that were not considered previously. To keep a similar RTE, the PCM temperature was decreased, and the turbine isentropic efficiency was increased. The performance results after this study are shown in Table 6. Figure 5 shows the ETES architecture with all fluid thermodynamic states.

Table 6: Results for **HP/ORC + PRE** architecture before (B) and after (A) study case refinement.

	η_{orc} [%]	COP [-]	RTE [%]	$\dot{W}_{cp}$ [MW]	$\dot{W}_{net}$ [MW]	T_{PCM} [°C]
B	15.7	5.5	86	1.23	2.62	150
A	14.4	5.9	85	1.19	2.51	141

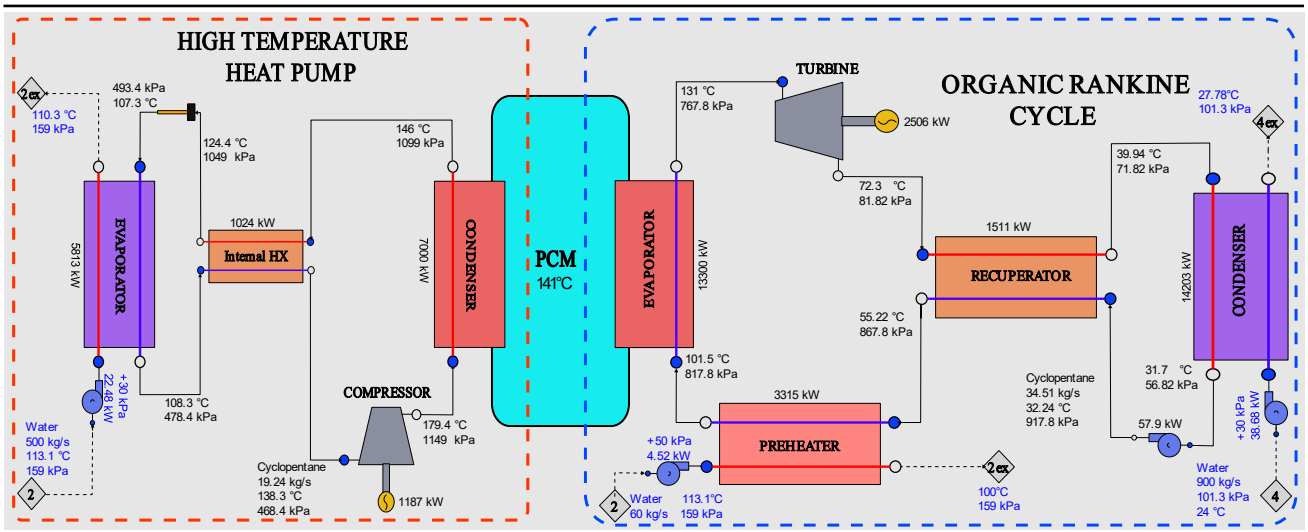


Figure 5: Chosen ETES architecture with thermodynamic states after parametric analysis.

4 Pre-Size of Components

This section aims to provide a pre-design of the main ETES components.

- For the heat exchangers: The technology and the heat transfer area. These are the pre-size parameters.
- For the turbomachines: The work, the inlet volumetric flowrate and the pressure ratio. These are the pre-size requirements.

4.1 Heat Exchangers

The heat exchanger area is pre-sized using the LMTD (Logarithmic Mean Temperature Difference) method. This method is commonly used for design and is based on temperatures at the inlet and outlet ports of a heat exchanger. It assumes that the heat duty ($\dot{Q}$) can be linked to the LMTD as follows:

$$\dot{Q} = U_{HX} \cdot A \cdot LMTD \cdot F \quad (11)$$

$$U_{HX} = \frac{1}{1/h_{cold} + 1/h_{hot}} \quad (12)$$

Where A [m²] is the heat exchanger area (to be determined), U_{HX} [W/(m² x K)] is the global heat transfer coefficient and F is the LMTD correction factor depending on the heat exchanger technology/configuration (computed using EES pre-built dedicated functions). U_{HX} is computed by considering the convective effects of both fluid sizes, meaning that the conduction resistance in the heat exchanger wall is neglected.

The heat exchanger technologies can be chosen based on their inlet fluid states and their heat duty. Due to the presence of mainly liquid secondary fluids, all heat exchangers (except the ones with PCM) were chosen to be shell-and-tube heat exchangers. The internal heat exchanger and the recuperator could feature finned tubes.

From Kakaç et. al. [11], generic heat transfer coefficient values were assumed for cyclopentane (considered between a light and a medium organic fluid) and water in shell-and-tube heat exchangers. Their values are summed up in Table 7.

Table 7: Typical Film Heat Transfer Coefficients for Shell-and-Tube Heat Exchangers.

Heat Transfer Mode	Fluid or Material	U $\left[\frac{W}{m^2 \times K}\right]$
Sensible Liquid	Water	5000
Latent solidification	PCM	1000
Latent Fusion	PCM	1000
Sensible Liquid	Cyclopentane	1500
Sensible Gas	Cyclopentane	600
Latent Evaporation	Cyclopentane	2000
Latent Condensation	Cyclopentane	2000

For the specific case of PCM-related heat exchanger, an equivalent heat transfer coefficient ($U_{eq,PCM}$) guess proved to be challenging. Because of the discussion on the pinch point value for one mode or the other in Section 3.2, the impact of the choice of this value on the areas of both modes had to be investigated. A sensitivity analysis on the ratio of required area for both modes (HTHP condenser and ORC evaporator) with respect to this parameter was performed. The results show that the value of $U_{eq,PCM}$ does not impact the area ratio significantly. Indeed, when varying the parameter from 500 to 5000 W/(m² × K), the required area of the heat pump condenser remained between 55 and 60% of the area

of the ORC evaporator. So, the effect on the pinch point temperature difference when trying to fit the two areas shall not depend significantly on this assumption. From a short literature review [12-14], the value for $U_{eq,PCM}$ for both solidification and melting processes were assumed at 1000 W/(m² × K). This consists in a first approximation for the design point when lacking experimental data. Table 8 shows the results of heat exchanger pre-size from these discussions.

From this table, it can be concluded that except for the PCM-related heat exchanger, the biggest heat exchanger is the HTHP evaporator. Because of the small pinch point temperature difference imposed for this heat exchanger, its heat flux (= 5.27 kW/m²) is much smaller than the one of the ORC condenser (= 13.14 kW/m²). This means that this heat exchanger is the first one on which the pinch point temperature difference value could be increased to reduce the total heat exchanger area of the machine. However, its size is quite close to the one of the ORC condenser. Another solution to reduce heat exchanger costs might be to mutualize these heat exchangers.

Table 8: Heat Exchangers pre-size results.

Heat Exchanger	***$\dot{Q}$ [kW]***	***Hot inlet fluid***	***Cold inlet fluid***	***HX Technology***	***A [m²]***
HTHP Evaporator	5813	Liquid (Shell)	Liquid (Tube)	**Shell & Tube**	**1103**
HTHP IHX	1024	Gas (Shell)	Liquid (Tube)	**Shell & Tube**	**262.6**
HTHP Condenser	7000	Liquid (Tube)	PCM	**Kelvin Cell**	**1525**
ORC Evaporator	13300	PCM	Liquid (Tube)	**Kelvin Cell**	**1618**
ORC Preheater	3315	Liquid (Shell)	Liquid (Tube)	**Shell & Tube**	**147.9**
ORC Recuperator	1511	Gas (Shell)	Liquid (Tube)	**Shell & Tube**	**374.1**
ORC Condenser	14203	Liquid (Tube)	Liquid (Shell)	**Shell & Tube**	**1081**

4.2 Turbomachines

Turbomachines are usually pre-sized according to their work ($\dot{W}$), inlet volumetric flowrate ($\dot{V}$) and pressure ratio (Π_r). These can be deduced from the data in Figure 5. They are listed in Table 9.

Table 9: Turbomachines pre-size requirements.

Turbomachine	***$\dot{W}$ [kWe]***	***$\dot{V}$ [m^3/s]***	***Π_r [-]***
HTHP Compressor	1187	1.85	2.45
ORC Pump	57.9	0.047	16.22
ORC Turbine	2506	1.95	9.38

From this table, it can be confirmed that heat exchanger pressure drops have a large impact on the turbine pressure ratio. This can be explained by the quite low temperature at the turbine inlet (131°C), lowering the evaporator saturation pressure. The compressor and ORC consumed/produced energy during a battery cycle (4h charge - 2h discharge) is also quite similar (4748 kWh for the compressor and 5012 kWh for the turbine). This shows a good charge/discharge balance in the machine parameters and operating conditions.

5 Conclusion

A novel Electro-Thermal Energy Storage (ETES) featuring a high temperature heat pump (HTHP), an Organic Rankine Cycle (ORC) and a Kelvin cell-based Phase Change Material (PCM) thermal storage was studied in this work. A preliminary investigation of this system as a thermally integrated electricity storage solution for the 80MWe Kızıldere-2 geothermal power-plant from Zorlu Enerji was performed. This investigation consisted in:

- **The choice of the working fluid**: 14 refrigerants were investigated. Cyclopentane was chosen because it offers a good compromise between performance (through a high round-trip efficiency (RTE)) and system compactness (through a high volumetric heat capacity), allowing better prospects for system profitability. It also satisfies the system requirements in terms of critical temperature and air leakage risks at ambient temperature.
- **The choice of architecture**: 5 architectures were tested. It showed that the reference case (HTHP with an internal heat exchanger together with an ORC featuring a recuperator) had the best RTE. Moreover, the addition of a preheater slightly decreased the efficiency (-1.15%) but increased the output work by 20.8%. This justified the choice of such an architecture. The ETES with these choices could reach a RTE of 86% with an input work of 1.23MWe and an output work of 2.62 MWe. The RTE can reach that high-value thanks to the use of waste heat from the plant process.
- **The introduction and assessment of impact on the performance of irreversibility factors**. This study allowed to choose coherent values for allowable heat exchanger pressure drops, secondary fluids use and heat exchanger pinch point temperature differences. This while optimizing the pre-established parameters for better performance. It shows that the pressure drops in low-pressure side heat exchangers were the most important for both machines. However,

the most important parameter for the whole system is the storage PCM melting temperature. The result of the addition of irreversibility factors and the tuning of ETES parameters is a system with a RTE of 85% with an input work of 1.19MWe and an output work of 2.51 MWe.

- The **pre-size** of the heat exchangers together with the **requirements** for the sizing of turbomachines.

This investigation shows positive prospects of the system performance, feasibility and profitability. However, these aspects still need to be proved by modelling the system in more details. Future work will consist in the detailed sizing of the components to verify their performance assumptions, the dynamic study and charge optimization of the whole system together with the study of an energy management system featuring this machine.

Acknowledgement

The project that produced the results presented in this paper has received funding from the European Union's Horizon Research and Innovation programme under grant agreement No. **101135763**, in the framework of the **SEHRENE** project.

References

[1] "IEA: Grid-scale Storage", [Online]. Available: https://www.iea.org/energy-system/electricity/grid-scale-storage [Accessed 15 November 2024]

[2] M. Gimeno-Gutiérrez and R. Lacal-Arántegui, "Assessment of the European potential for pumped hydropower energy storage based on two existing reservoirs", [Online]. Available: https://doi.org/10.1016/j.renene.2014.10.068

[3] Fan et. al., "Life cycle assessment of electric vehicles' lithium-ion batteries reused for energy storage", [Online]. Available: https://doi.org/10.1016/j.est.2023.108126

[4] Arpagaus et. al., "High temperature heat pumps: Market overview, state of the art, research status, refrigerants, and application potentials", *Energy*, vol. 152, pp. 985–1010, Jun. 2018, [Online]. Available: https://doi.org/10.1016/j.energy.2018.03.166

[5] Longo et. al, "Experimental assessment of the low GWP refrigerant HFO-1234ze(Z) for high temperature heat pumps", *Experimental Thermal and Fluid Science*, vol. 57, pp. 293–300, Sep. 2014, [Online]. Available: https://doi.org/10.1016/j.expthermflusci.2014.05.004

[6] Fukuda et. al., "Low GWP refrigerants R1234ze(E) and R1234ze(Z) for high temperature heat pumps", *International Journal of Refrigeration*, vol. 40, pp. 161–173, Apr. 2014, [Online]. Available: https://doi.org/10.1016/j.ijrefrig.2013.10.014

[7] Bamigbetan et. al, "Review of vapour compression heat pumps for high temperature heating using natural working fluids", *International Journal of Refrigeration*, vol. 80, pp. 197–211, Aug. 2017, [Online]. Available: https://doi.org/10.1016/j.ijrefrig.2017.04.021

[8] Frate et. al., "Analysis of suitability ranges of high temperature heat pump working fluids", *Applied Thermal Engineering*, vol. 150, pp. 628–640, Mar. 2019, [Online]. Available: https://doi.org/10.1016/j.applthermaleng.2019.01.034

[9] Gómez-Hernández et. al., "Carbon dioxide and acetone mixtures as refrigerants for industry heat pumps to supply temperature in the range 150–220 °C", *Energy*, vol. 269, p. 126821, Apr. 2023, [Online]. Available: https://doi.org/10.1016/j.energy.2023.126821

[10] Bertinat et. al., "Fluids for high temperature heat pumps", *International Journal of Refrigeration*, vol. 9, no. 1, pp. 43–50, Jan. 1986, [Online]. Available: https://doi.org/10.1016/0140-7007(86)90152-0 [Accessed 15 November 2024].

[11] Kakaç et. al., "Heat Exchangers: Selection, Rating, and Thermal Design", 3rd edition. Taylor & Francis Group, 2012.

[12] Esteves et. al., "Evolution of global heat transfer coefficient on PCM energy storage cycles", [Online]. Available: https://doi.org/10.1016/j.egypro.2017.10.318 [Accessed 15 November 2024].

[13] Esteves et. al., "Test of Two Phase Change Materials for Thermal Energy Storage: Determination of the Global Heat Transfer Coefficient", [Online]. Available: https://doi.org/10.3390/chemengineering2010010 [Accessed 15 November 2024].

[14] Horbatyuk et. al., "Comparative Heat Transfer Data for Solid-Liquid Phase Change of D-Mannitol and Adipic Acid", [Online]. Available: https://www.scirp.org/pdf/epe_20221123150730 62.pdf [Accessed 15 November 2024].

COMBINED TRILATERAL FLASH CYCLE AND ORGANIC FLASH CYCLE FOR LOW TO MEDIUM HEAT SOURCE ELECTRICITY GENERATION

José Mota*, Márcio Santos, Bernardo Almeida, Joel Morgado, José B. Ribeiro

Univ Coimbra, ADAI, Department of Mechanical Engineering, Rua Luís Reis Santos, Pólo II, 3030-788 Coimbra, Portugal.

** Corresponding Author: jose.mota@dem.uc.pt*

Abstract. In the last decade, most countries have made the commitment to reducing CO_2 emissions to mitigate the environmental impact derived from human behaviour. With that in mind, reducing energy waste is of the utmost importance. The ORC is a mature technology aimed at converting heat to power, which can be helpful for utilising waste heat in industrial processes and converting it to electricity.
A comparison analysis of the maximum exergy efficiency between a standalone ORC, TFC, OFC and an innovative configuration, the TFC-OFC is performed for different heat source inlet temperatures. Several hydrofluorochemicals are tested as the working fluid for each configuration. The results reveal that the ORC is still the preferred configuration for most of the heat source inlet temperatures. Nonetheless, the TFC-OFC reached the overall maximum exergy efficiency for every inlet temperature tested and can be a suitable option depending on the isentropic efficiency of the expander.

Keywords. Heat-to-power; Organic Rankine cycle; Alternative Configuration.

Nomenclature

E	Exergy
h	Specific enthalpy (J/kg)
OFC	Organic Flash Cycle
ORC	Organic Rankine Cycle
s	Specific enthalpy (J/kg.K)
T	Temperature (°C)
TFC	Trilateral Flash Cycle
W	Mechanical Work [W]
Special characters	
η	Efficiency (-)
Subscripts	
0	Reference
ex	Exergy
hs	Heat source
in	Inlet
out	Outlet

1 Introduction

With the rising concern regarding environmental sustainability comes the challenge of providing innovative and more efficient ways to produce electricity. On the spectrum of heat-to-power systems, the Organic Rankine Cycle (ORC) has gained popularity among the academic and R&D communities due to its potential to generate power from low to medium heat sources. One of the limitations of the ORC derives from the heating stage of this cycle. The evaporation of the working fluid present in the ORC is characterised by a high temperature mismatching between the heat source and the working fluid, leading to a decrement of the cycle's exergy efficiency. To overcome such limitation, several alternative Rankine-based configurations have been studied and developed, which aim to increase said temperature matching.

On the topic of this work, among those configurations, the Trilateral Flash Cycle (TFC) [1], [2], [3], [4] and the Organic Flash Cycle [5], [6], [7], [8] are of increased relevance as not only they are considered as an interesting alternative to the ORC but also they can be combined into one single configuration, the TFC-OFC, which is, of the author's knowledge, an innovative configuration.

In this work the TFC-OFC will be compared to a standalone ORC, OFC and TFC to determine potential efficiency improvements.

2 Description of the cycles

The ORC is a sufficiently sustained and mature technology to generate power from heat. Nonetheless, there are still limitations associated with this cycle, particularly the irreversibility associated with the isothermal evaporation of the working fluid during the heating stage, represented in Figure 1, due a temperature mismatching between the heat source and the working fluid.

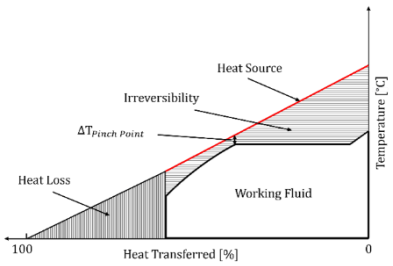


Figure 1. Temperature-heat diagram for a typical ORC.

This increment of the irreversibility of the process leads to an exergy efficiency reduction [9], which has motivated researchers to develop and investigate more efficient configurations, such as the OFC and TFC.

2.1 The OFC and TFC over the ORC

Both the OFC and TFC intend to decrease the temperature mismatching occurring in the ORC by altering the heating stage of the working fluid.

In the TFC, the working fluid enters the expander in a saturated liquid state, meaning that there is no evaporation during the heating stage. In this way, an efficiency increment is expected as the temperature matching is improved. However, special care regarding the expander selection is required due to the two-phase expansion. Moreover, lower values of vapour quality negatively influence the isentropic efficiency of the expander, directly influencing the amount of work produced by this component [10].

The OFC has a similar heating stage to the TFC, as the working fluid is only heated to a saturated liquid state. However, in the OFC, the working fluid is then guided to a flash tank where the liquid and vapour fractions are separated, with only the latter being responsible for producing mechanical work in the expander. This eliminates the two-phase expansion process, therefore not compromising the isentropic efficiency of the expander at the expense of having less working fluid mass performing mechanical work.

2.2 The TFC-OFC

Intending to make use of the strengths and eliminate the weaknesses of both the TFC and the OFC, a new configuration is proposed, the TFC-OFC, which derives from the combination of both cycles. The configuration of this cycle is presented in Figure 2.

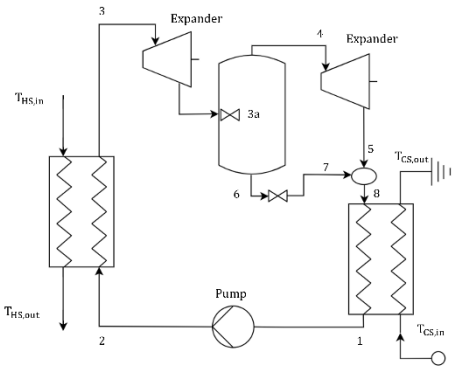


Figure 2. The configuration of the TFC-OFC

In this configuration, two expanders are present. The working fluid is heated to a saturated liquid state and enters a two-phase expander, producing mechanical work, as in the TFC. Then, the vapour and liquid fractions are separated in the flash tank, allowing for more work to be produced in a second expander, as in the OFC.

In this way, the efficiency of this cycle is expected to increase greatly compared to that of the standalone OFC or TFC.

3 Methodology

A comparison analysis is presented, assuming a steady-state operation of each cycle. The MATLAB software and the Coolprop database were used to model each configuration and calculate the thermodynamic properties of the fluids, respectively.

3.1 Optimisation Parameter

As mentioned in [11], the proper performance indicator to evaluate a cycle's technical performance is the exergy efficiency, η_{ex}, which is listed in equation (1).

$$\eta_{ex} = \frac{(\dot{W}_{out} - \dot{W}_{in})}{\dot{E}_{in}} \quad (1)$$

$\dot{W}_{out}$ Mechanical power delivered by the cycle [W].

$\dot{W}_{out}$ Mechanical power consumed by the cycle [W].

$\dot{E}_{in}$ Exergy rate of the heat source [W].

In turn, the exergy rate of the heat source, $\dot{E}_{in}$, can be written as displayed in equation (2).

$$\dot{E}_{in} = (h_{hs,in} - h_{hs,0}) - T_0 . (s_{hs,in} - s_{hs,0}) \quad (2)$$

$h_{hs,in}$ Specific enthalpy of the heat source at the inlet temperature [J/kg].

$h_{hs,0}$ Specific enthalpy of the heat source at the reference temperature [J/kg].

$s_{hs,in}$ Specific entropy of the heat source at the inlet temperature [J/kg.K].

$h_{hs,in}$ Specific entropy of the heat source at the reference temperature [J/kg.K].

T_0 Reference temperature [K].

In this way, for the same inlet temperature of the heat source, $\dot{E}_{in}$ remains the same, with η_{ex} being equivalent to maximising the mechanical work balance of the cycle, $(\dot{W}_{out} - \dot{W}_{in})$ in (1).

3.2 Modelling Parameters

For this analysis, the heating pressure varied for each configuration. On top of that, for the OFC and TFC-OFC, the temperature in the flash tank was varied. A pinch-point of 10K was considered for the heating heat exchanger. An isentropic efficiency of the expander of 70% was assumed for single-phase expansions, while 60% was considered for the two-phase expansion process, as it is considered a minimum value in order for the two-phase expansion cycles to be competitive with the single-phase expansion cycles [3]. A heat source mass flow of 1 kg/s was considered.

3.3 Working Fluid Selection

Regarding the working fluid, a short list of potential candidates was considered. As per requirements, the fluids must have a global warming potential (GWP) lower than 150 and a null ozone depletion potential (ODP) value. Furthermore, hydrofluorochemicals were prioritised, considering their good performance in this type of cycles [12]. The short list can be found in Table 1.

Table 1: List of working fluids considered.

Fluid	Critical Temperature [ºC]	Critical Pressure [bar]	GWP	ODP
R1234yf	34.70	33.82	4	0
R1234ze(E)	109.37	36.35	7	0
R1233zd(E)	166.45	36.24	7	0*

*Not strictly 0.

3.4 Case studies considered

At last, there were four different case studies considered, depending on the inlet temperature of the heat source, $T_{HS,in}$. They are represented in Table 2.

Table 2: List of case studies considered.

Case Study	1	2	3	4
$T_{HS,in}$ [ºC]	130	150	180	200

4 Results and Discussion

The results from the comparison analysis are displayed in Figure 3. In each square is presented the maximum exergy efficiency obtained for each combination of configuration and $T_{HS,in}$. The colour of the border of each square is respective to the optimal working fluid for that combination

As predicted, the TFC-OFC outperformed the standalone TFC and OFC configurations for every case study, apart from the TFC at a $T_{HS,in}$ of 130ºC. However, when it comes to the comparison with the basic ORC, only at a $T_{HS,in}$ of 180ºC, was the innovative configuration the preferred option.

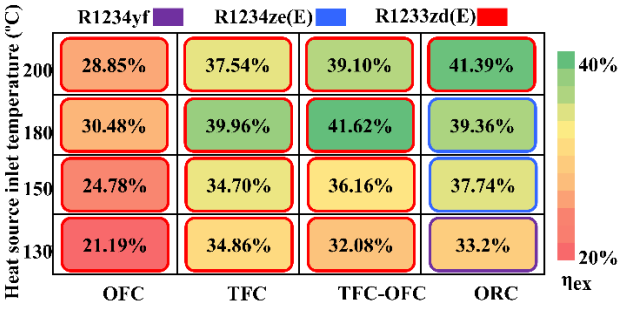


Figure 3. Summary matrix of the results.

Despite having a second expander, the TFC-OFC could not outperform the ORC in the remaining case studies. This is mainly due to the reduced isentropic efficiency of the two-phase expander, which play a critical role in the amount of delivered mechanical work. Additionally, it seems that the exergy efficiency improvement of the TFC-OFC reaches a *plateau* for a certain $T_{HS,in}$, while for the ORC it continuously increases.

5 Conclusions and Future Perspectives

In this work, a comparison analysis between a standalone ORC, TFC, OFC and a combined TFC-

OFC configurations as performed, and the following remarks are presented:

- The TFC-OFC outperformed the standalone TFC and OFC configurations for most case studies.
- The ORC is still the most viable option, exergy efficiency-wise, for every case study, with the exception of a $T_{HS,in}$ of 180ºC.

Nonetheless, with further developments of a two-phase expander and increasing its isentropic efficiency, this new configuration can pose an interesting, more efficient alternative to the basic ORC.

Acknowledgement

This research is financed by PRR - Recovery and Resilience Plan and by the Next Generation EU Funds, following NOTICE N.º 02/C05-i01/2022, Component 5 – Capitalization and Business Innovation - Mobilizing Agendas for Business Innovation under the AM2R project "Mobilizing Agenda for business innovation in the Two Wheels sector" (reference: 7253).

References

[1] I. K. Smith, "Development of the Trilateral Flash Cycle System: Part 1: Fundamental Considerations," *Proceedings of the Institution of Mechanical Engineers, Part A: Journal of Power and Energy*, vol. 207, no. 3, pp. 179–194, 1993, doi: 10.1243/PIME_PROC_1993_207_032_02.

[2] M. Yari, A. S. Mehr, V. Zare, S. M. S. Mahmoudi, and M. A. Rosen, "Exergoeconomic comparison of TLC (trilateral Rankine cycle), ORC (organic Rankine cycle) and Kalina cycle using a low grade heat source," *Energy*, vol. 83, pp. 712–722, Apr. 2015, doi: 10.1016/J.ENERGY.2015.02.080.

[3] K. Braimakis and S. Karellas, "Exergy efficiency potential of dual-phase expansion trilateral and partial evaporation ORC with zeotropic mixtures," *Energy*, vol. 262, p. 125475, 2023, doi: 10.1016/j.energy.2022.125475.

[4] G. Bianchi, M. Marchionni, J. Miller, and S. A. Tassou, "Modelling and off-design performance optimisation of a trilateral flash cycle system using two-phase twin-screw expanders with variable built-in volume ratio," *Appl Therm Eng*, vol. 179, p. 115671, 2020, doi: 10.1016/j.applthermaleng.2020.115671.

[5] T. Ho, S. S. Mao, and R. Greif, "Comparison of the Organic Flash Cycle (OFC) to other advanced vapor cycles for intermediate and high temperature waste heat reclamation and solar thermal energy," *Energy*, vol. 42, no. 1, pp. 213–223, 2012, doi: https://doi.org/10.1016/j.energy.2012.03.067.

[6] T. Ho, S. S. Mao, and R. Greif, "Increased power production through enhancements to the Organic Flash Cycle (OFC)," *Energy*, vol. 45, no. 1, pp. 686–695, Sep. 2012, doi: 10.1016/J.ENERGY.2012.07.023.

[7] S. Mondal and S. De, "Power by waste heat recovery from low temperature industrial flue gas by Organic Flash Cycle (OFC) and transcritical-CO2 power cycle: A comparative study through combined thermodynamic and economic analysis," *Energy*, vol. 121, pp. 832–840, 2017, doi: https://doi.org/10.1016/j.energy.2016.12.126.

[8] Z. Li *et al.*, "Comparison study of Trilateral Rankine Cycle, Organic Flash Cycle and basic Organic Rankine Cycle for low grade heat recovery," *Energy Procedia*, vol. 142, pp. 1441–1447, 2017, doi: https://doi.org/10.1016/j.egypro.2017.12.532.

[9] A. Schuster, S. Karellas, and R. Aumann, "Efficiency optimization potential in supercritical Organic Rankine Cycles," *Energy*, vol. 35, no. 2, pp. 1033–1039, Feb. 2010, doi: 10.1016/J.ENERGY.2009.06.019.

[10] S. Daniarta, P. Kolasiński, and A. R. Imre, "Thermodynamic efficiency of trilateral flash cycle, organic Rankine cycle and partially evaporated organic Rankine cycle," *Energy Convers Manag*, vol. 249, p. 114731, 2021, doi: https://doi.org/10.1016/j.enconman.2021.114731.

[11] K. Braimakis, M. Preißinger, D. Brüggemann, S. Karellas, and K. Panopoulos, "Low grade waste heat recovery with subcritical and supercritical Organic Rankine Cycle based on natural refrigerants and their binary mixtures," *Energy*, vol. 88, pp. 80–92, Aug. 2015, doi: 10.1016/J.ENERGY.2015.03.092.

[12] M. Bahrami, F. Pourfayaz, and A. Kasaeian, "Low global warming potential (GWP) working fluids (WFs) for Organic Rankine Cycle (ORC) applications," *Energy Reports*, vol. 8, pp. 2976–2988, Nov. 2022, doi: 10.1016/J.EGYR.2022.01.222.

INTEGRATED DEVELOPMENT OF COST-EFFECTIVE CARNOT BATTERIES USING NEAR-OPTIMUM ANALYSES

Antoine Laterre[1,2*], Vincent Lemort[1], Francesco Contino[2]

[1] Laboratory of Applied Thermodynamics, University of Liège, Belgium

[2] Université Catholique de Louvain, Belgium

** Corresponding Author: antoine.laterre@uclouvain.be*

Abstract. The design of Carnot batteries involves numerous trade-offs across several key parameters, as it requires a delicate balance between efficiency, density, cost, and technical feasibility. While the ideal thermodynamics offers 100% storage efficiency, real-world systems face inevitable losses due to internal and external irreversibilities. This work investigates the development of near-optimum designs for Carnot batteries, emphasizing cost-effective solutions without sacrificing performance. We explore various design options, such as unpressurized vs. pressurized thermal storage, sub-critical vs. trans-critical cycles, and the inclusion or exclusion of recuperators. Additionally, the use of standardized components, sub-cooling in the heat pump, and fluid selection (e.g., A3 or high GWP fluids) are evaluated for their impact on performance. This approach offers design alternatives that remain close to thermodynamic optima while incorporating practical considerations such as cost, manufacturability, and regulatory compliance. It provides a spectrum of design options that balance theoretical performance with real-world constraints, offering flexibility in integrating technical constraints, manufacturing preferences, supply chain capabilities, and economic viability, ultimately aiding in the decision-making process. Our findings reveal that while no single design can guarantee peak performance due to modelling uncertainties, near-optimum alternatives offer robust solutions for real-world applications. Our analysis aims to identify the "must-haves," "real choices," and "must-avoids" in the design process, presenting decision-makers with a variety of near-optimal solutions. By enabling flexibility in design choices, this approach helps bridge the gap between thermodynamic efficiency and economic viability, offering a pathway to more cost-effective Carnot batteries.

Keywords. Carnot Battery, Near-Optimum Analysis, Thermodynamic Optimisation, Cost-Effective Design.

COMPARISON OF THREE ARCHITECTURES OF THERMALLY INTEGRATED PUMPED THERMAL ENERGY STORAGES USING SIMULATION

Frédéric Ransy*, Vincent Lemort

[1] University of Liege, Thermodynamics Laboratory, Liege, Belgium

* *Corresponding Author: frederic.ransy@uliege.be*

Abstract. This paper compares three architectures of Thermally Integrated Pumped Thermal Energy Storages (TI-PTES) by simulating their performance and changing the waste heat and storage temperatures. The key performance indicators include the power-to-power efficiency, the volumetric energy density, and the waste heat ratio. The systems based on low-temperature storages are suitable for industrial processes with a high waste heat ratio, while the high temperature storage system provides higher energy density and is suitable for low waste heat ratio.

Keywords. Thermally Integrated Carnot Battery, simulation, waste heat, industrial process

Nomenclature

Abbreviations

CAES	Compressed Air Energy Storage
COP	Coefficient of Performance
HP	Heat Pump
LCOS	Levelized cost of storage
ORC	Organic Rankine Cycle
PCM	Phase Change Material
PHES	Pumped Hydro Energy Storage
PtP	Power-to-Power Efficiency
TI-	Thermally Integrated
PTES	Pumped Thermal Energy Storage
TRL	Technology Readiness Level
VEB	Volumetric Energy Density

Symbols

t	Duration (h)
T	Temperature (°C)
V	Volume (m³)
$\dot{W}_{el}$	Electric power (W)

Subscripts

ch	charge
dis	discharge
tot	total

1 Introduction

A pumped thermal energy storage is an energy storage system that stores electrical energy in form of heat. To do so, the system utilizes a HP to convert electricity into thermal energy, which is stored in one or two tanks. Then, the thermal energy is converted back to electricity through a heat-to-power cycle. As explained by Dumont et al. [1], this technology is suitable for medium and long storage duration (from 4 to 8 h or more). It has no environmental constraints (no need of an existing reservoir or cave), but the efficiency and the TRL compared to CAES and PHES are lower. Different configurations have been proposed in the literature, and many commercial projects are currently developed. Indeed, Novotny et al. [2] reviewed in 2022 more than 30 on-going projects from the kW to the MW scale with several TRL. In these systems, the PtP lies between 30 and 60 %. To increase the efficiency, a solution consists of integrating in the process a waste heat, for instance from an industrial process. Korhan et al. [3], Shuozhuo et al. [4] and Frate et al. [5] showed PtP higher than 80 %. The increase in efficiency is due to a higher COP of the HP in charging mode thanks to the utilization of the waste heat. The efficiency of this energy storage, called Thermally Integrated Pumped Thermal Energy Storage, is highly dependent on the process in which it is integrated, but also on parameters such as the waste heat temperature or the thermodynamic cycle architecture.

2 Methodology

This paper compares three different TI-PTES architectures and shows the impact of several parameters on the system performance, evaluated through three performance indicators.

2.1 Proposed TI-PTES architectures

Figure 1 shows the three TI-PTES architectures simulated in this paper. Those architectures are well

described in the literature, and are suitable for waste heat integration.

The first system (top in Figure 1) considers a vapor compression HP for charging, two pressurized liquid water storage tanks and an ORC with preheater for discharging. The working fluid for both the cycles is R1233zd(E). As explained by Liang et al. in [6], this fluid is a good compromise between efficiency, low equipment size and pressure ratio.

The second system (middle in Figure 1) considers the same fluid and thermodynamic architecture as in the first system (vapor compression HP + ORC), but with an additional latent storage with PCM.

The third system (bottom in Figure 1) considers a reversed Brayton cycle HP with supercritical CO_2 as working fluid for charging, two sensible molten salt storage tanks and a steam Rankine cycle for discharging. This system presented in [7] has a potential theoretical PtP of at least 50 %.

2.2 Simulation model description

The simulation models consist of determining at each point in the systems the thermodynamic state (pressure, enthalpy, entropy, etc.). Each component is modeled in steady state in considering the energy and the mass balances. For the heat exchangers, the temperature profiles are computed and a minimum pinch point, considered constant, is imposed. Pressure drops are not considered. The pumps, compressors and turbines are modeled with a constant isentropic efficiency. The heat losses are not computed. Expansion valves are considered as isenthalpic. The heat losses in the storage tanks are considered through a constant efficiency. In the cycle, constant ORC subcooling and superheating HP/ORC are imposed. The HP subcooling is optimized to maximize the efficiency.

2.3 Performance indicators definitions

Three performance indicators are generally utilized to define the performance of TI-PTES: the PtP, the VED and the LCOS. The latter is not considered in this paper. In the case of TI-PTES, the waste heat ratio is another indicator to consider. All these indicators are defined based on the energy exchanged over 1 charge/discharge cycle, which depends on the charging and discharging durations. These parameters depend on the application of the TI-PTES. In this paper, photovoltaic integration service is supposed, with a charging duration t_{ch} of 7 h and a discharging duration t_{dis} of 8 h.

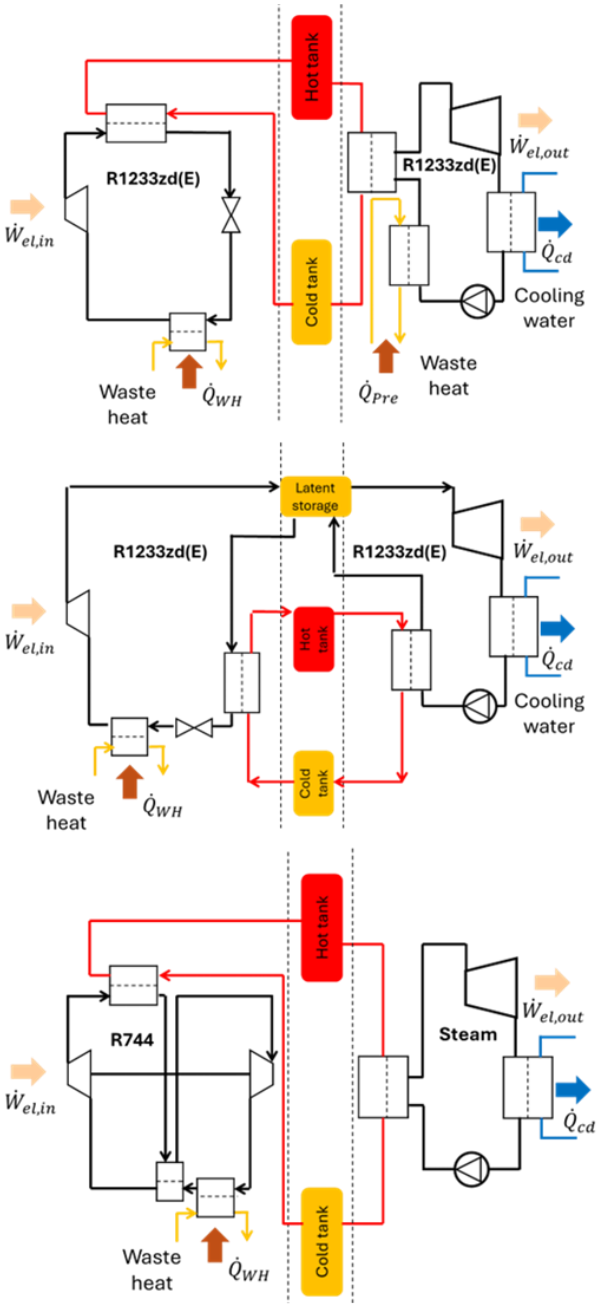


Figure 1: The three TI-PTES architectures. Top: system 1. Middle: system 2. Bottom: system 3

Based on the energy powers defined in Figure 1, the three performance indicators are defined as:

$$PtP = \frac{\dot{W}_{el,out}\ t_{dis}}{\dot{W}_{el,in}\ t_{ch}} \quad (1)$$

$$VED = \frac{\dot{W}_{el,out}\ t_{dis}}{V_{tank,tot}} \quad (2)$$

$$f_{waste} = \frac{\dot{Q}_{WH}\ t_{ch} + \dot{Q}_{Pre}\ t_{dis}}{\dot{W}_{el,out}\ t_{dis}} \quad (3)$$

The PtP expresses the power-to-power efficiency, and is computed with the net inlet and outlet electrical energies. The VED expresses the electrical energy released by the system in relation with the total system volume, taking into account the sensible and latent storage tanks $V_{tank,tot}$. The waste heat ratio expresses the ratio between the amount of waste heat energy necessary during charging and the amount of electric energy released during discharging. This factor indicates how a Carnot Battery architecture can effectively be integrated in a given industrial process, characterized by an electric energy need and a waste energy potential.

2.4 Parameters and boundary conditions

The parameters defining the system components and the boundary conditions for the three architectures are summarized in Table 1. The inlet waste heat temperature, which has a considerable impact on the results, is varied between 50°C and 90°C. The storage temperature is also varied. The maximum and minimum storage temperatures are constrained by technological limitations and the storage materials. For the systems 1 and 2, as water is considered as the storage material, the storage temperature is limited from minimum 70 °C to maximum 140 °C. For the system 1, the min/max storage temperature difference between the two tanks is 25/50°C, respectively. As explained in [8], in this range, the LCOS of the system is minimized. For system 3, as molten salt is considered as the storage material, the storage temperature is limited from minimum 300°C to maximum 540°C. The storage temperature difference between the two tanks is varied between 140 K and 240 K.

Table 1: Parameters imposed in the models

Item	Symbol	Value
Compressor efficiency	$\eta_{is,comp}$	80 %
Motor efficiency	η_{motor}	98 %
Turbine efficiency	$\eta_{is,turb}$	85 %
Generator efficiency	η_{gen}	98 %
Pump efficiency	$\eta_{is,pump}$	70 %
Heat storage efficiency	η_{sto}	95 %
Pinch points in HX's (systems 1 and 2, **or** 3)	ΔT_{pp}	3 or 20 K
Superheating degree HP/ORC	ΔT_{SH}	8 K
Subcooling degree ORC	ΔT_{SC}	2 K
Discharging power capacity	$\dot{W}_{el,out}$	1 MW
Input cooling water temperature	$T_{w,cw,su}$	20°C
Cooling water temperature lift	ΔT_{cw}	10 K
Inlet waste heat temperature	$T_{w,WH,su}$	50-90°C
Waste heat temperature lift	ΔT_{WH}	10 K

3 Results and discussion

This section presents the three performance indicators described in section 2.3 for the three architectures. In all figures, system 1 is in orange, system 2 in blue and system 3 in green. The results are similar to the work conducted in [8] and [9].

Figure 2 represents the variation of the PtP (top) and the waste heat ratio (bottom) with the inlet waste heat temperature. In Figure 2, for the systems 1, 2 and 3, the storage temperatures are fixed to 90-140°C (1), 103°C (2), and 305-540°C (3), respectively. For systems 1 and 2, the PtP curves are similar, and the inlet waste heat temperature has a strong impact. Indeed, the PtP is multiplied by 214 % when the waste heat temperature changes from 50 to 90°C. However, for system 3, the PtP is only multiplied by 108 %. Concerning the waste heat ratio f_{waste}, for each system, it increases with the waste heat temperature. Moreover, this indicator is highly dependent on the system considered and lies between 0.5 and 8.

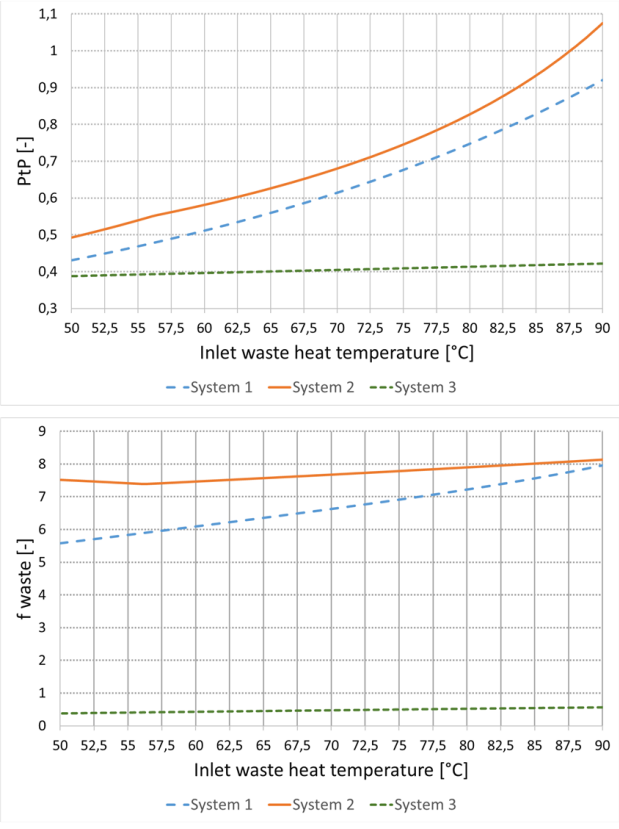


Figure 2: Variation of PtP (top) and waste heat ratio (bottom) with the inlet waste heat temperature

Figure 3 represents the operating envelopes for the three systems. These maps represent the PtP and the VED as a function of the waste heat ratio f_{waste}. The orange, blue and green surfaces represent, for the

three architectures, all the possible performance indicator values when the storage and the waste heat temperatures are varied within the ranges described in the section 2.4. The system 1 and 2 are characterized by high values of PtP and waste heat ratio, and also large variations of these factors. However, the VED is lower with small variations. For the system 3, it is the opposite. Indeed, the PtP and the waste heat ratio are small with small variations, while the VED is much higher with large variations. These maps can be utilized to successfully chose and design the architecture of a TI-PTES according to the characteristics of the industrial process.

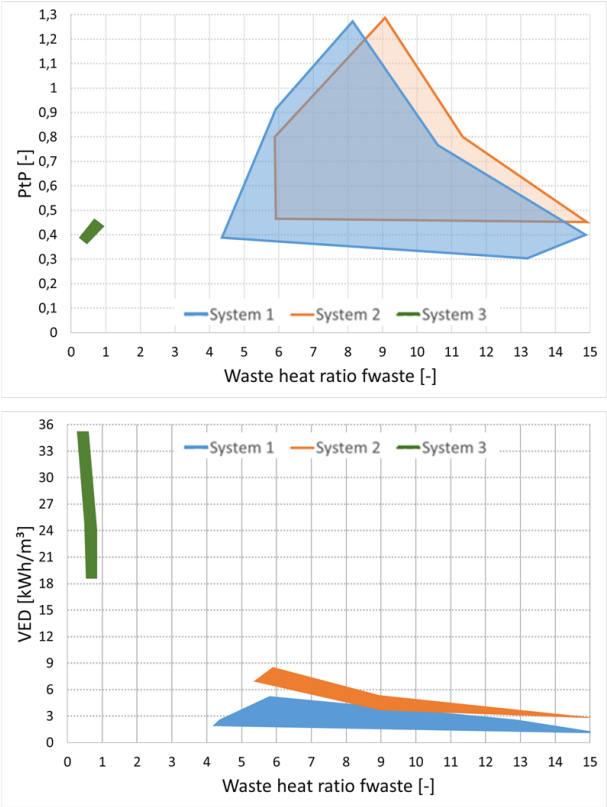


Figure 3: Operating envelope for the three systems. Top: PtP. Bottom: VED

4 Conclusion

This paper compares three TI-PTES architectures to help in the choice and design of such system when integrated in an industrial process. The systems 1 and 2 should be chosen for industrial processes with waste heat ratio higher than 4. In that case, the choice between 1 and 2 depends on the desired VED. The efficiency of such system will be highly dependent on the waste heat temperature, and this impact must not be omitted during the design phase. For industrial processes with waste heat ratio lower than 1, the system 1 is the most appropriate. In that case, the waste heat temperature has a much lower impact on the efficiency. To complete the analysis, a future work will consist of calculating the LCOS for the three architectures, and also adding technical constraints on the thermodynamic cycles, such max/min operating pressures and temperatures.

References

[1] Dumont O. et al., "Carnot battery technology: A state-of-the-art review.", in Journal of Energy Storage, Vol. 32, 2020.

[2] Novotny V. et al., "Review of Carnot Battery Technology Commercial Development", in Energies, 2022.

[3] Korhan Ökten and Burak Kurşun, "Thermo-economic assessment of a thermally integrated pumped thermal energy storage system combined with an absorption refrigeration cycle driven by low-grade heat source", in Journal of Energy Storage, Vol 51, 2022.

[4] Shuozhuo Hu et al., "Thermo-economic analysis of the pumped thermal energy storage with thermal integration in different application scenarios", in Energy Conversion and Management, Vol. 236, 2021.

[5] Frate, G.F. et al., " Rankine Carnot Batteries with the Integration of Thermal Energy Sources: A Review", in Energies , 13, 2020.

[6] Ting Liang et al., "Key components for Carnot Battery: Technology review, technical barriers and selection criteria", in Renewable and Sustainable Energy Reviews, Volume 163, 2022.

[7] Aga V. et al., "Supercritical CO2-Based Heat Pump Cycle for Electrical Energy Storage for Utility Scale Dispatchable Renewable Energy Power Plants", in 5th International Symposium - Supercritical CO2 Power Cycles, San Antonio, Texas, 2016.

[8] Yuemao Jiang et al., "Enhanced thermally integrated Carnot battery using low-GWP working fluid pair: Multi-aspect analysis and multi-scale optimization", in Applied Energy, Volume 376, Part A, 2024.

[9] Shuozhuo Hu et al., "Thermo-economic analysis of the pumped thermal energy storage with thermal integration in different application scenarios", in Energy Conversion and Management, Volume 236, 2021.

DECARBONISATION OF EXISTING BUILDING STOCK THROUGH LOW-TEMPERATURE DISTRICT HEATING NETWORK

Mazarine Roquet[1*], Pierre Dewallef[1]

[1] Laboratory of Applied Thermodynamics, University of Liège, Belgium

* *Corresponding Author: mazarine.roquet@uliege.be*

Abstract. Low temperature district heating networks are a promising solution for decarbonising existing building stocks. However, they present challenges such as operational strategies, network design and the need for building refurbishment. This research focuses on developing an integrated dynamic model of the network and buildings, taking into account the thermal inertia of both, and exploring control strategies to ensure thermal comfort under both design and operational conditions. The methodology involves coupling calibrated building models with a dynamic district heating network model. System design is integrated into the model to optimise network operation. The models, developed in Modelica and simulated using the Dymola platform, use return-temperature-based control strategies based on measured data. Two control strategies are evaluated: pump speed control based on the return temperature at the heat source and at the output of the most critical consumer. The results highlight the importance of integrated building and network models to avoid errors in design, control or refurbishment, particularly for low temperature systems. It also shows that a simple control strategy based on temperature measurement can achieve the desired thermal comfort. Future work will focus on improving model fluidity between design and operation, scaling up the system, investigating other control strategies, and linking building models to a geographic information system.

Keywords. Building stock, Low temperature district heating network, Building simulation.

STOCHASTIC GENERATOR FOR RESIDENTIAL LOAD PROFILES

Stegen Thomas[1]*, Joakim Castiaux[1], Noé Diffels[1], Maxime Duchesne[1], Bertrand Cornélusse[1]

[1] Montefiore Institute, University of Liège, Belgium

** Corresponding Author: tstegen@uliege.be*

Abstract. The energy transition brings a lot of challenges for the electric distribution networks. Due to both the electrification of usages and the development of distributed energy resources (DERs):

- The consumption patterns of residential users are going through a total change. In addition to the classical home appliances a roll-out of electric vehicles (EVs), controllable thermoelectric appliances (Water boilers, Heat pumps, and Air conditioners), and other controllable loads (Wet appliances) is drastically changing the power and energy consumption in residential area.
- The energy transition fosters new investment in less CO2 intensive generation units. Many of these are directly connected to the distribution grids and can cause deleterious reverse flows of power.

These two simultaneous paradigm changes are causing high stresses on the power grids.

The loads in residential areas are increasingly uncertain and hard to predict. This constitutes a challenge for DSOs, the low-voltage network monitoring is still incomplete or nearly absent in certain regions. Moreover, where it is present, assessing the evolution of electricity use and how it affects individual profiles is impossible without intrusive pieces of equipment.

We propose a tool to generate residential electric load profiles stochastically, this includes a baseload on which all previously listed controllable appliances can be added. Some boundaries for the flexibility of said appliances are also provided to assess the maximal efficiency of demand response mechanisms. All the data is synthetic, coming from stochastic occupancy of the houses, and designed to match statistical data when aggregated.

Keywords. Electrical Consumption, Flexible Load, Load Profiles, Profile Generator

RAPID DESIGN OF ENERGY COMMUNITIES: A HEAT-DRIVEN OPTIMIZATION APPROACH

Natalia Kozlowska[1*], Julien Jacquemin[1], Arthur Lefebvre[2], Pierre Dewallef[1]

[1] Laboratory of Applied Thermodynamics, University of Liège, Belgium.

[2] Catholic University of Louvain.

* *Corresponding Author:* natalia.kozlowska@uliege.be

Abstract. The building sector plays a critical role in achieving the goal of a climate-neutral economy by 2050 and the intermediate target of at least a 55% reduction in greenhouse gas emissions by 2030. One of the primary challenges in this transition is the decarbonization of the heating and cooling sector, with district heating and cooling networks playing a pivotal role in the process. To further accelerate the transition towards a sustainable energy system, energy communities have emerged as a key concept. These networks of interconnected buildings produce, consume, and share renewable energy locally, optimizing resources. The ongoing work focuses on multi-vector energy communities, with a particular emphasis on the heat dimension. The key challenges include the integration of district heating networks within these communities, balancing centralized heat production with decentralized building scale solutions, and accounting for temperature levels. An optimization-based approach is planned to be used to evaluate these interactions, ensuring adherence to thermodynamic principles for both building- and district-level systems. The Renewable Energy Hub Optimizer (REHO), a decision-support tool, is utilized in this work to optimize the design and operation of energy communities. REHO facilitates decision-making by providing insights into investment strategies and operational performance. The tool includes the integration of temperature-level considerations at the building scale, with plans to extend this to the district scale. Additionally, the modelling of the district heating network will incorporate distance-based building connections and accounts for heat losses, providing a more realistic and practical representation of energy flow within the community. Future contributions include the integration and feasibility analysis of geothermal energy within low-temperature district heating networks. This will further enhance the potential for renewable energy integration and provide a pathway for achieving efficient and sustainable heating solutions.

Keywords. Optimization, Energy Communities, District Heating Network.

Carnot

2024

Liège, BE

